MAGMA DYNAMICS OF THE PHONOLITIC DIEGO HERNÁNDEZ FORMATION, TENERIFE, CANARY ISLANDS

By

PAUL HESSEL OLIN

A dissertation submitted in partial fulfillment
of the requirements for the degree of

DOCTOR OF PHILOSOPHY

WASHINGTON STATE UNIVERSITY
School of Earth and Environmental Science

December 2007

To the Faculty of Washington State University:

The members of the Committee appointed to examine the dissertation of PAUL HESSEL OLIN find it satisfactory and recommend that it be accepted.

_____
Chair

_____

_____

ACKNOWLEDGMENTS

There are many people who have contributed scientifically to this research and to whom I owe my thanks. I thank John Wolff for inviting me to participate in the Tenerife project years ago, and when funding was exhausted he kept the research going anyway. John provided me with a Research Assistantship in the Washington State University GeoAnalytical Laboratory for several years, which allowed me to focus on my research. Thanks to other WSU contributors Holly Nichols, Hunter Hickes, and Peter Larson. I thank our international collaborators, Joán Martí, Ras Cas, Campbell Edgar, Adrian Pitarri, and Jill Middleton. Working with these folks was truly a first class experience and together we were able to make a significant impact in the understanding of the geology of Tenerife. Thanks to the WSU GeoAnalytical Laboratory staff, Charles Knaack, Diane Johnson Cornelius, Scott Cornelius, and Rick Conrey for their invaluable help during all these years.

I also thank Mom, Dad, Jane, and Tim for their ceaseless support over my many years as a student through emotional and financial support, and hand-me-down vehicles. Most importantly, I thank my wife, Kristin. Although I originally told her we would be in Pullman two years, she patiently let seven years go by for me to succeed.

MAGMA DYNAMICS OF THE PHONOLITIC DIEGO HERNÁNDEZ FORMATION, TENERIFE, CANARY ISLANDS

Abstract

Paul Hessel Olin, Ph.D.
Washington State University
December 2007
Chair: John A. Wolff

The Diego Hernandez Formation (DHF; 600-196 ka) represents the products of the most recent complete cycle of phonolitic explosive volcanism on Tenerife (Canary Islands, Spain). Two distinct phonolite lineages have persisted, or have been regenerated, throughout the history of the DHF. During any one eruption a single phonolite type dominates, but detailed geochemical investigations show that both magmas did exist simultaneously, for example, in the Fasnia Member.

In this dissertation, Chapter 1 describes laser ablation ICP-MS methods developed to analyze *in situ* trace element contents in pumices and minerals from DHF deposits, data from which are presented in other chapters. Chapter 2 is summary of DHF stratigraphy, geochronology, and physical volcanological interpretation of the DHF that provides context for the geochemistry to follow. Chapter 3 is a detailed study of the geochemistry of the Fasnia Member in which the chemical heterogeneity of whole rocks and glasses are described. Chapters 4 and 5 describe the different clinopyroxene and titanite compositions, respectively, found in the Fasnia and their importance in understanding Fasnia magmatism. Chapter 6 describes geochemical relationships between the DHF chemostratigraphic units and provides an interpretation of magmatic events throughout DHF time relative to the geochemistry.

TABLE OF CONTENTS

Page

APPENDICES

LIST OF FIGURES

Page

LIST OF TABLES

Page

Chapter 1

Laser ablation ICP-MS of minerals and glass from volcanic rocks

Abstract

Laser ablation ICP-MS is becoming a powerful petrologic tool, providing rapid, minimally destructive *in situ* analyses of trace elements (i.e. REE, HFSE, LILE). Washington State University GeoAnalytical Laboratory LA procedure utilizes a ThermoFinnigan Element2® high resolution ICP-MS coupled to a New Wave UP213 Nd:YAG laser. Sample is carried from the laser to the ICP-MS using He gas. Most instrument parameters are robust over a wide range of mineral and glass compositions, and from day to day runs, however some parameters need to be optimized for a given sample (e.g., laser beam parameters), or checked daily (e.g., gas flows). Data reduction is performed offline using MS Excel. All data are exported in counts per second (cps), background corrected and internally normalized using ^{29}Si (or ^{43}Ca) for the target, predetermined using the electron microprobe. Concentrations are calculated on a one- or two-point calibration using standard glasses (BCR, BIR, N610, N612, N614). A remarkable comparison of multiple LA tracks and several ~1 mg dissolution analyses of clinopyroxene (TF_PX4) validate the LA method. Results for minerals and glasses from volcanic rocks demonstrate the utility of LA-ICP-MS for petrologic applications.

Introduction

Laser ablation (LA) ICP-MS is quickly becoming a powerful tool in petrologic studies in all types of rocks. The method allows fine-scale *in situ* elemental and isotopic analysis of rock constituents (i.e., minerals and glass) that is minimally destructive and usually preserves textural information. This chapter outlines the LA-ICP-MS procedure used in the Washington State University (WSU) GeoAnalytical Laboratory for minerals and glasses from volcanic rocks, and may be used as a guideline for future LA-ICP-MS investigations by others.

General procedure

Instrumentation and parameters

In the WSU GeoAnalytical Laboratory, LA-ICP-MS is performed using a ThermoFinnigan Element2® ICP-MS, coupled with a New Wave UP213® Nd:YAG laser. The Element2® is a high resolution mass spectrometer designed for fast multi-element analyses in low, medium or high resolution. In the procedure outlined here, low resolution is used. The UP213® laser is a high performance laser in which the Nd:YAG rod generates 1064 nm radiation. This wavelength is reduced by passing the beam through a series of crystals, generating different harmonic wavelengths, ultimately to 213 nm, the wavelength used for ablation. Delivery of the ablated material from the laser ablation cell to the mass spectrometer is accomplished using a constant flow of helium (He) gas (~1.2 L/min) through the laser ablation cell, merging with the argon gas stream, and ionized in the plasma. This type of sample introduction and plasma generation is usually referred to as "dry plasma."

Operating parameters for the Element2® and UP213® for this method are summarized in Table 1. Many of these parameters remain unchanged for daily operation, or are sample dependent (e.g., beam size and traverse speed, see Samples), but occasional tuning of the Element2® may involve small adjustments to the torch position, sample and auxiliary argon gas flows (both of which are ~1 L/min), and ion lens settings to obtain optimal peak shape and sensitivity. Experience has shown that UP213 may require daily adjustments to fluence (~8-15 J/cm^2), and although the reason is not yet well understood, it is most likely linked to the power supply. These simple tuning steps are recommended if a few days have passed since last operation, and quite necessary if any hardware has been tinkered with (i.e., Element2® cone changes). For the most part however, the laser operates daily with little change to parameters. For sample-specific parameters, see Samples.

Internal normalization

For quantitative results using the LA method, internal normalization is required to correct for the effects of matrix, drift, and most importantly volume (or mass) of ablated material. This means that one needs to know the concentration of at least one element (or element oxide) naturally occurring in both the standard and sample in order to normalize the raw data in counts per second (cps) and calculate elemental concentrations. This is easily accomplished using the electron microprobe to acquire major element data for the sample, often a basic first step to any petrologic investigation. Both Ca and Si (i.e., ^{43}Ca, and ^{29}Si) are good choices for internal normalization, however Si is better for most igneous materials because it is abundant, and usually varies less than Ca. For Si, the 4.67% abundance isotope ^{29}Si is used; for Ca, the 0.135% abundance isotope ^{43}Ca is

Element2®

Torch Position		Gas Flows (L/min)		Power (W)	Lenses (V)		Additional Parameters	
X	3.3	Cool	15.00	1250	Extraction	-2000.0	Ua/Ub (%)	0.6
Y	2.2	Auxilary	1.20		Focus	-975.0	Focus Offset (%)	20
Z	-4.2	Sample	1.00-1.10		X-Deflection	4.30	SEM Voltage (V)	optimized
					Y-Deflection	7.00		
					Shape	120.0		

UP213®

Fluence* (J/cm^2)	Power * (mJ)	Firing Rate (Hz)	Beam Width ** (microns)	Traverse Rate* (microns/s)	Helium Flow Rate (L/min)
8 to 15 * optimized for sample	0.002 to 0.100	20	5 to 30 ** as small as possible	3 to 20	1.2

Table 1.1: Operating parameters for the Element2 and UP213. Some parameters remain unchanged for all samples, while fluence (or power) are optimized for each sample type. Traverse rate and beam parameters are also sample specific (see Samples), with the goal to have the beam size as small as possible for a given range of concentrations. For example, phonolitic glass analyses can be performed using an 8 micron beam while lower element concentrations in pyroxene require at least a 12 micron beam. Minimum useable count rates are on the order of 1000 counts per second.

used. ^{43}Ca has proven to have background interferences, possibly $^{28}Si^{15}N$ + $^{29}Si^{14}N$. ^{29}Si is preferable to ^{43}Ca because ^{29}Si background has been far more consistent over a period of years, and although ^{29}Si is also prone to background interferences (e.g., $^{13}C^{16}O$), they are more predictable and correctable.

Data collection

An Element2® software Method (Table 1.2) is set up to define the protocols of data collection for an ablation analysis (here ~2 minutes each). In this case, each analysis collects data for 32 selected elements, counting on each element peak 50 times, advancing in order of increasing atomic mass, equivalent to one scan. For each analysis this scan is repeated 30 times. Background measurements are taken by scanning 25 seconds prior to target ablation (~4 scans) with the laser firing and shutter closed. Continuing to scan, at 25 seconds the shutter opens and ablation of the target can occur for up to ~95 seconds before scanning ceases (~25 scans).

Offline data reduction

Raw data are generated in the form of counts per second (cps) of an element. The raw cps data are then exported to MS Excel as text and treated offline. The treatment consists of first delineating the two useable portions of the total analysis (Fig. 1.1), the background scans (~4 scans), and scans covering the stable portion of the target ablation signal (up to 22 scans) during which signal intensities form a plateau. Three to four scans between these portions cover the period of sample wash-in and are unusable. The target ablation signal is further scrutinized for consistency in cps and spurious data are removed. A target signal consisting of fewer than 15 scans is used with caution, fewer than 8 scans is discarded. The average

Entry	Locked	Isotope	Accurate Mass	Mass Window	Mass Range	Magnet Mass	Settling Time	Sample Time	Samples Per Peak	Segment Duration	Search Window	Integration Window	Scan Type	Detection Mode	IS Index	IS Name	Internal Standard	Peak Shift
1	No	Si29	28.976	20	28.966 - 28.986	28.976	0.35	0.002	50	0.02	60	80	EScan	Both			yes	0
2	No	Ca43	42.9582	20	42.944 - 42.973	42.958	0.036	0.01	50	0.1	60	80	EScan	Both			yes	1
3	No	Sc45	44.9554	20	44.940 - 44.970	42.958	0.001	0.01	50	0.1	60	80	EScan	Both	2	Ca43		0
4	No	Ti47	46.9512	20	46.936 - 46.967	42.958	0.001	0.002	50	0.02	60	80	EScan	Both	3	Ca43		0
5	No	Rb85	84.9113	20	84.883 - 84.940	84.911	0.078	0.01	50	0.1	60	80	EScan	Both	2	Ca43		1
6	No	Sr88	87.9051	20	87.876 - 87.934	84.911	0.001	0.01	50	0.1	60	80	EScan	Both	2	Ca43		1
7	No	Y89	88.9053	20	88.876 - 88.935	84.911	0.001	0.01	50	0.1	60	80	EScan	Both	2	Ca43		0
8	No	Zr90	89.9042	20	89.874 - 89.934	84.911	0.001	0.01	50	0.1	60	80	EScan	Both	2	Ca43		0
9	No	Nb93	92.9058	20	92.875 - 92.937	84.911	0.001	0.01	50	0.1	60	80	EScan	Both	2	Ca43		0
10	No	Cs133	132.905	20	132.861 - 132.949	132.905	0.07	0.01	50	0.1	60	80	EScan	Both	2	Ca43		0
11	No	Ba138	137.905	20	137.859 - 137.951	132.905	0.001	0.01	50	0.1	60	80	EScan	Both	2	Ca43		1
12	No	La139	138.906	20	138.860 - 138.952	132.905	0.001	0.01	50	0.1	60	80	EScan	Both	2	Ca43		1
13	No	Ce140	139.905	20	139.858 - 139.952	132.905	0.001	0.01	50	0.1	60	80	EScan	Both	2	Ca43		1
14	No	Pr141	140.907	20	140.860 - 140.954	132.905	0.001	0.01	50	0.1	60	80	EScan	Both	2	Ca43		0
15	No	Nd146	145.913	20	145.864 - 145.961	132.905	0.001	0.01	50	0.1	60	80	EScan	Both	2	Ca43		1
16	No	Sm147	146.914	20	146.865 - 146.963	132.905	0.001	0.01	50	0.1	60	80	EScan	Both	2	Ca43		1
17	No	Eu151	150.919	20	150.869 - 150.970	132.905	0.001	0.01	50	0.1	60	80	EScan	Both	2	Ca43		0
18	No	Gd157	156.923	20	156.871 - 156.976	156.923	0.07	0.01	50	0.1	60	80	EScan	Both	2	Ca43		0
19	No	Tb159	158.925	20	158.872 - 158.978	156.923	0.001	0.01	50	0.1	60	80	EScan	Both	2	Ca43		0
20	No	Dy163	162.928	20	162.874 - 162.983	156.923	0.001	0.01	50	0.1	60	80	EScan	Both	2	Ca43		0
21	No	Ho165	164.93	20	164.875 - 164.985	156.923	0.001	0.01	50	0.1	60	80	EScan	Both	2	Ca43		0
22	No	Er166	165.93	20	165.874 - 165.985	156.923	0.001	0.01	50	0.1	60	80	EScan	Both	2	Ca43		1
23	No	Tm169	168.934	20	168.877 - 168.990	156.923	0.001	0.01	50	0.1	60	80	EScan	Both	2	Ca43		0
24	No	Yb172	171.936	20	171.879 - 171.993	156.923	0.001	0.01	50	0.1	60	80	EScan	Both	2	Ca43		1
25	No	Lu175	174.94	20	174.882 - 174.999	156.923	0.001	0.01	50	0.1	60	80	EScan	Both	2	Ca43		0
26	No	Hf178	177.943	20	177.884 - 178.002	156.923	0.001	0.01	50	0.1	60	80	EScan	Both	2	Ca43		0
27	No	Ta181	180.948	20	180.887 - 181.008	180.947	0.07	0.01	50	0.1	60	80	EScan	Both	2	Ca43		0
28	No	Pb206	205.974	20	205.905 - 206.043	180.947	0.001	0.01	50	0.1	60	80	EScan	Both	2	Ca43		1
29	No	Pb207	206.975	20	206.906 - 207.044	180.947	0.001	0.01	50	0.1	60	80	EScan	Both	2	Ca43		0
30	No	Pb208	207.976	20	207.907 - 208.045	180.947	0.001	0.01	50	0.1	60	80	EScan	Both	2	Ca43		1
31	No	Th232	232.038	20	231.960 - 232.115	232.038	0.065	0.01	50	0.1	60	80	EScan	Both	2	Ca43		1
32	No	U238	238.05	20	237.971 - 238.130	232.038	0.001	0.01	50	0.1	60	80	EScan	Both	2	Ca43		1

Table 1.2: These are the Method parameters for analyses presented herein. The table appears as it would in Method Editor software for Element2. Thirty-two elements are collected (31 unknowns + ^{29}Si).

of the background scans is then subtracted from the average of the target ablation signal, and these data are internally normalized using predetermined Si concentration and ^{29}Si cps. The normalized, background-subtracted cps data for the standards are used to construct calibration lines for the elements, from which concentrations can be calculated for samples (from normalized, background-subtracted cps). Data presented herein are based on a single-point or two-point calibration, and because standards for calibration should be appropriate for the trace element contents of the sample of interest, the following standard glasses may be used; BCR, BIR, N610, N612, and N614. Element concentrations based on fewer than 1000 cps should be avoided, or at least used with caution.

Confirmation of Method

To evaluate the accuracy of the laser ablation procedure, dissolution analyses of clinopyroxene fragments from a single large pyroxene (TF_PX4) were compared with results obtained using LA-ICP-MS from within the same crystal. TF_PX4 (50 Wt% SiO_2) was chosen for this experiment because of the low abundances of trace elements, smooth REE patterns, homogeneous major elements, and large sample size (2x1.25x1 cm single crystal). This pyroxene is from an alkali basalt scoria cone on Tenerife that contains very large pyroxene crystals, some >5 cm.

TF_PX4 was first sliced in two, and one portion of the crystal was mounted on a glass slide. Then this mounted crystal was cut leaving it still rather thick (~5mm), and the saw marks were removed from this thick section by a diamond lap wheel. A final 3-4 mm wafer was cut again from this thick section and the saw marks were carefully removed from the wafer. The section was polished for LA-ICP-MS use and the wafer was crushed

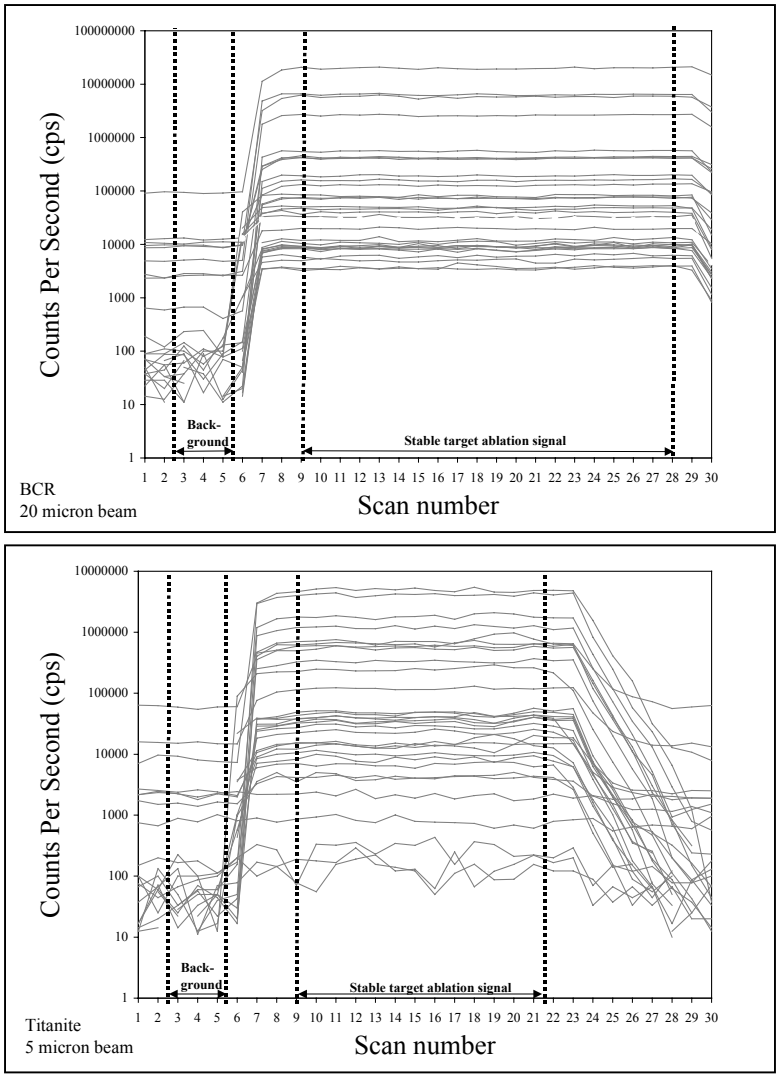

Figure 1.1: These are raw counts per second (cps) data for 32 elements showing the two useable portions of the scan, background and stable target ablation signal. Individual elements are not identified. These scans are for the standard BCR and a titanite sample. Note the poor quality of data <500 cps.

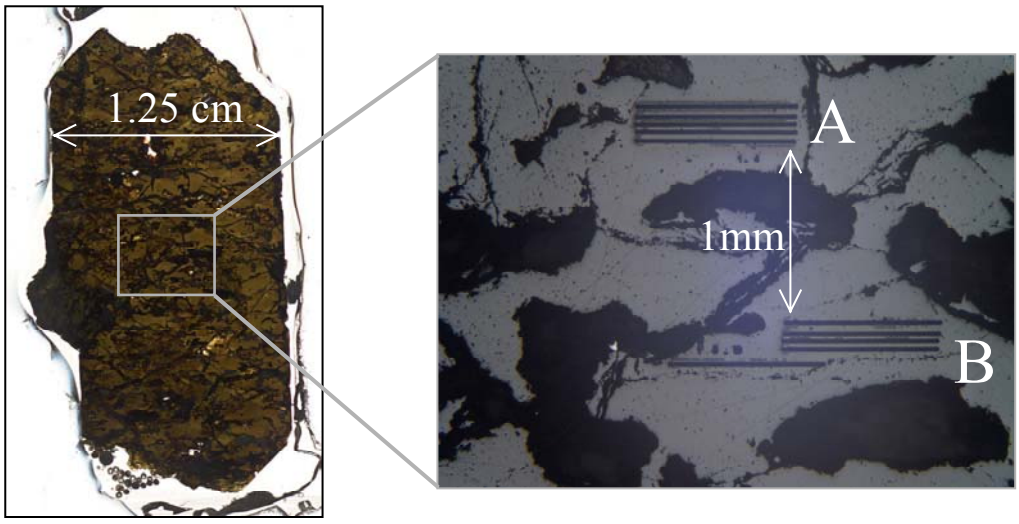

Figure 1.2: This is TF_PX4, a single large clinopyroxene (left). This sample was analyzed using both laser ablation (LA) and dissolution methods (DIS) to verify LA procedure. A & B in the reflected light image (right) refer to the two sites where 5 repeat analyses were performed (10 total laser tracks). Dark patches are epoxy-filled cracks and voids in the crystal.

into crystal fragments for use in dissolutions. All fragments were hand picked and visually scrutinized under a microscope for surface alteration and the presence of mineral and glass inclusions prior to dissolution. Three different size fractions are analyzed (F=fine, M=med, C=coarse) in duplicate (1 & 2), weighing between 0.7 – 1.7 mg. Four fragments are combined in sample F1 and three in F2. M1, M2, C1 and C2 are all single fragments of TF_PX4.

The fragments were dissolved in a two-step digestion process. First, 1 ml pure H_2O, 0.020 ml 37% HCl, 0.020 ml 70% HNO_3, 0.050 ml 50% HF, and 0.020 ml 71% $HClO_4$ were added to each sample vial, capped overnight and held on a hotplate at 130^oC, then uncapped and allowed to evaporated to dryness. Next, 0.5 ml pure H_2O and 0.020 ml 70% $HClO_4$ were added, and again this was evaporated to dryness. The final solutions were brought up in 3 ml 2% HNO_3 with 1 drop 30% H_2O_2, and 0.020 ml 0.5 ppm Rh solution as an internal monitor of the run.

LA-ICP-MS analyses were performed using a 20 micron beam in a linear traverse (a.k.a. a trough or track), not a pit or spot analysis (Fig. 1.2). Traversing is preferred over pits because there is no signal deterioration during the analysis (Fig. 1.1) and there is often better visual control over the sampled area. Pits are necessary where space is minimal, i.e., glass inclusions, but all data presented herein come from traversing the samples' surfaces. Two areas of TF_PX4 ~1 mm apart (A & B) were each analyzed five times (Fig. 1.2).

All analyses for both solutions and LA were performed on the Element2. The general agreement between data from each procedure validates the LA method (Table 1.3 and Figure 1.3). The apparent scatter of the patterns does not appear to be due to error

because the replicates at each of the two sites agree with one another, rather the data show real compositional variability in TF_PX4. The agreement between REE from each method is remarkable, and in fact the relative deviations for many LA REE are less than for dissolutions. Clearly the fragment picking method for the dissolutions did not screen out contaminants as evidenced by high concentrations of several incompatible trace elements in dissolution samples (i.e., La, Ba, Nb, Pb, U, & Th), elements consistent with contamination by glass inclusions. These results suggest that LA may be better than dissolution methods at small sample sizes because this type of contamination is better avoided. Even though the same BCR standard values are used, differences in concentrations obtained from the two methods are attributed to using two different standard materials, i.e., BCR-2g and BCR-P for the LA and dissolution methods, respectively. It should be noted that this experiment approaches the minimum sample size that can be analyzed by solution methods without extraordinary measures (i.e., clean room preparation and isotope dilution).

Precision

Short-term precision of the LA method is determined using 12 repeat analyses of BCR-2g collected over an eight hour period using a 20 micron beam, calibrated on itself at the beginning of the session. Results are given in Table 1.4. Generally, elements with higher concentrations have lower relative deviations. Gd has the worst precision of all elements (>3% relative), followed by the HREE, Ta, and Pb (2-3%). All other elements deviate <2% relative. Ba deviates the least (~1%). It should be noted that concentrations using ^{157}Gd are shown here, but since these data were acquired it has been demonstrated

TF_PX4 Dissolution														
	F1	M1	C1	F2	M2	C2						Ave	StdDev	%RelDev
Method	DIS	DIS	DIS	DIS	DIS	DIS								
Mass (mg)	1.24	0.71	1.71	0.95	0.92	1.55						n=5	n=5	n=5
ppm Rb	0.37	0.33	0.64	0.30	0.34	2.66						0.77	0.14	17.75
Sr	91.0	81.1	88.6	77.1	95.4	86.6						86.63	7.42	8.56
Y	15.3	13.3	13.2	13.0	15.9	13.7						14.07	1.33	9.44
Zr	50.0	45.5	46.3	43.7	52.8	52.7						48.50	3.66	7.55
Nb	1.50	1.08	1.73	0.88	1.39	2.15						1.46	0.34	23.25
Cs	0.01	0.01	0.01	0.01	0.02	0.04						0.02	0.00	21.80
Ba	3.88	4.64	7.28	2.57	5.56	23.3						7.87	1.77	22.51
La	3.72	2.98	3.43	2.75	3.94	7.41						4.04	0.49	12.25
Ce	12.0	10.4	10.9	10.0	12.2	16.9						12.06	0.96	7.94
Pr	2.14	1.84	1.95	1.81	2.23	2.58						2.09	0.18	8.80
Nd	12.1	10.6	10.8	10.5	12.7	12.9						11.60	1.00	8.62
Sm	3.89	3.40	3.32	3.39	4.01	3.57						3.60	0.32	8.91
Eu	1.30	1.14	1.11	1.14	1.34	1.19						1.20	0.11	8.76
Gd	4.32	3.77	3.65	3.76	4.40	3.91						3.97	0.35	8.83
Tb	0.62	0.54	0.53	0.54	0.63	0.56						0.57	0.05	8.73
Dy	3.35	2.93	2.82	2.94	3.44	3.01						3.08	0.28	8.99
Ho	0.57	0.50	0.48	0.50	0.58	0.51						0.52	0.05	9.13
Er	1.36	1.19	1.14	1.20	1.40	1.22						1.25	0.12	9.20
Tm	0.18	0.15	0.15	0.15	0.18	0.16						0.16	0.02	9.40
Yb	0.91	0.79	0.76	0.80	0.94	0.81						0.83	0.08	9.30
Lu	0.13	0.11	0.10	0.11	0.13	0.11						0.12	0.01	10.19
Hf	2.46	2.34	2.07	2.22	2.56	2.32						2.33	0.19	8.33
Ta	0.13	0.09	0.14	0.09	0.13	0.16						0.13	0.02	17.94
Pb	0.57	0.45	0.06	0.29	0.12	0.19						0.28	0.22	77.58
Th	0.14	0.09	0.11	0.09	0.10	0.19						0.12	0.02	17.87
U	0.09	0.06	0.04	0.02	0.07	0.12						0.07	0.02	36.14

TF_PX4 Laser ablation														
	A1	A2	A3	A4	A5	B1	B2	B3	B4	B5		Ave	StdDev	%RelDev
Method	LA	LA	LA	LA	LA	LA	LA	LA	LA	LA				
												n=10	n=10	n=10
ppm Rb	0.02	-	0.03	-	0.02	0.00	0.01	0.00	0.04	0.01		0.01	0.01	101.17
Sr	93.9	95.5	94.4	93.6	90.3	81.9	81.6	84.1	83.6	86.6		88.55	5.57	6.29
Y	13.4	14.4	14.2	14.0	13.9	12.3	12.3	12.7	12.6	13.5		13.32	0.81	6.07
Zr	50.0	54.4	53.4	52.2	51.0	41.2	41.7	44.5	43.0	47.6		47.91	5.00	10.43
Nb	0.39	0.43	0.42	0.38	0.41	0.30	0.31	0.33	0.39	0.34		0.37	0.05	12.76
Cs	0.01	0.00	-	0.00	0.01	0.01	0.01	-	-	0.00		0.00	0.00	103.13
Ba	0.11	0.10	0.12	0.18	0.24	0.08	0.10	0.09	0.88	0.11		0.20	0.24	121.23
La	3.27	3.46	3.37	3.21	3.05	2.61	2.71	2.77	2.85	2.88		3.02	0.30	9.84
Ce	13.5	14.1	13.9	13.3	12.7	10.9	11.0	11.5	11.4	11.9		12.42	1.22	9.82
Pr	2.43	2.55	2.52	2.37	2.33	1.99	1.97	2.10	2.07	2.20		2.25	0.22	9.55
Nd	13.0	14.0	13.2	13.2	12.5	10.8	10.8	11.4	11.1	11.9		12.19	1.14	9.39
Sm	3.90	4.12	4.18	3.91	3.88	3.30	3.45	3.46	3.47	3.81		3.75	0.31	8.17
Eu	1.38	1.39	1.40	1.36	1.34	1.16	1.16	1.24	1.19	1.29		1.29	0.10	7.47
Gd	3.94	4.08	4.13	3.86	4.05	3.39	3.52	3.51	3.55	3.95		3.80	0.28	7.25
Tb	0.59	0.63	0.60	0.60	0.59	0.52	0.52	0.56	0.55	0.58		0.57	0.04	6.36
Dy	3.21	3.32	3.28	3.19	3.18	2.76	2.81	2.91	2.95	3.13		3.07	0.20	6.48
Ho	0.56	0.56	0.56	0.55	0.53	0.49	0.47	0.50	0.50	0.53		0.53	0.03	6.20
Er	1.23	1.33	1.27	1.27	1.28	1.12	1.13	1.14	1.19	1.23		1.22	0.07	5.80
Tm	0.15	0.16	0.17	0.16	0.16	0.15	0.14	0.15	0.14	0.15		0.15	0.01	6.88
Yb	0.81	0.89	0.91	0.81	0.88	0.77	0.80	0.75	0.78	0.80		0.82	0.05	6.46
Lu	0.11	0.12	0.11	0.12	0.11	0.10	0.10	0.11	0.11	0.11		0.11	0.01	5.10
Hf	2.56	2.84	2.70	2.66	2.67	2.13	2.20	2.32	2.32	2.56		2.50	0.24	9.58
Ta	0.08	0.09	0.08	0.08	0.08	0.06	0.06	0.06	0.08	0.07		0.07	0.01	14.53
Pb	0.06	0.06	0.06	0.06	0.04	0.04	0.05	0.06	0.06	0.03		0.05	0.01	19.30
Th	0.04	0.04	0.03	0.04	0.03	0.03	0.03	0.03	0.04	0.03		0.03	0.00	12.08
U	0.01	0.01	0.01	0.01	0.01	0.01	0.00	0.01	0.01	0.01		0.01	0.00	15.67

Table 1.3: Comparison between dissolution (DIS) and laser ablation (LA) trace element analysis. Three size fractions (F=fine, M=med, C=coarse) of TF_PX4 fragments were repeated (1 & 2) in the dissolutions. Laser ablation analyses were repeated five times at two locations (A & B). A single-point BCR calibration was used for both analysis types because it is closer in composition to TF_PX4 than other available standards. C2 is omitted from the statistical calculations due to issues of glass contamination.

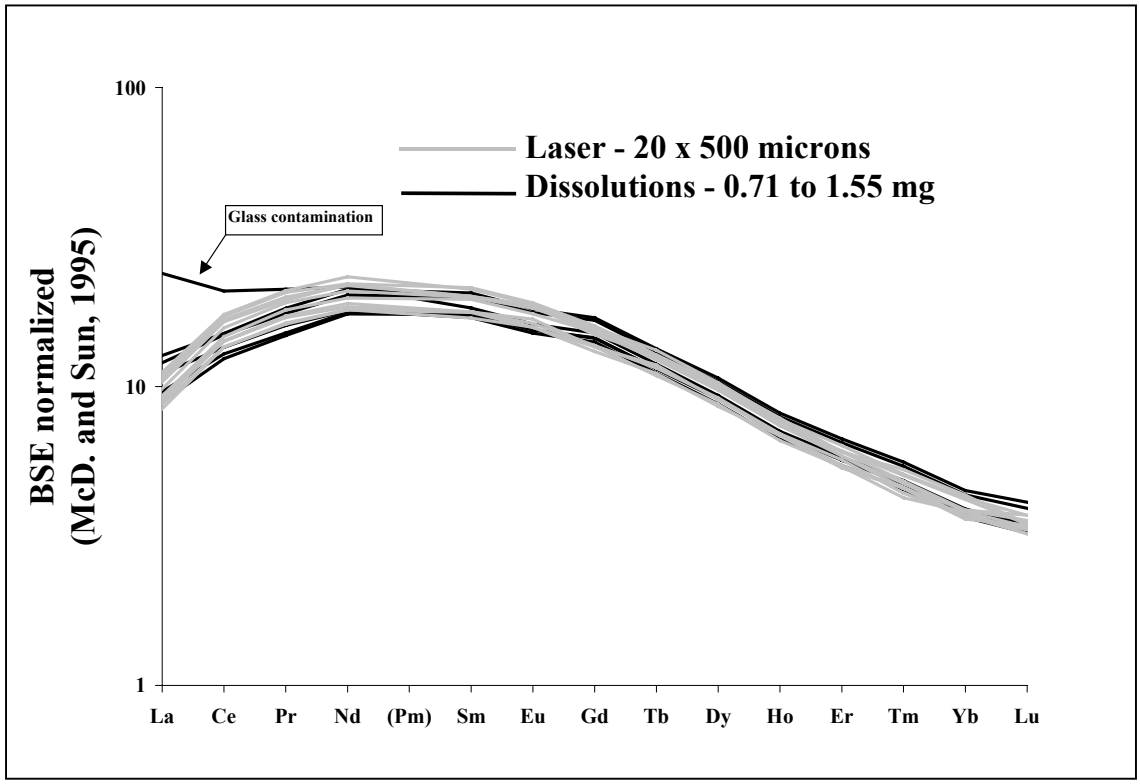

Figure 1.3: REE diagram (normalized to Bulk Silicate Earth (BSE), McDonough and Sun, 1995) for dissolution and laser ablation analyses for TF_PX4. The clear agreement between data from each procedure validates the LA method. High La and Ce in one dissolution sample (C2, the largest fragment) is likely due to glass contamination.

Sample	BCR	BCR-2g	BCR-2g	BCR-2g	BCR-2g	BCR-2g	BCR-2g	BCR-2g	BCR-2g	BCR-2g	BCR-2g	BCR-2g	BCR-2g	Max	Min	Ave	StdDev	%RelDev	%Dev of Ave. from Std. values
	Std. values	1	2	3	4	5	6	7	8	9	10	11	12	n=12	n=12	n=12	n=12	n=12	
ppm Rb	47.2	46.6	47.9	47.0	47.4	47.3	47.9	47.3	47.9	46.8	48.6	47.0	46.4	48.6	46.4	47.3	0.6	1.34	0.28
Sr	346	338	350	343	346	336	343	340	343	335	340	339	337	350	335	341	4	1.31	1.51
Y	37.0	35.8	37.0	36.5	36.8	35.7	36.1	36.2	36.1	35.4	36.0	36.2	35.5	37.0	35.4	36.1	0.5	1.37	2.41
Zr	188	185	186	186	188	182	185	184	185	181	185	184	180	188	180	184	2	1.13	2.04
Nb	14.0	13.8	14.1	14.0	14.0	13.8	13.8	13.8	13.8	13.5	14.0	14.0	13.6	14.1	13.5	13.8	0.2	1.18	1.18
Cs	0.96	0.94	0.99	0.96	0.96	0.95	0.98	0.96	0.98	0.96	1.00	0.97	0.96	1.00	0.94	0.97	0.02	1.82	0.99
Ba	681	673	683	674	680	670	688	673	688	670	683	685	676	688	670	679	7	1.00	0.37
La	24.9	24.5	25.0	24.9	25.0	25.0	25.3	25.0	25.3	24.9	25.7	25.8	25.3	25.8	24.5	25.1	0.4	1.44	0.94
Ce	53.7	52.6	54.9	54.3	54.1	54.0	55.2	54.5	55.2	53.9	55.7	55.7	55.4	55.7	52.6	54.6	0.9	1.67	1.76
Pr	6.80	6.75	6.86	6.81	6.85	6.71	6.84	6.84	6.84	6.70	6.87	6.97	6.76	6.97	6.70	6.82	0.08	1.14	0.24
Nd	28.8	28.9	28.3	28.7	28.9	28.3	28.3	28.9	28.3	27.7	28.4	28.7	28.0	28.9	27.7	28.4	0.4	1.33	1.32
Sm	6.59	6.48	6.57	6.55	6.51	6.43	6.46	6.40	6.46	6.33	6.54	6.41	6.30	6.57	6.30	6.45	0.08	1.29	2.08
Eu	1.95	1.89	1.92	1.93	1.94	1.84	1.87	1.91	1.87	1.86	1.90	1.90	1.86	1.94	1.84	1.89	0.03	1.57	3.02
Gd	6.68	6.58	6.43	6.47	6.55	6.17	6.28	6.29	6.28	6.06	6.18	6.10	5.81	6.58	5.81	6.27	0.22	3.54	6.21
Tb	1.05	1.05	1.04	1.05	1.05	1.00	1.01	1.03	1.01	0.97	1.03	1.05	0.99	1.05	0.97	1.02	0.03	2.59	2.45
Dy	6.34	6.21	6.21	6.26	6.47	6.01	6.37	6.12	6.37	6.02	6.23	6.33	6.15	6.47	6.01	6.23	0.14	2.27	1.75
Ho	1.26	1.23	1.23	1.23	1.28	1.18	1.25	1.25	1.25	1.20	1.22	1.26	1.19	1.28	1.18	1.23	0.03	2.45	2.27
Er	3.63	3.60	3.61	3.57	3.74	3.39	3.48	3.51	3.48	3.38	3.54	3.53	3.42	3.74	3.38	3.52	0.10	2.97	3.02
Tm	0.56	0.55	0.56	0.56	0.56	0.53	0.55	0.56	0.55	0.53	0.54	0.56	0.52	0.56	0.52	0.55	0.01	2.72	2.36
Yb	3.38	3.31	3.37	3.25	3.42	3.27	3.29	3.22	3.29	3.12	3.28	3.32	3.17	3.42	3.12	3.28	0.08	2.50	3.09
Lu	0.51	0.51	0.50	0.51	0.50	0.49	0.49	0.48	0.49	0.48	0.48	0.48	0.48	0.51	0.48	0.49	0.01	2.42	3.65
Hf	4.95	4.84	4.99	4.83	4.91	4.69	4.78	4.72	4.78	4.80	4.80	4.71	4.68	4.99	4.68	4.80	0.09	1.89	3.12
Ta	0.81	0.78	0.79	0.79	0.80	0.77	0.76	0.77	0.76	0.77	0.77	0.78	0.74	0.80	0.74	0.77	0.02	2.07	4.47
Pb	11.0	11.0	11.3	11.0	10.9	10.5	10.5	10.9	10.5	10.6	11.1	10.6	10.6	11.3	10.5	10.8	0.3	2.67	2.00
Th	6.20	6.17	6.15	6.11	6.14	6.06	6.05	6.09	6.05	6.12	6.19	6.10	5.93	6.19	5.93	6.10	0.07	1.14	1.68
U	1.69	1.67	1.67	1.67	1.69	1.64	1.67	1.68	1.67	1.69	1.71	1.65	1.69	1.71	1.64	1.68	0.02	1.11	0.77

Table 1.4: This table shows the precision of the LA method using BCR-2g analyzed 12 times over 8 hours. Gd is the least precise element, and all other elements analyzed here have relative deviations of <3%. Ba deviates the least

that ^{160}Gd may be better under some circumstances, especially when PrO interferes with ^{157}Gd. It is now general practice to collect these two Gd isotopes and use the one that fits more smoothly between neighboring elements (i.e., Eu and Tb).

Accuracy

The data here are insufficient to properly address accuracy. Accuracy could be addressed if more well-characterized standard glasses were available for use as unknowns, but the current paucity of these materials in the lab impedes the formal assessment of accuracy for unknowns. A comparison of the average of BCR unknowns with BCR standard values shows that apart from Gd and Ta, trace element concentrations for the unknowns are within 4% of the accepted values. Ba and Rb deviate the least, <0.4%.

Standards and samples

Sample preparation

The laser ablation cell is designed to accommodate standard 2.5 cm wide petrographic slides or 2.5 cm diameter circular mounts. Standards and samples are mounted and polished to microprobe quality. Typical 30 micron thick thin sections are useable for some targets, however thicker sections are preferable, especially for targets requiring ablation of a relatively large volumes of material. Grain mounts are an option where preservation of textural information is not important. The opening sample chamber has limited clearance that restricts slide mounted samples to <5 mm thickness, but because of the cylindrical opening which allows the passage of transmitted light through the sample block, circular mounts can be thicker.

Standards

Standards used for LA trace element analysis at WSU include basaltic whole rock glasses BCR-2g and BIR, and National Institute of Standards and Technology (NIST) Standard Reference Materials (SRMs) 610, 612 and 614, with the nominal trace element concentrations of 500 ppm, 50 ppm and 1 ppm, respectively (Gladney & Roelandts, 1987; USGS, 1996; Pearce et al., 1997; Horn et al., 1997). Standards are mounted and polished on petrographic slides. Standards and unknowns should be treated in exactly the same the same manner when possible, however experience has shown that different laser beam sizes may be used on a common calibration line since all data are Si normalized. Standard values used for calibration are given in Table 1.5.

Titanite

Titanite in phonolitic volcanic rocks from Tenerife have HFSE, REE and LILE in trace, minor, and in some cases, major element concentrations. In addition, these elements show significant variation with little change in SiO_2. This allows the analysis of most of these elements using laser beam widths as small as 5 microns traversing at speeds of 3 μm/s, in tracks 150-300 microns long or shorter. Currently, the lack of appropriate standards for samples with high "trace" element concentrations is a real problem, however Nb and Zr from the microprobe and from LA compare very well (Fig. 1.4) showing that the results are reasonable. Representative results for titanite are given in Table 1.6.

Clinopyroxene

Clinopyroxenes in volcanic rocks have a wide range in composition. On Tenerife for example, diopside occurs in the most mafic rocks, titanaugite in basalts, salite in

Element	BCR	BIR	N610	N612	N614
SiO2 wt%	55	48	70	72	72
CaO wt%	5.09	13.24	8.42	8.42	8.42
ppm Sc	32.6	44.0	441	41.1	2.00
Ti	13600	9600	434	50.00	3.20
Rb	47.2	0.27	431	31.63	0.82
Sr	346	108	497	76.15	45.5
Y	37.0	16.0	450	38.25	0.79
Zr	188	22.0	440	35.99	0.81
Nb	14.0	2.00	419	38.06	0.85
Cs	0.96	0.45	361	41.64	0.65
Ba	681	7.70	424	37.74	3.29
La	24.9	0.88	457	35.77	0.74
Ce	53.7	2.50	448	38.25	0.79
Pr	6.80	0.50	430	37.16	0.78
Nd	28.8	2.50	431	35.24	0.75
Sm	6.59	1.08	451	36.72	0.77
Eu	1.95	0.54	461	34.44	0.77
Gd	6.68	1.90	420	36.95	0.73
Tb	1.05	0.41	443	35.92	0.77
Dy	6.34	2.40	427	35.97	0.76
Ho	1.26	0.50	449	37.87	0.78
Er	3.63	1.80	426	37.43	0.78
Tm	0.56	0.27	420	37.55	0.77
Yb	3.38	1.70	462	39.95	0.76
Lu	0.51	0.26	435	37.71	0.78
Hf	4.95	0.58	418	34.77	0.75
Ta	0.81	0.06	377	39.77	0.86
Pb	11.0	3.20	413	38.96	2.30
Th	6.20	0.03	451	37.23	0.78
U	1.69	0.01	457	37.15	0.83

Table 1.5: This is a table of standard values used in analysis of minerals and glass discussed herein. BCR and BIR are whole rock basaltic glasses, whereas N610, 612, and 614 are synthetic glasses produced by NIST. Data sources: Gladney & Roelandts, 1987; USGS, 1996; Pearce et al., 1997; Horn et al., 1997.

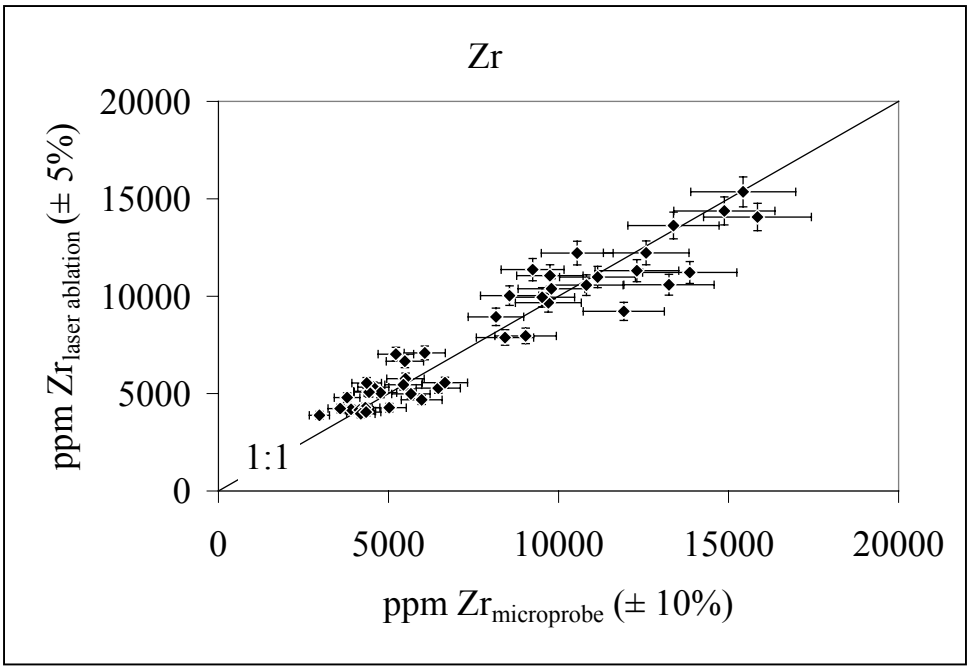

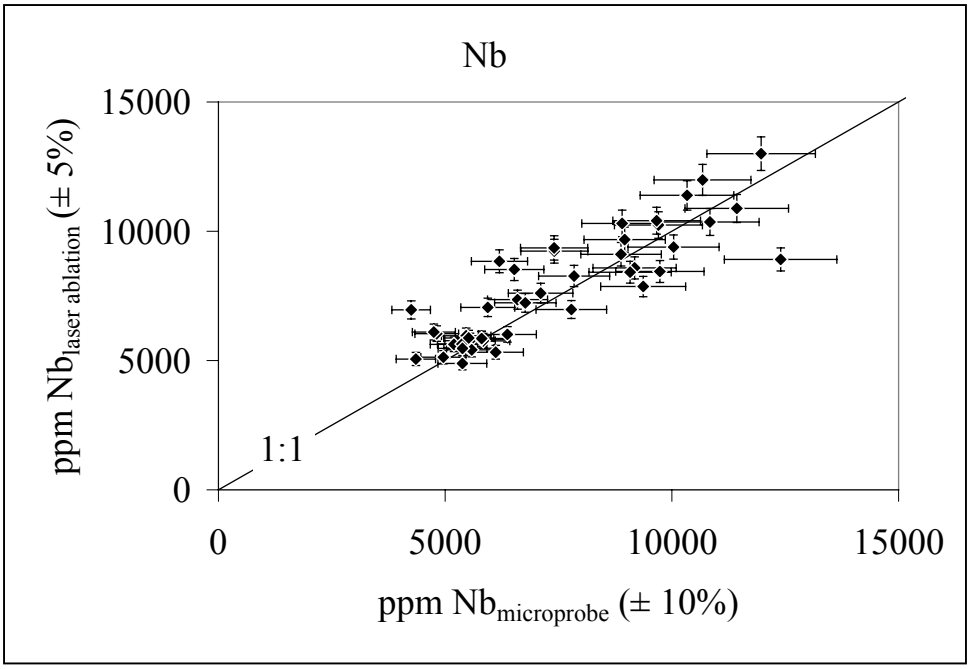

Figure 1.4: Comparison of Zr and Nb concentrations in titanite determined by microprobe and LA showing that there is good agreement between the two methods, although there is some scatter about the 1:1 line.

Sample ID	00TF95	99TF6	99TF6	99TF6	99TF6	99TF6	99TF6	99TF6	99TF6	99TF8D	99TF8D	99TF8D	84-13-1	00-86a
	sph_3C	sphB_sph12	PB_3sph1	sphB_px9	sphA_px2	sphB_px3	sphA_px1	9	10	14	7	5	6	1	1
Sample Type	Titanite	Titanite	Titanite	Clinopyroxene	Clinopyroxene	Clinopyroxene	Clinopyroxene	Feldspar	Feldspar	Feldspar	Phon. Glass	Phon. Glass	Phon. Glass	Rhyo. Glass	Rhyo. Glass
Si %	30	30	29	50	50	50	50	62	65	60	59	59	59	75	75
Ave. Si^{29} cps	532,740	912,326	430,617	12,587,042	11,694,694	12,522,030	11,898,675	51,745,760	47,588,212	44,717,917	2,510,871	2,354,585	1,994,687	2,484,236	3,185,284
ppm Rb	0.00	-	0.15	0.01	0.02	0.05	-	20.34	200.60	4.03	143.96	281.31	271.34	369.85	322.38
Sr	76.12	5.89	6.82	24.06	4.76	3.01	4.38	918.04	26.86	2,001.04	203.08	25.46	52.48	3.95	0.02
Y	2,019.35	771.88	855.52	49.66	26.05	33.71	33.11	0.28	-	1.43	25.47	20.73	28.22	91.36	60.75
Zr	3,886.67	8,940.02	16,188.90	362.80	1,404.84	1,866.45	2,141.50	0.11	0.09	7.51	586.39	1,600.00	2,186.78	259.82	163.70
Nb	5,476.50	8,841.70	10,553.45	2.41	4.38	3.59	8.08	0.05	0.03	2.73	203.14	273.85	283.13	203.25	188.05
Cs	-	0.08	-	-	-	-	0.01	0.00	0.10	0.01	1.09	4.25	4.09	10.49	9.50
Ba	28.85	20.99	20.49	0.57	0.43	0.76	0.47	2,201.03	14.26	1,385.11	804.11	38.30	79.18	13.67	0.39
La	3,082.34	3,051.74	3,151.48	48.92	56.92	104.17	73.45	15.23	1.31	16.49	99.70	101.17	124.66	33.72	27.65
Ce	8,707.50	5,682.65	5,506.92	151.67	112.75	174.79	143.23	17.13	0.68	24.10	187.47	136.60	141.24	70.12	78.71
Pr	1,207.54	545.75	514.23	20.94	10.92	15.89	14.08	0.77	0.01	1.47	16.89	8.65	9.50	7.99	7.01
Nd	5,385.60	1,637.49	1,646.81	85.43	33.65	46.93	43.04	1.51	0.02	3.66	57.07	21.57	26.48	31.45	26.13
Sm	1,042.61	233.57	251.20	16.96	5.03	6.69	6.24	0.08	-	0.39	8.81	3.83	4.11	9.55	7.53
Eu	224.91	40.51	40.41	3.69	0.90	1.14	1.18	1.54	0.12	1.39	2.30	0.53	0.68	0.01	(0.01)
Gd	731.83	187.43	177.24	13.36	4.37	5.67	5.61	0.15	0.00	0.28	6.69	2.67	3.02	9.83	6.19
Tb	105.23	26.20	28.96	1.99	0.67	0.80	0.87	0.00	0.00	0.02	0.95	0.38	0.54	2.15	1.43
Dy	520.89	150.05	159.55	10.97	4.07	5.01	5.28	0.01	0.00	0.09	5.25	2.84	3.44	14.57	9.29
Ho	85.39	29.34	30.73	2.01	0.91	1.09	1.22	0.00	0.00	0.02	1.04	0.72	0.84	3.06	1.95
Er	183.67	76.69	82.04	5.06	3.15	3.90	4.03	0.00	-	0.03	2.64	2.47	2.89	8.63	5.21
Tm	20.63	10.48	10.96	0.70	0.69	0.84	0.86	-	-	0.01	0.37	0.44	0.56	1.36	0.81
Yb	100.68	57.45	63.29	4.68	7.34	8.54	9.18	0.00	-	0.02	2.68	3.85	5.03	10.08	6.02
Lu	10.76	6.36	6.98	0.90	2.12	2.32	2.57	-	0.00	0.01	0.34	0.60	0.74	1.43	0.81
Hf	112.90	232.04	502.05	10.93	35.44	52.51	53.38	0.02	0.00	0.37	10.89	28.41	37.53	12.34	6.96
Ta	709.76	514.77	639.89	0.38	0.41	0.32	0.74	0.06	0.00	0.44	11.63	7.81	7.76	13.50	9.91
Pb	0.48	0.98	1.21	0.32	0.51	0.54	0.50	5.84	7.63	4.77	12.31	31.55	27.41	51.79	29.78
Th	109.89	81.93	90.35	0.12	0.12	1.30	0.22	0.00	0.00	0.49	16.91	50.75	68.19	40.68	28.12
U	8.63	13.64	18.02	0.01	0.02	0.09	0.03	0.00	0.00	0.14	4.68	16.74	18.16	17.27	15.81

Table 1.6: Representative analyses for minerals (titanite, clinopyroxene and feldspar) and glass (phonolitic and rhyolitic) from volcanic rocks. Parameters for each sample type are discussed in the text.

intermediate rocks, and Na-salite in phonolites. Minor and trace element compositions span orders of magnitude. Zr concentrations can be as low as 18 ppm or as high as 20,000 ppm (2 wt%). Concentrations for most elements of interest (i.e., REE) may range over 10s to 100s of ppm with little change in SiO_2. For the most Mg-rich pyroxenes (poor in the trace elements analyzed here), beam widths of 16-20 microns traversing at 8-11 μm/s were used, resulting in track lengths of 300-500 microns. Other more evolved pyroxene compositions with higher trace element concentrations were analyzed using a 12 micron wide beam traversing at ~6 μm/s, resulting in 200-400 micron long tracks. Representative results for clinopyroxene are given in Table 1.6.

Feldspar

Generally, most of the trace elements analyzed here are present at low concentrations in feldspars, except for Sr, Ba, and Rb. Therefore, a larger sampling volume is required for feldspar trace element analyses than for titanite or clinopyroxene. Beam widths 30 microns or larger provide useable results for many of the REE. The 30 micron beam traverses at 18 μm/s, resulting in track lengths ~1 mm. Representative results for feldspar are given in Table 1.6.

Volcanic glass

Volcanic glasses can range in composition from basaltic to phonolitic, or rhyolitic, and it is not uncommon for multiple compositions to occur within individual pumice clasts or lavas. The focus here is the analysis of glass bubble walls within individual pumice clasts. Beam widths of 5-12 microns traversing at 3-8 μm/s were used resulting in troughs of different lengths. Troughs were essentially placed on bubble walls thick enough to accommodate the laser beam and long enough to get enough sampling

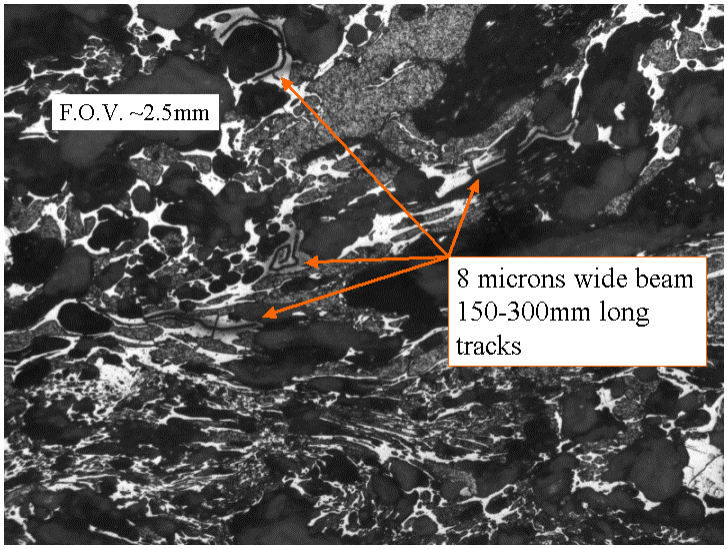

Figure 1.5: Reflected light image of rhyolitic pumiceous glass from the Bandelier Tuff. Arrows indicate several laser tracks, 8 microns wide, 150-300 microns long. Chemical heterogeneities in pumice clasts are often observed at the scale of this image, demonstrating the value of the LA-ICP-MS method in identifying different components.

time (Fig. 1.5). Representative results for pumiceous glass from Tenerife phonolites and from high silica rhyolites in the Bandelier Tuff are given in Table 1.6.

Pitfalls

Several pitfalls may be encountered using LA-ICP-MS. If unchecked these pitfalls may result in spurious data, but if recognized they are also easily overcome. Poorly constrained internal standardization values due to insufficient electron microprobe coverage could cause systematic offsets in calculated concentrations, especially in cases of extreme major element zoning within a sample. This can be addressed by careful petrographic investigation and detailed electron microprobing of the sample. Also, any unseen inclusions in the sample may cause spikes in the data for particular elements which if not removed can give misleading results. These data spikes are often quite obvious and can easily be omitted from averages. Experience has also shown that mismatches between laser beam size and traverse rate can cause erratic or pulsatory signals. A general rule of thumb is to traverse approximately half the beam diameter per second. For example, if the beam is 20 microns wide, a traverse rate of 10-12 microns per second is appropriate.

Concluding remarks

LA-ICP-MS is a robust procedure to analyze for many trace elements of petrologic significance *in situ* in a minimally-destructive manner. The set-up and procedure are reliable, and precision is comparable to, or exceeds small-scale (~1 mg) solution analyses. In the near future, it is likely that this type of data will routinely supplement XRF, ICP and microprobe data in petrologic investigations.

References

Gladney, E.S., Roelandts, I., 1987. 1987 Compilation of Elemental Concentration Data for USGS BIR-1, DNC-1 and W-2. Geostandards Newsletter: The Journal of Geostandards and Geoanalysis 12: 63-118.

Horn, I., Hinton, R.W., Jackson, S.E., Longerich, H.P., 1997. Ultra-trace element analysis of NIST SRM 616 and 614 using laser ablation microprobe-inductively coupled plasma-mass spectrometry (LAM-ICP-MS): A comparison with secondary ion mass spectrometry (SIMS). Geostandards Newsletter: The Journal of Geostandards and Geoanalysis 21:191-203.

McDonough, W.F., Sun, S.-s., 1995. The composition of the Earth. Chem. Geol. 120: 223-253.

Pearce, N.J.G., Perkins, W.T., Westgate, J.A., Gorton, M.P., Jackson, S.E., Neal, C.R., Chenery, S.P., 1997. A compilation of new and published major and trace element data for NIST SRM 610 and NIST SRM 612 glass reference materials. Geostandards Newsletter: The Journal of Geostandards and Geoanalysis 21:115-141.

USGS, 1996. Microbeam Standard Columbia River Basalt (Glass) BCR-2G, United States Geological Survey Special Bulletin (Reference Materials Project). US Geological Survey. Preliminary report, 10pp.

Chapter 2

The late Quaternary Diego Hernandez Formation, Tenerife: A complex cycle of voluminous explosive phonolitic eruptions

Abstract

The Diego Hernandez Formation (DHF; 600-196 ka) represents the products of the most recent complete cycle of phonolitic explosive volcanism on Tenerife (Canary Islands, Spain). Edgar et al. (2007) provide a revised and detailed stratigraphy, new $^{40}Ar/^{39}Ar$ and (U-Th)/He age determinations for major eruptive units, a summary of new chemical data and an overview of the key characteristics of the cycle, including volume estimates, dispersal patterns, eruption styles, phreatomagmatic influences and caldera collapse episodes. The complex stratigraphy of the DHF is divided into 8 named members, each representing a major eruption, as well as numerous named and unnamed minor deposits of limited present-day exposure. The major eruptions are represented by the Fortaleza (370 ka), Roque (347 ka, 3 km^3), Aldea (319 ka, 3 km^3), Fasnia (309 ka, 13 km^3), Poris (268 ka, 3.5 km^3), Arafo (4 km^3), Caleta (223 ka, 3.5 km^3) and Abrigo (between 196 and 171 ka, 20 km^3) members. The Aldea, Fasnia and Poris members consist of highly complex successions of plinian fall, surge and flow deposits and several of the eruptions produced widespread and internally complex ignimbrite sheets. Phreatomagmatism occurred most frequently in the opening phase of the eruptions but also recurred repeatedly throughout many of the sequences. Inferred sources of water include a shallow caldera lake and groundwater, and intermittent phreatomagmatic activity was an important influence on eruption style. Another important factor was conduit and vent instability, which frequently loaded the eruption column with dense

lithic debris and occasionally triggered column collapse and ignimbrite formation. Most of the major DHF eruptions were triggered by injection of mafic magma into existing phonolitic magma bodies. Two phonolitic magma types were available for eruption during the lifetime of the DHF, but each was dominant at different times. The results presented here lend support to the caldera collapse model for the origin of the Las Cañadas Caldera, although the evolution of the caldera is evidently more complex and incremental than first thought.

Introduction

Edgar et al. (2007) present a very detailed description of DHF geochronology, deposits, and volcanology. This chapter is made up of portions of that paper that are most relevant given the focus of this dissertation (the Fasnia Member), such as Tenerife geologic background, DHF stratigraphy and member ages, and an overview of the evolution DHF magmatic system. The author's contribution of geochemical data to this paper, on which he is a coauthor, provided a means to correlate caldera and distal deposits, and in fact, provided the basis for designating the four chemostratigraphic units of the DHF. Deposits descriptions are primarily the work of Edgar (2003), and the geochronology is from Nichols (2001).

Tenerife has a Quaternary history of explosive phonolitic eruptions, the products of which have an aggregate volume on the order of 100 km^3 dense rock equivalent (DRE). Some of these eruptions covered 90% of the island with pyroclastic flow deposits and were accompanied by caldera formation and lateral collapse episodes. The island has a large residential population (655,000), a well-developed rural and civic infrastructure, and has seen an explosive growth in tourism and associated industries over the past few decades. Consequently, a precise understanding of the Quaternary geologic record on Tenerife is a high priority, and a large body of geochronological, volcanological, petrological and geochemical data on the phonolitic pyroclastic rocks has been collected in recent years (Martí et al., 1990, 1994; Ablay et al., 1995, 1998; Bryan et al., 1998, 2002; Huertas et al., 2002; Edgar et al., 2002; Brown et al., 2003; Brown and Branney, 2004; see also the volumes edited by Martí and Mitjavila, 1995, and Martí and Wolff, 2000). Conflicting interpretations remain in two critical areas: the origin of the

central Las Cañadas depression (caldera versus lateral collapse scar; see Ancochea et al., 1990, 1998, 1999; Carracedo, 1994; Martí et al., 1994, 1997; Watts and Masson, 1995; Bryan et al., 1998; Cantagrel et al., 1999), and details of the very complex stratigraphy of the pyroclastic deposits (Bryan et al., 1998, 2002; Edgar et al., 2002; Brown et al., 2003; Brown and Branney, 2004). This chapter is a summary of the event stratigraphy and geochronology of the Diego Hernández Formation (DHF), which represents the last complete major cycle of explosive phonolitic activity on Tenerife.

Geologic background

Tenerife (Fig. 2.1) is the largest of the Canary Islands. The basal subaerial part, the Old Basaltic Series, consists mostly of lavas of at least three mafic alkaline shield volcanoes constructed between 12 and 3.9 Ma (Fuster et al., 1968; Ancochea et al., 1990; Martí et al., 1995, Thirlwall et al., 2000; Guillou et al., 2004), and now exposed as eroded massifs in the extremities of the island. These are overlain by the Las Cañadas edifice (Araña, 1971), a large composite stratovolcano consisting of a dominantly mafic to intermediate Lower Group (3.5 - 2.2 Ma), and an Upper Group (1.6 - 0.19 Ma) that includes the products of three basaltic-to-phonolitic volcanic cycles, represented by the Ucanca, Guajara, and Diego Hernandez formations. In the Las Cañadas caldera wall, the three formations are separated by major erosional disconformities, interpreted as the results of caldera collapse and associated lateral collapse episodes that terminated each cycle (Martí et al., 1994, 1997). Stratigraphically equivalent major disconformities outside the caldera are due to extended periods of non-deposition, when phonolitic eruptions of wide dispersal did not occur following cycle-ending collapse episodes. Basaltic eruptive activity, contemporaneous with growth of the Las Cañadas edifice, was

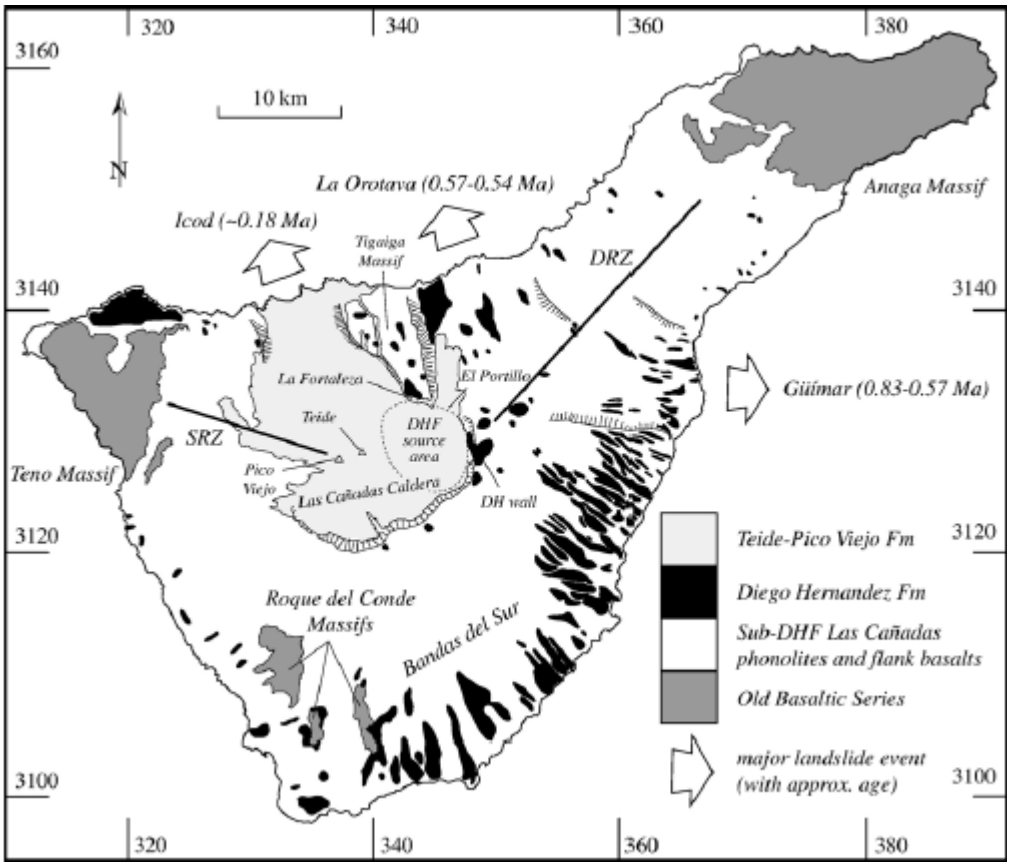

Figure 2.1. Map of Tenerife showing the present-day distribution of the Diego Hernandez Formation (in black) and other major stratigraphic subdivisions. Note: 1) the inferred source area of the DHF in the eastern part of the Las Cañadas caldera complex and its subsequent burial by products of the Teide-Pico Viejo Formation; 2) the location of the two DHF caldera wall sequences: the DH wall to the east and La Fortaleza to the north, which are separated by a gap (El Portillo); 3) the three large valleys bounded by steep scarps produced by major landslides that have punctuated the history of Tenerife; 4) the remnants of the Old Basaltic shield exposed in the three corners of the island; and 5) the two main rift zones along which flank basaltic volcanism has been concentrated (DRZ – Dorsal Rift Zone, SRZ – Santiago Rift Zone). Co-ordinates are U.T.M.

plentiful in both the summit areas and flanks of Tenerife, and has continued into the historic period. The two main zones of basaltic eruptions are the northwestern Santiago Rift Zone and the northeastern Dorsal Rift Zone (DRZ; Fig. 2.1). Within the summit caldera of Las Cañadas are situated the twin stratovolcanoes of Teide (3,718 m) and Pico Viejo (3,103 m), along with numerous satellite vents, all formed since the last caldera collapse at 0.19 Ma (Ridley, 1970, 1971; Mitjavila & Villa, 1993; Ablay et al., 1998). The most recent eruptions of phonolitic magma occurred from this complex at ≤ 2 ka (Ablay et al., 1995; Ablay & Marti, 2000). Similarities between the Teide-Pico Viejo record and the basal portions of earlier cycles (Martí et al., 1994, Ablay et al., 1995, and below) suggest the Holocene phonolitic activity represents the start of a fourth Quaternary explosive cycle with the potential to produce future catastrophic caldera-forming events.

Overview of DHF stratigraphy

The Diego Hernandez Formation (DHF) represents the youngest of the three complete magmatic cycles in the Upper Group. Following Martí et al. (1994), the DHF includes all volcanic units erupted from the Las Cañadas caldera (LCC) that are stratigraphically above the Granadilla Member of the underlying Guajara Formation (Bryan et al., 1998, 2000), up to and including the Abrigo Member (Fig. 2.2). The Granadilla eruption was the terminal caldera-forming event of the Guajara cycle, and has been dated by $^{40}Ar/^{39}Ar$ at 600 ± 18 ka (Brown et al., 2003). In the type section at the easternmost part of the Las Cañadas caldera wall (hereafter referred to as the DH wall, Fig. 2.1), the DHF contains several sedimentary interbeds and minor phonolitic pumice deposits near the base, and interfingers with mafic scoria beds and lava flows of the

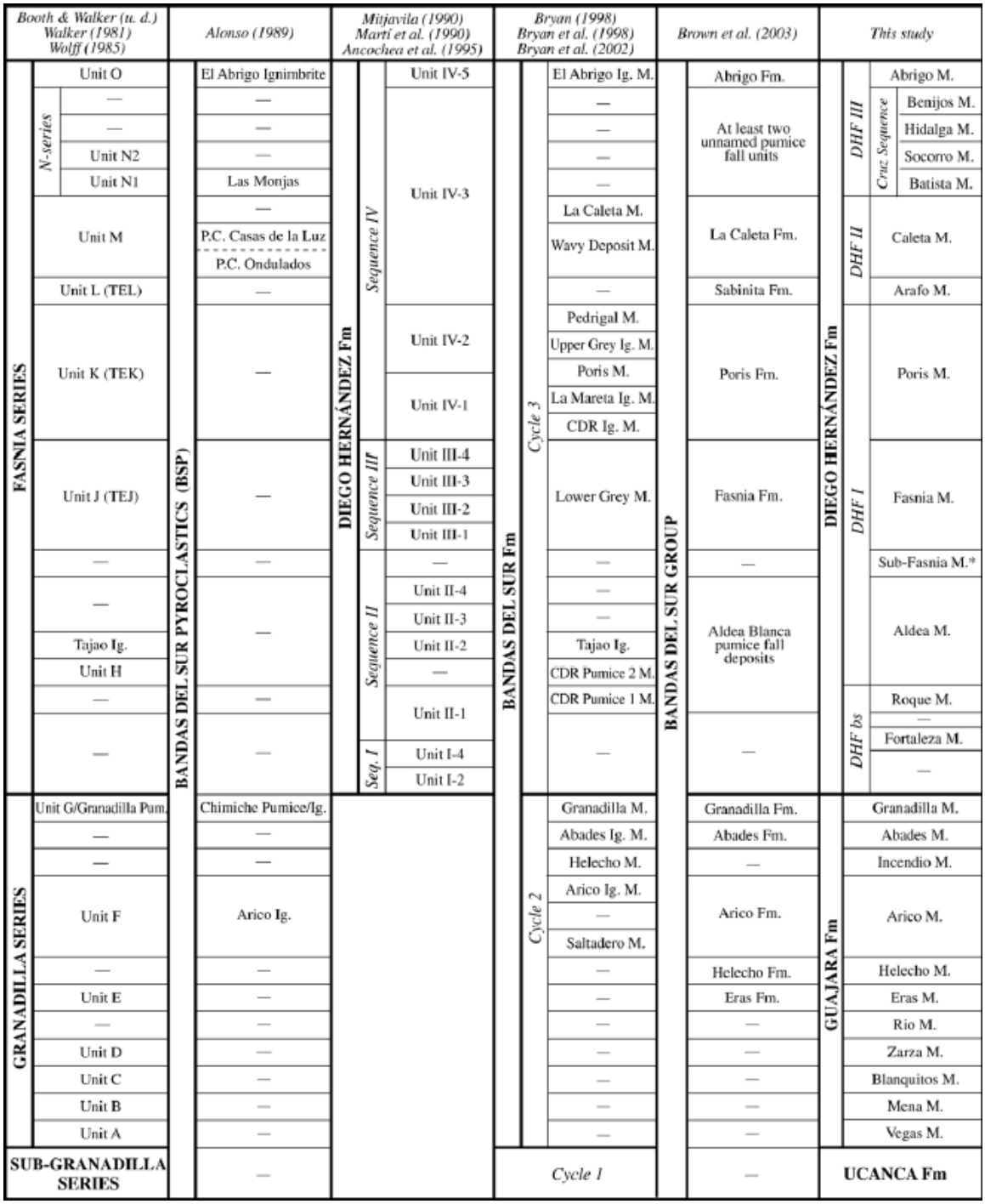

Figure 2.2: Comparison between this study and previous stratigraphic schemes for the phonolitic pyroclastic succession of Tenerife (basaltic units not shown).

* Sub-Fasnia M. includes the Cabezon, Tarasca, Guirres, Espigon, Tosca, Tarta and Taco members, although their stratigraphic relationship to the Aldea and Roque members and to each other is unknown. CDR – Caldera del Rey, Fm. – Formation, Ig. – Ignimbrite, M. – Member, P.C. – Piroclastos de Caida (Sp. pyroclastic fall deposit), Pum. – Pumice. [Guajara Formation stratigraphy from J. Middleton (unpubl. data)]

Dorsal Series, erupted from vents located near the intersection of the Dorsal Ridge with the DH wall. The type section infills the head region of the Orotava valley, a large collapse scar in the north flank of Tenerife (Fig. 2.1). In the southern coastal zone of Tenerife, known as the Bandas del Sur, members of the DHF are typically separated by paleosols, erosion horizons, or, occasionally, coarse fluvial gravels. Wolff et al. (2000) subdivided the principal phonolitic units of the DHF into three chemostratigraphic sequences, DHF I (oldest) to DHF III (youngest). Another subdivision beneath DHF I in the type section has since been identified, the basal sequence (DHFbs), which is dominated by sediments and mafic lavas.

In the stratigraphic scheme used here, a member is defined as a sequence of volcanic deposits that are bounded by palaeosols and an eruption is defined as a sequence of events that produces a member. This usage follows established practice for mapping of volcanic areas, where members are separated by significant time breaks and a formation consists of one or more such related members. Members are given locality-based names and are subdivided into units and subunits on the basis of facies characteristics and inferred mode of deposition. Fall and surge units are labelled alphabetically from base to top and subunits have been labelled alphanumerically. Ignimbrite units have been given locality-based names, although where only one ignimbrite unit has been identified within a member, it is referred to by the member name (e.g. the Caleta ignimbrite).

Geochronology

Prior attempts to date DHF units include the K/Ar studies of Mitjavila (1990), Ancochea et al. (1990, 1995) and Bryan et al. (1998). The K/Ar dates are often

inconsistent with stratigraphy, suggesting that they may be affected by excess argon or the presence of xenocrysts and, in general, the uncertainties associated with them are too large to resolve repose periods between major eruptions. In general, $^{40}Ar/^{39}Ar$ determinations on alkali feldspars are preferred for dating young felsic volcanic rocks. Mitjavila and Villa (1993) provided the first DHF $^{40}Ar/^{39}Ar$ plateau age, on step-heated sanidine phenocrysts from the Abrigo Member, of 183 ± 8 ka (all uncertainties reported or quoted in this paper are 2σ), and Brown et al. (2003) dated the Fasnia, Poris, Caleta and Abrigo Members using $^{40}Ar/^{39}Ar$. New $^{40}Ar/^{39}Ar$ dates for DHF units are reported and discussed in detail below. In addition, titanite separates from the Roque, Fasnia, Poris and Abrigo members were dated using (U-Th)/He.

$^{40}Ar/^{39}Ar$ dating

The most intractable problem in $^{40}Ar/^{39}Ar$ dating of young volcanic rocks arises from xenocrysts that are largely reset and yield ages similar to those of true phenocrysts. Consequently, we employed laser fusion of individual crystals in order to identify and reject xenocrysts. The ages of several crystals from a single sample are then combined to yield a mean age, and are plotted on inverse isochron diagrams (procedures of York, 1969; Wendt and Carl, 1991) to check for the presence of excess argon. Individual samples of a single or a few identical, cleaned pumice clasts were lightly crushed, and inclusion-free alkali feldspars ($Or_{48-15}Ab_{52-70}An_{0-15}$) separated by hand picking. The separates were briefly etched in 5% HF to remove adhering glass, followed by re-picking to select completely clean grains, which were analyzed using a MAP215-50 mass spectrometer at the Nevada Isotope Geochronology Laboratory. Samples and standards (Fish Canyon Tuff sanidine) were irradiated at the Ford Reactor at the University of

Member and unit	Sample number	$^{40}Ar/^{39}Ar$ isochron age (ka)	$^{40}Ar/^{39}Ar$ weighted mean age (ka)	Preferred $^{40}Ar/^{39}Ar$ age (ka)	(U–Th)/He age (ka)
Abrigo, upper flow unit	TF00-153N*	188±12	197±9 [n=8(13)]	196±6	194±16 (n=1)
Abrigo, upper flow unit	TF00-178N	212±19	196±8 [n=9(14)]		
Batista fallout	TF00-9	224±20	234±7 [n=12(13)]	234±7	
Poris, Abona ignimbrite	TF00-17	269±18	285±7 [n=13(14)]	268±8[a]	263±18 (n=4)
Poris, Unit B fallout	TF00-37*	No isochron	268±8 [n=10(12)]		
Fasnia, Santo ignimbrite	TF00-89*	324±9	313±8 [n=10(11)]	309±6	335±27 (n=1)
Fasnia, Subunit F4 fallout	TF99-12	No isochron	305±8 [n=10(11)]		
Aldea, Tajao ignimbrite	TF00-117	No isochron	319±7 [n=11(11)]	319±5	
Aldea, lower plinian	TF00-73	334±5	320±8 [n=9(12)]		
Roque fallout	TF00-71*	351±10	347±8 [n=9(12)]	347±8	324±23 (n=2)

Table 2.1: New isotopic age data for DHF units. For $^{40}Ar/^{39}Ar$ dates, the weighted mean age is generally preferred over the isochron age (see text); [n = x(y)] where x = number of individual crystals used to calculate the weighted mean age, y = total number of crystals analyzed. For members where more than one $^{40}Ar/^{39}Ar$ determination was made, the preferred age is the average of the weighted mean ages, except [a]see text. Asterisks on sample numbers indicate source of titanite grains separated for (U,Th)/He dating. For the Poris Member, titanites separated from TF00-18 and TF00-42 were also used; both samples come from the Quinta ignimbrite unit of the Poris Member (Edgar et al., 2002). All uncertainties are 2σ. Full analytical detials may be obtained by application to the authors.

Michigan. An age of 27.9 Ma was used for the Fish Canyon Tuff sanidine fluence monitor (Steven et al., 1967; Cebula et al., 1986). Irradiated crystals (11 – 14 per sample, 3 – 4 for fluence monitors) were fused using a 20 W CO_2 laser to release Ar. Weighted mean ages are calculated by weighting the inverse of the variance, after rejecting individual crystals that yield ages outside two standard deviations of the mean (Table 2.1).

In general, the weighted mean age is preferred over the isochron age for these samples, due to low radiogenic ^{40}Ar yields and consequent high blank corrections that propogate into the isochron data; this is a common problem when attempting to date individual small crystals from young rocks (Spell et al., 1996, 2001). Nonetheless, valid isochrons that were obtained are within uncertainty of, or very close to, weighted mean ages. Where more than one sample from a unit was used, the preferred age (Table 2.1) is a weighted mean age. All but two of the nine dated samples contained at least one xenocryst, and two samples show evidence for excess argon. A potential problem with weighted mean ages is that xenocrysts only slightly older than the eruption age may be included in, and may skew, the age (Gansecki et al., 1996). Xenocrysts become more abundant upwards in the DHF, indicating that recycling of earlier magmatic components became more significant with time. Results are summarized in Table 2.1. $^{40}Ar/^{39}Ar$ ages from other studies are recalculated based on intercalibrations between fluence monitors (Renne et al., 1998) so that ages are directly comparable to our results where possible.

(U-Th)/He dating

(U-Th)/He dating has not yet been widely applied to young volcanic rocks, but has considerable potential (Min et al., 2006), not least because, in contrast to Ar, He retention

times in minerals at magmatic temperatures are effectively zero and xenocrystic contamination should therefore not be a problem. Titanite has a (U-Th)/He closure temperature of about 200°C (Reiners and Farley, 1999), strongly partitions U and Th from melt, and is ubiquitous among the DHF phonolites.

Titanite separates from pumice clasts were prepared as for feldspars, except that glass was physically removed instead of by etching with HF. This typically left a coating of ~5 – 25 μm of glass adhering to the rims of grains. This is actually desirable because the relatively low-(U, Th) glass acts as a jacket that mitigates α-ejection from the core crystal. Thus, no α-ejection correction was applied. Ten to 20 titanite grains per sample were placed in foil packets and either furnace- or laser-heated to >1200°C to extract He, which was analyzed by ^{3}He isotope dilution, cryogenic purification, and quadrupole mass-spectrometry. Quantitative extraction was checked by multiple heating and analysis steps. U and Th concentrations were determined by ^{229}Th and ^{233}U isotope dilution on a quadrupole ICP-MS**.** Although U, Th, and He analytical precision is ~1-2%, based on replicate analyses of standards and other titanite samples we estimate a 2σ reproducibility of 8% for these titanite He ages (Reiners and Farley, 1999).

Results

The Roque Member, within the DHFbs sequence, yielded a weighted mean ^{40}Ar/^{39}Ar age of 347 ± 8 ka, indistinguishable from the isochron age of 351 ± 10 ka (Table 2.1). Two titanite separates from the same sample yielded an average age of 324 ± 23 ka, within uncertainty of the ^{40}Ar/^{39}Ar date. The weighted mean ^{40}Ar/^{39}Ar age of the Roque Member is taken as the preferred age.

Mitjavila (1990) reported a K/Ar date of 266 ± 34 ka for the Tajao ignimbrite unit of the Aldea Member (his Unit II-2, Fig. 2.2), however this age is probably too young. We obtained $^{40}Ar/^{39}Ar$ weighted mean ages of two samples from the Aldea Member, one from the DH wall and one from the Bandas del Sur, that are indistinguishable. One sample also yielded a statistically valid isochron, just outside of 2σ analytical error of the weighted mean age. The mean of the two weighted mean ages is taken as the preferred age of 319 ± 5 ka (Table 2.1).

Mitjavila (1990) reported a K/Ar date for the Fasnia Member (his unit III-1) of 377 ± 32 ka, inconsistent with his result for the Aldea. We obtained two overlapping $^{40}Ar/^{39}Ar$ ages for the Fasnia Member, for which the preferred age is again taken as the mean of the two weighted mean ages, i.e. 309 ± 6 ka (Table 2.1). A (U-Th)/He age of 335 ± 27 ka from a single titanite separate is within uncertainty of the preferred age. The close similarity in measured ages of the Aldea and Fasnia members is consistent with the generally poor development of the weathering profile separating the two members in the Bandas del Sur. Brown et al. (2003) report a $^{40}Ar/^{39}Ar$ age of 292 ± 12 ka (recalculated) for the Fasnia Member, slightly younger than, but overlapping the 2σ uncertainty of, our results.

Mitjavila (1990, his Unit IV-2, Fig. 2.2) and Bryan et al. (1998) dated the Poris Member by K/Ar at 225 ± 52 ka, and 316 ± 20 ka respectively. We obtained $^{40}Ar/^{39}Ar$ ages from two samples of the Poris Member that are barely consistent (Table 2.1), most likely due to the presence of partly reset xenocrysts with closely similar "ages" to the eruption age. Because the effect of xenocrysts should be to increase the apparent age of a sample, the younger of the two weighted mean ages is preferred here, and the age of the

Poris Member is therefore taken as 268 ± 8 ka (note that the statistically indistinguishable 277 ka average of the two weighted mean ages was reported as the age of the Poris Member by Edgar et al., 2002). Brown et al. (2003) report a $^{40}Ar/^{39}Ar$ age of 276 ± 10 ka age (recalculated) for the Poris Member, indistinguishable from our results. (U-Th)/He ages were determined on five titanite separates from three different Poris pumice samples. One of these fell outside 2σ error and was rejected. The average of the remaining four is 263 ± 18 ka, within error of the preferred $^{40}Ar/^{39}Ar$ age.

The Batista sample yields a $^{40}Ar/^{39}Ar$ weighted mean age of 234 ± 7 ka, indistinguishable from the isochron age of 224 ± 10 ka. Brown et al. (2003) dated the Caleta Member, which underlies the Batista, at 223 ± 10 ka (recalculated), indistinguishable from our result for the Batista Member.

The two Abrigo samples contained the highest proportion of xenocrysts, all "older" than the eruption age, that were rejected from the weighted means (Table 2.1). No accepted crystals yielded an age younger than 180 ka. The two weighted mean ages are indistinguishable and the mean of 196 ± 6 ka is hence taken as the age of the Abrigo Member. This value is within uncertainty of the $^{40}Ar/^{39}Ar$ step-heating plateau age of 183 ± 8 ka reported by Mitjavila and Villa (1993; uncorrected as fluence monitor data was not given). The abundance of xenocrysts suggests that this is likely to be a maximum age. A single (U-Th)/He age is within uncertainty at 194 ± 16 ka. Brown et al. (2003) report a $^{40}Ar/^{39}Ar$ age of 171 ± 2 ka (recalculated) for the Abrigo Member, which is inconsistent with our results.

Discussion

The ages reported here are stratigraphically consistent (Table 2.1), and generally agree with prior $^{40}Ar/^{39}Ar$ results of Mijavila and Villa (1993) and Brown et al. (2003), whereas the earlier K/Ar results are frequently inconsistent and show widely varying results for the same unit. The congruence between our ages and those of Brown et al. (2003) represents a significant step towards a precise, rigorous geochronology for the DHF, although minor discrepancies remain. The agreement of the (U-Th)/He ages with the preferred $^{40}Ar/^{39}Ar$ ages (Table 2.1) is encouraging, and indicates that this technique has great potential for dating Quaternary felsic volcanic suites that contain U,Th-rich phases and where excess ^{40}Ar or feldspar xenocrysts are potential problems.

Significant differences exist between our results and those of Brown et al. (2003) for the Abrigo Member, most likely related to the presence of partly degassed xenocrysts, which may vary in abundance from sample to sample. The Abrigo Member contains a much higher proportion of feldspars with inherited ^{40}Ar than the other dated DHF members (Table 2.1), suggesting that the magma was actively assimilating the Tenerife edifice at the time of eruption. Individual single crystal Abrigo ages obtained in this study overlap those reported by Brown et al. (2003). Pittari et al. (2006), based on all available $^{40}Ar/^{39}Ar$ dates, gave the date of the Abrigo Member as 188 ± 19ka. Because of the potential xenocryst problem, the youngest $^{40}Ar/^{39}Ar$ ages reported for the Abrigo Member are likely more accurate.

Eruption volumes

The lack of an accessible distal record hampers plinian fall deposit volume calculations on oceanic islands. The method of Pyle (1989), which assumes a constant

exponential thinning rate with distance from source, was applied to on-land isopachs of DHF fall deposits. The resulting tephra volume estimates (Table 2.2) are high, e.g. Aldea: 25 km^3, Arafo: 15 km^3, Caleta: 15 km^3 of tephra. It is possible that significant variations in wind direction and strength during the course of some eruptions distorted the geometry of the isopachs to produce an artificially low thinning rate. This effect was minimized where possible by separately treating each fall unit within a member. Pyle's (1989) method tends to underestimate true volumes (Hildreth & Drake, 1992; Fierstein & Nathenson, 1992; Pyle, 1995; Bonadonna et al., 1998, 2002), and the volumes so calculated are regarded as minimum values; consequently maximum fall deposit volumes (Table 2.2) were also found using the approach of Carey et al. (1995).

Maximum volume estimates for ignimbrites were obtained by extrapolation from the volume of preserved onshore deposits. The proportion of ignimbrite deposited offshore was estimated by consideration of dispersal patterns, observed onshore thickness and facies variations, and offshore drillhole data (Schmincke and Sumita, 1998). Possible intracaldera fill was ignored because the subsurface geology of the Las Cañadas Caldera is still poorly understood. The maximum volumes obtained (Table 2.2) are very high and are regarded as order-of-magnitude estimates only. It seems likely, however, that the major DHF eruptions each produced 5-30 km^3 of tephra (1-10 km^3 dense rock equivalent, DRE) and are therefore comparable to other well-studied large plinian eruptions. The total volume of the DHF cycle is estimated to be 70 km^3 of magma (DRE).

In addition to problems noted above, accurate estimation of deposit volumes on Tenerife is undermined by difficulties arising from highly complex PDC deposit geometries, and poor preservation within 10 km of vent, burial and caldera collapse. The

Member	This study				Previous estimates[a]		
	V_{min} (km^3)	V_{max} (km^3)	$V_{DRE(max)}$ (km^3)	$V_{lithics}$ (km^3)	V_{teph} (km^3)	V_{DRE} (km^3)	Source
Abrigo	1.8	–	~20	–	>13	–	a
					1.0	0.4	b
Cruz Sequence[b]	–	~25	~5	–	–	–	–
Benijos[c]	–	~5	~1	–	–	–	–
Hidalga[c]	–	~5	~1	–	–	–	–
Socorro	1.9	4.9	1.0	–	7	1.4[d]	e
Batista	0.8	10.1	2.0	–	0.4	0.13	b
Caleta	1.5	10.1	2.2	–	8	1.6	e
					0.66	0.142	b
Ignimbrite	0.13	0.3	0.2	–	–	–	–
Ash/surge	–	–	–	–	–	–	–
Plinian fall	1.4	9.8	2.0	–	–	–	–
Arafo	3.0	18.6	3.7	–	6	1.2	e
					~10	–	d
Ash/surge	0.05	0.15	0.03	–	–	–	–
Plinian fall	2.9	18.4	3.7	–	–	–	–
Poris	2.7	12.4	3.5	–	4.5	0.9	e
					>5	–	d
Ignimbrite	0.85	5.5	2	–	–	–	–
Ash/surge	0.15	0.2	0.1	–	–	–	–
Plinian fall	1.7	6.7	1.5	–	–	–	–
Fasnia	13.5	62.0	13.3	13.3	24	4.8	e
					~30	–	d
Ignimbrite	1.2	11.2	3.7	4.2	–	–	–
Ash/surge	0.15	0.23	0.08	0.08	–	–	–
Plinian fall	12.2	50.6	9.5	9.0	–	–	–
Aldea	–	~13.5	3.1	–	–	–	–
Ignimbrite	–	<1	0.6	–	0.1	0.05	e
Ash/surge	–	–	–	–	–	–	–
Plinian fall (A)	4.8	12.5	2.5	–	–	–	–
Roque	1.6	13.6	2.7	–	–	–	–
Other sub-Fasnia	–	~30	~10	–	–	–	–
Total DHF	32	210	70	–	–	–	–

Sources: a — Martí et al. (1994)
b — Alonso (1989)
c — B. Booth and G.P.L. Walker (unpubl. data)
d — Walker (1981)
e — Wolff (1985, Tajao ignimbrite only).

[a] Estimates of previous studies, for both tephra and dense rock equivalent (DRE) where available.
[b] Unnamed plinian deposits of the Cruz sequence, based on the assumption of ten members with 2.5 km^3 each.
[c] Estimate based on limited thickness data (no well constrained isopachs).
[d] Quoted simply as "Unit N", which may correspond to either the Socorro Member or the Batista Member or both.

Table 2.2: Summary of volume estimates for the major members of the DHF, with complex members broken down into three deposit types. Refer to text for explanation of minimum and maximum values. The estimates of previous studies are shown for comparison.

current study represents the most complete mapping of individual DHF units undertaken to date, and the volume estimates in Table 2.2 are therefore the most reliable available at the present time. Improved volume estimates will be possible in the future if detailed correlation with offshore ash layers (Schmincke and Sumita, 1998) can be achieved.

Evolution of the DHF eruptions, caldera complex and magma systems

Vent locations and dispersal patterns

The identification of proximal-distal facies variations and the isopach patterns of the major plinian fall deposits indicate DHF source vent locations in the area now occupied by the NE sector of the Las Cañadas Caldera, consistent with the caldera collapse model of Martí et al. (1994) and Martí & Gudmundsson (2000) in which the locus of phonolitic explosive activity migrated to the NE during the Upper Group cycles. Wind directions varied greatly during the DHF period, but the most common dispersal directions were to the east and southeast, and only the western slopes of the island lack preserved fall deposits. Pyroclastic flows were dispersed in all directions and many reached the sea. The extent of offshore dispersal is unknown, but seafloor ashes of similar ages occur widely in this region of the Atlantic (Moreno et al., 2001). PDCs varied widely in size and mobility: the most powerful lithic-rich flows (Ravelo and Abrigo ignimbrites) were dispersed radially and deposited widespread ignimbrite veneer deposits in addition to complex valley-ponded deposits. In contrast, many smaller flows (e.g. Tajao, Antagas, and ignimbrites within the Fasnia Member) were confined to one or two deep barrancos and left behind only valley-ponded deposits, although they are correlated with thin co-ignimbrite ash beds of much greater extent. For more detailed

discussions of the transport and deposition of PDCs on Tenerife, see Edgar et al., 2002; Edgar, 2003;Brown and Branney, 2004a,b; Pitarri, 2004; and Pittari et al., 2005, 2006.

Eruption styles

Despite their predominantly plinian character, the deposits of the DHF display a diversity which reflects a wide range of eruption styles and processes. The major members consist of complex sequences of intercalated fall, surge and ignimbrite units (Fig. 2.3). Even individual plinian fall deposits diverge in many ways from the homogeneous or simple reverse graded pattern which is considered the characteristic product of simple sustained plinian-style outbursts (Walker, 1981; Jurado-Chichay & Walker, 2001). Some ignimbrites (e.g. Tajao, Santo, Bueno) occur above thick, reverse-graded plinian deposits as in the classic model of Sparks et al. (1973) and in these cases column collapse may have been caused by vent widening leading to an insupportable eruption intensity and magma discharge rate. However, the same eruptive sequences contain several intra-plinian ignimbrites and surges, indicating repeated and/or partial column collapse. Intra-plinian ignimbrite formation in the DHF indicates the influence of other, reversible, destabilizing factors, notably phreatomagmatic explosions and vent collapse. The high lithic content of many ignimbrites and ignimbrite facies testifies to the mechanical weakness of the conduit-vent systems.

Welded rocks occur in the Fortaleza Member (welded fallout sequence) and in proximal facies of the Santo ignimbrite (Fasnia Member) but are otherwise absent. The dearth of welded rocks in the DHF is in stark contrast with the extensive welded fall deposits and welded ignimbrites of the Ucanca and Guajara formations. This may partly reflect both the destruction of near-vent welded facies by caldera collapse and an

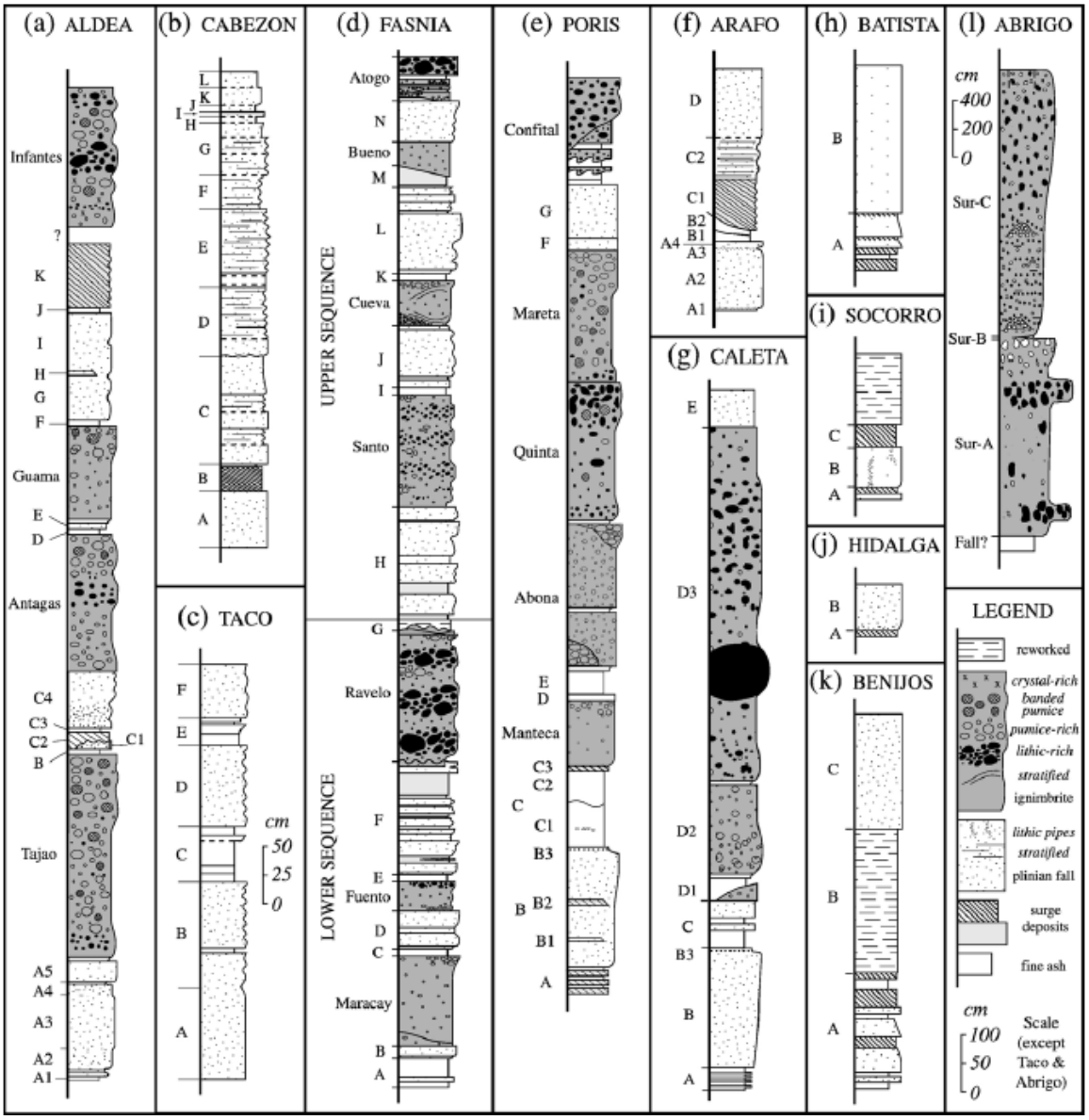

Figure 2.3: Composite stratigraphic sections of major members of the DHF. Note the stratigraphic complexity of many members, particularly the Aldea, Fasnia and Poris members. An approximate scale bar is given in the legend at bottom right but the complex members are not strictly to scale (for example, the thicknesses of many units in the Fasnia section are underrepresented). [Poris section modified from Edgar et al. (2002); Abrigo section modified from Pittari et al., in preparation]

increased role for cooling of the erupting magma by magma-water interaction, since phreatomagmatic deposits are far more abundant in the DHF.

Phreatomagmatism and the role of hydrothermal systems

The influence of external water is apparent among products of all the major eruptions and many of the minor ones. Basal phreatomagmatic fall and/or surge units occur in the Fasnia, Poris, Caleta and Batista members. The basal sequences of the Fasnia and Caleta Members include vegetation-draping wet ashes that fell as mud, indicating high water-ash ratios. They are interpreted to record initial contact between rising magma and open water. Other members (e.g. Fortaleza, Tosca, Aldea, Arafo, Socorro, Hidalga and several other members of the Cruz Sequence) display a weaker phreatomagmatic influence in their basal units or subunits. The persistent recurrence of these features is strong evidence for a long-lived or periodically re-established caldera lake in the DH source area. Phreatomagmatic deposits are also common in the middle and upper parts of many units (Taco, Cabezon, Espigon, Tosca, Aldea, Fasnia, Poris, Arafo, Caleta, Socorro, Benijos), indicating repeated interactions between rising magma and persistent external water.

The Aldea, Fasnia and Poris members are rich in hydrothermally altered lithic fragments and display dramatic upsequence variations in their abundance. The stratigraphic complexity of these members can largely be attributed to conduit and vent instability that may have been enhanced by the long-term action of a subvolcanic hydrothermal system. There is a trend towards increasing simplicity in the internal stratigraphy in the upper half of the formation which might indicate destruction of the hydrothermal system by caldera collapse (see below), resulting in increased stability of

feeder conduits. The Arafo and Caleta members and most Cruz sequence members are relatively lithic-poor, and the dominant phreatomagmatic influence is the continued presence of a shallow, exhaustible caldera lake. However, up to 40% of the lithic clasts within the Abrigo ignimbrite are hydrothermally altered, indicating large-scale excavation of a pre-existing hydrothermal system along with seemingly complete evisceration of the magma chamber.

The Poris and Caleta members both exhibit a return to a strongly phreatomagmatic eruption style after the main dry plinian phase which followed the initial phreatomagmatic activity. In both members, the top of the coarse plinian deposit is mantled by a lithic-rich fall layer interpreted to record vent-wall collapse, followed by accretionary lapilli-bearing fine ash surge deposits which indicate an immediate new influx of water into the vent. The most likely source is a caldera lake that was denied access to the magma during peak magma discharge associated with the dry plinian phase, perhaps by construction of a pyroclastic cone around the vent that was subsequently destroyed by vent-wall collapse recorded as the lithic layer. A similar lithic-rich fall deposit occurs at the top of the Arafo A plinian deposit and is immediately followed by the intra-plinian phreatomagmatic surge (Units B and C), which may indicate the same sequence of events. The strong stratigraphic similarities between these members, therefore, seems to indicate the persistence of a caldera lake, and vent-wall instability, which had a major influence on the course of DHF eruptions.

Caldera evolution

The Las Cañadas Caldera (LCC) has a complex history stretching back more than 1 million years. Its origins have long been controversial (Hausen, 1956; Bravo, 1962;

Fuster et al., 1968; Araña, 1971; Ridley, 1971) and recent debate has seen the elaboration of two competing models. In the lateral collapse model (Ancochea et al., 1990, 1999; Huertas et al., 2002), the caldera rim is interpreted as the head wall produced by one or more north-directed landslides, with vertical caldera collapse playing an insignificant role. The vertical caldera collapse model (Martí et al., 1994, 1997; Martí & Gudmundsson, 2000) identifies the primary mechanism as collapse into a magma chamber associated with large plinian eruptions, with secondary modification of the caldera depression by lateral collapse. The fundamental difficulty is that the structural floor of the caldera is unavailable for inspection due to burial by Teide-Pico Viejo lavas, and the debate has perforce revolved around less direct geologic evidence. The problem is compounded by different stratigraphic schemes for the Las Cañadas edifice and disputes about radiogenic dating and the timing of collapse events.

The results of the present study lend support to the vertical collapse model for the genesis of the caldera. The estimated single eruption volumes of 1-15 km^3 DRE are consistent with caldera collapse associated with several major DHF eruptions (Fasnia, Poris, Arafo, Caleta; Table 2.2) in addition to the Abrigo. The large number of lithic-rich fall deposits and ignimbrites in the DHF indicates a high degree of conduit and vent instability. Lithic population variations in the climactic Abrigo ignimbrite (Pittari, 2004) suggest that radially-dispersed pyroclastic flow pulses were fed from several vents along a ring fissure system. Vent-derived cobble LCZs at different levels in the Abrigo, Fasnia (Ravelo, Santo and Atogo ignimbrites), Poris (Quinta and Confital ignimbrites) and Caleta ignimbrites are inferred to record individual piecemeal caldera collapse events which contributed to the progressive enlargement of the LCC during the DHF period..

The persistence, or recurrence, of a caldera lake of sufficient size to produce the voluminous phreatomagmatic deposits that record high water/ash ratios in the Fasnia, Poris and Caleta members clearly requires the existence of a closed depression(s) in Las Cañadas during DHF I - II time, over a period of some 70 ka. The required topography is more consistent with vertical collapse than with landsliding.

The most recent version of the caldera collapse model (Martí & Gudmundsson, 2000) focused on climactic caldera collapse events terminating each major volcanic cycle of the Upper Group. It is increasingly clear that caldera growth was more complex and incremental than this. The climactic eruption of the DHF (Abrigo Member) still represents the largest caldera collapse event, but at least three collapse events are likely earlier in the cycle (Fasnia, Poris and Caleta). Some indication of multiple caldera subsidence events comes from the scalloped geometry of the current topographic rim of the caldera. Although mass wasting and scarp retreat (e.g. Lipman, 1976, 1997) may have contributed to some of these irregularities, they could also reflect the outlines of smaller-scale collapse structures that contributed to the progressive enlargement of the LCC.

Temporal variations in magma types

Two phonolite magma types persisted, or were repeatedly generated, during the lifetime of the DHF (discussed in detail in Chapter 6). High-Nb/Zr magma, similar to that erupted during earlier explosive phonolitic cycles on Tenerife, produced most of the DHFbs (excepting the Roque Member) and DHF III deposits, but was also available during the intervening 85 ka which was dominated by the low-Nb/Zr magma type (DHF I and II). This type first appeared with eruption of the Espigon pumice early in the DHF

cycle, reappeared in the Roque Member at 347 ka, near the end of DHFbs time, and reached a maximum flux with eruption of the Aldea and Fasnia members at 319 and 309 ka. The Fasnia contains an intermixed component of high-Nb/Zr magma (discussed in detail in subsequent chapters), which is also represented in the 268 ka Poris Member (Edgar et al., 2002). Low-Nb/Zr magma (DHF II) again dominated the period between 268 and 234 ka. The latter finally disappeared with the onset of Cruz sequence activity at 234 ka, culminating in the Abrigo eruption at <196 ka. This pattern of episodes of alternating dominance of two phonolitic magma types, each of varying degrees of evolution, is perhaps difficult to reconcile with continuous co-existence of two distinct magma chambers throughout DHF time, but is consistent with repeated generation and fractionation of magma, or repeated melting of different protoliths, following structural re-arrangement after major eruptions (Fasnia, Poris, Caleta). The occurrence of basaltic magma in 5 of the 7 major members (Aldea, Fasnia, Poris, Caleta, Abrigo) members attests to a crucial role for basalt in mobilizing, and perhaps generating, significant volumes of phonolitic magma through the transfer of heat to shallow levels within the island edifice. This is consistent with the ongoing shield-building basaltic volcanism in both the LCC and the rest of the island during the eruptive activity of the DHF. Following the major structural disturbance associated with the Abrigo event, phonolitic volcanism in Las Cañadas ceased until the last few tens of thousands of years when it began to re-appear during the eruptive activity associated with the growth of the Teide-Pico Viejo stratovolcano complex.

Conclusions

Detailed field mapping and volcanological analysis has produced the most detailed stratigraphy yet of one of the major explosive phonolitic eruptive cycles of the Upper Group of Tenerife, the Diego Hernandez Formation. This is augmented by new $^{40}Ar/^{39}Ar$ and corroborating (U-Th)/He geochronology, combined with critical analysis of previous geochronological work to produce a detailed chronostratigraphy that forms the basis for calculating eruption frequency, and for volcanic hazard prediction. This work has demonstrated that the DHF cycle lasted for about 400 k.y., that phonolitic explosive activity began with relatively minor eruptions, and that the period of major explosive eruptions occupied the last ~150 k.y. of the cycle, with significant repose periods between major eruptions. Most eruptions were complex, involving variations in eruption styles and dispersal processes of erupted products. Variations in eruption styles were caused by variations in eruption conditions, including the presence or absence of a caldera lake and hydrothermal system during each eruption. Two major phonolite magma types were repeatedly erupted during the history of the DHF. The dynamics of the two (single or multiple magma chambers) and life span of each magma type is uncertain. It is clear, however, that recurrent basaltic magmatism has played a major role in phonolite magma generation in this oceanic island shield volcano setting.

References

Ablay, G.J., Martí, J., 2000. Stratigraphy, structure, and volcanic evolution of the Pico Teide-Pico Viejo formation, Tenerife, Canary Islands. J. Volc. Geotherm. Res. 103, 175-208.

Ablay, G.J., Ernst, G.G.J., Martí, J., Sparks, R.S.J., 1995. The ~2 ka subplinian eruption of Montaña Blanca, Tenerife. Bull. Volcanol. 57, 337-355.

Ablay, G.J, Carroll, M.R., Palmer, M.R., Martí, J., Sparks, R.S.J., 1998. Basanite-phonolite lineages of the Teide-Pico Viejo volcanic complex, Tenerife, Canary Islands. J. Petrol. 39, 905-936.

Ancochea, E., Fúster, J.M., Ibarrola, E., Cendrero, A., Coello, J., Hernán, F., Cantagrel, J.M., Jamond, C., 1990. Volcanic evolution of the island of Tenerife (Canary Islands) in the light of new K-Ar data. J. Volcanol. Geotherm. Res. 44, 231-249.

Ancochea, E., Huertas, M.J., Fuster, J.M., Cantagrel, J.M., Coello, J., Ibarrola, E., 1995. Geocronologia de la pared de la caldera de las Canadas (Tenerife, Islas Canarias). Bol. Real Soc. Esp. Hist. Nat. 90, 107-124.

Ancochea, E., Cantagrel., J.M., Fuster, J.M., Huertas, M.J., Arnaud, N.O., 1998. Vertical and lateral collapses on Tenerife (Canary Islands) and other volcanic ocean islands: Comment. Geology 26, 861-862.

Ancochea, E., Huertas, M.J., Cantagrel, J.M., Coello, J., Fúster, J.M., Arnaud, N., Ibarrola, E., 1999. Evolution of the Cañadas edifice and its implications for the origin of the Cañadas Caldera (Tenerife, Canary Islands). J. Volcanol. Geotherm. Res. 88, 177-199.

Araña, V., 1971. Litología y estructura del edificio Cañadas, Tenerife (Islas Canarias). Est. Geol. 27, 95-137.

Bonadonna, C., Ernst, G.G.J., Sparks, R.S.J., 1998. Thickness variations and volume estimates of tephra fall deposits: the importance of particle Reynolds number. J. Volcanol. Geotherm. Res. 81, 173-187.

Bonadonna, C., Mayberry, G.C., Calder, E.S., Sparks, R.S.J., Choux, C., Jackson, P., Lejeune, A.M., Loughlin, S.C., Norton, G.E., Rose, W.I., Ryan, G., Young, S.R., 2002. Tephra fallout in the eruption of Soufrière Hills Volcano, Montserrat. In: Druitt, T.H., Kokelaar, B.P. (Eds.), The Eruption of Soufrière Hills Volcano, Montserrat, from 1995 to 1999. Geol. Soc. Lon. Mem. 21, 483-516.

Bravo, T., 1962. El circo de Cañadas y sus dependencias. Bol. Real Soc. Esp. Hist. Nat. 40, 93-108.

Brown, R.J., Barry, T.L., Branney, M.J., Pringle, M.S., Bryan, S.E., 2003. The Quaternary pyroclastic succession of southern Tenerife, Canary Islands: explosive eruptions, related subsidence and sector collapse. Geol. Mag. 140, 265-288.

Brown, RJ and Branney, MJ, 2004a. Event stratigraphy of a caldera-forming ignimbrite eruption on Tenerife: the 273 ka Poris Formation. Bull. Volcanol. 66, 392-416.

Brown, R.J. and Branney, M.J., 2004b. Bypassing and diachronous deposition from density currents: evidence froma giant regressive bed form in the Poris ignimbrite, Tenerfie, Canary Islands. Geology 32, 445-448.

Bryan, S.E., Martí, J., Cas, R.A.F., 1998. Stratigraphy of the Bandas del Sur Formation: an extracaldera record of Quaternary phonolitic explosive eruptions from the Las Cañadas edifice, Tenerife (Canary Islands). Geol. Mag. 133, 605-636.

Bryan, S.E., Martí, J., Leosson, M., 2002. Petrology and geochemistry of the Bandas del Sur Formation, Las Cañadas Edifice, Tenerife (Canary Islands). J. Petrol. 43, 1815-1856.

Cantagrel, J.M., Arnaud, N.O., Ancochea, E., Fúster, J.M., Huertas, M.J., 1999. Repeated debris avalanches on Tenerife and genesis of Las Cañadas caldera wall (Canary Islands). Geology 27, 739-742.

Carey, S., Gardner, J., Sigurdsson, H., 1995. The intensity and magnitude of Holocene plinian eruptions from Mount St. Helens volcano. J. Volcanol. Geotherm. Res. 66, 185-202.

Carracedo, J.C., 1994. The Canary Islands: an example of structural control on the growth of large oceanic-island volcanoes. J. Volcanol. Geotherm. Res. 60, 225-241.

Cebula, G.T., Kunk, M.J., Mehnert, H.H., Naeser, C.W., Obradovich, J.D., Sutter, J.F., 1986. The Fish Canyon Tuff, a potential standard for the ^{40}Ar-^{39}Ar and fission-track dating methods. Terr. Cogn. 6, 139 (Abstracts of the 6th International Conference on Geochronology, Cosmochronology and Isotope Geology).

Edgar, C.J., 2003. The Stratigraphy and Eruption Dynamics of a Quaternary Phonolitic Plinian Eruption Sequence: The Diego Hernandez Formation, Tenerife, Canary Islands (Spain). Ph.D. Thesis, Monash Univ., Australia, 264 pp.

Edgar, C.J., Wolff, J.A., Nichols, H.J., Cas, R.A.F., Martí, J., 2002. A complex Quaternary ignimbrite-forming phonolitic eruption: the Poris Member of the Diego Hernández Formation (Tenerife, Canary Islands). J. Volcanol. Geotherm. Res. 118, 99-130.

Edgar, C., Wolff, J.A., Olin, P.H., Nichols, H.J., Pitarri, A., Cas, R.A.F, Reiners, P.W., Spell, T.L., Martí, J., 2007. The late Quaternary Diego Hernandez Formation, Tenerife: a cycle of repeated voluminous explosive phonolitic eruptions. J. Volcanol. Geotherm. Res. 160, 59-85.

Fierstein, J., Nathenson, M., 1992. Another look at the calculation of fallout tephra volumes. Bull. Volcanol. 54, 156-167.

Fúster, J.M., Araña, V., Brandle, J.L., Navarro, J.M., Alonso, U., Aparicio, A., 1968. Geology and volcanology of the Canary Islands: Tenerife. Inst. Lucas Mallada, CSIC, Madrid, 218 pp.

Gansecki, C.A., Mahood, G.A., McWilliams, M.O., 1996. $^{40}Ar/^{39}Ar$ geochronology of rhyolites erupted following collapse of the Yellowstone caldera, Yellowstone Plateau volcanic field: implications for crustal contamination. Earth Planet. Sci. Lett. 142, 91-107.

Guillou, H., Carracedo, J.C., Paris, R., Torrado, F.J.P., 2004. Implications for the early shield-stage evolution of Tenerife from K/Ar ages and magnetic stratigraphy. Earth Planet. Sci. Lett. 222, 599-614.

Hausen, H., 1956. Contributions to the geology of Tenerife. Soc. Sci. Fenn. Comm. Phys.-Math. 18, 1-247.

Hildreth, W., Drake, R.E., 1992. Volcano Quizapu, Chilean Andes. Bull. Volcanol. 54, 93-125.

Huertas, M.J., Arnaud, N.O., Ancochea, E., Cantagrel, J.M., Fúster, J.M., 2002. $^{40}Ar/^{39}Ar$ stratigraphy of pyroclastic units from the Cañadas Volcanic Edifice (Tenerife,

Canary Islands) and their bearing on the structural evolution. J. Volcanol. Geotherm. Res. 115, 351-365.

Jurado-Chichay, Z., Walker, G.P.L., 2001. Variability of plinian fall deposits: examples from Okataina Volcanic Centre, New Zealand. J. Volcanol. Geotherm. Res. 111, 239-263.

Lipman, P.W., 1976. Caldera collapse breccias in the western San Juan Mountains, Colorado. Geol. Soc. Am. Bull. 87, 1397-1410.

Lipman, P.W., 1997. Subsidence of ash-flow calderas: relation to caldera size and magma-chamber geometry. Bull. Volcanol. 59, 198-218.

Martí, J., Gudmundsson, A., 2000. The Las Cañadas caldera (Tenerife, Canary Islands): an overlapping collapse caldera generated by magma-chamber migration. J. Volcanol. Geotherm. Res. 103, 161-173.

Martí, J., Mitjavila, J. (eds.), 1995. A field guide to the Central Volcanic Complex of Tenerife (Canary Islands). Serie Casa de Los Volcanes No.4, Cabildo Insular de Lanzarote, Lanzarote.

Martí, J., Wolff, J.A., 2000. Introduction: the geology and geophysics of Tenerife. J. Volcanol. Geotherm. Res. 103, vii-x.

Martí, J., Mitjavila, J., Villa, I.M., 1990. Stratigraphy and K-Ar ages of the Diego Hernández wall and their significance on the Las Cañadas Caldera formation (Tenerife, Canary Islands). Terra Nova 2, 148-153.

Martí, J., Mitjavila, J., Araña, V., 1994. Stratigraphy, structure and geochronology of the Las Cañadas caldera (Tenerife, Canary Islands). Geol. Mag. 131, 715-727.

Martí, J., Mitjavila, J., Araña, V., 1995. The Las Cañadas Edifice and Caldera. In: Martí, J., Mitjavila, J. (Eds.), A field guide to the Central Volcanic Complex of Tenerife (Canary Islands). Serie Casa de Los Volcanes No.4, Cabildo Insular de Lanzarote, Lanzarote, pp. 19-38.

Martí, J., Hurlimann, M., Ablay, G.J., Gudmundsson, A., 1997. Vertical and lateral collapses on Tenerife (Canary Islands) and other volcanic ocean islands. Geology 25, 879-882.

Min, K., Reiners, P.W., Wolff, J.A., Mundil, R., Winters, R.L., 2006. (U-Th)/He dating of volcanic phenocrysts with high-U, Th inclusions, Bandelier Tuff, New Mexico. Chem. Geol. 227, 223-235.

Mitjavila, J.M., 1990. Aplicació de tècniques de geoquimica isotòpica i de geocronologia a l'estudi volcanologic de l'edifici de Diego Hernández i la seva relació amb la Caldera de Las Cañadas (Tenerife). PhD thesis, Univ. of Barcelona (microfilm no.1312), Spain, 258 pp.

Mitjavila, J.M., Villa, I.M., 1993. Temporal evolution of the Diego Hernández Formation (Las Cañadas, Tenerife) and confirmation of the age of the caldera using the $^{40}Ar/^{39}Ar$ method. Rev. Soc. Geol. Esp. 6, 61-65.

Moreno, A., Targarona, J., Henderiks, J., Canals, M., Freudenthal, T., Meggers, H., 2001. Orbital forcing of dust supply to the North Canary Basin over the last 250 kyr. Quat. Sci. Rev. 20, 1327-1339.

Nichols, H.J., 2001. Petrologic and geochemical variation in a caldera-forming ignimbrite: the Abrigo Member, Diego Hernández Formation, Tenerife, Canary Islands (Spain). MSc thesis, Washington State Univ., USA, 126 pp.

Pittari, A., 2004. Eruption Dynamics and Emplacement Processes for the Climactic Abrigo Member, Tenerife, Canary Islands. PhD thesis, Monash Univ., Australia, 327 pp.

Pittari, A., Cas, R.A.F., Marti, J., 2005. The occurrence and origin of prominent massive, pumice-rich ignimbrite lobes within the Late Pleistocene Abrigo Ignimbrite, Tenerife, Canary Islands. J. Volcanol. Geotherm. Res. 139, 271-293.

Pittari, A., Cas, R.A.F., Edgar, C.J., Nichols, H.J., Wolff, J.A., Marti, J., 2006. The influence of palaeotopography on pyroclastic flow processes and facies architecture of a lithic-rich ignimbrite in a high gradient setting: the Abrigo Ignimbrite, Tenerife, Canary Islands. J. Volcanol. Geotherm. Res.

Pyle, D.M., 1989. The thickness, volume and grainsize of tephra fall deposits. Bull. Volcanol. 51, 1-15.

Pyle, D.M., 1995. Assessment of the minimum volume of tephra fall deposits. J. Volcanol. Geotherm. Res. 69, 379-382.

Reiners, P.W., Farley, K.A., 1999. He diffusion and (U-Th)/Pb thermochronometry of titanite. Geochim. Cosmochim. Acta 63, 3845-3859.

Renne, P.R., Swisher, C.C., Deino, A.L., Karner, D.B., Owens, T.L., DePaolo, D.J., 1998. Intercalibration of standards, absolute ages and uncertainties in $^{40}Ar/^{39}Ar$ dating. Chem. Geol. 145, 117-152 (Isotope Geoscience Section).

Ridley, W.I., 1970. The petrology of the Las Cañadas volcanoes, Tenerife, Canary Islands. Contr. Mineral. Petrol. 26, 124-160.

Ridley, W.I., 1971. The origin of some collapse structures in the Canary Islands. Geol. Mag. 108, 477-484.

Schmincke, H.U., Sumita, M., 1998. Volcanic evolution of Gran Canaria reconstructed from apron sediments: synthesis of VICAP project drilling. In: Weaver, P.P.E., Schmincke, H.U., Firth, J.V., Duffield, W. (Eds.), Proceedings of the Ocean Drilling Program, Scientific Results 157, 443-469.

Sparks, R.S.J., Self, S., Walker, G.P.L., 1973. Products of ignimbrite eruptions. Geology 1, 115-118.

Spell, T.L., McDougall, I., Doulgeris, A., 1996. Cerro Toledo Rhyolite, Jemez Volcanic Field, New Mexico: $^{40}Ar/^{39}Ar$ geochronology of the transition between two caldera forming eruptions. Geol. Soc. Am. Bull. 108, 1549-1566.

Spell, T.L., Smith, E.I., Sanford, A., Zanetti, K.A., 2001. Systematics of xenocrystic contamination: preservation of discrete feldspar populations at McCullough Pass Caldera revealed by $^{40}Ar/^{39}Ar$ dating. Earth Planet. Sci. Lett. 5890, 1-13.

Steven, T.A., Mehnert, H.H., Obradovich, J.D., 1967. Age of volcanic activity in the San Juan Mountains, Colorado. US Geol. Surv. Prof. Pap., 575-D, 47-55.

Thirlwall, M.F., Singer, B.S., Marriner, G.F., 2000. $^{39}Ar/^{40}Ar$ ages and geochemistry of the basaltic shield stage of Tenerife, Canary Islands, Spain. J. Volcanol. Geotherm. Res. 103, 247-297.

Walker, G.P.L., 1981. Plinian eruptions and their products. Bull. Volcanol. 44, 223-240.

Watts, A.B., Masson, D.G., 1995. A giant landslide on the north flank of Tenerife, Canary Islands. J. Geophys. Res. 100, 487-498.

Wendt, I., Carl, C., 1991. The statistical distribution of the mean squared weighted deviation. Chem. Geol., 86, 275-285.

Wolff, J.A., Grandy, J.S., Larson, P.B., 2000. Interaction of mantle-derived magma with island crust? Trace element and oxygen isotope data from the Diego Hernandez Formation, Las Cañadas, Tenerife. J. Volcanol. Geotherm. Res. 103, 343-366.

York, D., 1969. Least squares fitting of a straight line with correlated errors. Earth Planet. Sci. Lett., 5, 320-324.

Chapter 3

Scales of chemical heterogeneity in the Diego Hernández Formation: the magmatic complexity of the Fasnia Member as an example

Abstract

The 309 ± 6 ka, 13 km^3 Fasnia Member of the Diego Hernández Formation (DHF), Tenerife, Canary Islands, is the most complex deposit of an explosive phonolitic eruption in the DHF. The Fasnia is complex in many ways: 1) physically, with 21 distinctive units and numerous subunits representing plinian fallout, surge, and ignimbrite deposition, 2) texturally, in the variability of clast textures (e.g., uniform white to mingled pumices), 3) chemically, at least three magmatic end members are identified and variably mixed (i.e., two phonolitic and one mafic-intermediate magma), and 4) chemostratigraphically, the Fasnia shows both systematic and random changes in trace element contents with stratigraphy on a variety of scales. Two end member phonolitic magmas do not share a simple common genesis, rather each represents long-lived or repeatedly generated felsic magmatic lineages seen in other DHF members. All three magmatic end members are chemically heterogeneous prior to the mixing event, and in fact the most chemically and physically homogenous magma is the resulting near-hybrid magma. These features point to a system in which multiple magmas are generated in isolation and mixed shortly before eruption, possibly triggered by a mafic magmatic event, and progressively homogenized. These geochemical details cannot be resolved using traditional whole-rock bulk analyses, rather they are revealed using small-scale laser ablation (mm^3) and electron microprobe analytical methods.

Introduction

The 309 ± 6 ka, 13 km^3 Fasnia Member is in the middle of the DHF I chemostratigraphic unit (Fig. 2.2), bounded by the 0.32 Ma Aldea Member below and the 0.27 Ma Poris Member above (Edgar et al., 2002; Brown et al., 2004a; Edgar et al., 2007). Having both physical volcanological and geochemical complexity, the Fasnia Member is one of the most interesting explosive eruption products in the history of Tenerife. The Fasnia has a dominant plinian dispersal direction of E-SE from its vent area and exposures of Fasnia ignimbrites can be found across the island, attesting to the devastating nature of this event (Fig. 3.1).

The stratigraphy and geochronology of the Diego Hernández Formation (DHF) is outlined in Chapter 2. The petrology and whole-rock geochemistry of the DHF is outlined in Chapter 6. This chapter focuses on the Fasnia Member whole-rock and small-scale (mm^3) laser ablation geochemical data from glasses, revealing greater chemical heterogeneity than is apparent in the whole-rock data. Physical processes responsible for the observed chemical heterogeneity and differences in pumice textures (e.g., banded vs. nonbanded clasts) likely influenced the progress of the eruption that is recorded by the Fasnia deposits. The deposit descriptions are summarized below, followed by a detailed multi-scaled geochemical investigation.

The Fasnia Member

Fasnia deposit descriptions

The relationship of the Fasnia Member to other DHF members and its internal stratigraphy and physical volcanology are outlined by Edgar et al. (2007). However,

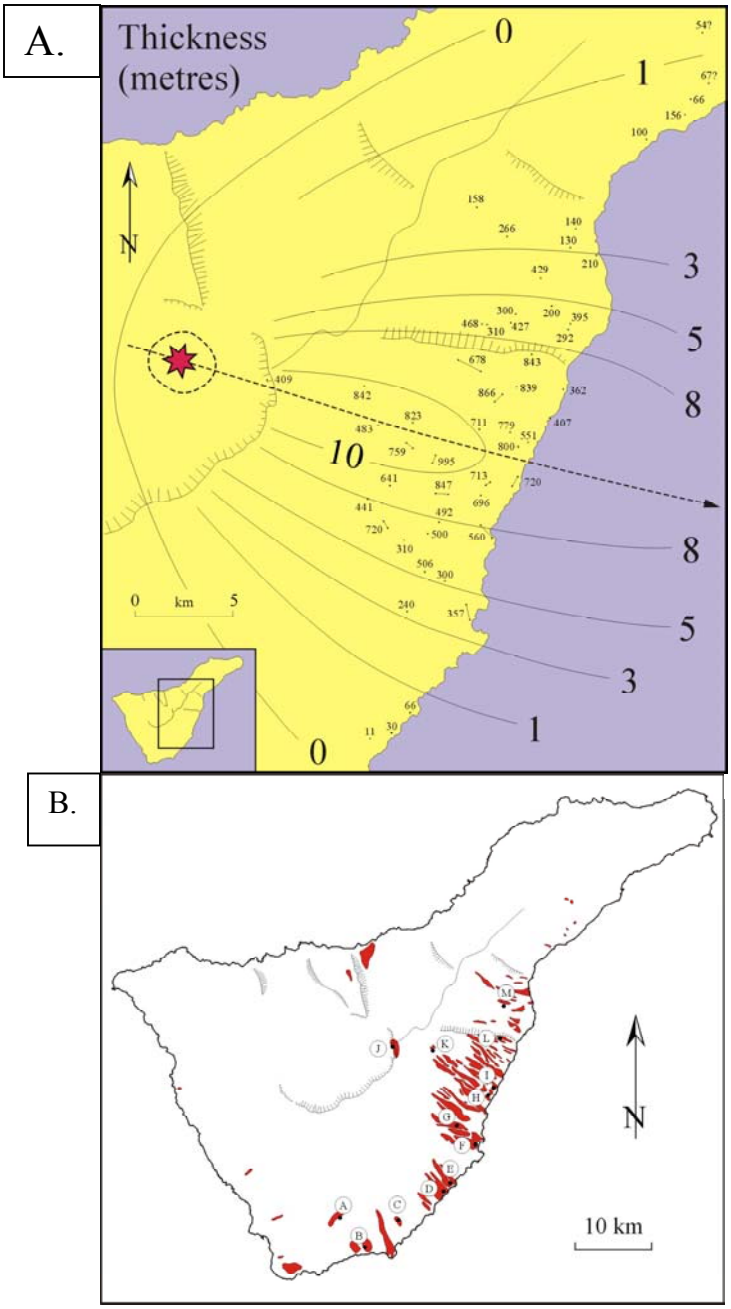

Figure 3.1: A.) Plinian dispersal isopach map showing cumulative thickness (meters) of Fasnia Member plinian fallout deposits. B.) Outcrop locations of the Fasnia Member ignimbrites. The pattern of the ignimbrite deposits reflect ponding in barrancos (ravines). Letters in panel B are sample locations from Edgar (2003). (From Edgar, 2003)

discussion of the chemical variations observed in the Fasnia requires a stratigraphic and physical volcanologic context, so Edgar's (2003) detailed work is summarized here. Full descriptions of the complex structures of the deposits of each unit are omitted. Subunits are mentioned where it is necessary for the later geochemical discussion.

The Fasnia is divided into lower and upper portions based on minor localized reworking and gullying at a distinct stratigraphic interval (Figs. 3.2 and 3.3) interpreted to represent a pause in the eruption. The lowest mapped unit at the base of the lower Fasnia is Unit A, an extensive white ash bed which drapes vegetation, contains accretionary lapilli, and is capped by a thin bed of pumice lapilli. Fasnia initial activity recorded in Unit A was clearly phreatomagmatic (Fig. 3.4), highly explosive, and involved a significant volume of magma. Water was present as a lake, or if no lake existed, a shallow aquifer.

Unit B, conformably overlying Unit A, is a thin, medium-grained white plinian fallout deposit. Unit B records the generation of a high plinian eruption column under fairly dry conditions. The lithic-rich base of Unit B probably represents a vent clearing episode or rapid erosion of vent walls.

Above Unit B is the first pyroclastic flow deposit of the Fasnia, the Maracay ignimbrite and its equivalent widespread co-ignimbrite ash cloud deposit, Unit C. These two units represent an early phase of plinian eruption column collapse. Weak mingling textures between light-medium gray and white phonolite are observed in 10% of the pumice clasts and are interpreted to represent an advanced degree of mixing between magmas.

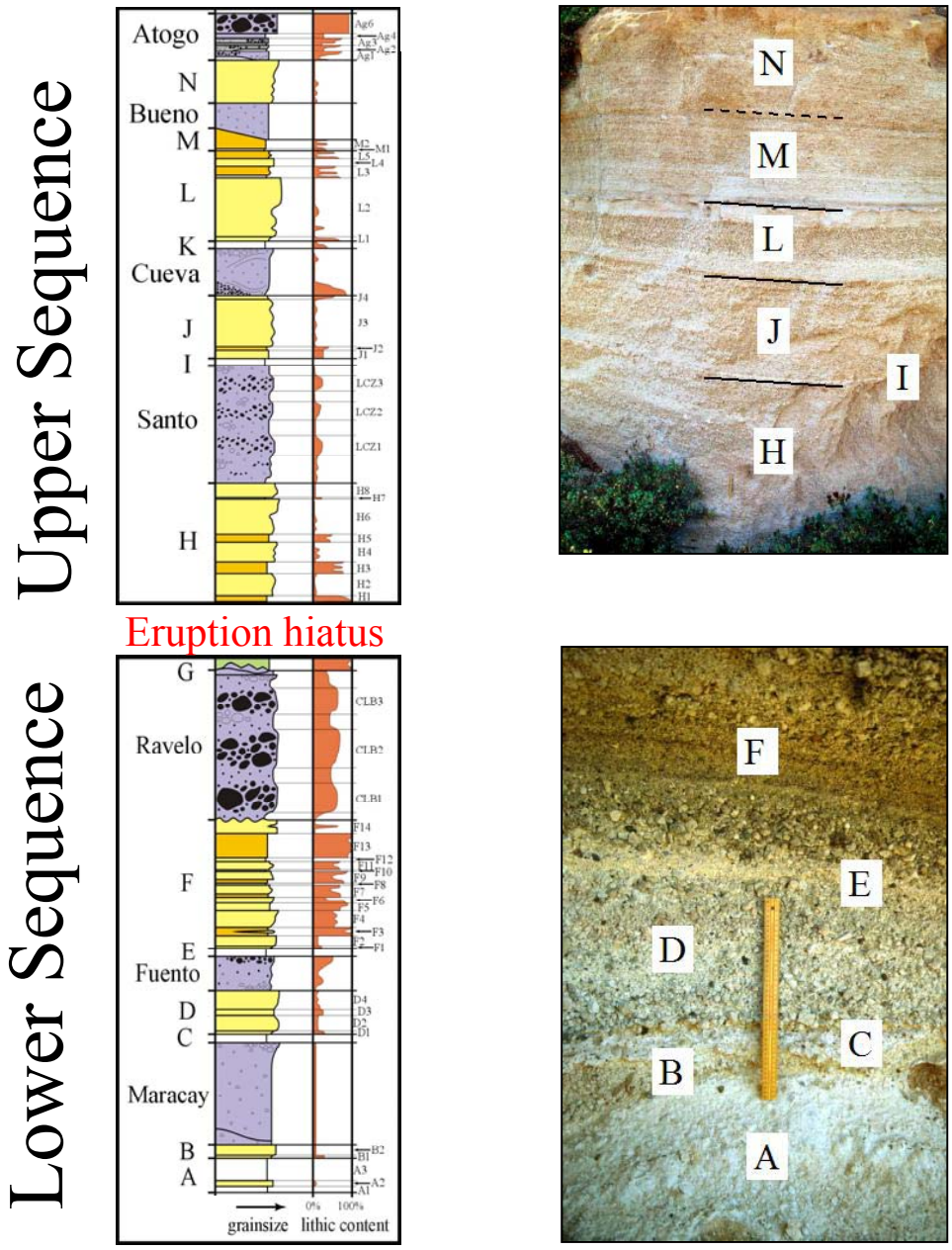

Figure 3.2: Stratigraphy of the Fasnia Member, which is divided into the lower and the upper Fasnia sequences based on an interpreted eruption hiatus (Edgar, 2003). Also shown are two photographs representative of portions of the lower and upper Fasnia. From Edgar (2003). Ash (white), plinian air fall (yellow), surge (orange), pyroclastic flow (gray), reworked sediments (green).

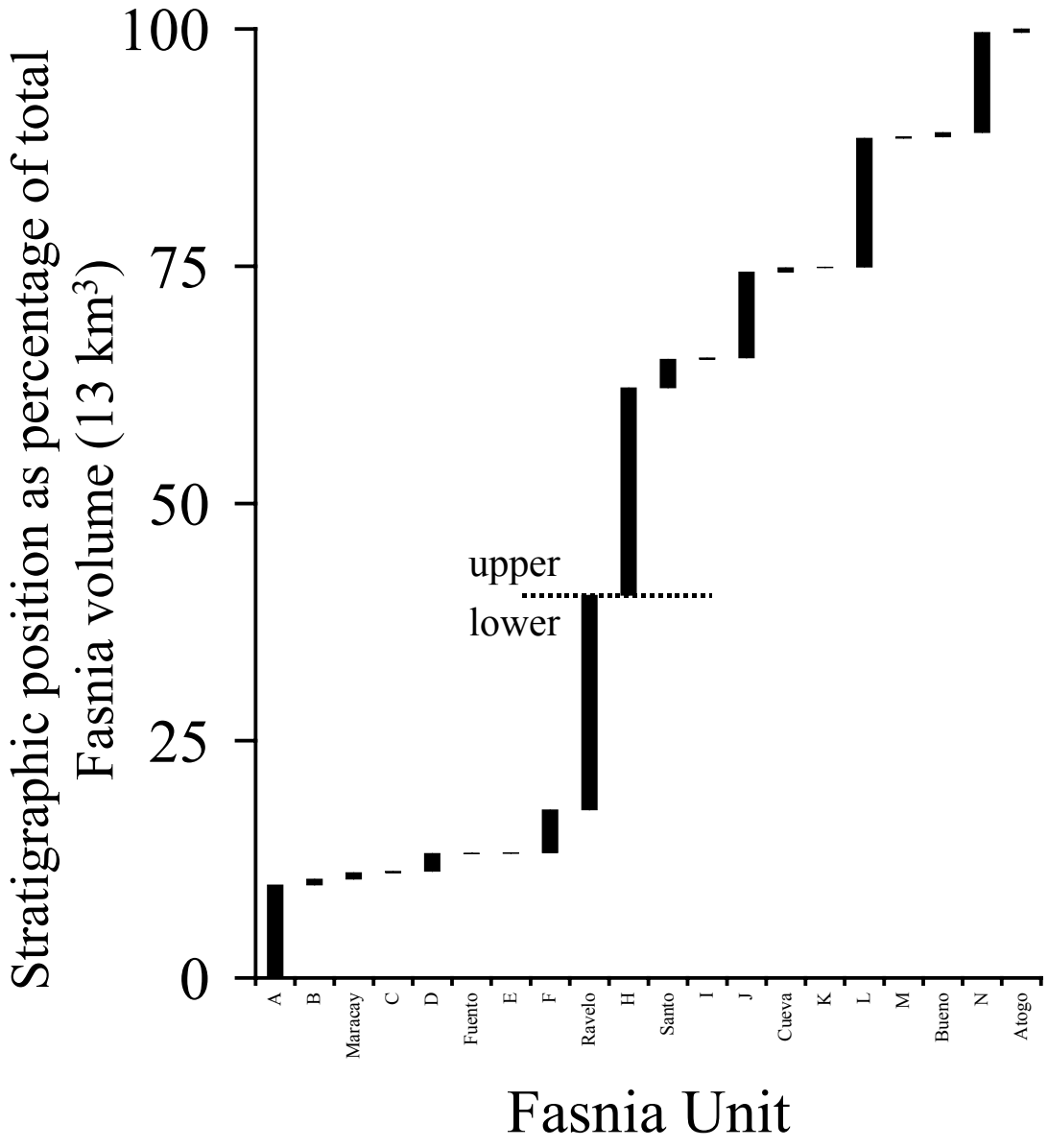

Figure 3.3: Normalized cumulative volume plot showing normalized stratigraphic position for the units as a percentage of the total Fasnia volume. The lower-upper division is indicated between the Ravelo and H units, at ~41%.

Overlying the Maracay ignimbrite and Unit C is Unit D, a plinian deposit, coarser grained and more widely dispersed than Unit B. Unit D represents renewed, or continued fallout from a high eruption column. Stratification and high lithic contents suggest instability at the vent. Banded pumice is prevalent in Unit D, reaching a maximum concentration of ~80% at the top. Mingled pumices have a range of textures, from sharp to diffuse banding of colors from black through to white. Some pumice clasts have highly vesicular, spheroidal "cores," mantled by black to white, less vesicular glass (Fig. 3.5A & B).

Above Unit D, the second pyroclastic flow deposit identified in the Fasnia sequence is the Fuento ignimbrite and its associated co-ignimbrite ash cloud deposit, Unit E. The Fuento ignimbrite is only present in the caldera wall, however the co-ignimbrite ash deposit, Unit E, is widely dispersed similar to Unit C, suggesting that the Fuento pyroclastic flow did indeed breached the caldera. However, the main deposition of the Fuento must have occurred entirely offshore and the wind dispersed the co-ignimbrite ash from the proximal region over a wide area. The Fuento ignimbrite is thought to be a product of minor instability and limited collapse at the eruption column margins.

Conformably overlying Unit E is the thickest fall-dominated deposit in the lower Fasnia, Unit F. At least four interruptions of fallout deposition are interpreted as surge deposits. Stratification in Unit F is very complex, with over 30 areally extensive layers, grouped into 14 subunits (F1-F14). Unit F reflects a series of complicated events occurring at the vent. Elevated lithic contents (consistently above 30%, apart from Subunit F2) and phreatomagmatic indicators, such as accretionary lapilli, throughout the deposit represent large-scale vent-conduit erosion. Maximum measured thickness of Unit F is 2 meters, however this is less than the maximum depositional thickness due to

Figure 3.4: A.) A column-like remnant of plinian beds representing Fasnia Units A-J. B.) Creamy white phreatomagmatic base of the Fasnia draping vegetated older deposits and extending stratigraphically to within Unit H. The gullying in the right of image B represents the Ravelo ignimbrite and subsequent hiatus. C.) A close-up of the Santo ignimbrite showing flame structures between two depositional pulses. D.) A close up the phreatomagmatic base (Unit A, plus Units B through D) of the Fasnia seen draping over vegetation (pocket-knife for scale).

extensive erosion by the overlying Ravelo ignimbrite. Subunits of special interest include F6, a thin fall deposit, and F2 and F14, coarse- and very coarse-grained fall deposits, respectively. Abundant mingled pumice clasts occur in F2, F6 and F14, having similar textural complexity and associated geochemical complexity to those observed in Unit D.

The most complex unit of the Fasnia is the highly erosive Ravelo ignimbrite. The Ravelo may be the most extensive eruptive unit on Tenerife, after the caldera-forming Abrigo ignimbrite (Nichols, 2001; Pitarri, 2004). The Ravelo is found overlying earlier erupted Fasnia units (A-F), or on older substrate, having eroded through all of the earlier erupted Fasnia units. Confident identification of juvenile clasts specific to the Ravelo ignimbrite is impeded due to this extensive and obvious erosion of underlying units. In some distal locations, the Ravelo ignimbrite is the only representative of the Fasnia Member. The sedimentology of the Ravelo ignimbrite is extremely complex, with identification of five deposit types and 22 distinct facies (Edgar, 2003). Clearly, Ravelo deposits represent a catastrophic collapse of the first Fasnia eruption column, and closure of the lower Fasnia eruption.

Atop the Ravelo, and capping the lower Fasnia are localized sediments, Unit G, and an associated paraconformity. Unit G sediments are not widely observed in outcrop, rather an apparently conformable contact exists between the Ravelo and Unit H fall deposits in most locations. Where exposed, Unit G clearly represents a limited hiatus in Fasnia eruptive activity during which surface erosion and resedimentation occurred, seen as gullying and redeposition within gullies that crosscut Lower Sequence deposits. These features may reflect localized heavy rains during the hiatus, resulting in high-energy fluvial events. For several reasons Edgar (2003) suggests this hiatus is on the order of

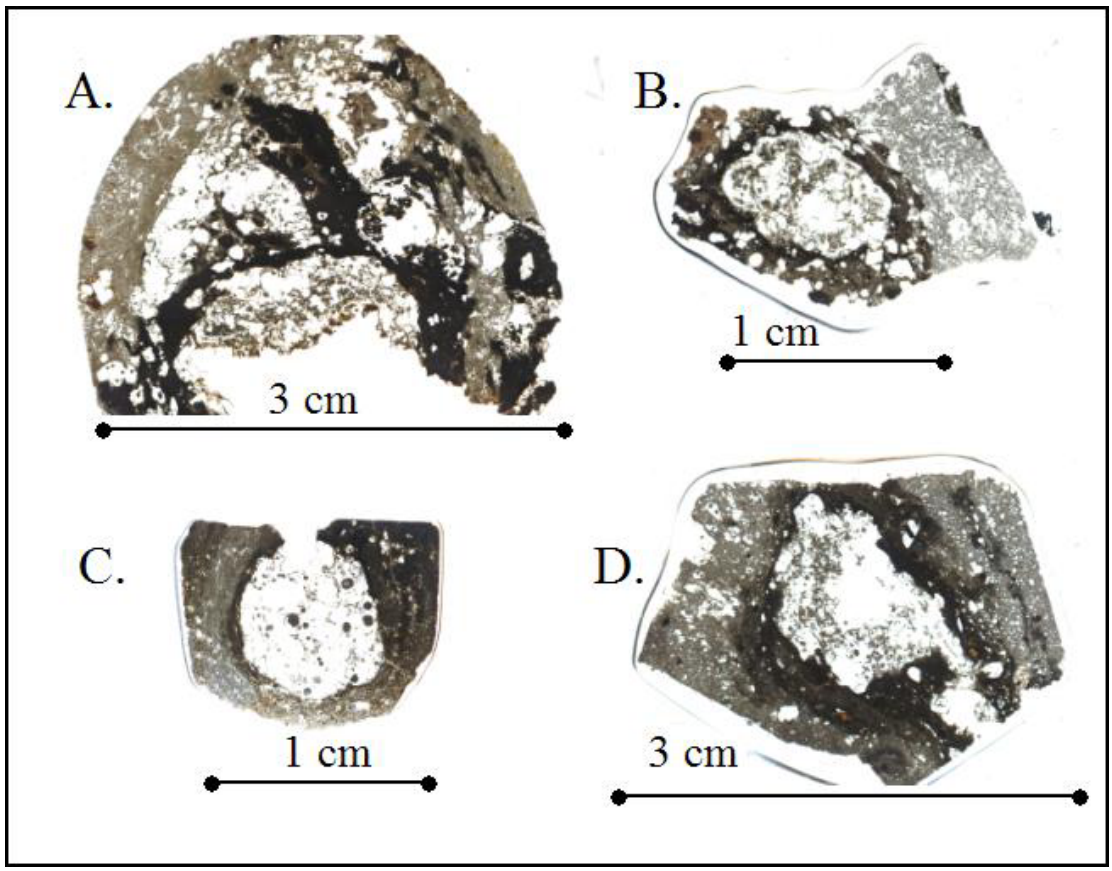

Figure 3.5: Examples of mingled pumices from the lower Fasnia. Pumices A (05TF82a2) is from Unit D and contains finely vesicular glass mantling coarsely vesicular glass and a mafic component. Pumice B (99TF8d) is also from Unit D and contains finely vesicular glass mantling coarsely vesicular glass, but in this case the dark glass interface is actually a mixture between the two phonolitic glasses, not a true mafic component. Pumice C (05TF83b) is from Unit F and has coarsely vesicular glass in the core mantled by finely vesicular glass. Pumice D (01TF122a) is from Unit F and has coarsely vesicular glass in the core mantled by finely vesicular glass. Analysis has shown that the finely vesicular glasses and coarsely vesicular glasses represent two fundamentally different phonolitic magmas.

hours to days; the amount of incision into the Lower Sequence is small, there is no evidence for soil development, angularity of grains and clasts in Unit G indicate localized, short lived transport, and the Ravelo ash, where observed, preserves delicate ripple structures that would have likely degraded within days of exposure to strong, low level winds. This hiatus is not only interesting volcanologically, but it appears to be very important petrologically, because it may represent a period of vigorous mixing within the Fasnia magma chamber.

Overlying Unit G and the extensive paraconformity, the lowest deposit in the upper Fasnia is Unit H. Unit H is the thickest (up to 3.8 m) and most widely dispersed fall-dominated unit in the Fasnia Member, with most of its volume likely deposited offshore. Unit H may be found in contact with the Ravelo ignimbrite or earlier deposits, down to the substrate, where variable erosion by the Ravelo ignimbrite has occurred, but Ravelo deposition did not. Beyond the dispersal areas of the lower Fasnia units, Unit H lies directly on the substrate. Unit H is well stratified and has been divided into eight subunits (H1-H8). Similar to Unit F, a surge component is identified in three subunits (H1, H3 and H5). Unit H signifies the resumption of the Fasnia eruption with prolonged plinian activity. It initiated with an explosive vent-clearing phase, followed by a sustained plinian column with several phases of vent instability. The greatest column heights (>30 km) were attained in Subunit H6, and at distances of 10-12 km from the vent, pumice clasts up to 68 cm long and lithics up to 10 cm diameter are found.

Above Unit H, the Santo ignimbrite is the second largest pyroclastic flow deposit in the Fasnia Member. In the Diego Hernández caldera wall, the Santo has a welded facies, the only example of a welded ignimbrite in the entire DHF. The Santo and

associated Unit I ash cloud deposit represent column instability following the prolonged plinian activity of Unit H. Less internally complex than the Ravelo ignimbrite, the Santo is stratified in its lithic and pumice content. Unit I is noteworthy for the abundance of accretionary lapilli, especially at the top of the deposit, interpreted as late fallout.

Unit J is the next plinian fall unit of the Fasnia Member with a maximum measured thickness of 1.9 meters. Unit J lies conformably on Unit I, and has a more limited dispersal area than Units H and L in the upper Fasnia. The bulk of Unit J is diffusely stratified medium- to coarse-grained plinian fallout. Lithic contents are variable and coarser than other plinian units, with a maximum at the base. Unit J records an episode of vent clearing following the Santo pyroclastic flow, fluctuating column height and eruption intensity, which ended with an influx of fine lithics.

Unit J is overlain by the Cueva ignimbrite and associated ash cloud, Unit K, representing another pyroclastic flow event due to the collapse of the Fasnia eruption column. The Cueva collapse may have been triggered by an influx of lithic debris into the vent, initiated late in the Unit J plinian event, and observed in the basal Cueva ignimbrite. Unit K is overlain conformably by Unit L.

Unit L is the third plinian fall unit in the Upper Sequence (up to 2.6 m), similar in complexity to Unit H. Distinctive layers in Unit L are defined by abrupt changes in grain size, lithic content and sorting, allowing five areally significant subunits to be identified (L1-L5). Subunit L2 is the thickest part of Unit L (up to 1.5 m), and its upper portion is extremely coarse and well sorted, a texture that is unmatched in other Fasnia units. Geochemically, Subunit L2 shows an equally dramatic shift in composition to a distinct near-end member phonolite composition, discussed in detail later. Unit L represents

relatively stable eruption column conditions between the Cueva and Bueno pyroclastic flow events. The eruption column that produced subunit L2 reached exceptional heights (>30 km) and high eruption intensity due to explosive volatile exsolution in dry vent conditions, rather than phreatomagmatic activity.

Unit M conformably overlies Unit L in scattered locations, and in a coastal ignimbrite-dominated sequence it is found between Unit K or Cueva ignimbrite and underlying the Bueno or Atogo ignimbrites. Unit M is a fairly thick, widely dispersed, well sorted, but poorly preserved coarse surge deposit. In some locations Unit M is well stratified, containing planar layering, either substrate- or Unit L-parallel. In other locations stratified and cross-stratified divisions exist. Unit M has gradational contacts with the overlying Bueno ignimbrite or plinian Unit N, making these contacts difficult to identify in the field. An abundance of field evidence further suggests that Unit M and Bueno ignimbrite are the result of a single event.

The Bueno ignimbrite lies conformably on Unit M or Unit L, and conformably under Unit N. At one location, it rests unconformably on Unit H as a result of pronounced pyroclastic flow erosion by the bypassing Santo and/or Cueva ignimbrites. The Bueno ignimbrite is thin but widely dispersed, and remarkably uniform in composition and outcrop appearance. A co-ignimbrite ash cloud deposit, Subunit M3, lies between the Bueno ignimbrite and Unit N.

The uppermost plinian fall deposit of the Fasnia Member is Unit N. Originally quite thick (maximum measured thickness of 1.8 m, 10 km from vent), Unit N is only preserved in eight scattered outcrops, having been extensively eroded in its high, vulnerable stratigraphic position. Unit M and Unit N form a continuum at several

localities, representing a continuation and slow restabilization of a fluctuating plinian column. Unit N is geochemically significant, with detectable amounts of the highly evolved phonolite compositions observed early in the lower Fasnia.

The Atogo ignimbrite is the uppermost primary deposit in the Fasnia Member sequence. The Atogo rests conformably on Unit M or Unit N, or on any preceding Fasnia ignimbrite. The Atogo is poorly preserved, although widely dispersed outcrops suggest a much greater extent of original deposition. Abundant lithics in the Atogo, similar to the Ravelo, indicates further vent and conduit destruction. The Atogo and Ravelo ignimbrites are interpreted to represent catastrophic column collapse, resulting in presumed caldera formation, and both close an eruption sequence, albeit temporary in the case of the Ravelo of the lower Fasnia.

Any reworked deposit lying on top of the upper Fasnia, apparently derived from Fasnia deposits due to surface erosion and redeposition, is designated Unit O.

Pumice clast color and textural variability – plinian deposits

All pumices observed in the field have weathered surfaces to varying degrees, usually brown or gray in color, obscuring the "true" color of the pumiceous glass. Furthermore, vesicle size and density affects the color of glass observed. Colors described below refer to interiors of freshly broken clasts.

Pumices in Units A and B are typically white, finely vesicular, and essentially aphyric. Occasional clasts have a very delicate frothy vesicular texture and are slightly greenish. Sometimes this variability in vesiculation is observed in a single clast. In Units D and F, white non-banded pumice clasts give way to abundant clasts exhibiting variable degrees of mingling, from simple bimodal banding to texturally complex types (Fig. 3.5).

Banding colors range from white to black, with any combination resulting from the mixing of the end member colors possible (e.g. cream, brown, gray, etc.). Close examination of these types of clasts reveals that the banding can persist to fine scales, limiting the usefulness of whole-rock analysis (or bulk analysis of hand-picked like-colored pieces) of such clasts. Vesiculation is also quite variable, with dense glass, or poorly to finely vesicular glass adjacent to frothy, highly vesicular portions. Some clasts have highly vesicular portions with bubble-like geometries surrounded by finely vesicular or dense mafic glass, which is further encapsulated by white or cream colored finely vesicular glass. Units H and J lack banded pumice, but are dominated by white pumice with juvenile mafic clots up to 10 mm diameter, with most clots being much smaller (<1-2 mm). The larger clots are often are associated with larger vesicles in the pumice and, because of their size, can easily be separated from the felsic portions during sample preparation for geochemical analyses. However, smaller clots and unseen clots internal to pumice clasts may not (or cannot) be completely eliminated from whole-rock analyses. In addition to the clots, pumices from Units H and J have a greater proportion of eye-catching blue haüyne (<1%) than earlier erupted pumice clasts. Variability in vesiculation like that described for Units A and B is also present. Pumices from Units L – N are very similar to H and J pumices (i.e., dominantly white to cream in color, containing mafic clots and haüyne), but banding of white and cream colors is observed in some clasts.

Measuring trace element abundances in rocks with the textural complexities described above is problematic when using traditional XRF or ICP-MS methods that require hundreds of milligrams to grams of material for an analysis. However, this problem can be overcome by using LA-ICP-MS, which allows *in situ* measurement of

trace elements in pumiceous glass on a scale comparable to fine-scale banding observed. This approach is able to get at the true trace element variability of the glasses within the clast and allow identification of near end member compositions within the Fasnia. These heterogeneities are apparent at the mm^3 scale. LA-ICP-MS results for both banded and apparently non-banded clasts are described below.

Analytical Procedures

All whole-rock major and trace elements were determined using X-ray fluorescence (XRF) and inductively coupled plasma (ICP) spectrometers in the Washington State University GeoAnalytical Laboratory. Methods and procedures for whole-rocks are detailed in Chapter 6. Whole-rock analyses are of two types, combined multiple pumices and single pumice clasts. There is no apparent difference between these two sample types, but where necessary they are distinguished from one another. During sample preparation care was taken to screen out mafic material, and in some cases different components within a single sample were analyzed individually. Selected glasses were also analyzed for major elements, and subsequently F and Cl using the electron microprobe.

Laser ablation (LA-ICP-MS) analyses were performed at Washington State University, using a New Wave UP213 Nd-YAG laser coupled with a ThermoFinnigan Element2 high-resolution mass spectrometer. The laser was operated at 20 Hz, and delivered 10-15 J/cm^2 to the sample surface. He was used as the carrier gas. Pumiceous glass samples, prepared as polished petrographic sections 30 – 100 microns thick, were ablated in troughs 0.3 - 1 mm long, 5 - 8 microns wide that followed bubble walls. A complete description of WSU laser ablation procedures and methodology is in Chapter 1.

Fasnia minerals

The Fasnia juvenile clasts have minerals that fit into three assemblages, similar to those described by Wolff (1985a) and Edgar et al. (2002 & 2007). An assemblage representing mafic magma consisting of calcic plagioclase + clinopyroxene (titanaugite) + olivine + Fe-Ti oxides is attributed to mafic material seen in mingled pumices and mafic clots. An assemblage associated with tephriphonolitic (or trachyandesitic) to phonolitic compositions consists of sodic (ternary) feldspar + salite + kaersutite + haüyne + titanite + oxides. The third assemblage, crystallized from evolved phonolitic compositions, consists of alkali feldspar + sodian salite + titanite + biotite + sodalite + oxides. As mentioned previously, titanite plays a major role in affecting trace element budgets of DHF magmas, providing an approach for distinguishing liquids that are otherwise chemically similar. This chapter focuses on the compositions of whole-rocks and glasses, Chapters 4 & 5 will address the importance of clinopyroxene and titanite and their usefulness as recorders of crystal transference in the Fasnia magma system.

Geochemistry

Major and minor element oxides in whole-rocks and glasses

Major element analyses presented here are of both single and multiple pumice whole-rock samples. Nine tephriphonolitic and phonotephritic samples, most of which are obviously the result of phonolite contaminated by mafic magma are not included. The data for the 94 samples presented have been scrutinized for loss or addition of elements (e.g., Ca & Mg) due to post-depositional processes, i.e., leaching or precipitation (e.g., calcite) due to groundwater. Of the original 94 samples analyzed by XRF, 39 are omitted from Figures 3.6 and 3.7 on the basis of anomalous CaO and MgO contents, however the

ICP-MS determined trace element data is used in the next section. The remaining 55 Fasnia whole-rock samples plot predominantly in the phonolite field on a total alkalis versus silica (TAS) diagram (Fig. 3.6). Three samples that plot in the trachyte field are most likely phonolites that have experienced a small degree of post-depositional alkali loss. Also shown in Figures 3.6 and 3.7 are electron microprobe data for glasses from selected pumices used for laser ablation trace element analyses. The glasses show approximately the same range in composition as the whole-rocks, but exhibit differences between the two phonolitic end members that are not resolvable in the whole-rock data. Higher alkali contents are from high-Zr glasses (>1800 ppm Zr) and correspond to the finely vesicular glasses that mantle the lower alkali, low-Zr glasses (500-800 ppm Zr) in Figure 3.5. The lower Fasnia is notable for the fact that these two compositions occur in their pure forms juxtaposed within single clasts, whereas the upper Fasnia whole-rocks and glasses primarily represent a hybrid of the two phonolite types (an idea developed throughout this paper), although pure low-Zr magma is erupted briefly. Glasses from an upper Fasnia hybrid clast indeed plot between the two end members on the TAS diagram and glasses from a representative upper Fasnia low-Zr pumice plot with highly vesicular glasses in lower Fasnia mingled clasts. A few whole-rocks and glasses trend toward less evolved compositions.

SiO_2 in the Fasnia phonolitic whole-rocks (Figs. 3.6 and 3.7) ranges from 56.2 to 60.9 wt%. Apart from a few exceptions, high-Zr glasses have <58.8 wt% SiO_2 versus low-Zr glasses with >58.8 wt% SiO_2. Al_2O_3 and TiO_2 contents are negatively correlated

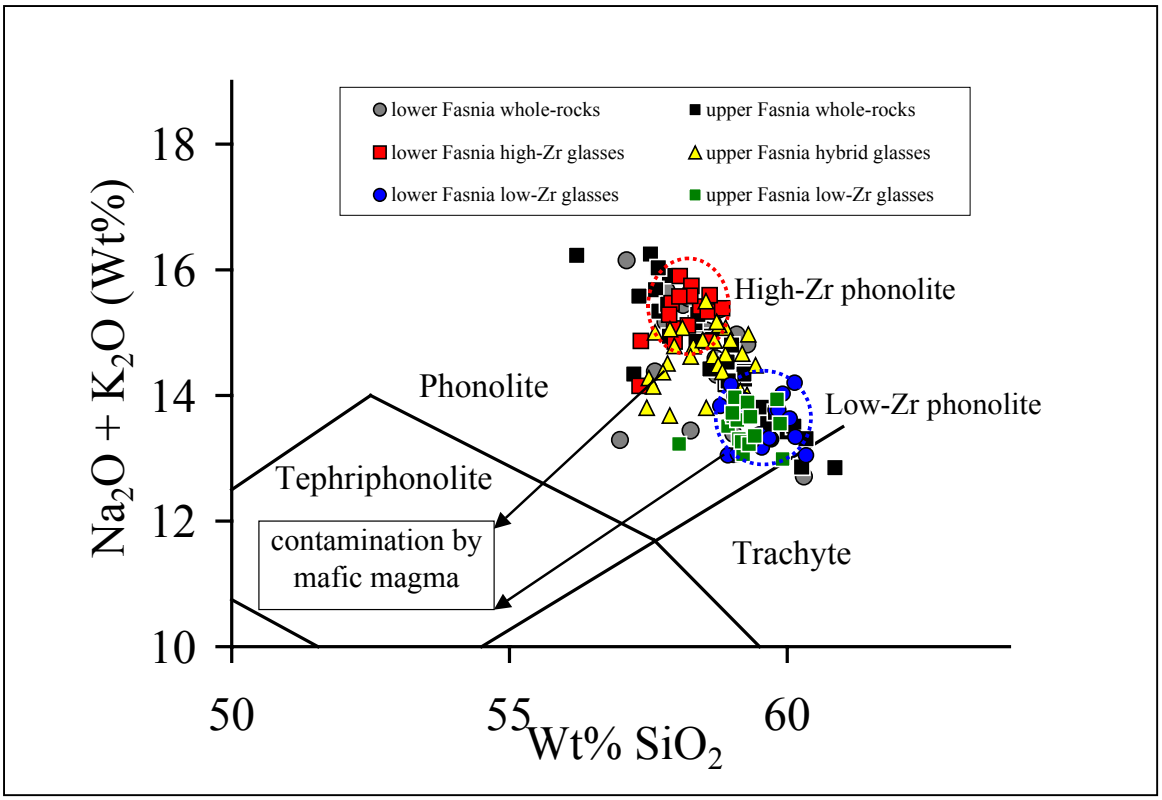

Figure 3.6: TAS diagram (after Le Bas et al., 1986) for Fasnia whole-rock samples and selected glasses. Whole-rocks were analyzed by XRF and glasses were analyzed by electron microprobe. Arrows showing contamination by mafic magma are drawn on.

and glasses define the high and low extremes of the trend. High Zr glasses have the lowest TiO_2 and highest Al_2O_3 concentrations, 0.25 wt% and 22.3 wt% respectively. Low-Zr glasses have the highest TiO_2 and the lowest Al_2O_3 concentrations, 0.92 wt% and 19.5 wt% respectively. Whole-rock TiO_2 and Al_2O_3 contents plot between these extremes, some overlapping hybrid glasses. CaO and MgO in whole-rocks and glasses show very similar behavior and are positively correlated. Some whole-rocks have low CaO and MgO contents overlapping hybrid and low-Zr glasses, but many scatter to higher values. High-Zr glasses have the lowest CaO and MgO contents, as low as 0.50 wt% and 0.12 wt%, respectively. Low-Zr glasses have CaO contents from 0.98 to 2.16 wt%, and MgO contents range from 0.33 to 0.60 wt%. FeO* in whole-rocks and glasses show a slight negative correlation with Al_2O_3 albeit with some scatter, but overall it does not vary greatly, 1.91 to 3.01 wt%. Generally, but not exclusively, high-Zr glasses have lower FeO* than low-Zr glasses. Whole-rock FeO* generally plots between the glasses, but some have higher values. In general, high-Zr and low-Zr populations are similar to evolved DHF I and DHF III rocks, respectively (see Ch. 2 & 6).

Whole-rock trace element concentrations

Complementing the 94 single and multiple pumice samples analyzed using both XRF and ICP methods (presented above and in Chapter 6), an additional 154 single pumices from upper Fasnia plinian deposits were analyzed by ICP-MS for trace elements to create a chemostratigraphic profile through the upper Fasnia. All whole-rock (n=248) trace element data are presented together here along with 11 basalts stratigraphically constrained between the Aldea and Fasnia Members. These basalts represent possible mafic contaminants involved in pre-eruptive magmatic events in the Fasnia. Trace

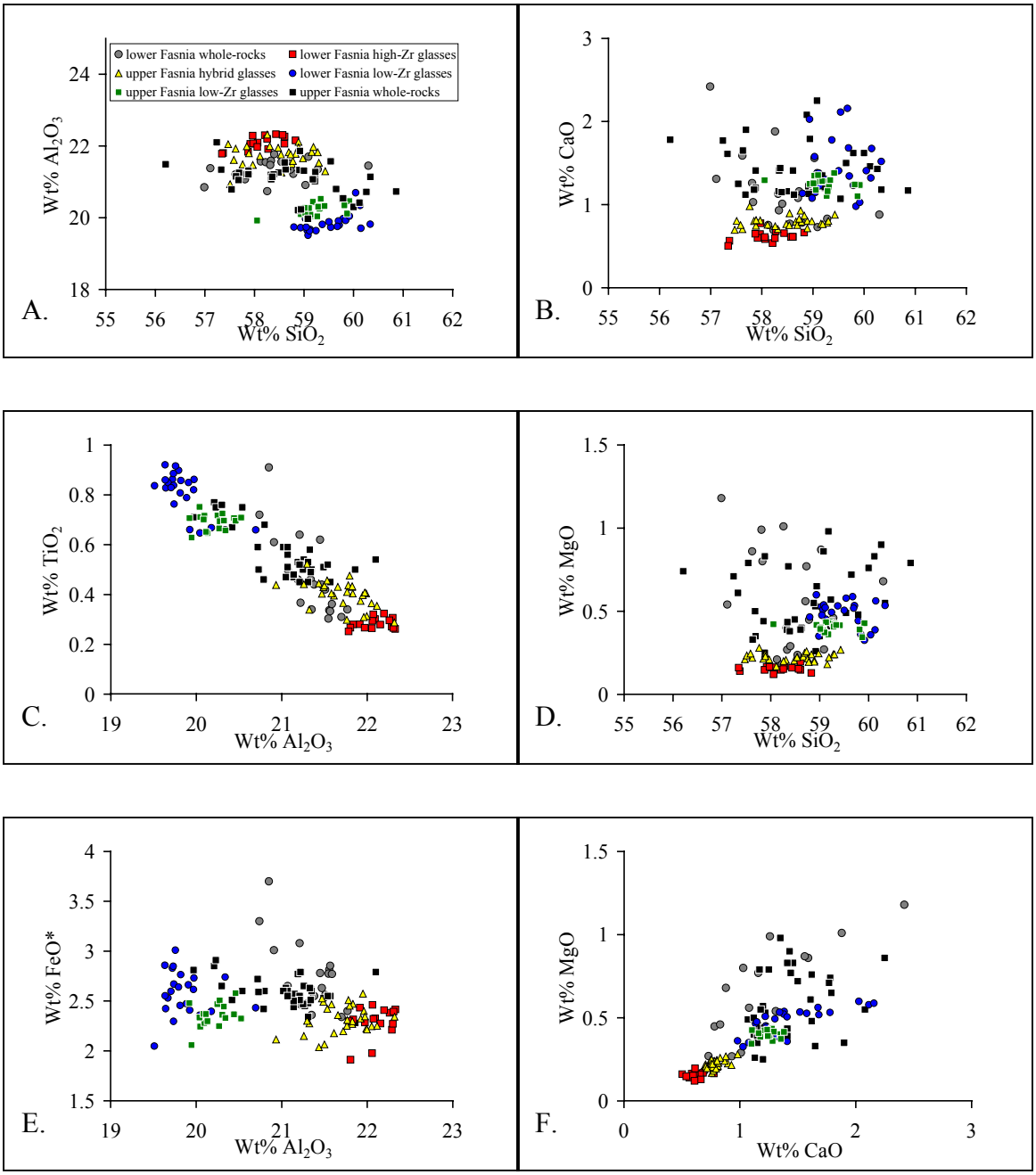

Figure 3.7: XRF and microprobe major element oxides for Fasnia whole-rocks and glasses.

element compositions of glasses are addressed in a later section, and in that section possible fractionation and mixing models relating the phonolites to one another are described. Zr is used as an indicator of fractionation throughout because of its strong enrichment with progressive evolution. Trace element contents vary significantly in the Fasnia (Fig. 3.8). High field strength (HFSE), large ion lithophile (LILE), and rare earth (REE) elements occur in trace and minor amounts, ranging in concentration two- to six-fold. Many elements are incompatible throughout, such as Pb, Th, Hf, Cs, and U. Pb (9.8-34.3 ppm; Fig. 3.8) is positively correlated with Zr (607-2044 ppm). Typically considered incompatible, Nb, Ta, and MREE are in fact significantly compatible into titanite, and therefore strongly influenced by small degrees of titanite fractionation (titanite partition coefficients for Nb, Ce, Ta, and Sm average 30, 52, 90, and 120, respectively; Ch. 5). Nb (172 to 290 ppm) is positively correlated with Zr. Sm (2.5 to 8.7 ppm) is negatively correlated with Zr. A few samples scatter towards higher Sm contents.

Selected elements ratios demonstrate the fractionation of elements that in many systems behave similarly. Ce becomes progressively depleted with increasing Zr, reflected in increasing Pb/Ce. Likewise, Ta becomes depleted relative to Nb, increasing Nb/Ta with evolution. Progressive MREE (i.e., Sm) depletion relative to LREE is apparent in increasing La/Sm with increasing Zr, and similar to MREE/HREE vs. Zr (e.g., Lu/Sm; not shown).

The lower Fasnia contains the most evolved whole-rock compositions, i.e., highest Zr, ~2000 ppm. The upper Fasnia contains the least evolved phonolites, i.e.,

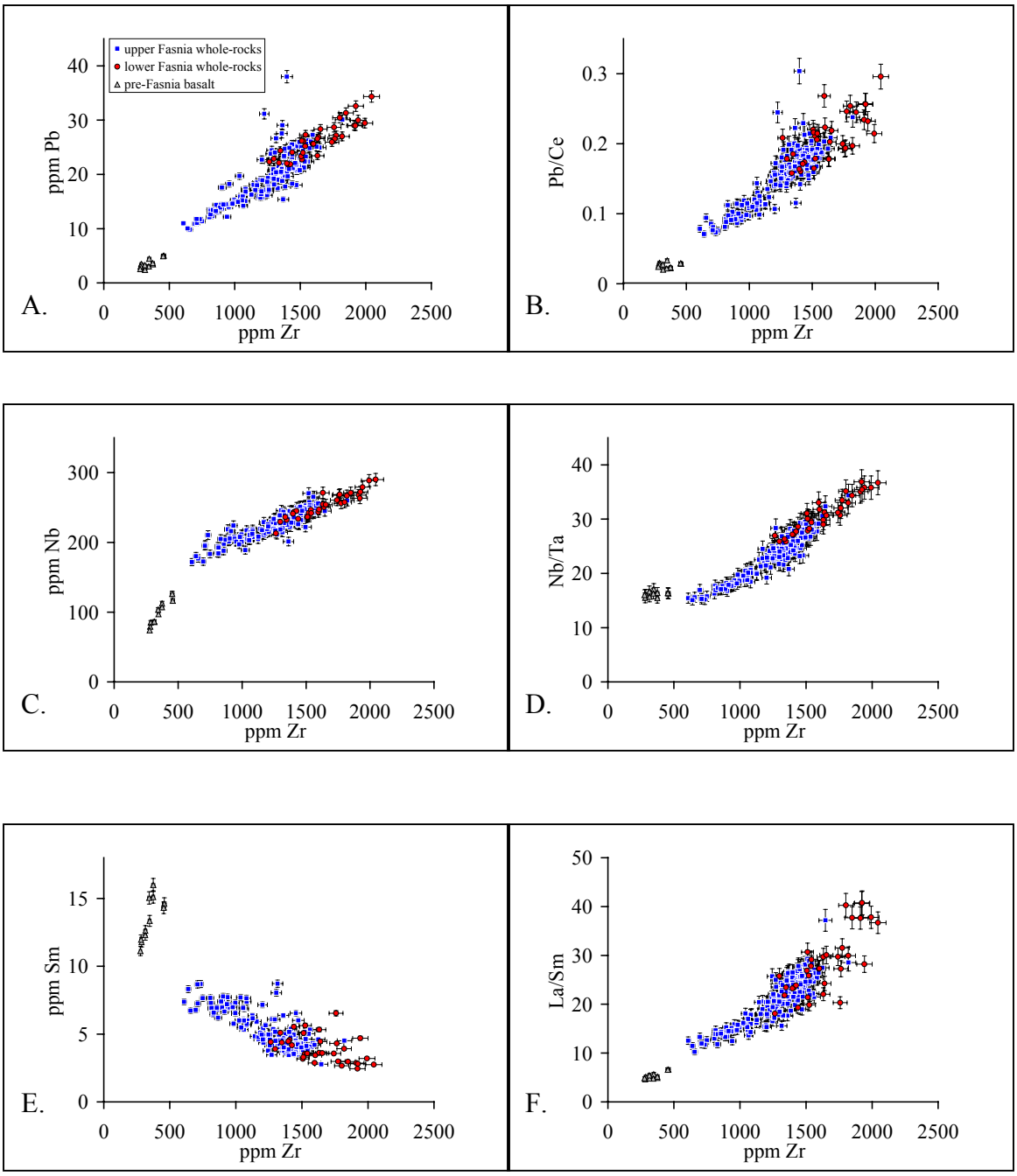

Figure 3.8: ICP-MS determined whole rock trace element data for the Fasnia Member and 11 pre-Fasnia basalts.

lowest Zr, ~600 ppm. Most of the samples plot between ~1100 and ~1600 ppm, representing hybrid whole-rock compositions.

Whole-rock REE patterns and abundance diagrams for DHF phonolites are shown in Figure 3.9. These data are normalized to primitive Dorsal Ridge Zone basalt, 01TF276. REE patterns are clearly MREE depleted, a feature consistent with fractionation of titanite from the magmas. The normalized abundance diagram shows the Fasnia is depleted in Ba, Sr, P and Ti, and has elevated Cs, Rb, Th, U and Pb. Nb and Ta are depleted due to titanite fractionation.

Volatile elements F and Cl in Fasnia glasses

The volatile elements F and Cl were measured in glasses from a few selected clasts from the lower and upper Fasnia by electron microprobe (Fig. 3.10). Clasts from and Unit L were chosen to compare F and Cl concentrations in a mingled clast containing both high-Zr and low-Zr glasses (Unit D), a hybrid and pure low-Zr phonolite clast bounding the sharp compositional transition in Subunit L2. F and Cl were analyzed independently from other major elements assuming a single bulk glass composition representing average high-Zr phonolite, therefore these data are considered preliminary and represent a first order look at these elements in lower Fasnia glasses. These data are NOT intended for publication.

For all glasses, F concentrations range from 0.1 to ~1.0 wt% and Cl concentrations range from 0.0 to ~0.5 wt%. Glasses from sample 99TF8, a Unit D mingled clast, show a lot of scatter towards lower Cl contents relative to the other samples. These lower Cl contents are generally associated with the finely vesicular high-

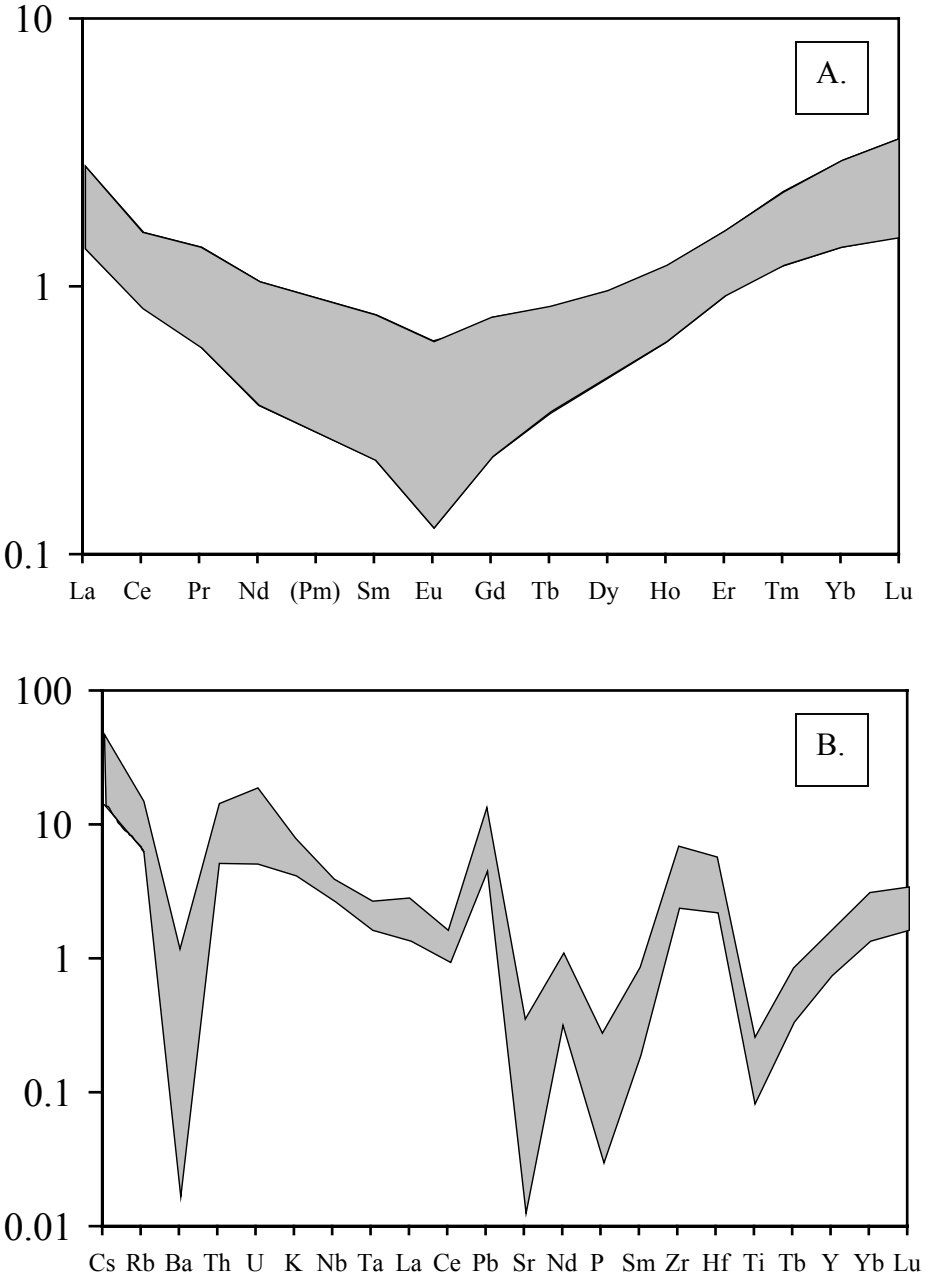

Figure 3.9: REE (A) and trace element (B) abundance diagrams for the Fasnia Member. These data are normalized to Dorsal Series basalt 01TF276. Note the pronounced MREE and Nb-Ta depletion, and depletions in Ba and Sr, attributed to titanite and feldspar fractionation, respectively.

Zr glasses from the outer portions of the clast (Fig. 3.5). The highest-Cl glasses that lie near the 1:1 line are from coarsely vesicular low-Zr interiors and clearly overlap Unit L hybrid and low-Zr glasses. The highest F contents are from high-Zr glasses, however overall F does not vary systematically among the glass types.

Glasses from sample 03TF16, Subunit L1, have the highest measured F and Cl concentrations, both as high as ~0.5 wt% in some glasses. These glasses are dominated by hybrid compositions (i.e., 1146 to 1518 ppm Zr), but glasses with Zr contents as low as 623 ppm have been observed. Some glasses extend to lower F and Cl contents along the 1:1 line and to values associated with low-Zr glasses.

Glasses from sample 03TF13, Subunit L2, have low to intermediate F and intermediate Cl contents. These glasses represent fairly pure low-Zr glass with 587 to 790 ppm Zr. F and Cl data plot down the 1:1 line from the hybrid glasses and a few scatter towards lower and higher Cl contents.

Fasnia Member chemostratigraphy – plinian deposits

The Fasnia Member shows changes in composition with stratigraphy. Figure 3.11 shows volume-normalized stratigraphic position of plinian deposits only (ignimbrite volumes are included in the calculation) versus the whole-rock concentrations of two incompatible elements (Zr, Th) and one titanite-compatible element (Sm). Geochemical data for pyroclastic flow deposits are not included in this profile because field evidence, such as ignimbrites observed eroding underlying deposts, and scatter in such data suggests that recycled clasts may make up a significant volume of these deposits, and stratigraphic position of clasts within flow deposits does not systematically reflect order

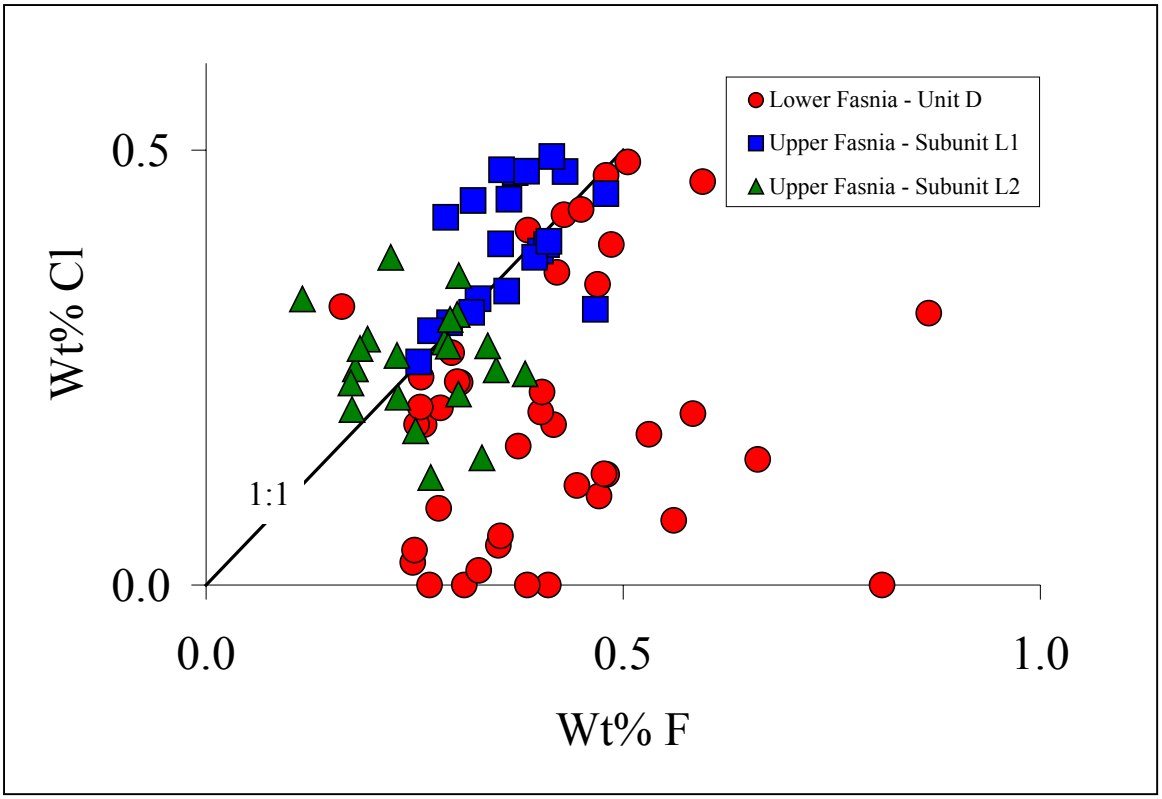

Figure 3.10: Volatile elements fluorine and chlorine in glasses determined by electron microprobe. These data were not collected with the major elements, rather a single bulk compositon was assumed. These data are preliminary and NOT intended for publication.

of clast eruption (Branney and Kokelaar, 2002). Zr and Th have essentially identical trends, but because Sm is compatible it generally behaves opposite to Zr and Th. The first erupted magma has the most evolved compositions (~2000 ppm Zr). Then Zr and Th decrease from Unit A though F to hybrid phonolite compositions (1200 – 1500 ppm Zr WR) observed late in Unit F. A lower Fasnia trend for Sm is less well defined, likely reflecting contamination by mafic material (see *Trace elements in lower Fasnia glasses)*. This hybrid compositional range persists through Ravelo ignimbrite (not shown), and accounts for >4 km^3 of hybrid magma represented by Units H and J, after the lower–upper hiatus. The compositional variation observed in Units H and J is much greater than analytical uncertainty and reflects true heterogeneity of the hybrid magma. Another compositional shift occurs in Unit L from hybrid phonolite to relatively pure low-Zr phonolite (~600 ppm Zr). In Units M and N, compositions steadily return to hybrid phonolite on the whole-rock scale, but high-Zr phonolite is detected at fine scales by LA-ICP-MS.

Statistical treatment of the upper Fasnia compositional profile

It has long been recognized that the juvenile component(s) in felsic pyroclastic deposits commonly exhibit internal stratigraphic chemical variations that are interpreted to represent systematic chemical zoning within the source magma chamber (Smith and Bailey, 1966; Lipman, 1967; McBirney, 1968; Smith, 1979; Hildreth, 1979, 1981). From the standpoint of magma genesis, there is now a consensus that such variations may arise through the operation of crystal-liquid fractionation and crystal transfer (e.g., Wolff and Storey, 1984; Cameron and Cameron, 1986; Storey et al., 1989; Troll and Schmincke,

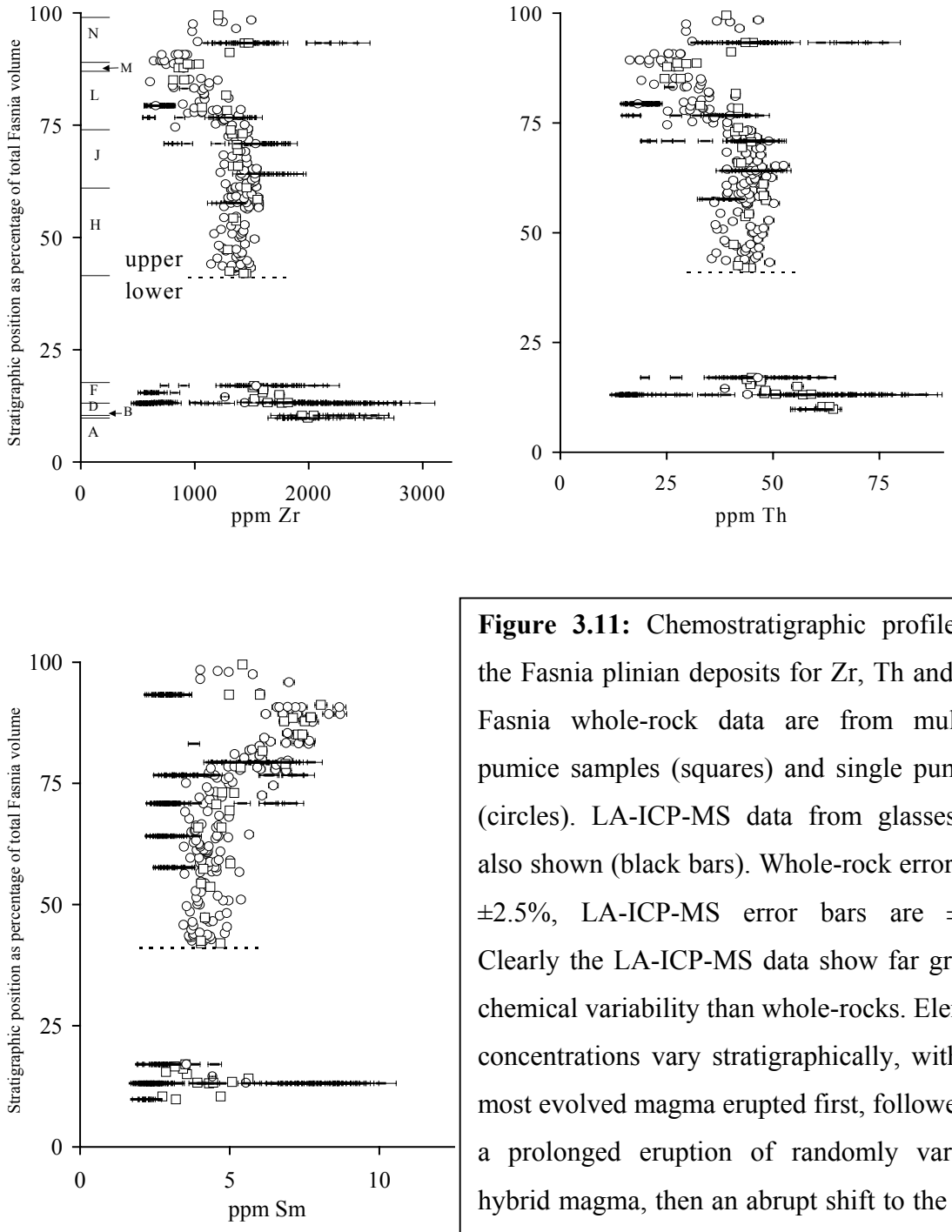

Figure 3.11: Chemostratigraphic profiles of the Fasnia plinian deposits for Zr, Th and Sm. Fasnia whole-rock data are from multiple pumice samples (squares) and single pumices (circles). LA-ICP-MS data from glasses are also shown (black bars). Whole-rock errors are ±2.5%, LA-ICP-MS error bars are ±5%. Clearly the LA-ICP-MS data show far greater chemical variability than whole-rocks. Element concentrations vary stratigraphically, with the most evolved magma erupted first, followed by a prolonged eruption of randomly variable hybrid magma, then an abrupt shift to the least evolved phonolites, and finally a recovery to hybrid compositions.

2002), recharge (e.g., Neumann et al., 1999; Fowler et al., 2004; Wark et al., 2007) and, often, contamination from the walls of the magma chamber (Johnson, 1989; Tegtmeyer and Farmer, 1990; Knesel and Davidson, 1997; Wolff and Ramos, 2003). What is less clear is the amount of information carried by the fine structure of chemical profiles through pyroclastic deposits. This is important for an understanding of magma chamber and eruption dynamics, because physical models predict significant perturbations to simple density-stabilized layering structure in magma prior to and during eruption (Spera, 1984; Oldenburg et al., 1989; Folch et al., 1998, 2001), and further scrambling of compositions is expected during post-fragmentation transport of pyroclasts in the eruption column and atmosphere (Wolff, 1985b).

We have applied a spatial correlogram analysis, based on fundamental statistical descriptions of turbulence and mixing (Taylor, 1935; Danckwerts, 1952) to the upper Fasnia single pumice data (n=154), in order to quantitatively evaluate the significance of the chemical variations within the upper Fasnia plinian deposits, and to estimate the implied spatial scales of compositional variation in the magma prior to fragmentation. Fragmentation is the transition from bubbly continuous melt to parcels of melt within a continuous gas phase (Cashman et al., 2000). This occurs as bubble growth and nucleation of volatile species (i.e., H_2O, CO_2, S, F and Cl) drive rapid expansion of the magma to the point of brittle failure. The "parcels of melt" quench as they are accelerated up volcanic conduits forming pumice and other pyroclasts. If magma is extractable from the magma chamber in a systematic top-down manner into the conduit prior to fragmentation and entrainment into the eruption column, then the resulting deposits should record the inverted chemical zonation of the magma body. Spatial correlogram

analysis has previously been used to predict spatial scales of compositional change in forward modeling of magma mixing (Oldenburg et al., 1989), and was more recently applied to geochemical data bearing on the size of mantle compositional domains (Graham et al., 2001).

Avoidance of issues arising from clast recycling

The spatial correlogram analysis relies on accurately measured distances between clasts, which in this study we directly relate to the volume of erupted magma. Geochemical data for pyroclastic flow deposits are not included in this statistical treatment for two reasons: 1.) Field evidence, such as ignimbrites observed eroding underlying deposits, suggests that recycled clasts may make up a significant volume of ignimbrite deposits, and 2). Depositional complexities preclude simply equating stratigraphic position of clasts to volume of magma erupted (e.g., Branney and Kokelar, 2002).

The single pumice data used below was scrutinized for trends induced by potential clast recycling using clast shape plotted against selected trace elements (i.e., Zr, Th, etc.), ultimately showing no correlation (Fig. 3.12), however the incidence of rounded clasts, approximately 20%, suggests that some recycling occurred. At the mass eruption rate of ~10^5 m^3 s^{-1} (~2 x 10^8 kg s^{-1}) and column heights ~30 km (H_B=~25 km, H_T=~35 km) of the upper Fasnia (Edgar, 2003), the average sampling density represented by pumices in the profile, 0.05 km^3, exceeds the maximum possible volume separation of two similarly-sized clasts, <0.01 km^3 (Wolff, 1985b), obscuring any scrambling effects that simply falling from different parts of the umbrella cloud may have on the profile.

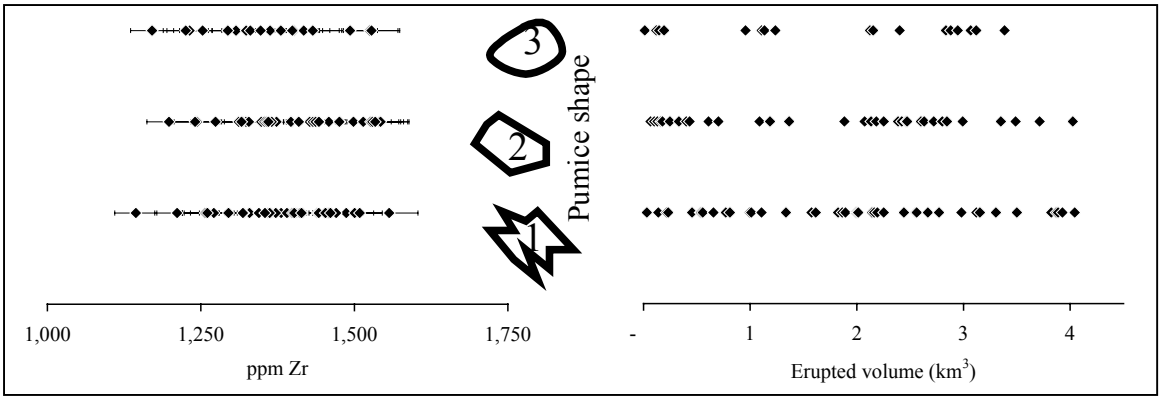

Figure 3.12: Occurrence of clast shape categories (1=angular, 2=subrounded, 3=rounded) as a function of compositon (i.e., Zr) and volume of magma erupted.

Spatial correlogram analysis

First, normalized composition, $\hat{E}$, is defined:

$$\hat{E} = (E - E_l)/(E_h - E_l)$$

where E equals the concentration of the chemical component and l and h denote the low and high extremes of the compositional range. If $\hat{E}_1$ and $\hat{E}_2$ represent compositions at two points a distance r apart within the magma, the deviations from the mean form the product:

$$(\hat{E}_1 - \hat{E}_{av})(\hat{E}_2 - \hat{E}_{av})$$

If a number of such pairs are taken the mean value of the products of the deviations is known as the space correlation and is written:

$$R^*(r) = \overline{(\hat{E}_1 - \hat{E}_{av})(\hat{E}_2 - \hat{E}_{av})}$$

where the overbar indicates the mean at constant r. The composition correlation function, $R(r)$, for all values of $\hat{E}$ a distance r apart is:

$$R(r) = R^*(r)/s^2$$

where s^2 is the population variance. A value of $R(r)$ close to 1 means that a particular concentration with respect to the mean at some location in the magma is likely to be associated with a similar value a distance r away, while a value near zero means a random relationship. $R(r)$ at $r = 0$ equals unity by definition. A value of $R(r)$ close to –1 indicates a negatively correlated relationship. For heterogeneous mixtures, $R(r)$ is >0 at small r because neighboring points are derived from the same compositional domain, but decreases with increasing r. The lowest value of r at which $R(r)$ = zero is denoted by r^*. The integral of $R^*(r)$ between $r = 0$ and $r = r^*$ corresponds to the length scale of

segregation *L*, which is related to the size of compositional anomalies or "lumps" within a mixture. The result of this treatment is plotted as a correlogram (Fig. 3.13).

Correlograms

Three correlograms for Zr, Th, and Sm data from the ~7 km^3 upper Fasnia plinian deposits are shown in Figure 3.11, one for Units H and J, one for Units J and L, and one for Units H, J, L and N. The data are plotted as bins of constant population. For data collected from a linear traverse, there are few points at large *r*, hence, at large *r*, results using bins of constant population are more robust than for bins of constant width.

The correlograms confirm the visual impressions of Figure 3.11. The correlogram for Units H and J (100 members per bin) reflects the random relationship of clast compositions. In other words, the erupted phonolite mixture exhibits complete randomness during this time at the scale of 0.05 km^3, but it is not yet a smooth mixture. The correlogram for Units J and L (50 members per bin) almost continuously decreases from R(r) = 1 to –1, with a spike at r = ~0.2. The magma erupted from Unit J to Unit L time clearly transitions from a Unit J "end member" to a Unit L "end member." The spike indicates a brief pulse of more J-like magma during the transition.

The correlogram for Units H-N (200 members per bin) show the same features as above, but they are compressed due to the change in scale. The rapid drop of R(r) from 1 to 0, at r = ~0.1, reflects the sharp compositional transition from H- and J-type to L-type magma, with the spike still evident at r = ~0.05 (equivalent to ~0.2 for J & L). The randomness of H and J compositions is apparent between r = 0.2 – 0.4, at R(r) approximately equal to –0.2, consistent with incomplete but completely random mixing. The anticorrelation (approach to *R(r)* = -1) at *r* = ~0.65 in the data is the correlogram

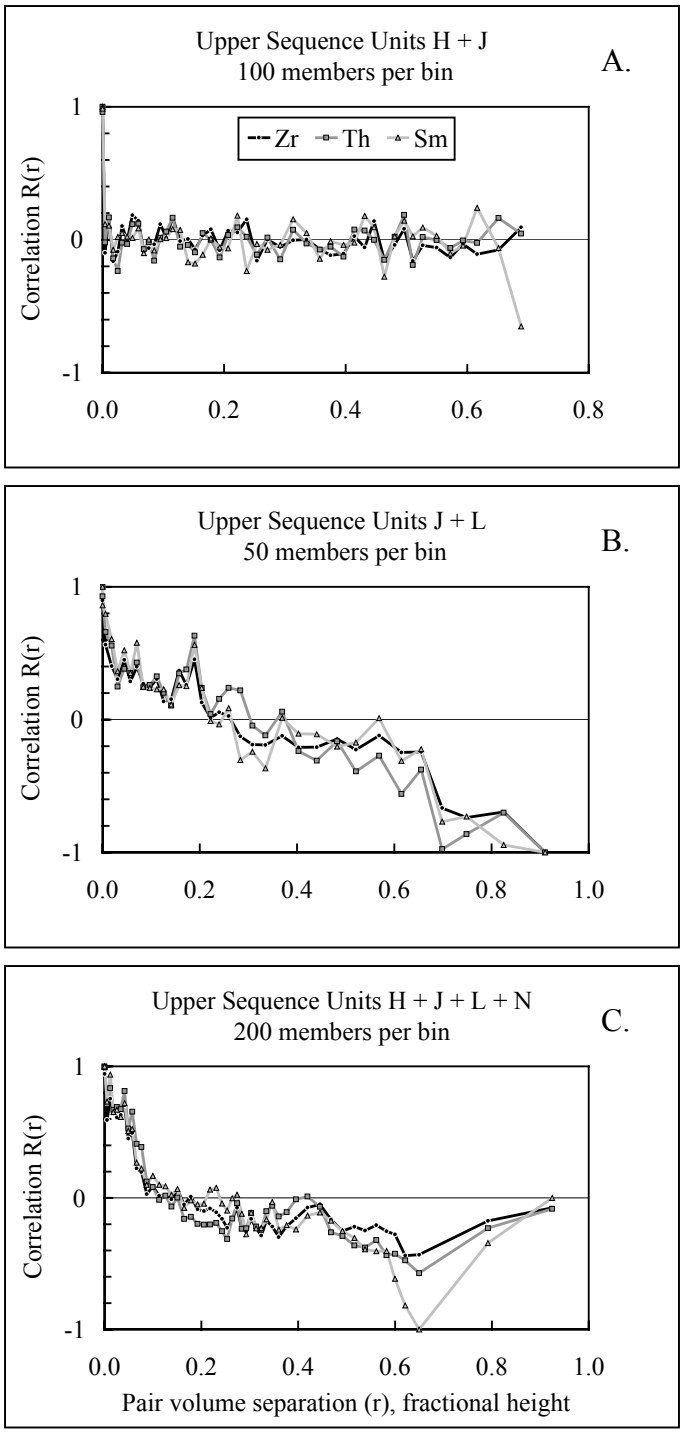

Figure 3.13: Correlograms for the statistical treatment of the compositional profile for elements Zr, Th, and Sm. See text for description and interpretation.

representation of the excursion to low Zr and Th, and higher Sm in unit L. The correlation of –1 implies that relatively unadulterated low-Zr phonolite dominates L and evolved phonolite is essentially absent. In other words, over this volume there is a distinct coarsening of the mixture and a change from compositional randomness to segregation. For the elements used in this ~7 km^3 DRE upper Fasnia profile $r^* = 0.12$ (0.8 km^3 magma), and the length scale of the segregation (or compositional lump size), L corresponds to a volume of 0.32 km^3 (~4.3% of the upper Fasnia volume) at an average sampling density of 0.05 km^3.

Intraclast trace element chemical variations

Laser ablation (LA-ICP-MS) techniques were employed to investigate chemical heterogeneities of glasses within pumices. In general, the results reveal compositional extremes not resolved by the whole-rock approach, and provide greater insight into fine-scale magma dynamics operating in the Fasnia system. The lower Fasnia glasses are described first and data are plotted according to unit along with several basaltic samples that are stratigraphically constrained between the Aldea and Fasnia Members. These glasses cover a wide compositional range and many have been contaminated by mafic magma. Lower Fasnia glasses showing evidence of a mafic component are filtered out and the relationships between the remaining lower Fasnia phonolitic glasses are described. The upper Fasnia glasses are then described and compared to the lower Fasnia.

Trace elements in lower Fasnia glasses

All Fasnia glasses are characterized by incompatible trace element contents that are positively correlated with Zr (416-2958 ppm; Fig. 3.14). Th (9-85 ppm) is strongly correlated with Zr, but Cs (0.5-6.2 ppm) and Pb (6.8-40 ppm) show more scatter at high

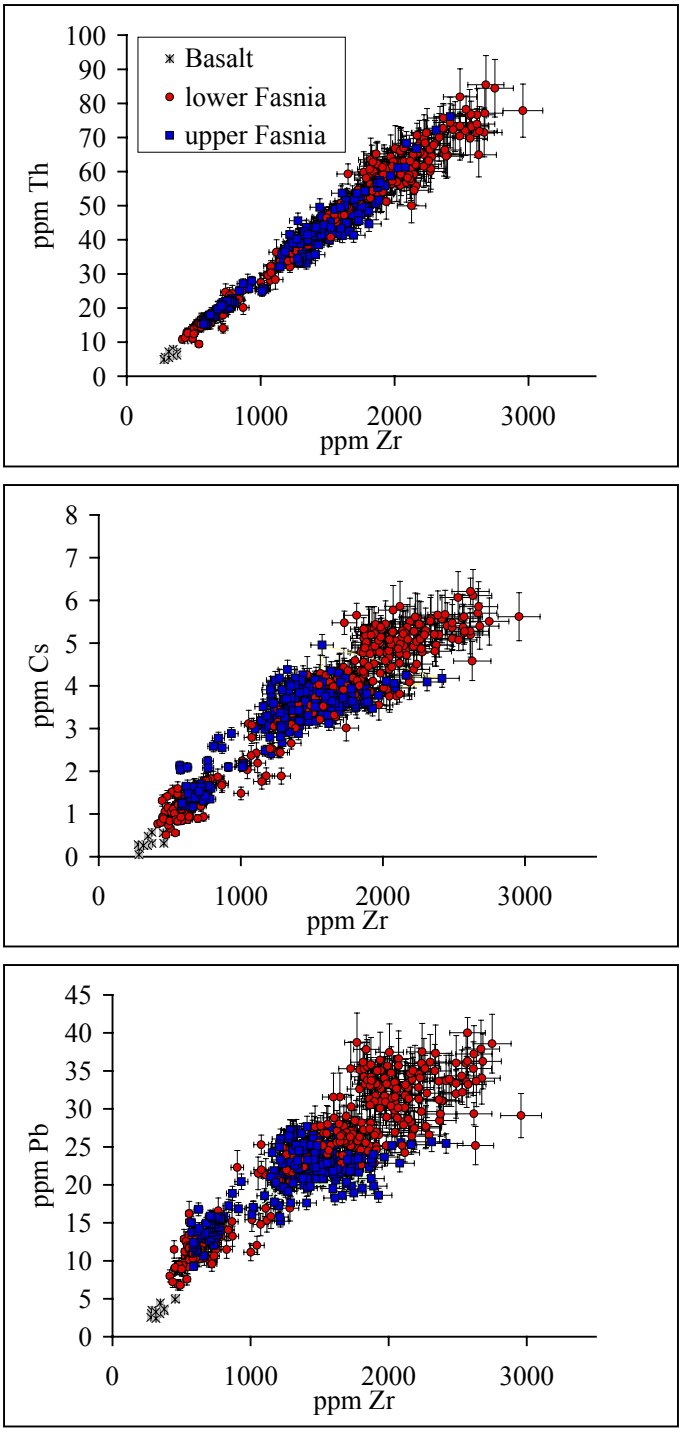

Figure 3.14: LA-ICP-MS data for incompatible trace elements in glasses from the lower and upper Fasnia. Error bars ±5%.

Zr contents, probably reflecting some degree of post eruptive mobility. Some glasses from lower Fasnia clasts yield the most enriched incompatible trace element abundances, exceeding whole-rock values by 50%, and the most depleted compatible trace element concentrations in the Fasnia.

Compatible vs. compatible element diagrams show the openness of the lower Fasnia magma system and many compositions intermediate to the three end members probably reflect any of the numerous possible mixing lines (Fig. 3.15), as seen in Ba vs. Sr or Sm vs. Ta (Fig. 3.15) in this system. On Figure 3.15 three mixing lines are shown forming a triangular mixing envelope. Although mixing between any of the compositions is possible, endpoints of the mixing lines are fixed at compositions representative of the least evolved low-Zr glass, the least evolved high-Zr glass, and a mafic glass. Almost the entire range of phonolites could have mixed with mafic magma to some degree, but as a first order filter, glasses within the Ta vs. Sm, Ta vs. Nb, and Ba vs. Sr mixing envelopes are subsequently removed so relationships between the phonolitic end members can be better evaluated in Figures 3.18 to 3.19. Of the 339 lower Fasnia glasses in Figure 3.15, 73 are filtered out for being significantly contaminated by mafic magma.

Unit A glasses (2 clasts, 24 analyses) and Unit B glasses (2 clasts, 11 analyses) are from white, nearly aphyric, finely vesicular pumices. These high-Zr glasses have some of the highest Zr and Nb contents in the Fasnia, but Ba, Sr, Sm, and Ta contents are among the lowest (Fig. 3.16). None of the Unit A glasses show signs of significant contamination by mafic magma, however one Unit B glass analysis is contaminated by mafic magma and screened out.

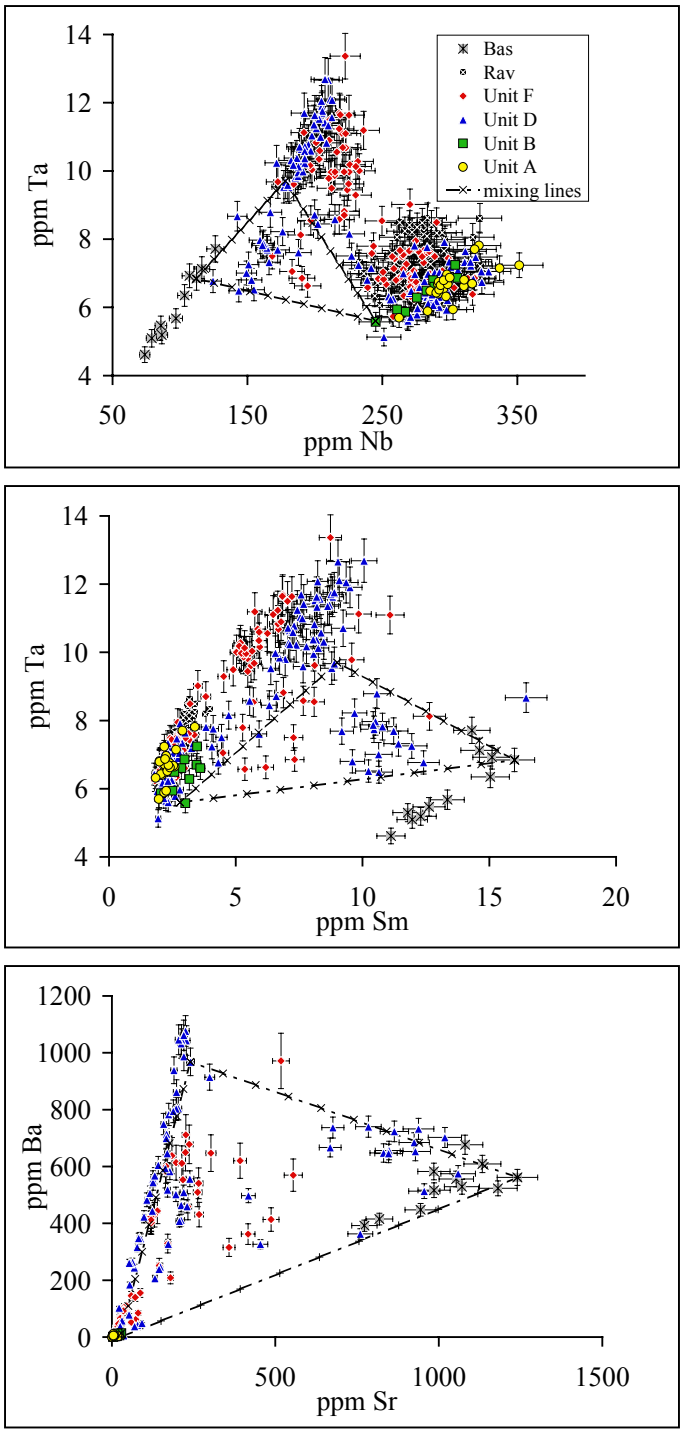

Figure 3.15: Compatible vs. compatible element diagrams for lower Fasnia glasses plotted according to unit. Glasses that lie within ternary mixing envelope are omitted from further plots.

Unit D glasses (7 clasts, 139 analyses) are from texturally complex mingled and banded pumices, such as those in Figure 3.5. These pumices contain the most evolved high-Zr glasses with the highest Zr and Nb contents, low-Zr glasses with the highest Ba and Ta concentrations, and the most mafic glasses analyzed in the lower Fasnia. Figure 3.15 clearly shows that many glasses have been contaminated with mafic magma and fall within the triangular mixing envelope. Glasses contaminated by mafic magma do not plot along any particular mixing trend (e.g., high-Zr phonolite mixing with mafic magma) suggesting that these are either ternary mixtures, involving the three magmatic end members, or that the two end member components are compositionally heterogeneous. Thirty-seven (37) Unit D glasses showing contamination by mafic magma are omitted from later descriptions of phonolite relationships. Similar to Unit D, Unit F glasses (7 clasts, 119 analyses) are also from texturally complex mingled and banded pumices. The evolved high-Zr glasses in Unit F are equivalent to high-Zr glasses in Units A, B, and D.Unit F also contains low-Zr glasses, as in Unit D, but at slightly lower Ba and Sm contents. Twenty-eight glasses contaminated by mafic magma are identified and are screened out. The most striking feature of the Unit F glasses is the first appearance of a population of 1000-2000 ppm Zr glasses that have elevated compatible elements relative to high-Zr phonolite. These glasses represent a third phonolite type interpreted to be a hybrid of low-Zr and high-Zr phonolitic magmas. This hybrid phonolite composition dominates the upper Fasnia and its genesis will be addressed in detail below. Trends extending from Unit F low-Zr glasses towards high-Zr glasses can be attributed to either mixing with high-Zr phonolite, or fractionation from low-Zr phonolite to slightly more

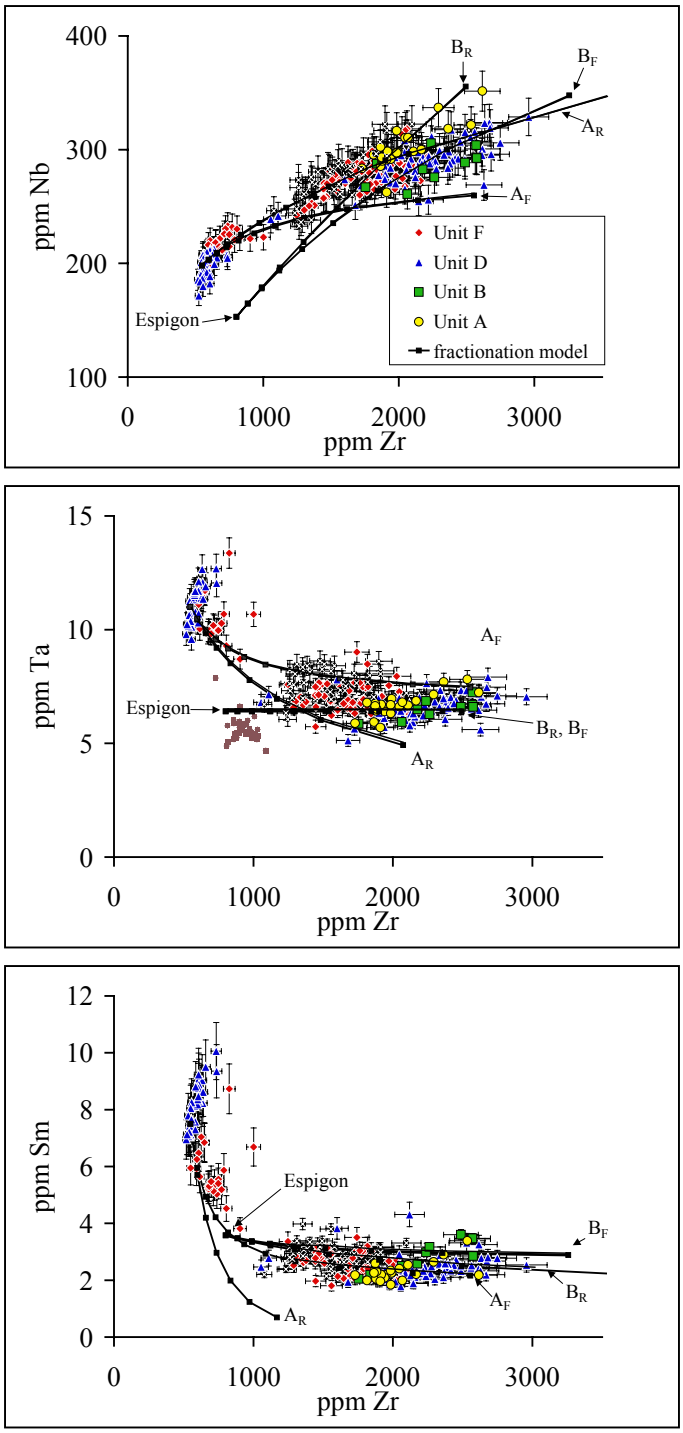

Figure 3.16: Titanite-compatible elements in lower Fasnia glasses plotted by unit. Model curves are for both Rayleigh and batch fractionation initiated from two different starting compositions. See text for model parameters and interpretation. The Espigon is a DHF bs unit used as a fractionation starting point.

evolved compositions. Possible fractionation paths for the phonolites will be discussed fully below. Glasses from Ravelo ignimbrite (2 clasts, 46 analyses), not shown in the stratigraphic profile, are also hybrid phonolite in composition, similar to the Unit F hybrid. Pure high-Zr or low-Zr glasses are not detected; Seven Ravelo glasses are filtered out due to mafic magma contamination.

With glasses contaminated by mafic magma screened out, the remaining 266 lower Fasnia phonolitic glasses are shown in Figure 3.17. Following Edgar et al. (2007), relationships between low-Zr and high-Zr glasses are evaluated using fractionation models (both Rayleigh and batch) initiated from two different starting compositions, roughly corresponding to their A & B trends. Models are plotted in 10% increments. Starting compositions are the least evolved low-Zr glass (500 ppm Zr, 187 ppm Nb) and a whole-rock analysis from the sub-Fasnia Espigon Member (802 ppm Zr, 153 ppm Nb). This sample was chosen to represent a volume of DHF II type phonolite, observed in DHF bs, that might fractionate to produce DHF I type phonolite. Zr is used as the fractionation indicator. Model curves initiated at low-Zr glass are labeled A_R and A_F (R=Rayleigh, F=batch), and correspond to 3% titanite in the fractionating assemblage. Curves with the Espigon starting composition are labeled B_R and B_F and correspond to 1% titanite in the fractionating assemblage. Care was taken to constrain titanite trace element partition coefficients in this system (see Chapter 5), and in light of the significant variation observed corresponding to DHF I and III type glasses, the use of different values in the models is justified. The most significant differences are partition coefficients for Ta and Sm. Titanite partition coefficients used in the model A curves are;

D_{Zr}=5.8, D_{Nb}=25, D_{Ta}=50, D_{Sm}=85. Titanite partition coefficients for model B curves are; D_{Zr}=5.8, D_{Nb}=30, D_{Ta}=100, D_{Sm}=125.

Figure 3.16 shows that the lower Fasnia data can be reconciled with the models by >75% fractionation from either starting composition. To achieve glasses with ~2000 ppm Zr from low-Zr phonolite glasses requires >85% fractionation for both Rayleigh and batch models for Nb and Ta. Actual data for these two elements lie within the region created by A_R and A_F, whereas Sm data fit the batch model curve much better than the Rayleigh curve. To achieve ~2000 ppm Zr glasses starting from the Espigon parental composition requires ~>60% fractionation for both schemes. In this case, Rayleigh and batch fractionation models do not differ significantly. If operable, mixing processes would form linear arrays on Figure 3.16, and given the range of trace element contents, numerous mixing paths are possible. For example, in Nb vs. Zr and Ta vs. Zr, most of the hybrid glasses (1000-2000 ppm Zr) could be either products of fractionation model A, or mixing between high-Zr and low-Zr glasses. Sm does not behave in the same way, and values in the hybrid glasses are more consistent with fractionation.

Trace elements in upper Fasnia glasses

The majority of analyzed glasses from the upper Fasnia (which generally lacks mingled pumice) have trace element concentrations intermediate to the high-Zr and low-Zr glasses observed in the lower Fasnia (1100 – 1800 ppm Zr), and similar to hybrid glasses from Unit F and the Ravelo ignimbrite. Unlike the lower Fasnia in which many glasses were contaminated by a mafic component and subsequently screened out, no upper Fasnia glasses are significantly contaminated by mafic magma. Incompatible trace elements in these hybrid glasses plot between low-Zr and high-Zr phonolite (Fig. 3.16).

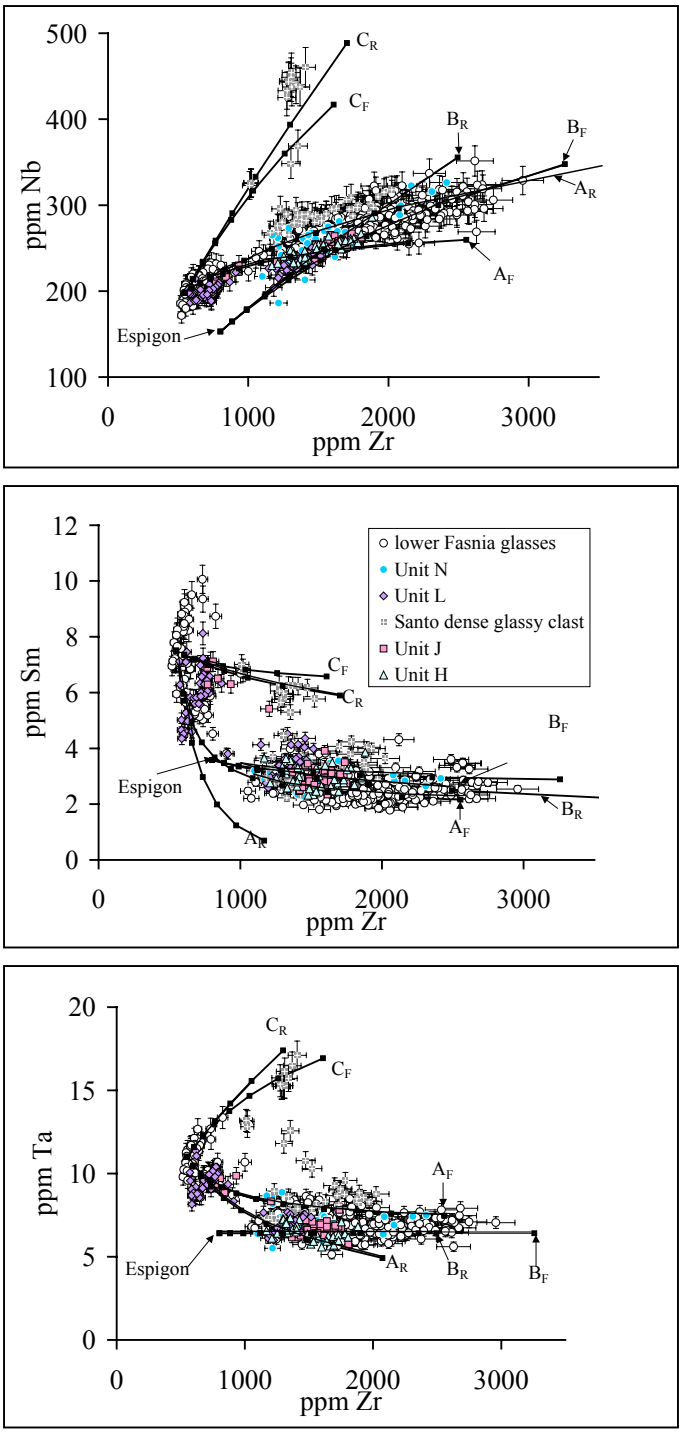

Figure 3.17: Titanite-compatible elements in upper Fasnia glasses plotted by unit. Model curves are for both Rayleigh and batch fractionation initiated from two different starting compositions. See text for model parameters and interpretation.

Selected trace elements Nb, Ta, and Sm are again used in Figure 3.18 to clarify relationships among the phonolitic glasses. Here the upper Fasnia data are plotted according to unit and the lower Fasnia data are treated as a single series. In addition to the two sets of fractionation curves shown in Figure 3.17 a third set, C_R and C_F, is added with the same starting composition and partition coefficients as model A curves and represent 1% titanite in the fractionation assemblage. Model C curves represent the likely fractionation path of DHF III phonolites. Although in the discussion below many of the upper Fasnia glasses are described as and interpreted to be hybrids, the fractionation models are included to show that fractionation processes have probably had at least some impact on compositions.

All Unit H glasses (2 clasts, 37 analyses) are hybrid phonolite in composition. No pure low-Zr or high-Zr glasses are observed. These glasses record the lowest Sm contents in the upper Fasnia, and except for one Unit N glass and two lower Fasnia glasses, the lowest Ta contents in the member.

The Santo ignimbrite is clearly a complex deposit and by no means represented by a single clast. However, 61 analyses from a single dense, glassy juvenile clast are included here. This clast contains disparate phonolitic glasses juxtaposed with little change in texture, but with sharply contrasting Nb and Ta contents (Fig. 3.17). Most notable are the glasses with high Nb and Ta (>400 ppm, >15 ppm, respectively) relative to all other Fasnia glasses. These high Nb glasses are in fact consistent with DHF III-type magma (see Chapters 2 & 6), and represent another possible component or contaminant in the Fasnia system, the significance of which is unclear. Most of the glasses are similar to other hybrid compositions in Sm and Y contents, however Nb and Ta (to a lesser

extent) have trends at higher concentrations relative to the other units. A few glasses have >1800 ppm Zr, but slightly higher Ta and Sm contents suggest these glasses have also been contaminated by the DHF III-type component.

Unit J glasses (1 clast, 47 analyses) are dominated by hybrid compositions most similar to Unit H glasses. Four glasses with low Zr contents representing relatively pure low-Zr are also observed.

Unit L glasses (2 clasts, 76 analyses) are both hybrids (1100 to 1500 ppm Zr) and the purest low-Zr (585 to 1516 ppm Zr) glasses in the upper Fasnia. Apart from a few glasses at low Zr contents, the two Unit L populations correspond to two different phonolite types. The clast dominated by hybrid glasses is from Subunit L2 and occurs just prior to the abrupt compositional shift (Fig. 3.11) that occurs during Subunit L2. The other clast is from the least evolved end of the Subunit L2 compositional shift (lowest Zr and Th contents. All glasses analyzed within this clast (03TF13) are low-Zr phonolite, suggesting that this clast as a whole represents fairly pure low-Zr phonolitic magma. However, trace element trends do not rule out contamination of these glasses by high-Zr phonolite or mafic magma.

Unit N glasses (3 clasts, 40 analyses) are dominated by hybrid compositions, but a few high-Zr glasses are present, as are a few glasses that trend towards lower Zr compositions that may reflect minor contamination by low-Zr or mafic magma. Hybrid glasses are consistent with the whole-rock compositions. Relatively pure high-Zr glasses are observed in a very small area in one clast mantling two nepheline crystals.

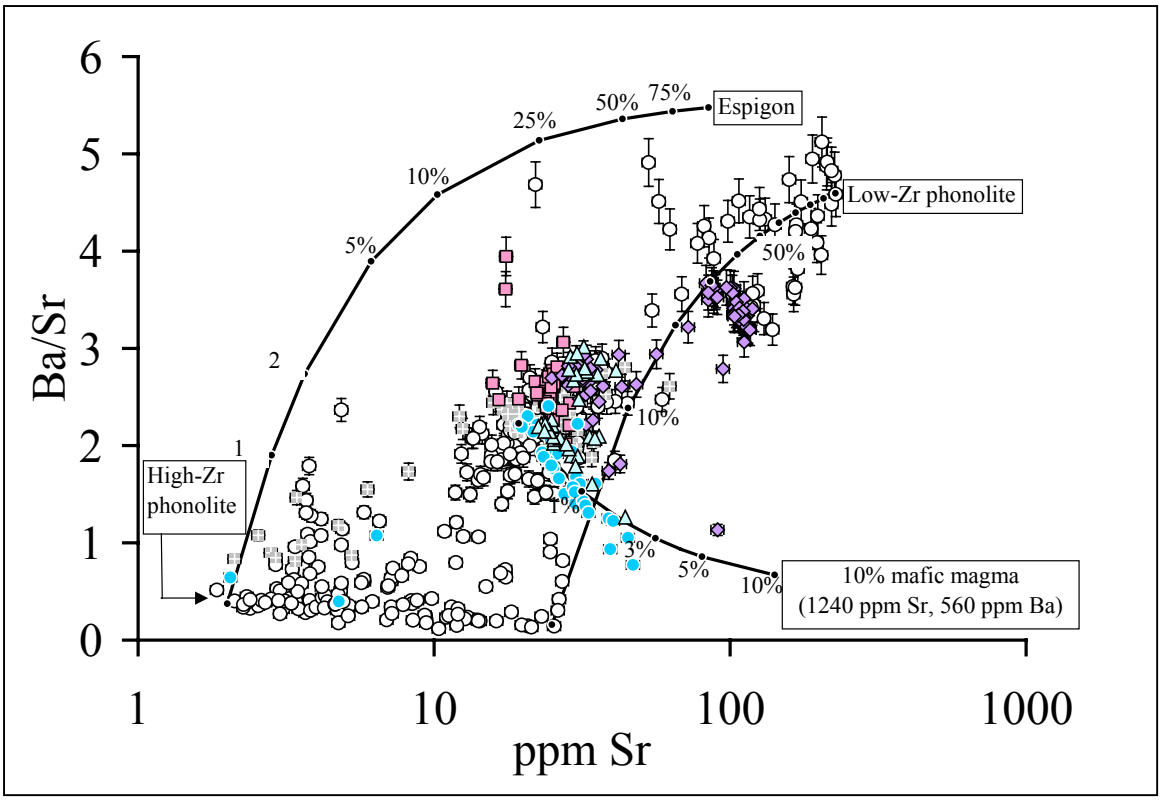

Figure 3.18: Ba/Sr vs. Sr for Fasnia glasses. Three possible mixing lines are also shown. These elements are controlled primarily by feldspar.

Figure 3.18 shows Ba/Sr vs. Sr, elements controlled by primarily by feldspar. Three mixing lines are also shown between the most evolved high-Zr glasses and the Espigon, the least evolved high-Zr glasses and low-Zr glasses, and hybrid glasses and mafic magma. This figure clearly shows that some Unit N hybrid glasses indeed contain up to 3% admixed mafic magma.

Figure 3.19 shows Th/Ba vs. Zr/Sm, ratios that increase due to feldspar and titanite fractionation, respectively. It is clear that high-Zr magma has fractionated both phases in its history because both ratios are elevated in high-Zr glasses, however the strong sharp increase in Th/Ba at Zr/Sm = ~1000 signifies late stage crystallization dominated by feldspar. Positively correlated Th/Ba and Zr/Sm ratios for low-Zr and hybrid phonolite reflect possible co-precipitation of feldspar and titanite in these magmas, but these trends could also arise through magma mixing processes. In summary, trace elements in glasses in the Fasnia support the presence of two distinct phonolitic magmas (high-Zr and low-Zr), mafic magma, and a volumetrically minor DHF III-type phonolite component in the Fasnia magma chamber. All of these magmas have innate chemical heterogeneity. The lower Fasnia glasses reflect a fairly coarse magma mixture of high-Zr phonolite, low-Zr phonolite, and mafic magma. The upper Fasnia glasses reflect a greatly homogenized magma mixture, and although maficmagma is not detectable in significant amounts, trace elements require an admixed mafic component. The presence of a few high-Zr glasses reveals that the mixing is still incomplete at fine scales.

Eruption style and degree of mingling

Changes associated with textural and compositional attributes of the Fasnia magma system appear to play an important role in the different styles of eruption

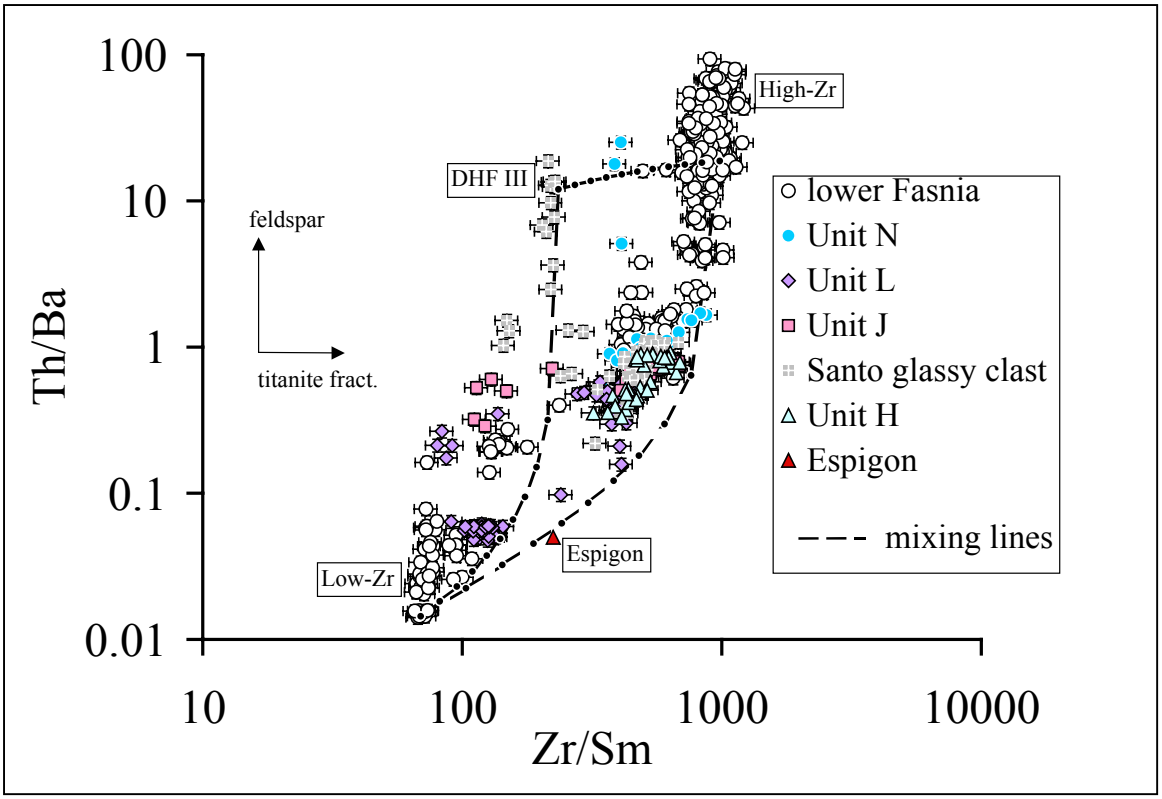

Figure 3.19: Th/Ba vs. Zr/Sm for Fasnia glasses. Three possible mixing lines are also shown. Increasing Th/Ba is attributed to feldspar fractionation, increasing Zr/Sm is attributed to titanite fractionation.

recorded in the Fasnia stratigraphy. Considered at the deposit, clast, and intraclast scales, these sources of data reveal an initially chaotic magma chamber erupting during lower Fasnia time that after the hiatus has transitioned to a more homogenous state reflected in the deposits and geochemistry.

The Fasnia eruption initiated with a phreatomagmatic eruption of ~1.38 km^3 DRE of highly evolved high-Zr phonolite magma as it encountered groundwater at shallow levels. Texturally uniform white pumices in lower Fasnia plinian fallout Units A and B have proven to be chemically distinct, relatively pure high-Zr phonolite. These deposits most likely represent the uppermost portions of magma chamber that has not been significantly contaminated by either low-Zr or mafic magma even though both were probably already present at slightly lower levels. The first signs of low-Zr and mafic magma appears in the 0.1 km^3 DRE Maracay ignimbrite, seen in mingled pumices (~10%) and the structurally and texturally complex Unit D deposits occur during period of greatest geochemical heterogeneity recorded in the entire Fasnia. Unit D represents 0.25 km^3 DRE of chaotically mixed magma of the three end member types, and in fact these magmas are observed juxtaposed. The nature of this eruption was pulsatory, and the deposit is punctuated by up to 80% mingled pumices and high lithic contents. Following Unit D, the small volume Fuento ignimbrite (0.02 km^3 DRE) in deposited. Next, Unit F represents continued chaotic magmatic environment and violent eruption of an additional 0.6 km^3 DRE of coarsely mixed magma. These conditions are reflected in the very complex stratigraphy, abundant mingled clasts, and high lithic contents (up to 30%) of the deposit. Unit F contains the first significant volume of hybrid magma, as well as fairly pure high-Zr and low-Zr phonolite, and mafic magma. It is clear that in Units D and

F, complexity and violence of the eruption is associated with the chaotic nature of the heterogeneous magma mixture. The lower Fasnia climaxes with the voluminous Ravelo ignimbrite, 3 km^3 DRE minimum, which represents a fountaining of magma and lithic debris which spread across most of the island of Tenerife, possibly during an early stage of caldera collapse. The Ravelo contains magma compositions similar to the lower Fasnia, but confident identification and rigorous evaluation of juvenile clasts is hampered due to clear evidence of basal erosion during emplacement and entrainment of clasts from underlying units. The Ravelo not only marks the end of the lower Fasnia eruption, but chaotic conditions represented by deposits like Units D and F are not seen in again in the upper Fasnia. Although these observations suggest a cause and effect relationship between mixing events themselves and eruptive style, and the degree of chemical heterogeneity and eruption style, it is not clear, nor resolvable at this time, which is more important.

The upper Fasnia deposits are characterized by hybrid phonolitic magma and punctuated by a late and limited eruption of low-Zr magma. The upper Fasnia eruption opens with a prolonged plinian phase recorded by the 2.9 km^3 DRE Unit H deposits, although minor eruption instabilities are apparent in the deposits (i.e., surge-like components) and simultaneous pyroclastic flow activity. Unit H is hybridized magma that is both compositionally and texturally homogenous at the clast and intraclast scale, relative to the extremes observed in the lower Fasnia. No mingled clasts are observed, but small (<1-5 mm) mafic clots are seen. Unit H is followed by the ~0.4 km^3 DRE Santo ignimbrite in which pumices of variable compositions and textures are again observed. In fact, the most mafic pumice clast of the upper Fasnia was recovered from this deposit. A

glassy juvenile fragment from the Santo also contains a fourth (albeit minor) magmatic component, evolved DHF III-type magma that has clearly mixed with Fasnia hybrid and high-Zr magma. After the Santo, plinian activity deposited the 1.2 km^3 DRE Unit J. Unit J is texturally and compositionally similar to Unit H hybridized magma, but low-Zr glasses are detectable. Unit J is capped by the lithic-rich ~0.07 km^3 DRE Cueva ignimbrite. Unit L (1.8 km^3 DRE) plinian activity initiates with the eruption of more hybrid magma in Subunit L1, but within Subunit L2 there is a sharp transition from hybrid magma to a volumetrically limited, but sharp excursion towards low-Zr phonolite. Apart from one clast collected from the Santo, this is the only time that whole pumices of low-Zr phonolite are erupted. This transition is not only compositionally distinct, but corresponding changes in the structure of the deposit and in clast texture also occur. The low-Zr portion of Subunit L2 is well sorted and coarser than earlier erupted portions of the deposit and distinct from all other Fasnia units. The explosivity and exceptional column heights attained during this period (>30 km) were driven by volatile exsolution and dry vent conditions, not phreatomagmatism (Edgar, 2003). The Unit M surge deposits and the Bueno ignimbrite (0.08 km^3 DRE combined) represent the initiation of the progressive return to hybrid and more evolved magma compositions. These deposits are uniform in appearance and whole-rock chemistry. The plinian fall out deposits of Unit N (1.4 km^3) continue the trend towards more evolved compositions (i.e., higher Zr and Th; Fig. 3.11). Although Unit N whole-rocks primarily represent hybrid magma, relatively unadulterated high-Zr glasses are detected. Trace elements from the population of hybrid glasses show signs of contamination by mafic magma. The Atogo ignimbrite is the last primary deposit in the stratigraphy and represents a dramatic end to the Fasnia

eruption. The 0.05 km^3 DRE Atogo is very similar to the much more voluminous Ravelo ignimbrite. Both deposits have very high lithic contents and a high degree of internal complexity. Evaluation of Atogo juvenile clasts is similarly problematic, but a range in magma compositions are suggested by a few whole-rocks from the Atogo that have Zr contents from ~1000-2000 ppm.

Discussion

Fasnia magma mixing

The many scales of observable chemical heterogeneity within the Fasnia Member exemplify the complexity of magmatic processes associated with DHF volcanism. Both whole-rock and microscale LA-ICP-MS geochemical data clearly reflect open behavior of the Fasnia magma system. The observed chemical variations require two distinct phonolitic magmas that are variably mixed with one another and with a third mafic magma. The evolved DHF III component in the Santo glassy clast appears to be volumetrically insignificant. The phonolitic magmas are in fact representative of two either long-lived or repeatedly generated evolved felsic lineages (DHF I/II and DHF III) that cannot be genetically related by simple crystal fractionation processes (Edgar et al., 2002; Wolff et al., 2000). The dominant Fasnia magma type is DHF I-type high-Zr phonolite. Low-Zr phonolite is most consistent with the DHF III lineage and is a significant component in the 268 ka Poris Member. Low-Zr phonolite is likely parental to more evolved DHF III magmas erupted later in the DHF, in the Cruz Sequence and Abrigo Member.

Most geochemical diagrams presented throughout the paper require three compositional end members. Almost none of the whole-rocks presented here represent

any of the pure end member magmas, rather most are mixtures of the two phonolites or are ternary mixtures. Viewed in isolation, the LA-ICP-MS glass data could be misinterpreted as representing a fractionation relationship between the low-Zr and high-Zr magma, corresponding to ~3% titanite in the fractionating assemblage. However, relationships between whole-rock major and trace element contents, chemostratigraphy, and pumice textures supports mixing between these two different magmas as the dominant process.

Relating chemistry back to the deposits

Perhaps one of the most striking features of the Fasnia eruption is the progression from the early-erupted, coarsely-mixed heterogeneous tri-modal magma, to a more greatly homogenized, fairly hybridized voluminous magma erupted during the upper Fasnia. The lower Fasnia Units B, D & F are dominated by thin, bedded, and often lithic-rich deposits that represent small volume, pulsatory plinian eruptions (Edgar, 2003), and within Units D & F are abundant coarsely mingled clasts exhibit chemical heterogeneity on the cm^3 scale. On the other hand, post hiatus upper Fasnia Units H & J are thick, voluminous, continuous, stratified plinian deposits (Edgar, 2003) which are geochemically restricted to hybrid compositions and erupted in a geochemically random order. This suggests that the state of the magma body itself fundamentally changed from lower Fasnia time to upper Fasnia time, and this change took place during the eruption hiatus. The magma chamber was probably mixing by vigorous convection, and not enough time passed to reestablish compositional zoning in the chamber before initiation of the upper Fasnia eruption. The geochemical and textural transition in Unit L from H- and J-like hybrid magma to a distinctly different thick voluminous plinian deposit

associated with an influx of relatively homogenous low-Zr phonolite implies a link between the style of eruption and magma composition. The low-Zr magma in Unit L probably represents the evacuation of deep, unmixed portions of the Fasnia system, perhaps in response to caldera forming processes.

In summary, this relationship in the Fasnia between composition, the degree of chemical homogeneity, and style of eruption is very interesting. It is possible that the early pulsatory activity recorded in the lower Fasnia deposits is a response to the coarse heterogeneous mixture in the conduit, but high lithic contents in some beds and the recurrence of accretionary lapilli throughout the lower Fasnia indicate other possible influences, i.e., vent and conduit erosion, and the influx of water (Edgar, 2003). Although phreatic and lithic influences are still apparent in the upper Fasnia deposits (Edgar, 2003), the periods of sustained high plinian activity recorded by these deposits are consistent with the eruption of a fairly homogenized magma (both hybrid and low-Zr phonolite) in which all components, especially volatile species are essentially evenly distributed.

Conclusions

The Fasnia Member represents an eruption dominated by mixed phonolitic and mafic-intermediate magmas. The two phonolitic end members (high-Zr and low-Zr) are distinct both chemically and genetically, but these components cannot be fully resolved by whole-rock analytical methods. LA-ICP-MS not only resolves the end members, but it also reveals the chemical heterogeneity within each end member magma.

The chemical and textural features of the Fasnia pumices and the structure of the plinian deposits suggest a relationship between eruptive style and degree of chemical heterogeneity. The eruption of the Fasnia progressed from early pulsatory plinian

eruptions of poorly mixed magma to prolonged high plinian eruptions of the hybridized magma, to distinctive fairly homogenous low-Zr phonolite. The late and progressive return to hybrid magma in the Fasnia indicates the continued presence or generation of hybrid magma at depth, in which traces of slightly modified high-Zr phonolite and mafic-intermediate magma are identifiable.

Based on the physical, textural, geochemical, and chemostratigraphic complexities observed, the Fasnia is justifiably the most interesting deposit in the Diego Hernández Formation and on all of Tenerife.

References

Branney, M.J., Kokelar, P., 2002. Pyroclastic density currents and the sedimentation of ignimbrites. Geol. Soc. Mem. 27, 143p.

Brown, R.J., Branney, M.J., 2004a. Event stratigraphy of a caldera-forming ignimbrite eruption on Tenerife: the 273 ka Poris Formation. Bull. Volcanol. 66, 392-416.

Cameron, K.L., Cameron, M., 1986. Whole-rock/groundmass differentiation trends of rare earth elements in high-rhyolites. Geochim. Cosmochim. Acta 50, 759-769.

Cashman, K.V., Sturtevant, B., Papale, P., Navon, O., 2000. Magmatic fragmentation. In: Sigurdsson (Ed.), Encyclopedia of Volcanoes. Academic Press, pp. 421-445.

Danckwerts, P.V., 1952. The Definition and Measurement of Some Characteristics of Mixtures. Appl. Sci. Res., A3, 279-296.

Edgar, C.J., Wolff, J.A., Nichols, H.J., Cas, R.A.F., Martí, J., 2002. A complex Quaternary ignimbrite-forming phonolitic eruption: The Poris Member of the Diego Hernandez Formation (Tenerife, Canary Islands). J. Volcanol. Geotherm. Res. 119, 99-130.

Edgar, C., 2003. The Stratigraphy and Eruption Dynamics of a Quaternary Phonolitic Plinian Eruption Sequence, The Diego Hernandez Formation, Tenerife, Canary Islands (Spain). PhD thesis, Monash University, Australia, 264 pgs.

Edgar, C., Wolff, J.A., Olin, P.H., Nichols, H.J., Pitarri, A., Cas, R.A.F, Reiners, P.W., Spell, T.L., Martí, J., 2007. The late Quaternary Diego Hernandez Formation, Tenerife: a cycle of repeated voluminous explosive phonolitic eruptions. J. Volcanol. Geotherm. Res. 160, 59-85.

Folch, A., Codina, R., Martí, J., 2001. Numerical modeling of magma withdrawal during explosive caldera-forming eruptions. J. Geophys. Res. 106, 163-175.

Folch, A., Martí, J., 1998. A numerical model for temporal variations during explosive central-vent eruptions. Annales Geophysicae 16, suppl. 1, p. 188.

Fowler, S.J., Bohrson, W.A., Spera, F.J., 2004. Magmatic evolution of the Skye igneous centre, western Scotland; modelling of assimilation, recharge and fractional crystallization. J. Petrol. 45, 2481-2505.

Graham, D.W., Lupton, J.E., Spera, F.J., Christie, D.M., 2001. Upper-mantle dynamics revealed by helium isotope variations along the southeast Indian ridge. Nature 409, 701-703

Hildreth, W., 1979. The Bishop Tuff: evidence for the origin of compositional zonation in silicic magma chambers. Geol. Soc. Am., Spec. Pap., 180, 43-75.

Hildreth, W., 1981. Gradients in Silicic Magma Chambers: Implications fro Lithospheric Magmatism. J. Volcanol. Geotherm. Res. 86, 10153-10192.

Johnson, C.M., 1989. Isotopic zonations in silicic magma chambers. Geology 17, 1136-1139.

Knesel, K.M., Davidson, J.P., 1997. The origin and evolution of large-volume silicic magma systems; Long Valley Caldera. Inter. Geol. Rev. 39, 1033-1052.

Le Bas et al., 1986. A Chemical Classification of Volcanic Rocks Based on the Total Alkali-Silica Diagram. J. Petrol. 27 (3), 745-750.

Lipman, P.W., 1967. Mineral and chemical variations within an ash-flow sheet from Aso Caldera, South Western Japan. Contrib. Mineral. Petrol. 16, 300-327.

McBirney, A.R., 1968. Compositional variations of the climactic eruption of Mount Mazama. Oregon Dept. of Geol. & Min. Ind. Bull., p.53-56.

Neumann, E.-R., Wulff-Pedersen, E., Simonsen, S.L., Pearson, N.J., Martí, J., Mitjavila, J., 1999. Evidence for fractional crystallization of periodically refilled magma chambers in Tenerife, Canary Islands. J. Petrol. 40, 1089-1123.

Nichols, H.J., 2001. Petrologic and geochemical variation in a caldera-forming ignimbrite: the Abrigo Member, Diego Hernández Formation, Tenerife, Canary Islands (Spain). MSc thesis, Washington State Univ., USA, 126 pp.

Oldenburg, C.M., Spera, F.J., Yuen, D.A., Sewell, G., 1989. Dynamic Mixing in Magma Bodies: Theory, Simulations, and Implications. J. Geophys. Res. 94, 9215-9236.

Pitarri, A., 2004. Eruption dynamics and emplacement processes for the climactic Abrigo Member, Tenerife, Canary Islands. PhD thesis, Monash Univ., Australia, 327 pp.

Smith, R.L., Bailey, R.A., 1966. The Bandelier Tuff: study of ash-flow eruption cycles from zoned magma chambers. Bull. Volcanol., 29, 83-104.

Smith, R.L., 1979. Ash-flow magmatism. Geol. Soc. Am., Spec. Pap., 108, 5-27.

Spera, F.J., 1984. Some numerical experiments on the withdrawal of magma from crustal reservoirs. J. Geophys. Res. 89, 8222-8236.

Storey, M., Wolff, J.A., Norry, M.J., Marriner, G.F., 1989. Origin of hybrid lavas from Agua de Pau Volcano, Sao Miguel, Azores. Geol. Soc. Spec. Publ., 42, 161-180.

Taylor, G.I., 1935. Statistical Theory of Turbulence. Proc. R. Soc. London, Ser. A, 151, 421-478.

Tegtmeyer, K.J., Farmer, G.L., 1990. Nd isotopic gradients in upoper crustal magma chambers; evidence for in situ magma-wall-rock interaction. Geology 18, 5-9.

Troll, V.R., Schmincke, H.R., 2002. Magma mixing and crustal recycling recorded in ternary feldspar from compositionally zoned peralkaline ignimbrite "A," Gran Canaria, Canary Islands. J. Petrol. 43, 243-270.

Veitch, G., Woods, A.W., 2000. Particle recycling in volcanic plumes. Bull. Volcanol. 64, 31-39.

Wark, D.A., Hildreth, W., Spera, F.S., Cherniak, D.J., Watson, E.B., 2007. Pre-eruption recharge of the Bishop magma system. Geology 35, 235-238.

Wolff, J.A., Storey, M., 1984. Zoning in highly alkaline magma bodies. Geol. Mag., 121, 563-575.

Wolff, J.A., 1985. Zonation, mixing and eruption of silica-undersaturated alkaline magma: a case study from Tenerife, Canary Islands. Geol. Mag. 122, 623-640.

Wolff, J.A., 1985b. The effect of explosive eruption processes on geochemical patterns within pyroclastic deposits. J. Volcanol. Geotherm. Res. 26, 189-201.

Wolff, J.A., Ramos, F.R., 2003. Pb isotopic variation among Bandelier Tuff feldspars: No evidence for a long-lived silicic magma chamber. Geology 31, 533-536.

Chapter 4

Deciphering crystal transfer in magmas using trace elements: constraints from REE partitioning of the Fasnia Member pyroxenes

Abstract

Four compositionally distinct clinopyroxene populations are found in the phonolitic Fasnia Member. Titanaugites are associated with the minor mafic magmatic component, Ti-salites grew in transitional tephriphonolitic to phonolitic magma, salites grew in low-Zr phonolite magma, and Na-salites grew in hybrid phonolite magma with higher Zr contents. Using ~500 phonolitic glass analyses from Fasnia pumices, parental glasses have been identified for the salite and Na-salite populations by applying the lattice strain model equation of Blundy and Wood (1994) for crystal-liquid partitioning of REE in pyroxenes and glasses. Na-salites have HREE contents that do not match simple model predictions, but can be modeled if the REE are present in two coordination states, i.e., eight- and six-fold coordination. REE are typically modeled to substitute for ^{VIII}Ca in the pyroxene M2 site because ionic radii for the $^{VIII}REE^{3+}$ (1.16 to 0.977 Å) are very similar to the preferred ionic radius of Ca^{2+} (1.12 Å). Because Fe^{2+} or Mn^{2+} may also occur in M2 in octahedral coordination, especially in the Na-salites with higher Fe and Mn concentrations, REE^{3+} substitution into a M2 site with a preferred ionic radius near $^{VI}Fe^{2+}$ (0.78Å) and ^{VI}Mn (0.83Å) favors $^{VI}HREE^{3+}$ relative to the other $^{VI}REE^{3+}$ (e.g., ^{VI}Lu 0.860 Å). Modeling results support the interpretation that salites crystallized in low-Zr phonolite magma and that Na-salites later crystallized in hybrid phonolite magma that is a product of mixing between low-Zr phonolite and distinct pyroxene-free high-Zr phonolite magma.

Introduction

The Fasnia Member

The 309±6 ka Fasnia Member of the Diego Hernández Formation (ca. 600 to 180 ka; Edgar et al., 2007), Tenerife, represents the explosive eruption of ~13 km^3 of phonolitic magma to produce a geochemically and stratigraphically complex deposit. The Fasnia magma is a mixture between two phonolitic magmas (low-Zr and high-Zr) and a volumetrically minor mafic magma. The geochemistry and amount of mingled pumices change with stratigraphy, representing a transition from a coarse magma mixture resulting in abundant mingled clasts to a relatively homogenous hybrid phonolite erupted as uniform white to gray pumices. End member components are identifiable on the basis of glass and whole-rock geochemistry (see Ch. 3).

Pyroxenes

Pyroxenes from Tenerife span a large compositional range, from chrome diopside in primitive basalts to aegirine in syenites (Scott, 1976). Neumann et al. (1999) investigated pyroxenes of different ages and from different parts of Tenerife and in their study they identified different compositional groups including Al-salites and Na-salites and concluded that the pyroxenes studied recorded processes of fractional crystallization in magma chambers that experienced periods of recharge.

The phonolitic Fasnia Member contains four different pyroxene compositional groups that have geneses in distinct parental magmas. On the basis of major element contents, many of the Fasnia pyroxenes are nearly identical to the groups observed in the Tajao ignimbrite (Wolff, 1985) of the 319±5 ka Aldea Member (Edgar et al., 2007). Using petrographic and compositional evidence, Wolff (1985) assigned each of the

groups to mafic, intermediate or phonolitic magmatic components, respectively. The Fasnia deposits are geochemically and physically similar to the Aldea, but the Fasnia whole-rocks and especially the glasses (Ch.3) clearly show that at least two distinct phonolite magmas and a volumetrically minor mafic magma have mixed and homogenized to varying degrees, resulting in a significant volume of hybrid magma.

This chapter addresses relationships between pyroxenes and the magmatic components identified in the Fasnia Member. The lattice strain model (LSM) of Blundy and Wood (1994), which predicts partition coefficients for trace elements in minerals based on cation radius and the Young's Modulus for the lattice site of substitution, is used to identify suitable pyroxene-glass pairs for salite and Na-salite pyroxenes by comparing the model fit for each pyroxene and ~500 potential parental glasses. However, because the model does not predict elevated HREE contents observed in the Na-salites, the LSM is also used to consider rare earth elements (REE) in other than the 8-fold coordination state. This modeling approach reasonably replicates observed HREE enrichment in Na-salites and can be applied to other iron-rich pyroxenes (e.g., hedenbergites from the Bandelier Tuff, New Mexico, and aegirine and aegirine-augites from the Illimaussaq alkaline intrusion, Greenland (Marks et al., 2004).

Analytical Methods

Fasnia pyroxenes were analyzed for major elements using the Cameca electron microprobe in the Washington State University GeoAnalytical Laboratory. The instrument was operated at 15kv, using a spot diameter of ~4 microns and a beam current of 12nA.

Trace element concentrations in pyroxenes and glasses were acquired using LA-ICP-MS methods developed at Washington State University. Pyroxene grains were either analyzed *in situ* in polished pumice petrographic sections, or where few to no grains were exposed this way, pumice was crushed and sieved, and the crystals recovered were prepared as grain mounts. Glass was analyzed *in situ* in pumice polished sections. The analyses were performed using a New Wave UP213 Nd:YAG laser ablation system coupled to a ThermoFinnigan Element2 mass spectrometer. The laser troughs are 8-16 microns wide, and 0.5-1 mm long. The laser fluence was ~12 J/cm^2, the firing rate 20 Hz, and He was used as the carrier gas. Elemental concentrations were determined by normalizing averaged and background-corrected counts per second (cps) data to ^{29}Si cps and wt% SiO_2 in the target (see Chapter 1). Glasses BCR-2g and Nist610 were used for daily instrument tuning, offline calibration and data reduction. All LA-ICP-MS data for cpx and glasses are in the Appendices.

Petrography

Four type of pyroxenes have been identified in the Fasnia; titanaugites, salites, titanium-rich (Ti-) salites, and sodium-rich (Na-) salites. All pyroxene types might be found in a single thin section or grain mount, but differ in appearance. Titanaugites (<1 to 2 mm) are often tan-pink and euhedral to subhedral. They might show zoning and are sometimes observed to mantle green cores of salite and Na-salite. Ti-salites and salites occur as blocky euhedral grains to subhedral fragments with rounded or broken terminations. They are pale green to brownish-green and are <0.5 to 1.5 mm in size. Na-salites are deep green and strongly pleochroic euhedral to subhedral grains. Many grains are elongate and range from <0.5 to 2 mm in length. Na-salites are sometimes associated

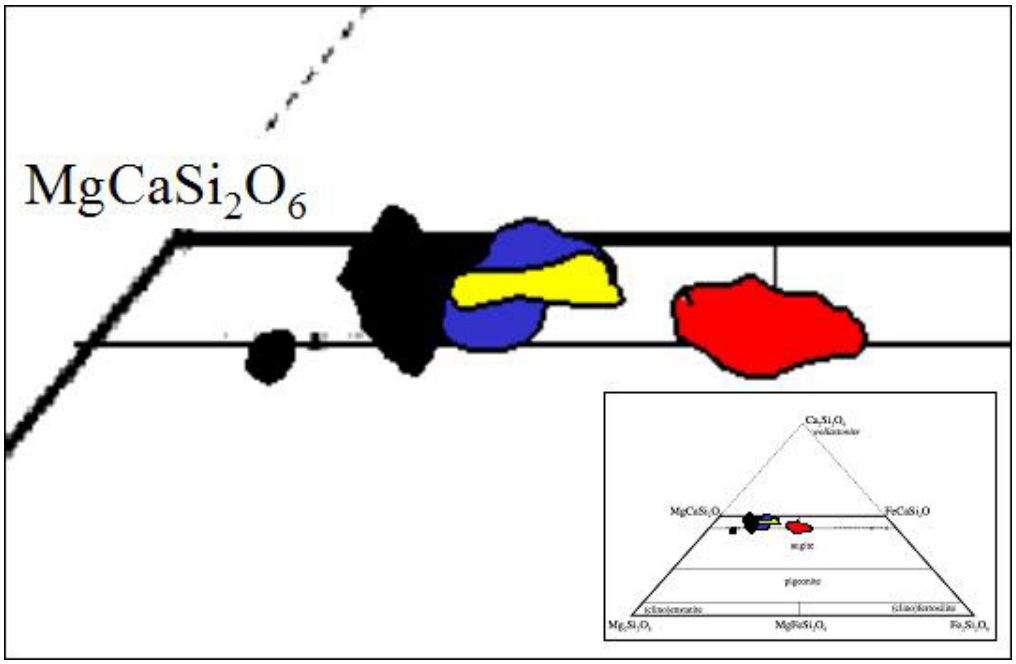

Figure 4.1: Pyroxene quadrilateral (or pyroxene ternary diagram, inset) showing fields for the four (4) pyroxene compositional groups in the Fasnia Member; titanaugites (black), salites (blue), Ti-salites (yellow), and Na-salites (red).

with small euhedral titanite grains either poikilitically enclosed or located along the margins of the Na-salites.

Geochemistry

Major element compositions

The four clinopyroxene compositional groups identified in the Fasnia phonolitic deposits are: salites with low Na, Fe and Mn contents (similar to the Al-salites of Neumann et al., 1999); Na-salites with higher Na, Fe and Mn contents; titanaugites; and a few Ti-salites with Na similar to salites, but with elevated Ti and Al contents. These compositions are plotted on the pyroxene quadrilateral in Figure 4.1. Titanaugites are consistent with the presence of a mafic magmatic component. Titanaugites have low Na_2O (<1 wt%) and a range in Mg# from 74 to 87 (Fe* as FeO). Al_2O_3 and TiO_2 contents are strongly correlated reflecting Tschermak's substitutions (Fig. 4.2). The salites have a relatively narrow range in Mg# from 70.7 to 76.1 and Na_2O contents from 0.69 to 1.23 wt%. Al_2O_3 and TiO_2 contents range from 1.98 to 3.62 wt% and 0.77 to 1.63 wt%, respectively. Ti-salites have 0.75 to 1.34 wt% Na_2O, similar to the other salites, but Ti-salites have higher TiO_2 and Al_2O_3, 2.85 to 3.30 wt% and 6.06 to 7.28 wt%, respectively. Ti-salites have a range in Mg# from 65.2 to 70.4. Although few Ti-salites have been observed, they are important because they could indicate an additional volumetrically minor magmatic component. Na-salites are clearly set apart from the other pyroxenes by higher Na_2O contents, 1.59 to 2.47 wt%, and lower Mg#, 48.2 to 59.3. Al_2O_3 and TiO_2 contents overlap the salites, but also extend to lower values, 1.33 to 2.75 wt% and 0.42 to 1.14 wt%, respectively.

Major-element oxides are stoiciometrically recast on the basis of four cations per 6-oxygen formula unit (pfu; Figs. 4.2 and 4.3). Because Na contents in pyroxene generally increase with degree of melt evolution, Na is used as an index of fractionation. Total Fe (Fe^T) is partitioned into Fe^{3+} and Fe^{2+} by setting Fe^{3+} equal to Na. For all the pyroxenes investigated here, Na is generally positively correlated with Fe^T, Mn, and Si (Fig. 4.2), and negatively correlated with Ca, Mg, Al, and Ti (Fig. 4.3). Al and Ti trends are strongly correlated and antithetical to Si, consistent with differing amounts of Tschermak's substitutions.

Titanaugites have the least evolved compositions (i.e., low Na and high Mg), consistent with crystallization in mafic to intermediate magmas (Fig. 4.2). Ti-salites have similar Si (1.68 to 1.73 pfu), Al (0.27 to 0.32 pfu), and Ti (0.081 to 0.092 pfu) contents to some titanaugites, but they also have Na contents (0.056 to 0.099 pfu) like the salites (0.050 to 0.088 pfu). Ti-salites have lower Mg (0.60 to 0.66 pfu), and higher Fe (0.28 to 0.33 pfu) when compared to salites. Na has the greatest range in Ti-salites and other elements vary neither significantly nor systematically over this range. Salites have 1.83 to 1.92 pfu Si, 0.087 to 0.160 pfu Al, and 0.022 to 0.046 pfu Ti. Salites have 0.70 to 0.76 pfu Mg, similar to titanaugites, 0.23 to 0.29 pfu Fe^T, between titanaugites and Ti-salites, and 0.013 to 0.019 pfu Mn, higher than titanaugites and Ti-salites. Fe^T and Mn are weakly positively correlated with Na, and although significant variation is observed in other elements, contents do not vary systematically with Na (apart from Ca). Na-salites have the highest Na and Mn contents of the pyroxenes, 0.12 to 0.18 pfu and 0.035 to 0.047 pfu, respectively. Na-salites also have the lowest Al and Ti contents.

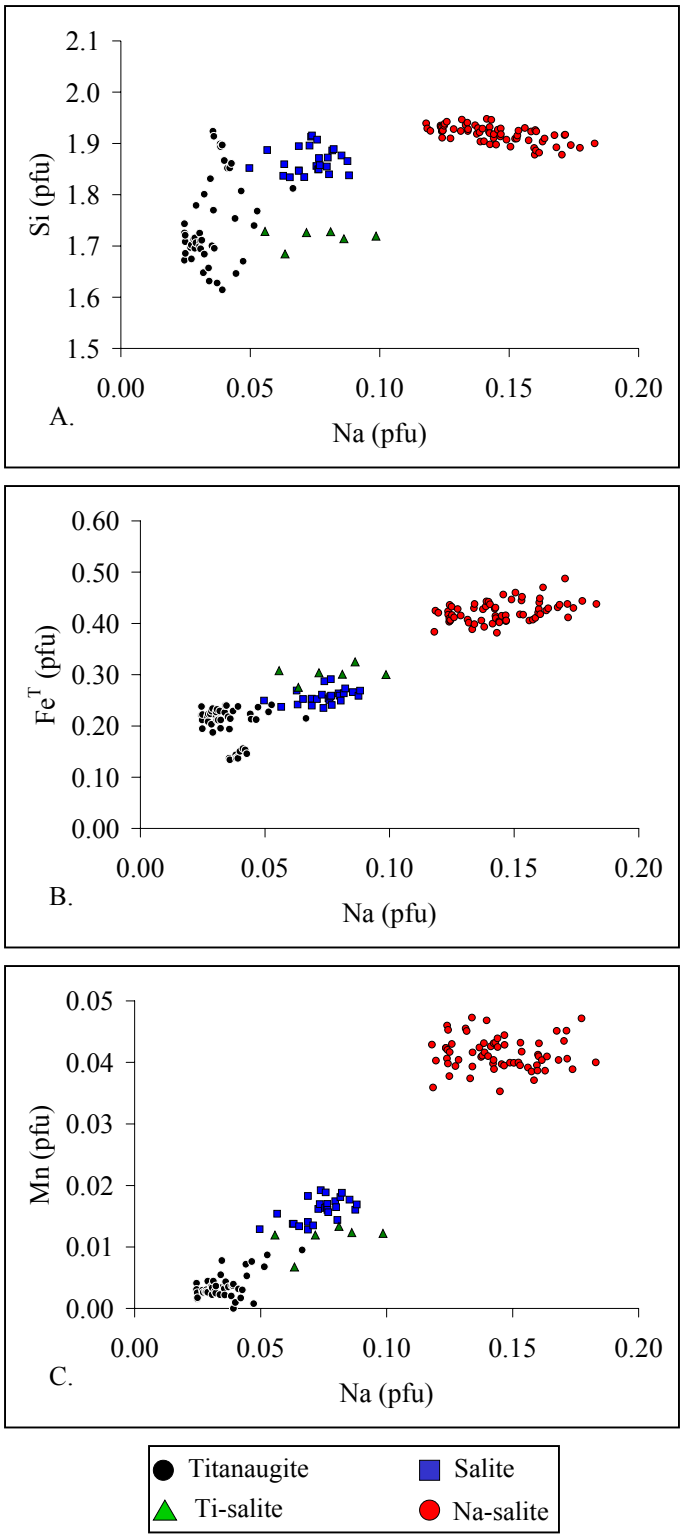

Figure 4.2: Pyroxene major element cations stoiciometrically recast on the basis of four cations per 6-oxygen formula unit (pfu).

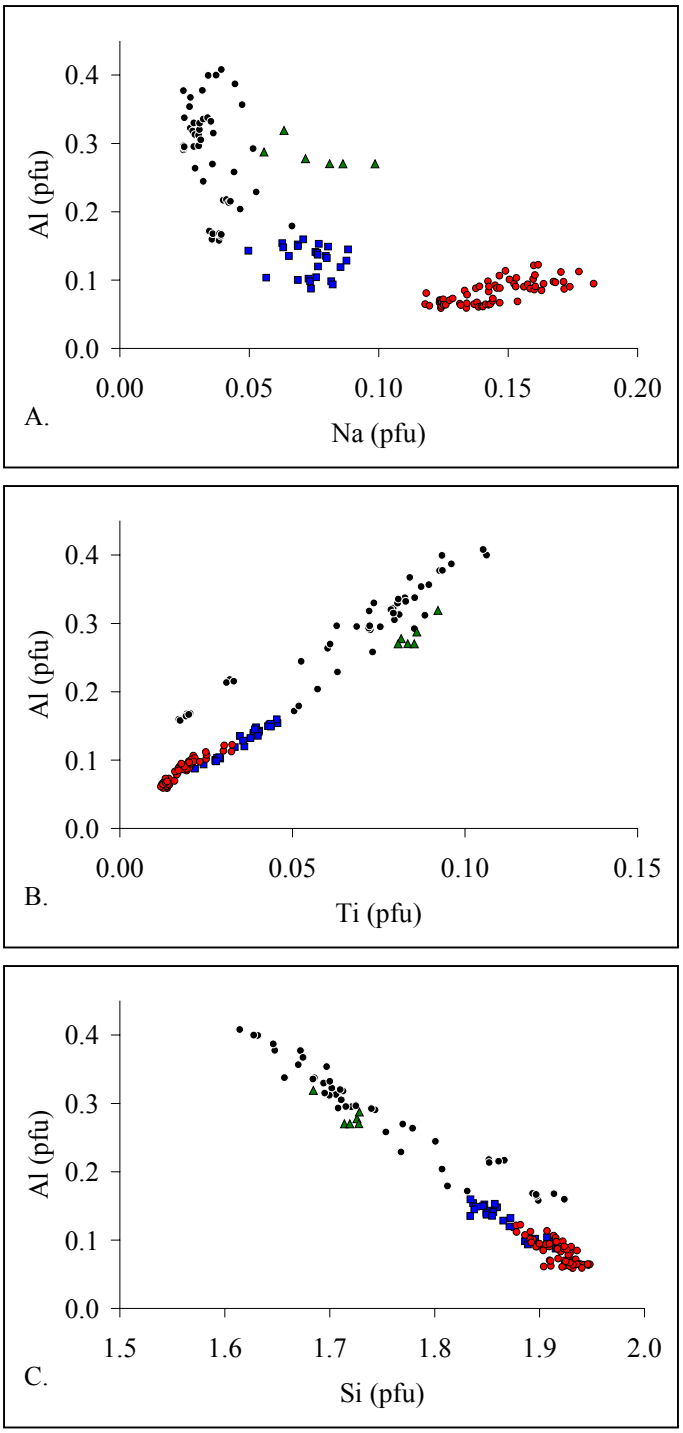

Figure 4.2 continued.

As Na increases in the Na-salites, so do Al contents (Fig. 4.2). Si is antithetical to Al and Ti. Ca and Mg decrease with increasing Na and Fe^T, but Mn does not vary systematically with Na.

Si/Al and Fe/Ti (Fig. 4.3) show very similar behavior. This reflects the relationship between the Ti-Al Tschermak's components and the elements for which they substitute, Si and Fe. In the plot of Fe/Ti versus Si/Al salites, Ti-salites, and titanaugites fall along the same trend, but salites have higher Fe/Ti and Si/Al values. Na-salites form a steeper linear array at slightly higher Fe/Ti values than the other pyroxenes.

Major element structural constraints

Pyroxene has the general formula $[M2][M1][T_2O_6]$. The tetrahedral site (T) is filled with Si and lesser amounts of ^{IV}Al. The M2 polyhedron is larger and always more distorted than M1 (Cameron and Papike, 1980) and will accommodate 6-, 7- and 8-coordinated univalent, divalent and trivalent cations with ionic radii from ~0.72 Å (^{VI}Mg) to ~1.16 Å (^{VIII}Na). Seven-coordination has only been described for some pigeonites (Cameron and Papike, 1980) and is not considered further here. M1 is the smaller of the two cation sites and accommodates divalent, trivalent, and tetravalent cations in octahedral coordination, with ionic radii between ~0.53 Å ($^{VI}Al^{3+}$) and ~0.83 Å (Mn^{2+}). A preference for either M1 or M2 is influenced by anion configuration around each site, and by the ionic radius and electronegativity of the cations (Cameron and Papike, 1980). Larger cations such as ^{VIII}Na (1.18 Å), ^{VIII}Ca (1.12 Å), and ^{VI}Mn (0.83 Å) will prefer M2 over M1 (Robinson, 1980).

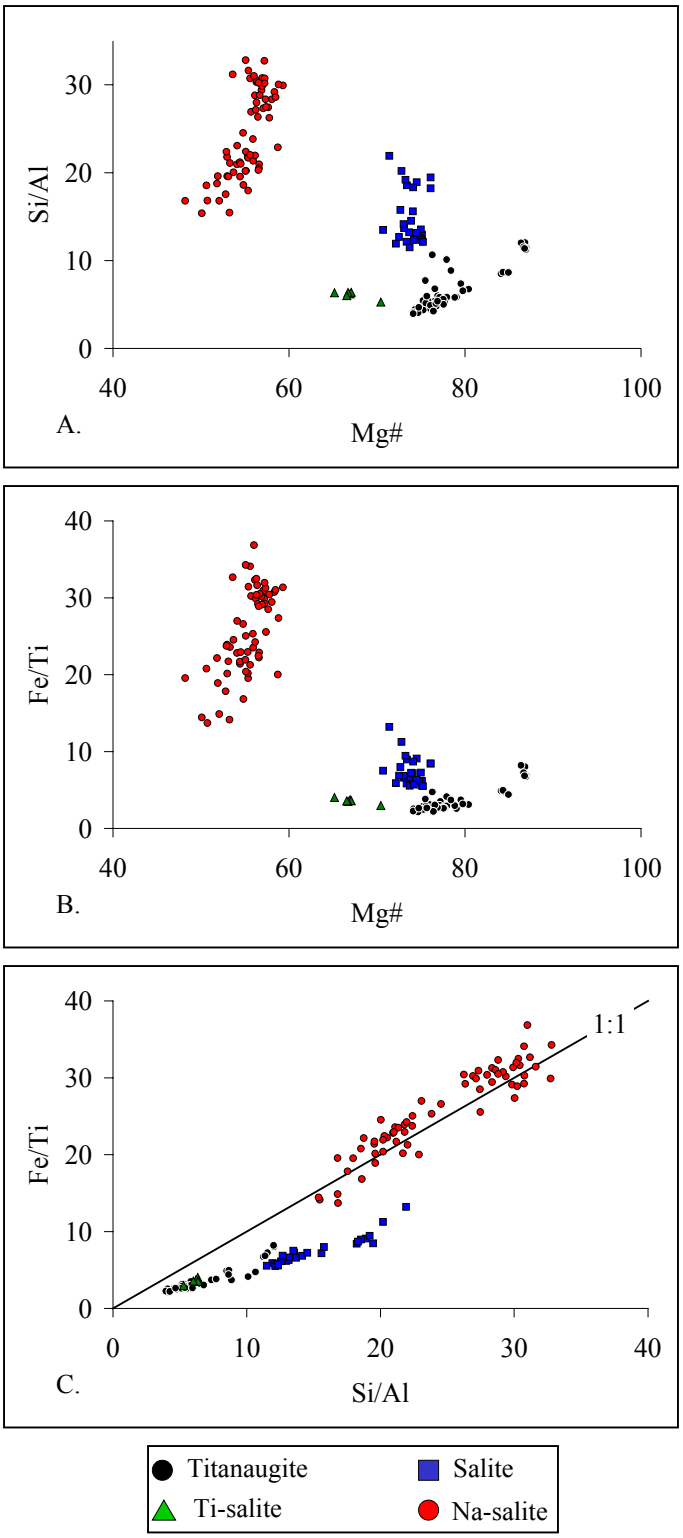

Figure 4.3: Selected cation ratios for Fasnia pyroxenes.

Cation site assignments for the salites and Na-salites require different major element configurations. In both cases, Si and some Al occupy the T-site in tetrahedral coordination, and accordingly Si+Al is approximately equal to two per 6-oxygen formula unit. A shortfall in T-site occupancy could be made up with small amounts of Fe^{3+}, but more likely all Fe^{3+} is in the M1 site (Cameron and Papike, 1980). Al that is not accommodated in the T-site would also occupy M1. In addition to Al and Fe^{3+}, M1 also hosts Ti^{4+} and Mg. A shortfall in M1 occupancy is made up by placing some Fe^{2+} and Mn in the site, and the remaining $Fe^{2+}$and Mn cations are accommodated in M2. It is assumed that Fe^{2+}/Mn ratios in M1 and M2 are the same. In both the M1 and M2 site, Fe^{2+} and Mn are in octahedral coordination. Because of their larger sizes, Na and Ca are assigned to M2 and occur in 8-coordination. When comparing Ti+Mg+Fe^{T}+Mn and Ca+Na for salites and Na-salites (Fig. 4.4), salites require more M2 occupancy of Fe^{2+} and Mn than Na-salites, both on the basis of an overfilled M1 site (i.e., Ti+Mg+Fe^{T}+Mn > 1) and an under filled M2 site (i.e., Ca+Na < 1); For Na-salites, Ca+Na is ~1 and Ti+Mg+Fe^{T}+Mn is ~1 suggesting more limited Fe^{2+} and Mn occupancy in M2 even though the contents of Fe and Mn are greater in the Na-salites.

The lattice strain model of trace element partitioning (Brice, 1975; Blundy and Wood, 1994) employed below depends on clinopyroxene structural elements that are related to its chemistry (Wood and Blundy, 1997). Most experiments constraining the model have used calcic pyroxenes with Mg contents consistent with basaltic environments (Hauri et al, 1994; Blundy and Wood, 1994; Wood and Blundy, 1997; Hill

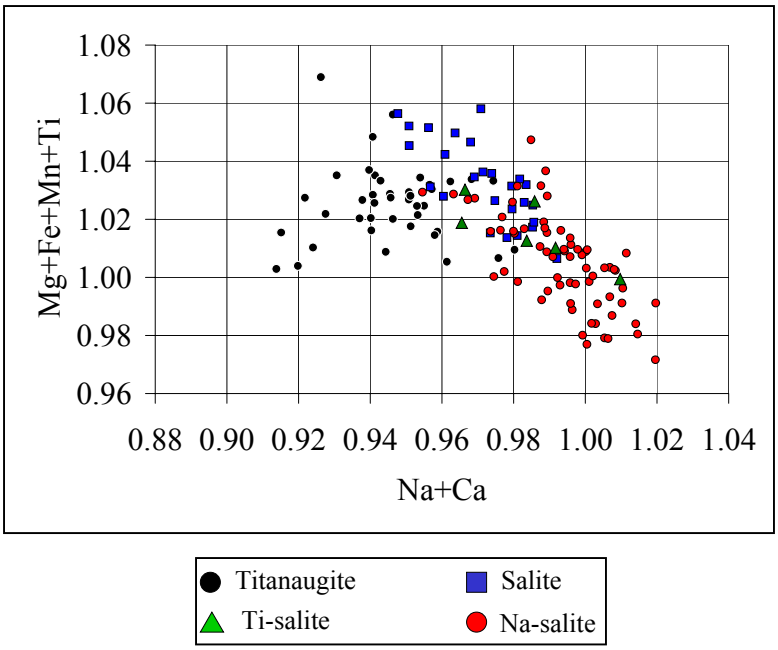

Figure 4.4: Sums of selected cations according to likely site occupancy; M1-site=Mg+Fe+Mn+Ti; M2-site=Na+Ca.

et al., 2000), but as pyroxene compositions becomes more Na- and Fe-rich, and to an extent Mn-rich, the structure changes to accommodate the larger ionic radii of these elements (Cameron and Papike, 1980). In turn, these structural changes must have consequences for trace element partitioning behavior. Trace element differences between the salite and Na-salite populations likely reflect the effects of increasing iron because salites (with low Na, Fe, and Mn) have REE patterns similar to the titanaugites, but at higher concentrations, and Na-salites (with elevated Na, Fe and Mn) have HREE enriched patterns (Fig. 4.5).

Trace element compositions

There are four trace element compositional groups in the Fasnia that correspond to the titanaugite, salite, Ti-salite, and Na-salite populations. Zr contents generally increase with Na_2O (Fig. 4.6), and analogous to Na, Zr is used with the trace element data as an index of fractionation. Titanaugites have low Zr contents, <258 ppm, and high Sr contents (Fig. 4.6). Titanaugites also have generally low REE and incompatible element contents. Ti-salites have Zr contents from 406 to 503 ppm and high Sr and Ti similar to titanaugites. REE contents for Ti-salites, however, are like the salites except that Ti-salites do not have a negative Eu anomaly (Fig. 4.5). Salites have Zr contents ranging from 222 to 663 ppm. Salites have high REE contents compared to titanaugites, and negative Eu anomalies. Na-salites have Zr contents ranging from 889 to 3411 ppm. Na-salites have strongly MREE depleted patterns with negative Eu anomalies and significant HREE enriched tails.

REE and Y concentrations are shown in Figure 4.7. For the following discussion, La, Sm, and Lu represent LREE, MREE, and HREE behavior, respectively. Ti-salites and

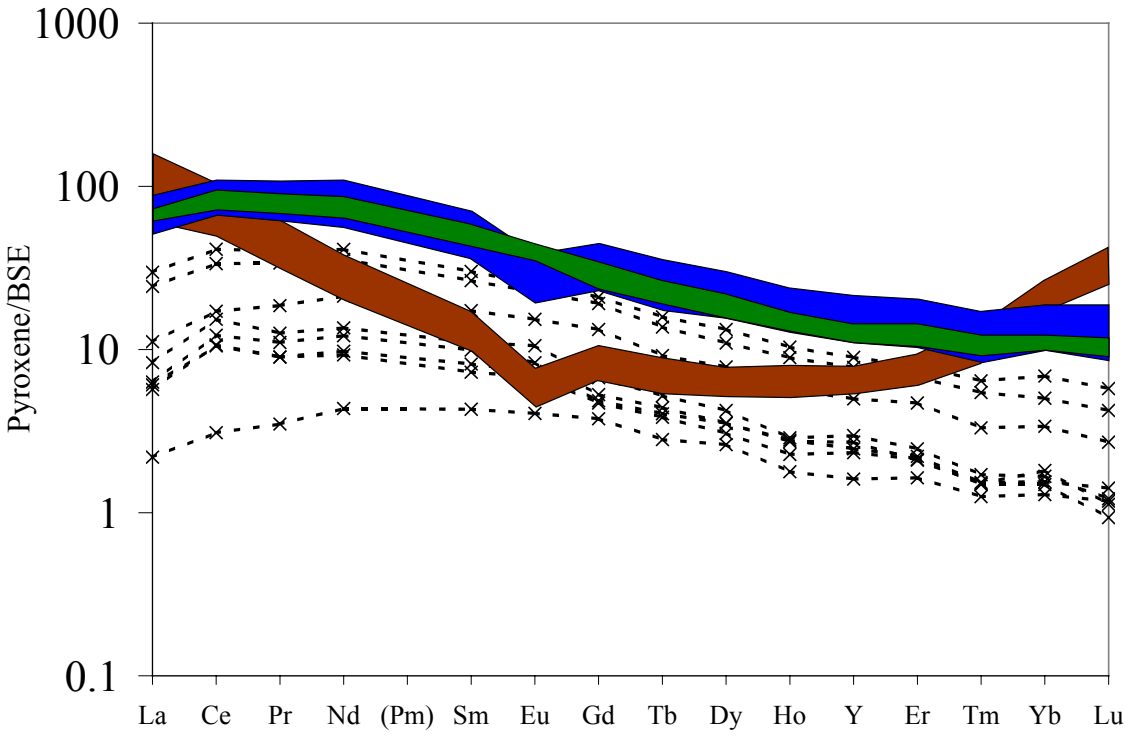

Figure 4.5: REE data for titanaugites (black dashed lines), Ti-salites (green field), salites (blue field), and Na-salites (red field) normalized to Bulk Silicate Earth (BSE; McDonough and Sun, 1995). Note the clear overlap of Ti-salites and salites patterns, but whereas most salites have a negative Eu anomaly, Ti-salites lack this feature.

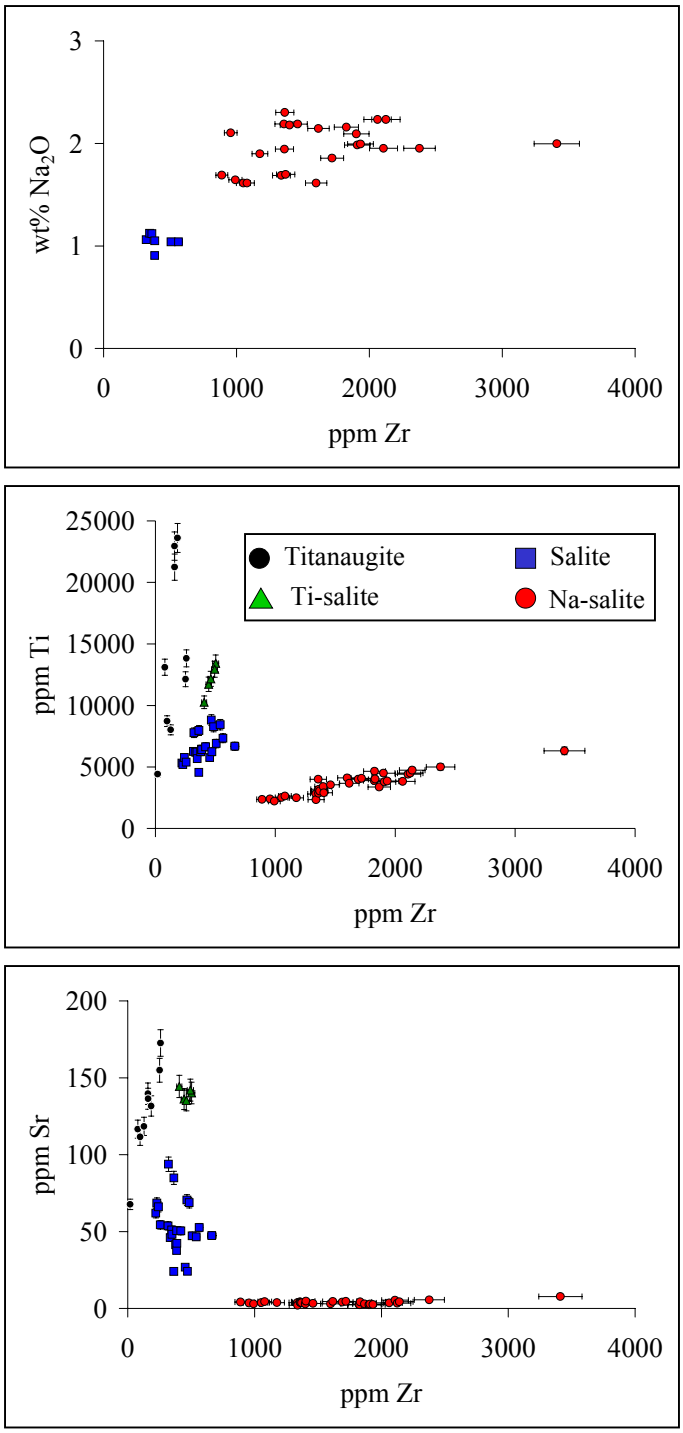

Figure 4.6: Zr, Ti and Sr LA-ICP-MS data for Fasnia pyroxene compositional groups. Na_2O (shown for salites and Na-salites only) is from the microprobe at the same locations as LA-ICP-MS data.

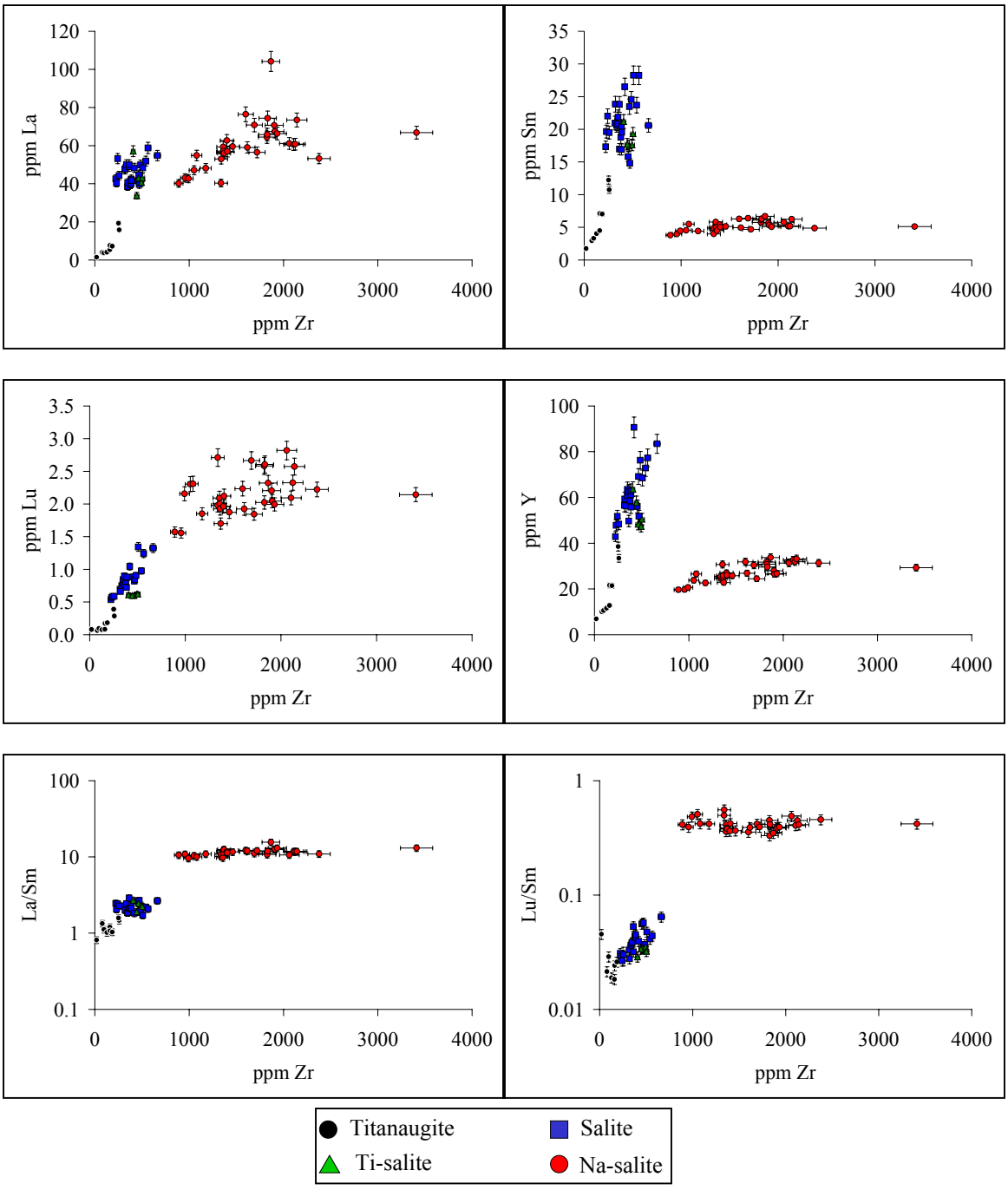

Figure 4.7: REE and Y contents and ratios for pyroxene compositional groups versus Zr.

salites have the following ranges in concentrations for selected REE and Y: La from 38 to 59 ppm; Sm from 15 to 28 ppm; Lu from 0.54 to 1.34 ppm; and Y from 43 to 91 ppm. At higher Zr contents, Na-salites have: La contents from 40 to 104 ppm; Sm contents from 3.8 to 6.7 ppm; Lu contents from 1.56 to 2.82 ppm; and Y contents from 20 to 34 ppm. La does not vary systematically with Zr in salites, but is positively correlated with Zr in Na-salites. In plots that appear very similar, Sm and Y are positively correlated with Zr in salites, but in the Na-salites Y is positively correlated with Zr and Sm does not vary significantly. In salites and Na-salites, Lu and Zr are positively correlated.

La/Sm values are much higher for Na-salites than for salites, but the values do not change significantly with increasing Zr. Lu/Sm values are higher for Na-salites than for salites. Lu/Sm is positively correlated with Zr in salites, but remains fairly constant with increasing Zr in Na-salites. Na-salites are clearly more MREE-depleted than Ti-salites and salites, consistent with crystallization from an evolved phonolitic liquid with a history of titanite fractionation.

High field strength elements (HFSE) show different trends versus Zr (Fig. 4.8). Hf is strongly positively correlated with Zr, reaching concentrations >50 ppm in Na-salites. Nb concentrations in salites range from 1.61 to 3.45 ppm and Ta contents range from 0.28 to 0.73 ppm. Ti-salites have Nb contents from 2.80 to 5.63 ppm and Ta contents from 0.56 to 0.93 ppm, extending to higher values than salites. In Na-salites Nb contents range from 1.51 to 9.98 ppm and Ta contents range from 0.07 to 1.30 ppm. Nb, Ta, and Zr contents are positively correlated with one another within each pyroxene compositional group. A step-like increase of Nb and Ta concentrations in Na-salites at approximately 1350 to 1400 ppm Zr is also accompanied by increasing Ti.

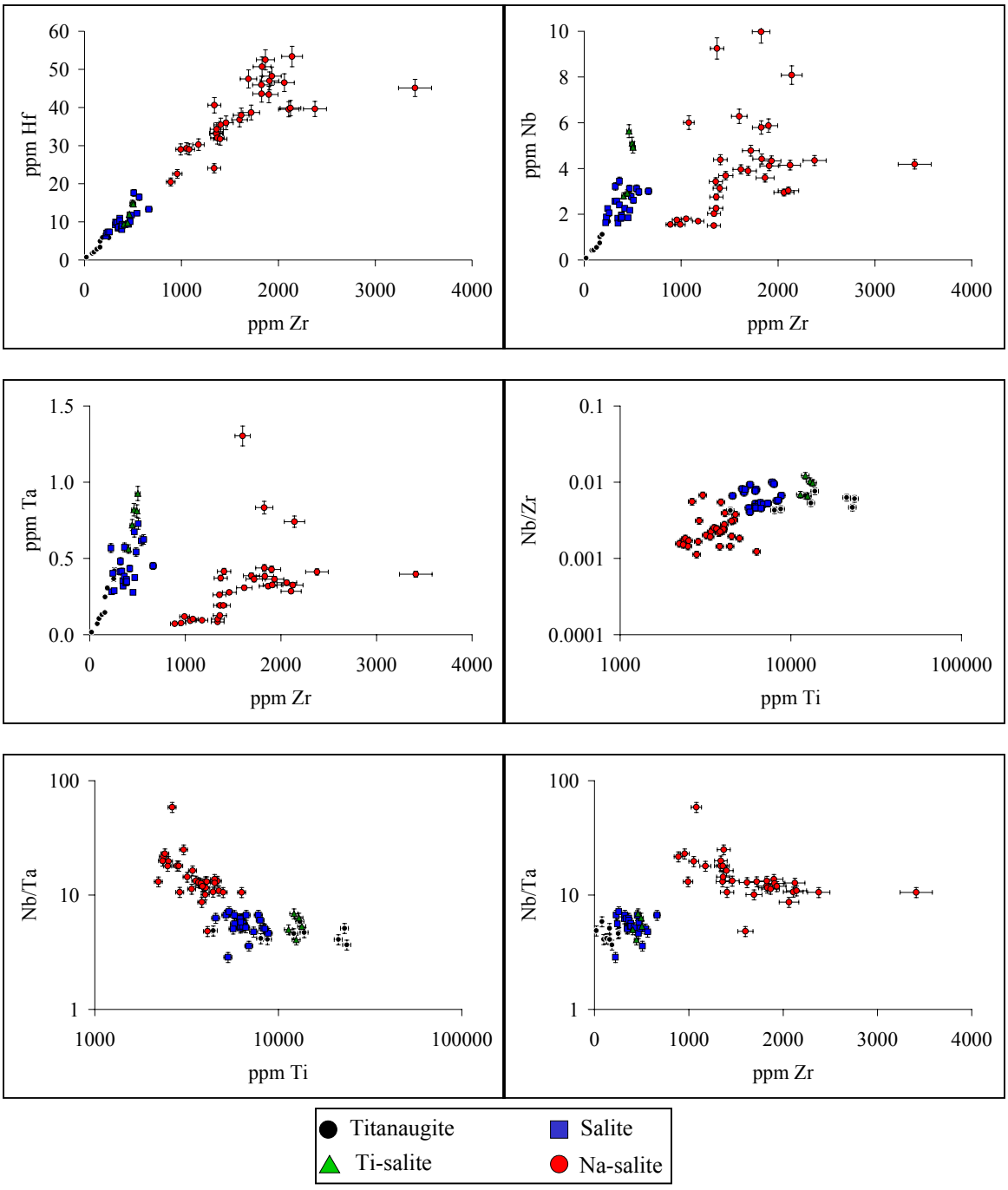

Figure 4.8: HFSE contents and ratios for pyroxene compositional groups versus Zr and Ti.

Contrasting Nb/Zr and especially Nb/Ta values for salites and Na-salites are the result of different histories of titanite fractionation in the parental magmas (Fig. 4.8). Nb/Ta increases with titanite removal while Nb/Zr decreases. Nb/Ta does not seem to vary systematically in salites, but decreases overall in Na-salites with increasing Zr and Ti contents. Between approximately 1350 and 1400 ppm Zr, Nb/Ta in Na-salites distinctly steps to lower values as Ti contents show a step-like increase (Figs. 4.6 and 4.8). This must be a structural effect since Nb/Ta is increasing in the liquids.

Plots of Zr/Ti and Nb/Ta versus La/Sm (Fig. 4.9) clearly distinguish salites from Na-salites. Salites have low La/Sm and Zr/Ti values contrasting with the elevated values for Na-salites. Nb/Ta overlaps slightly.

Trace element partitioning between pyroxenes and glasses

REE partitioning model

The lattice strain model (LSM) of Blundy and Wood (1994) postulates that for a series of cations of like charge (i.e., 3+ for REE), with radius r_i, the partition coefficient D_i for an element entering a crystal lattice site M can be related by three parameters: r_0, the preferred radius of the site; E_M, the Young's modulus of the site, which determines the elastic response of the site to strain caused by site-size mismatch; and D_0, the fictive strain-compensated partition coefficient for an ion with radius r_0. This relationship is expressed as follows (Blundy and Wood, 1994),

$$D_i = D_0 * \exp\{-4\pi E_M N_A [r_0(r_i - r_0)^2/2 + (r_i - r_0)^3/3]/RT\} \quad (1)$$

where N_A is Avogadro's Number, R is the ideal gas constant, and T is temperature in Kelvin. This equation is most often plotted as partition coefficient versus ionic radius, producing a parabolic distribution (Fig. 4.10). The partition coefficient D_0 for cation with

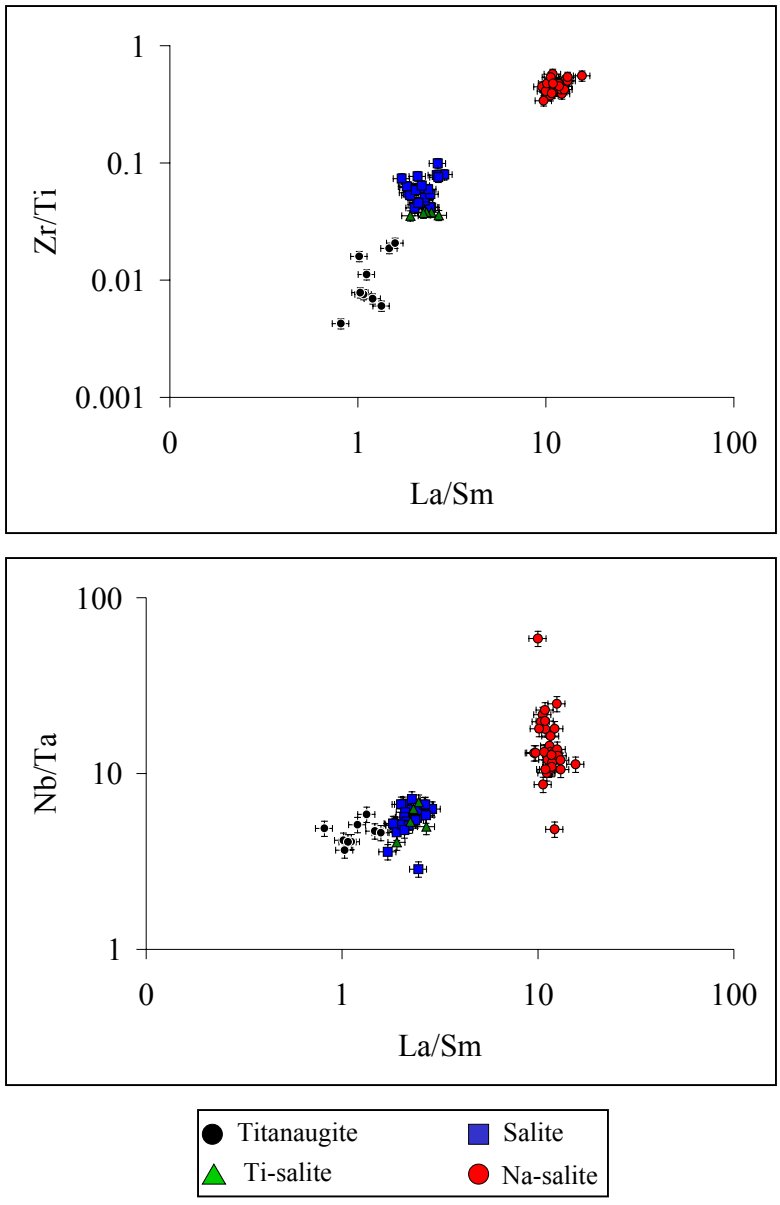

Figure 4.9: Element ratio plots for pyroxene compositional groups.

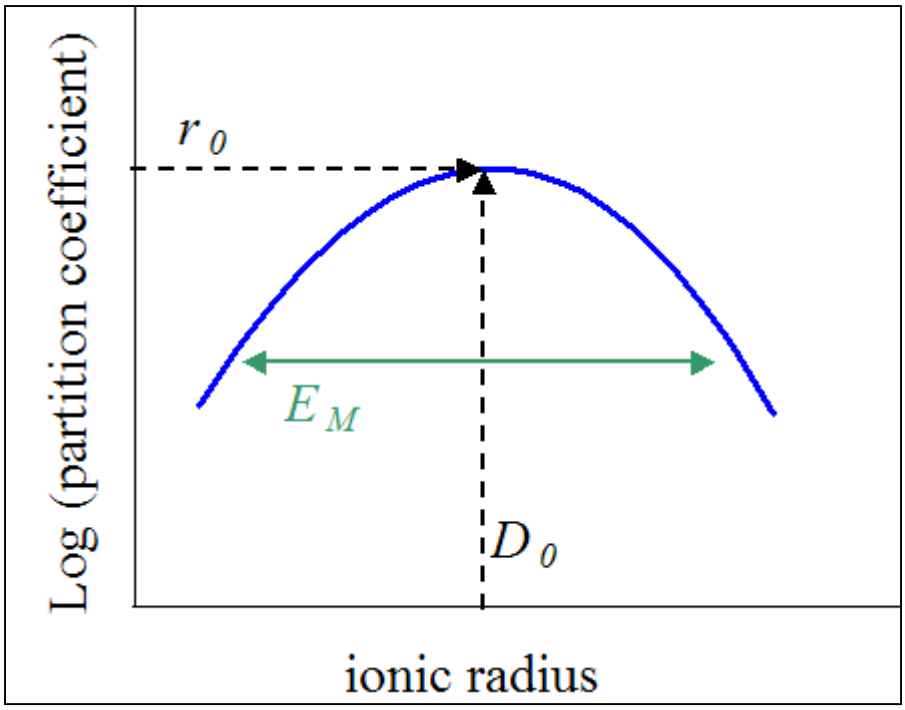

Figure 4.10: Idealized schematic parabolic distribution of partition coefficients versus ionic radius for a suite of like elements (i.e., REE^{3+}) according to the lattice strain compensation model of trace element partitioning (Blundy and Wood, 1994). D_0 is the fictive strain-compensated partition coefficient for an ion with radius r_0. E_M, the Young's modulus, controls the tightness of the parabola.

optimal radius r_0 fixes the apex of the parabola and its "tightness" is controlled by the Young's modulus (E_M) for the site. Higher E_M values tighten the parabola, reflecting greater stiffness of the site and therefore narrower range of permissible ionic radii that substitute into the site to a significant degree. Conversely, lower E_M values open the parabola, reflecting greater accommodation of ionic radii mismatches by expansion or contraction of the site. For the application of the model below, it is not necessary to know r_0 and D_0 *a priori* as long as there are enough elements to plot.

The LSM has been used many times to model trace element mineral-melt partitioning for different phases under experimental and natural conditions (e.g., Bottazzi et al., 1999; Prowatke and Klemme, 2004; Marks et al., 2004), but because Ca-Mg pyroxenes exist in so many geologic environments, they have received more attention than sodium and iron rich compositions (e.g., Wood and Blundy, 1997; Vannucci et al., 1998; Hill et al., 2000; Wood and Trigila, 2001; Tiepolo et al., 2002). Many of these studies report fairly uniform parabolic distributions of partition coefficients (D values) for REE in pyroxenes that can be suitably modeled by assuming that all REE^{3+} are substituting for 8-coordinated Ca^{2+} and indeed fit a single parabolic function. However iron rich aegirine-augites and aegirines from alkaline and peralkaline rocks from the Illímaussaq alkaline intrusion, Greenland described by Marks et al. (2004) are HREE enriched and have REE patterns that are strikingly similar to the Fasnia HREE enriched Na-salites in Figure 4.5. Marks et al. (2004) found that applying the one-eightfold-site LSM model to the Illimaussaq system generated unrealistic partition coefficients, and hence concluded that melt compositions were inappropriate. Therefore, Marks et al. (2004) suggested that more experimental work should be done to constrain trace element

partitioning behavior in alkaline systems. Early attempts at applying the model to Fasnia salites and especially Na-salites encountered similar difficulties with respect to the HREE. LREE and MREE contents were similar to model predictions, but Na-salite HREE enrichment required liquids that had not been identified anywhere in the magma system. Because Fasnia salites and Na-salites, and the HREE-enriched pyroxenes of Marks et al. (2004) have in common elevated Na, Fe, and Mn contents, and because HREE have ionic radii similar to Fe and Mn in octahedral coordination (e.g., ^{VI}Lu 0.86 Å, $^{2+}$Fe 0.78 Å, Mn 0.83 Å), consideration was given to the possibility that REE in Fe-rich pyroxenes can occur in either 8-coordination (substituting for Na or Ca in M2) or in 6-coordination (substituting for Fe and Mn in M1 or M2). If this is the case, then each coordination state ($^{VI}REE^{3+}$ and $^{VIII}REE^{3+}$) is governed by a LSM equation, and that mineral/melt D values are in fact a sum of the two parabolic functions represented by $^{VIII}D_i$ and $^{VI}D_i$ (Fig. 4.11), and D_{HREE} are enhanced relative to the rest of the REE.

Identification of pyroxene-glass pairs

In petrologic studies it is common to calculate partition coefficients using minerals and adjacent glasses (e.g., Wörner et al., 1983) or at least pyroxenes and glasses from within the same sample. The Fasnia, however, is clearly an example where mixing magma has not only brought together magmas of different compositions, but associated processes have scrambled minerals and glasses. This added complexity precludes confident identification of minerals and parental glasses. The method outlined below predicts trace element partition coefficients independent of major element compositions and does not rely on textural relationships.

For each of the 28 salites and 31 Na-salites, apparent trace element D values were calculated using pyroxene REE concentrations divided by REE concentrations for each of the approximately 500 phonolitic glass analyses. The evaluation of the fit of potential pyroxene–glass pairs to the model equation is performed by rewriting equation (1) and plotting it as a linear function (y = mx) as follows:

$$[RT/(-4\pi N_A)] * [Ln(D_i/D_0)] = E_M[r_0/2*(r_i - r_0)^2 + 1/3*(r_i - r_0)^3] \qquad (2)$$

The slope of the line is, by definition, E_M. Using equation (2) with $^{VIII}REE^{3+}$, the pyroxene-glass pair with the best correlation coefficient for the linear regression (r-squared or RSQ value) is considered an equilibrium pair (Fig. 4.12). Not all the REE are used however. Gd is omitted for analytical reasons concerning the glass, Eu is omitted due to its unconstrained 2+ oxidation state, and HREE are omitted. Pairs can then be used to calculate pyroxene-melt partition coefficients. Because the style of REE variation of the in the Fasnia liquids is quite distinct (i.e., due to varying degrees of titanite fractionation), the system is especially favorable for this particular application. This approach is more rigorous than simply using predicted absolute D values because the fit relies on multiple elements, and the calculated partition coefficients for the suite of elements are robust. When all pairs are considered, the actual natural variability within the system can be addressed.

From the numerous pyroxene-glass combinations possible, the 28 salites are fit with 13 different low-Zr glasses (466-808 ppm Zr; Fig. 4.14). One salite is paired with a glass having 1169 ppm Zr. The 31 Na-salites pair with only seven different hybrid phonolite glasses (1169-1645 ppm Zr).

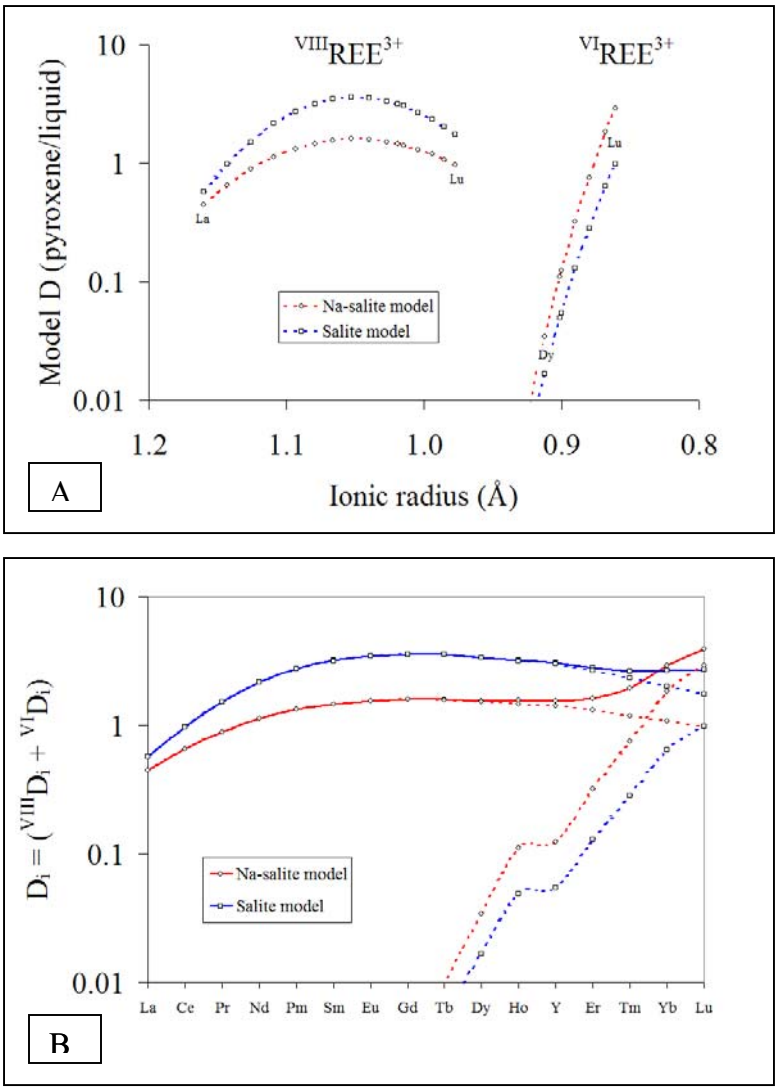

Figure 4.11: Two examples of REE distribution models for salites (blue) and Na-salites (red). Panel A shows D_i vs. ionic radius (r_i) as a function of REE in 8-coordination (VIII) and octahedral coordination (VI), in which $^{VIII}REE^{3+}$ form a parabolic arc and $^{VI}REE^{3+}$ lie form a steep limb of a parabola, with increasing D from Dy to Lu (LREE and MREE lie a low values not shown). Panel B shows D_i vs. element in traditional order, where $D_i = {}^{VIII}D_i + {}^{VI}D_i$.

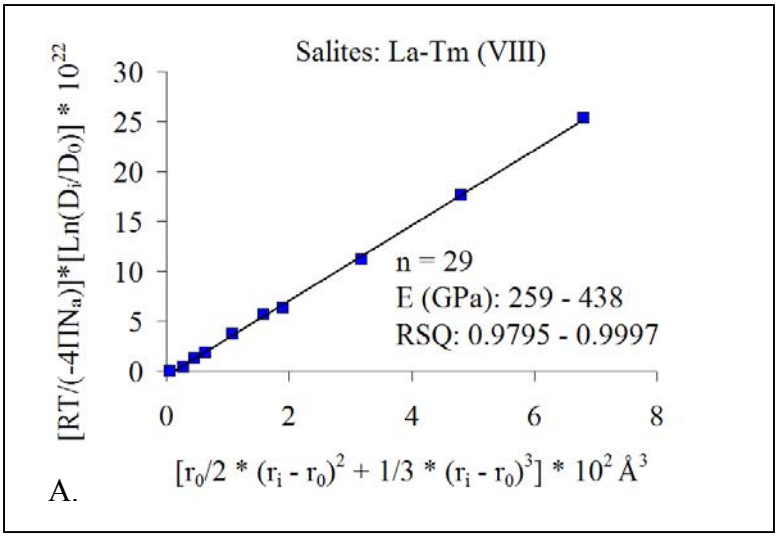

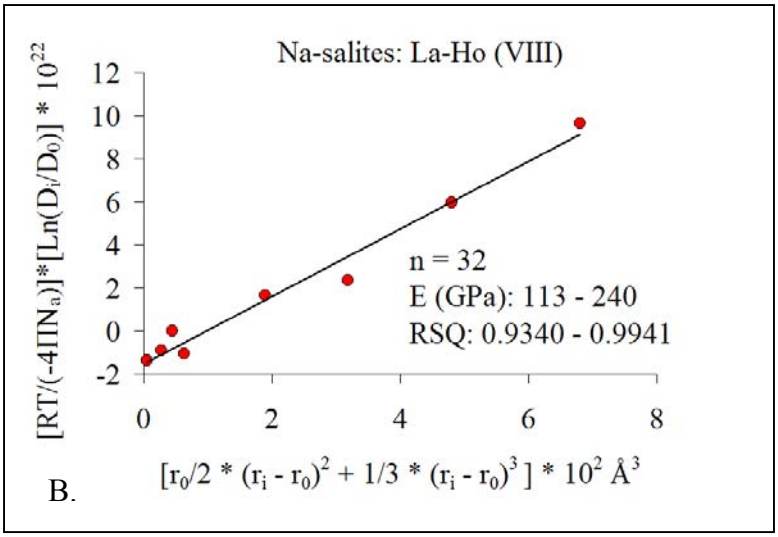

Figure 4.12: Two representative linear fits for the salites (A) and Na-salites (B). The number of analyses (n), ranges of calculated $^{VIII}E_{M2}$, and ranges of best correlation coefficients (RSQ) for the linear regressions are given for salite and Na-salite populations. The 28 salites fit with 13 different low-Zr glasses. The 32 Na-salites fit with 7 hybrid glasses.

Calculated $^{VIII}E_{M2}$ values for the Na-salites range from 113 to 240 GPa (aver. 177 GPa; Fig. 4.14). $^{VIII}E_{M2}$ for salites range from 259 to 438 GPa (aver. 342 GPa). The predicted $^{VIII}E_{M2}$ value at 800-900°C and 0.2 GPa is represented by the dashed line at ~280 GPa in Figure 4.14A. These results imply that $^{VIII}E_{M2}$ decreases with increasing Na_2O (Fig. 4.14A), and because Na is larger than Ca, the M2 site becomes more distorted and can therefore accommodate a larger range of cation misfits.

To address the HREE enrichment observed primarily in Na-salites, equation (2) is applied to the HREE in octahedral coordination. A first approximation for ^{VI}E is attained from the slope between Yb and Lu in the linear expression of the octahedral LSM equation. Values for ^{VI}E determined in this way range from 660 to 1400 GPa (aver. ~1020 GPa) for Na-salites (Fig. 4.14). The ^{VI}E values are reasonable when compared to recently experimentally determined ^{VI}E values of 1635 GPa for 3+ cations in M1 (Hill et al., 2000). In general, high ^{VI}E values reflect the very narrow range of acceptable cations in octahedral coordination, or the "stiffness" of the octahedral site, and therefore are significantly higher than $^{VIII}E^{3+}$ (Fig. 4.14B).

REE partition coefficients

Three model curves are plotted along with the calculated pyroxene/glass D values on Figure 4.15. These curves representing the upper limit, lower limit, and average D_{REE} for salite and Na-salite populations. Parameters for each model curve are given in Table 4.1. Salites are modeled at 900°C and Na-salites are modeled at 800°C. For the salites and Na-salites alike $^{VIII}r_0$ is 1.05 Å. $^{VIII}D_0$ for salites is

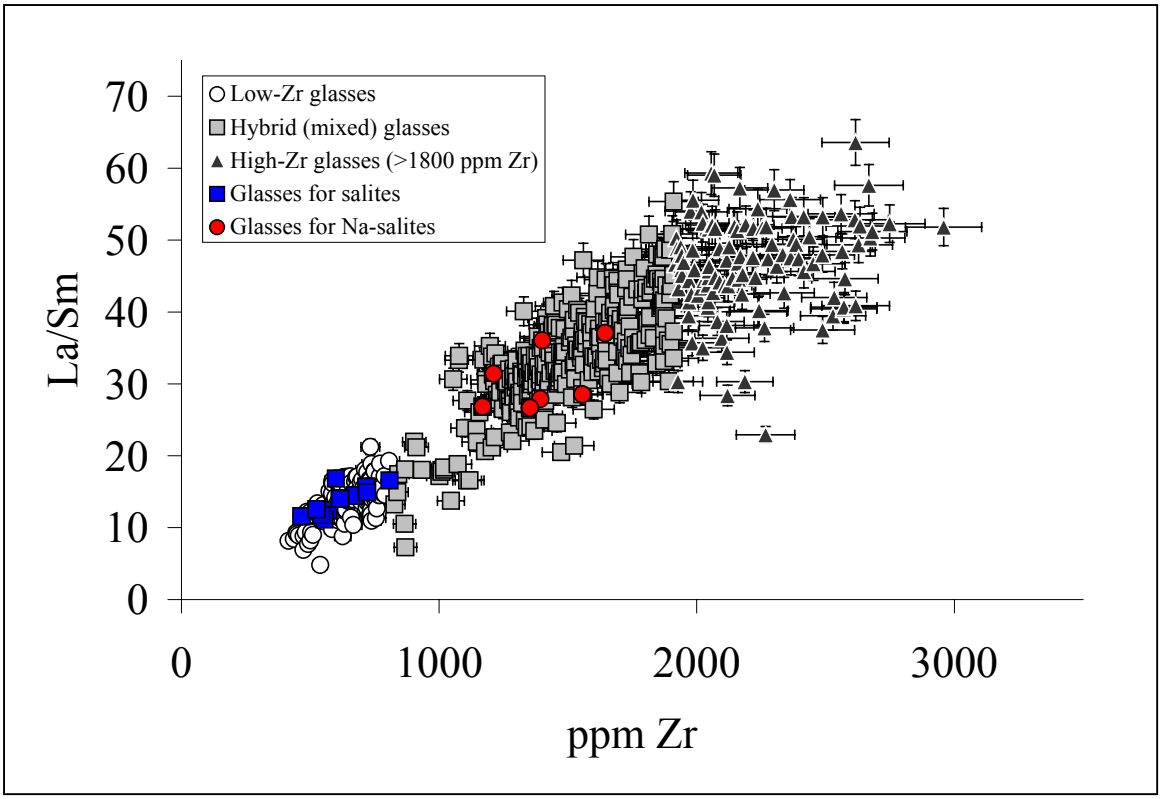

Figure 4.13: Best-fit glasses for Fasnia salites and Na-salites.

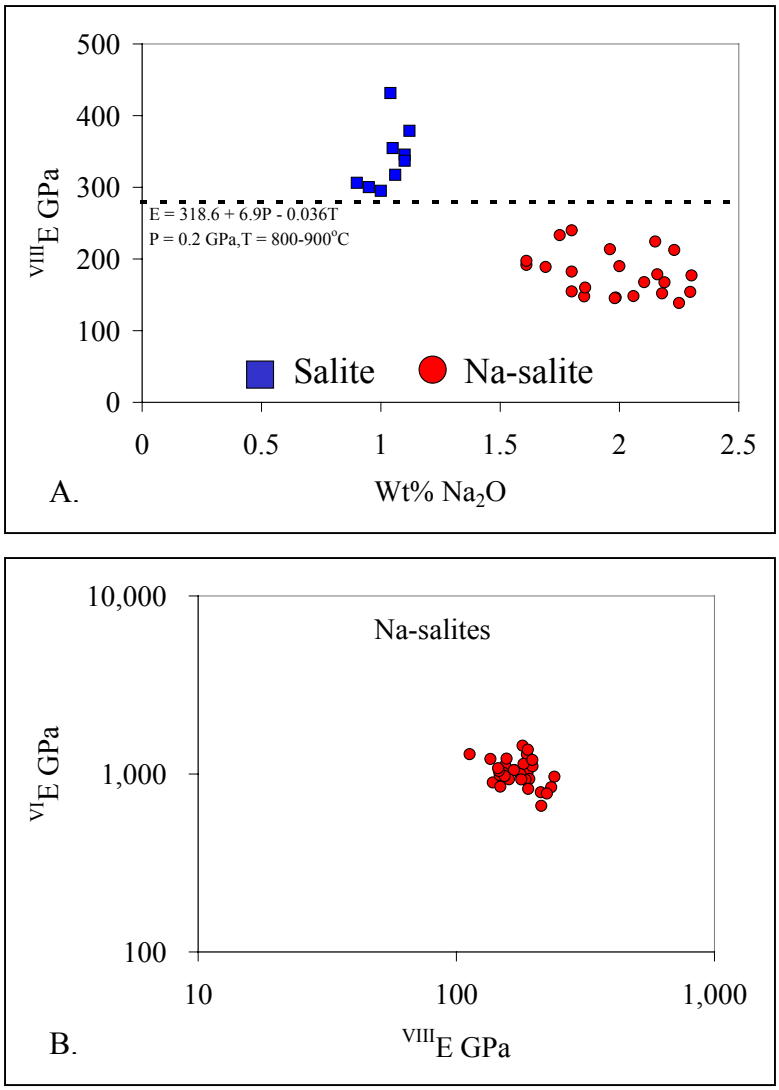

Figure 4.14: Calculated ^{VIII}E vs. Na_2O in cpx (A) and ^{VI}E vs. ^{VIII}E for Na-salites (B). The dashed line in panel A represents ^{VIII}E (~280 GPa) calculated using the equation for E^{3+} from Wood and Blundy (1997).

2.2 to 7.7, and for Na-salites ^{VIII}D ranges from 1.2 to 2.2. ^{VIII}E for salites is 350 to 470 GPa, and for Na-salites ^{VIII}E is 220 GPa. For the octahedral models, $^{VI}r_0$ for the salites and Na-salites is 0.79 Å, which is approximately the combined effective ionic radius (weighted average) of the Fe^{2+} and Mn ratio of the pyroxenes. $^{VI}D_0$ for the salites is 2.2 to 15 and $^{VI}D_0$ for Na-salites is 20 to 30. These values were chosen by trial and error fitting of the model curves to the data. ^{VI}E is 1200 GPa. It should be noted that the octahedral model equation is quite sensitive to small changes in r_0, and hence D_0 values can change significantly. This is a function of the higher E_M values for this coordination state.

Salites and Na-salites require a significant range in D_{REE} to explain the observed variation within each population and an even greater range when considering all modeled pyroxenes. Salites have the following ranges in D values for selected REE and Y: D_{La} 0.3 to 0.7; D_{Sm} 2.0 to 6.3; D_{Lu} 1.6 to 5.0; and D_Y 1.9 to 4.6. Na-salites have the D values: D_{La} 0.4 to 1.1; D_{Sm} 1.0 to 2.4; D_{Lu} 3.5 to 5.9; and D_Y 0.9 to 1.3. D values for the REE and Y correlate with each other as observed in the uniform increase of D values in Figure 4.15, and in the plot of D_Y versus D_{Ho} (Fig. 4.16). Whereas D_Y shows no correlation with glass compositions (Fig. 4.16), D_{Sm} is lower in glasses with low Sm and higher in glasses with higher Sm although no strong correlation exists within either salite or Na-salite groups. D values for Y and Ho plot close to the 1:1 line in Figure 4.16 and although a slight preference for Ho is suggested in the figure, these pyroxenes clearly do not significantly fractionate Y and Ho from one another. Calculated D values for LREE and MREE are generally comparable to other published values (e.g., Sisson, 1991; Hart and Dunn, 1993; Schosnig and Hoffer, 1998; Hill et al., 2000; Bennett et al., 2003; Huang et al., 2006;

Model Parameters	T (^{o}C)	P (GPa)	VIII E (GPa)	VIII r_0 (Å)	VIII D_0	VI E (GPa)	VI r_0 (Å)	VI D_0
Salite								
lower limit	900	0.2	350	1.05	2.2	1200	0.79	2.2
upper limit	900	0.2	470	1.05	7.7	1200	0.79	15
average	900	0.2	350	1.05	3.6	1200	0.79	7.0
							0.79	
Na-salite							0.79	
lower limit	800	0.2	220	1.05	1.2	1200	0.79	20
upper limit	800	0.2	220	1.05	2.2	1200	0.79	30
average	800	0.2	220	1.05	1.6	1200	0.79	25

Table 4.1: Model parameters for each of the three curves in Fig. 4.14 A and B. Roman numerals refer to the coordination state of the variable of interest.

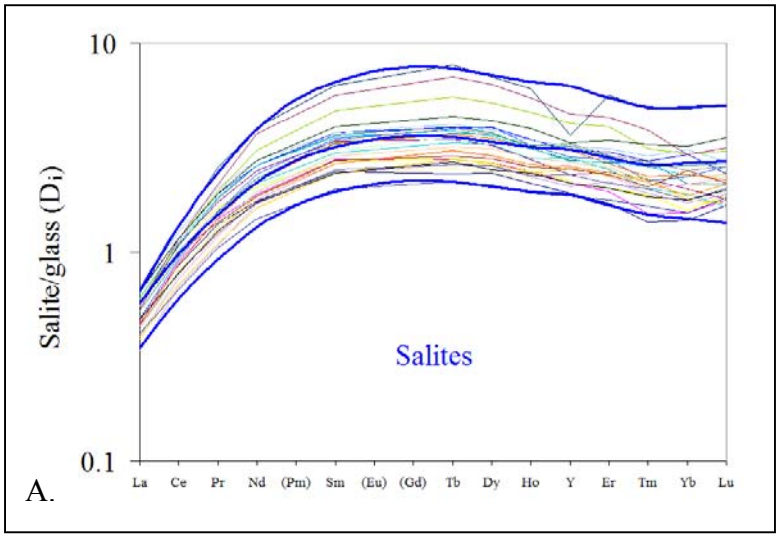

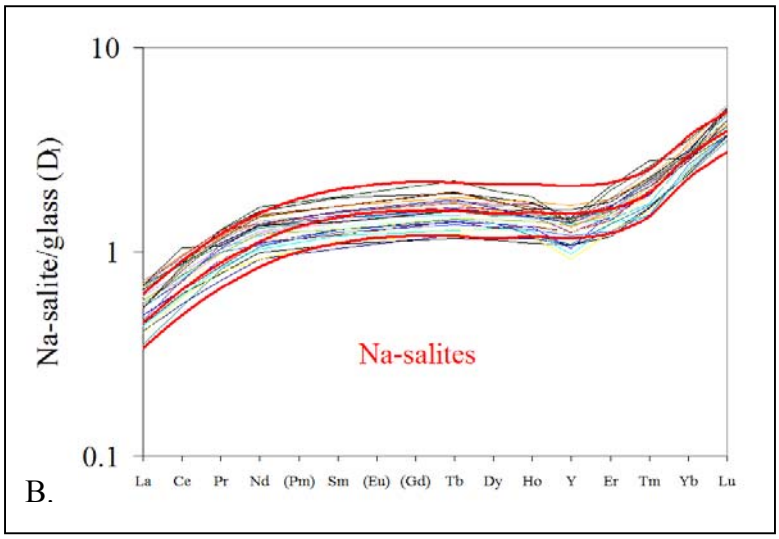

Figure 4.15: Pyroxene/glass and model curves for salites (A) and Na-salites (B). The three models shown on each diagram represent the upper limit, lower limit, and average D_{REE} for the pyroxene populations. Model parameters are summarized in Table 4.1.

Lofgren et al., 2006), but values for HREE are significantly higher than these studies, similar to calculated values (albeit erroneously) of Marks et al. (2004).

HFSE partition coefficients

Partition coefficients for HFSE are shown in Figures 4.18 and 4.19, and in general they are positively correlated with one another, especially Hf and Zr, and Ti, Nb and Ta. Salites have the following D_{HFSE}: D_{Ti} 0.8 to 2.6; D_{Zr} 0.4 to 1.1; D_{Hf} 0.6 to 1.7; D_{Nb} 0.01 to 0.03; and D_{Ta} 0.03 to 0.09. Na-salites have the following D_{HFSE}: D_{Ti} 0.8 to 1.9; D_{Zr} 0.7 to 1.7; D_{Hf} 1.0 to 2.8; D_{Nb} 0.006 to 0.04; and D_{Ta} 0.011 to 0.16.

In Figure 4.18, there is a slight tendency for higher D_{Zr} to be associated with higher Zr glasses (although some overlap with lower Zr glasses exists), but D_{Zr} does not appear to vary systematically with glass composition within either population. Ratios of HFSE D values show that Ti is more compatible than Zr in salites, but in Na-salites the D values for Ti and Zr are nearly the same. An interesting feature in the ratio plots (Fig. 4.18) is the step-like increase in D_{Nb}/D_{Zr} at approximately 1350 to 1400 ppm Zr and overall decreasing D_{Nb}/D_{Ta} with Zr increasing. These features are consistent with the element concentration data (Figs. 4.6 and 4.8) and suggest that pyroxene composition is controlling this behavior, perhaps reflecting a change in a primary substitution mechanism (see discussion). Calculated HFSE partition coefficients are generally comparable to other published values (e.g., Sisson, 1991; Hart and Dunn, 1993; Schosnig and Hoffer, 1998; Hill et al., 2000; Bennett et al., 2003; Marks et al., 2004; Huang et al., 2006; Lofgren et al., 2006).

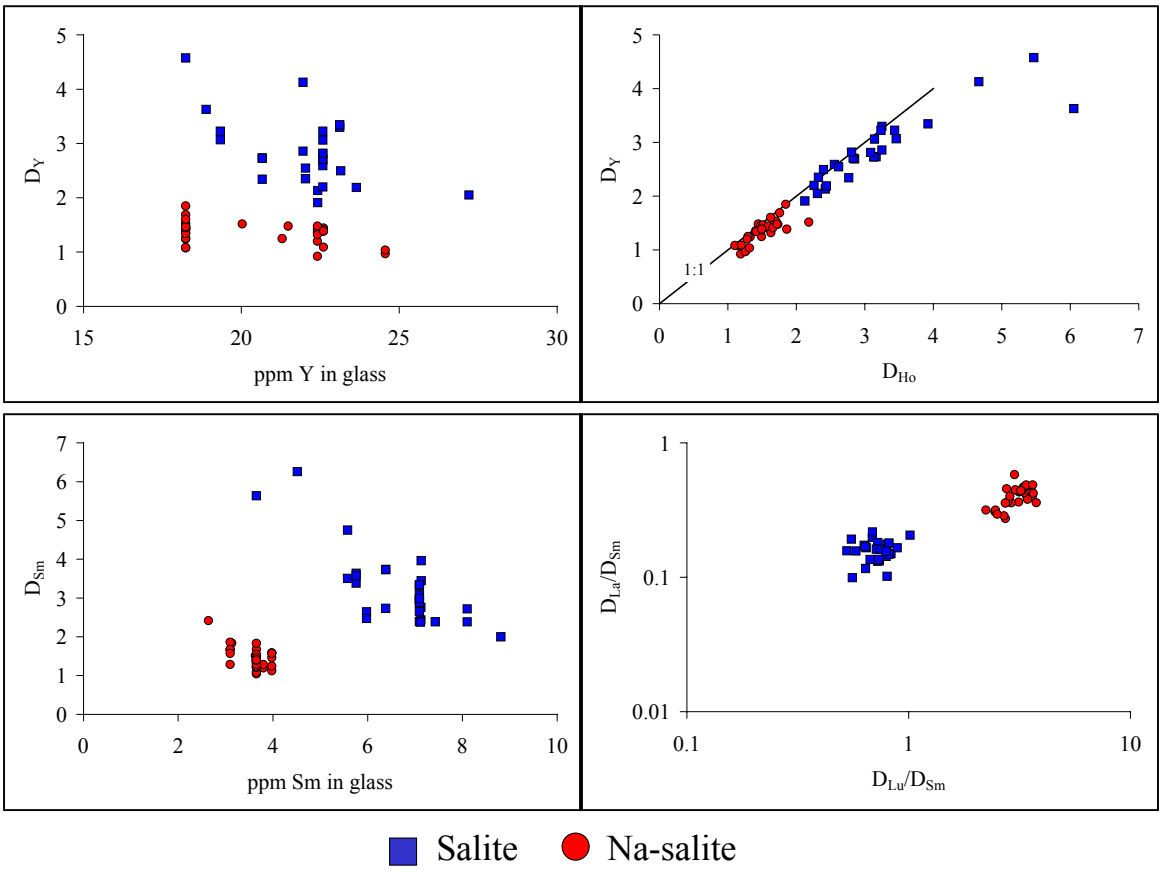

Figure 4.16: Calculated REE and Y partition coefficients and selected partition coefficient ratios for salites and Na-salites.

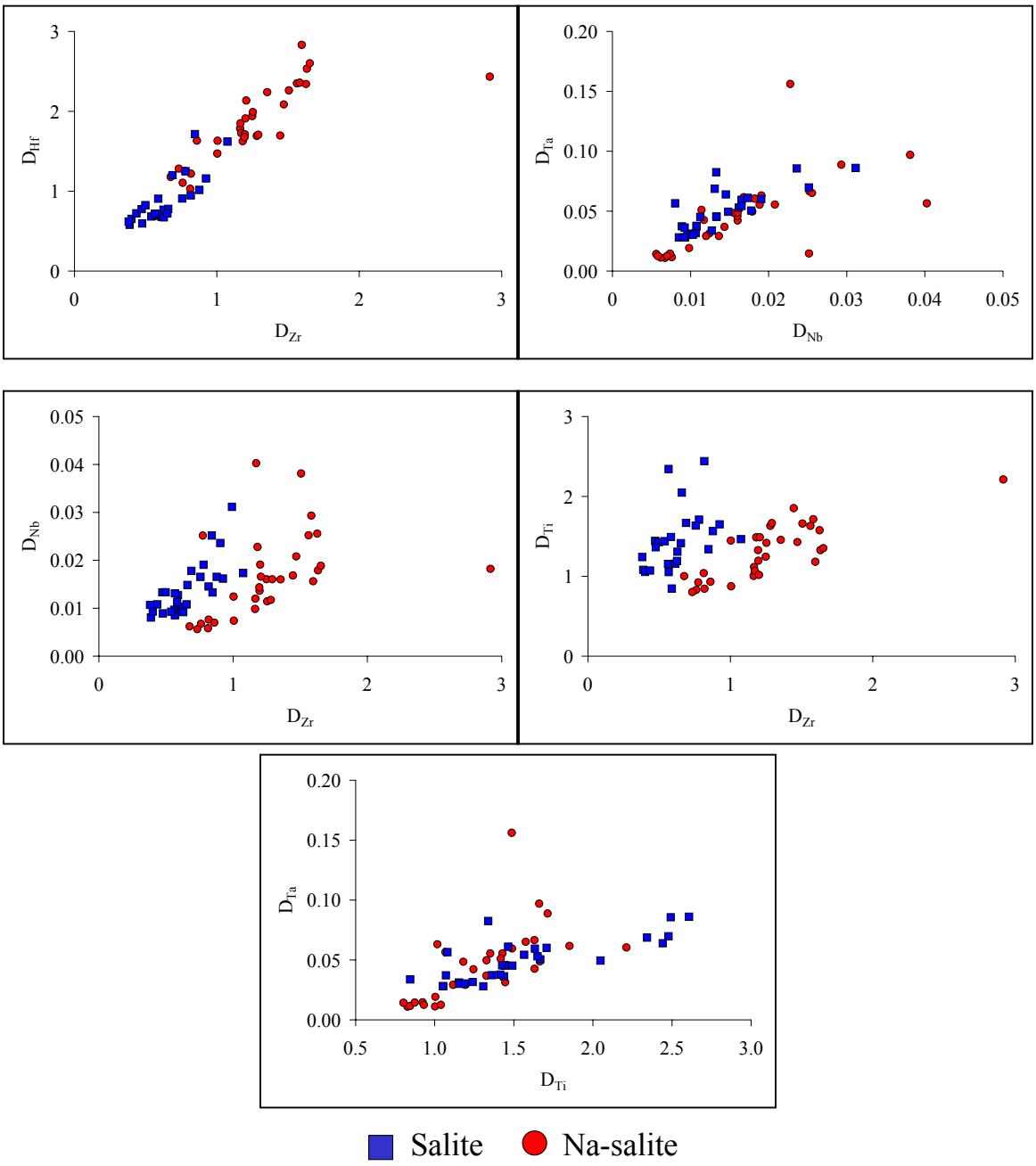

Figure 4.17: Calculated partition coefficients for HFSE.

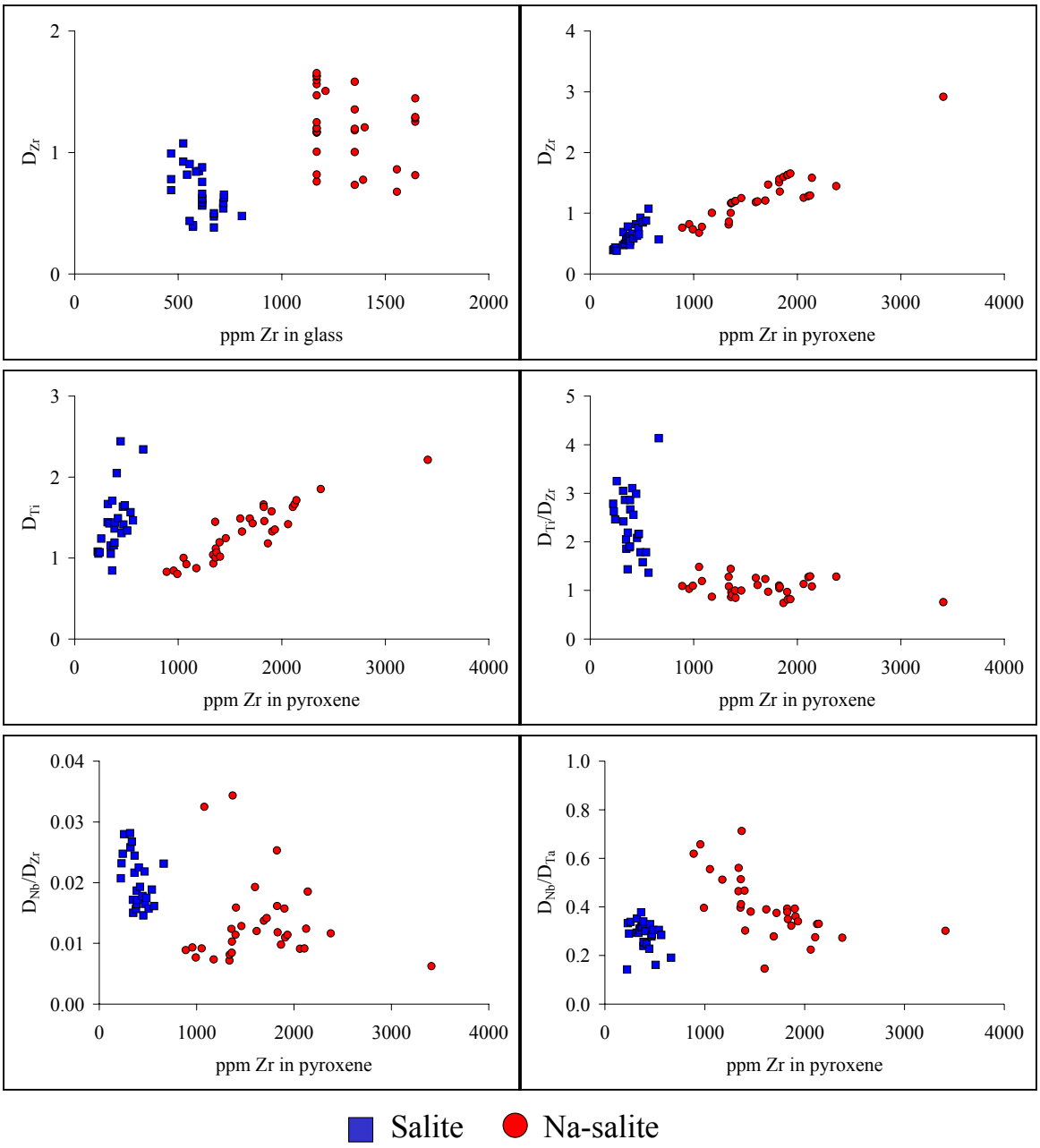

Figure 4.18: Calculated HFSE partition coefficients and selected ratios vs. Zr contents in glasses and pyroxenes.

Discussion

The salite and Na-salite populations crystallized from two distinct phonolitic magmas, low-Zr phonolite and the hybridized product of low-Zr and high-Zr phonolite mixing. The pure high-Zr phonolite appears to have been pyroxene free since no crystals can be paired with any high-Zr glasses. This suggests that this high-Zr liquid may in fact represent a liquid that has been separated from its crystals. Unless high-Zr phonolite is superheated, there is no apparent reason why this liquid would not be crystallizing pyroxenes since even the most evolved syenites on Tenerife contain pyroxenes. Representative pyroxenes of all types were transferred from parental magmas, including the hybrid magma, into more evolved high-Zr phonolitic liquids prior to eruption and quenching since most of the Na-salites occur in some of the most evolved clasts that were erupted early in the Fasnia, but their parental hybrid glasses appear afterwards, becoming prolific midway through the eruption. Most of the salites are associated with these hybrid glasses, but their parental glasses are identified in the coarsely mixed magma erupted early that is only erupted *en masse* for a limited period of time late in the Fasnia. So in general, no genetic relationship should be assumed between any pyroxene and its host glass, and in fact, it is more likely that, at least in the Fasnia, pyroxenes and host glasses are not related. The lack of reaction rims or mantling on all pyroxenes studied suggests that the initial magma mixing event, crystallization of Na-salites from hybrid phonolite, and the transfer of pyroxenes occurred shortly before eruption, precluding the development of such disequilibrium textures. Simple fractionation processes cannot relate low-Zr and high-Zr magmas; rather they represent two long-lived or repeatedly generated magmatic lineages on Tenerife (see Chs. 2 and 3).

Salites and Na-salites crystallized from two distinct magmas, however, calculated partition coefficients have a significant range of values that vary uniformly among the elements within each population and is clearly linked to changing D_0 values. This does not appear to be a function of progressive evolution of each respective magma batch because there is no correlation between D values and glass compositions. The most likely variable responsible for this behavior is temperature. Decreasing temperature has the effect of increasing D_0 values (Wood and Blundy, 1997). It is reasonable to assume that a temperature gradient does exist within the magma chambers, especially with respect to the hybrid phonolite, considering that the end member phonolites are initially quite different, and in general any magma should be losing heat through the roof and walls of the chamber.

Consistent with previous findings (e.g., Wood and Blundy, 1997), pyroxene composition in this study appears to more strongly control trace element partitioning than melt composition. This is most apparent in the partitioning behavior of Nb and Ta observed in the Na-salites. The changes in D values for these elements, and hence concentrations in the Na-salites, appear to be related to Ti and Al contents in the pyroxenes themselves. Increases in Ti and Al correspond to increases in Nb and Ta partition coefficients, with D_{Ta} enhanced relative to D_{Nb}. D values for Zr and Hf also increase, but the effect is not as dramatic. In salites and Na-salites, $D_{Ta} \leq 5\ D_{Nb}$. This effect may signify a fundamental change in substitution mechanisms. On the basis of charge balancing requirements, one possible substitution mechanism may be related to $NaTiAlSiO_6$. As this component increases in pyroxene, it is more likely that substitution of $NaNbAlAlO_6$ or $NaTaAlAlO_6$ will occur.

Elevated sodium contents in melt has been shown to have the effect of increasing trace element partition coefficients in pyroxene (Bennett et al., 2004). While higher Na contents in the melts can explain overall higher partition coefficients for salite and Na-salites compared to titanaugites (i.e., phonolite vs. basalt, respectively), it does not account for the differences between salites and Na-salites, which in fact crystallized from liquids with very similar Na contents. Differences between salites and Na-salites are therefore more directly related to different pyroxene compositions.

Yttrium in salites and Na-salites is clearly behaving like the REE. In this system, Y is most like Ho. Because calculated D_Y values are consistently < D_{Ho}, Y is placed between Ho and Er. Although Y is more similar to Ho than Er, the observed Y anomalies in Figure 4.15 reflect that Y is slightly less compatible than any of these elements. An anomaly is especially apparent in many Na-Salites. This feature is most likely related to the increased role of REE in octahedral coordination described for the Na-salites in general, and suggests that the REE will more easily occupy octahedral sites than Y (i.e., REE become overall more compatible than Y). This would have the effect of partitioning Y from like REE.

REE occupation of two coordination states has also been described in amphibole (i.e., K-richterite; Bottazzi et al., 1999). Like the Na-salites, this behavior is best explained by HREE substitution for Fe^{2+} (and Mg) in octahedral coordination in addition to substitution for 8-coordinated Ca (Bottazzi, et al., 1999).

Conclusions

Salites and Na-salites in the Fasnia Member have geneses in distinct phonolitic magmas. Salites crystallized from low-Zr phonolite magma whereas Na-salites

crystallized in a hybrid phonolitic magma that is a product of mixing between low-Zr and high-Zr phonolites that are not related by fractional crystallization processes, rather each represents two different long-lived or repeatedly generated felsic lineages. Titanaugites are consistent with the minor mafic component and the few identified Ti-salites likely represent a volumetrically insignificant intermediate to transitional phonolite magma that is less evolved than low-Zr phonolite. The high-Zr phonolite liquid appears to be pyroxene free because no pyroxene was paired with these glass compositions.

The lattice strain model equation of Blundy and Wood (1994) provides a robust approach to calculating appropriate partition coefficients for Fasnia pyroxenes with the consideration of REE elements in octahedral coordination in addition to 8-fold coordination. Calculated D values and modeling results require a significant range in D values for REE in both salite and Na-salite populations that is most likely related to temperature variations within the host magmas. D values for pyroxenes and trace element contents in parental glasses are not strongly correlated, implying decoupling between evolution of the magmas and pyroxene trace element contents. Rather partitioning of trace elements between pyroxenes and melts is more strongly controlled by the crystal composition.

References

Cameron, M., Papike, J.J., 1980. Crystal chemistry of silicate pyroxenes. Reviews in Mineralogy Volume 7, Pyroxenes, 5-92.

Bennett, S.L., Blundy, J., Elliott, T., 2004. The effect of sodium and titanium on crystal-melt partitioning of trace elements. Geochim. Cosmochim. Acta 68, 2335-2347.

Blundy, J., Wood, B., 1994. Prediction of crystal-melt partition coefficients from elastic moduli. Nature 372, 452-454.

Bottazzi, P., Tiepolo, M., Vannucci, R., Zanetti, A., Brumm, R., Foley, Oberti, R., 1999. Distinct site preferences for heavy and light REE in amphibole and the prediction of $^{Amph/L}D_{REE}$. Contrib. Mineral. Petrol. 137, 36-45.

Brice, J.C., 1975. Some thermodynamic aspects of the growth of strained crystals. Journal of crystal growth 28, 249-253.

Deer, W.A., Howie, R.A., Zussman, J., 1997. Rock-forming minerals, single-chain silicates, 2A, second edition, 668pp.

Edgar, C., Wolff, J.A., Olin, P.H., Nichols, H.J., Pitarri, A., Cas, R.A.F, Reiners, P.W., Spell, T.L., Martí, J., 2007. The late Quaternary Diego Hernandez Formation, Tenerife: a cycle of repeated voluminous explosive phonolitic eruptions. J. Volcanol. Geotherm. Res. 160, 59-85.

Hart, S.R., Dunn, T., 1993. Experimental cpx/melt partitioning of 24 trace elements. Contrib. Mineral. Petrol. 113, 1-8.

Hill, E., Wood, B., Blundy, J., 2000. The effect of Ca-Tschermaks component on trace element partitioning between clinopyroxene and silicate melt. Lithos 53, 203-215.

Huang, F., Lundstrom, C.C., McDonough, W.F., 2006. Effect of the melt structure on trace-element partitioning between clinopyroxene and silicic, alkaline, aluminous melts. Am. Mineral. 91, 1385-1400.

Lofgren, G.E., Huss, G.R., Wasserburg, G.J., 2006. An experimental study of trace-element partitioning between Ti-Al-clinopyroxene and melt: Equilibrium and kinetic effects including sector zoning. Am. Mineral. 91, 1596-1606.

Marks, M., Halama, R., Wenzel, T., Markl, G., 2004. Trace element variations in clinopyroxene and amphibole from alkaline to peralkaline syenites and granites: implications for mineral-melt trace-element partitioning. Chem. Geol. 211, 185-215.

McDonough, W.F., Sun, S.-s., 1995. The composition of the earth. Chem. Geol. 120, 223-253.

Neumann, E.-R., Wulff-Pedersen, E., Simonsen, S.L., Pearson, N.J., Martí, J., Mitjavila, J., 1999. Evidence for fractional crystallization of periodically refilled magma chambers in Tenerife, Canary Islands. J. Petrol. 40, 1089-1123.

Robinson, P., 1980. The composition space of terrestrial pyroxenes – internal and external limits. Reviews in Mineralogy Volume 7, Pyroxenes, 419-494.

Schosnig, M., Hoffer, E., 1998. Compositional dependence of REE partitioning between diopside and melt at 1 atmosphere. Contrib. Mineral. Petrol. 133, 205-216.

Scott, P.W., 1976. Crystallization trends of pyroxenes from the alkaline volcanic rocks of Tnerife, Canary Islands. Mineral. Mag. 40, 805-816.

Sisson, T.W., 1991. Pyroxene-high silica rhyolites trace element partition coefficients measured by ion microprobe. Geochim. Cosmochim. Acta 55, 1575-1585.

Tiepolo, M., Oberti, R., Vannucci, R., 2002. Trace-element incorporation in titanite: constraints from experimentally determined solid/liquid partition coefficients. Chem. Geol. 191: 105-119.

Vannucci, R., Bottazzi, P., Wulff-Pedersen, E., Neumann, E.-R., 1998. Partitioning of REE, Y, Sr, Zr and Ti between clinopyroxene and silicate melts in the mantle under La Palma (Canary Islands): implications for the nature of the metasomatic agents. Earth Planet. Sci. Lett., 158, 39-51.

Wolff, J.A., 1985a. Zonation, mixing and eruption of silica-undersaturated alkaline magma: a case study from Tenerife, Canary Islands. Geol. Mag. 122, 623-640.

Wood, B., Blundy, J., 1997. A predictive model for rare earth element partitioning between clinopyroxene and anhydrous silicate melt. Contrib. Mineral. Petrol. 129, 166-181.

Wood, B., Trigila, R., 2001. Experimental determination of aluminous clinopyoxene-melt partition coefficients for potassic liquids, with application to the evolution of the Roman province potassic magmas. Chem. Geol. 172, 213-223.

Wörner, G., Beusen, J.M., Duchateau, N., Gijbels, R., Schmincke, H.-U., 1983. Trace element abundances and mineral/melt distribution coefficients in phonolites from the Laacher See Volcano (Germany). Contrib. Mineral. Petrol. 84, 152-173.

Chapter 5

The role of titanite in the phonolitic Fasnia Member, Diego Hernández Formation

Abstract

Titanite is an important phase in the petrogenesis of the Fasnia Member and other Diego Hernández Formation felsic magmas. It strongly fractionates REE and HFSE (e.g., Nb and Ta) from one another, imparting distinct trace element signatures to magmatic components (i.e., glasses and other minerals). Four different types of titanites are identified, having geneses in low-Zr phonolite and different products of mixing between low-Zr and high-Zr phonolite magmas. Application of the lattice strain model (Blundy and Wood, 1994) results in a significant range in titanite – melt trace element partition coefficients, best explained by differences in temperature, mineral chemistry, and melt compositional effects. Modeling results compare well with experimental data on trace element partitioning in titanite. The variation observed in Fasnia titanites reflects the magmatic complexities of the Fasnia Member and is consistent with other lines of geochemical evidence from pyroxenes and glasses.

Introduction

Whole-rock and microscale trace element variability in the Fasnia Member, Diego Hernández Formation (DHF), clearly requires separation of phonolitic liquid from titanite during petrogenesis. This chapter focuses on the variable chemistry of Fasnia titanites in order to identify and constrain the variables controlling trace element partitioning. The lattice strain model (LSM) equation (Blundy and Wood, 1994) is used to match individual titanites to glasses described in Chapter 3 and to constrain titanite – melt trace element partition coefficients for this system.

Titanite occurs in small (~1 %) quantities in phonolitic pumices and in syenitic xenoliths in Fasnia ignimbrites. It is distinctly straw yellow to yellow-orange in color and generally ranges in size from a few tens of microns to 0.5 mm, but occasionally large (~1mm) grains are seen. Small grains are often euhedral, but larger grains are more complex.

Structure and cation substitutions

Titanite CaTi (SiO_4) (O,OH,F) contains SiO_4 tetrahedra with groups of CaO_7 and TiO_6 polyhedra (Zachariasen, 1930). In addition to Ca, the irregular seven coordination polyhedra will also accommodate Na, Sr, Ba, rare earth elements (REE), and Y. The octahedral site contains Ti, Al, Fe^{3+}, Mg, Fe^{2+}, and Mn. In this study all Fe is treated as Fe^{3+}. The high field strength elements (HFSE; i.e., Zr, Hf, Nb, Ta) occur in the octahedral Ti site. Uranium and Th have ionic radii in octahedral coordination that are large for the Ti site, and fit better in the Ca site (Shannon, 1976; Table 5.1).

In addition to ionic radius, coupled substitutions in titanite are constrained by the need to maintain charge balance and by the presence of OH^- and F^- (Sahama, 1946; Jaffe,

Element	Coordination number	Charge	Ionic radius Å
Al	6	3+	0.535
Ti	**6**	**4+**	**0.605**
Ta	6	5+	0.640
Nb	6	5+	0.640
Fe	6	3+	0.645
Hf	6	4+	0.710
Zr	6	4+	0.720
Th	7	4+	
U	7	4+	0.950
Lu	7	3+	
Yb	7	3+	0.925
Tm	7	3+	
Er	7	3+	0.945
Y	7	3+	0.960
Ho	7	3+	
Dy	7	3+	0.970
Tb	7	3+	0.980
Gd	7	3+	1.000
Eu	7	3+	1.010
Sm	7	3+	1.020
Pr	7	3+	
Nd	7	3+	
Ca	**7**	**2+**	**1.060**
Ce	7	3+	1.070
La	7	3+	1.100
Na	7	1+	1.120
Sr	7	2+	1.180
Ba	7	2+	1.380

Table 5.1: Ionic radii of major and trace element cations in titanite with respect to the coordination number (Shannon, 1976)

1947; Zabavnikova, 1957; Mongiorgi and Sanseverino, 1968; Cerny and Povondra, 1972; Higgins and Ribbe, 1976). In general the most important coupled substitutions are:

$$(Al^{3+}, Fe^{3+}) + (OH^-, F^-) = Ti^{4+} + O^{2-}$$

$$Na^+ + (OH^-, F^-) = Ca^{2+} + O^{2-}$$

In an environment rich in trace elements (e.g., REE, HFSE, Y, Sr and Ba) other substitutions are also possible (Zabavnikova, 1957; Hollabaugh, 1980; Green and Pearson, 1986; Cérny et al., 1995; Tiepolo et al., 2002; Prowatke and Klemme, 2005):

$$Na^+ + (Nb^{5+}, Ta^{5+}) = Ca^{2+} + Ti^{4+}$$

$$Na^+ + (REE^{3+}, Y^{3+}) = 2\ Ca^{2+}$$

$$(Sr^{2+}, Ba^{2+}) = Ca^{2+}$$

$$(Zr^{4+}, Hf^{4+}) = Ti^{4+}$$

$$(Fe^{3+}, Al^{3+}) + (Nb^{5+}, Ta^{5+}) = 2\ Ti^{4+}$$

$$(REE^{3+}, Y^{3+}) + (Fe^{3+}, Al^{3+}) = Ca^{2+} + Ti^{4+}$$

And if vacancies are considered more substitutions may occur, such as:

$$2\ Ca^{2+} + O^{2-} = (REE^{3+}, Y^{3+}) + \square + F^-,$$

where □ symbolizes a vacancy in the structure (Prowatke and Klemme, 2005). In light of these possible substitutions, a more appropriate formula for Fasnia titanites is:

$$(Na^+, Ca^{2+}, REE^{3+}, Y^{3+})\ (Al^{3+}, Fe^{3+}, Ti^{4+}, Zr^{4+}, Hf^{4+}, Nb^{5+}, Ta^{5+})\ (SiO_4)\ (O^{2-}, OH^-, F^-).$$

Mineral chemistry

Major and minor elements – microprobe

Major and minor element compositions were determined using the Cameca Instruments electron microprobe at the Washington State University GeoAnalytical Laboratory. All microprobe data for titanite are tabulated in the Appendices.

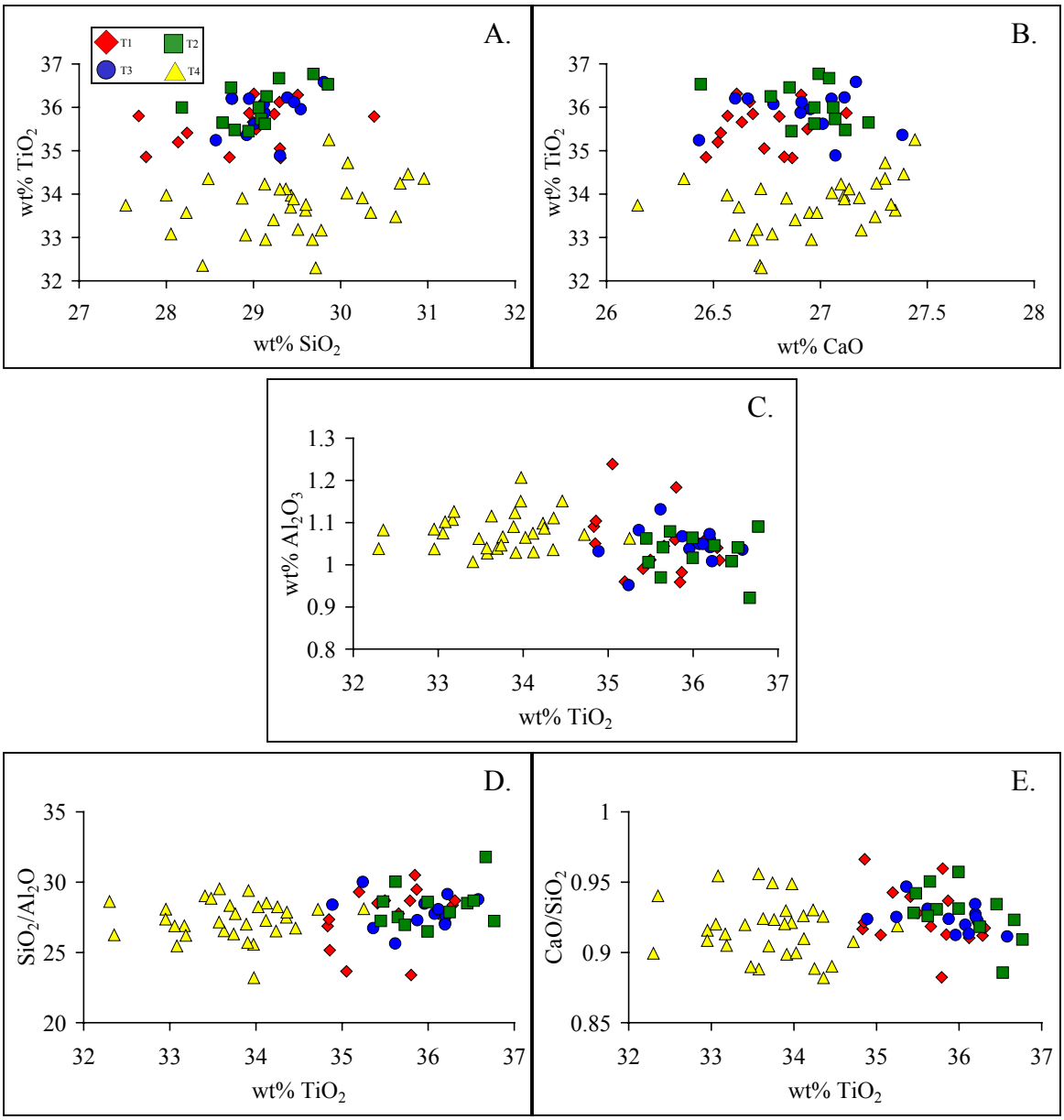

Figure 5.1: Microprobe determined major and minor element oxides and selected oxide ratios. See text for description of titanite types T1-T4.

Fasnia titanites are grouped into four types (T1 through T4). The four different types are distinguished based on differences between trace element contents and calculated trace element partition coefficients presented below. Major elements for T1 and T2 titanites (18 and 12 grains, respectively) are not different, nor do they have distinct differences in trace element contents, but T1 and T2 have different calculated partition coefficients presented below. T3 titanites (26 grains) have trace element concentrations, element ratios, and calculated model parameters that are distinguishable from the other titanites, and in fact T3 often plot between T1/T2 and T4 types. Type T4 (32 grains) is the most distinct population and corresponds to titanites with low TiO_2 (<34.5 wt%) and high ZrO_2 (>1 wt%) and FeO (>1.5 wt%) contents. Type T4 titanites are fairly tightly grouped with respect to trace element contents, element ratios, and calculated model parameters. Some titanites do show compositionally zoning.

TiO_2 shows the greatest range in concentration relative to the major element constituents, ranging from 34.9 to 36.8 wt% in T1-T3 and 32.3 to 35.3 wt% in T4 (Fig. 5.1). SiO_2, CaO, and Al_2O_3 contents do not vary systematically with TiO_2. SiO_2 ranges from 27.5 to 31.0 wt%, CaO ranges from 26.2 to 27.4 wt%, and Al_2O_3 range from 0.92 to 1.24 wt%. Although some scatter in observed in SiO_2/Al_2O_3 and CaO/SiO_2, values do not change systematically with TiO_2.

TiO_2 contents are strongly negatively correlated with ZrO_2 (Fig. 5.2). ZrO_2 contents range from 0.38 to 0.89 wt% in T1-T3 titanites and from 0.99 to 2.55 wt% in T4. Several elements are positively correlated with ZrO_2. FeO ranges from 1.28 to 1.79 wt% in T1-T3 titanites and from 1.47 to 2.32 in T4. Nb_2O_5 ranges from 0.61 to 1.06 wt% in T1-T3, and from 0.89 to 1.82 wt% in T4. Na_2O ranges from <0.01 to 0.15 wt% in T1-T3

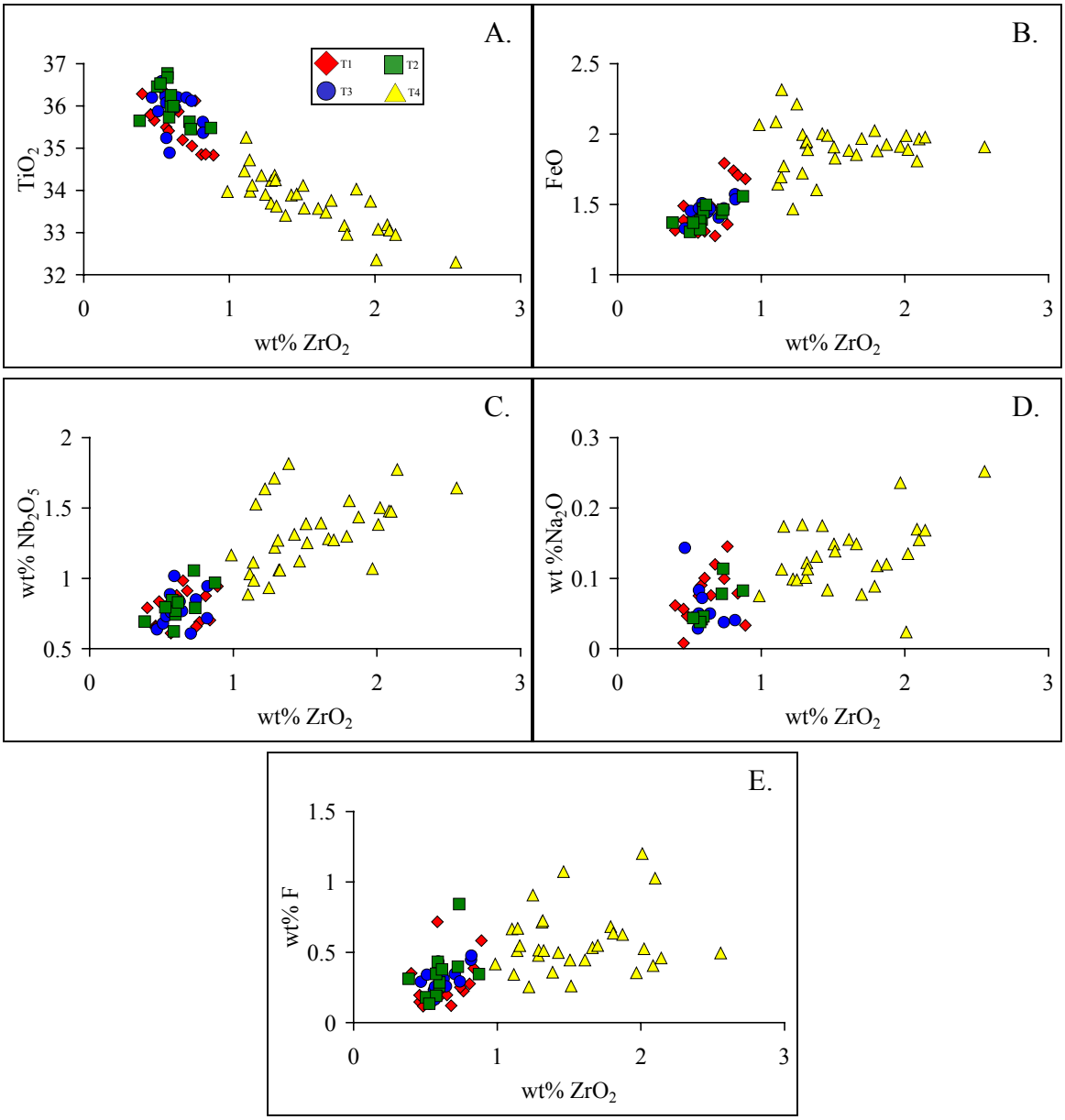

Figure 5.2: Selected titanite element oxides versus ZrO_2. Microprobe determined values.

and 0.02 to 0.25 wt% in T4. Fluorine contents range from 0.12 to 0.84 wt% in T1-T3 titanites and from 0.25 to 1.20 wt% in T4.

Selected element ratios are shown in Figure 5.3 and are used to evaluate substitution mechanisms discussed early. Nb/Zr values sharply decrease with increasing ZrO_2 in T1-T3 titanites. Nb/Zr in T4 titanites also decreases with increasing ZrO_2, but more gradually than T1-T3. Five T4 titanites plot at higher Nb/Zr values, defining a different trend. Fe/Al values increase sharply with ZrO_2 in T1-T3 titanites, but little change with Zr contents in occurs in T4. Fe/Nb values are positively correlated with ZrO_2, especially in T4 titanites. Fe/F values show an overall increase with ZrO_2, with significant scatter. Na/Fe and Nb/Na values also show significant scatter and do not strongly vary systematically with Zr.

Minor and trace elements – LA-ICP-MS

Complementing the microprobe data, additional minor and trace element concentrations were acquired using LA-ICP-MS methods developed at Washington State University. Titanite grains (40 grains, 88 analyses) were either analyzed *in situ* in polished pumice petrographic sections (Fig. 5.4), or because few to no grains are exposed this way, pumice was crushed and sieved, and the few crystals recovered were prepared as grain mounts. The analyses were performed using a New Wave UP213 Nd:YAG laser ablation system coupled to a ThermoFinnigan Element2 mass spectrometer. The laser troughs are 5 – 8 microns wide, and ~500 microns long. The laser fluence was ~12 J/cm^2, the firing rate 20 Hz, and He was used as the carrier gas. Elemental concentrations were determined by normalizing averaged and background-corrected counts per second (cps) data to ^{29}Si cps and SiO_2 determined on the microprobe (see Chapter 1). Glasses BCR-2g

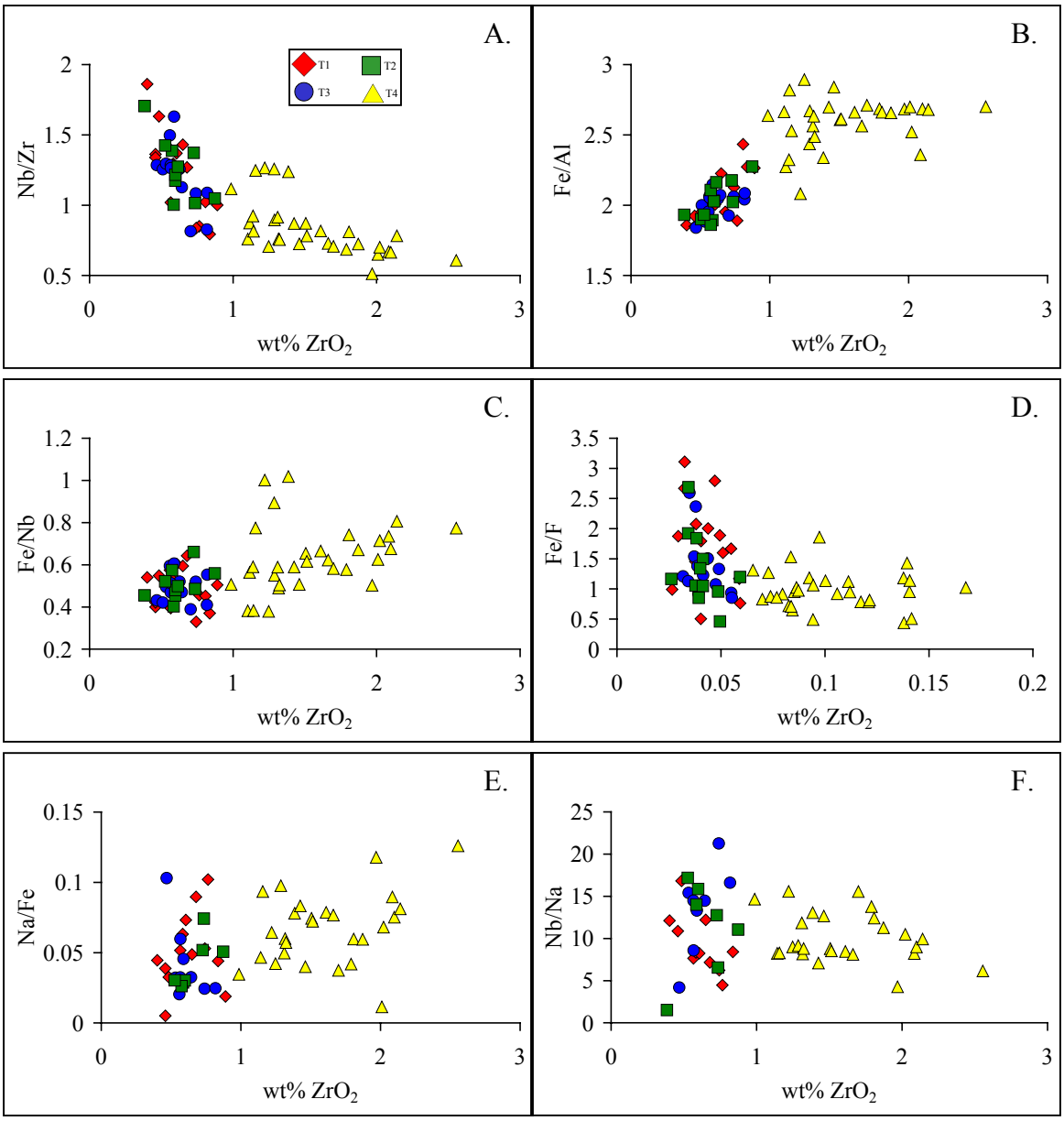

Figure 5.3: Selected titanite element ratios versus ZrO_2 content, Fe = Fe^{3+}. Microprobe determined values.

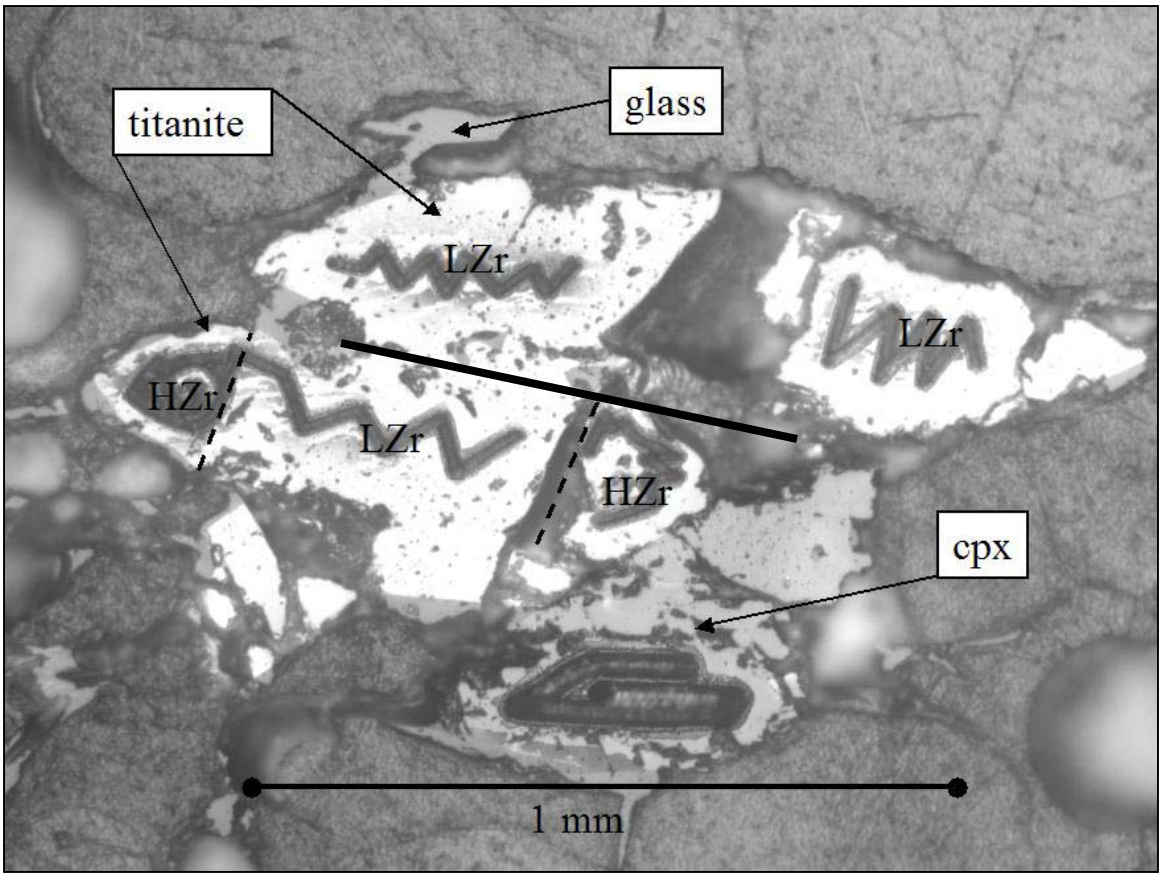

Figure 5.4: Reflected light image of two titanite grains (separated by the heavy black line), one of which shows extreme compositional changes, i.e., low Zr contents immediately adjacent to high Zr (LZr and HZr, respectively; sharp compositional change is indicated by the dashed lines). The zigzag pattern of the laser tracks allows for greater data acquisition time. Pyroxene and glass are also present in this image.

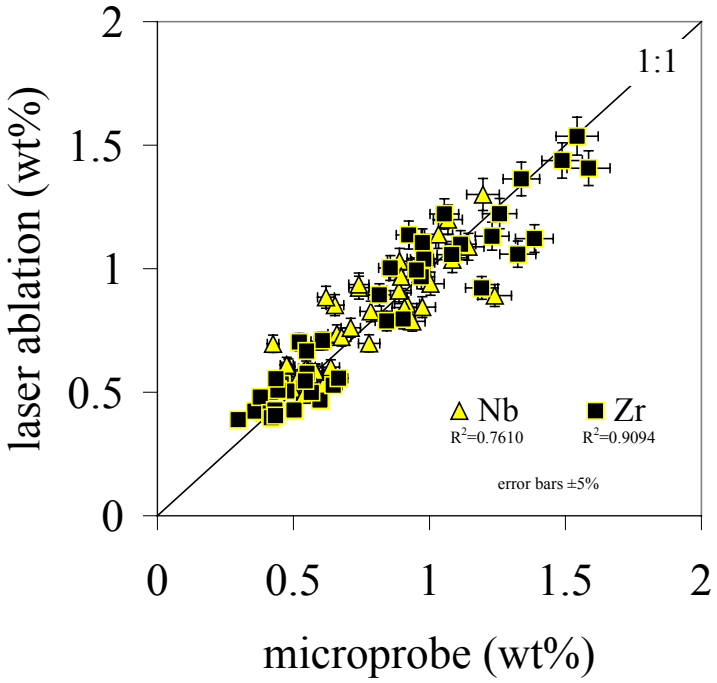

Figure 5.5: Niobium and zirconium concentrations determined by laser ablation (LA-ICP-MS) versus electron microprobe. Error bars 10%.

and Nist610 were used as standards. A plot of Zr and Nb contents determined by microprobe and LA-ICP-MS at the same locations within titanite grains (Fig. 5.5) shows that these two very different methods return very similar results, justifying the application of LA-ICP-MS methods for these titanites. Titanite LA-ICP-MS data are tabulated in the Appendices.

HFSE, Th and U contents are shown in Figure 5.6. All titanites have Hf and Nb concentrations that are positively correlated with Zr. Uranium is also positively correlated with Zr (not shown), but U is more tightly correlated with Nb. Tantalum and Th versus Zr plots are strikingly similar, showing that Ta and Th contents do not vary continuously with Zr when considering all titanites, rather each titanite type (i.e., T1/T2, T3 and T4) has a distinct array. Tantalum does not vary systematically with Nb when considering all titanites, but each type plots along a positive array. Type T1/T2 titanites have 0.40 to 0.65 wt% Zr, 0.49 to 0.67 wt% Nb, 113 to 184 ppm Hf, 523 to 824 ppm Ta, 7.6 to 11.5 ppm U and 92 to 135 ppm Th. Type T3 titanites have 0.49 to 0.89 wt% Zr, 0.57 to 1.09 wt% Nb, 132 to 266 ppm Hf, 548 to 957 ppm Ta, 9.5 to 16.2 ppm U, and 85 to 150 ppm Th. Type T4 titanites have 0.89 to 1.62 wt% Zr, 0.81 to 1.30 wt% Nb, 232 to 502 ppm Hf, 430 to 761 ppm Ta, 12.6 to 23.9 ppm U and 69 to 142 ppm Th.

Selected ratios of HFSE, Th and U are shown in Figure. 5.7. Type T1/T2 titanites have the lowest Nb/Ta values, 7.4 to 10.3, followed by T2, 8.8 to 15.4, and T4, 14.7 to 18.9. T1/T2 and T3 values Nb/Ta increase with increasing Zr while T4 values do not vary systematically over the range in Zr contents. U/Th values show a similar pattern with respect to Zr contents, although T4 U/Th shows greater scatter than Nb/Ta.

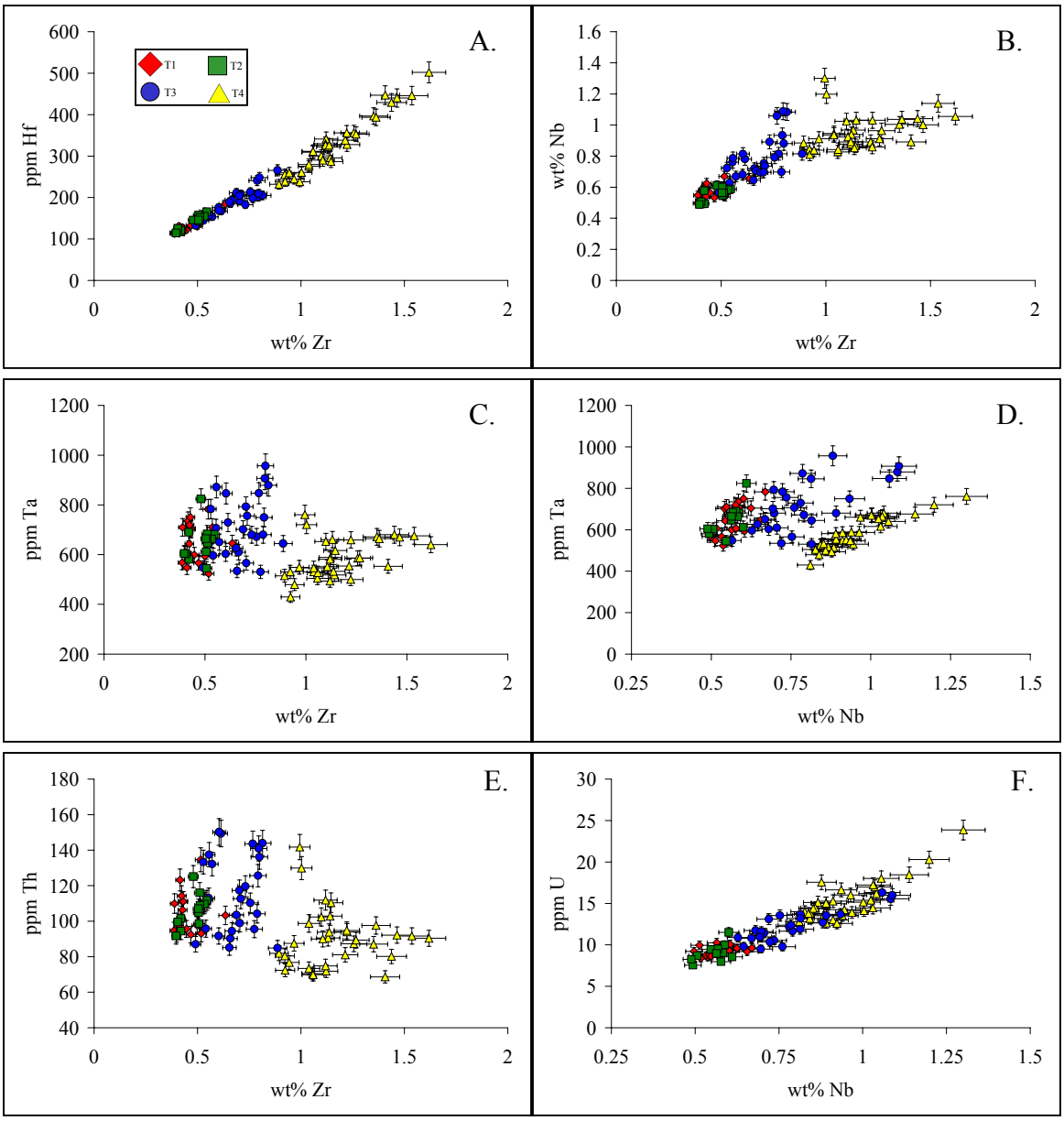

Figure 5.6: Selected trace element contents in Fasnia titanites.

U/Th values 0.07 to 0.11 in T1/T2, 0.08 to 0.16 in T3, and 0.13 to 0.23 in T4. Nb/U and Ta/Th values do not vary systematically with Zr contents, suggesting that the contents of these two element pairs are similarly controlled. Nb/U values are 515 to 724 in T1/T2, 550 to 780 in T3, and 500 to 733 in T4. Ta/Th values are 5.5 to 6.8 in T1/T2, 4.9 to 7.9 in T3, and 5.0 to 8.5 in T4. Zr/Hf values do not vary systematically with Zr contents in T1/T2 and T3 titanites, but T4 shows a slight systematic decrease in Zr/Hf values with increasing Zr contents. Zr/Hf values are 31 to 38 in T1/T2, 32 to 40 in T3, and 31 to 42 in T4. Nb/Zr values show a systematic decrease with increasing Zr contents, however whereas T1/T2 and T4 values are strongly correlated with Zr, T3 shows significant scatter to higher Nb/Zr values. Nb/Zr values are 1.0 to 1.4 in T1/T2, 0.9 to 1.4 in T3, and 0.6 to 1.3 in T4.

Selected REE, Y, Sr and Ba contents are shown in Figure 5.8. REE and Y are compatible into titanite, and because it prefers middle REE (MREE), especially Sm, to light REE (LREE) and heavy REE (HREE), so even small degrees of titanite fractionation have strong effects on REE patterns of evolving liquids (Green and Pearson, 1986). La, Sm, and Lu are selected to represent the behavior of LREE, MREE and HREE, respectively. La contents do not vary systematically with Zr, rather La behaves much like Ta and Th. La contents are 2726 to 3642 ppm in T1/T3, 2797 to 4037 ppm in T3 , and 2541 to 3710 in T4. Sm contents decrease sharply and continuously with increasing Zr in T1/T2 and T3, but in T4 Sm does not change significantly with increasing Zr. Sm concentrations are 569 to 1043 ppm in T1/T2, 326 to 798 ppm in T3,

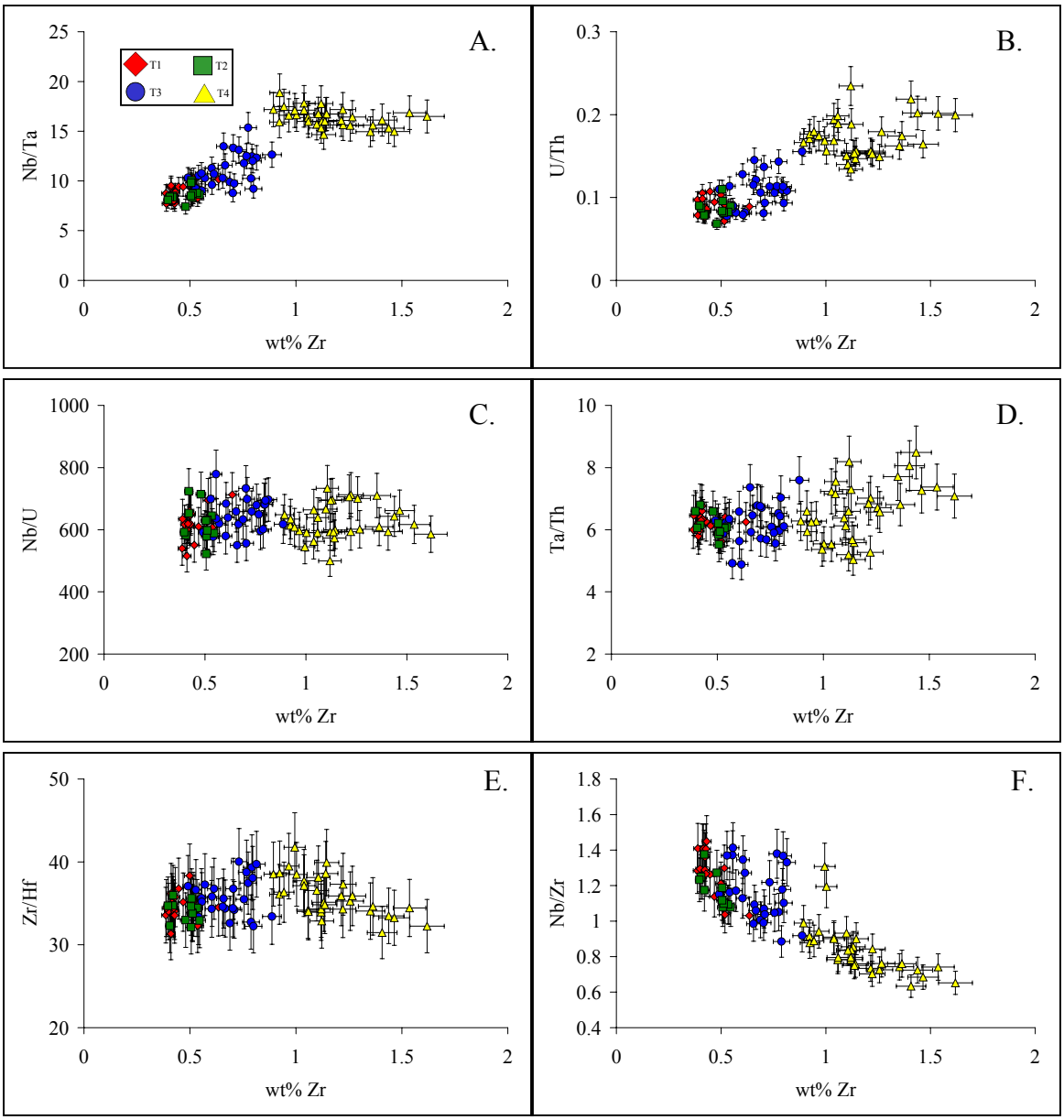

Figure 5.7: Selected element ratio versus Zr concentrations. LA-ICP-MS determined values. Error bars on concentration data ±5%, ratios ±10%.

and 203 to 300 ppm in T4. Lu contents generally decrease with increasing Zr contents, but within each group the variation is not systematic. Lu concentrations are 9.5 to 12.9 ppm in T1/T2, 7.6 to 12.5 ppm in T3, and 5.2 to 9.8 ppm in T4. Yttrium behaves essentially the same as Sm. Yttrium concentrations are 1493 to 2130 ppm in T1/T2, 896 to 1825 ppm in T3, and 657 to 1037 ppm in T4. Sr contents sharply decrease with increasing Zr in T1/T2, but the lower concentrations in T3 and T4 do not vary systematically with Zr. Sr concentrations are 12 to 76 ppm in T1/T2, 3.8 to 23 ppm in T3, and 3.7 to 15 ppm in T4. Ba does not behave like Sr, rather the trends are like Lu, Ta, Th, and to a lesser extent La. Ba concentrations are 24 to 31 ppm in T1/T2, 21 to 33 ppm in T3, and 17 to 24 ppm in T4. It is noteworthy that elements with different ionic radii and charge appear to behave so similarly in these titanites.

More selected element ratios are shown in Figure 5.9. Increasing values for La/Sm and Lu/Sm reflect progressive MREE depletion with increasing Zr, a feature consistent with the separation of titanite from evolving magmas, and the observed trends are similar to Nb/Ta. La/Sm values are 2.9 to 5.6 in T1/T2, 4.4 to 9.4 in T3, and 11.2 to 14.1 in T4. Lu/Sm values are 0.010 to 0.019 in T1/T2, 0.014 to 0.024 in T3, and 0.025 to 0.033 in T4.

The elements Y and Ho behave very similar geochemically because they have very similar ionic radii and electronegativities (Bau, 1996 and references therein), and these elements are often treated as geochemical twins. However, ratios of Y/Ho and Y/Er (Fig. 5.9) shows that Y behaves more like Er than Ho in this system, i.e., Y/Er varies less than Y/Ho with increasing Zr contents. Y/Ho versus Y is also shown along with the boundaries of the charge and radius controlled (CHARAC) boundaries of Bau (1996).

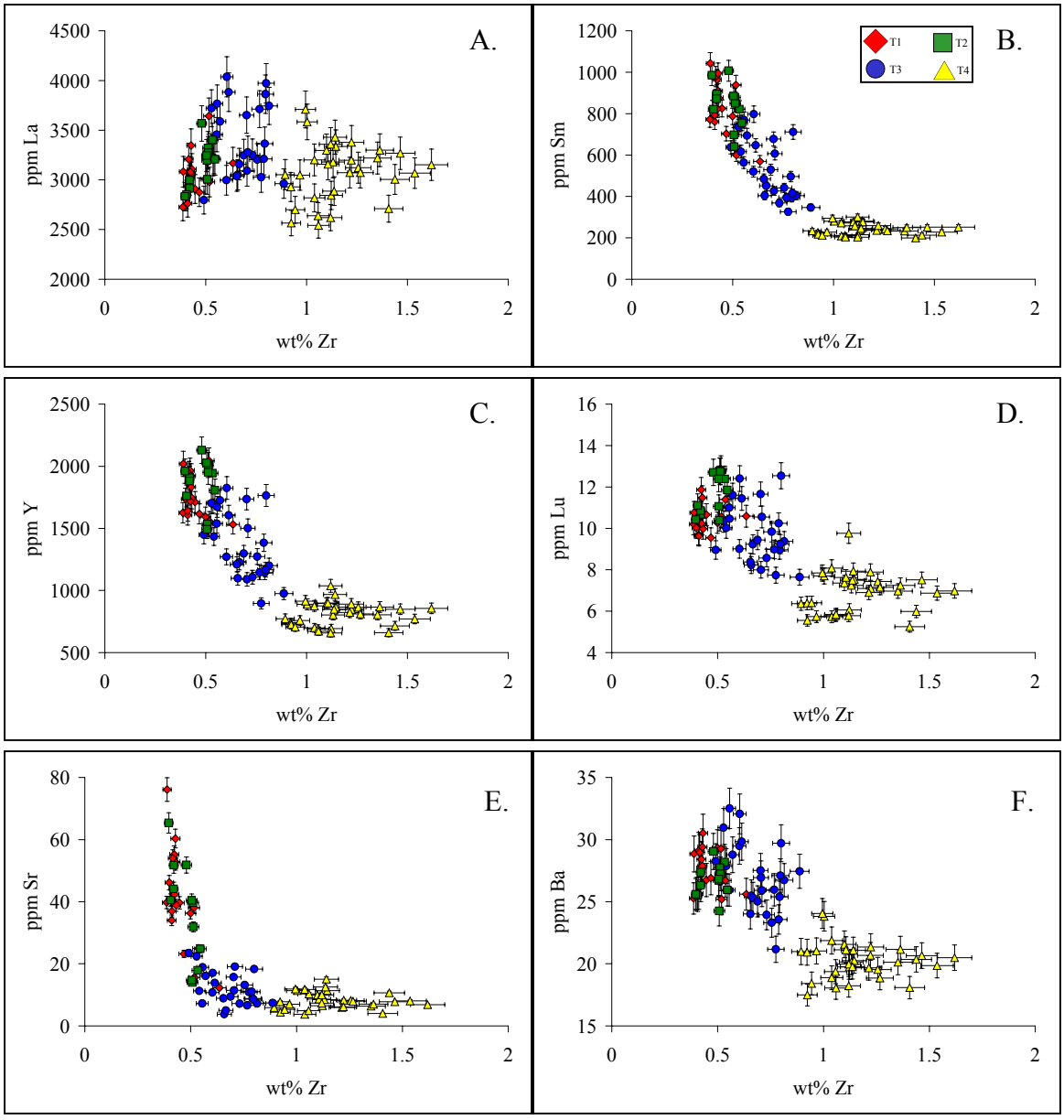

Figure 5.8: Selected REE, Y, Sr, and Ba versus Zr concentration. LA-ICP-MS determined values. Error bars ±5%.

These boundaries represent the region where most igneous rocks (and hence most igneous rock components) plot, reflecting that little to no fractionation of Y from Ho occurs during the magmatic evolution of most magmas. Clearly this is not the case for all igneous rocks since Y/Ho does vary systematically in DHF phonolites. Note that T1/T2 Y/Ho ratios plot just below the lowest values reported by Bau (1996). Y/Ho values are 22 to 25 in T1/T2, 23 to 27 in T3, and 25 to 28 in T4. Y/Er values do not change significantly, varying from 9.3 to 11.0 for all titanites.

Increasing values for La/Sm, Lu/Sm, Nb/Ta and U/Th are clearly correlated (Fig. 5.10). Y/Ho versus Zr/Hf shows that although Y/Ho values for T1/T2 titanites lie near the minimum of the CHARAC field, Zr/Hf values for all titanites are within this field. However, titanite Zr/Hf values are significantly lower than values for mafic liquids (i.e., basalts) associated with Diego Hernández Formation magmatism. This two facts provide a mechanism to fractionate Zr from Hf and Y from Ho, subsequently increasing these ratios in the evolving liquids. Basalts and Fasnia phonolitic glasses are plotted in Fig. 5.10d to show that this is indeed the case.

Core and rim variations

Different compositional types occur within some single grains. Three titanite grains shown normal zoning with respect to Zr (i.e., increasing Zr from core to rim) and nine grains show reverse zoning (i.e., decreasing Zr core to rim). This also applies to Nb contents, but oppositely to Sm contents (Fig. 5.11). Of the three grains that show normal zoning in Zr and Nb, one has increasing Sm from core to rim, the opposite of what is expected. Eight of the nine reversely zoned grains fall along the same trend in Nb, but one core has much higher Nb than the rest defining a different trend. In general, reversely

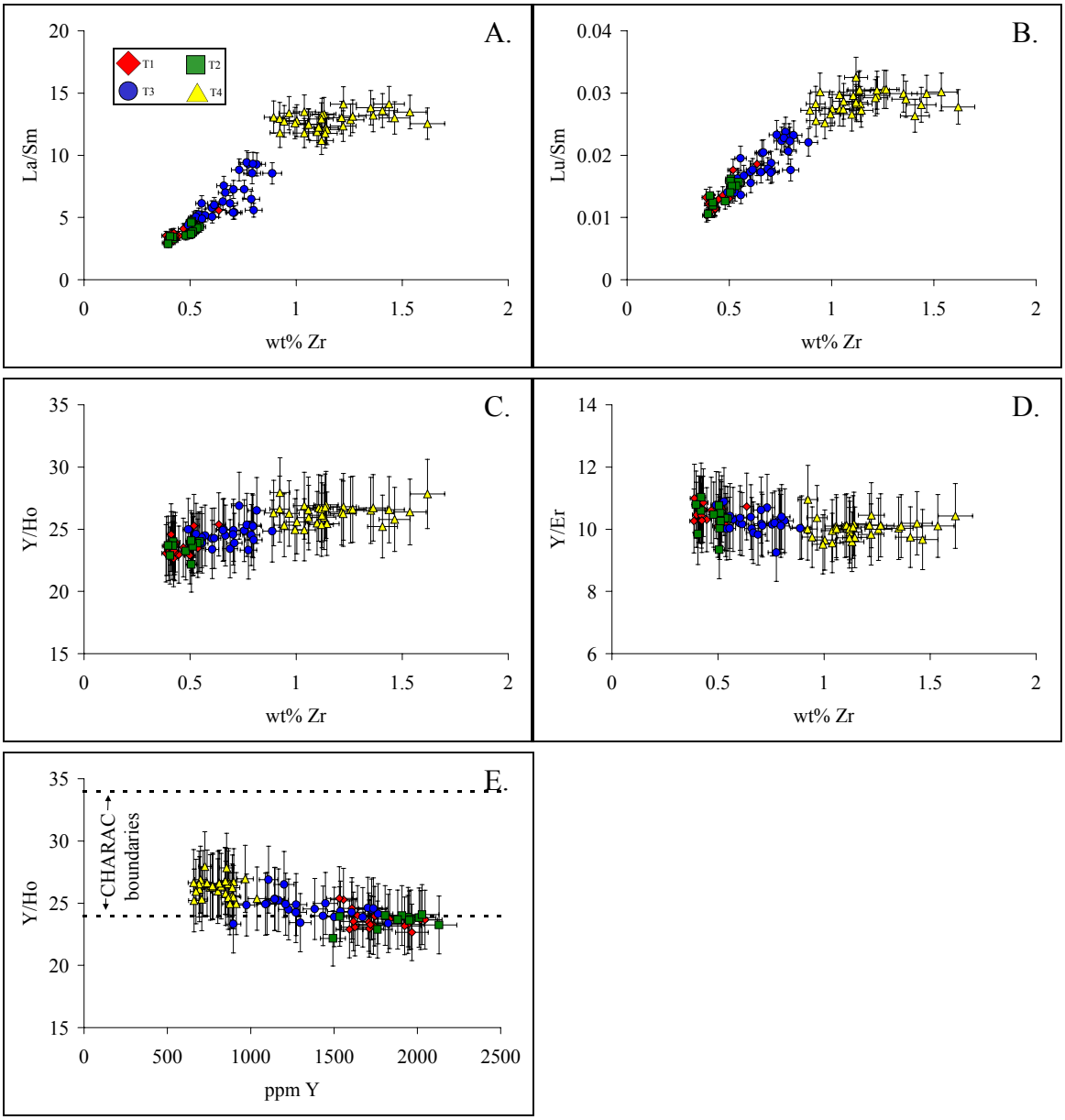

Figure 5.9: Selected element ratios emphasizing the REE and Y. LA-ICP-MS determined values. Error bars concentration data ±5%, ratios ±10%.

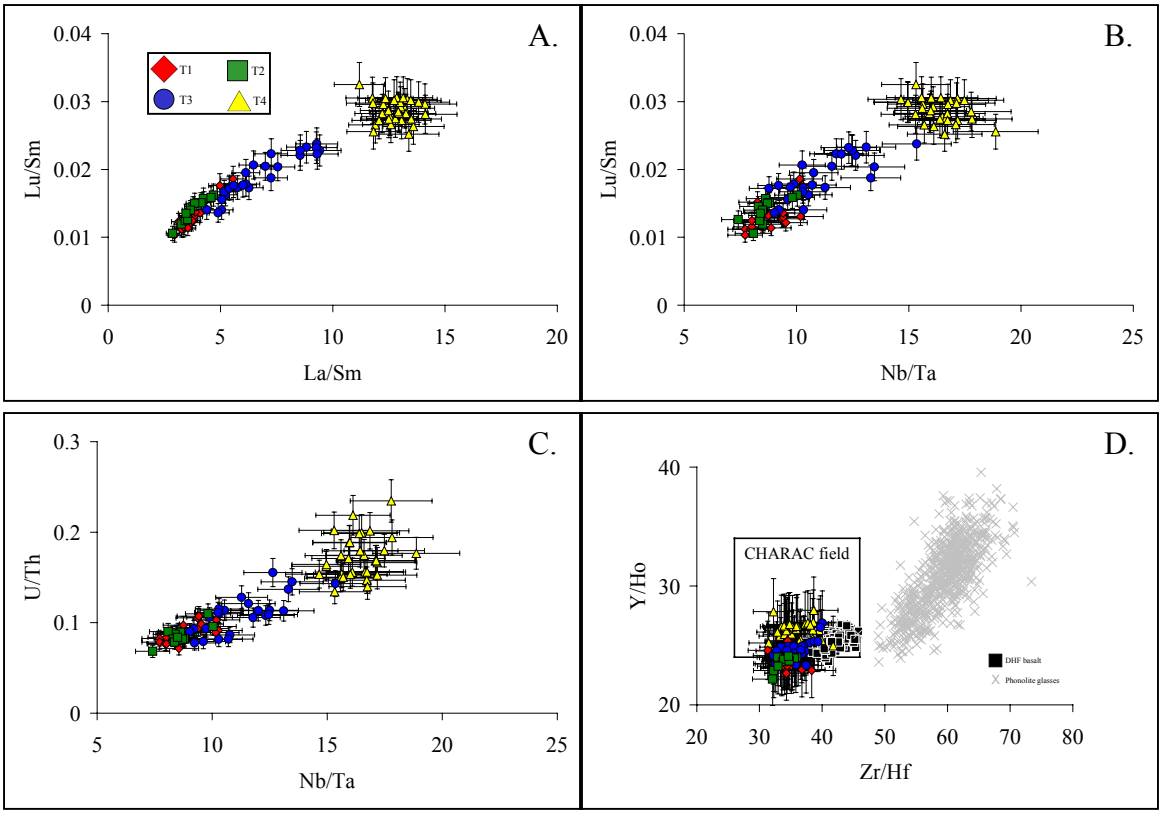

Figure 5.10: Ratio versus ratio plots emphasizing relationships between REE, HFSE, and U/Th. Error bars on ratios ±10%. Panel D contains the charge and radius controlled (CHARAC) domain of igneous rocks (Bau, 1996), and includes basalt whole-rocks and LA-ICP-MS phonolitic glasses.

zoned grains could arise from any of the following scenarios: 1) evolved magma that is being progressively recharged or contaminated by less evolved magma, 2) cores crystallized in a more evolved liquid are transferred into a less evolved magma by crystal settling or rapid mixing between magma reservoirs, or 3) the cores may be xenocrystic, either from syenitic plutons or deeply buried phonolitic rocks. The single titanite core with high Nb is more consistent with crystallization from DHF III-type phonolite, and therefore might be xenocrystic. Although the current data cannot distinguish between scenarios 1 or 2, scenario 2 is favored in light of other petrologic evidence (e.g., glass compositional data) to explain the other reversely zoned grains, and in fact, crystal transfer during magma mixing also explains the apparent normal zoning too. For example, one grain has an extremely sharp transition from very low Zr and Nb contents to the highest Zr and Nb contents measured in these Fasnia titanites (Fig. 5.11), requiring different magma environments, consistent with scenario 2 processes.

Titanite - melt partition coefficients

The lattice strain model of trace element partitioning (LSM; Blundy and Wood, 1994) is described in Chapter 4. The LSM model equations are applied to the REE in the Fasnia titanites in the same way they are applied to REE in Fasnia clinopyroxenes. Different to pyroxenes however, REE elements partition onto a seven coordinated Ca-site instead of an eight coordinated site. Therefore REE partitioning in titanite is related to the similarity of the 7-coordinated ionic radii of the REE (1.100 to < 0.925 Å) to that of ^{VII}Ca (1.06 Å). All titanite analyses are compared to the approximately 500 phonolitic glass analyses and best-fit titanite-glass pairs are identified by the best correlation coefficient for the linear fit (or RSQ value). Seven-coordination ionic radii used in the calculations

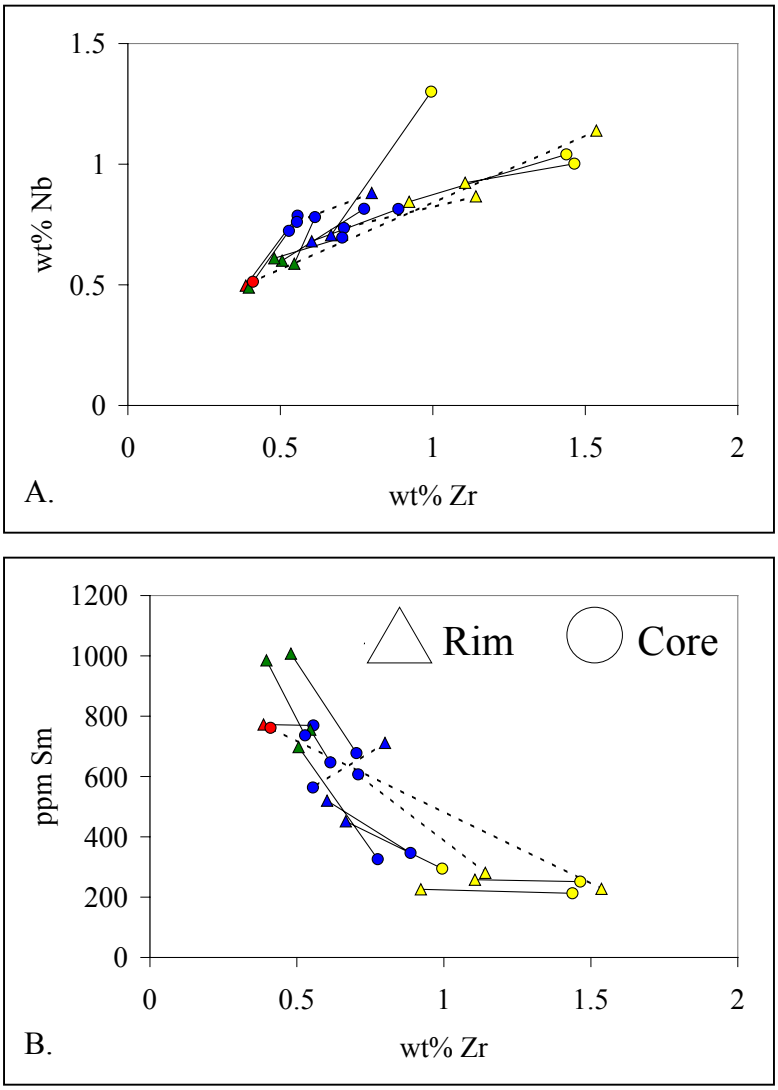

Figure 5.11: Normal (dashed lines) and reverse (solid lines) compositional zoning in some titanites. Colors are consistent with other figures.

are from Shannon (1976; Table 5.1), however values are not determined for Pr, Nd, Ho or Tm and therefore these element are not included in the fitting exercise. Eu is also not included because of its unconstrained oxidation state (2+ or 3+), and Gd is omitted for analytical reasons concerning the glasses, but any of these values can be subsequently interpolated from the model curves. Partition coefficients for elements NOT directly included in the modeling (e.g., HFSE) are calculated from the LSM determined titanite-glass pairs.

Best-fit RSQ values for all titanite-glass pairs range between 0.9419 and 0.9949 (ave. 0.9757), and these pairs are interpreted to represent possible conditions of mineral-melt equilibrium. Plots of $^{VII}E^{3+}$ and selected calculated partition coefficients versus RSQ values show that there is no systematic correlation between the RSQ value and these variables (Fig. 5.12) which means that differences in calculated partition coefficients are not directly related to the model fit. T4 also has essentially unchanging $^{VII}E^{3+}$ values. It is also interesting to note that T2 titanites now plot with T3, not T1.

Values obtained for Young's Moduli (i.e., $^{VII}E^{3+}$) from the slope of the best-fit line (see chapter 4) show a significant range: T1, 250 to 496 GPa; T2, 519 to 776 GPa; T3, 517 to 701 GPa; and T4, 398 to 469 GPa (Figs. 5.12 and 5.13). These values are reasonable when compared to recent published experimental values for titanites of variable compositions (Tiepolo et al., 2002; Prowatke and Klemme, 2005). In fact the Fasnia titanites clearly plot along the experimentally determined arrays for D_{Nb}/D_{Ta} and D_{La}/D_{Sm} versus $^{VII}E^{3+}$ (Fig. 5.13). D_{Nb}/D_{Ta} and D_{La}/D_{Sm} values increase with decreasing $^{VII}E^{3+}$, consistent with the LSM model. This is not the case for D_U/D_{Th}, which does not vary systematically with $^{VII}E^{3+}$, but values do plot with experimental data at lower $^{VII}E^{3+}$.

	max	min	ave
La	48	19	26
Ce	119	35	52
Pr	179	41	73
Nd	262	50	94
Sm	306	60	120
Tb	252	51	98
Dy	177	45	80
Ho	124	39	64
Y	104	24	46
Er	90	33	50
Tm	61	24	36
Yb	43	16	24
Lu	25	10	16
Zr	9	2	5.1
Hf	19	4	9.1
Nb	52	19	30
Ta	149	41	91
Sr	7	0.04	1.1
Ba	20	0.06	1.6
Th	3	1.7	2.4
U	2	0.5	0.9

Table 5.2: Calculated maximum, minimun, and average titanite – melt partition coefficients. See text for details.

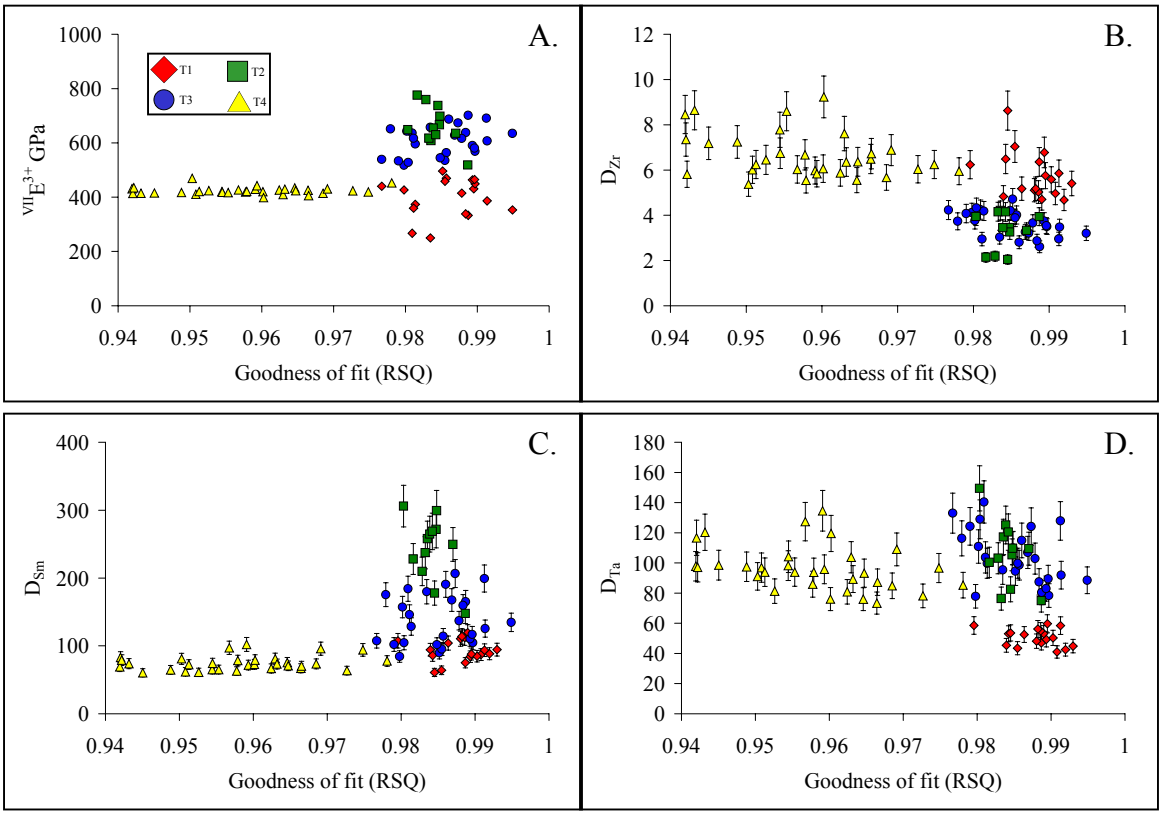

Figure 5.12: Calculated $^{VII}E^{3+}$ and selected partition coefficients versus the goodness of fit to lattice strain model equation (RSQ value). Error bars on D values 10%.

D_{Zr}/D_{Hf} values for the Fasnia titanites and the experiments are quite similar, and all these data show a slight increase in D_{Zr}/D_{Hf} values at lower $^{VII}E^{3+}$. D_{Zr} and D_{Sm} of Fasnia titanites appear to correlate with $^{VII}E^{3+}$, but whereas experimentally determined D_{Sm} values lie along a different array with respect to $^{VII}E^{3+}$, experimental D_{Zr} values do not appear to vary systematically with $^{VII}E^{3+}$. Changes in $^{VII}E^{3+}$ values do not directly correlate with overall titanite compositional variation, represented by Zr contents (Fig. 5.14), rather each titanite type has a different trend: T1 and T2 show little change in Zr contents over a significant range in $^{VII}E^{3+}$; Zr contents in T3 are negatively correlated with $^{VII}E^{3+}$; and T4 has a significant range in Zr contents with little change in $^{VII}E^{3+}$. Glass compositions are positively correlated with $^{VII}E^{3+}$ as a whole, but for the specific glasses corresponding to the titanite types no obvious trend is observed. For example all T3 titanites fit a single glass composition, but calculated $^{VII}E^{3+}$ values show a significant range.

Modeling curves and calculated REE partition coefficients for Fasnia titanites are presented in Figures 5.15, 5.16, and 5.17. Parameters for each model curve pertaining to the different titanite types are given in panels 5.15 A – D. Also presented is a comparison of published D_{REE} from natural samples and experiments. The ideal cation radius for T1 and T4 models is r_0 = 1.018 Å, and for T2 and T3 r_0 = 1.015 Å, both values between Sm and Eu. The ideal partition coefficient D_0 is different for each model: T1=90; T2=75; T3= 150; and T4=200. Model values for $^{VII}E^{3+}$ are: T1 and T2 = 400 GPa; T3 = 600 GPa; and T4 = 660 GPa. All models are calculated at T = 850 ^{o}C and P = 0.2 GPa.

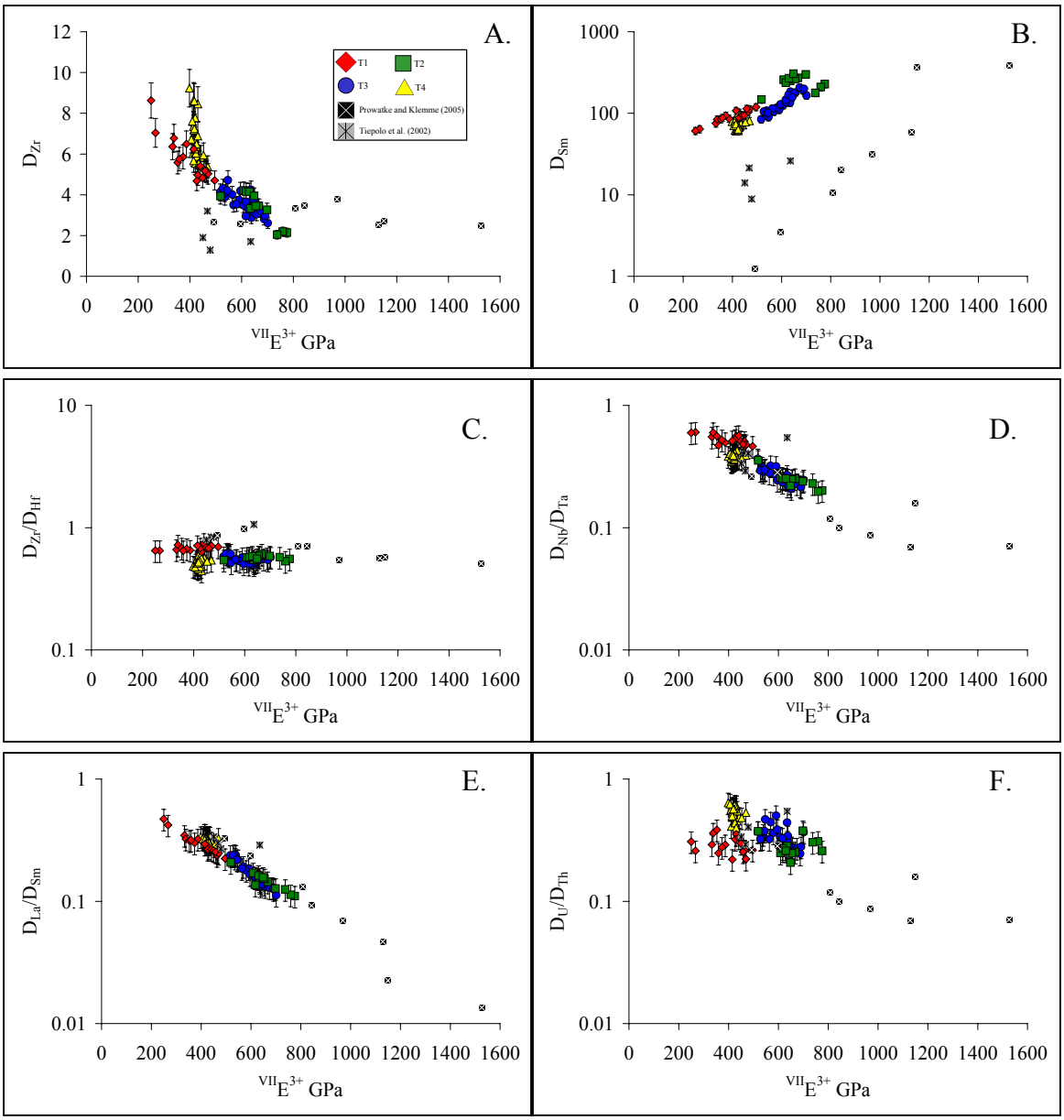

Figure 5.13: Selected calculated partition coefficients and partition coefficient ratios versus $^{VII}E^{3+}$. Error bars on D values 10%, ratios 20%.

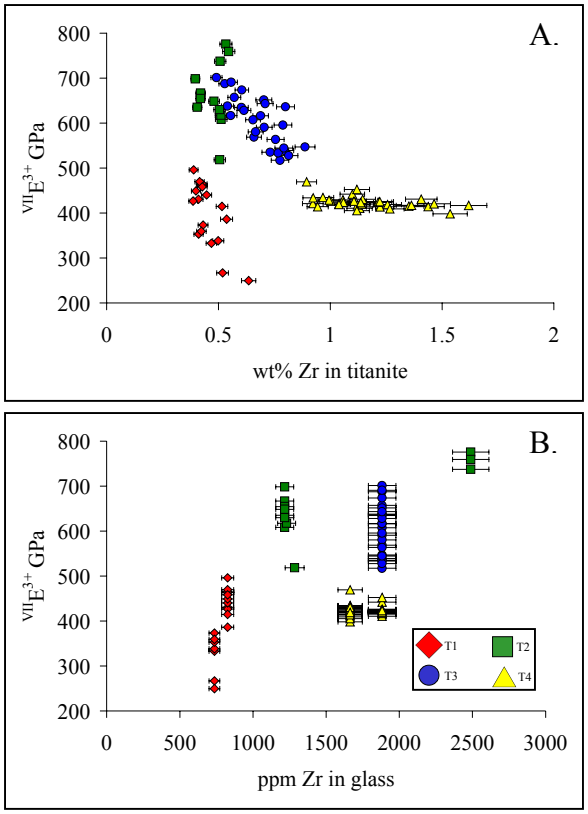

Figure 5.14: $^{VII}E^{3+}$ versus glass (A) and titanite (B) composition. Error bars 10% on Zr contents.

Modeling and calculation results show that titanite – melt partition coefficients (D values) for REE and Y have a significant range in values. Sm is the most compatible trace element investigated in these titanites (D_{Sm} = 60 to 300), and as the model predicts, D values for other REE decrease away from Sm. Although D_{REE} and D_Y are generally positively correlated with one another (5.16 and 5.17), there are clearly two divergent trends for D_{Sm} and D_{Lu}. The range in D_{REE} ratios (i.e., D_{Lu}/D_{Sm}) correlate positively with D_{Nb}/D_{Ta}.

Calculated D_{REE} for Fasnia titanites are higher than experimental results of Green and Pearson (1986; not shown) and Tiepolo et al. (2002), and similar to the upper limit of the range of values reported by Prowatke and Klemme (2005). Titanites from the dacitic Fish Canyon Tuff (Bachmann et al., 2005) are reported to have higher D_{REE} and exceptionally high D_{HREE} when compared to the Fasnia samples. The range in D_{REE} reported by Wörner et al. (1983) for titanites in the phonolitic Laacher See Volcano overlap values determined for Fasnia titanites.

The changing relationship between the partition coefficients of Y and the REE is an interesting result (Fig. 5.17). T1 and T2 titanites have D_Y values that are most similar to D_{Ho}, a relationship that is consistent with their ionic radii and like charge. But T3 and T4 titanites have D_Y values closer to D_{Tm}, a significantly smaller ion with an ionic radius between 0.945 Å (Er) and 0.925 Å (Yb), compared to 0.960 Å (Y).

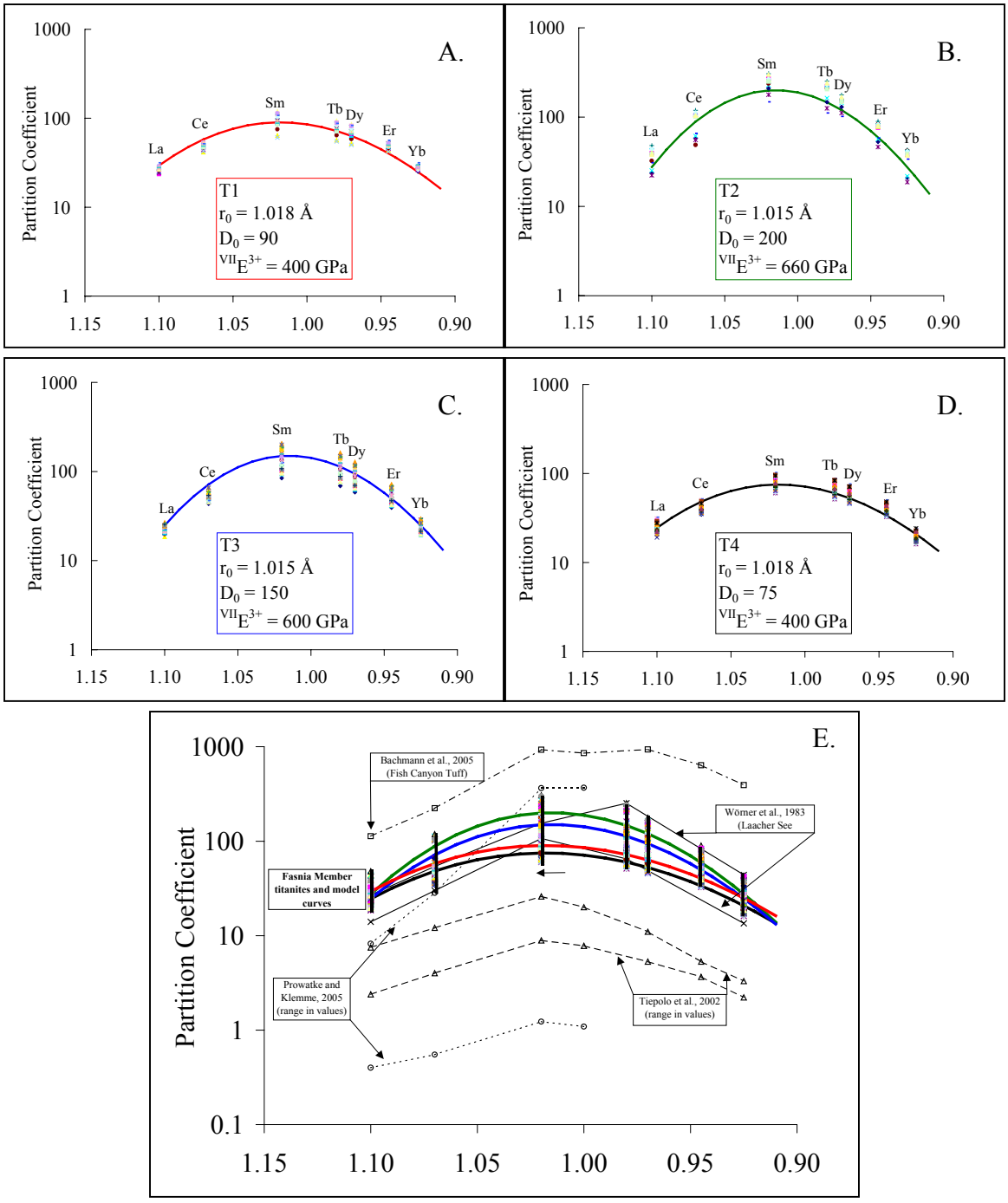

Figure 5.15: Model curves and calculated partition coefficients for Fasnia titanites versus ionic radius (panels A – D). Model curves represent average D values. Parameters are given for each type. Panel E is a comparison of published values and Fasnia titanites. Other data sources: Wörner et al., 1983; Tiepolo et al., 2002; Prowatke and Klemme, 2005; and Bachman et al., 2005.

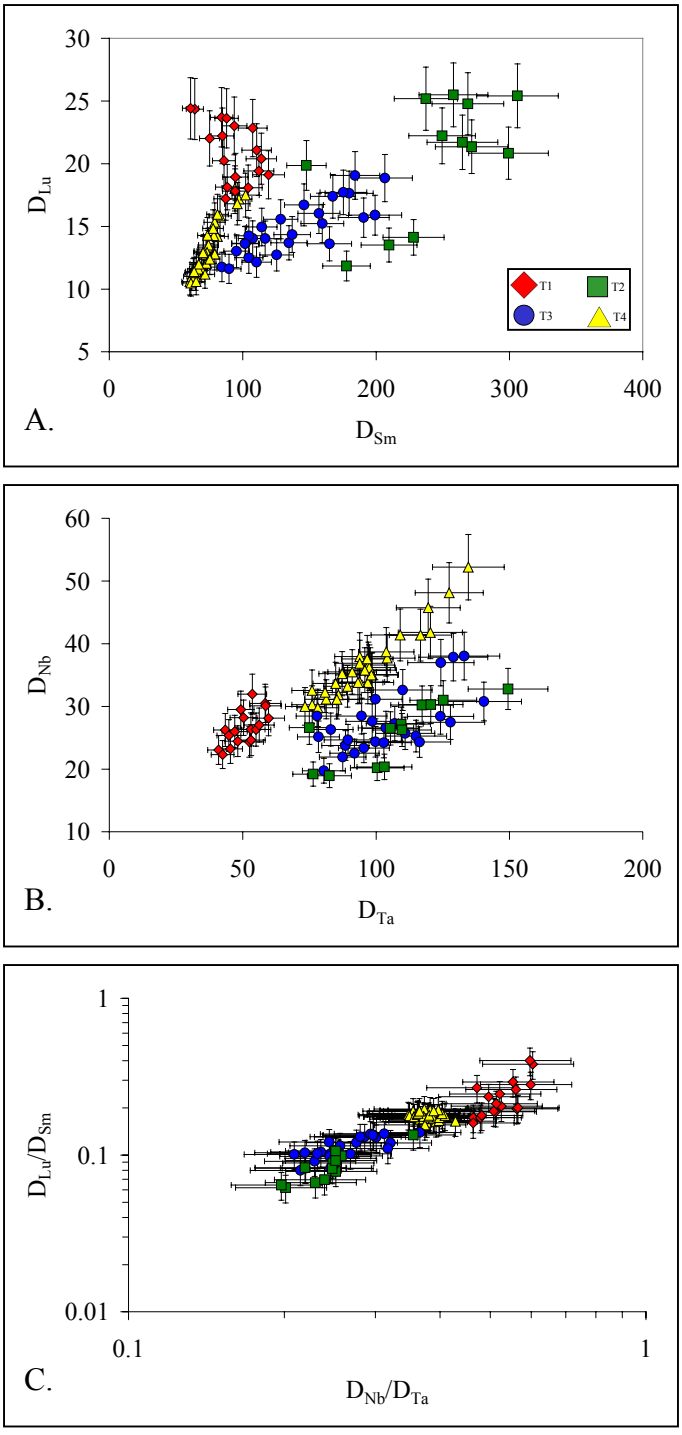

Figure 5.16: Calculated D_{Lu} vs. D_{Sm}, D_{Nb} vs D_{Ta}, and D_{Lu}/D_{Sm} vs. D_{Nb}/D_{Ta} for Fasnia titanites. Note the positive correlelation of the partition coefficient ratios. Error bars 20%.

Discussion

Cation substitution mechanisms

Variations in major, minor, and trace element contents in the Fasnia titanites reflect several important substitution mechanisms operating in this system. The octahedral Ti-site has at least two major mechanisms for Ti^{4+} substitution:

$(Zr^{4+}, Hf^{4+}) = Ti^{4+}$, and

$(Fe^{3+}, Al^{3+}) + (Nb^{5+}, Ta^{5+}) = 2\ Ti^{4+}$.

Fe^{3+} is probably more important than Al^{3+} in this system because Al_2O_3 does not vary significantly or systematically in the titanites. Relationships between Nb, Fe, Na and F (Fig. 5.3) suggest other mechanisms, such as the following coupled substitutions:

$Na^{1+} + (Nb^{5+}, Ta^{5+}) = Ca^{2+} + Ti^{4+}$,

$Na^{1+} + Zr^{4+} + F^{-} = Ca^{2+} + Ti^{4+} + O^{2-}$, and

$Fe^{3+} + F^{-} = Ti^{4+} + O^{2-}$. CaO does not vary systematically, but substitution by Sr, Ba, REE, Y, and Na on the seven-coordinated site could be attributed to these substitutions:

$(Sr^{2+}, Ba^{2+}) = Ca^{2+}$, and

$Na^{+} + (REE^{3+}, Y^{3+}) = 2\ Ca^{2+}$.

But as Na increases, the overall REE and Y contents systematically decrease, an effect also observed by Prowatke and Klemme (2005), calling into question the viability of this mechanism. Another feasible mechanism of REE and Y substitution more consistent with these data is:

$(REE^{3+}, Y^{3+}) + (Fe^{3+}, Al^{3+}) = Ca^{2+} + Ti^{4+}$.

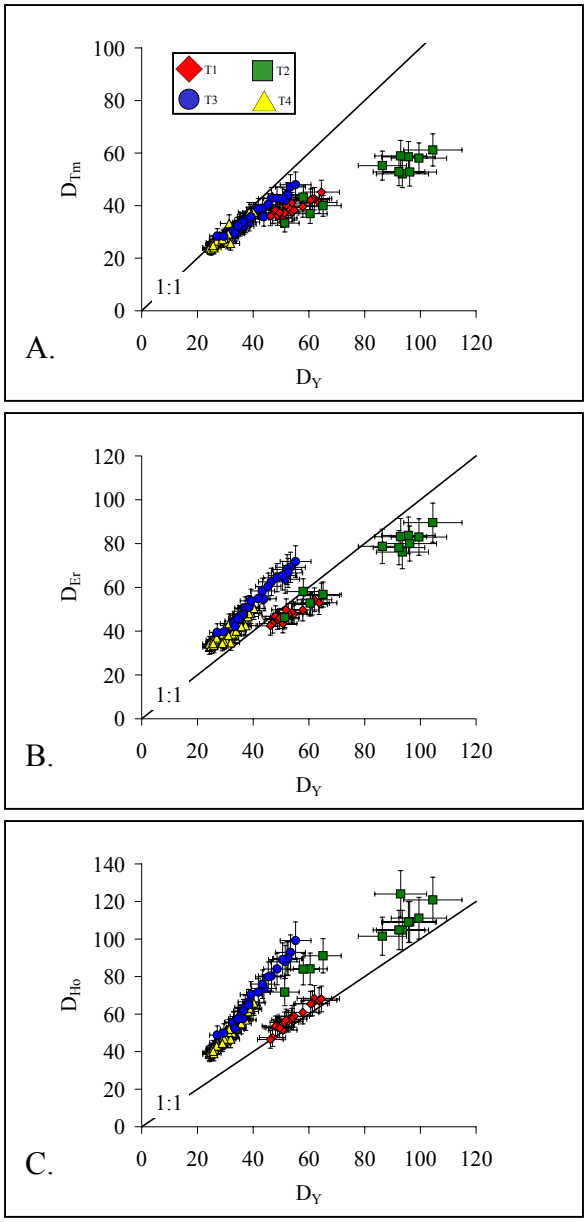

Figure 5.17: D_{REE} vs D_Y. Note that Y partitioning behavior changes relative to Ho, and in fact, in T3 and T4 titanites Y partitions more like Tm.

Fluorine also increases with Na, possibly reflecting the greater importance of this substitution as REE and Y decrease:

$$Na^{1+} + F^{-} = Ca^{2+} + O^{2-}.$$

The substitution of more highly charged cations (i.e., Th^{4+} and U^{4+}) in the Ca-site is most likely achieved by:

$$(Th^{4+}, U^{4+}) + \square = 2\ Ca^{2+},$$

where $\square$ is a vacancy in the Ca-site, but other mechanisms are possible, such as:

$$(Th^{4+}, U^{4+}) + (Fe^{2+}, Mg^{2+}, Mn^{2+}) = Ca^{2+} + Ti^{4+}.$$

What is controlling titanite partition coefficients?

Perhaps the most remarkable result of the LSM modeling is the wide range in calculated partition coefficients for many trace elements of interest (Table 5.2). The relationship between titanite ${}^{VII}E^{3+}$ values and the ratios of REE partition coefficients (i.e., D_{La}/D_{Sm}; Fig. 5.13) is consistent with the LSM model predictions. Accordingly, T2 and T3 titanites that have similar ${}^{VII}E^{3+}$ values have similar D value ratios, as do T1 and T4 titanites, however, all titanites fall along a continuous array. D_0 values (~D_{Sm}; Fig. 5.13) are positively correlated with ${}^{VII}E^{3+}$. This most likely reflects the influence of pyroxene composition on partitioning of the REE in titanite.

Prowatke and Klemme (2005) show that D_{REE} values increase with degree of alumina saturation, and in fact they attained D_{REE} values similar to the Fasnia titanites in melts with similar Al_2O_3 contents to Fasnia phonolitic melts. Prowatke and Klemme (2005) showed that Zr and Hf are far less sensitive to the composition of the bulk melt, nonetheless, the higher D_{Zr} and D_{Hf} of the Fasnia titanites are most likely a result of the high concentrations of these elements in the melts combined with the increasing degree

of substitution in increasingly Ti-deficient titanites. The observed range in $^{VII}E^{3+}$ and D values within any titanite type is best explained by temperature differences within the chemically homogenous liquid from which each type grew.

Titanite clearly fractionates Nb and Ta, strongly preferring Ta over Nb more than 2:1 (Table 5.2), and over the range in titanite compositions D_{Nb}/D_{Ta} varies significantly and systematically with $^{VII}E^{3+}$ and changing D_{REE} ratios (Figs. 5.13 and 5.16). Generally, increasing D_{Nb} and D_{Ta} values can be attributed to decreasing temperature (Green and Pearson, 1986). But the changing D_{Nb}/D_{Ta} values are more difficult to explain because the ionic radii of Nb and Ta are essentially equal (Shannon, 1976), and so should be unaffected by changes in $^{VII}E^{3+}$, whereas changing D_{REE} ratios (i.e., D_{La}/D_{Sm}, D_{Lu}/D_{Sm}) are predicted. Tiepolo et al. (2000) have suggested based on measured changes in the M1-O distance in amphibole that Ta is indeed slightly smaller than Nb, and hence, more compatible. But until this is verified by direct measurement, it is only circumspect. Surely the suggested difference in ionic radii based on fitting data to the lattice strain model (0.66 Å and 0.64 Å for Nb and Ta, respectively; Shannon, 1976; Blundy and Wood, 2003; Schmidt, 2004) could be resolved by X-ray diffraction techniques. Tiepolo et al. (2000) argued that because D_{Ta} increases with increasing Al^{3+} substitution in their experiments, which has the effect of decreasing the size of the octahedral site (Hollabaugh, 1980), Ta must be smaller than Nb. Tiepolo et al. (2002) also show that in their experiments D_{Nb}/D_{Ta} decreases with increasing Al. However in the Fasnia titanites Al contents do not vary systematically with titanite composition (i.e., with Ti and Zr contents) nor do D_{Ta} values (Figs. 5.1 and 5.12), however Fe/Al varies (Fig. 5.3). T4 titanites have both high Fe/Al and high D_{Nb}/D_{Ta}, but T1 titanites have low Fe/Al and the

highest D_{Nb}/D_{Ta} values. So although Fe and Al are very likely exerting some influence on Nb and Ta partitioning, it is clearly more complicated. Until differences in ionic radii for Nb and Ta are verified, this explanation of fractionation can only be treated as speculation.

Proceeding with the assumption that the ionic radii of Nb and Ta are truly the same (Shannon, 1976), inherent differences in the electronic structures of the elements may in fact be responsible for the different partitioning behavior of the elements. One possibility is the differences in charge densities, such that Nb has 36/41 electrons and Ta has 68/73 electrons, hence Ta has a lower charge density than Nb at the surface of the ion. In addition, the electrons in the *f* orbital of Ta (Nb has no *f* orbital) screen the full charge effect of the nucleus from outer electrons and adjacent ions (Brown et al., 1994). Quite possibly it is this combined effect of lower charge density and screening in the Ta atom that allows Ta to make slightly weaker bonds in the liquid than Nb, and therefore Ta is more compatible in the solid. Horng and Hess (2000) attribute Nb/Ta fractionation in rutile to differences in the molecular electronic polarizabilities (α_G; Jaffe, 1988) of Nb_2O_5 and Ta_2O_5, 26.239 and 24.274, respectively (Horng and Hess, 2000). The lower polarizability of Ta causes less distortion of the octahedral Ti site in rutile because it forms weaker bonds than Nb, and consequently a smaller amount of Nb is incorporated into the structure. Ta also has a different electronegativity than Nb (1.5 compared to 1.6 on the Pauling scale, respectively), suggesting that Ta is more able to part with the melt and be incorporated into a solid.

The possible electronic mechanisms of Nb and Ta fractionation, if responsible, should apply to other "identical" element pairs such as Zr/Hf and Y/Ho. Y has already

been shown to have variable behavior relative to the REE, behaving more like Ho, Er or Tm depending on the titanite type. The atomic structures of Hf and the REE include *f* orbitals, whereas Zr and Y do not. Like Nb and Ta, Zr and Hf have different electronegativities (1.4 and 1.3 on the Pauling scale, respectively). One might predict based on their positions next to Nb and Ta that Zr and Hf would behave similarly, but D_{Zr}/D_{Hf} does not vary like D_{Nb}/D_{Ta}, and in fact T1 titanites have only slightly higher D_{Zr}/D_{Hf} compared to the rest. So although the more compatible element in each pair similarly contains *f* electrons, subtle but important differences in atomic structure appear to result in differences in partitioning behavior.

It is clear that mechanisms and controls of trace element partitioning in this system (or any system for that matter) are complex. The most important factors controlling partitioning behavior are the charge and radius of substituent cations, composition of the mineral and melt, and availability of other cations to allow reasonable charge balanced substitutions. The subtleties of the fractionation of elements with like charge and ionic radii appear to be controlled by the slight differences in the electronic properties of the elements themselves, most important being the presence or absence of *f* electrons. This behavior signifies a limit to what the lattice strain model can predict on the basis of radius and charge alone.

Petrogenetic implications of titanite compositions

Titanite compositional variability, like the glasses described in Chapter 3 and the pyroxenes in Chapter 4, reflect the complex magma dynamics operating during the Fasnia magmatic event. Based on the REE lattice strain modeling, T1 titanites grew in distinct low-Zr phonolite magma (Fig. 5.14). Most T2 titanites are consistent with a

genesis in hybrid phonolite with approximately 1200 ppm Zr, but three T2 titanites pair with high-Zr phonolite with 2488 ppm Zr. Interestingly, the model results suggest that all T3 titanites have an origin in a single liquid composition, hybrid phonolite with 1882 ppm Zr. The large range in $^{VII}E^{3+}$ values for these titanites reflects that this single liquid composition probably had a significant temperature gradient (Blundy and Wood, 2003). Many T4 titanites also grew in the hybrid phonolite with 1882 ppm Zr and several pair with phonolite with 1663 ppm Zr. $^{VII}E^{3+}$ values for these T4 titanites do not vary, signifying perhaps that the magma, or at least the portion crystallizing T4 titanites, is in thermal equilibrium (Blundy and Wood, 2003).

In Chapter 4, modeling of salites and Na-salites led to conclusions that the pyroxenes grew in low-Zr and hybrid phonolite, respectively. Ti-salites represent a transitional magma (i.e., less evolved than low-Zr phonolite) and titanaugites represent the mafic magmatic component. In Chapter 3, three dominant glass compositions representing three different magma types were identified: low-Zr phonolite, pyroxene free high-Zr phonolite, and hybrid phonolite which itself a product of mixing between low- and high-Zr phonolite. The interpretation of the Fasnia titanites in the context of these other Fasnia magmatic components (i.e., glasses and pyroxenes) suggests the following series of events. Prior to the Fasnia mixing event, low-Zr phonolite crystallized T1 titanites and salites in isolation. Pyroxene free high-Zr phonolite and low-Zr phonolite were mixed. T2 titanites are interpreted to have crystallized in the early stages of the mixing event. T3 titanites crystallized later as hybridization progresses, followed by T4 titanites that crystallized along with Na-salites. Similar trends showing little variation in La/Sm, Lu/Sm, and Nb/Ta values versus Zr contents provides sound geochemical

evidence for the co-precipitation of T4 titanites and Na-salites. Just prior to the Fasnia eruption, the magma system was severely disrupted causing transfer of crystals from parental liquids into different compositions that were then erupted.

The significance of the observed variation in D values for titanite trace elements implies that a single titanite partition coefficient is insufficient for accurate fractionation modeling in the Fasnia system, and probably in systems with comparable geochemical and physical complexities. The variation in titanite D values observed in the Fasnia, for example, allow for differences in the amount of titanite in a fractionating assemblage to achieve similar geochemical trends. Using Ta as an example, the difference between using D_{Ta} = 100 versus D_{Ta} = 50 essentially constitutes a doubling in the amount of titanite in a model fractionating assemblage. Therefore geochemical modeling of the Fasnia (and other Diego Hernández Formation members) is more complicated than simply choosing a set of appropriate D values for the system, it really involves assessing the appropriateness of partition coefficients at different points of evolution or in mixing processes.

Conclusions

The four titanite compositions identified in the Fasnia Member have geneses in different phonolitic magma compositions. T1 titanites grew in low-Zr phonolite, whereas T2, T3, and T4 titanites grew in liquids resulting from mixing between low-Zr and high-Zr phonolite end members. The significant range in D values for the titanites probably reflects melt compositional and temperature effects primarily, but titanite composition (i.e., Ti contents, Fe/Al) also influences trace element partitioning behavior. Titanites, pyroxenes, and glasses all support the interpretation that the Fasnia represents a complex

magmatic event involving distinct low-Zr and high-Zr phonolite magmas (and volumetrically minor mafic magma) that came together, mixed to varying degrees with portions becoming hybridized. The hybrid phonolite crystallized (at least) titanite and Na-salites before eruption.

References

Bachmann, O., Dungan, M.A., Bussy, F., 2005. Insights into shallow magmatic processes in large silicic magma bodies: the trace element record in the Fish Canyon magma body, Colorado. Contrib. Mineral. Petrol. 149, 338-349.

Bau, M., 1996. Controls on the fractionation of isovalent trace elements in magmatic and aqueous systems: evidence from Y/Ho, Zr/Hf, and the lanthanide tetrad effect. Contrib. Mineral. Petrol. 123, 323-333.

Blundy, J.D., Wood, B.J., 1994. Prediction of crystal-melt partition coefficients from elastic moduli. Nature 372, 452-454.

Blundy, J.D., Wood, B.J., 2003. Partitioning of trace elements between crystals and melts. Earth Planet. Sci. Lett. 210, 383-397.

Cerny, P., Povondra, P., 1972. An Al, F-rich metamict titanite from Czechoslovakia. N. Jb. Miner. Mh., 9, 400-406.

Cérny, P., Novak, M., Chapman, R., 1995. The Al(Nb)TaTi-2 substitution in titanite: the emergence of a new species? Mineral. Petrol. 52, 61-73.

Green, T.H., Pearson, N.J., 1986. Rare-earth element partitioning between sphene and coexisting silicate liquid at high pressure and temperature. Chem. Geol. 55, 105-119.

Green, T.H., Pearson, N.J., 1987. An experimental study of Nb and Ta partitioning between Ti-rich minerals and silicate liquids at high pressure and temperature. Geochim. Cosmochim. Acta 51, 55-62.

Higgins, J.B., Ribbe, P.H., 1976. The crystal chemistry and space groups of natural and synthetic titanites. Am. Mineral. 62, 878-888.

Hollabaugh, C.L., 1980. Experimental mineralogy and crystal chemistry of sphene in the system soda-lime-alumina-titanina-silica-water. Ph.D. Thesis, Washington State University, 107 pp.

Horng, W.S., Hess, P.C., 2000. Partition coefficients of Nb and Ta between rutile and anhydrous haplogranite melts. Contrib. Mineral. Petrol. 138, 176-185.

Jaffe, H.W., 1947. Reexamination of sphene (titanite). Am. Mineral. 32, 637-642.

Jaffe, H.W., 1988. Crystal chemistry and refractivity. Cambridge University Press, Cambridge, p118-140.

McDonough, W.F., Sun, S.-s.. 1995. The composition of the Earth. Chem. Geol. 120, 223-253.

Mongiorgi, R., Sanseverino, L.R. di, 1968. A reconsideration of the structure of titanite, $CaTiOSiO_4$. Mineral. Petrogr. Acta 14, 123-141.

Prowatke, S., Klemme, S., 2005. Effect of melt composition on the partitioning of trace elements between titanite and silicate melt. Geochim. Cosmochim. Acta 69, 695-709.

Sahama, T.G., 1946. On the chemistry of the mineral titanite. Bulletin de la Commission Geologiue de Finland. 138, 88-120.

Shannon, R.D., 1976. Revised effective ionic radii and systematic studies of interatomic distances in halides and chalcogenides. Acta Cryst. A32, 751-767.

Tiepolo, M., Vannucci, R., Oberti, R., Foley, S., Bottazzi, P., Zanetti, A., 2000. Nb and Ta incorporation and fractionation in titanian pargasite and kaersutite: Crystal-chemical constraints and implications for natural systems. Earth Planet. Sci. Lett. 176, 185-201.

Tiepolo, M., Oberti, R., Vannucci, R., 2002. Trace-element incorporation in titanite: constraints from experimentally determined solid/liquid partition coefficients. Chem. Geol. 191, 105-119.

Wolff, J.A., 1984. Variation in Nb/Ta during differentiation of phonolitic magma, Tenerife, Canary Islands. Geochim. Cosmochim. Acta 48, 1345-1348.

Wörner, G., Beusen, J.M., Duchateau, N., Gijbels, R., Schmincke, H.-U., 1983. Trace element abundances and mineral/melt distribution coefficients in phonolites from the Laacher See Volcano (Germany). Contrib. Mineral. Petrol. 84, 152-173.

Zabavnikova, I.I., 1957. Diadochic substitution in sphene. Geochemistry 3, 271-278.

Zachariasen, W.H., 1930. The crystal structure of titanite. Z. Krystallogr. 73, 7-16.

Chapter 6

The Diego Hernández Formation: the geochemistry of a multi-cyclic explosive phonolitic sequence

Abstract

The 0.35 – 0.19 Ma Diego Hernández Formation (DHF) represents the most recent explosive phonolitic eruptive period on the island of Tenerife, Canary Islands. Two distinct phonolite lineages have persisted, or have been regenerated, throughout the history of the DHF. Apart from differences in Si/Al, these phonolites have very similar major element compositions. Differences in trace element contents with stratigraphy allow four chemostratigraphic units, DHF bs, DHF I, DHF II and DHF III, to be distinguished. MREE, Nb, and Ta are very compatible in titanite and sensitive to small changes in the degree of titanite fractionation, therefore, the observed trace element variations in the DHF arise from variable titanite fractionation histories. Nb/Zr makes a good reference value for the two phonolitic lineages; DHF I and DHF II phonolites have Nb/Zr <0.2, and DHF III and most of DHF bs phonolites have Nb/Zr >0.2. During any one eruption a single phonolite type dominates, but detailed geochemical investigations show that both magmas exist simultaneously. Phonolite types remain relatively isolated from one another until precursory eruptive events, or the eruption itself, mingles the magmas. Syenite blocks associated voluminous ignimbrites throughout the DHF have chemistries consistent with the two phonolite lineages, and likely represent solidified and variably altered phonolitic equivalents at depth. Trace element data supports an origin for DHF I- and DHF II-type phonolitic magmas through melting of these preexisting syenite plutons. Geochemical data from the 0.31 Ma Fasnia Member support the existence of a

zoned phonolitic magma body with syenite derived high-Zr phonolitic melts at the roof, low-Zr phonolite at the base, and a zone of near-hybridized phonolite in the middle. High-Zr phonolite appears to be relatively crystal poor, whereas hybrid and low-Zr phonolite crystallized distinct clinopyroxene and titanite populations. The Fasnia eruption was triggered by a mafic recharge event that disrupted the entire system, causing the transference of the different crystal assemblages throughout the magma body and juxtaposing low-Zr (base) and high-Zr phonolitic (roof) liquids seen early in the eruption sequence in banded and mingled pumices.

The Fasnia is the second major DHF I eruption, bounded by the 0.32 Ma Aldea Member below and the 0.27 Ma Poris Member above. Geochemical data suggest a link between these three events in which the melting of syenite began prior to the Aldea and continued until the eruption of Fasnia, at which time either the conditions of melting became unfavorable or syenite was no longer available to be melted. Some hybrid magma generated during the Fasnia remained at depth and was later rejuvenated and subsequently exhausted during the Poris eruption. The Poris also contains low-Zr phonolite that is geochemically similar to the Fasnia, suggesting ongoing or renewed low-Zr phonolite genesis during this time, or rejuvenation of Fasnia low-Zr phonolite.

Introduction

This chapter describes the geochemistry of the Diego Hernández Formation, Tenerife, Spain, and is complementary to Edgar et al.'s (2007) description of the stratigraphy, geochronology, and general physical volcanology of the formation, summarized in Chapter 2. Some data used within have been presented in previous publications referenced throughout this chapter (e.g., Wolff, 1985a & 1987; Wolff et al., 2000; Edgar et al., 2002; Edgar et al., 2007), but the dataset presented here contains additional data and therefore supersedes previous publications.

The stratigraphy and general volcanology of the Diego Hernàndez Formation (DHF) is thoroughly treated by Edgar et al. (2007), and detailed physical volcanological aspects of some members are discussed by Wolff (1985), Edgar (2002), Brown et al. (2003), and Pitarri (2005). Refer to Chapter 2 for a summary of Tenerife geology and descriptions of DHF stratigraphy and geochronology.

Analytical Procedures

Sample preparation

Whole-rock major and trace elements were determined using x-ray fluorescence (XRF) and inductively coupled plasma (ICP) spectrometers in the Washington State University GeoAnalytical Laboratory. Where possible for pyroclastic deposits, single pumice clasts were analyzed, but in some cases multiple clasts were combined for an analysis. Weathered surfaces on all samples were removed using a diamond lap and deionized water and samples were then dried in an oven overnight. Samples were prepared according to laboratory procedures outlined by Knaack et al. (1994) and Johnson et al. (1999), except that the pumice method (Olin, 2003) was applied to pumice

clasts. In contrast to hard rocks in which fines are removed after a sample is coarsely chipped, in the pumice method the whole pumice sample is conserved for XRF and ICP analyses. Fines conservation is preferred because during the chipping process, phenocrysts from pumices are far more likely to be separated from the matrix, therefore resulting in whole-rock data biased toward an incorrect, more highly fractionated composition for a given sample (Wolff, 1985b). This is not the case for hard rocks (e.g., basaltic rocks) because phenocrysts are seen to break with the matrix and not be separated on a scale that will bias the analysis.

XRF

Prior to January, 2002, samples were analyzed on a Rigaku 3370 X-ray fluorescence spectrometer. Beginning in January 2003, samples were analyzed on a ThermoARL Advant'XP+ sequential X-ray fluorescence spectrometer. Both spectrometers use a rhodium (Rh) target, run at 50kV/50mA with full vacuum and a 25 mm mask for all elements and all samples. Every attempt was made to assure that data from both instruments are compatible, and therefore data are treated as such here.

ICP-MS

Whole-rock ICP analyses were performed on a Hewlett-Packard 4500 Series Quadrupole inductively coupled mass spectrometer (ICP-MS) operating at 1300 watts, optimized for low oxides and calibrated against 3 whole-rock in-house standards. Two methods of sample dissolution were used, fusion-dissolution and straight dissolution. The fusion-dissolution method (Knaack et al., 1994) consists of a 1:1 dilithium tetraborate and rock powder mixture (about 2 grams each) fused in a muffle furnace for five minutes at 1000^{o}C, cooled and powdered. Fusion-dissolution uses 250 mg of this powder, whereas

the straight dissolution method uses 200 mg pure rock powder, in many cases from single clasts, but the two-stage digestion of both powders is very similar. In an open Teflon vial, all samples are wetted with 2 ml 70% HNO_3 (+ 2 ml 37% HCl for straight dissolution), 6 ml 50% HF and 2 ml 71% $HClO_4$ are added and evaporated to dryness on a 110°C hotplate (~24 hours). Each vial is rinsed with ultra-pure deionized water and 2 ml 71% $HClO_4$ is added (to convert insoluble fluorides to soluble perchlorates), and the sample is evaporated to dryness again, this time at 165°C (~6 hours). To all samples, 3 ml 70% HNO_3, 8 drops 30% H_2O_2, 3 drops of 50% HF, and 1 ml of internal standard of In, Re, and Ru are added, and then diluted to 60 ml final volume. During the analysis, a further 10X dilution occurs with sample delivery to the ICP-MS. The fusion-dissolution procedure ensures the complete dissolution of zircons and other refractory phases such as garnets, however no such phases have been identified in these rocks and straight dissolution results agree with fusion-dissolution results.

LA-ICP-MS

LA-ICP-MS determined trace element contents in glasses are included in some diagrams in this chapter. See Chapters 1 and 3 for additional analytical details and detailed discussion of glass compositional variability.

Geochemistry

The general petrology and geochemistry of the DHF has been described by Wolff et al. (2000), while more detailed descriptions of the Aldea and Poris members are given by Wolff (1985) and Edgar et al. (2002) respectively. In this section, temporal and geochemical evolution of the DHF phonolites is discussed in the context of the chronology and erupted volumes of magma, in particular the repeated eruption of

phonolitic magma with two distinct trace-element signatures and similarities between the Aldea, Fasnia, and Poris events.

Major element compositions of phonolites range from metaluminous to weakly peralkaline, with up to 16 weight % total alkalies (Fi.g 6.1). The phenocryst assemblage is sodic sanidine or anorthoclase + clinopyroxene + magnetite + biotite + titanite + häuyne or sodalite ± nepheline. The least evolved phonolites may additionally have small amounts of kaersutite and ilmenite, while sodalite and nepheline are restricted to the more evolved compositions. There are no significant differences in phenocryst assemblage between DHF I, II and III phonolites, although häuyne is more prominent in DHF I units. Total phenocryst contents vary widely; most pumices have ≤ 5% phenocrysts, but highly porphyritic pumices occur in the Aldea, Poris and Abrigo members. Many samples have been at least slightly modified by loss of alkalies and Na/K exchange, but the freshest DHF I pumices have compositions very close to the 1 kbar water-saturated phonolitic minimum in the *Ne-Ks-Q* system (Fig. 6.1) and are mildly peralkaline with (Na+K)/Al ≈ 1.1. Those from DHF III have lower Al_2O_3 ((Na+K)/Al ≈ 1.2) and are slightly less silica undersaturated, although still strongly *ne*-normative.

Six of the major members (Aldea, Fasnia, Poris, Arafo, Caleta, Abrigo) and some minor units of the DHF additionally bear a mafic magmatic component, which most commonly appears as black streaks and patches in banded pumice. In any one unit, the mafic component itself typically includes both basaltic and intermediate (tephriphonolite) compositions introduced by pre-eruptive magma mixing (Wolff, 1983, 1985; Edgar et al., 2002).

Major and minor element oxides in phonolite

Evolved DHF magmas plot dominantly in the phonolite and trachyte fields on a total alkalies versus silica (TAS) diagram (Fig. 2.1). Samples plotting in the trachyte field are most likely phonolites that have experienced post-eruptive alkali loss, and although Fasnia samples have been screened for this effect (see Chapter 3), samples from other members have not been. No fresh trachytes have been identified in the DHF, therefore samples plotting in the trachyte field in Figure 6.1 are treated as phonolites in subsequent descriptions and discussions. Samples from all units with clear physical (e.g., banding) or geochemical (e.g., elevated Ni contents) indicators of mafic contamination have been filtered from the dataset.

Small but significant differences in major element contents exist between the chemostratigraphic units (Fig. 6.2). Much of DHF III has lower Al_2O_3 than other units (<20 wt% Al_2O_3 vs. >20 wt%, respectively), although several DHF III samples, mostly from the Cruz Sequence, have higher Al contents. TiO_2 contents are also generally higher in DHF III phonolites with most samples having >0.6 wt% TiO_2, compared to DHF I and II phonolites that have TiO_2 as low as 0.3 wt%. DHF bs generally plots between these two end members in TiO_2, but DHF bs clearly has elevated MnO and slightly higher FeO compared to the other units. SiO_2, CaO, and P_2O_5 contents overlap significantly and cannot distinguish the units.

Si/Al best distinguishes phonolite types (Fig. 6.3). Interestingly, DHF bs has Si/Al values more like DHF I, II than DHF III. Most DHF III phonolites have higher Si/Al values (>2.6) than the other units. Si/Al versus Nb clearly distinguishes the chemostratigraphic units. Trace element contents are discussed further below.

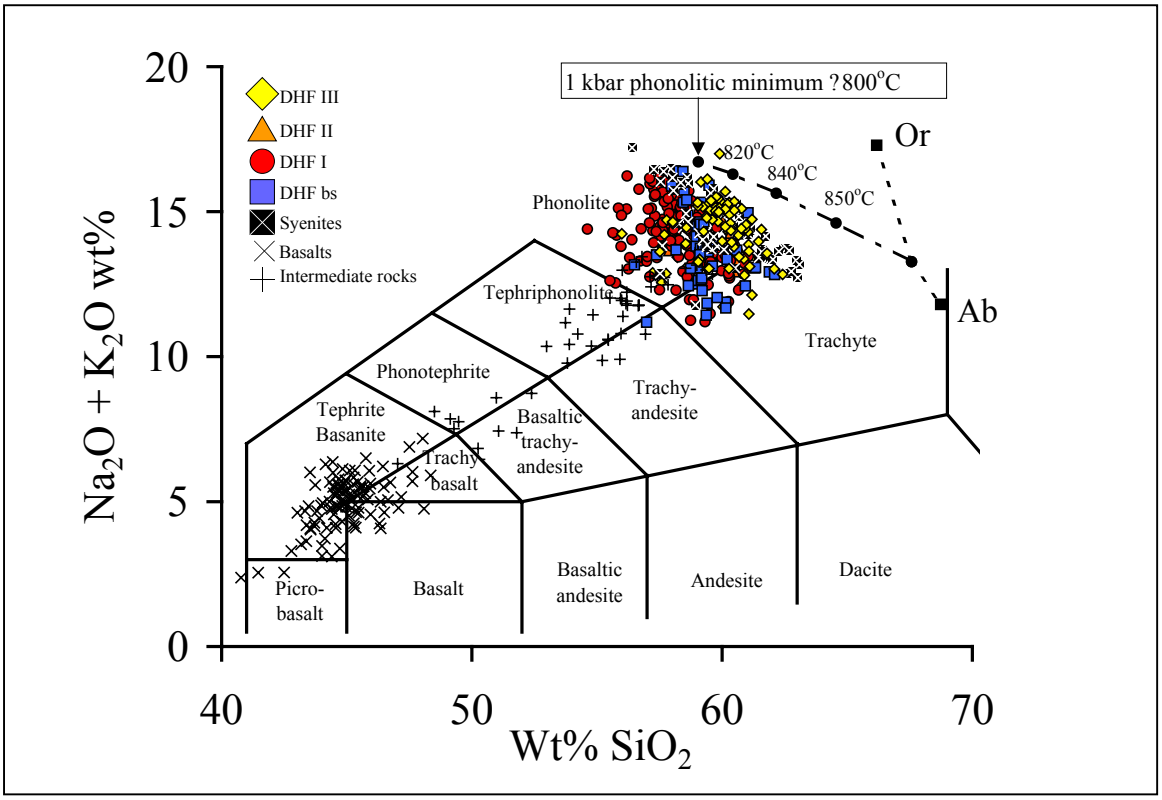

Figure 6.1: Evolved DHF magmas are clearly dominated by phonolites, with lesser trachytes. Samples at lower Na_2O + K_2O values in the trachyte and trachyandesite fields, have lost alkalies. The lack of distinction between DHF major elements reflects that the magma compositions lie at or near the phonolitic minimum (see text; after Le Bas et al., 1986). Phonolitic minimum from Hamilton and Mackenzie (1965).

Major and minor element oxides in syenites

The syenites recovered from DHF pyroclastic deposits cover the major and trace element geochemical spectrum of the phonolitic whole-rocks, and are therefore believed to represent fully crystallized phonolitic magmas (Wolff, 1987). Major and minor element oxides for DHF syenites show less overall scatter than the phonolites and plot in two distinct populations geochemically equivalent to DHF I, II phonolites and DHF III phonolites (Wolff et al., 2000). DHF I, II type syenites have higher Al_2O_3, and lower TiO_2 and MnO contents than DHF III type syenites (Fig. 6.2). Syenite Si/Al values also mimic the phonolites, with two groups plotting at values consistent with DHF III and DHF I, II phonolites. DHF III phonolites and syenites are also geochemically similar to older Guajara age phonolites (Wolff et al., 2000).

Trace elements in phonolite

In addition to providing petrologic information, significant resolvable differences in trace element contents of DHF pumices allow better resolution of chemostratigraphic units and individual DHF members. High field strength (HFSE), large ion lithophile (LILE) and rare earth (REE) elements, such as Zr, Nb, Ta, Sm and Th occur in minor and trace amounts, and range in concentration two- to six-fold (Fig. 6.4). Many elements that normally exhibit incompatible behavior in magmatic systems are compatible into titanite (i.e. Nb, Ta, MREE). The ranges in concentrations of these elements in the DHF phonolites have been attributed to 0.5 – 5% titanite in the fractionating assemblage (Wolff, 1984; Wolff et al., 2000), however the results of the Fasnia geochemical study presented in Chapters 3 through 5 implies that the processes responsible for the observed geochemical differences are probably more complicated. Zr is used as an indicator of

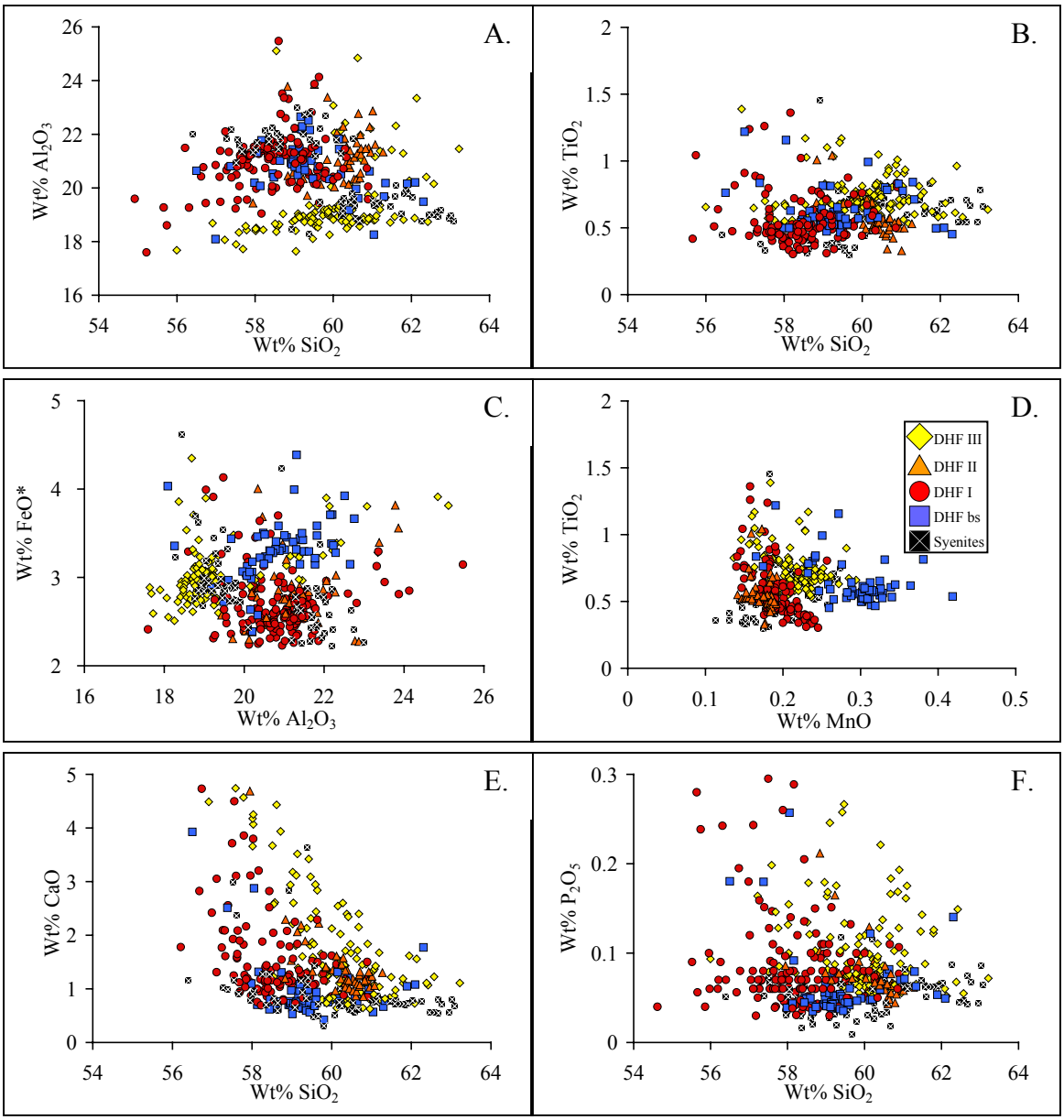

Figure 6.2: Major element oxide contents in DHF phonolites and syenites.

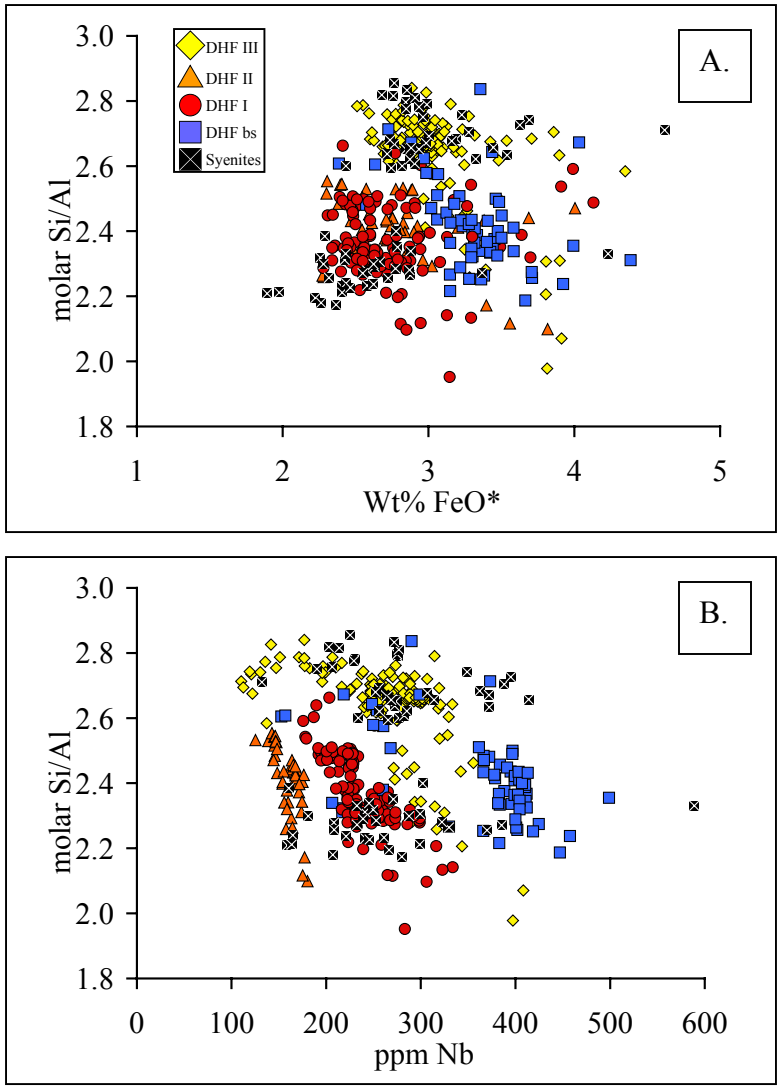

Figure 6.3: Si/Al values for DHF phonolites and syenites.

fractionation, and although it is compatible into titanite (D_{Zr} = 2 to 9; Chapter 5), bulk D_{Zr} remains low due to the low abundance of titanite, typically accounting for ~1% of the fractionating assemblage.

Zr for the entire DHF shows a broad negative correlation with TiO_2 (Fig. 6.4), consistent with late stage fractionation of Ti-rich minerals such as titanite and Ti-oxides. Most of the DHFbs samples are quite similar to DHF III phonolites, but with distinctly higher Nb and Ta contents, as well as elevated Zr, Th, and Sm. A few DHF bs units are noteworthy for having DHF I, II compositions (Figs. 6.4). Apart from these few units, DHFbs element ratios are fairly restricted, e.g., Nb/Ta, La/Sm and Pb/Ce (Fig. 6.5), and most similar to DHF III compositional trends.

DHF I has been analyzed most intensively, and is characterized by well correlated Zr and Th (Fig. 6.4). DHF I has intermediate Nb contents and is depleted in Ta and Sm, indicative of titanite fractionation. Titanite-sensitive element ratios, in the DHF are negatively correlated with increasing Zr contents, i.e., Nb/Ta, La/Sm, Pb/Ce, and Nb/Zr (Fig. 6.5).

DHF II is characterized by lower Zr contents (730 – 1088 ppm). It is also more depleted in Nb, Ta, Sm, and Y than any other chemostratigraphic unit (Fig. 6.4). DHF II also extends to highly fractionated Nb/Ta, La/Sm and Pb/Ce values, similar to the most evolved DHF I samples, but at lower Zr concentrations. Titanite must play a significant role in the petrogenesis of these rocks in order to account for these features.

Like DHF I, DHF III samples have a large range in composition. Zr, Th and Pb trend from low to intermediate concentrations and have intermediate to high Nb, Ta, and Sm compared to DHF I, II phonolites. Nb/Ta, La/Sm and Pb/Ce are generally lower than

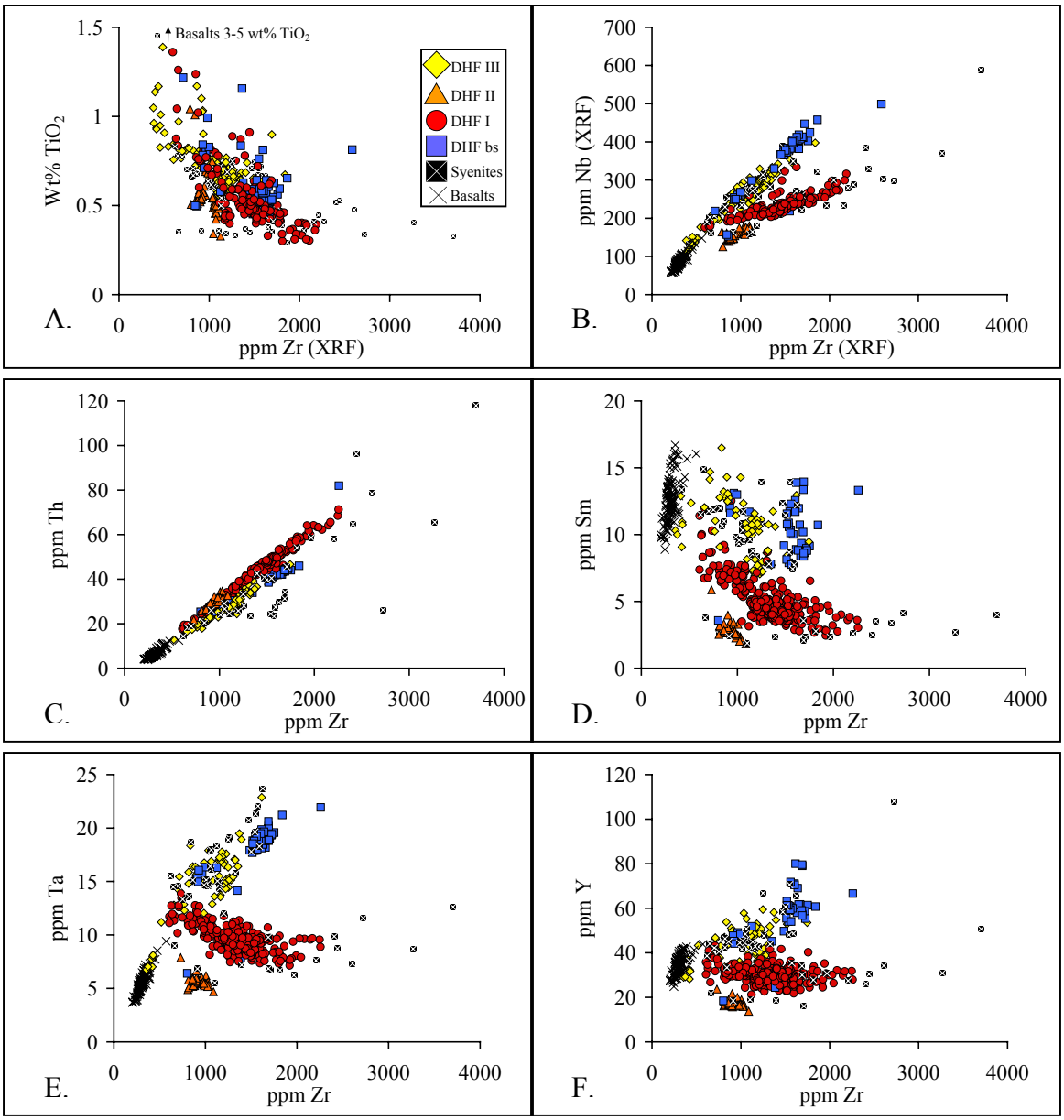

Figure 6.4: Trace element contents in DHF phonolites, syenites, and related basalts.

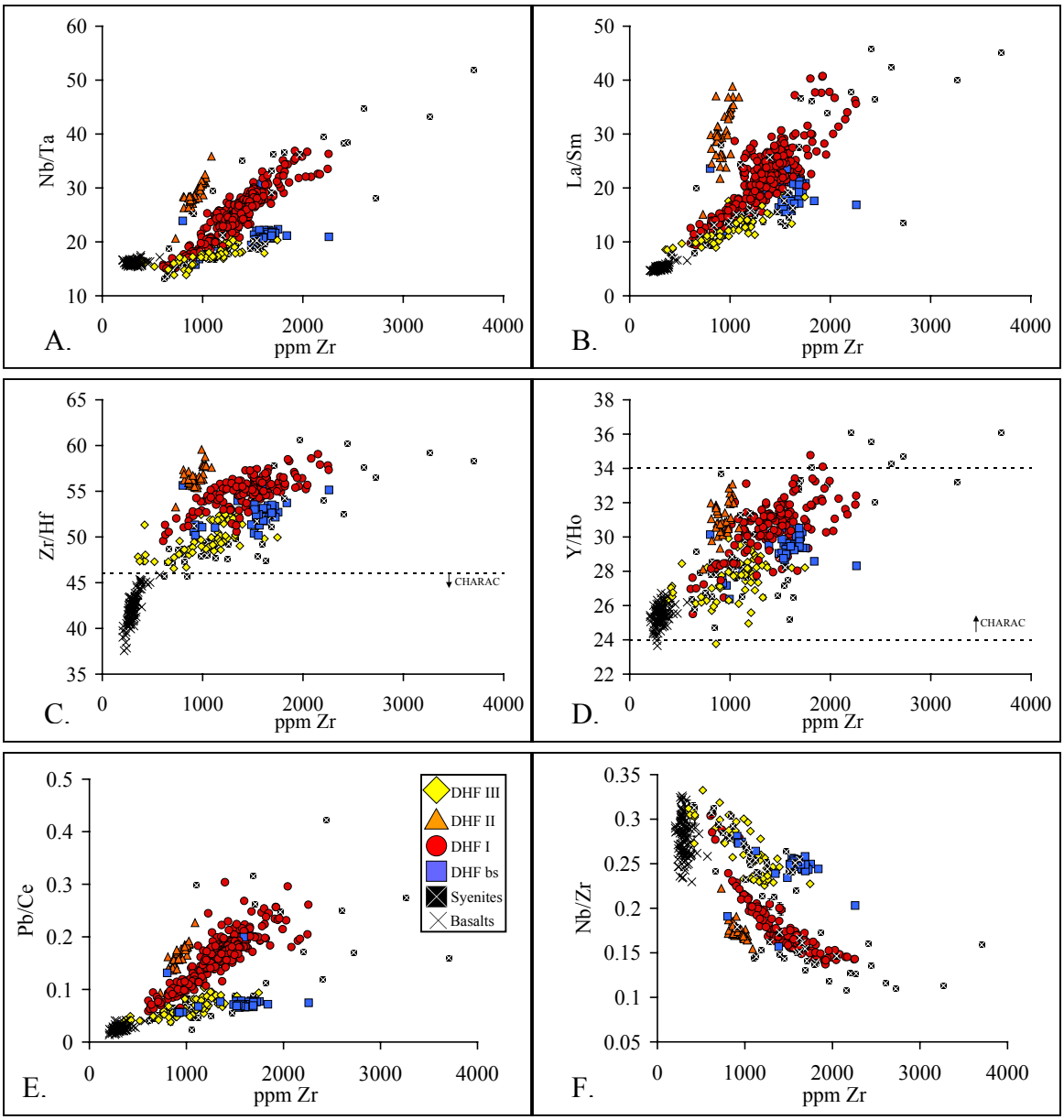

Figure 6.5: Selected trace element ratios for DHF phonolites, syenites, and related basalts.

DHF I, II values. A few juvenile clasts in DHF III have very high Ba contents (>3000 ppm) and are thought to represent tephriphonolite that has accumulated Ba-rich feldspar (Storey et al., 1989). Because these very few high-Ba samples imply a rather limited role for this composition in the DHF volumetrically speaking, they are not treated separately from the rest of DHF III, they do however consistently plot at less evolved compositions, e.g., lower Zr contents.

Whole-rock REE patterns and abundance diagrams for DHF chemostratigraphic units are shown in Figures 6.6 and 6.7. These data are normalized to Bulk Silicate Earth (McDonough and Sun, 1995). REE patterns for the phonolites are variably MREE depleted, which could be due, in part, to kaersutite fractionation from tephriphonolitic magmas (Ablay et al., 1998). But strong Nb/Ta fractionation implies that titanite is more important in causing differences between units. DHF bs is most simlar to DHF III type phonolite, but s few units are similar to DHF I, II. In general, the range in REE concentrations in DHF I phonolites are rather large, whereas DHF bs, II, and III phonolites are more chemically restricted.

Normalized abundance diagrams for chemostratigraphic units are quite similar overall (Fig. 6.7), but subtle and significant differences exist between them. All units have pronounced depletions in Ba, Sr, P and Ti, features consistent with a history of feldspar, clinopyroxene, and apatite fractionation. Enrichments in Cs, Pb, Zr and Hf reflect the continued incompatibility of these elements in the evolved phonolitic magmas. Other distinguishing features are related to differing titanite fractionation histories, such as Nb, Ta and MREE depletions. The greatest depletions in these elements are observed

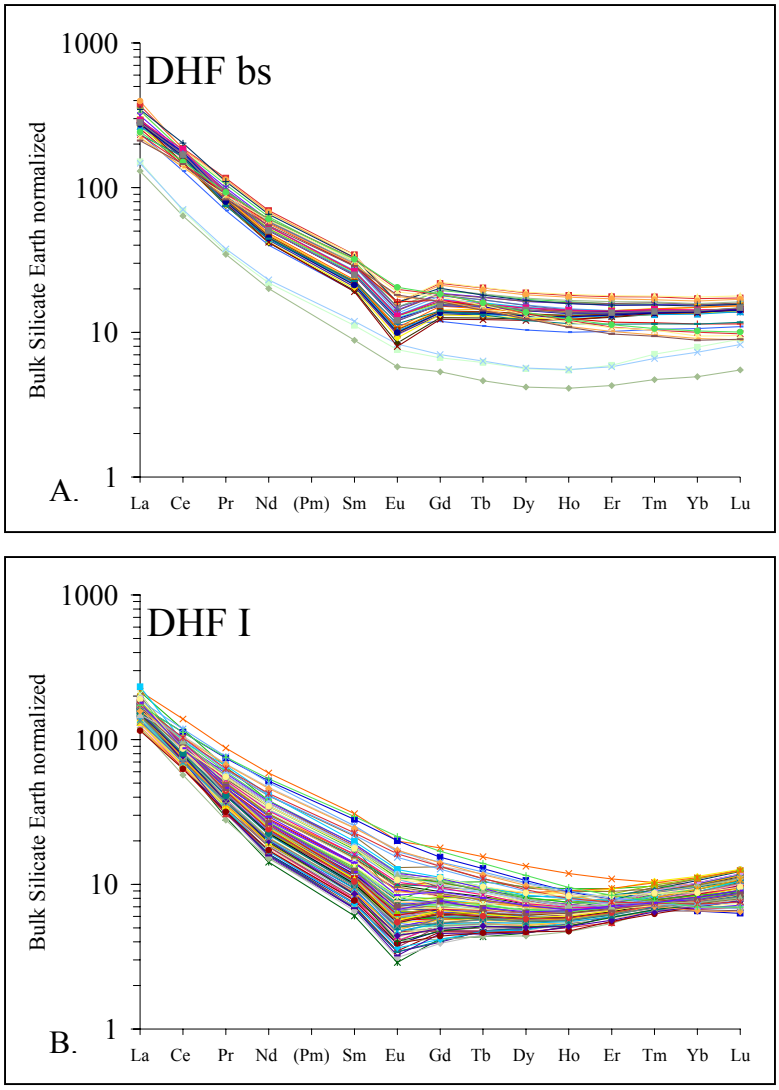

Figure 6.6a: Bulk Silicate Earth (McDonough and Sun, 1995) normalized REE contents in DHF bs and DHF I phonolites.

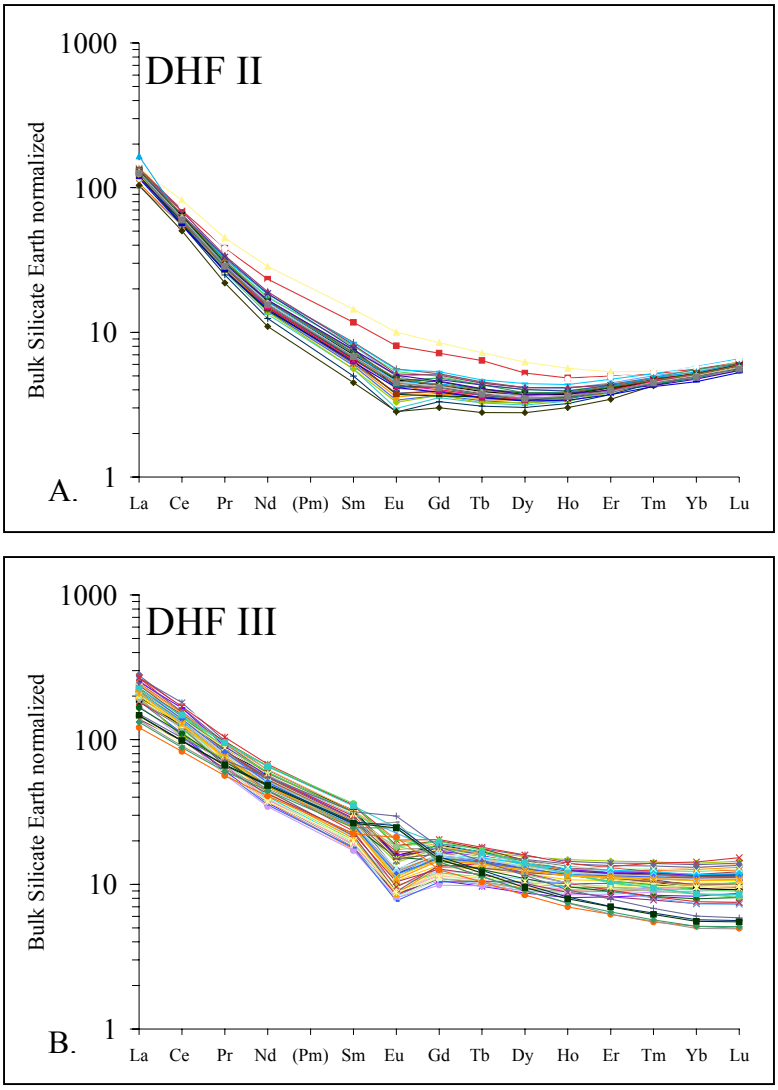

Figure 6.6b: Bulk Silicate Earth (McDonough and Sun, 1995) normalized REE contents in DHF II and DHF III phonolites.

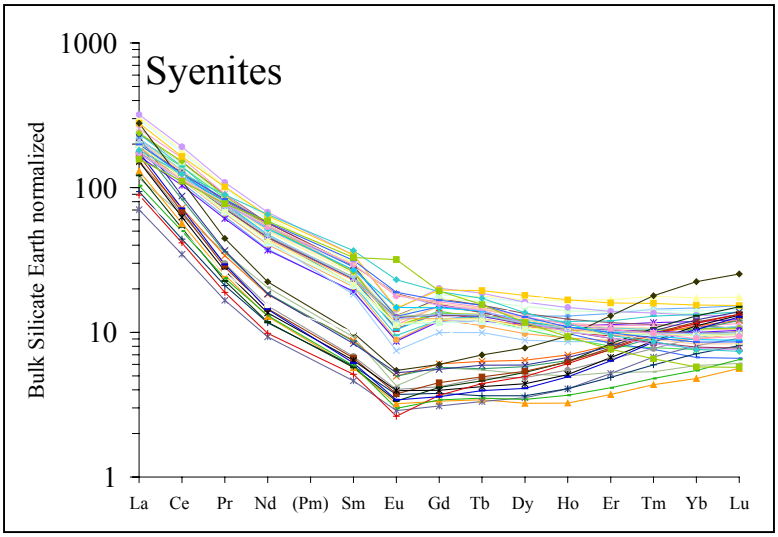

Figure 6.6c: Bulk Silicate Earth (McDonough and Sun, 1995) normalized REE contents in DHF syenites.

in DHF I, II and hence these phonolites are interpreted as having crystallized and separated the most titanite.

Trace elements in syenites

Syenite trace element contents mimic the phonolites. Syenites plot in two groups corresponding primarily to DHF I, II and DHF III phonolites (Fig. 6.4 & 6.5). REE and normalized abundance diagrams (Fig. 6.6 and 6.7) show the significant differences between the syenite type, most apparent in MREE, Nb and Ta depletion.

Basalt geochemistry

The compositions of Dorsal Ridge Zone basalts associated with DHF magmatism are discussed in detail by Olin (2003) and summarized here. Mafic rocks on Tenerife are variable in composition and fall into several fields on the total alkalis versus silica diagram (Fig. 6.1). Of the 116 samples analyzed, the majority (51%) are basanites with normative olivine (*ol*) >10%, 15% are tephrites (*ol*<10%), 13% are alkali basalts, 11% hawaiites, 2% picrobasalts, and one sample is a nephelinite (<41% SiO_2). Decreasing concentrations of FeO*, MgO, CaO and TiO_2, and increasing SiO_2, Al_2O_3, K_2O, Na_2O (not shown) are consistent with fractional crystallization of clinopyroxene (titanaugite), olivine and Fe-Ti oxides from basaltic magma. Ever increasing Al_2O_3 and decreasing CaO/Sr imply little role for plagioclase in the crystallizing assemblage.

Basalt Nb/Ta (15-17) and Pb/Ce (0.02-0.03) values (Fig. 6.5) are generally consistent with other ocean island basalts (Hofmann et al., 1986; Newsom et al., 1986; Weaver, 1991; Chauvel et al., 1997; Thirwall et al., 1997 and references therein). The higher values (>17 for Nb/Ta and > 0.035 for Pb/Ce) probably indicate contamination by phonolitic material, as does MREE depletion observed in some samples.

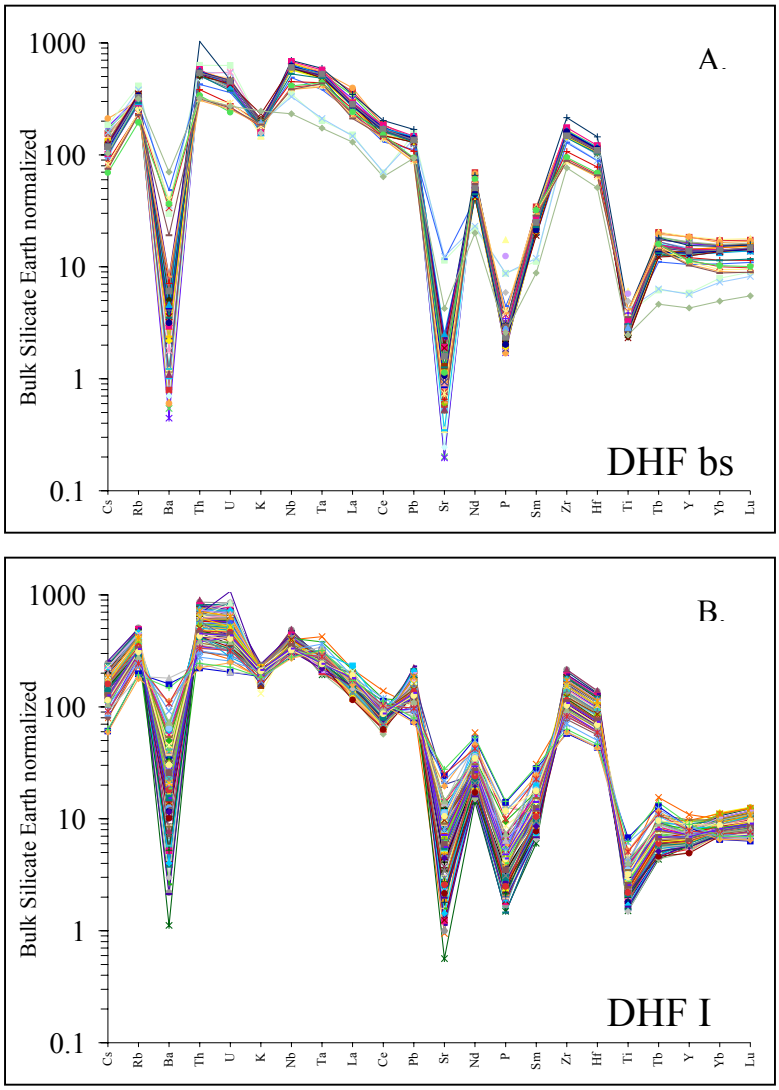

Figure 6.7a: Abundance diagrams for DHF bs and DHF I phonolites normalized to Bulk Silicate Earth (McDonough and Sun, 1995).

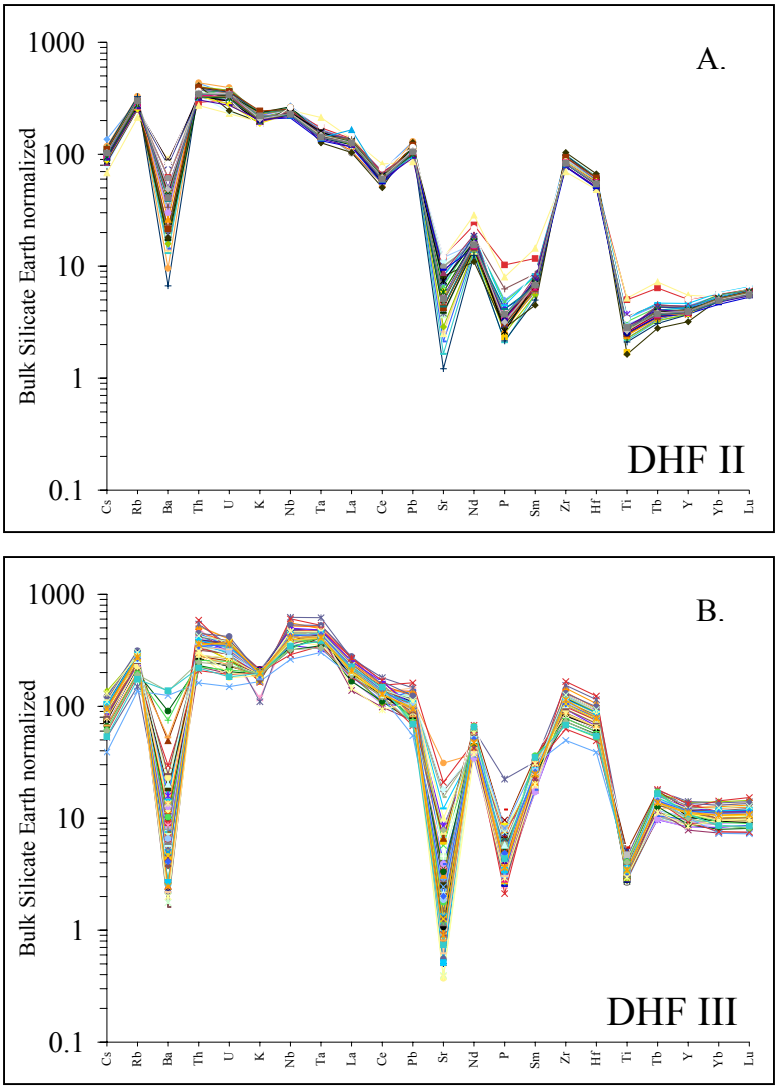

Figure 6.7b: Abundance diagrams for DHF II and DHF IIII phonolites normalized to Bulk Silicate Earth (McDonough and Sun, 1995).

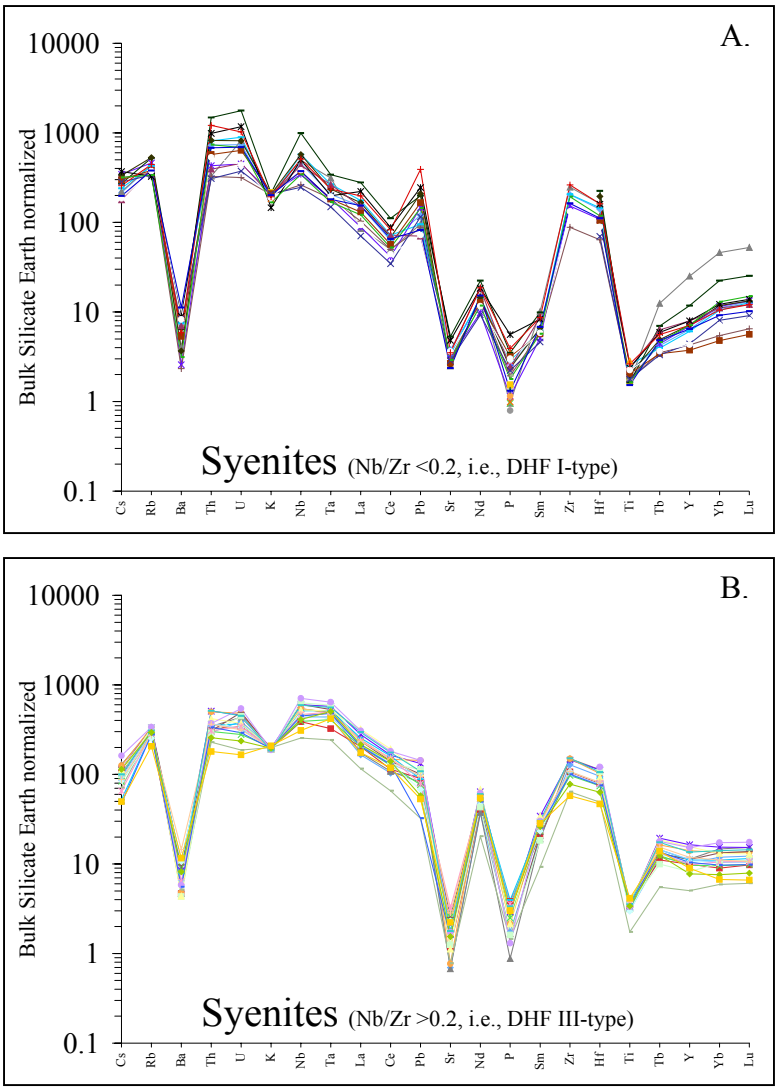

Figure 6.7c: Abundance diagrams for DHF syenites normalized to Bulk Silicate Earth (McDonough and Sun, 1995).

Intermediate rocks

Rocks with intermediate compositions represent perhaps the least constrained magmatic component in the DHF system. Most of the rocks plotting in the intermediate fields in Fig. 6.1 are visibly mixed rocks (e.g., banded pumices) and not true fractionated intermediates. In fact, unequivocal identification of true intermediate fractionates is, in general, problematic. The overall paucity of samples with intermediate compositions is interesting, and supports the observation that volcanism on Tenerife is dominantly bimodal. This, in part, can be explained by the relationship between basaltic volcanism and syenite melting discussed in detail later. It should be noted, however, that intermediate rocks are much more abundant in the recent Teide-Pico Viejo complex.

Discussion

There is clearly a fundamental difference between the genesis of DHF I, II and DHF III type phonolites and syenites. Relations between trace element contents in the phonolites are highly variable and systematic (Fig. 6.4 & 6.5; see also Wolff et al., 2000). Most DHFbs phonolites have relatively high Nb/Zr and low Nb/Ta. This chemistry characterizes the earlier Guajara Formation, and at least some of the Ucanca Formation and Lower Group phonolites. DHF I phonolites, in contrast, have lower Nb/Zr over a wide range of Zr contents. DHF II phonolites have very low Nb/Zr and show much less compositional variation. DHF III phonolites mark a return to the high-Nb/Zr, Guajara-like chemistry.

The differing degrees of enrichment of trace elements (i.e., Nb) with increasing Zr are due to a varying role for residual titanite at some point in phonolite petrogenesis (Wolff et al., 2000); either during fractional crystallization or due to melting of pre-

existing syenites with differing titanite fractionation histories (Wolff et al., 2000). Edgar et al. (2007) show that DHF I and II phonolites could be related by simple fractional crystallization involving titanite, however, no such relation exists between DHF I and III phonolites. The crucial point, fully supported by the expanded data set, is that the high-Nb/Zr and low-Nb/Zr phonolite cannot be related by any simple evolutionary mechanism. Regardless of petrogenetic details, the salient feature of DHF magma chemistry is that two phonolite types that lack a simple evolutionary relationship persisted, or were repeatedly generated, throughout the lifetime of the DHF. The fact that the syenites exhibit this compositional polarity, and that pre-DHF units have DHF III compositions further indicates that the processes have been at work prior to DHF time, probably operating at depth within the island rather than being shallow, short-lived, late-stage processes.

Once formed, preexisting syenite plutons become a possible source for phonolite magmas via anatexis. Syenite textures are quite variable, but generally speaking DHF III-type syenites are fresher than DHF I, II type syenites. DHF III syenites occasionally contain glass, thought to have quenched upon eruption (Wolff, 1987; Wolff and Toney, 1993). Thus far, no glass has been observed in any DHF I, II syenite, and in fact most of these rocks have clearly undergone low temperature alteration, as evidenced by sericitization of feldspar, replacement of sodalite by analcite and nepheline by cancrinite, and some veining in samples (although the veins could be late stage magmatic). DHF III syenites, on the other hand, are more consistent with fresh, young crystallized (at depth) equivalents of DHF III phonolite magma (Wolff , 1987; Wolff and Toney, 1993).

DHF I magmatism

Based on the geochemistry for all DHF phonolitic and syenitic rocks, two dominant felsic magmatic lineages, DHF I, II and DHF III, persisted or were repeatedly generated on Tenerife. Each phonolite type may be differentiated to different degrees. Either magma type may dominate during any one eruption, as in the Arafo and Caleta Members (DHF II) or the Abrigo Member (DHF III), or both may be erupted together as in the Fasnia (Chapter 3) and Poris Members (Edgar et al., 2002; Edgar et al., 2007). Two contrasting lineages have been proposed to reconcile subtle differences between Teide and Pico Viejo eruptive products (Ablay et al., 1998), but both are in fact like DHF III with small differences in feldspar histories. The scenarios represented by the Aldea, Fasnia, and Poris members (Edgar et al, 2002; Edgar, 2003, Edgar et al., 2007) are more complex.

The geochemistry of low-Zr phonolite is consistent with a phonolite that is the product of fractionation from tephriphonolitic magma (Wolff & Storey, 1984; Ablay et al., 1998; Edgar et al. 2002). However, the very evolved nature of high-Zr phonolite is more consistent with melting of preexisting syenitic plutons (Wolff et al., 2000; Edgar et al., 2002). The feasibility of crustal melting by basaltic magma emplacement at depth and within networks of shallow dikes and sills has been demonstrated by numerical modeling (Litvinovsky & Podladchikov, 1993; Laube & Springer, 1998; Annen & Sparks, 2002; Dufek & Bergantz, 2005; Annen et al., 2006). Although the models primarily focus on arc volcanism, the premise can be applied to Tenerife. In general, these models predict that if hot basaltic intrusions are emplaced in the crust at a rate such that the ambient crustal temperatures increase (i.e., rate of heat input > rate heat dissipation), crustal

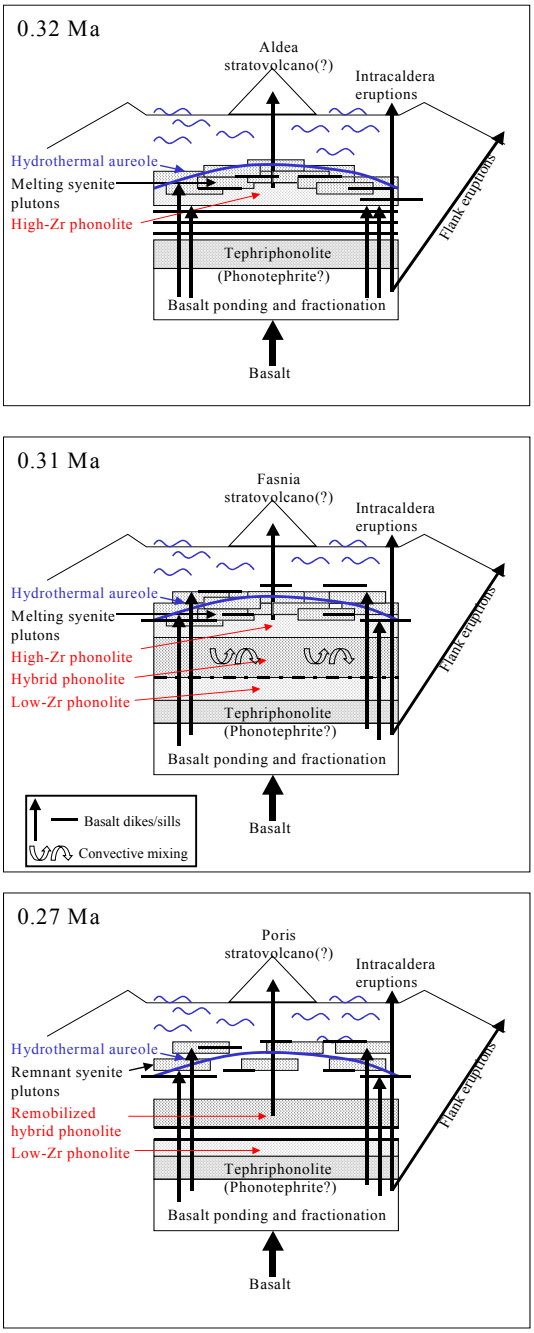

Figure 6.8: Conceptual diagrams for magmatism through DHF I time. Syenite melting produces a substantial volume of high-Zr phonolite during Aldea and Fasnia time that is mixed with low-Zr phonolite and tephriphonolite (which are continually or repeatedly generated at depth through this 50 ka period) to produce hybrid phonolite. Hybrid phonolite remaining after the Fasnia is remobilized during the Poris to produce the Poris "high-Zr" phonolite of Edgar et al. (2002). Region of magmatism depicted above is approximately 4-5 km deep below Las Cañadas.

melting will eventually be induced. In these scenarios, crustal melt production rates are directly related to basaltic intrusion rates. This model has been called upon to explain the "abundant phonolites" of Ua Pou Island, Marquesas (Legendre et al., 2005). On Ua Pou Island, as in the DHF, mafic, intermediate and felsic liquids are simultaneously erupted over a short period of time, (Wolff, 1985; Edgar et al., 2002; Edgar et al., 2007; Legendre et al., 2005), implying that these magmas coexist at depth for some time. This allows for mixing processes to advance and, in some cases, complete hybridization of magmas.

If DHF I time is an example of significant crustal melting due to basaltic injection, then prior to the Aldea there must have been shallow intrusion of voluminous basaltic magma that heated up the shallow crust below Las Cañadas and triggered the melting of preexisting syenite plutons that were erupted as the Aldea high-Zr phonolite (Fig. 6.8). Continued syenite melting (with or without continued basaltic injections), created the Fasnia high-Zr phonolite magma (generally compositionally similar to but resolvably different from Aldea phonolite) and low-Zr phonolite magma either simultaneously fractionates from intermediate magmas (Wolff & Storey, 1984; Ablay et al., 1998; Edgar et al. 2002), or is itself a product of crustal melting of a different protolith, an option that has not been explored. The Fasnia hybrid phonolite is a result of advanced mixing of these two endemembers (Fig. 6.8 & 6.9), although mixing in the Fasnia system probably occurred shortly before the Fasnia eruption because complete hybridization is never observed in the clasts described in Chapter 3. The mixing event and the Fasnia eruption was likely triggered when mafic magma intersected the phonolite bodies.

The Poris Member has similar magmatic complexity to the Fasnia, i.e., two phonolites are observed mixing with intermediate and mafic magmas (Edgar et al., 2002). Edgar et al.'s high-Zr phonolite (1000-1200 ppm Zr) is in fact very similar to the Fasnia's intermediate-Zr phonolite (a hybrid magma; see Chapter 3), and Edgar et al.'s low-Zr phonolite is almost identical to Fasnia low-Zr phonolite. These features are not likely coincidental, rather they suggest a link between Fasnia and Poris magmatism in which some Fasnia hybrid phonolite magma remained at depth after the termination of the Fasnia eruption, and was rejuvenated during the early phases of the Poris event. Poris low-Zr phonolite could also be rejuvenated Fasnia magma, or it was replenished by means of fractionation from tephriphonolitic magmas (Wolff & Storey, 1984; Ablay et al., 1998; Edgar et al. 2002). In the Poris it appears that these two phonolites remained isolated until a mafic recharge event disturbed the entire system and triggered the Poris eruption (Edgar et al., 2002).

To summarize Aldea-Fasnia-Poris phonolitic magmatism, large-scale melting of preexisting DHF I type syenite plutons (Nb/Zr <0.2) began prior to the Aldea event resulting in at least 3.1 km^3 DRE of eruptible phonolite magma during this period (Table 2.2; Edgar et al., 2007). If considered in light of the Fasnia whole-rock and glass data, much of the Aldea magma is hybrid, or at least mixed in composition at the whole-rock scale, and high-Zr phonolitic liquids are a major component. The Aldea eruption was likely triggered by a mafic recharge event that caused the mingling of mafic, intermediate, and evolved magma shortly before eruption (Wolff, 1985). Within ~10,000 years, further melting of near identical, but compositionally resolvable syenites produced Fasnia high-Zr phonolite magma, significantly greater in volume than the Aldea. Fasnia

high-Zr phonolite mixed with low-Zr phonolite to produce the Fasnia layered magma system with relatively pure high-Zr phonolite at the top, a voluminous hybrid magma in the middle, and low-Zr phonolite and tephriphonolitic magma at the base. Fasnia stratigraphic and textural relationships suggest that, again, a mafic recharge event is the trigger of the eruption. During the Fasnia eruption, pure high-Zr phonolite is erupted en masse early on, and after this point pure high-Zr phonolite is never erupted again on Tenerife, suggesting the syenites that were generating high-Zr phonolite at depth were no longer melting, although syenite blocks and lithic fragments of DHF I composition are observed in deposits younger than the Fasnia, occurring in the Abrigo ignimbrite ~100 ka later. After ~30,000 years of relative quiescence, what remains of the Fasnia hybrid magma is thermally in isolation from new or rejuvenated low-Zr phonolite. Rejuvenated Fasnia hybrid phonolite and low-Zr phonolite are again intersected by a mafic recharge event that triggers the Poris eruption in which the high-Zr is erupted early on and low-Zr appears later. This is the last eruption of a significant volume of DHF I type phonolite on Tenerife.

Geochemical plots in Figure 6.9 support the relationship between the Aldea, Fasnia, and Poris described above. Aldea and Fasnia phonolites are compositionally similar with respect to Zr and MgO contents, for example, but Aldea Ta contents fall along a slightly different array than Fasnia samples. The Poris high-Zr samples are compositionally similar to Fasnia hybrid pumices and glasses (~1200 ppm Zr). These samples also plot along the Fasnia array for Nb/Ta vs. Ta and Nb/Zr vs. Zr. This supports the conclusion that Poris high-Zr phonolite (Edgar et al., 2002) is in fact rejuvenated Fasnia hybrid magma. Low-Zr phonolite in the Fasnia and

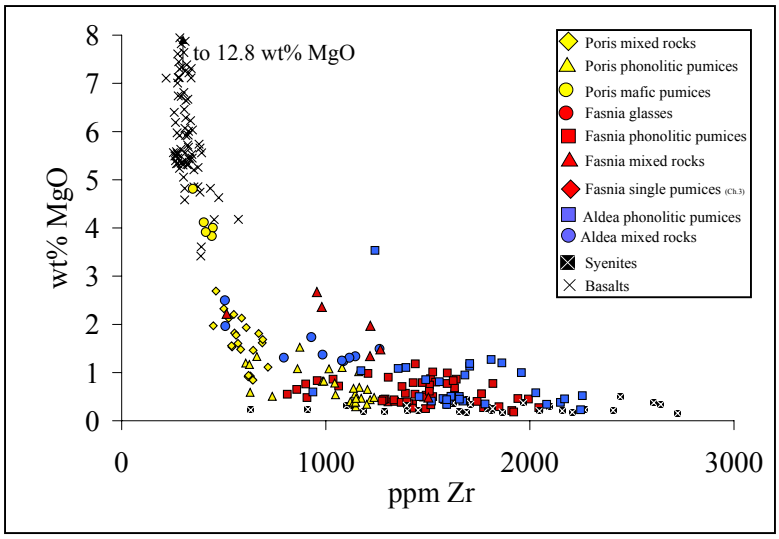
to 12.8 wt% MgO
wt% MgO
ppm Zr
0
1
2
3
4
5
6
7
8
0
1000
2000
3000
Poris mixed rocks
Poris phonolitic pumices
Poris mafic pumices
Fasnia glasses
Fasnia phonolitic pumices
Fasnia mixed rocks
Fasnia single pumices (Ch.3)
Aldea phonolitic pumices
Aldea mixed rocks
Syenites
Basalts

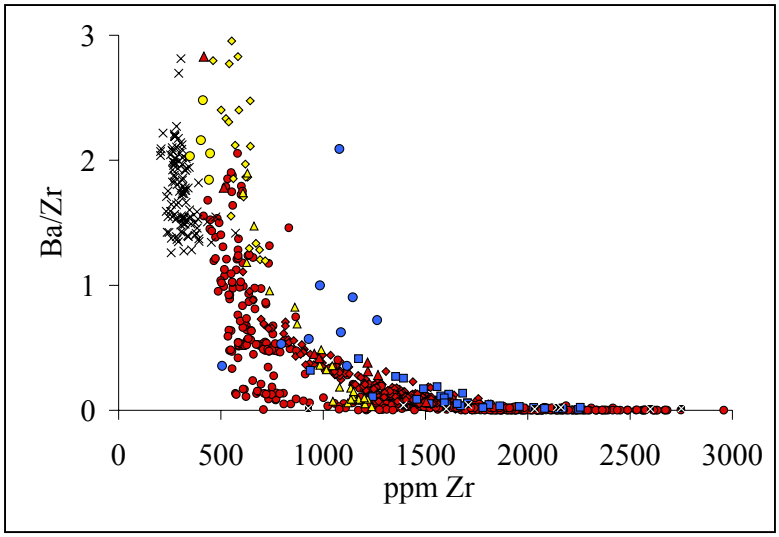
Ba/Zr
ppm Zr
0
1
2
3
0
500
1000
1500
2000
2500
3000

Figure 6.9a:

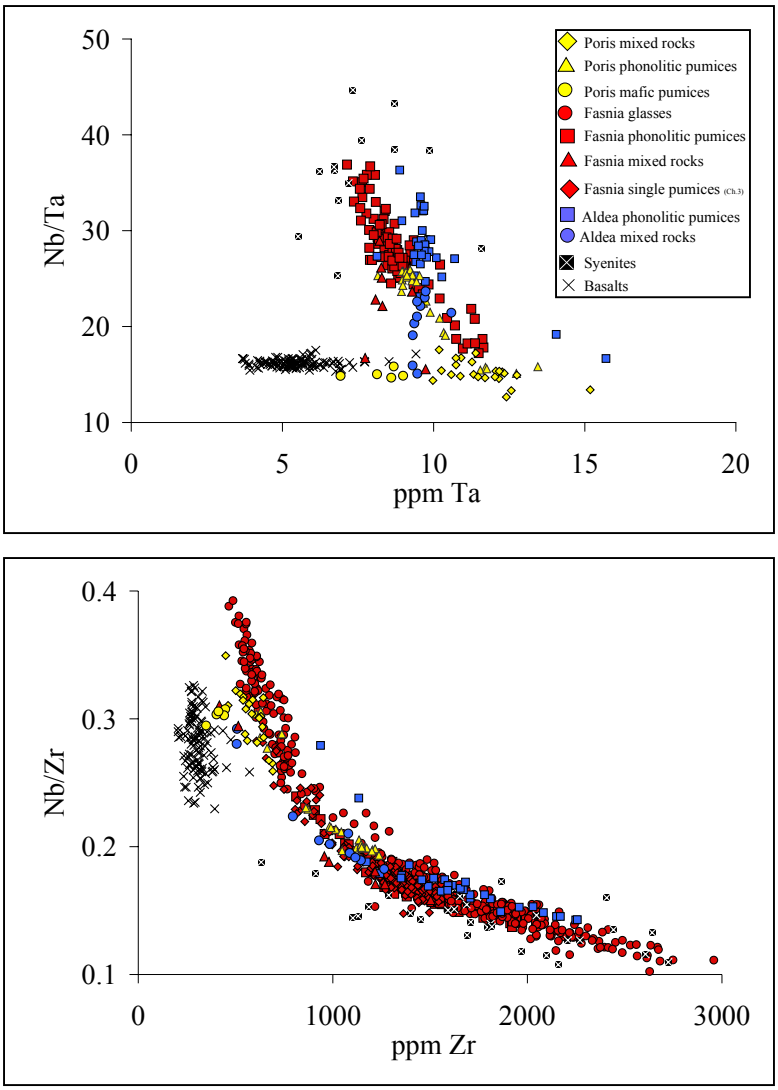
Poris mixed rocks
Poris phonolitic pumices
Poris mafic pumices
Fasnia glasses
Fasnia phonolitic pumices
Fasnia mixed rocks
Fasnia single pumices (Ch.3)
Aldea phonolitic pumices
Aldea mixed rocks
Syenites
Basalts
Nb/Ta
ppm Ta
50
40
30
20
10
0
5
10
15
20
Nb/Zr
ppm Zr
0.4
0.3
0.2
0.1
0
1000
2000
3000

Figure 6.9b:

Poris could be similarly related by rejuvenation, or low-Zr magma was replenished by fractionation processes.

When considering other deposits outside of DHF I, several observations deserve attention. The Roque Member (DHF bs) has DHF I composition, but occurs prior to the Aldea, and has a similar volume to the Aldea (Chapter 2; Edgar et al., 2007). It is quite likely that the Roque in fact presents the first appearance of DHF I magma, i.e., phonolitic magma generated by melting DHF I type syenite. Occurring before the Roque, the Espigon Member (DHF bs) has DHF II compositions ~100 ka prior to the eruption of DHF II members. The Espigon and DHF II phonolites are also good candidates for syenitic melts for similar reasons as the DHF I phonolites and some syenites have equivalent compositions. Therefore, except for the Cruz Sequence and the Abrigo Member, melting of syenites may actually be a dominant feature of DHF magmatism. Although the scheme outline here is consistent with the data, it is indeed speculative.

Further understanding of DHF magmatism and the relationships between members would be achieved through additional study of the glasses and minerals (i.e., pyroxene and titanite) from numerous members, like the comprehensive LA-ICP-MS study presented for the Fasnia in Chapters 3 through 5.

Conclusions

All factors considered, DHF magmatism is very chemically complex. Variations at the formation scale require the persistence or repeated generation of two phonolitic magmatic lineages that erupt episodically, and may be mixing to varying degrees or are co-erupted (i.e., DHF I). Phonolitic magma genesis is likely occurring by processes of

fractional crystallization of intermediate parental magmas (i.e., tephriphonolite) and melting and assimilation of variably altered, preexisting syenite plutons.

References:

Ablay, G.J., Martí, J., 2000. Stratigraphy, structure, and volcanic evolution of the Pico Teide-Pico Viejo formation, Tenerife, Canary Islands. J. Volc. Geotherm. Res. 103, 175-208.

Ablay, G.J, Carroll, M.R., Palmer, M.R., Martí, J., Sparks, R.S.J., 1998. Basanite-phonolite lineages of the Teide-Pico Viejo volcanic complex, Tenerife, Canary Islands. J. Petrol. 39, 905-936.

Ablay, G.J., Ernst, G.G.J., Martí, J., Sparks, R.S.J., 1995. The ~2 ka subplinian eruption of Montaña Blanca, Tenerife. Bull. Volcanol. 57, 337-355.

Ancochea, E., Fúster, J.M., Ibarrola, E., et al., 1990. Volcanic evolution of the island of Tenerife (Canary Islands) in the light of new K-Ar data. J. Volc. Geotherm. Res. 44, 231-249.

Araña, V., 1971. Litología y estructura del edificio Cañadas, Tenerife (Islas Canarias). Est. Geol. 27, 95-137.

Brown, R.J., Barry, T.L., Branney, M.J., Pringle, M.S., Bryan, S.E., 2003. The Quaternary pyroclastic succession of southern Tenerife, Canary Islands: explosive eruptions, related subsidence and sector collapse. Geol. Mag. 140, 265-288.

Chauvel, C., McDonough, M., Guille, G., Maury, R., and Duncan, R., 1997. Contrasting old and young Rurutu Island, Austral chain. Chem. Geol. 139, 125-143.

Edgar, C.J., Wolff, J.A., Nichols, H.J., Cas, R.A.F., Martí, J., 2002. A complex Quaternary ignimbrite-forming phonolitic eruption: The Poris Member of the Diego Hernandez Formation (Tenerife, Canary Islands). J. Volc. Geotherm. Res. 119, 99-130.

Edgar, C.J., Wolff, J.A., Olin, P.H., Nichols, H.J., Pitarri, A., Cas, R.A.F., Reiners, P.W., Spell, T.L., Martí J., 2007. The late Quaternary Diego Hernández Formation, Tenerife: Volcanology of a complex cycle of voluminous explosive phonolitic eruptions. J. Volc. Geotherm. Res. 160 (1-2), 59-85.

Fúster, J.M., Araña, V., Brandle, J.L., Navarro, J.M., Alonso, U., Aparicio, A., 1968. Geology and Volcanology of the Canary Islands. Inst. Lucas Mallada, CSIS, Madrid. 218 pp.

Guillou, H., Carrecedo, J.C., Paris, R., Torrado, F.J.P., 2004. Implications for the early shield-stage evolution of Tenerife from K/Ar ages and magnetic stratigraphy. Earth Planet. Sci. Lett. 222, 599-614.

Hofmann, A.W., Jochum, K.P., Seufert, M. and White, W.M., 1986. Nb and Pb in oceanic basalts: new constraints on mantle evolution. Earth Planet. Sci. Lett. 79, 33-45.

Johnson, D.M., Hooper, P.R. and Conrey, R.M., 1999. XRF analysis of rocks and minerals for major and trace elements on a single low dilution Li-tetraborate fused bead. Advances in X-ray Analysis, 41, 843-867.

Knaack, C., Cornelius, S. and Hooper, P.R., 1994. Trace element analysis of rocks and minerals by ICP-MS. Unpublished web page, GeoAnalytical Laboratory, Department of Geology, Washington State University. URL:http://www.wsu.edu:8080/~geology/Pages/Services/ICP.html (2007).

Le Bas et al., 1986. A Chemical Classification of Volcanic Rocks Based on the Total Alkali-Silica Diagram. J. Petrol. 27 (3), 745-750.

Martí, J., Hurlimann, M., Ablay, G.J., Gudmundsson, A., 1997. Vertical and lateral collapses on Tenerife (Canary Islands) and other volcanic ocean islands. Geology 25, 879-882.

Martí, J., Mitjavila, J. (Eds.), 1995. A field guide to the Central Volcanic Complex of Tenerife (Canary Islands). Serie Casa de Los Volcanes, vol. 4. Cabildo Insular de Lanzarote, Lanzarote.

Martí, J., Mitjavila, J., and Araña, V., 1994. Stratigraphy, structure and geochronology of the Las Cañadas caldera (Tenerife, Canary Islands). Geol. Mag. 131, 715-727.

McDonough, W.F., and Sun, S.S., 1995. The composition of the Earth. Chemical Geology 120 (3-4), p.223-253.

Mitjavila, J.M., Villa, I.M., 1993. Temporal evolution of the Diego Hernández Formation (Las Cañadas, Tenerife) and confirmation of the age of the caldera using the $^{40}Ar/^{39}Ar$ method. Rev. Soc. Geol. Esp. 6, 61-65.

Newsom, H.E., White, W.M., Jochum, K.P. and Hoffman, A.W., 1986. Siderophile and chalcophile element abundances in oceanic basalts, Pb isotopic evolution and growth of the Earth's core. Earth Planet. Sci. Lett. 80, 299-313.

Olin, P.H., 2003. Trace element signatures of contamination of basalt by phonolite: the Diego Hernández formation and the Dorsal Series, Tenerife, Canary Islands. MSc thesis, Washington State Univ., USA, 114 pp.

Pitarri, A., Cas, R.A.F., Martí, J., 2005. The occurance and origin of prominent massive, pumice-rich ignimbrite lobes within the Late Pleistocene Abrigo Ignimbrite, Tenerife, Canary Islands. J. Volcanol. Geotherm. Res. 139, 271-293.

Ridley, W.I., 1970. The petrology of the Las Cañadas volcanoes, Tenerife, Canary Islands. Contr. Mineral. Petrol. 26, 124-160.

Ridley, W.I., 1971. The origin of some collapse structures in the Canary Islands. Geol. Mag. 108, 477-484.

Storey, M., Wolff, J.A., Norry, M.J., Marriner, G.F., 1989. Origin of hybrid lavas from Agua de Pau volcano, Sao Miguel, Azores. Magmatism in the ocean basins, Geol. Soc. Spec. Pub. 42, 161-180.

Thirwalll, M.F., Jenkins, C., Vroon, P.Z. and Mattey, D.P., 1997. Crustal interaction during construction of ocean islands: Pb-Sr-Nd-O isotope geochemistry of the shield basalts of Gran Canaria, Canary Islands. Chem. Geol. 135, p.233-262.

Thirwall, M.F., Singer, B.S., Marriner, G.F., 2000. $^{39}Ar/^{40}Ar$ ages and geochemistry of the basaltic shield stage of Tenerife, Canary Islands, Spain. J. Volcanol. Geotherm. Res. 103, 247-297.

Weaver, B.L., 1991. The origin of ocean island basalt end member compositions: trace element and isotopic constraints. Earth Planet. Sci. Lett. 104, 381-397.

Wolff, J.A., 1983. Petrology of the Quaternary pyroclastic deposits from Tenerife, Canary Islands. Ph.D. Thesis, University of London, 542 pp.

Wolff, J.A., 1984. Variation in Nb/Ta during differentiation of phonolitic magma, Tenerife, Canary Islands. Geochim. Cosmochim. Acta. 48, 1345-1348.

Wolff, J.A., 1985. Zonation, mixing and eruption of silica-undersaturated alkaline magma: a case study from Tenerife, Canary Islands. Geol. Mag. 122(6), 623-640.

Wolff, J.A., 1985b. The effect of explosive eruption on geochemical patterns within pyroclastic deposits. J. Volcanol. Geotherm. Res. 26, 189-201.

Wolff, J.A., 1987. Crystallisation of nepheline syenite in a subvolcanic magma system: Tenerife, Canary Islands. Lithos 20, 207-223.

Wolff, J.A., Grandy, J.S., Larson, P.B., 2000. Interaction of mantle-derived magma with island crust? Trace element and oxygen isotope data from the Diego Hernandez Formation, Las Cañadas, Tenerife. J. Volcanol. Geotherm. Res. 103, p. 343.

Wolff, J.A., Storey, M., 1983. The volatile component of some pumice-forming alkaline magmas from the Azores and Canary Islands. Contrib. Mineral. Petrol. 82, 66-74.

Wolff, J.A., Toney, J.B., 1993. Trapped liquid from a nepheline syenite: a re-evaluation of Na-, Zr-, F-rich interstitial glass in a xenolith from Tenerife, Canary Islands. Lithos 29, 285-293.

Appendix A

Whole-rock concentration data for the Diego Hernández Formation

Appendix A.
DHF Whole-rock data

ChemoUnit	DHF bs	DHF bs	DHF bs	DHF bs	DHF bs	DHF bs	DHF bs	DHF bs	DHF bs
Member	BS	BS	BS	BS	BS	BS	BS	BS	BS
sample #	03TF174	03TF177A	03TF177C	03TF177D	03TF177E	03TF177F	03TF177G	03TF179A	03TF179B
XRF Major element oxides (Wt%)									
SiO2	59.40	58.13	61.30	58.64	59.13	58.45	60.64	58.48	58.92
Al2O3	22.16	20.07	19.67	21.01	21.47	20.53	19.60	20.39	20.93
TiO2	0.59	0.50	0.84	0.51	0.57	0.56	0.78	0.56	0.52
FeO*	3.71	3.12	3.44	3.31	3.42	3.23	2.97	3.22	3.33
MnO	0.33	0.30	0.24	0.31	0.30	0.29	0.23	0.29	0.30
CaO	0.98	0.70	0.67	0.64	0.66	0.80	0.77	0.63	0.70
MgO	0.60	0.42	0.49	0.34	0.34	0.46	0.47	0.34	0.35
K2O	4.54	5.34	5.34	5.31	5.93	5.58	5.25	5.41	5.38
Na2O	7.30	11.06	7.71	9.57	7.80	9.74	8.98	10.33	9.19
P2O5	0.05	0.04	0.08	0.04	0.04	0.05	0.08	0.05	0.04
total	99.66	99.70	99.79	99.68	99.68	99.70	99.78	99.71	99.68
XRF Trace elements (ppm) Ni	6.3	3.1	1.0	0.0	0.0	2.1	1.0	1.0	1.0
Cr	8.4	2.1	3.1	0.0	0.0	1.0	0.0	1.0	0.0
Sc	1.1	0.0	7.2	0.0	0.0	4.1	0.0	0.0	1.0
V	23	24	23	20	21	14	13	19	28
Ba	0	0	31	0	0	0	220	0	0
Rb	202	213	144	216	220	219	151	214	218
Sr	70	21	14	25	12	20	15	16	24
Zr	1780	1525	928	1663	1627	1546	927	1494	1670
Y	58	56	46	60	60	61	47	58	59
Nb	425	384	248	412	396	378	254	366	410
Ga	42	37	29	37	39	40	29	38	39
Cu	21	1	0	0	4	2	0	1	3
Zn	200	185	147	196	200	190	136	182	197
Pb	21	20	10	19	20	19	10	18	18
La	179	174	153	204	200	182	156	188	188
Ce	305	291	252	290	305	306	253	287	311
Th	50	39	27	44	46	39	28	42	46
ICP-MS traces (ppm) La	171	187	143	190	192	181	145	180	184
Ce	287	265	232	279	284	268	233	269	272
Pr	20	21	22	22	23	22	22	22	21
Nd	55	57	71	59	67	65	74	65	56
Sm	8.8	8.9	12.0	9.1	10.7	10.3	12.7	10.6	8.6
Eu	1.6	1.5	2.7	1.6	2.0	1.9	2.9	2.0	1.5
Gd	7.4	7.6	9.0	7.7	8.9	8.6	9.6	8.7	7.4
Tb	1.3	1.4	1.4	1.4	1.6	1.5	1.5	1.5	1.4
Dy	8.7	8.9	8.4	9.4	9.9	9.7	8.9	9.6	8.8
Ho	1.9	2.0	1.6	2.1	2.1	2.1	1.8	2.0	1.9
Er	5.7	6.1	4.4	6.2	6.1	6.1	4.7	6.0	5.8
Tm	0.9	1.0	0.7	1.0	1.0	1.0	0.7	0.9	0.9
Yb	5.9	6.3	4.0	6.5	6.2	6.1	4.2	6.0	6.2
Lu	0.9	1.0	0.6	1.0	1.0	1.0	0.6	0.9	1.0
Ba	30	21	54	15	7	8	263	20	19
Th	45	42	24	44	43	41	25	42	45
Nb	420	402	253	437	403	387	256	383	419
Y	55	59	45	61	62	61	48	59	57
Hf	33	31	18	33	31	30	18	30	33
Ta	19	18	15	20	19	18	15	18	19
U	8.3	9.9	5.2	9.2	9.4	9.3	5.9	9.5	9.4
Pb	22	20	13	21	20	19	13	20	21
Rb	178	211	137	208	209	207	143	207	203
Cs	2.2	3.0	1.6	2.8	2.7	2.7	1.7	2.7	2.5
Sr	50	20	12	24	11	10	15	12	24
Sc	2.6	2.1	1.6	2.0	2.2	2.0	1.4	2.0	2.2
Zr	1725	1613	922	1752	1651	1556	911	1538	1702

Appendix A.
DHF Whole-rock data

ChemoUnit	DHF bs	DHF bs	DHF bs	DHF bs	DHF bs	DHF bs	DHF bs	DHF bs	DHF bs
Member	BS	BS	BS	BS	BS	BS	BS	BS	BS
sample #	03TF180A	03TF180B	03TF180C	03TF181A	03TF181B	03TF181C	03TF182A	03TF182B	03TF183A
XRF Major element oxides (Wt%)									
SiO2	59.13	59.22	58.98	59.26	61.34	59.05	59.14	60.14	59.91
Al2O3	21.39	21.23	21.06	20.86	20.18	22.21	20.72	21.82	20.33
TiO2	0.55	0.59	0.57	0.62	0.71	0.56	0.52	0.61	0.57
FeO*	3.44	3.40	3.45	3.58	2.99	3.71	3.28	3.58	3.46
MnO	0.32	0.31	0.31	0.36	0.23	0.33	0.31	0.30	0.32
CaO	0.77	0.77	0.73	0.74	0.78	0.73	0.70	0.82	0.75
MgO	0.45	0.43	0.40	0.44	0.42	0.42	0.40	0.48	0.42
K2O	5.62	5.83	5.68	5.65	5.38	5.18	5.63	5.28	5.42
Na2O	7.96	7.87	8.46	8.11	7.69	7.45	8.94	6.59	8.46
P2O5	0.04	0.05	0.05	0.05	0.06	0.04	0.04	0.05	0.05
total	99.67	99.70	99.69	99.68	99.78	99.67	99.69	99.69	99.69
XRF Trace elements (ppm) Ni	2.1	2.1	3.1	4.2	3.1	2.1	0.0	3.2	0.0
Cr	1.0	0.0	0.0	1.0	1.0	1.0	0.0	2.1	0.0
Sc	0.0	3.1	2.1	0.0	0.0	1.0	2.1	4.2	0.0
V	27	20	19	29	14	27	26	20	24
Ba	0	0	0	0	103	0	0	0	7
Rb	217	211	216	207	145	194	221	198	212
Sr	30	25	16	16	13	27	23	29	33
Zr	1702	1558	1634	1644	942	1758	1657	1655	1588
Y	58	57	60	60	44	52	57	54	61
Nb	411	383	388	404	250	402	400	382	397
Ga	41	40	38	36	27	42	39	39	40
Cu	0	0	0	2	0	3	1	2	0
Zn	201	188	195	198	135	199	194	183	197
Pb	22	17	18	19	11	23	17	21	21
La	194	180	176	175	183	177	174	161	183
Ce	307	298	318	326	275	331	294	318	307
Th	47	42	46	45	25	49	45	45	41
ICP-MS traces (ppm) La	186			182	137		178	150	185
Ce	279			295	244		269	275	283
Pr	21			22	21		20	19	22
Nd	58			63	68		54	55	63
Sm	9.0			10.2	11.6		8.4	9.2	10.0
Eu	1.6			1.9	2.8		1.5	1.8	1.8
Gd	7.6			8.3	8.9		7.2	7.7	8.5
Tb	1.4			1.5	1.4		1.3	1.3	1.5
Dy	9.1			9.5	8.3		8.7	8.1	9.6
Ho	1.9			2.0	1.6		1.9	1.7	2.0
Er	5.9			6.0	4.3		5.8	5.0	6.1
Tm	1.0			0.9	0.6		0.9	0.8	0.9
Yb	6.1			6.1	3.9		6.0	5.0	6.2
Lu	1.0			1.0	0.6		1.0	0.8	1.0
Ba	29			28	126		14	23	53
Th	44			44	25		43	41	42
Nb	418			412	253		410	348	396
Y	59			59	44		57	50	60
Hf	32			32	18		32	29	30
Ta	19			20	16		19	18	19
U	9.0			8.9	5.3		9.4	7.6	9.2
Pb	21			21	14		21	20	20
Rb	202			192	136		208	175	200
Cs	2.6			2.4	1.6		2.5	2.1	2.6
Sr	26			17	10		19	25	45
Sc	2.2			2.1	1.3		1.9	1.9	2.1
Zr	1719			1685	928		1691	1486	1582

Appendix A.
DHF Whole-rock data

ChemoUnit	DHF bs	DHF bs	DHF bs	DHF bs	DHF bs	DHF bs	DHF bs	DHF bs	DHF bs
Member	BS	BS	BS	BS	BS	BS	BS	BS	BS
sample #	03TF183B	03TF183C	03TF184A	03TF184B	03TF184C	03TF185A	03TF185B	03TF185C	03TF186F
XRF Major element oxides (Wt%)									
SiO2	59.61	60.20	59.02	59.27	59.17	58.16	59.37	58.99	60.93
Al2O3	20.80	20.51	20.79	20.65	22.65	21.77	22.51	21.25	20.62
TiO2	0.53	0.57	0.54	0.53	0.51	0.63	0.65	0.81	0.83
FeO*	3.41	3.48	3.32	3.30	3.15	3.15	3.92	3.99	3.21
MnO	0.34	0.32	0.42	0.33	0.27	0.26	0.32	0.38	0.24
CaO	0.79	0.77	0.64	0.63	0.86	1.32	0.84	0.97	0.99
MgO	0.44	0.43	0.41	0.38	0.40	0.64	0.55	0.58	0.44
K2O	5.47	5.44	5.31	5.57	5.42	5.14	4.57	5.27	4.84
Na2O	8.26	7.92	9.20	8.98	7.23	8.54	6.86	7.23	7.60
P2O5	0.04	0.05	0.04	0.04	0.04	0.09	0.05	0.06	0.07
total	99.68	99.69	99.68	99.68	99.69	99.70	99.65	99.54	99.76
XRF Trace elements (ppm) Ni	0.0	5.1	3.1	1.0	3.1	4.1	6.4	4.2	2.1
Cr	1.0	0.0	2.1	3.1	0.0	0.0	0.0	1.1	0.0
Sc	2.1	1.0	0.0	1.0	0.0	2.1	0.0	0.0	1.0
V	17	25	17	16	23	33	23	36	25
Ba	0	0	0	0	1	215	0	0	235
Rb	217	208	219	223	194	185	172	207	125
Sr	26	34	32	25	45	156	47	51	25
Zr	1693	1592	1622	1648	1570	1377	1865	2585	997
Y	58	59	59	60	53	45	59	73	47
Nb	413	397	399	403	383	330	458	499	268
Ga	37	36	37	38	41	36	39	41	27
Cu	0	4	0	1	1	0	3	5	0
Zn	197	197	199	194	178	164	192	209	144
Pb	17	21	19	21	17	15	20	28	14
La	177	179	192	187	193	162	185	258	160
Ce	310	321	316	303	307	243	342	452	256
Th	44	43	41	43	43	39	53	119	25
ICP-MS traces (ppm) La	177	183	183	173		153	189	225	157
Ce	279	283	271	252		218	307	340	253
Pr	20	22	21	19		18	23	28	24
Nd	56	63	57	53		50	67	82	76
Sm	8.6	10.1	8.8	8.1		7.8	10.7	13.3	13.0
Eu	1.5	1.9	1.6	1.4		1.7	2.0	2.5	3.2
Gd	7.4	8.4	7.5	7.2		6.5	9.1	11.0	10.0
Tb	1.3	1.5	1.3	1.3		1.1	1.6	1.8	1.6
Dy	8.7	9.6	8.9	8.5		7.0	9.9	11.2	9.3
Ho	1.9	2.0	2.0	1.8		1.5	2.1	2.4	1.8
Er	5.8	6.0	5.8	5.7		4.4	6.1	6.8	4.9
Tm	0.9	0.9	0.9	0.9		0.7	1.0	1.1	0.7
Yb	6.1	6.2	6.2	6.0		4.7	6.3	6.7	4.5
Lu	1.0	1.0	1.0	0.9		0.7	1.0	1.1	0.7
Ba	21	40	31	14		319	19	35	241
Th	44	43	44	42		34	46	82	27
Nb	409	397	402	378		322	449	459	272
Y	57	59	58	55		45	61	67	48
Hf	32	31	32	30		25	34	41	20
Ta	19	19	18	18		14	21	22	16
U	9.2	9.2	9.2	9.1		7.3	8.4	9.5	4.9
Pb	21	20	21	20		17	22	25	14
Rb	203	196	205	199		169	173	188	117
Cs	2.5	2.5	2.8	2.6		2.2	2.1	2.4	1.5
Sr	21	32	34	22		233	38	40	23
Sc	2.2	2.1	2.5	2.1		2.1	2.6	3.3	1.6
Zr	1692	1555	1633	1513		1349	1840	2260	996

Appendix A.
DHF Whole-rock data

ChemoUnit	DHF bs	DHF bs	DHF bs	DHF bs	DHF bs	DHF bs	DHF bs	DHF bs	DHF bs	DHF bs
Member	BS	BS	BS	BS	BS	BS	BS	BS	BS	BS
sample #	03TF186M	03TF187	03TF188	03TF189	03TF190	03TF81	05TF94	05TTF93	DH99-60B	DH99-60C
XRF Major element oxides (Wt%)										
SiO2	60.58	58.95	59.21	58.96	57.98	61.04	59.44	59.09	59.19	60.15
Al2O3	19.96	20.88	22.29	21.43	20.20	18.26	21.01	20.48	22.18	21.45
TiO2	0.80	0.53	0.59	0.64	0.50	0.78	0.47	0.47	0.81	0.99
FeO*	3.07	3.30	3.28	3.42	3.06	3.36	3.48	3.50	3.38	3.50
MnO	0.24	0.30	0.26	0.29	0.30	0.28	0.32	0.31	0.33	0.25
CaO	0.86	0.77	1.09	0.70	1.10	0.57	0.73	0.71	0.96	1.31
MgO	0.52	0.36	0.67	0.39	0.64	0.47	0.42	0.31	0.36	0.55
K2O	5.15	5.36	5.53	5.17	5.44	5.18	6.69	6.02	4.96	4.53
Na2O	8.52	9.19	6.74	8.64	10.44	9.78	6.96	8.62	7.75	7.15
P2O5	0.08	0.04	0.05	0.06	0.04	0.07	0.05	0.06	0.07	0.12
total	99.77	99.68	99.71	99.70	99.69	99.77	99.56	99.58	100.00	100.00
XRF Trace elements (ppm) Ni	2.0	2.1	4.3	4.2	2.1	1.0	9.1	5.4	6.0	7.0
Cr	0.0	1.0	2.1	2.1	0.0	0.0	0.4	2.3	0.0	3.0
Sc	3.1	0.0	1.1	0.0	0.0	4.1	0.1	-0.1	0.0	1.0
V	26	23	16	12	19	45	23	24	21	27
Ba	204	0	0	0	0	33	25	36		
Rb	147	214	181	186	217	139	238	229	187	125
Sr	18	36	22	23	20	4	40	41	67	245
Zr	963	1648	1488	1526	1597	994	1672	1600	1595	980
Y	49	62	55	61	57	59	56	56	69	47
Nb	260	410	366	383	395	290	407	391	401	260
Ga	28	38	36	35	34	26	42	39	36	30
Cu	0	0	3	2	1	0	4	2	1	4
Zn	136	194	178	188	188	166	196	188	201	144
Pb	13	21	18	18	14	12	23	23		
La	152	203	173	177	200	176	204	189		
Ce	240	295	277	316	291	303	277	280		
Th	25	44	42	43	41	25	46	44		
ICP-MS traces (ppm) La	151	191	166	187	181		182	174		
Ce	244	269	239	287	262		249	248		
Pr	23	22	23	24	20		20	19		
Nd	76	61	71	73	55		52	52		
Sm	13.1	9.3	11.7	12.0	8.4		7.7	7.9		
Eu	3.0	1.7	2.5	2.3	1.5		1.2	1.3		
Gd	9.9	8.2	9.1	9.8	7.4		6.7	6.9		
Tb	1.6	1.4	1.5	1.7	1.3		1.2	1.2		
Dy	9.1	9.5	9.0	10.3	8.8		8.2	8.3		
Ho	1.8	2.1	1.9	2.1	1.9		1.8	1.8		
Er	4.8	6.2	5.1	6.2	5.8		5.6	5.6		
Tm	0.7	1.0	0.8	1.0	0.9		0.9	0.9		
Yb	4.4	6.5	5.0	6.0	6.1		6.0	6.0		
Lu	0.7	1.0	0.8	0.9	1.0		1.0	1.0		
Ba	221	21	47	28	12		24	33		
Th	26	43	30	40	42		41	40		
Nb	265	409	297	384	403		400	393		
Y	49	62	52	61	58		54	54		
Hf	19	32	22	29	31		31	30		
Ta	16	19	16	19	18		18	18		
U	5.4	9.2	5.8	7.9	11.2		8.6	8.9		
Pb	14	21	16	19	19		19	19		
Rb	142	197	140	171	202		211	208		
Cs	1.6	2.6	1.8	2.3	2.6		2.6	2.6		
Sr	15	31	13	21	17		37	40		
Sc	1.4	2.1	2.1	2.2	2.3		1.7	1.8		
Zr	965	1666	1124	1545	1658		1566	1536		

Appendix A.
DHF Whole-rock data

ChemoUnit	DHF bs	DHF bs	DHF bs	DHF bs	DHF bs	DHF bs	DHF bs	DHF bs	DHF bs
Member	BS	BS	Espigon	Fortelaza	Fortelaza	Fortelaza	Fortelaza	Fortelaza	Fortelaza
sample #	DH99-61	DH9981	05TF90	01TF640	03TF246	03TF247	03TF248	03TF249A	03TF249B
XRF Major element oxides (Wt%)									
SiO2	59.48	59.61	61.89	59.57	59.16	59.01	59.80	59.36	59.45
Al2O3	20.34	21.40	20.16	20.13	20.21	22.23	21.82	21.30	21.50
TiO2	0.52	0.53	0.50	0.57	0.57	0.61	0.64	0.58	0.58
FeO*	2.57	3.15	2.63	3.06	3.18	3.36	3.47	3.32	3.29
MnO	0.31	0.28	0.18	0.28	0.29	0.34	0.31	0.32	0.31
CaO	0.62	0.94	1.05	0.68	0.65	0.53	0.42	0.59	0.56
MgO	0.21	0.59	0.34	0.45	0.30	0.52	1.14	0.46	0.35
K2O	5.61	6.00	7.10	5.57	5.58	4.72	4.25	5.10	5.18
Na2O	10.30	7.12	5.82	9.35	9.74	8.34	7.79	8.64	8.44
P2O5	0.04	0.06	0.05	0.04	0.04	0.04	0.05	0.04	0.04
total	100.00	99.68	99.72	99.71	99.71	99.70	99.70	99.70	99.71
XRF Trace elements (ppm) Ni	4.0	2.1	6.5	1.0	2.0	5.2	3.2	2.1	2.1
Cr	0.0	0.0	0.5	0.0	3.1	3.1	3.2	0.0	0.0
Sc	2.0	0.0	-0.2	2.0	1.0	0.0	0.0	1.0	0.0
V	18	35	17	27	15	13	10	14	15
Ba		20	487	0	0	0	0	0	0
Rb	215	216	210	211	214	198	184	203	210
Sr	24	72	91	10	12	16	10	6	7
Zr	1516	1580	860	1422	1448	1655	1631	1589	1605
Y	57	59	19	62	61	79	81	70	71
Nb	372	399	153	361	366	419	412	403	404
Ga	33		28	33	36	39	39	40	42
Cu	0		3	1	1	0	0	2	0
Zn	184		102	181	178	200	195	192	191
Pb			15	14	17	19	24	19	19
La			93	203	187	241	222	206	223
Ce			121	303	313	343	362	319	335
Th			28	36	38	47	43	44	45
ICP-MS traces (ppm) La			84		188	239	219	221	204
Ce			107		276	313	301	300	292
Pr			9		24	30	28	27	25
Nd			25		72	87	84	79	74
Sm			3.6		11.6	13.9	13.9	12.6	12.0
Eu			0.9		2.1	2.5	2.5	2.3	2.2
Gd			2.9		9.7	11.8	12.1	10.6	10.1
Tb			0.5		1.7	2.0	2.0	1.8	1.7
Dy			2.8		10.4	12.6	12.8	11.4	11.0
Ho			0.6		2.2	2.7	2.7	2.4	2.4
Er			1.9		6.2	7.7	7.8	6.9	6.7
Tm			0.3		1.0	1.2	1.2	1.1	1.1
Yb			2.2		6.2	7.5	7.7	6.9	6.8
Lu			0.4		0.9	1.2	1.2	1.1	1.0
Ba			463		5	5	8	4	3
Th			25		39	44	43	42	42
Nb			153		378	421	404	408	409
Y			18		63	79	80	71	69
Hf			14		28	32	30	31	31
Ta			6		19	20	20	20	20
U			5.5		8.9	8.8	8.1	8.4	8.6
Pb			14		19	21	20	20	20
Rb			190		202	182	164	185	197
Cs			2.2		2.0	3.3	2.9	3.6	3.7
Sr			85		11	12	7	4	4
Sc			1.0		2.1	2.4	2.5	2.3	2.2
Zr			802		1517	1691	1616	1604	1640

Appendix A.
DHF Whole-rock data

ChemoUnit	DHF bs	DHF bs	DHF bs	DHF bs	DHF bs	DHF bs	DHF bs	DHF bs	DHF bs	DHF bs
Member	Fortelaza	Fortelaza	Fortelaza	Fortelaza	Fortelaza	Roque	Roque	Roque	Tace	Taco
sample #	03TF250	03TF251	03TF252	03TF253	03TF254	00TF70	00TF71	DH9959	03TF658	03TF656
XRF Major element oxides (Wt%)										
SiO2	58.65	59.12	58.74	58.59	58.44	56.50	57.38	58.05	56.99	60.41
Al2O3	22.76	21.62	21.77	20.49	20.06	20.64	20.81	21.31	18.09	19.18
TiO2	0.63	0.60	0.58	0.55	0.54	0.76	0.84	1.16	1.22	0.58
FeO*	3.66	3.29	3.22	3.15	3.02	3.30	3.36	4.39	4.03	2.88
MnO	0.34	0.31	0.29	0.29	0.29	0.17	0.17	0.27	0.19	0.25
CaO	0.76	0.75	1.31	0.68	0.62	3.93	2.51	2.87	5.08	1.20
MgO	0.41	0.46	0.72	0.49	0.31	1.05	0.98	1.31	2.47	1.43
K2O	4.72	4.93	4.70	5.31	5.48	5.41	5.53	5.04	4.30	5.62
Na2O	7.73	8.58	8.34	10.10	10.90	7.75	7.97	5.04	6.88	8.14
P2O5	0.03	0.04	0.04	0.05	0.04	0.18	0.18	0.26	0.36	0.06
total	99.70	99.70	99.70	99.71	99.71	99.70	99.72	99.69	99.62	99.73
XRF Trace elements (ppm) Ni	0.0	2.1	1.0	3.1	1.0	5.2	4.1	5.2	9.4	8.5
Cr	0.0	0.0	0.0	1.0	0.0	0.0	0.0	2.1	5.3	8.8
Sc	0.0	0.0	1.0	1.0	0.0	2.1	7.1	0.0	3.8	0.8
V	25	21	21	14	24	34	46	65	60	29
Ba	0	0	0	0	0	175	227	316	1360	305
Rb	207	191	195	212	216	245	224	204	105	144
Sr	22	16	17	8	7	247	259	408	773	88
Zr	1719	1587	1581	1502	1454	1551	1350	1364	710	1123
Y	84	70	73	62	60	26	26	30	44	43
Nb	447	404	400	378	367	218	206	217	219	299
Ga	43	41	40	34	32	35	33	32	26	31
Cu	1	0	0	2	0	1	0	7	5	6
Zn	217	193	194	190	180	129	114	141	121	146
Pb	22	19	19	19	18	23	23	19	14	23
La	263	189	208	183	179	102	79	98	127	138
Ce	346	341	320	295	293	153	139	155	219	227
Th	47	45	44	39	42	48	41	41	20	35
ICP-MS traces (ppm) La	257	188	191	180	187	98	95			
Ce	308	294	285	273	275	116	118			
Pr	29	24	24	23	23	9	10			
Nd	85	72	73	67	67	27	29			
Sm	13.4	11.7	12.3	10.9	10.8	4.5	4.8			
Eu	2.4	2.2	2.3	2.0	2.0	1.2	1.3			
Gd	11.5	10.0	10.8	9.2	8.9	3.6	3.8			
Tb	1.9	1.7	1.8	1.6	1.5	0.6	0.6			
Dy	12.3	11.0	11.6	10.0	9.7	3.8	3.8			
Ho	2.6	2.4	2.5	2.1	2.0	0.8	0.8			
Er	7.5	6.9	7.1	6.2	5.9	2.6	2.5			
Tm	1.1	1.1	1.1	1.0	0.9	0.5	0.4			
Yb	7.3	6.9	7.0	6.2	6.0	3.5	3.2			
Lu	1.1	1.1	1.1	1.0	0.9	0.6	0.6			
Ba	4	8	7	7	5	197	233			
Th	44	42	42	41	39	50	43			
Nb	436	404	395	384	378	230	218			
Y	80	70	72	61	61	25	24			
Hf	32	30	30	29	29	29	25			
Ta	21	19	19	19	19	7	8			
U	8.2	8.2	8.0	9.3	9.0	12.8	10.9			
Pb	21	20	19	19	19	23	21			
Rb	184	179	175	196	214	247	228			
Cs	4.4	3.1	3.3	2.8	2.7	3.9	3.3			
Sr	17	11	12	7	5	227	246			
Sc	2.4	2.3	2.3	2.1	1.9	2.4	2.7			
Zr	1689	1605	1559	1534	1518	1592	1387			

Appendix A.
DHF Whole-rock data

ChemoUnit	DHF I	DHF I	DHF I	DHF I	DHF I	DHF I	DHF I	DHF I	DHF I	DHF I
Member	Cabezon	Aldea	Aldea	Aldea	Aldea	Aldea	Aldea	Aldea	Aldea	Aldea
sample #	01TF611	03TF178A	03TF178B	03TF178C	01TF73	01TF75	01TF78	01TF77	01TF81	01TF82
XRF Major element oxides (Wt%)										
SiO2	58.99	58.47	58.78	57.27	57.52	57.62	57.70	58.09	57.32	57.85
Al2O3	21.81	21.71	22.60	20.66	20.49	21.17	21.53	21.27	20.79	20.75
TiO2	0.50	0.40	0.39	0.89	0.75	0.60	0.40	0.40	0.46	0.46
FeO*	2.67	2.71	2.82	3.49	3.13	2.88	2.71	2.71	2.64	2.49
MnO	0.19	0.23	0.23	0.18	0.18	0.19	0.22	0.23	0.21	0.20
CaO	1.03	0.79	0.80	2.09	1.93	1.57	0.95	0.96	2.09	2.16
MgO	0.38	0.34	0.38	1.04	1.10	0.85	0.58	1.00	1.27	1.13
K2O	5.88	6.20	6.15	5.51	5.27	5.39	5.63	5.61	5.48	5.56
Na2O	8.20	8.78	7.44	8.42	9.22	9.34	9.92	9.36	9.37	9.03
P2O5	0.05	0.04	0.04	0.16	0.13	0.08	0.04	0.04	0.07	0.08
total	99.70	99.67	99.64	99.71	99.72	99.70	99.67	99.66	99.70	99.71
XRF Trace elements (ppm) Ni	6.1	0.0	0.0	3.1	9.3	9.2	5.2	7.2	6.3	5.2
Cr	1.0	1.0	1.0	2.1	0.0	2.1	0.0	0.0	0.0	0.0
Sc	2.0	0.0	8.2	1.0	2.1	0.0	1.0	1.0	1.1	3.1
V	23	22	22	47	45	48	33	26	27	37
Ba	277	0	0	411	356	289	0	7	65	88
Rb	238	296	281	199	200	220	281	290	250	240
Sr	108	46	93	284	217	162	34	47	66	85
Zr	1541	2027	2190	1256	1293	1502	1988	2066	1747	1658
Y	28	33	32	31	29	29	32	34	32	31
Nb	252	298	316	223	220	239	286	289	258	248
Ga	35	40	44	32	32	36	43	43	40	37
Cu	0	0	0	5	0	0	0	0	0	0
Zn	124	162	162	123	119	126	149	156	145	137
Pb	20	23	27	16	16	19	31	28	24	23
La	91	134	133	100	104	117	127	141	109	113
Ce	182	196	206	170	167	184	184	202	175	175
Th	46	62	67	39	39	49	59	64	53	51
ICP-MS traces (ppm) La	98	126	118	104	111	94	114	112	115	110
Ce	133	149	147	146	145	124	137	131	140	130
Pr	10	10	10	13	12	10	10	10	12	11
Nd	29	27	25	39	35	29	26	28	33	33
Sm	4.4	4.0	3.6	6.7	5.7	4.6	3.8	4.3	5.1	5.0
Eu	0.9	0.8	0.7	1.7	1.4	1.1	0.7	0.8	1.0	1.0
Gd	3.7	3.4	3.2	5.3	4.7	3.9	3.3	3.7	4.3	4.1
Tb	0.6	0.6	0.6	0.8	0.8	0.7	0.6	0.6	0.7	0.7
Dy	4.1	4.2	3.9	5.0	4.6	4.1	4.1	4.2	4.7	4.5
Ho	0.9	1.0	0.9	1.0	1.0	0.9	1.0	1.0	1.1	1.0
Er	3.0	3.4	3.2	3.0	3.1	2.9	3.3	3.3	3.5	3.3
Tm	0.5	0.6	0.6	0.5	0.5	0.5	0.6	0.6	0.6	0.6
Yb	3.8	4.5	4.4	3.3	3.6	3.5	4.5	4.4	4.4	4.2
Lu	0.7	0.8	0.8	0.5	0.6	0.6	0.8	0.8	0.8	0.7
Ba	205	30	22	484	358	257	47	58	81	101
Th	51	62	64	35	42	45	63	60	56	52
Nb	280	309	312	220	259	252	310	299	288	272
Y	27	32	30	30	31	26	30	31	32	31
Hf	30	36	36	21	25	28	37	35	32	31
Ta	10	10	10	10	10	9	10	9	10	9
U	7.2	15.6	14.2	8.7	10.0	7.7	13.0	11.9	11.6	10.9
Pb	24	27	28	17	21	24	32	31	28	26
Rb	237	282	256	181	206	213	280	269	247	236
Cs	3.5	4.4	3.7	2.4	2.9	3.2	4.5	4.4	3.9	3.8
Sr	71	46	93	311	203	141	39	46	58	67
Sc	2.0	2.5	2.5	4.2	3.0	2.0	2.0	2.0	2.0	1.9
Zr	1624	2082	2150	1173	1393	1490	2029	1959	1810	1706

Appendix A.
DHF Whole-rock data

ChemoUnit	DHF I	DHF I	DHF I	DHF I	DHF I	DHF I	DHF I	DHF I	DHF I	DHF I	DHF I
Member	Aldea	Aldea	Aldea	Aldea	Aldea	Aldea	Aldea	Aldea	Aldea	Aldea	Aldea
sample #	01TF83	01TF84	01TF85	01TF86	01TF610	01TF614	01TF612	01TF613	01TF622	01TF620	01TF621
XRF Major element oxides (Wt%)											
SiO2	57.79	57.67	56.68	57.91	58.21	57.97	58.39	58.37	58.99	58.32	58.47
Al2O3	20.84	21.34	20.77	21.25	21.39	21.53	21.57	21.78	21.32	21.35	21.58
TiO2	0.50	0.44	0.47	0.45	0.53	0.43	0.47	0.41	0.57	0.48	0.47
FeO*	2.77	2.54	2.47	2.53	2.84	2.57	2.69	2.65	2.76	2.63	2.56
MnO	0.22	0.20	0.18	0.20	0.20	0.20	0.20	0.21	0.21	0.20	0.19
CaO	1.83	0.92	2.82	1.08	1.18	0.87	0.96	0.86	1.08	0.99	0.94
MgO	1.19	0.50	0.50	0.42	0.46	0.40	0.45	0.35	0.51	0.34	0.41
K2O	5.54	5.81	5.68	5.86	6.20	5.84	6.04	6.30	5.81	6.04	6.10
Na2O	8.95	10.25	10.09	9.97	8.64	9.86	8.90	8.74	8.38	9.33	8.95
P2O5	0.07	0.04	0.06	0.05	0.06	0.04	0.04	0.03	0.06	0.05	0.04
total	99.69	99.71	99.73	99.71	99.71	99.72	99.71	99.70	99.70	99.71	99.73
XRF Trace elements (ppm) Ni	12.4	6.1	3.1	5.1	4.1	6.1	6.1	5.1	8.1	5.1	6.1
Cr	0.0	1.0	0.0	0.0	1.0	0.0	0.0	0.0	0.0	0.0	0.0
Sc	4.1	6.1	0.0	2.0	5.1	0.0	2.0	2.0	1.0	0.0	0.0
V	31	30	31	35	27	28	31	29	39	24	31
Ba	96	36	106	56	80	18	69	11	234	96	65
Rb	256	264	237	258	257	267	260	276	245	257	253
Sr	66	38	82	45	65	31	56	30	121	72	45
Zr	1755	1689	1469	1639	1666	1672	1643	1790	1573	1633	1551
Y	32	29	30	30	31	28	29	31	31	30	29
Nb	266	259	241	258	263	260	259	273	257	259	252
Ga	35	37	33	37	39	36	39	39	36	38	37
Cu	0	0	0	0	0	0	0	0	0	0	0
Zn	149	136	120	132	134	133	135	138	131	131	125
Pb	27	25	24	26	25	21	26	28	22	19	24
La	139	95	115	126	117	112	96	106	114	125	113
Ce	195	200	170	161	174	176	195	196	181	182	163
Th	54	51	47	49	49	51	50	55	49	51	45
ICP-MS traces (ppm) La	110	97	105	95	89	77	101	95	101	107	77
Ce	134	123	135	123	119	106	130	123	135	137	108
Pr	11	10	10	10	9	8	10	9	10	10	8
Nd	31	26	29	27	27	22	27	24	30	29	23
Sm	4.8	4.0	4.5	4.1	4.2	3.3	4.0	3.7	4.7	4.4	3.7
Eu	0.9	0.8	0.9	0.8	0.9	0.7	0.8	0.7	1.1	1.0	0.7
Gd	3.9	3.4	3.9	3.5	3.5	2.9	3.5	3.1	3.9	3.8	3.1
Tb	0.7	0.6	0.6	0.6	0.6	0.5	0.6	0.6	0.7	0.6	0.5
Dy	4.4	3.9	4.2	3.9	3.9	3.5	3.9	3.7	4.4	4.1	3.6
Ho	1.0	0.9	1.0	0.9	0.9	0.8	0.9	0.9	1.0	0.9	0.8
Er	3.2	2.9	3.1	2.9	2.9	2.8	3.0	3.0	3.1	3.0	2.7
Tm	0.6	0.5	0.5	0.5	0.5	0.5	0.5	0.6	0.5	0.5	0.5
Yb	4.1	3.8	3.8	3.8	3.7	3.7	3.8	4.1	4.0	3.8	3.5
Lu	0.7	0.7	0.7	0.6	0.6	0.7	0.7	0.7	0.7	0.7	0.6
Ba	99	82	127	83	180	58	87	38	207	158	80
Th	53	51	45	49	48	46	52	53	49	49	43
Nb	277	276	254	271	274	278	277	289	274	270	266
Y	30	27	30	27	26	23	27	26	29	28	23
Hf	31	30	26	29	29	31	30	32	30	29	28
Ta	10	10	10	10	10	10	10	10	10	10	10
U	10.5	9.4	12.2	9.4	6.7	9.4	9.5	9.7	10.1	10.2	7.6
Pb	27	27	23	26	26	26	26	27	24	25	24
Rb	241	253	227	244	238	244	252	261	239	241	231
Cs	3.7	3.8	3.2	3.6	3.5	3.8	3.7	3.9	3.5	3.5	3.3
Sr	62	46	82	44	84	32	44	25	107	85	38
Sc	1.8	1.7	1.9	1.8	1.6	1.8	1.8	1.7	2.3	2.1	1.7
Zr	1705	1655	1458	1602	1575	1671	1655	1780	1614	1592	1518

Appendix A.
DHF Whole-rock data

ChemoUnit	DHF I	DHF I	DHF I	DHF I	DHF I	DHF I	DHF I	DHF I	DHF I	DHF I	DHF I
Member	Aldea	Aldea	Aldea	Aldea	Aldea	Aldea	Aldea	Aldea	Aldea	Aldea	Aldea
sample #	01TF617	01TF616	00TF72	00TF73	00TF74B	00TF75	01TF55	01TF258	01TF259	00TF78	00TF76
XRF Major element oxides (Wt%)											
SiO2	60.89	58.19	57.98	58.13	57.64	57.40	55.22	59.64	58.60	53.83	54.92
Al2O3	20.05	21.45	21.46	21.45	20.85	20.39	17.59	24.13	25.47	19.50	19.59
TiO2	0.80	0.45	0.36	0.39	0.57	0.87	0.47	0.39	0.62	0.42	0.66
FeO*	3.02	2.55	2.67	2.73	2.94	3.64	2.41	2.85	3.15	2.64	2.93
MnO	0.26	0.20	0.23	0.23	0.20	0.19	0.16	0.24	0.22	0.21	0.18
CaO	0.85	0.95	1.12	1.00	2.09	2.56	9.02	1.07	1.61	7.94	6.71
MgO	0.60	0.44	0.23	0.45	0.81	1.08	3.53	0.52	0.95	1.20	1.51
K2O	5.09	6.02	5.99	6.12	5.82	5.47	4.47	6.05	4.64	5.53	5.40
Na2O	8.14	9.42	9.58	9.11	8.68	7.95	6.76	4.69	4.31	8.35	7.69
P2O5	0.08	0.04	0.03	0.05	0.09	0.15	0.11	0.05	0.09	0.05	0.11
total	99.77	99.72	99.65	99.66	99.70	99.70	99.75	99.63	99.65	99.68	99.70
XRF Trace elements (ppm) Ni	3.0	3.0	2.0	6.2	6.1	5.1	8.5	5.3	7.4	0.0	2.1
Cr	0.0	0.0	0.0	0.0	0.0	0.0	0.0	0.0	0.0	0.0	0.0
Sc	0.0	1.0	4.1	1.0	0.0	9.2	0.0	6.4	0.0	0.0	0.0
V	17	20	22	22	30	51	42	17	33	29	32
Ba	294	70	0	0	158	380	123	4	173	47	419
Rb	144	256	310	300	251	210	200	293	191	265	205
Sr	22	59	24	34	123	265	206	196	398	175	307
Zr	933	1598	2172	2080	1630	1349	1273	2264	1750	1837	1309
Y	48	28	32	31	28	32	27	30	31	33	30
Nb	251	254	299	293	257	227	204	306	283	267	220
Ga	29	35	39	40	35	36	32	44	45	35	31
Cu	0	0	0	0	0	0	4	2	1	0	0
Zn	144	128	164	165	136	125	111	169	150	139	119
Pb	14	24	33	32	20	26	20	28	24	28	23
La	140	116	129	126	135	108	96	118	134	117	99
Ce	242	172	192	196	174	170	158	190	196	189	160
Th	25	47	66	62	48	39	38	71	53	51	40
ICP-MS traces (ppm) La	140	93	131	130	114	114	95	108	113	122	118
Ce	233	121	152	152	147	153	120	128	152	141	149
Pr	22	9	10	10	11	13	9	8	11	11	11
Nd	73	25	25	27	33	38	26	21	31	30	33
Sm	12.5	3.8	3.6	3.8	5.2	6.1	4.1	3.0	4.8	4.5	5.2
Eu	3.1	0.8	0.6	0.7	1.2	1.5	0.9	0.6	1.1	0.9	1.2
Gd	9.7	3.2	2.8	3.0	4.1	4.8	3.4	2.8	4.0	3.6	4.1
Tb	1.5	0.6	0.6	0.6	0.7	0.8	0.6	0.5	0.7	0.7	0.7
Dy	9.0	3.8	4.1	4.2	4.5	4.9	3.7	3.6	4.3	4.2	4.6
Ho	1.8	0.9	1.0	1.0	1.0	1.0	0.8	0.9	1.0	1.0	1.0
Er	4.8	2.9	3.5	3.4	3.1	3.1	2.6	3.1	3.1	3.3	3.1
Tm	0.7	0.5	0.6	0.6	0.6	0.5	0.5	0.6	0.5	0.6	0.5
Yb	4.4	3.8	4.8	4.7	4.0	3.6	3.4	4.5	4.0	4.4	4.0
Lu	0.7	0.6	0.9	0.8	0.7	0.6	0.6	0.8	0.7	0.8	0.7
Ba	300	95	14	34	294	366	135	52	230	66	223
Th	25	48	68	66	49	42	39	71	53	57	50
Nb	262	270	321	315	257	240	222	322	290	278	264
Y	47	26	32	32	30	31	25	28	30	32	31
Hf	19	29	39	37	28	25	22	39	30	32	29
Ta	16	10	10	10	9	10	8	9	11	9	10
U	5.4	8.8	17.2	16.3	12.2	10.4	9.9	10.8	6.7	14.5	12.4
Pb	15	26	31	30	23	21	21	33	26	26	24
Rb	139	245	304	296	233	211	190	285	179	254	244
Cs	1.7	3.5	5.2	4.8	3.5	3.0	2.8	4.4	2.9	4.0	3.6
Sr	19	59	20	36	189	247	199	178	402	162	150
Sc	1.2	1.7	1.9	2.0	2.4	3.1	2.1	2.1	2.1	1.9	3.4
Zr	938	1593	2248	2170	1557	1355	1242	2257	1682	1863	1591

Appendix A.
DHF Whole-rock data

ChemoUnit	DHF I	DHF I	DHF I	DHF I	DHF I	DHF I	DHF I	DHF I	DHF I	DHF I	DHF I
Member	Aldea	Aldea	Fasnia	Fasnia	Fasnia	Fasnia	Fasnia	Fasnia	Fasnia	Fasnia	Fasnia
sample #	00TF77	00TF79	TF99-3	TF99-4	05TF76	05TF78	05TF79A	05TF79B	TF99-6	TF01-125	TF01-65
XRF Major element oxides (Wt%)											
SiO2	56.62	57.09	59.98	58.78	58.55	58.13	58.23	58.33	59.28	59.09	57.18
Al2O3	20.42	20.41	20.80	21.22	21.56	21.57	21.55	21.59	21.35	21.70	21.24
TiO2	0.54	0.46	0.47	0.37	0.34	0.33	0.30	0.36	0.34	0.31	0.31
FeO*	2.87	2.72	2.32	2.47	2.81	2.85	2.77	2.77	2.36	2.34	2.26
MnO	0.20	0.20	0.50	0.21	0.23	0.24	0.25	0.24	0.22	0.23	0.21
CaO	3.53	3.44	0.97	0.78	0.77	0.76	0.69	0.93	0.83	0.73	2.73
MgO	1.50	0.93	1.60	0.45	0.24	0.21	0.18	0.27	0.46	0.27	0.59
K2O	5.65	5.86	5.99	6.59	6.50	6.26	6.27	6.35	6.85	6.99	5.85
Na2O	8.25	8.51	6.97	8.78	8.54	9.18	9.28	8.69	7.96	7.98	9.27
P2O5	0.08	0.06	0.08	0.04	0.04	0.04	0.03	0.05	0.04	0.03	0.03
total	99.68	99.69	99.68	99.68	99.57	99.56	99.55	99.58	99.69	99.67	99.67
XRF Trace elements (ppm) Ni	4.1	5.2	80.0	7.3	7.8	7.2	22.0	6.9	8.0	5.2	5.3
Cr	0.0	0.0	4.0	0.0	2.1	1.6	2.8	1.6	1.0	0.0	1.1
Sc	0.0	3.1	7.0	0.0	1.3	0.3	-0.4	0.5	0.0	1.0	0.0
V	30	29	25	23	17	17	16	19	12	14	22
Ba	225	97	152	16	29	27	2	80	0	0	0
Rb	250	254	261	299	314	317	327	298	302	307	291
Sr	173	117	72	35	28	24	10	74	41	22	52
Zr	1671	1756	1671	1924	2001	2025	2110	1893	1962	2075	1947
Y	30	32	37	31	27	26	28	27	35	31	27
Nb	251	265	248	268	265	268	273	255	265	273	254
Ga	34	39	36	41	43	42	45	42	39	43	39
Cu	0	0	0	0	3	3	3	4	4	0	0
Zn	139	141	140	144	158	163	169	156	152	155	147
Pb	27	22	35	26	32	33	34	31	30	23	28
La	112	129	125	111	115	118	122	110	131	125	126
Ce	155	182	193	189	141	143	149	143	190	182	174
Th	53	53	53	59	66	64	67	60	61	51	62
ICP-MS traces (ppm) La	109	139	133	121		108	100	94	133	101	114
Ce	142	197	149	137		124	113	110	129	116	127
Pr	12	16	13	9		8	7	8	11	8	8
Nd	35	47	39	23		20	18	20	30	19	20
Sm	5.7	7.4	6.5	3.2		2.9	2.5	3.0	4.7	2.8	2.8
Eu	1.4	1.2	1.5	0.6		0.5	0.4	0.6	1.0	0.5	0.5
Gd	4.5	5.6	5.5	2.9		2.6	2.3	2.6	4.0	2.2	2.2
Tb	0.8	1.0	0.9	0.5		0.5	0.4	0.5	0.7	0.5	0.5
Dy	4.7	6.5	5.9	3.7		3.3	3.1	3.3	4.5	3.4	3.4
Ho	1.0	1.4	1.3	0.9		0.8	0.8	0.8	1.1	0.8	0.8
Er	3.1	4.1	4.1	3.2		2.9	2.8	2.7	3.6	3.1	2.9
Tm	0.5	0.7	0.7	0.6		0.6	0.5	0.5	0.6	0.6	0.6
Yb	3.7	4.3	5.0	4.5		4.2	4.1	3.9	4.8	4.5	4.4
Lu	0.6	0.7	0.9	0.8		0.7	0.7	0.7	0.8	0.8	0.8
Ba	365	17	166	34		26	7	77	56	26	25
Th	42	32	56	64		60	59	53	62	63	64
Nb	237	270	268	289		268	263	256	279	290	272
Y	30	41	40	30		26	24	24	35	26	28
Hf	24	22	31	35		33	34	31	34	37	35
Ta	9	14	9	8		8	7	8	8	8	8
U	10.6	7.5	13.3	15.6		14.4	13.8	10.4	14.6	15.0	16.9
Pb	21	17	29	29		29	29	27	30	34	33
Rb	208	180	260	296		280	279	260	289	301	285
Cs	2.9	2.1	4.8	4.7		4.4	4.5	4.1	4.5	5.4	5.0
Sr	274	31	66	24		25	11	68	44	22	44
Sc	2.2	1.5	2.3	2.6		1.5	1.6	1.5	2.6	2.1	2.6
Zr	1351	1134	1758	1993		1912	1921	1774	1942	2044	1924

Appendix A.
DHF Whole-rock data

ChemoUnit	DHF I	DHF I	DHF I	DHF I	DHF I	DHF I	DHF I	DHF I	DHF I	DHF I
Member	Fasnia	Fasnia	Fasnia	Fasnia	Fasnia	Fasnia	Fasnia	Fasnia	Fasnia	Fasnia
sample #	TF01-66	TF99-8	TF99-10f	TF-01-115F	TF-01-116	Tf99-11f	TF99-12	TF01-123	TF99-13	TF01-122
XRF Major element oxides (Wt%)										
SiO2	54.62	58.71	58.73	57.62	56.99	59.03	58.26	57.02	58.32	57.81
Al2O3	20.12	21.51	21.34	21.21	20.85	20.91	20.74	20.28	21.47	21.07
TiO2	0.30	0.42	0.46	0.64	0.91	0.61	0.72	0.78	0.44	0.50
FeO*	2.24	2.56	2.62	3.08	3.70	3.01	3.30	3.45	2.63	2.65
MnO	0.20	0.21	0.22	0.20	0.19	0.20	0.22	0.19	0.21	0.19
CaO	7.05	1.08	1.16	1.59	2.42	1.56	1.88	2.10	1.13	1.26
MgO	0.72	0.56	0.77	0.86	1.18	0.87	1.01	2.34	0.40	0.99
K2O	5.76	6.71	6.37	6.00	5.56	6.32	6.00	5.62	6.46	6.25
Na2O	8.64	7.88	7.96	8.38	7.73	7.07	7.44	7.83	8.58	8.92
P2O5	0.04	0.06	0.06	0.11	0.18	0.10	0.12	0.12	0.06	0.06
total	99.69	99.70	99.69	99.69	99.71	99.68	99.69	99.73	99.70	99.70
XRF Trace elements (ppm) Ni	0.0	9.0	12.0	2.1	5.1	18.0	12.0	8.1	5.2	5.2
Cr	0.0	0.0	0.0	0.0	4.1	0.0	6.0	18.2	0.0	0.0
Sc	2.1	3.0	2.0	0.0	1.0	6.0	6.0	3.0	6.3	4.1
V	21	27	27	39	60	41	46	53	19	24
Ba	0	43	50	121	246	223	252	235	52	132
Rb	278	280	271	267	230	235	236	218	275	252
Sr	93	65	75	141	251	179	202	192	78	112
Zr	1811	1784	1829	1690	1447	1576	1539	1395	1785	1615
Y	28	25	26	29	29	29	33	29	27	28
Nb	241	255	253	242	217	234	229	215	250	236
Ga	35	38	38	37	37	35	31	33	37	37
Cu	0	0	0	0	0	0	6	0	5	0
Zn	135	144	144	137	126	134	142	118	140	131
Pb	27	31	23	26	19	18	26	10	22	17
La	108	108	114	101	108	105	106	99	106	119
Ce	173	172	174	158	164	174	195	165	179	152
Th	61	58	51	42	33	37	44	29	54	38
ICP-MS traces (ppm) La	107	118	117	108	107	109	112	80	106	78
Ce	120	137	137	132	139	138	146	107	130	96
Pr	8	10	10	10	11	11	11	9	9	7
Nd	19	28	26	28	33	31	34	26	23	19
Sm	2.7	4.3	3.9	4.4	5.5	5.1	5.6	4.4	3.6	2.9
Eu	0.5	0.9	0.8	1.1	1.5	1.3	1.4	1.1	0.7	0.6
Gd	2.1	3.8	3.3	3.5	4.4	4.3	4.6	3.4	3.0	2.3
Tb	0.4	0.6	0.6	0.6	0.7	0.7	0.8	0.6	0.5	0.4
Dy	3.2	4.2	3.9	4.1	4.6	4.5	4.9	3.8	3.6	3.0
Ho	0.8	1.0	0.9	0.9	1.0	1.0	1.1	0.8	0.8	0.7
Er	2.9	3.1	3.0	2.9	3.0	3.2	3.4	2.5	2.9	2.4
Tm	0.6	0.6	0.6	0.5	0.5	0.6	0.6	0.4	0.5	0.4
Yb	4.2	4.2	4.3	3.9	3.7	4.1	4.2	3.1	3.9	3.4
Lu	0.8	0.7	0.7	0.7	0.6	0.7	0.7	0.5	0.7	0.6
Ba	20	88	89	199	328	284	275	286	116	111
Th	58	57	59	51	44	48	48	39	56	45
Nb	258	269	267	250	234	237	237	213	261	243
Y	28	30	29	29	30	31	33	23	26	22
Hf	32	32	33	29	26	27	27	24	32	28
Ta	7	8	8	8	8	9	8	8	8	7
U	17.5	14.0	14.2	12.7	11.2	11.6	11.4	8.4	12.3	9.4
Pb	30	27	27	27	24	23	26	22	26	26
Rb	274	270	274	248	223	230	231	200	262	243
Cs	4.7	4.1	4.2	4.3	3.7	3.3	3.4	3.5	3.9	4.1
Sr	83	71	79	173	286	201	199	198	76	73
Sc	2.5	1.8	2.0	3.4	4.2	2.9	4.5	3.5	2.7	1.7
Zr	1802	1764	1819	1640	1439	1514	1525	1265	1742	1596

Appendix A.
DHF Whole-rock data

ChemoUnit	DHF I	DHF I	DHF I	DHF I	DHF I	DHF I	DHF I	DHF I	DHF I	DHF I
Member	Fasnia	Fasnia	Fasnia	Fasnia	Fasnia	Fasnia	Fasnia	Fasnia	Fasnia	Fasnia
sample #	TF01-121	TF01-120	TF01-118	TF01-119	TF99-24	TF01-87	TF01-52	TF01-53	TF01-54	TF01-51
XRF Major element oxides (Wt%)										
SiO2	57.27	57.12	57.23	57.83	57.11	57.90	56.77	56.40	58.40	57.59
Al2O3	21.10	20.80	20.91	21.19	21.38	21.20	20.35	20.39	21.77	20.95
TiO2	0.47	0.48	0.45	0.46	0.44	0.51	0.40	0.41	0.34	0.44
FeO*	2.62	2.60	2.45	2.51	2.55	2.38	2.25	2.27	2.40	2.23
MnO	0.20	0.19	0.18	0.19	0.19	0.17	0.18	0.19	0.20	0.16
CaO	1.15	1.16	0.99	1.03	1.31	2.41	4.41	5.00	1.01	2.21
MgO	1.07	1.33	1.43	0.80	0.54	0.50	0.89	0.97	0.29	0.27
K2O	6.19	6.25	6.46	6.35	5.69	5.67	5.57	5.39	5.78	5.88
Na2O	9.58	9.71	9.58	9.32	10.46	8.92	8.84	8.64	9.48	9.97
P2O5	0.06	0.06	0.05	0.05	0.06	0.07	0.08	0.07	0.04	0.06
total	99.71	99.70	99.73	99.73	99.73	99.73	99.74	99.73	99.71	99.76
XRF Trace elements (ppm) Ni	3.1	3.2	4.2	2.1	5.3	2.1	3.1	1.1	5.1	2.1
Cr	0.0	0.0	0.0	0.0	0.0	0.0	0.0	0.0	0.0	0.0
Sc	0.0	0.0	0.0	0.0	1.1	0.0	0.0	0.0	0.0	0.0
V	26	19	32	25	29	38	24	29	22	25
Ba	88	83	112	88	74	189	59	78	0	100
Rb	258	254	244	250	245	219	246	250	284	217
Sr	91	89	98	72	100	140	92	123	25	78
Zr	1675	1617	1489	1523	1579	1327	1517	1586	1807	1228
Y	29	28	26	27	26	26	28	28	28	27
Nb	239	235	224	231	232	214	222	230	248	205
Ga	39	38	37	39	35	32	31	36	35	30
Cu	0	0	0	0	4	0	0	0	0	0
Zn	134	130	123	123	130	113	122	122	142	106
Pb	19	14	16	19	22	25	27	26	30	24
La	114	106	93	105	106	106	113	95	106	89
Ce	168	176	151	172	163	147	156	160	158	143
Th	39	37	35	33	47	43	49	51	58	41
ICP-MS traces (ppm) La	94	85	91	99	108	103	101	108	112	100
Ce	115	106	114	122	131	131	121	130	128	128
Pr	8	8	8	9	9	10	9	9	8	10
Nd	23	21	23	24	25	28	23	24	21	26
Sm	3.4	3.2	3.5	3.6	3.6	4.4	3.3	3.6	3.0	3.9
Eu	0.8	0.7	0.7	0.8	0.8	1.0	0.7	0.7	0.6	0.8
Gd	2.7	2.6	2.7	2.8	3.1	3.4	2.6	2.7	2.3	2.9
Tb	0.5	0.5	0.5	0.5	0.5	0.6	0.5	0.5	0.5	0.5
Dy	3.4	3.2	3.4	3.6	3.6	3.8	3.4	3.6	3.3	3.6
Ho	0.8	0.7	0.8	0.8	0.8	0.9	0.8	0.8	0.8	0.8
Er	2.6	2.4	2.6	2.6	2.8	2.6	2.6	2.8	2.8	2.5
Tm	0.5	0.5	0.5	0.5	0.5	0.5	0.5	0.5	0.5	0.5
Yb	3.6	3.4	3.5	3.6	3.8	3.4	3.5	3.7	3.9	3.2
Lu	0.6	0.6	0.6	0.6	0.7	0.6	0.6	0.7	0.7	0.6
Ba	198	111	105	110	124	200	83	91	27	109
Th	47	44	45	46	52	42	48	52	59	40
Nb	247	236	242	247	255	232	237	254	271	230
Y	25	23	24	26	27	27	25	27	27	25
Hf	28	27	27	28	29	25	26	29	32	23
Ta	8	8	8	8	9	9	8	8	8	9
U	11.1	10.9	10.9	11.6	13.0	11.5	12.4	13.3	14.8	11.4
Pb	26	23	24	25	23	24	26	28	31	23
Rb	246	235	239	244	250	220	235	251	277	218
Cs	4.1	3.9	3.9	4.0	3.6	3.5	3.9	4.2	4.7	3.3
Sr	124	75	66	67	89	125	96	113	29	74
Sc	1.6	1.3	1.3	1.3	2.7	2.4	2.4	2.6	2.6	2.1
Zr	1601	1507	1521	1538	1631	1348	1511	1654	1849	1298

Appendix A.
DHF Whole-rock data

ChemoUnit	DHF I	DHF I	DHF I	DHF I	DHF I	DHF I	DHF I	DHF I	DHF I
Member	Fasnia	Fasnia	Fasnia	Fasnia	Fasnia	Fasnia	Fasnia	Fasnia	Fasnia
sample #	TF01-49	DH99-48	TF-01-109	TF-01-124	TF76-JF1	TF76-JF2	TF01-110	TF76-JF3	TF01-106
XRF Major element oxides (Wt%)									
SiO2	56.19	60.30	58.12	57.54	58.33	58.49	58.16	58.63	58.79
Al2O3	20.74	21.45	21.00	20.79	21.19	21.26	20.50	21.35	21.03
TiO2	0.42	0.62	0.54	0.46	0.53	0.54	0.51	0.50	0.52
FeO*	2.38	2.78	2.54	2.42	2.77	2.65	2.57	2.60	2.76
MnO	0.18	0.21	0.18	0.18	0.18	0.18	0.18	0.18	0.18
CaO	4.20	0.88	2.32	1.25	1.16	1.16	2.29	1.12	1.20
MgO	0.46	0.68	0.82	0.79	0.39	0.45	1.65	0.40	1.99
K2O	5.67	3.80	6.24	6.49	6.28	6.31	6.08	6.43	6.16
Na2O	9.42	8.91	7.87	9.76	8.84	8.63	7.71	8.46	7.02
P2O5	0.06	0.07	0.08	0.06	0.07	0.07	0.08	0.06	0.07
total	99.72	99.70	99.71	99.74	99.74	99.74	99.73	99.73	99.72
XRF Trace elements (ppm) Ni	2.1	10.5	2.1	4.2	3.1	3.0	3.2	3.1	7.3
Cr	0.0	8.4	0.0	0.0	2.0	2.0	0.0	6.1	0.0
Sc	0.0	3.2	0.0	0.0	0.0	1.0	0.0	5.1	0.0
V	22	23	38	24	27	27	36	32	37
Ba	60	133	171	108	96	130	129	123	131
Rb	247	275	233	231	242	238	232	243	238
Sr	87	103	163	93	92	103	134	93	115
Zr	1523	1667	1410	1445	1416	1402	1433	1462	1490
Y	29	33	29	28	26	28	27	27	35
Nb	224	256	219	224	232	229	218	232	220
Ga	34	35	32	33	34	34	33	35	35
Cu	0	4	0	0	2	1	0	4	0
Zn	119	151	121	116	108	108	140	108	130
Pb	27	25	24	15	13	12	26	13	22
La	93	115	79	102	90	101	73	90	87
Ce	151	187	163	146	148	171	144	168	156
Th	50	51	41	31	42	45	38	46	46
ICP-MS traces (ppm) La	104	118	109	83	88	85	106	93	114
Ce	127	149	139	110	114	114	131	117	135
Pr	9	11	11	9	9	9	10	9	11
Nd	24	33	30	25	26	26	28	26	32
Sm	3.6	5.3	4.7	4.0	4.0	4.2	4.4	4.0	5.3
Eu	0.8	1.2	1.1	0.9	0.9	0.9	1.0	0.9	1.2
Gd	2.7	4.1	3.5	3.1	3.1	3.2	3.2	3.2	4.4
Tb	0.5	0.7	0.6	0.6	0.6	0.6	0.6	0.6	0.8
Dy	3.5	4.8	4.2	3.7	3.7	3.8	3.9	3.8	5.2
Ho	0.8	1.1	0.9	0.8	0.8	0.8	0.9	0.8	1.2
Er	2.7	3.4	2.9	2.8	2.7	2.7	2.7	2.8	3.8
Tm	0.5	0.6	0.5	0.5	0.5	0.5	0.5	0.5	0.7
Yb	3.6	4.1	3.7	3.4	3.4	3.5	3.5	3.5	4.9
Lu	0.6	0.7	0.6	0.6	0.6	0.6	0.6	0.6	0.8
Ba	118	159	196	162	142	165	172	159	123
Th	50	52	45	43	42	41	44	44	50
Nb	242	271	241	240	224	222	234	224	242
Y	26	33	29	23	25	25	27	26	36
Hf	27	30	26	27	25	25	26	26	29
Ta	8	9	9	9	9	9	9	8	8
U	17.1	12.3	10.2	9.3	8.6	8.7	10.0	9.6	11.5
Pb	27	27	25	25	21	21	29	22	26
Rb	238	268	226	229	228	224	219	236	237
Cs	3.8	4.8	3.7	3.9	3.1	3.0	3.7	3.2	3.9
Sr	97	93	163	97	94	105	135	97	92
Sc	2.4	3.4	1.6	1.9	1.1	1.0	1.4	1.1	2.2
Zr	1541	1631	1451	1429	1305	1291	1364	1338	1561

Appendix A.
DHF Whole-rock data

ChemoUnit	DHF I	DHF I	DHF I	DHF I	DHF I	DHF I	DHF I	DHF I	DHF I	DHF I
Member	Fasnia	Fasnia	Fasnia	Fasnia	Fasnia	Fasnia	Fasnia	Fasnia	Fasnia	Fasnia
sample #	TF01-111	TF01-108	TF01-107	TF01-88	TF01-127	TF01-128	TF99-18	TF99-20	TF99-21	TF01-129
XRF Major element oxides (Wt%)										
SiO2	58.04	58.61	59.13	56.21	59.23	58.91	57.88	57.69	57.63	59.54
Al2O3	20.74	20.74	20.70	21.49	21.27	21.33	21.31	21.25	21.15	21.57
TiO2	0.47	0.53	0.46	0.51	0.52	0.58	0.45	0.50	0.47	0.45
FeO*	2.52	2.60	2.45	2.53	2.45	2.63	2.48	2.47	2.57	2.55
MnO	0.18	0.18	0.18	0.17	0.18	0.19	0.19	0.17	0.18	0.18
CaO	2.34	1.40	1.28	1.78	1.20	1.22	1.20	1.90	1.65	1.07
MgO	1.45	2.84	2.77	0.74	0.57	0.53	0.25	0.35	0.33	0.49
K2O	6.29	5.99	6.02	5.29	6.25	5.68	5.92	5.75	5.86	6.29
Na2O	7.63	6.76	6.67	10.94	8.01	8.57	9.99	9.59	9.82	7.52
P2O5	0.07	0.08	0.06	0.07	0.07	0.08	0.06	0.07	0.06	0.05
total	99.73	99.73	99.72	99.73	99.75	99.72	99.73	99.74	99.72	99.71
XRF Trace elements (ppm) Ni	3.1	10.3	9.3	1.1	2.1	5.1	2.1	1.0	1.0	6.1
Cr	0.0	0.0	0.0	0.0	0.0	1.0	0.0	0.0	0.0	0.0
Sc	1.0	0.0	0.0	3.2	0.0	2.0	4.1	0.0	5.2	2.0
V	25	34	38	33	22	37	24	21	28	21
Ba	119	132	138	154	190	164	97	128	83	149
Rb	243	229	236	205	223	198	251	225	246	241
Sr	136	130	119	134	123	118	82	127	86	113
Zr	1491	1451	1480	1442	1374	1477	1529	1377	1490	1502
Y	27	33	38	28	29	30	26	27	28	30
Nb	223	215	215	223	223	232	236	223	231	229
Ga	36	33	32	30	37	36	35	30	33	38
Cu	0	0	0	0	0	0	1	0	0	0
Zn	124	118	124	116	113	127	127	119	123	115
Pb	23	26	23	19	15	16	23	20	23	15
La	105	120	114	95	95	120	101	101	101	105
Ce	159	148	150	174	142	182	158	150	154	164
Th	41	43	45	48	29	34	45	38	47	32
ICP-MS traces (ppm) La	112	112	125	106	95	102	105	105	106	103
Ce	132	129	131	134	124	128	130	133	130	117
Pr	10	10	13	10	10	10	10	10	10	10
Nd	27	30	38	28	27	28	26	28	27	28
Sm	4.1	5.0	6.5	4.2	4.4	4.3	4.0	4.2	4.0	4.3
Eu	0.9	1.1	1.5	0.9	1.0	1.0	0.9	0.9	0.9	1.0
Gd	3.2	4.2	5.6	3.4	3.3	3.3	3.2	3.4	3.4	3.3
Tb	0.6	0.7	0.9	0.6	0.6	0.6	0.6	0.6	0.6	0.6
Dy	3.9	4.8	5.9	3.9	3.9	3.9	3.7	3.8	3.8	3.9
Ho	0.9	1.1	1.3	0.9	0.9	0.9	0.8	0.9	0.9	0.9
Er	2.9	3.5	4.1	2.8	2.8	2.9	2.7	2.7	2.9	2.8
Tm	0.5	0.6	0.7	0.5	0.5	0.5	0.5	0.5	0.5	0.5
Yb	3.9	4.4	4.9	3.7	3.5	3.6	3.6	3.6	3.7	3.7
Lu	0.7	0.8	0.8	0.6	0.6	0.6	0.6	0.6	0.6	0.6
Ba	117	130	139	175	208	182	156	153	118	165
Th	48	48	48	47	43	46	48	45	48	46
Nb	247	242	239	250	239	245	243	242	246	239
Y	28	35	42	28	25	26	26	27	28	26
Hf	28	28	28	27	26	27	26	25	27	27
Ta	8	8	8	9	9	9	9	9	9	8
U	11.6	11.1	11.3	10.3	9.6	10.7	12.7	11.5	13.1	11.0
Pb	26	26	25	21	24	26	23	21	23	25
Rb	241	233	230	199	228	198	236	227	240	236
Cs	4.0	3.9	3.9	3.2	3.8	4.2	3.3	3.1	3.4	4.0
Sr	107	105	106	131	110	109	96	106	69	101
Sc	1.5	1.7	2.0	2.5	1.9	2.4	2.5	2.5	2.6	1.9
Zr	1563	1551	1455	1509	1390	1492	1489	1426	1515	1479

Appendix A.
DHF Whole-rock data

ChemoUnit	DHF I	DHF I	DHF I	DHF I	DHF I	DHF I	DHF I	DHF I	DHF I	DHF I
Member	Fasnia	Fasnia	Fasnia	Fasnia	Fasnia	Fasnia	Fasnia	Fasnia	Fasnia	Fasnia
sample #	TF00-88	TF00-91	TF00-92	TF00-89	TF00-90	TF01-89	TF00-95	TF76-JF4	TF01-112	TF01-113
XRF Major element oxides (Wt%)										
SiO2	57.85	55.96	57.68	57.30	57.05	57.33	57.24	58.34	55.52	56.26
Al2O3	21.22	21.02	21.05	21.13	21.15	21.34	22.10	21.07	19.23	19.67
TiO2	0.52	0.61	0.47	0.49	0.48	0.49	0.54	0.51	0.45	0.49
FeO*	2.79	2.88	2.63	2.57	2.50	2.51	2.79	2.56	2.31	2.36
MnO	0.19	0.17	0.19	0.18	0.18	0.18	0.17	0.18	0.17	0.17
CaO	1.18	4.26	1.12	2.02	2.76	1.61	1.77	1.41	6.79	5.74
MgO	0.44	0.95	0.50	0.45	0.45	0.61	0.71	0.43	2.56	1.94
K2O	5.94	5.40	5.81	5.74	5.83	5.58	5.58	6.51	5.81	5.92
Na2O	9.51	8.40	10.22	9.78	9.26	10.00	8.76	8.65	6.81	7.10
P2O5	0.07	0.10	0.06	0.07	0.07	0.07	0.07	0.06	0.09	0.09
total	99.71	99.75	99.73	99.73	99.73	99.72	99.73	99.72	99.74	99.74
XRF Trace elements (ppm) Ni	10.3	2.1	6.1	4.1	3.1	3.1	7.3	4.0	4.3	3.2
Cr	0.0	1.0	0.0	0.0	0.0	0.0	0.0	1.0	0.0	0.0
Sc	0.0	2.1	4.1	0.0	4.1	2.1	4.2	4.0	0.0	1.1
V	22	33	24	27	29	34	25	30	19	29
Ba	77	215	90	138	83	152	139	117	94	161
Rb	252	203	249	242	240	234	216	242	226	221
Sr	63	225	74	115	82	133	128	93	205	204
Zr	1564	1344	1533	1492	1507	1475	1442	1454	1390	1341
Y	30	28	27	27	28	26	27	26	28	27
Nb	246	218	233	228	235	223	239	232	207	204
Ga	35	30	38	36	34	30	33	32	33	35
Cu	0	0	0	3	2	0	0	0	0	0
Zn	141	121	136	124	128	120	121	112	117	108
Pb	28	19	21	25	25	22	24	13	20	19
La	104	97	97	108	101	123	109	102	112	90
Ce	177	157	170	160	174	158	179	164	148	143
Th	49	36	45	44	45	50	44	44	33	30
ICP-MS traces (ppm) La	110	104	109	106	108	106	98	85	106	110
Ce	140	137	136	132	136	131	137	111	123	128
Pr	10	10	10	10	10	10	10	9	10	11
Nd	28	29	27	26	27	27	29	25	29	32
Sm	4.3	4.7	4.1	4.0	4.1	4.1	4.7	4.0	4.7	5.0
Eu	0.9	1.1	0.9	0.9	0.9	0.9	1.1	0.8	1.1	1.1
Gd	3.3	3.6	3.2	3.1	3.1	3.1	3.6	3.1	3.7	3.9
Tb	0.6	0.6	0.6	0.6	0.6	0.6	0.6	0.6	0.6	0.7
Dy	4.0	4.0	3.8	3.8	3.9	3.8	4.0	3.6	4.1	4.3
Ho	0.9	0.9	0.9	0.9	0.9	0.9	0.9	0.8	0.9	1.0
Er	3.0	2.9	2.9	2.8	2.9	2.8	2.8	2.7	2.9	3.0
Tm	0.5	0.5	0.5	0.5	0.5	0.5	0.5	0.5	0.5	0.5
Yb	3.8	3.5	3.8	3.8	3.7	3.6	3.5	3.5	3.7	3.8
Lu	0.7	0.6	0.6	0.6	0.6	0.6	0.6	0.6	0.7	0.7
Ba	129	219	152	143	134	167	232	143	133	133
Th	50	42	48	50	46	47	42	42	43	43
Nb	256	228	246	252	244	245	240	225	222	226
Y	29	28	27	27	27	27	27	25	29	30
Hf	28	25	28	28	28	27	25	26	25	25
Ta	9	9	9	9	9	9	10	9	8	8
U	12.1	9.7	11.8	13.0	11.6	12.1	8.8	8.4	10.1	10.3
Pb	26	22	24	25	24	25	22	21	23	23
Rb	245	197	245	246	236	232	190	230	214	216
Cs	3.9	3.1	4.1	3.9	3.8	3.8	3.0	3.2	3.6	3.6
Sr	74	212	86	98	82	128	178	97	230	162
Sc	2.8	2.7	2.4	2.6	2.0	2.8	2.5	1.0	1.7	1.4
Zr	1582	1360	1524	1572	1504	1508	1374	1335	1380	1377

Appendix A.
DHF Whole-rock data

ChemoUnit	DHF I	DHF I	DHF I	DHF I	DHF I	DHF I	DHF I	DHF I	DHF I	DHF I
Member	Fasnia	Fasnia	Fasnia	Fasnia	Fasnia	Fasnia	Fasnia	Fasnia	Fasnia	Fasnia
sample #	TF76-JF5	TF99-56	TF01-114	TF99-55	TF99-25	TF00-97	TF01-97	TF01-98	TF01-99	TF00-7
XRF Major element oxides (Wt%)										
SiO2	58.39	57.98	58.28	60.28	55.86	57.64	57.37	58.36	58.06	57.94
Al2O3	21.21	20.16	20.56	20.19	21.02	19.92	20.49	21.14	20.75	19.85
TiO2	0.52	0.56	0.51	0.49	0.33	0.51	0.48	0.47	0.54	0.60
FeO*	2.55	2.64	2.52	2.52	2.28	2.59	2.46	2.44	2.56	2.66
MnO	0.18	0.18	0.18	0.17	0.19	0.18	0.17	0.18	0.17	0.16
CaO	1.15	3.07	2.53	1.35	4.50	2.38	3.61	1.44	2.31	3.25
MgO	0.38	1.26	1.07	1.88	0.39	1.81	0.76	0.77	0.93	1.19
K2O	6.47	6.11	6.28	5.79	5.65	5.79	5.76	5.92	5.78	5.95
Na2O	8.82	7.69	7.73	6.99	9.47	8.83	8.55	8.94	8.55	8.04
P2O5	0.06	0.08	0.07	0.07	0.04	0.08	0.08	0.07	0.08	0.10
total	99.73	99.73	99.73	99.73	99.73	99.73	99.73	99.73	99.73	99.74
XRF Trace elements										
(ppm) Ni	5.0	5.3	3.1	15.0	2.1	4.2	3.1	4.1	6.2	4.2
Cr	0.0	1.1	0.0	0.0	0.0	0.0	0.0	0.0	1.0	0.0
Sc	1.0	1.1	0.0	2.0	9.4	0.0	2.1	0.0	0.0	5.2
V	36	31	27	23	18	33	28	28	35	34
Ba	136	149	119	128	0	147	128	125	208	278
Rb	240	229	238	220	260	224	230	243	220	197
Sr	88	140	118	125	45	113	123	99	152	191
Zr	1424	1381	1419	1444	1650	1414	1359	1469	1281	1158
Y	26	28	26	39	25	38	27	28	27	28
Nb	232	224	221	217	238	222	214	224	211	209
Ga	35	31	33	35	37	33	30	31	31	31
Cu	0	3	0	0	0	0	0	0	0	0
Zn	112	124	118	137	132	123	111	119	113	111
Pb	12	19	23	19	24	23	20	23	22	15
La	112	109	98	141	98	110	80	88	90	111
Ce	160	169	155	166	167	162	164	172	146	182
Th	44	41	34	34	51	44	45	49	40	33
ICP-MS traces										
(ppm) La	104	105	105	136	103	113	101	111	103	
Ce	133	136	134	134	120	138	127	134	135	
Pr	10	11	10	16	8	12	10	10	11	
Nd	29	32	30	51	20	38	27	27	32	
Sm	4.6	5.2	4.7	8.7	2.8	6.4	4.1	4.2	5.2	
Eu	1.0	1.2	1.0	2.0	0.5	1.5	0.9	0.9	1.2	
Gd	3.4	4.2	3.6	7.2	2.5	5.3	3.3	3.4	4.0	
Tb	0.7	0.7	0.6	1.1	0.4	0.9	0.6	0.6	0.7	
Dy	4.0	4.3	4.1	6.4	3.1	5.6	3.9	4.1	4.3	
Ho	0.9	0.9	0.9	1.3	0.8	1.2	0.9	0.9	0.9	
Er	2.9	2.9	2.8	3.9	2.7	3.7	2.8	3.0	2.9	
Tm	0.5	0.5	0.5	0.6	0.5	0.6	0.5	0.5	0.5	
Yb	3.6	3.5	3.6	4.4	3.8	4.2	3.5	3.9	3.5	
Lu	0.6	0.6	0.6	0.7	0.7	0.7	0.6	0.7	0.6	
Ba	165	216	152	193	14	244	156	115	265	
Th	45	41	43	42	54	43	44	50	39	
Nb	236	227	237	215	245	229	232	256	228	
Y	28	28	28	42	25	39	27	30	29	
Hf	26	24	26	24	29	24	25	29	23	
Ta	11	9	9	8	8	9	9	9	9	
U	11.0	9.7	10.6	10.1	21.9	10.6	10.9	12.5	9.7	
Pb	15	20	24	27	25	28	25	27	23	
Rb	227	213	225	206	250	213	231	257	216	
Cs	3.1	2.9	3.6	2.9	3.7	3.5	3.7	4.2	3.4	
Sr	91	169	125	138	39	152	118	67	179	
Sc	1.3	2.7	1.3	3.8	2.5	3.0	2.3	2.5	2.5	
Zr	1370	1330	1421	1315	1647	1359	1383	1595	1288	

Appendix A.
DHF Whole-rock data

ChemoUnit	DHF I	DHF I	DHF I	DHF I	DHF I	DHF I	DHF I	DHF I	DHF I	DHF I
Member	Fasnia	Fasnia	Fasnia	Fasnia	Fasnia	Fasnia	Fasnia	Fasnia	Fasnia	Fasnia
sample #	TF00-169W	TF01-60	01TF59F	TF01-61	TF76-JF6	TF01-62	TF76-JF7	TF01-63	TF01-58	TF00-2
XRF Major element oxides (Wt%)										
SiO2	59.65	59.23		59.22	58.88	59.79	58.94	60.00	60.12	59.08
Al2O3	20.80	21.07		21.02	20.21	20.54	20.23	20.30	20.42	19.97
TiO2	0.68	0.56		0.59	0.77	0.75	0.75	0.76	0.67	0.71
FeO*	2.60	2.60		2.60	2.85	2.60	2.91	2.65	2.51	2.81
MnO	0.16	0.18		0.18	0.15	0.15	0.15	0.14	0.15	0.16
CaO	1.50	1.21		1.29	2.08	1.62	1.79	1.62	1.46	2.25
MgO	0.72	0.44		0.41	0.55	0.48	0.65	0.76	0.83	0.86
K2O	6.23	6.32		6.36	6.34	6.21	6.29	6.26	6.21	6.08
Na2O	7.32	8.06		7.98	7.83	7.52	7.94	7.16	7.30	7.70
P2O5	0.09	0.07		0.08	0.11	0.10	0.11	0.10	0.08	0.11
total	99.75	99.74	0.00	99.73	99.77	99.76	99.76	99.75	99.75	99.73
XRF Trace elements (ppm) Ni	12.0	6.2		5.2	2.1	3.1	5.2	6.2	2.1	8.0
Cr	4.0	0.0		0.0	2.1	0.0	5.2	0.0	0.0	0.0
Sc	0.0	3.1		7.2	0.0	3.1	5.2	0.0	0.0	4.0
V	34	38		36	43	48	47	47	46	50
Ba	339	192		245	472	492	415	461	373	389
Rb	192	230		217	163	168	171	165	185	180
Sr	185	107		137	229	249	206	222	183	209
Zr	1082	1371		1268	857	906	895	882	1027	984
Y	29	30		30	31	31	28	30	32	31
Nb	204	223		218	199	195	201	192	200	206
Ga	28	32		27	29	25	29	23	25	30
Cu	0	0		0	0	0	3	0	0	4
Zn	106	117		121	92	88	93	89	93	102
Pb	11	22		21	10	15	12	14	17	15
La	105	102		103	96	110	104	115	104	116
Ce	162	165		173	170	164	191	150	164	176
Th	22	42		40	26	31	26	30	34	28
ICP-MS traces (ppm) La	111	106	117	116	98	108	98	109	113	122
Ce	151	138	147	150	146	157	146	154	153	165
Pr	14	11	12	13	14	14	13	14	14	15
Nd	42	33	33	38	43	45	41	45	44	47
Sm	6.9	5.4	5.2	6.1	7.3	7.4	6.8	7.5	7.1	7.7
Eu	1.7	1.3	1.1	1.4	1.8	1.8	1.7	1.8	1.7	1.9
Gd	5.4	4.1	4.2	4.6	5.2	5.6	5.0	5.6	5.4	5.9
Tb	0.8	0.7	0.7	0.8	0.9	0.9	0.9	0.9	0.9	0.9
Dy	5.0	4.4	4.4	4.7	5.2	5.3	5.1	5.2	5.1	5.5
Ho	1.0	1.0	1.0	1.0	1.0	1.1	1.0	1.0	1.0	1.1
Er	2.9	2.9	3.1	3.1	2.8	2.9	2.9	2.9	3.0	3.2
Tm	0.5	0.5	0.5	0.5	0.4	0.5	0.5	0.5	0.5	0.5
Yb	3.2	3.6	3.8	3.5	2.9	3.0	2.9	3.0	3.1	3.3
Lu	0.5	0.6	0.7	0.6	0.4	0.5	0.5	0.5	0.5	0.5
Ba	380	272	158	248	464	443	419	430	422	456
Th	33	42	48	41	25	28	25	28	30	32
Nb	215	228	270	234	194	208	198	203	201	217
Y	29	28	30	29	29	30	29	29	29	32
Hf	20	24	28	24	16	17	17	17	18	20
Ta	11	10	10	10	11	12	11	11	11	12
U	7.9	10.1	11.7	10.0	5.8	6.6	5.9	6.4	7.0	7.6
Pb	16	24	24	24	14	18	14	18	18	20
Rb	186	214	243	216	152	166	160	164	172	186
Cs	2.3	3.5	3.3	3.5	1.7	2.5	1.8	2.4	2.6	2.8
Sr	194	134	83	119	229	193	206	193	200	217
Sc	2.0	2.5	2.4	2.6	1.2	2.0	1.4	2.1	2.0	2.1
Zr	1064	1283	1521	1276	812	908	858	902	958	1036

Appendix A.
DHF Whole-rock data

ChemoUnit	DHF I	DHF I	DHF I	DHF I	DHF I	DHF I	DHF I	DHF I	DHF I	DHF I
Member	Fasnia	Fasnia	Fasnia	Fasnia	Fasnia	Fasnia	Fasnia	Fasnia	Fasnia	Fasnia
sample #	TF00-170W	TF99-26	TF01-69	TF99-23	TF01-56	TF01-57	TF00-171W	TF01-64	TF00-24	TF01-68
XRF Major element oxides (Wt%)										
SiO2	60.66	55.98	57.10	57.88	60.26	60.34	60.86	59.18	58.70	55.64
Al2O3	20.19	20.41	19.99	21.21	20.72	21.14	20.73	21.07	20.43	20.08
TiO2	0.77	0.43	0.55	0.45	0.59	0.48	0.50	0.59	0.71	0.47
FeO*	2.78	2.43	2.39	2.51	2.72	2.50	2.59	2.55	2.97	2.48
MnO	0.15	0.18	0.16	0.22	0.17	0.18	0.17	0.17	0.16	0.20
CaO	1.67	4.58	3.99	1.41	1.43	1.18	1.17	1.35	1.95	5.31
MgO	1.15	0.79	0.88	0.83	0.90	0.55	0.79	0.98	1.24	0.99
K2O	6.02	5.72	5.52	5.76	6.15	6.24	6.23	6.28	5.70	5.56
Na2O	6.27	9.15	9.09	9.18	6.71	7.07	6.62	7.51	7.79	8.71
P2O5	0.11	0.06	0.08	0.26	0.07	0.05	0.06	0.08	0.10	0.28
total	99.77	99.73	99.75	99.71	99.72	99.73	99.72	99.76	99.74	99.72
XRF Trace elements (ppm) Ni	11.0	1.1	0.0	6.3	7.3	5.2	8.0	8.2	4.2	3.2
Cr	0.0	0.0	0.0	0.0	0.0	0.0	0.0	1.0	2.1	0.0
Sc	3.0	0.0	0.0	1.0	1.0	0.0	0.0	2.0	2.1	0.0
V	35	24	35	23	44	34	29	42	32	32
Ba	359	75	235	83	273	137	129	245	382	130
Rb	172	244	202	255	220	249	240	215	183	236
Sr	199	121	177	88	167	110	101	142	220	153
Zr	963	1526	1224	1599	1320	1491	1451	1251	1090	1442
Y	31	28	28	34	34	30	31	28	28	27
Nb	195	232	205	238	214	226	223	211	206	217
Ga	30	34	29	35	30	30	35	29	29	32
Cu	0	0	0	1	0	0	0	0	4	0
Zn	94	124	106	153	110	115	116	104	106	137
Pb	12	19	19	22	23	21	20	17	19	25
La	117	98	100	124	135	111	126	95	100	93
Ce	172	166	139	177	179	169	151	170	171	162
Th	19	46	43	52	42	49	32	40	32	50
ICP-MS traces (ppm) La	117	104	95	126	150	124	135	106	118	109
Ce	157	127	126	130	162	134	137	143	153	127
Pr	15	9	10	11	17	12	13	11	15	10
Nd	47	24	29	31	52	33	39	34	45	27
Sm	7.7	3.5	4.6	4.6	8.0	5.0	6.0	5.4	7.4	4.3
Eu	1.8	0.8	1.1	1.0	2.0	1.1	1.3	1.3	1.8	0.9
Gd	6.0	3.0	3.6	3.8	6.1	3.9	4.9	4.1	5.4	3.4
Tb	0.9	0.5	0.6	0.7	1.0	0.7	0.7	0.7	0.9	0.6
Dy	5.3	3.5	3.9	4.4	5.7	4.1	4.4	4.3	5.3	3.9
Ho	1.1	0.8	0.8	1.0	1.2	0.9	1.0	0.9	1.0	0.9
Er	3.0	2.6	2.6	3.3	3.4	2.9	3.0	2.8	3.0	2.9
Tm	0.5	0.5	0.5	0.6	0.5	0.5	0.5	0.5	0.5	0.5
Yb	3.0	3.5	3.2	4.3	3.7	3.7	3.6	3.3	3.2	3.8
Lu	0.5	0.6	0.5	0.7	0.6	0.6	0.6	0.6	0.5	0.7
Ba	421	133	216	118	406	186	163	301	423	136
Th	27	48	37	53	40	45	44	39	32	48
Nb	208	242	211	252	246	232	237	225	218	237
Y	31	26	25	34	36	28	31	28	31	29
Hf	17	27	22	29	24	27	26	23	20	27
Ta	11	8	9	8	11	9	9	10	10	8
U	6.5	12.4	8.9	13.6	9.8	11.2	10.6	9.5	7.4	13.5
Pb	14	22	19	25	24	26	21	23	17	26
Rb	169	238	185	248	218	235	231	210	178	237
Cs	1.9	3.5	3.0	3.7	3.3	3.9	3.1	3.3	2.9	4.0
Sr	217	133	175	82	226	113	107	146	226	126
Sc	2.0	2.5	3.2	2.8	2.8	2.6	2.2	2.5	2.5	2.7
Zr	937	1511	1171	1625	1307	1438	1473	1207	1082	1494

Appendix A.
DHF Whole-rock data

ChemoUnit	DHF I	DHF I	DHF I	DHF I	DHF I	DHF I	DHF I	DHF I	DHF I	DHF I
Member	Fasnia	Fasnia	Fasnia	Fasnia	Fasnia	Fasnia	Fasnia	Maja	Maja	Maja
sample #	TF01-90	DH99-46	DH99-44	DH99-43	DH99-42	01TF141	01TF141M	01TF221	01TF222	03TF166B
XRF Major element oxides (Wt%)										
SiO2	58.08	59.32	59.00	58.92	58.61	59.54	60.26	59.52	58.70	59.24
Al2O3	20.90	21.00	21.31	21.86	21.54	21.33	21.75	23.87	23.52	22.05
TiO2	0.40	0.60	0.53	0.50	0.52	0.53	0.45	0.47	0.52	0.49
FeO*	2.38	2.60	2.34	2.28	2.55	2.72	2.66	2.81	2.95	2.96
MnO	0.20	0.18	0.19	0.18	0.19	0.19	0.21	0.20	0.18	0.20
CaO	2.06	3.96	1.15	1.13	1.41	1.33	1.31	0.99	1.04	1.12
MgO	1.14	0.82	0.35	0.26	0.39	0.72	1.08	0.34	0.81	0.40
K2O	5.88	5.54	6.26	6.23	6.15	6.50	6.42	6.23	5.53	5.75
Na2O	8.51	5.66	8.54	8.30	8.27	6.78	5.47	5.25	6.44	7.41
P2O5	0.14	0.04	0.07	0.06	0.10	0.08	0.07	0.04	0.06	0.07
total	99.69	99.72	99.74	99.72	99.73	99.72	99.69	99.73	99.73	99.70
XRF Trace elements (ppm) Ni	5.2	4.0	2.1	5.2	3.1	5.3	3.1	3.1	14.5	43.4
Cr	0.0	0.0	0.0	0.0	0.0	0.0	0.0	0.0	0.0	6.2
Sc	0.0	2.0	3.1	0.0	2.1	0.0	2.1	0.0	6.2	0.9
V	29	27	31	24	33	57	52	37	43	26
Ba	55	222	183	97	146	140	52	39	65	143
Rb	266	269	233	240	236	242	258	198	185	213
Sr	81	171	112	103	124	123	94	131	161	214
Zr	1767	1415	1369	1462	1461	1496	1786	1446	1409	1464
Y	33	28	26	28	27	27	29	27	30	43
Nb	238	229	223	232	231	238	252	270	265	299
Ga	34	36	33	33	36	35	40	39	38	38
Cu	0	6	2	3	6	5	2	5	1	7
Zn	130	120	119	126	125	124	143	141	156	138
Pb	26	21	19	20	19	19	23	23	19	25
La	126	103	95	109	117	103	128	132	122	130
Ce	186	163	173	159	176	171	170	198	140	187
Th	58	44	41	45	42	45	58	45	43	47
ICP-MS traces (ppm) La	129	111	107	100	104	98	107	115	114	
Ce	127	140	136	128	135	126	125	152	147	
Pr	11	11	10	10	10	9	9	11	11	
Nd	29	32	29	27	28	26	24	28	32	
Sm	4.5	5.1	4.6	4.2	4.5	3.9	3.6	3.9	4.6	
Eu	0.9	1.2	1.0	0.9	1.0	0.9	0.7	0.7	0.9	
Gd	3.5	4.0	3.5	3.2	3.4	3.4	3.2	3.2	3.8	
Tb	0.7	0.7	0.6	0.6	0.6	0.6	0.5	0.6	0.6	
Dy	4.3	4.3	4.1	3.9	3.9	3.8	3.7	3.9	4.1	
Ho	1.0	0.9	0.9	0.9	0.9	0.9	0.9	0.9	0.9	
Er	3.3	3.0	2.8	2.7	2.7	2.8	3.0	2.9	3.0	
Tm	0.6	0.5	0.5	0.5	0.5	0.5	0.5	0.5	0.5	
Yb	4.5	3.5	3.5	3.5	3.5	3.7	4.1	3.6	3.6	
Lu	0.8	0.6	0.6	0.6	0.6	0.6	0.7	0.6	0.6	
Ba	64	246	175	156	210	138	94	62	107	
Th	58	43	44	45	44	50	57	46	46	
Nb	260	236	244	245	241	262	272	281	279	
Y	34	28	27	26	26	26	28	27	29	
Hf	33	24	26	26	25	29	32	26	25	
Ta	8	9	9	9	9	9	8	11	11	
U	13.8	9.2	11.4	10.3	10.5	10.5	13.0	8.2	7.1	
Pb	30	22	22	22	22	24	28	23	22	
Rb	270	255	232	229	224	240	250	192	174	
Cs	4.7	3.0	3.3	3.2	3.2	3.5	3.9	2.5	2.6	
Sr	63	175	93	109	141	113	94	128	168	
Sc	2.9	2.8	2.4	2.7	2.7	2.0	2.7	2.1	2.3	
Zr	1821	1338	1407	1425	1397	1607	1807	1416	1396	

Appendix A.
DHF Whole-rock data

ChemoUnit	DHF I	DHF I	DHF I	DHF I	DHF I	DHF I	DHF I	DHF I	DHF I
Member	Maja	Maja	Maja	Maja	Maja	Poris	Poris	Poris	Poris
sample #	03TF166D	03TF166A	03TF166C	01TF223	03TF167M	TF99-61	TF99-60	TF99-59	TF99-58
XRF Major element oxides (Wt%)									
SiO2	58.86	58.72	58.74	59.45	54.05	59.51	59.46	57.80	56.74
Al2O3	23.32	21.23	23.36	22.81	20.68	20.15	20.37	19.56	19.43
TiO2	0.50	0.78	0.64	0.48	1.78	0.43	0.47	0.46	0.82
FeO*	3.13	3.40	3.29	2.71	6.00	2.39	2.51	2.48	3.26
MnO	0.20	0.18	0.19	0.20	0.19	0.19	0.19	0.18	0.18
CaO	1.22	1.83	1.54	1.10	4.31	1.52	1.22	3.86	4.73
MgO	0.39	0.67	0.50	0.46	2.09	0.69	0.65	1.02	1.07
K2O	5.31	5.47	5.23	5.44	4.04	6.30	6.42	6.20	5.83
Na2O	6.64	7.27	6.02	7.03	6.15	8.51	8.41	8.11	7.47
P2O5	0.09	0.15	0.12	0.05	0.38	0.07	0.08	0.10	0.19
total	99.67	99.69	99.64	99.73	99.68	99.77	99.77	99.77	99.74
XRF Trace elements (ppm) Ni	50.9	12.8	57.3	8.3	14.1	6.3	4.2	7.4	5.3
Cr	7.5	8.3	8.0	1.0	11.3	0.0	0.0	1.1	4.2
Sc	0.9	1.8	0.5	2.1	6.8	5.2	0.0	0.0	6.3
V	26	42	30	42	105	28	39	29	58
Ba	175	582	368	64	587	32	42	42	325
Rb	207	169	186	194	124	218	217	207	179
Sr	298	365	479	197	613	76	82	128	315
Zr	1627	1096	1498	1357	940	1197	1209	1178	1015
Y	36	35	40	32	41	28	27	31	33
Nb	334	260	323	258	232	226	226	223	206
Ga	38	33	37	36	35	30	32	30	28
Cu	9	5	7	0	13	6	2	6	5
Zn	157	124	152	132	138	119	122	123	118
Pb	28	22	25	22	14	17	20	18	16
La	119	123	124	95	122	117	111	107	109
Ce	180	194	200	210	187	185	163	180	194
Th	56	34	51	41	29	36	38	35	31
ICP-MS traces (ppm) La				110		106	105	121	119
Ce				154		136	137	145	161
Pr				11		10	10	12	14
Nd				30		28	27	32	43
Sm				4.3		4.1	3.9	4.6	7.1
Eu				0.9		0.8	0.7	0.9	1.7
Gd				3.3		3.4	3.0	3.7	5.7
Tb				0.6		0.6	0.5	0.7	0.9
Dy				4.1		3.9	3.6	4.3	5.4
Ho				0.9		0.9	0.8	1.0	1.1
Er				3.0		2.8	2.7	3.1	3.4
Tm				0.5		0.5	0.5	0.5	0.5
Yb				3.6		3.5	3.4	3.8	3.7
Lu				0.6		0.6	0.6	0.7	0.6
Ba				93		95	62	94	330
Th				40		36	37	36	32
Nb				263		232	238	231	217
Y				29		28	25	32	34
Hf				24		22	22	21	19
Ta				10		9	9	9	10
U				7.7		7.5	7.6	8.6	7.6
Pb				21		20	21	20	18
Rb				179		209	208	199	177
Cs				2.8		2.7	2.7	2.6	2.3
Sr				194		82	64	145	286
Sc				1.9		2.1	2.1	2.2	2.9
Zr				1284		1164	1204	1161	1016

Appendix A.
DHF Whole-rock data

ChemoUnit	DHF I	DHF I	DHF I	DHF I	DHF I	DHF I	DHF I	DHF I	DHF I	DHF I
Member	Poris	Poris	Poris	Poris	Poris	Poris	Poris	Poris	Poris	Poris
sample #	TF99-57P	TF99-28	TF99-27	TF00-64	TF00-62	TF00-56	TF00-53	TF00-49	TF00-47	TF00-40
XRF Major element oxides (Wt%)										
SiO2	58.17	59.59	57.60	59.38	58.53	57.96	58.47	58.43	55.66	58.03
Al2O3	19.04	20.65	20.06	20.48	20.00	20.65	21.01	19.94	19.27	19.97
TiO2	1.36	0.45	0.80	0.43	0.44	0.40	0.60	0.70	0.42	0.43
FeO*	3.99	2.31	3.23	2.48	2.43	2.43	2.55	2.91	2.34	2.48
MnO	0.16	0.19	0.18	0.19	0.19	0.18	0.15	0.18	0.18	0.18
CaO	3.20	1.09	3.11	1.24	2.04	3.11	1.35	2.82	7.15	3.80
MgO	1.20	0.44	0.78	0.46	0.40	0.48	0.47	0.82	0.54	0.55
K2O	5.40	6.09	5.44	5.98	5.90	5.57	5.63	5.39	5.69	5.55
Na2O	6.89	8.91	8.39	9.07	9.77	8.95	9.50	8.42	8.46	8.71
P2O5	0.29	0.05	0.15	0.05	0.05	0.04	0.08	0.14	0.06	0.06
total	99.70	99.76	99.74	99.77	99.76	99.77	99.81	99.74	99.77	99.77
XRF Trace elements (ppm) Ni	3.1	2.1	3.1	16.5	27.5	10.3	12.1	15.5	16.2	16.7
Cr	0.0	0.0	0.0	4.1	6.6	3.1	8.1	4.1	3.2	0.0
Sc	5.1	0.0	2.1	0.0	5.5	0.0	4.0	3.1	4.3	1.0
V	88	29	45	26	26	26	36	42	35	33
Ba	1057	111	335	57	51	5	123	395	57	53
Rb	116	212	181	211	217	200	171	172	204	191
Sr	501	60	262	51	56	64	102	206	94	120
Zr	596	1205	1065	1207	1237	1226	888	999	1171	1184
Y	36	28	31	29	27	27	23	33	27	27
Nb	176	228	213	229	234	230	223	209	224	229
Ga	22	31	28	32	31	29	27	30	31	27
Cu	4	2	2	1	0	2	3	4	0	1
Zn	96	115	117	118	124	116	74	108	113	118
Pb	6	19	16	18	19	15	5	14	17	15
La	111	111	101	95	112	122	82	115	97	112
Ce	188	186	182	170	165	162	127	175	185	167
Th	18	35	30	34	42	37	18	32	36	38
ICP-MS traces (ppm) La	111	118	113	89	75	97		102	100	102
Ce	188	149	159	116	105	132		146	129	135
Pr	19	11	13	9	8	10		13	10	10
Nd	65	31	40	25	21	24		38	25	28
Sm	11.4	4.4	6.5	3.8	3.1	3.5		6.2	3.5	4.0
Eu	3.1	0.9	1.6	0.7	0.6	0.6		1.5	0.7	0.8
Gd	8.4	3.6	5.1	2.9	2.4	2.6		4.7	2.7	2.9
Tb	1.3	0.6	0.8	0.5	0.5	0.5		0.8	0.5	0.6
Dy	7.2	4.0	5.0	3.6	3.2	3.4		4.8	3.4	3.7
Ho	1.3	0.9	1.0	0.8	0.7	0.8		1.0	0.8	0.8
Er	3.4	2.9	3.0	2.6	2.4	2.6		3.0	2.5	2.7
Tm	0.5	0.5	0.5	0.5	0.4	0.5		0.5	0.4	0.5
Yb	2.9	3.5	3.3	3.2	3.1	3.2		3.3	3.1	3.3
Lu	0.4	0.6	0.5	0.5	0.5	0.6		0.5	0.5	0.6
Ba	1058	108	371	103	67	35		355	76	101
Th	18	38	33	35	34	38		29	33	33
Nb	185	241	221	233	223	239		212	206	229
Y	36	28	31	25	21	24		30	24	26
Hf	12	22	19	21	20	22		18	19	21
Ta	12	10	10	9	9	9		10	8	9
U	4.1	9.7	8.4	5.6	6.9	8.3		6.8	8.6	6.6
Pb	11	19	17	20	19	19		17	18	19
Rb	118	203	173	194	186	186		161	174	176
Cs	1.3	2.8	2.3	3.3	3.2	3.1		2.7	2.9	3.0
Sr	482	55	282	46	43	55		180	89	112
Sc	3.0	2.2	3.0	1.8	1.6	1.6		2.1	1.4	1.5
Zr	608	1217	1044	1174	1120	1237		983	1048	1144

Appendix A.
DHF Whole-rock data

ChemoUnit	DHF I	DHF I	DHF I	DHF I	DHF I	DHF I	DHF I	DHF I	DHF I	DHF I
Member	Poris	Poris	Poris	Poris	Poris	Poris	Poris	Poris	Poris	Poris
sample #	TF00-39	TF00-37	TF00-21	TF00-16	DH99-66	DH99-63	DH97-2e	CE337-1	01TF630	01TF629
XRF Major element oxides (Wt%)										
SiO2	59.64	59.59	60.89	60.00	59.36	59.81	58.94	55.74	59.79	59.14
Al2O3	19.44	20.40	19.57	20.41	20.59	20.64	20.98	18.60	20.37	20.10
TiO2	0.87	0.45	0.84	0.44	0.59	0.55	0.63	1.04	0.51	0.81
FeO*	2.95	2.46	2.77	2.41	2.48	2.48	2.94	3.29	2.64	3.17
MnO	0.15	0.18	0.14	0.19	0.19	0.19	0.18	0.15	0.19	0.18
CaO	2.29	0.95	1.50	0.86	1.29	1.16	1.27	7.23	1.29	1.84
MgO	0.59	0.29	0.51	0.34	0.37	0.38	0.39	1.17	0.46	0.82
K2O	5.54	5.78	6.00	6.03	5.95	6.01	5.50	5.25	6.04	5.40
Na2O	8.10	9.59	7.42	9.04	8.84	8.46	8.83	7.29	8.41	8.12
P2O5	0.13	0.06	0.11	0.05	0.10	0.08	0.10	0.24	0.07	0.15
total	99.70	99.76	99.75	99.77	99.76	99.76	99.75	100.00	99.76	99.74
XRF Trace elements (ppm) Ni	17.3	17.6	13.2	19.5	4.1	6.2	4.1	3.1	6.2	5.1
Cr	1.0	0.0	4.1	5.1	0.0	5.2	2.0	2.1	0.0	3.0
Sc	2.0	4.1	3.0	2.1	0.0	0.0	0.0	0.0	4.1	8.1
V	49	24	46	35	41	39	36	61	30	50
Ba	1210	103	833	61	171	76	181	742	97	406
Rb	118	207	131	207	202	205	194	116	207	174
Sr	301	65	181	49	127	80	146	396	80	264
Zr	634	1187	652	1173	1144	1196	1136	643	1180	995
Y	37	30	33	27	29	29	31	34	28	30
Nb	187	227	190	228	224	227	226	178	228	207
Ga	22	30	21	30	33	30	32	23	31	29
Cu	4	0	0	2	5	0	0	2	2	5
Zn	93	117	87	112	120	121	119	90	121	110
Pb	11	15	12	18	16	18	17		17	15
La	111	120	119	120	105	119	124		134	106
Ce	213	170	193	187	179	178	186		170	157
Th	23	38	19	36	35	36	35		34	28
ICP-MS traces (ppm) La	96	86	121	116	112	113	113	102	115	113
Ce	177	118	198	147	151	149	153	173	154	164
Pr	17	9	19	11	12	12	12	17	12	14
Nd	58	26	63	30	33	34	37	57	33	44
Sm	10.0	3.9	10.3	4.2	4.9	5.1	5.7	9.9	5.0	7.2
Eu	2.7	0.8	2.6	0.8	1.1	1.1	1.3	2.6	1.1	1.8
Gd	7.3	3.0	7.7	3.4	3.7	3.9	4.8	7.7	4.2	5.8
Tb	1.2	0.6	1.2	0.6	0.7	0.7	0.8	1.2	0.7	0.9
Dy	6.8	3.8	6.9	3.9	4.3	4.5	4.8	6.6	4.3	5.3
Ho	1.3	0.8	1.3	0.9	0.9	1.0	1.0	1.3	0.9	1.1
Er	3.4	2.7	3.5	2.8	2.9	3.0	3.0	3.3	2.9	3.1
Tm	0.5	0.5	0.5	0.5	0.5	0.5	0.5	0.5	0.5	0.5
Yb	3.1	3.3	3.1	3.4	3.4	3.5	3.5	2.9	3.4	3.3
Lu	0.5	0.6	0.5	0.6	0.6	0.6	0.6	0.4	0.6	0.5
Ba	1194	151	705	119	202	123	189	740	171	480
Th	19	32	22	38	36	37	30	18	36	31
Nb	192	230	213	236	233	231	230	179	229	213
Y	33	25	36	27	28	29	31	35	28	31
Hf	13	21	14	22	21	21	20	12	21	19
Ta	13	9	13	9	9	9	10	12	10	10
U	4.1	6.4	5.2	9.4	8.6	8.6	8.5	5.0	9.0	7.7
Pb	12	19	14	21	19	19	18	11	19	17
Rb	112	190	140	207	197	193	181	107	195	168
Cs	1.9	3.3	2.2	3.4	2.7	2.6	2.5	1.3	2.6	2.2
Sr	275	68	159	51	119	126	142	390	117	288
Sc	1.3	1.5	1.5	1.6	2.3	3.5	1.8	2.7	2.2	2.9
Zr	629	1147	738	1201	1135	1146		626	1148	991

Appendix A.
DHF Whole-rock data

ChemoUnit	DHF I	DHF I	DHF I	DHF I	DHF I
Member	Poris	Poris	Poris	Poris	Poris
sample #	01TF626	01TF625	01TF18	01TF17	01TF11
XRF Major element oxides (Wt%)					
SiO2	57.11	58.43	56.31	57.50	57.55
Al2O3	19.48	19.86	19.26	19.23	19.54
TiO2	1.24	1.02	0.64	1.26	0.51
FeO*	4.13	3.48	2.75	3.91	2.56
MnO	0.18	0.18	0.17	0.16	0.18
CaO	3.05	2.52	5.86	3.72	4.50
MgO	1.53	1.08	1.10	1.33	0.67
K2O	4.88	5.13	6.04	5.30	6.17
Na2O	7.87	7.80	7.38	7.00	7.99
P2O5	0.24	0.21	0.24	0.30	0.09
total	99.71	99.71	99.75	99.71	99.77
XRF Trace elements (ppm) Ni	13.2	7.1	2.1	5.1	2.1
Cr	11.2	4.1	0.0	5.1	0.0
Sc	0.0	0.0	2.1	1.0	1.0
V	83	65	54	91	35
Ba	607	691	244	937	108
Rb	147	152	179	121	197
Sr	448	431	276	486	157
Zr	850	878	1010	657	1111
Y	33	32	47	36	33
Nb	192	194	199	179	218
Ga	27	27	30	24	33
Cu	5	6	0	0	0
Zn	114	110	108	91	111
Pb	14	15	18	10	17
La	102	107	121	110	125
Ce	190	176	159	168	158
Th	24	25	32	18	35
ICP-MS traces (ppm) La	111	112	123	112	117
Ce	170	173	145	188	146
Pr	16	16	14	19	12
Nd	51	53	43	67	33
Sm	8.9	9.2	7.2	11.9	4.9
Eu	2.4	2.5	1.6	3.3	1.0
Gd	6.9	7.2	6.1	9.2	4.2
Tb	1.0	1.1	1.0	1.4	0.7
Dy	6.0	6.2	5.9	7.8	4.4
Ho	1.2	1.2	1.2	1.4	1.0
Er	3.3	3.3	3.7	3.7	3.1
Tm	0.5	0.5	0.6	0.5	0.5
Yb	3.2	3.2	3.9	3.1	3.6
Lu	0.5	0.5	0.6	0.5	0.6
Ba	603	711	199	976	101
Th	27	26	34	19	36
Nb	200	198	211	183	218
Y	33	34	38	38	30
Hf	17	17	20	13	21
Ta	10	10	9	12	9
U	6.5	6.5	8.3	4.6	8.8
Pb	15	15	19	12	20
Rb	148	147	186	115	197
Cs	1.9	1.9	2.4	1.3	2.7
Sr	435	498	210	550	111
Sc	4.0	3.6	2.3	4.2	1.6
Zr	873	861	1080	662	1136

Appendix A.
DHF Whole-rock data

ChemoUnit	DHF II	DHF II	DHF II	DHF II	DHF II	DHF II	DHF II	DHF II	DHF II	DHF II
Member	ARAFO	ARAFO	ARAFO	ARAFO	ARAFO	ARAFO	ARAFO	ARAFO	ARAFO	ARAFO
sample #	05TF57	96TF-4	05TF19	05TF10	01TF200-2	05TF58	05TF36	01TF266	01TF200	01TF149
XRF Major element oxides (Wt%)										
SiO2	58.83	58.84	59.23	59.84	59.85	60.09	60.12	60.23	60.25	60.29
Al2O3	23.78	20.45	20.34	21.06	23.38	22.06	20.96	21.83	22.30	21.85
TiO2	0.69	1.01	1.04	0.64	0.75	0.49	0.71	0.56	0.69	0.52
FeO*	3.82	3.69	4.00	3.20	3.40	2.96	3.38	2.60	3.02	2.49
MnO	0.19	0.16	0.17	0.18	0.16	0.19	0.18	0.16	0.16	0.16
CaO	1.20	2.29	2.19	1.39	1.41	0.97	1.61	1.19	1.46	1.58
MgO	0.47	0.80	0.91	0.50	0.63	0.28	0.58	0.83	1.05	0.73
K2O	5.56	5.80	5.62	6.15	5.47	6.32	6.57	5.62	5.69	5.80
Na2O	5.06	6.76	6.01	6.63	4.63	6.31	5.46	6.71	5.06	6.29
P2O5	0.10	0.21	0.16	0.10	0.09	0.06	0.13	0.06	0.09	0.07
total	99.69	100.00	99.68	99.71	99.76	99.72	99.71	99.78	99.77	99.78
XRF Trace elements (ppm) Ni	9.4	6.0	20.9	9.3	6.3	6.6	9.3	5.2	8.3	5.3
Cr	7.5	1.0	7.6	3.7	8.4	2.1	-0.3	0.0	10.3	0.0
Sc	1.9	4.0	1.8	1.8	1.1	0.9	2.1	4.1	5.2	8.4
V	37	66	61	38	32	28	44	20	45	23
Ba	207		622	266	271	64	227	271	280	322
Rb	196	158	138	188	173	208	192	172	172	157
Sr	143	279	249	143	206	77	171	209	176	237
Zr	1097	842	787	1019	1032	1101	1000	958	959	900
Y	19	25	24	20	23	17	20	19	22	18
Nb	180	161	164	168	177	174	165	160	163	156
Ga	35	31	28	33	32	33	32	30	30	29
Cu	15	1	7	4	7	6	4	1	2	1
Zn	119	97	101	109	110	114	107	102	104	99
Pb	22		15	19	18	22	19	12	16	11
La	92		92	91	98	89	91	87	83	86
Ce	134		149	121	145	116	119	109	152	135
Th	34		23	30	31	35	30	28	29	26
ICP-MS traces (ppm) La	86	89	89	85		88	89	84	81	72
Ce	118	116	137	105		105	109	107	106	92
Pr	8	10	11	8		7	8	8	8	7
Nd	22	29	36	22		18	23	20	23	20
Sm	3.3	4.8	5.9	3.3		2.4	3.5	2.8	3.4	2.7
Eu	0.8	1.2	1.5	0.8		0.5	0.9	0.7	0.9	0.8
Gd	2.8	3.9	4.6	2.7		2.0	2.8	2.3	2.9	2.3
Tb	0.4	0.6	0.7	0.4		0.3	0.5	0.4	0.5	0.4
Dy	2.8	3.5	4.2	2.7		2.3	2.8	2.4	3.0	2.3
Ho	0.6	0.7	0.8	0.6		0.5	0.6	0.6	0.6	0.5
Er	2.0	2.2	2.3	1.9		1.8	1.9	1.8	2.1	1.7
Tm	0.3	0.4	0.4	0.3		0.3	0.3	0.3	0.4	0.3
Yb	2.4	2.5	2.3	2.4		2.4	2.3	2.3	2.6	2.1
Lu	0.4	0.4	0.4	0.4		0.4	0.4	0.4	0.4	0.4
Ba	199	410	596	256		63	222	282	289	325
Th	34	23	22	30		35	30	29	29	27
Nb	177	163	162	163		174	164	165	169	162
Y	19	22	24	18		17	19	18	20	16
Hf	18	15	14	17		18	16	17	17	16
Ta	6	6	8	6		6	6	6	6	6
U	7.0	6.3	4.7	6.9		8.0	7.2	6.3	6.1	4.9
Pb	20	15	13	17		19	17	17	17	16
Rb	182	155	128	168		197	179	167	168	153
Cs	2.9	1.9	1.4	2.2		2.5	2.2	2.1	2.2	1.7
Sr	137	238	235	131		75	164	201	162	219
Sc	3.3	2.6	3.2	1.6		1.7	2.1	1.4	2.5	1.1
Zr	1006		731	924		1030	926	949	960	907

Appendix A.
DHF Whole-rock data

ChemoUnit	DHF II	DHF II	DHF II	DHF II	DHF II	DHF II	DHF II	DHF II	DHF II	DHF II
Member	ARAFO	ARAFO	ARAFO	ARAFO	ARAFO	ARAFO	ARAFO	ARAFO	ARAFO	ARAFO
sample #	05TF5	05TF24	01TF267	05TF14	05TF12	05TF15	05TF23	05TF22	05TF8	01TF150-2
XRF Major element oxides (Wt%)										
SiO2	60.33	60.34	60.34	60.39	60.43	60.44	60.54	60.61	60.62	60.64
Al2O3	21.19	20.95	21.53	20.86	21.39	21.01	21.13	21.67	21.29	22.77
TiO2	0.52	0.49	0.61	0.54	0.54	0.49	0.46	0.44	0.46	0.34
FeO*	2.92	2.75	2.70	2.86	2.90	2.75	2.71	2.72	2.74	2.28
MnO	0.19	0.18	0.16	0.18	0.19	0.18	0.18	0.19	0.18	0.18
CaO	1.11	1.03	1.34	1.17	1.16	1.01	0.96	0.87	0.95	1.09
MgO	0.34	0.31	0.91	0.36	0.35	0.29	0.27	0.23	0.25	0.26
K2O	6.56	6.46	5.98	6.53	6.38	6.59	6.47	6.67	6.64	5.84
Na2O	6.49	7.17	6.12	6.76	6.32	6.90	6.94	6.31	6.53	6.33
P2O5	0.07	0.06	0.08	0.08	0.07	0.06	0.06	0.04	0.05	0.05
total	99.72	99.74	99.78	99.73	99.71	99.73	99.73	99.73	99.73	99.79
XRF Trace elements (ppm) Ni	12.0	11.7	8.3	8.8	6.6	14.8	6.7	12.4	10.9	3.1
Cr	0.0	1.8	0.0	1.1	1.6	0.9	2.5	1.0	0.2	0.0
Sc	0.1	0.1	0.0	0.2	0.4	1.1	0.5	0.9	0.2	5.2
V	33	30	25	34	33	30	27	25	27	26
Ba	128	97	235	149	207	97	98	88	113	105
Rb	202	201	175	203	196	206	200	203	206	177
Sr	82	50	266	95	115	55	44	34	63	141
Zr	1058	1041	946	1033	1055	1059	1063	1100	1077	1045
Y	18	16	19	18	18	17	17	17	17	17
Nb	168	164	159	165	169	169	167	171	170	158
Ga	31	32	30	32	32	33	33	34	33	31
Cu	3	4	5	2	7	3	3	4	3	1
Zn	109	106	105	105	110	108	106	112	109	111
Pb	20	19	15	20	20	21	21	21	20	14
La	91	89	82	91	90	90	90	87	90	88
Ce	111	112	127	111	115	109	115	111	110	119
Th	34	33	26	32	32	33	33	34	34	32
ICP-MS traces (ppm) La	84	80	84	80	82	84	83	80	83	
Ce	101	95	105	98	100	99	99	96	98	
Pr	7	7	8	7	7	7	7	7	7	
Nd	18	17	20	18	19	18	17	17	17	
Sm	2.5	2.4	2.9	2.6	2.8	2.4	2.4	2.3	2.3	
Eu	0.6	0.5	0.7	0.6	0.6	0.6	0.5	0.5	0.5	
Gd	2.1	2.1	2.4	2.2	2.3	2.2	2.0	1.9	2.0	
Tb	0.3	0.3	0.4	0.4	0.4	0.3	0.3	0.3	0.3	
Dy	2.3	2.2	2.5	2.4	2.4	2.3	2.2	2.1	2.2	
Ho	0.5	0.5	0.6	0.5	0.5	0.5	0.5	0.5	0.5	
Er	1.7	1.7	1.9	1.8	1.8	1.8	1.8	1.7	1.7	
Tm	0.3	0.3	0.3	0.3	0.3	0.3	0.3	0.3	0.3	
Yb	2.3	2.3	2.4	2.3	2.3	2.3	2.3	2.3	2.3	
Lu	0.4	0.4	0.4	0.4	0.4	0.4	0.4	0.4	0.4	
Ba	120	91	256	144	198	92	95	86	105	
Th	32	30	28	30	31	31	31	32	32	
Nb	161	166	160	165	166	167	168	170	164	
Y	16	16	18	17	17	17	17	16	16	
Hf	17	17	17	17	17	17	18	18	17	
Ta	5	5	6	5	6	5	5	5	5	
U	7.5	7.1	6.5	7.2	6.9	7.5	7.3	7.2	7.6	
Pb	18	18	17	17	18	18	18	18	18	
Rb	175	188	167	184	175	188	186	186	184	
Cs	2.3	2.3	2.0	2.3	2.2	2.4	2.3	2.3	2.4	
Sr	73	50	238	87	105	52	42	33	57	
Sc	1.2	1.6	1.5	1.4	1.3	1.3	1.4	1.3	1.0	
Zr	946	998	919	964	975	1001	1013	1034	983	

Appendix A.
DHF Whole-rock data

ChemoUnit	DHF II	DHF II	DHF II	DHF II	DHF II	DHF II	DHF II	DHF II	DHF II	DHF II
Member	ARAFO	ARAFO	ARAFO	ARAFO	ARAFO	ARAFO	ARAFO	ARAFO	ARAFO	ARAFO
sample #	05TF11	01TF237	05TF6	01TF238	05TF25	DH97-5a	96TF-3	01TF150	05TF7	05TF34
XRF Major element oxides (Wt%)										
SiO2	60.69	60.69	60.71	60.71	60.79	60.91	60.95	61.01	61.08	60.93
Al2O3	21.98	20.55	21.24	21.47	21.03	21.49	21.32	22.87	21.62	22.28
TiO2	0.48	0.57	0.51	0.57	0.42	0.54	0.50	0.33	0.50	0.55
FeO*	2.86	2.55	2.83	2.60	2.59	2.54	2.61	2.27	2.84	2.83
MnO	0.19	0.15	0.18	0.16	0.18	0.17	0.17	0.18	0.19	0.18
CaO	1.05	1.26	1.07	1.32	0.85	1.15	1.03	1.23	1.06	1.32
MgO	0.31	0.51	0.33	0.50	0.22	0.32	0.24	0.47	0.31	0.32
K2O	6.65	6.06	6.73	5.99	6.81	6.73	6.81	5.60	7.05	5.65
Na2O	5.44	7.38	6.05	6.39	6.78	5.85	6.10	5.76	5.01	5.56
P2O5	0.06	0.06	0.07	0.06	0.04	0.07	0.06	0.06	0.06	0.07
total	99.71	99.79	99.72	99.79	99.74	99.79	99.80	99.78	99.72	99.69
XRF Trace elements (ppm) Ni	15.0	3.1	13.6	2.0	9.8	4.2	5.3	6.3	12.4	12.0
Cr	0.1	3.1	1.4	1.0	0.9	1.0	0.0	0.0	0.4	2.1
Sc	0.5	2.0	1.0	4.1	1.2	5.2	0.0	2.1	1.5	1.1
V	28	44	31	34	23	27	25	19	28	25
Ba	183	327	146	296	47	89	81	100	149	584
Rb	200	175	203	169	211	198	204	165	204	162
Sr	94	124	81	154	25	92	73	179	93	182
Zr	1105	881	1053	934	1073	1039	1058	1124	1078	926
Y	17	17	18	17	16	20	18	15	17	19
Nb	174	148	168	154	167	175	176	164	172	159
Ga	35	27	32	28	34	30	32	31	34	31
Cu	6	0	8	0	2	2	2	4	4	1
Zn	111	94	106	96	107	107	107	105	110	94
Pb	21	18	21	16	21	13	15	16	21	18
La	93	82	94	75	89	108	81	79	92	93
Ce	118	115	117	121	115	135	136	133	119	126
Th	35	26	33	27	33	30	33	34	34	29
ICP-MS traces (ppm) La	84	69	83	66	79	89	78	67	84	87
Ce	98	92	97	92	92	101	94	84	99	115
Pr	7	7	7	7	6	8	7	6	7	9
Nd	18	19	18	20	16	21	18	14	19	24
Sm	2.5	2.7	2.5	3.0	2.0	3.0	2.6	1.8	2.6	3.3
Eu	0.6	0.7	0.6	0.8	0.4	0.7	0.6	0.4	0.6	0.8
Gd	2.1	2.0	2.1	2.3	1.8	2.6	2.0	1.6	2.1	2.8
Tb	0.3	0.4	0.3	0.4	0.3	0.4	0.4	0.3	0.4	0.4
Dy	2.3	2.4	2.3	2.6	2.0	2.6	2.3	1.9	2.3	2.8
Ho	0.5	0.5	0.5	0.6	0.5	0.6	0.5	0.4	0.5	0.6
Er	1.7	1.7	1.7	1.7	1.6	1.8	1.7	1.5	1.8	1.9
Tm	0.3	0.3	0.3	0.3	0.3	0.3	0.3	0.3	0.3	0.3
Yb	2.3	2.2	2.3	2.1	2.2	2.4	2.3	2.2	2.3	2.3
Lu	0.4	0.4	0.4	0.4	0.4	0.4	0.4	0.4	0.4	0.4
Ba	173	296	128	404	44	137	113	118	142	570
Th	32	26	30	26	31	28	26	33	32	27
Nb	168	160	164	162	168	166	175	168	166	159
Y	16	16	17	16	16	18	17	14	16	19
Hf	18	16	17	16	17	17	18	19	17	15
Ta	5	6	5	6	5	5	5	5	5	6
U	7.0	6.4	7.2	5.7	7.3	7.7	6.8	5.0	7.4	6.1
Pb	18	16	17	16	18	17	17	19	18	16
Rb	178	171	185	156	196	177	181	161	178	152
Cs	2.3	2.1	2.2	2.1	2.4	2.2	2.3	1.8	2.3	1.8
Sr	86	106	76	196	24	95	76	161	85	174
Sc	1.1	1.6	1.6	1.7	1.2	1.1	0.1	1.1	1.1	0.9
Zr	1006	900	990	900	1025			1088	982	860

Appendix A.
DHF Whole-rock data

ChemoUnit	DHF II	DHF II	DHF II	DHF II	DHF II	DHF II	DHF II	DHF II	DHF II	DHF II
Member	ARAFO	ARAFO	ARAFO	CALETA	CALETA	CALETA	CALETA	CALETA	CALETA	CALETA
sample #	05TF35	05TF48	05TF52	05TF61B	01TF92	01TF93	01TF96	01TF94	01TF95	05TF89G
XRF Major element oxides (Wt%)										
SiO2	61.27	60.83	59.52	57.95	58.98	59.13	59.34	59.68	60.03	60.27
Al2O3	21.34	21.47	23.86	19.43	20.58	20.19	19.71	20.12	20.03	20.19
TiO2	0.53	0.54	0.68	0.51	0.55	0.52	0.52	0.52	0.53	0.51
FeO*	2.71	2.81	3.56	2.57	2.47	2.38	2.31	2.30	2.40	2.83
MnO	0.18	0.17	0.19	0.17	0.14	0.15	0.15	0.15	0.15	0.16
CaO	1.30	1.16	1.32	4.69	1.53	2.06	1.89	2.22	1.35	1.05
MgO	0.35	0.29	0.39	0.61	0.79	0.62	0.75	0.62	0.63	0.67
K2O	6.01	5.71	5.09	5.94	5.45	5.64	5.71	5.70	5.79	5.82
Na2O	5.96	6.67	4.98	7.78	9.23	9.03	9.34	8.41	8.83	8.20
P2O5	0.06	0.05	0.07	0.09	0.08	0.07	0.08	0.07	0.07	0.07
total	99.70	99.70	99.66	99.73	99.80	99.80	99.80	99.80	99.81	99.76
XRF Trace elements (ppm) Ni	13.0	6.9	7.0	3.6	5.2	4.1	4.1	3.1	4.1	10.2
Cr	2.0	0.1	3.4	2.5	0.0	0.0	4.1	1.0	0.0	3.7
Sc	0.3	0.3	1.8	2.4	3.1	2.1	3.1	8.2	4.1	0.5
V	25	27	32	31	32	32	28	28	22	29
Ba	544	577	566	292	279	264	283	283	272	263
Rb	165	161	169	175	153	163	166	169	169	170
Sr	153	153	255	193	120	110	111	110	95	78
Zr	893	912	984	870	891	867	844	860	862	798
Y	19	18	22	17	17	17	18	16	16	14
Nb	155	154	175	139	148	146	143	145	145	125
Ga	29	31	32	29	25	27	25	28	27	28
Cu	3	3	8	3	3	0	4	0	1	10
Zn	99	100	112	96	98	93	93	90	94	103
Pb	17	16	20	16	10	13	13	14	12	23
La	89	84	104	83	81	75	89	78	67	76
Ce	121	116	140	101	123	122	129	109	118	102
Th	27	26	30	26	25	27	26	26	25	40
ICP-MS traces (ppm) La	86	81	95	75	80	82	107	84	84	
Ce	109	108	125	92	104	102	100	103	105	
Pr	8	8	10	7	7	7	8	7	8	
Nd	23	20	27	18	19	19	20	19	21	
Sm	3.2	2.8	4.0	2.5	2.7	2.6	2.9	2.7	2.9	
Eu	0.6	0.7	1.0	0.6	0.7	0.7	0.7	0.7	0.7	
Gd	2.6	2.3	3.2	2.1	2.2	2.2	2.4	2.3	2.5	
Tb	0.4	0.4	0.5	0.4	0.4	0.4	0.4	0.4	0.4	
Dy	2.7	2.5	3.3	2.3	2.4	2.3	2.5	2.4	2.6	
Ho	0.6	0.6	0.7	0.5	0.5	0.5	0.6	0.5	0.6	
Er	1.9	1.8	2.2	1.6	1.7	1.7	1.9	1.8	1.8	
Tm	0.3	0.3	0.4	0.3	0.3	0.3	0.3	0.3	0.3	
Yb	2.2	2.2	2.5	2.0	2.2	2.2	2.3	2.3	2.3	
Lu	0.4	0.4	0.4	0.4	0.4	0.4	0.4	0.4	0.4	
Ba	526	566	543	280	303	279	306	298	310	
Th	26	26	29	26	26	26	26	26	26	
Nb	152	155	172	139	152	149	147	149	150	
Y	18	18	22	16	16	17	18	17	17	
Hf	14	15	16	14	16	16	15	16	16	
Ta	6	6	7	5	5	5	5	5	5	
U	6.2	6.0	6.2	6.7	5.7	7.0	6.6	6.5	6.4	
Pb	15	15	17	15	14	15	15	15	15	
Rb	150	153	157	166	152	161	164	164	165	
Cs	1.8	1.8	2.1	2.1	1.8	2.0	2.0	2.0	2.0	
Sr	143	148	242	185	119	103	104	99	117	
Sc	0.8	1.1	2.1	1.3	1.8	1.8	1.8	1.7	2.1	
Zr	813	860	902	809	897	882	860	876	870	

Appendix A.
DHF Whole-rock data

ChemoUnit	DHF II	DHF II	DHF II	DHF II	DHF II
Member	CALETA	CALETA	CALETA	CALETA	CALETA
sample #	01TF91	05TF89H	05TF39	05TF41	05TF40
XRF Major element oxides (Wt%)					
SiO2	60.39	60.43	60.53	60.59	60.68
Al2O3	20.13	20.75	20.33	20.32	20.37
TiO2	0.53	0.59	0.57	0.53	0.57
FeO*	2.41	3.01	2.88	2.78	2.89
MnO	0.16	0.17	0.17	0.17	0.18
CaO	1.34	1.14	1.19	1.13	1.24
MgO	0.46	0.58	0.38	0.32	0.40
K2O	5.85	5.83	6.29	5.98	6.37
Na2O	8.47	7.16	7.32	7.84	6.97
P2O5	0.06	0.07	0.09	0.07	0.08
total	99.80	99.73	99.74	99.73	99.73
XRF Trace elements (ppm) Ni	1.0	8.1	6.7	12.7	9.9
Cr	1.0	4.6	1.2	1.7	3.0
Sc	4.1	1.1	1.2	0.3	1.4
V	29	37	33	28	34
Ba	285	353	251	317	266
Rb	174	174	189	183	186
Sr	91	116	88	104	103
Zr	869	891	920	911	919
Y	17	17	17	17	18
Nb	146	144	147	146	147
Ga	27	29	30	29	32
Cu	0	4	3	2	3
Zn	94	94	100	98	101
Pb	13	17	18	17	17
La	99	86	82	81	82
Ce	110	117	110	111	111
Th	25	27	27	26	27
ICP-MS traces (ppm) La	88	76	81	83	81
Ce	109	99	100	104	100
Pr	8	7	7	7	7
Nd	21	21	19	20	19
Sm	2.9	3.1	2.7	2.8	2.7
Eu	0.7	0.8	0.6	0.7	0.7
Gd	2.3	2.5	2.3	2.3	2.3
Tb	0.4	0.4	0.4	0.4	0.4
Dy	2.5	2.5	2.4	2.3	2.3
Ho	0.6	0.6	0.5	0.5	0.5
Er	1.9	1.7	1.7	1.7	1.7
Tm	0.3	0.3	0.3	0.3	0.3
Yb	2.3	2.1	2.1	2.2	2.2
Lu	0.4	0.4	0.4	0.4	0.4
Ba	324	333	253	320	269
Th	26	24	27	28	27
Nb	151	143	148	152	149
Y	17	17	17	17	17
Hf	16	15	15	16	15
Ta	5	5	5	5	5
U	6.7	5.6	6.9	7.1	6.9
Pb	16	14	16	16	16
Rb	171	154	177	179	179
Cs	2.2	1.9	2.2	2.2	2.2
Sr	97	105	87	104	102
Sc	1.8	1.7	1.4	1.2	1.7
Zr	879	817	861	879	870

Appendix A.
DHF Whole-rock data

ChemoUnit	DHF III	DHF III	DHF III	DHF III	DHF III	DHF III	DHF III	DHF III	DHF III	DHF III
Member	N series	N series	N series	N series	N series	N series	N series	N series	N series	N series
sample #	01TF100	01TF101	01TF102	01TF104	01TF105	01TF167	01TF168	01TF169	01TF170	01TF172
XRF Major element oxides (Wt%)										
SiO2	60.24	60.32	58.96	59.02	57.22	61.95	62.57	62.38	61.07	63.22
Al2O3	19.27	19.24	18.74	18.81	18.06	20.27	20.15	20.41	21.16	21.46
TiO2	0.56	0.57	0.69	0.58	0.65	0.58	0.58	0.61	0.70	0.64
FeO*	2.76	2.69	3.02	2.70	2.77	2.97	2.90	3.02	3.24	2.97
MnO	0.21	0.21	0.20	0.19	0.18	0.21	0.22	0.22	0.23	0.21
CaO	1.52	1.44	2.94	3.18	6.14	1.62	1.23	1.11	1.08	1.11
MgO	0.84	0.98	1.44	1.51	1.69	1.43	0.68	0.72	0.70	0.66
K2O	6.17	6.14	5.73	5.83	5.59	5.08	5.10	5.48	4.88	4.88
Na2O	8.14	8.09	7.86	7.78	7.30	5.54	6.25	5.70	6.59	4.51
P2O5	0.08	0.09	0.18	0.16	0.16	0.06	0.05	0.07	0.08	0.07
total	99.77	99.77	99.76	99.77	99.77	99.71	99.73	99.73	99.72	99.72
XRF Trace elements (ppm) Ni	5.2	7.3	6.3	4.2	3.2	4.3	5.3	5.3	10.6	5.3
Cr	0.0	0.0	0.0	0.0	0.0	0.0	5.3	0.0	1.1	0.0
Sc	0.0	0.0	5.2	0.0	0.0	7.4	6.3	0.0	0.0	0.0
V	28	30	42	24	38	32	29	36	33	20
Ba	12	43	116	34	86	53	48	98	60	25
Rb	183	186	171	174	163	179	178	189	166	180
Sr	61	69	157	111	178	479	321	280	256	383
Zr	1116	1147	1069	1097	995	1232	1233	1208	1269	1263
Y	37	39	39	42	36	38	38	39	41	39
Nb	250	259	245	248	225	275	279	275	293	280
Ga	28	31	28	29	29	32	31	32	34	32
Cu	3	3	6	3	3	13	11	16	12	5
Zn	133	134	133	127	121	128	129	131	139	129
Pb	16	13	13	16	13	15	14	17	15	16
La	137	137	147	131	139	152	151	147	151	154
Ce	218	219	206	221	204	226	232	237	254	236
Th	29	31	30	30	26	36	34	34	37	33
ICP-MS traces (ppm) La	145	144	138	142	126	140	146	147	134	133
Ce	204	201	196	198	177	192	205	205	216	195
Pr	17	17	17	17	15	16	17	17	17	16
Nd	47	48	49	52	46	47	48	50	50	48
Sm	7.2	7.3	7.7	8.2	7.2	7.1	7.2	7.6	8.0	7.2
Eu	1.3	1.3	1.5	1.5	1.3	1.2	1.3	1.4	1.4	1.3
Gd	5.8	5.9	6.2	6.5	5.8	5.9	5.9	6.0	6.4	5.9
Tb	1.0	1.0	1.1	1.1	1.0	1.0	1.0	1.0	1.1	1.0
Dy	6.3	6.4	6.4	6.9	5.9	6.3	6.1	6.2	6.9	6.1
Ho	1.3	1.3	1.3	1.5	1.2	1.3	1.3	1.3	1.4	1.3
Er	4.0	4.1	4.0	4.3	3.6	3.9	3.9	3.9	4.2	3.8
Tm	0.6	0.7	0.6	0.7	0.6	0.6	0.6	0.6	0.7	0.6
Yb	4.2	4.2	4.0	4.4	3.6	4.1	4.1	4.1	4.4	4.0
Lu	0.7	0.7	0.7	0.7	0.6	0.7	0.7	0.6	0.7	0.6
Ba	50	60	128	94	104	92	72	125	96	51
Th	32	32	30	31	28	33	35	34	36	34
Nb	268	268	251	255	229	290	288	282	310	293
Y	39	40	39	43	36	37	38	39	39	37
Hf	23	22	21	21	19	24	24	23	24	24
Ta	14	14	13	14	12	15	14	14	15	15
U	7.5	7.5	6.9	7.0	6.5	6.1	6.8	7.2	5.8	6.0
Pb	18	17	16	16	15	17	18	18	19	19
Rb	181	179	166	168	151	175	172	181	160	173
Cs	2.2	2.1	1.9	2.0	1.7	2.1	2.0	2.0	2.3	2.1
Sr	57	67	152	114	169	618	347	307	243	358
Sc	2.2	2.1	2.7	2.3	2.3	1.6	2.3	2.4	2.2	1.8
Zr	1165	1164	1075	1100	984	1235	1250	1222	1280	1263

Appendix A.
DHF Whole-rock data

ChemoUnit	DHF III	DHF III	DHF III	DHF III	DHF III	DHF III	DHF III	DHF III	DHF III	DHF III
Member	N series	N series	N series	N series	N series	N series	N series	N series	N series	N series
sample #	01TF265	01TF273	01TF218	01TF219	01TF242	DH97-14	DH97-15	DH97-16	TF00102	01TF234
XRF Major element oxides (Wt%)										
SiO2	60.74	61.60	60.70	62.13	60.73	60.00	60.04	60.19	59.87	60.30
Al2O3	21.37	22.31	21.97	23.35	21.06	23.07	22.05	22.14	19.11	22.42
TiO2	0.63	0.66	0.65	0.69	0.68	0.65	0.65	0.77	0.69	0.74
FeO*	2.98	3.39	3.25	3.28	3.14	3.81	3.90	3.81	3.17	3.39
MnO	0.20	0.21	0.24	0.25	0.21	0.26	0.24	0.24	0.24	0.23
CaO	0.92	0.98	1.07	1.56	0.93	0.84	0.84	1.11	0.73	1.15
MgO	0.51	0.54	0.48	0.51	0.53	0.49	0.48	0.55	0.38	0.91
K2O	5.62	5.26	6.07	3.43	5.93	5.23	5.47	5.29	5.78	4.89
Na2O	6.71	4.71	5.25	4.49	6.48	5.60	6.24	5.83	9.70	5.64
P2O5	0.06	0.06	0.06	0.05	0.07	0.06	0.07	0.08	0.08	0.05
total	99.76	99.73	99.73	99.73	99.75	99.75	99.75	99.75	99.75	99.74
XRF Trace elements (ppm) Ni	7.3	5.3	5.2	6.4	6.2	8.0	8.0	10.0	6.2	7.3
Cr	0.0	0.0	1.0	0.0	0.0	1.0	2.0	3.0	0.0	1.0
Sc	1.0	0.0	1.0	2.1	5.2	1.0	2.0	0.0	0.0	2.1
V	29	32	43	46	49	42	36	39	38	42
Ba	15	48	41	36	73				4	21
Rb	188	178	185	125	188	184	197	148	185	151
Sr	78	188	135	91	75	134	78	122	12	147
Zr	1216	1286	1343	1403	1194	1587	1489	1188	1256	1184
Y	40	43	45	38	39	54	51	51	54	50
Nb	273	293	300	317	271	344	325	288	308	291
Ga	31	34	37	34	31	44	39	28	33	35
Cu	0	2	0	31	0	0	1	3	2	0
Zn	136	141	136	125	132	165	161	148	150	145
Pb	18	16	22	21	17				19	16
La	154	138	170	159	139				165	170
Ce	226	232	246	258	223				268	280
Th	35	34	35	36	35				33	29
ICP-MS traces (ppm) La	146	154	165	142	111	155	119	143	126	127
Ce	214	234	222	232	174	223	186	220	176	211
Pr	17	18	20	17	15	18	15	20	19	19
Nd	50	52	56	49	43	53	44	63	61	59
Sm	7.7	8.0	8.6	7.7	6.9	8.4	7.3	10.7	11.1	10.0
Eu	1.2	1.4	1.5	1.4	1.2	1.3	1.2	1.8	2.2	1.6
Gd	6.1	6.4	6.8	6.3	5.4	6.7	5.6	7.9	9.7	7.4
Tb	1.1	1.1	1.2	1.1	1.0	1.2	1.0	1.4	1.7	1.3
Dy	6.5	6.8	7.3	6.6	6.1	8.1	7.0	8.5	10.5	8.0
Ho	1.4	1.5	1.5	1.4	1.3	1.7	1.5	1.7	2.2	1.6
Er	4.1	4.3	4.4	4.0	3.7	5.2	4.4	4.9	6.4	4.6
Tm	0.7	0.7	0.7	0.6	0.6	0.9	0.7	0.7	1.0	0.7
Yb	4.3	4.5	4.7	4.1	3.9	5.8	5.0	4.7	6.2	4.5
Lu	0.7	0.7	0.8	0.6	0.6	0.9	0.8	0.7	1.0	0.7
Ba	47	79	52	57	83	36	51	50	17	29
Th	35	37	38	39	33	42	36	30	28	29
Nb	283	298	313	325	282	331	320	280	306	299
Y	40	42	44	39	36	52	42	48	59	44
Hf	24	24	25	26	23	30	28	22	25	23
Ta	15	15	15	16	15	17	16	16	16	17
U	7.2	7.2	6.7	5.9	6.8	8.1	6.8	5.9	5.2	5.3
Pb	19	19	20	21	18	22	21	17	17	17
Rb	179	165	178	131	176	178	179	136	167	149
Cs	2.0	2.1	2.2	2.1	2.2	2.7	2.6	1.9	2.9	1.6
Sr	91	199	127	68	78	125	77	122	22	124
Sc	1.6	2.2	2.3	2.4	2.6	1.6	1.6	1.8	2.0	2.2
Zr	1210	1260	1304	1355	1183				1248	1153

Appendix A.
DHF Whole-rock data

ChemoUnit	DHF III	DHF III	DHF III	DHF III	DHF III	DHF III	DHF III	DHF III	DHF III
Member	Abrigo	Abrigo	Abrigo	N series	N series	N series	N series	N series	N series
sample #	01TF179	01TF178	01TF177	01TF104N	01TF105N	01TF106N	01TF107N	01TF112N	01TF113N
XRF Major element oxides (Wt%)									
SiO2	61.79	61.49	60.63	61.19	59.11	58.21	58.62	60.40	59.94
Al2O3	21.29	21.42	24.84	19.19	18.95	18.43	18.64	20.11	20.04
TiO2	0.62	0.74	0.90	0.53	0.72	0.56	0.59	0.64	0.58
FeO*	3.27	3.26	3.91	2.93	3.09	2.63	2.81	3.15	3.09
MnO	0.23	0.24	0.28	0.24	0.20	0.19	0.20	0.23	0.23
CaO	1.19	1.22	1.56	1.68	3.12	5.33	4.43	0.71	0.82
MgO	0.71	0.75	0.90	1.79	0.80	0.93	0.62	0.44	0.39
K2O	4.81	4.88	3.17	5.47	5.66	5.84	6.15	5.89	5.82
Na2O	5.68	5.57	3.03	6.66	8.00	7.59	7.66	8.10	8.74
P2O5	0.12	0.14	0.46	0.08	0.12	0.08	0.06	0.06	0.07
total	99.71	99.72	99.69	99.76	99.77	99.78	99.78	99.73	99.73
XRF Trace elements (ppm) Ni	5.3	7.4	8.9	6.3	2.1	1.1	1.1	6.2	5.2
Cr	0.0	0.0	2.2	0.0	0.0	0.0	0.0	0.0	0.0
Sc	3.2	5.3	6.7	3.1	0.0	0.0	0.0	8.3	4.2
V	36	28	26	26	44	39	42	48	28
Ba	23	37	0	22	97	11	0	5	31
Rb	165	157	101	162	175	177	168	193	203
Sr	56	52	54	51	143	92	80	24	66
Zr	1550	1419	1693	1172	1062	1080	1055	1349	1381
Y	53	54	63	57	36	38	44	51	46
Nb	356	342	408	289	248	250	266	328	320
Ga	33	32	31	31	30	31	30	34	32
Cu	3	8	23	0	0	0	0	0	0
Zn	153	150	128	148	118	117	123	145	139
Pb	16	15	18	20	17	14	12	19	18
La	159	168	189	172	128	136	132	168	173
Ce	249	294	348	236	203	205	244	261	247
Th	41	37	45	32	30	28	30	35	36
ICP-MS traces (ppm) La	156	160	173						
Ce	233	257	302						
Pr	19	22	25						
Nd	53	65	77						
Sm	8.5	10.6	12.9						
Eu	1.3	1.8	2.2						
Gd	7.1	8.5	10.4						
Tb	1.3	1.5	1.7						
Dy	8.2	8.9	10.7						
Ho	1.8	1.9	2.1						
Er	5.3	5.3	6.1						
Tm	0.9	0.8	0.9						
Yb	5.6	5.4	6.0						
Lu	0.9	0.8	0.9						
Ba	68	71	36						
Th	41	37	43						
Nb	367	343	410						
Y	53	55	61						
Hf	30	27	32						
Ta	18	19	23						
U	8.1	7.6	7.1						
Pb	20	19	22						
Rb	151	149	90						
Cs	2.0	1.8	1.1						
Sr	61	52	52						
Sc	2.6	2.4	2.9						
Zr	1520	1395	1615						

Appendix A.
DHF Whole-rock data

ChemoUnit	DHF III	DHF III	DHF III	DHF III	DHF III	DHF III	DHF III	DHF III	DHF III	DHF III
Member	N series	N series	N series	N series	N series	N series	N series	N series	N series	N series
sample #	01TF168N	01TF86N	01TF98N	TF0010	TF00100	TF00101	TF0011	TF00114	TF0012	TF0013
XRF Major element oxides (Wt%)										
SiO2	60.96	58.01	59.64	58.72	60.48	59.14	57.76	61.20	58.51	57.59
Al2O3	22.21	18.48	18.71	19.03	19.29	18.91	18.58	21.38	18.66	18.34
TiO2	0.66	0.55	0.55	0.57	0.59	0.55	0.56	0.70	0.57	0.57
FeO*	3.31	2.86	2.61	2.76	2.95	2.74	2.69	3.23	2.75	2.72
MnO	0.21	0.24	0.19	0.19	0.23	0.21	0.18	0.22	0.18	0.18
CaO	0.63	3.66	2.84	3.94	1.67	3.52	5.15	1.04	3.67	4.74
MgO	0.27	0.90	1.81	1.33	0.75	0.98	1.86	0.40	2.25	2.86
K2O	5.16	5.64	5.75	5.82	5.69	5.70	5.57	5.62	5.53	5.36
Na2O	6.29	9.29	7.59	7.32	8.03	7.97	7.29	5.91	7.50	7.21
P2O5	0.06	0.13	0.08	0.10	0.06	0.05	0.13	0.06	0.13	0.20
total	99.75	99.75	99.77	99.77	99.74	99.77	99.77	99.76	99.77	99.77
XRF Trace elements (ppm) Ni	5.2	8.4	5.3	2.1	5.2	0.0	6.2	6.3	1.0	4.2
Cr	0.0	0.0	0.0	0.0	0.0	0.0	0.0	0.0	0.0	0.0
Sc	8.4	0.0	4.2	0.0	0.0	4.2	5.2	0.0	1.0	4.2
V	31	33	33	38	35	33	33	36	34	38
Ba	10	0	0	0	0	0	22	7	20	43
Rb	172	177	171	178	188	174	172	150	167	161
Sr	75	74	57	80	35	67	117	131	119	174
Zr	1268	1256	1148	1135	1299	1111	1101	1166	1119	1092
Y	46	50	44	44	55	41	40	48	41	45
Nb	315	305	250	253	301	260	244	285	248	238
Ga	36	31	30	28	31	30	30	30	28	31
Cu	0	0	0	0	0	0	0	5	0	0
Zn	138	140	120	121	144	130	118	147	123	116
Pb	9	16	13	15	21	14	18	17	18	19
La	127	153	187	134	166	143	120	136	153	150
Ce	252	226	200	205	237	229	213	259	212	197
Th	30	33	32	33	34	28	29	26	26	29
ICP-MS traces (ppm) La										
Ce										
Pr										
Nd										
Sm										
Eu										
Gd										
Tb										
Dy										
Ho										
Er										
Tm										
Yb										
Lu										
Ba										
Th										
Nb										
Y										
Hf										
Ta										
U										
Pb										
Rb										
Cs										
Sr										
Sc										
Zr										

Appendix A.
DHF Whole-rock data

ChemoUnit	DHF III	DHF III	DHF III	DHF III	DHF III	DHF III	DHF III	DHF III	DHF III
Member	N series	N series	N series	N series	N series	Abrigo	Abrigo	Abrigo	Abrigo
sample #	TF00145hn	TF00146hn	TF008	TF009	TF0099	01TF102N	01TF103N	01TF245	01TF108Na
XRF Major element oxides (Wt%)									
SiO2	60.16	61.06	61.34	59.59	60.22	59.94	59.79	58.54	61.80
Al2O3	19.32	19.74	19.64	19.33	19.07	18.92	19.05	25.11	18.81
TiO2	0.56	0.56	0.60	0.55	0.61	0.73	0.67	0.67	0.85
FeO*	2.77	2.74	2.91	2.73	2.81	3.08	3.00	3.81	2.83
MnO	0.19	0.19	0.20	0.19	0.19	0.23	0.24	0.28	0.18
CaO	2.54	0.90	0.82	2.95	2.02	1.27	1.23	1.23	1.11
MgO	0.88	0.65	0.80	1.01	1.09	0.38	0.36	0.54	0.55
K2O	5.84	6.13	5.98	5.91	5.85	5.77	5.69	4.72	5.84
Na2O	7.46	7.73	7.42	7.43	7.81	9.39	9.66	4.67	7.72
P2O5	0.07	0.06	0.07	0.09	0.09	0.07	0.07	0.04	0.13
total	99.78	99.78	99.77	99.77	99.77	99.77	99.75	99.63	99.81
XRF Trace elements (ppm) Ni	4.1	4.1	4.1	4.2	4.1	3.1	5.1	8.5	6.2
Cr	0.0	0.0	0.0	0.0	0.0	0.0	0.0	0.0	0.0
Sc	0.0	0.0	4.1	0.0	0.0	4.1	7.2	0.0	1.0
V	42	31	32	36	37	32	41	33	40
Ba	16	0	27	0	40	0	0	3	403
Rb	179	183	174	183	179	168	176	190	103
Sr	44	20	40	43	67	20	20	362	64
Zr	1115	1145	1100	1137	1135	1119	1196	1839	605
Y	40	38	46	43	40	51	50	58	35
Nb	249	259	255	258	247	291	301	397	171
Ga	31	32	32	29	29	30	33	54	27
Cu	0	0	0	0	4	0	0	2	0
Zn	120	125	124	123	123	135	140	192	95
Pb	15	11	16	23	20	11	14	26	8
La	124	131	156	137	124	141	172	191	132
Ce	211	197	231	207	241	252	264	301	173
Th	29	30	32	30	32	28	31	49	14
ICP-MS traces (ppm) La								173	
Ce								259	
Pr								21	
Nd								60	
Sm								9.5	
Eu								1.5	
Gd								7.3	
Tb								1.4	
Dy								8.7	
Ho								1.9	
Er								5.8	
Tm								1.0	
Yb								6.3	
Lu								1.0	
Ba								44	
Th								47	
Nb								397	
Y								54	
Hf								35	
Ta								20	
U								6.3	
Pb								24	
Rb								172	
Cs								2.4	
Sr								417	
Sc								3.0	
Zr								1745	

Appendix A.
DHF Whole-rock data

ChemoUnit	DHF III	DHF III	DHF III	DHF III	DHF III	DHF III	DHF III	DHF III	DHF III
Member	Abrigo	Abrigo	Abrigo	Abrigo	Abrigo	Abrigo	Abrigo	Abrigo	Abrigo
sample #	01TF108Nb	01TF109N	01TF111N	01TF116N	01TF121N	01TF142N	01TF145N	01TF170N	01TF171N
XRF Major element oxides (Wt%)									
SiO2	60.87	60.28	57.51	60.89	59.53	60.04	60.36	59.74	61.04
Al2O3	18.76	18.92	17.89	19.73	19.09	19.23	19.17	19.12	18.79
TiO2	0.97	0.63	0.70	0.90	0.69	0.69	0.73	0.71	0.81
FeO*	3.28	2.87	2.86	3.48	3.06	3.08	3.04	3.07	2.78
MnO	0.19	0.20	0.22	0.21	0.24	0.24	0.23	0.23	0.18
CaO	1.46	2.60	5.71	1.06	1.59	0.81	0.81	1.26	1.33
MgO	0.71	1.15	1.17	0.52	0.42	0.48	0.28	0.43	0.49
K2O	5.49	5.36	5.43	5.14	5.77	5.75	5.90	5.66	5.86
Na2O	7.88	7.67	8.19	7.67	9.29	9.35	9.17	9.49	8.44
P2O5	0.17	0.08	0.08	0.13	0.07	0.07	0.07	0.07	0.10
total	99.76	99.77	99.76	99.73	99.75	99.75	99.76	99.77	99.82
XRF Trace elements (ppm) Ni	3.1	6.3	1.1	9.2	4.1	7.2	3.1	5.1	4.1
Cr	0.0	0.0	0.0	0.0	0.0	0.0	0.0	0.0	0.0
Sc	0.0	2.1	2.1	0.0	2.1	2.1	3.1	0.0	0.0
V	46	36	42	55	38	44	44	37	37
Ba	734	108	147	622	67	10	1	0	87
Rb	108	168	156	133	172	175	172	166	120
Sr	153	116	123	133	60	32	18	20	33
Zr	660	1074	1062	934	1198	1211	1165	1155	729
Y	37	37	47	45	51	49	51	50	44
Nb	183	247	270	243	300	301	300	293	210
Ga	27	29	30	31	33	33	34	32	26
Cu	0	0	0	0	0	0	0	0	0
Zn	104	119	131	121	139	143	136	136	103
Pb	12	16	16	10	13	10	9	9	8
La	114	133	142	139	150	168	163	146	139
Ce	197	204	246	228	258	262	275	240	220
Th	14	30	28	23	29	28	26	27	15
ICP-MS traces (ppm) La									
Ce									
Pr									
Nd									
Sm									
Eu									
Gd									
Tb									
Dy									
Ho									
Er									
Tm									
Yb									
Lu									
Ba									
Th									
Nb									
Y									
Hf									
Ta									
U									
Pb									
Rb									
Cs									
Sr									
Sc									
Zr									

Appendix A.
DHF Whole-rock data

ChemoUnit	DHF III	DHF III	DHF III	DHF III	DHF III	DHF III	DHF III	DHF III	DHF III	DHF III
Member	Abrigo	Abrigo	Abrigo	Abrigo	Abrigo	Abrigo	Abrigo	Abrigo	Abrigo	Abrigo
sample #	01TF172N	01TF173Na	01TF35	01TF36	01TF37	01TF39	01TF72N	01TF76Na	01TF79N	01TF81NC
XRF Major element oxides (Wt%)										
SiO2	60.02	59.78	60.16	60.13	59.86	59.46	56.00	60.41	60.33	59.51
Al2O3	19.22	19.05	19.41	19.20	19.15	18.99	17.68	18.99	19.21	18.82
TiO2	0.68	0.68	0.58	0.68	0.67	0.68	0.66	0.77	0.67	0.79
FeO*	3.03	3.05	3.02	2.83	2.91	2.93	2.82	3.07	3.00	2.99
MnO	0.23	0.23	0.24	0.23	0.23	0.23	0.21	0.21	0.23	0.21
CaO	0.79	1.44	0.88	1.27	1.14	1.81	6.85	0.79	0.75	1.87
MgO	0.40	0.41	0.23	0.32	0.28	0.32	1.22	0.44	0.31	0.44
K2O	5.64	5.68	5.91	5.83	5.77	5.79	5.31	5.72	5.59	5.47
Na2O	9.64	9.37	9.24	9.21	9.68	9.48	8.92	9.31	9.62	9.56
P2O5	0.10	0.08	0.05	0.06	0.06	0.06	0.09	0.08	0.07	0.11
total	99.76	99.76	99.73	99.76	99.75	99.75	99.75	99.78	99.76	99.77
XRF Trace elements (ppm) Ni	5.1	4.1	3.1	5.2	4.1	2.1	8.5	8.2	4.1	2.1
Cr	0.0	0.0	0.0	0.0	0.0	0.0	2.1	0.0	0.0	0.0
Sc	5.1	0.0	0.0	0.0	0.0	0.0	0.0	1.0	0.0	0.0
V	43	33	44	42	44	46	37	40	40	38
Ba	0	0	0	10	0	4	115	41	0	243
Rb	172	171	199	177	183	180	155	150	172	140
Sr	15	21	18	25	18	32	147	22	23	77
Zr	1199	1189	1380	1188	1243	1223	1102	996	1173	940
Y	50	48	53	53	54	55	46	49	49	45
Nb	302	297	318	286	298	295	276	263	295	247
Ga	33	31	29	29	28	27	29	30	31	27
Cu	0	0	0	0	0	0	0	0	0	0
Zn	140	139	153	142	141	142	126	127	139	124
Pb	11	9	16	16	18	20	9	12	11	10
La	148	125	154	146	172	154	140	144	137	151
Ce	264	265	274	254	257	266	246	268	258	231
Th	27	27	35	34	35	33	21	21	28	23
ICP-MS traces (ppm) La			147	150	144	150				
Ce			226	239	229	237				
Pr			19	21	21	21				
Nd			55	66	63	65				
Sm			8.8	11.2	10.6	10.8				
Eu			1.4	1.9	1.8	1.8				
Gd			7.4	8.8	8.3	8.7				
Tb			1.3	1.5	1.4	1.5				
Dy			8.1	8.9	8.7	9.0				
Ho			1.7	1.8	1.8	1.8				
Er			5.0	5.1	5.1	5.2				
Tm			0.8	0.8	0.8	0.8				
Yb			5.2	5.0	5.0	5.0				
Lu			0.8	0.8	0.8	0.8				
Ba			11	31	14	39				
Th			33	29	29	30				
Nb			325	296	303	302				
Y			49	51	50	52				
Hf			26	23	24	23				
Ta			17	17	17	17				
U			7.8	7.0	6.7	7.2				
Pb			17	15	15	16				
Rb			186	169	170	171				
Cs			2.4	2.0	2.1	2.1				
Sr			18	28	22	38				
Sc			2.1	1.9	1.8	2.2				
Zr			1320	1146	1179	1173				

Appendix A.
DHF Whole-rock data

ChemoUnit	DHF III	DHF III	DHF III	DHF III	DHF III	DHF III	DHF III	DHF III	DHF III	DHF III
Member	Abrigo	Abrigo	Abrigo	Abrigo	Abrigo	Abrigo	Abrigo	Abrigo	Abrigo	Abrigo
sample #	01TF82Na	01TF89Nb	01TF91N	01TF94N	01TF99N	01TF85N	01TF93N	TF00180	01TF1	TF00178
XRF Major element oxides (Wt%)										
SiO2	59.15	59.23	57.69	60.30	59.89	60.13	61.07	59.73	59.77	60.38
Al2O3	18.91	18.95	17.72	18.96	19.24	19.20	18.81	18.97	19.19	19.03
TiO2	0.69	0.67	0.64	0.74	0.59	0.66	0.91	0.70	0.68	0.66
FeO*	2.96	2.93	2.59	3.01	3.02	2.91	2.97	3.00	3.19	3.07
MnO	0.22	0.23	0.22	0.22	0.25	0.23	0.17	0.23	0.25	0.25
CaO	1.39	2.11	5.83	0.86	1.25	0.64	1.37	1.66	0.81	0.68
MgO	0.34	0.38	0.73	0.67	0.31	0.25	0.65	0.38	0.27	0.34
K2O	5.56	5.66	5.33	5.77	5.91	5.57	5.41	5.58	5.57	5.61
Na2O	10.46	9.50	8.88	9.13	9.21	10.12	8.22	9.45	9.94	9.66
P2O5	0.07	0.09	0.15	0.09	0.07	0.06	0.16	0.07	0.07	0.06
total	99.77	99.76	99.77	99.76	99.74	99.76	99.75	99.76	99.73	99.74
XRF Trace elements (ppm) Ni	7.2	3.1	1.0	4.1	4.2	3.0	2.0	15.2	3.0	17.1
Cr	0.0	0.0	0.0	0.0	0.0	0.0	0.0	2.0	0.0	1.0
Sc	7.2	0.0	0.0	2.1	2.1	1.0	4.1	0.0	3.0	0.0
V	40	32	33	34	31	39	45	37	41	37
Ba	35	0	25	109	0	0	1088	0	0	0
Rb	163	171	156	162	193	171	89	176	191	188
Sr	25	37	100	42	28	11	130	19	9	9
Zr	1115	1171	1074	1082	1321	1170	504	1181	1353	1331
Y	47	49	46	48	50	49	32	52	58	54
Nb	286	296	273	278	321	296	147	296	333	319
Ga	29	33	27	29	34	31	22	29	32	29
Cu	0	0	0	0	0	0	0	1	0	4
Zn	135	139	129	135	149	136	92	143	157	157
Pb	11	13	14	15	19	13	8	13	24	14
La	140	147	136	139	164	142	97	153	180	165
Ce	248	258	216	245	261	271	183	268	294	283
Th	29	31	25	28	33	26	12	29	32	30
ICP-MS traces (ppm) La								144	180	139
Ce								235	279	218
Pr								21	24	20
Nd								66	72	61
Sm								11.1	11.7	10.3
Eu								1.9	1.9	1.8
Gd								8.8	9.4	8.1
Tb								1.5	1.6	1.4
Dy								9.2	10.0	8.6
Ho								1.8	2.1	1.8
Er								5.2	5.9	5.1
Tm								0.8	0.9	0.8
Yb								4.9	5.8	5.0
Lu								0.8	0.9	0.8
Ba								17	14	53
Th								29	36	29
Nb								284	350	276
Y								50	58	50
Hf								23	28	23
Ta								17	19	15
U								7.6	8.5	6.8
Pb								15	19	15
Rb								168	188	169
Cs								2.0	2.6	2.2
Sr								15	11	52
Sc								1.7	1.8	1.7
Zr								1206	1371	1224

Appendix A.
DHF Whole-rock data

ChemoUnit	DHF III	DHF III	DHF III	DHF III	DHF III	DHF III	DHF III	DHF III	DHF III	DHF III
Member	Abrigo	Abrigo	Abrigo	Abrigo	Abrigo	Abrigo	Abrigo	Abrigo	Abrigo	Abrigo
sample #	01TF119N	01TF71N	01TF144N	01TF3	01TF57N	01TF58N	01TF81Na	TF00153A	TF00193	01TF114N
XRF Major element oxides (Wt%)										
SiO2	62.42	59.48	61.57	59.37	59.26	61.20	58.57	60.93	58.54	59.10
Al2O3	18.74	18.10	18.93	18.91	18.73	19.35	18.55	18.90	18.36	19.04
TiO2	0.96	0.83	0.77	0.82	1.03	0.72	1.03	0.80	1.17	1.10
FeO*	2.98	2.55	2.72	2.99	3.71	2.60	3.54	2.83	3.86	3.90
MnO	0.15	0.14	0.18	0.21	0.23	0.16	0.23	0.19	0.23	0.22
CaO	1.07	2.32	0.87	2.13	1.60	0.75	2.61	1.17	2.58	1.81
MgO	0.55	3.28	0.32	0.40	0.69	0.24	0.68	0.47	0.94	0.92
K2O	5.88	5.54	5.92	5.55	5.45	5.83	5.48	5.82	5.49	5.04
Na2O	6.95	7.50	8.47	9.29	8.87	8.90	8.97	8.59	8.40	8.32
P2O5	0.15	0.13	0.09	0.10	0.18	0.06	0.12	0.09	0.18	0.25
total	99.86	99.86	99.83	99.78	99.75	99.81	99.78	99.80	99.77	99.69
XRF Trace elements (ppm) Ni	8.1	3.1	5.1	2.0	5.1	3.0	4.1	10.3	17.3	3.1
Cr	0.0	0.0	0.0	0.0	0.0	0.0	0.0	0.0	2.0	0.0
Sc	2.0	4.1	1.0	3.0	1.0	1.0	5.1	6.2	6.1	1.0
V	36	54	48	31	65	43	52	48	61	49
Ba	239	115	78	93	326	20	64	52	176	858
Rb	95	86	117	153	147	148	143	143	146	131
Sr	60	110	19	47	128	19	36	28	81	341
Zr	386	456	690	971	928	842	922	872	862	913
Y	38	37	39	53	53	42	54	49	57	45
Nb	142	151	197	261	248	225	269	237	257	240
Ga	22	22	25	26	26	26	25	25	26	29
Cu	0	0	0	0	0	0	0	3	2	0
Zn	80	77	97	125	131	95	135	123	137	126
Pb	7	0	4	17	15	12	6	14	8	10
La	94	108	119	147	150	133	163	135	180	124
Ce	218	217	233	265	270	220	292	247	296	217
Th	8	9	14	27	26	23	22	23	20	24
ICP-MS traces (ppm) La				127	146	90		118	160	
Ce				221	251	165		213	284	
Pr				22	25	16		21	28	
Nd				74	82	53		72	95	
Sm				12.8	14.3	9.1		13.2	16.5	
Eu				2.4	2.9	1.6		2.4	3.0	
Gd				9.7	10.9	6.9		10.2	12.4	
Tb				1.6	1.7	1.2		1.7	1.9	
Dy				9.0	9.9	6.8		9.7	11.1	
Ho				1.7	1.9	1.3		1.8	2.1	
Er				4.7	5.0	3.6		4.9	5.3	
Tm				0.7	0.7	0.5		0.7	0.7	
Yb				4.1	4.4	3.2		4.1	4.4	
Lu				0.6	0.7	0.5		0.6	0.6	
Ba				123	324	29		67	264	
Th				21	22	18		21	20	
Nb				245	256	235		221	255	
Y				45	51	34		44	54	
Hf				18	18	17		18	18	
Ta				16	16	16		15	18	
U				4.6	5.2	4.0		4.6	4.9	
Pb				12	12	11		12	11	
Rb				137	142	141		133	140	
Cs				1.6	1.6	1.4		1.5	1.5	
Sr				50	131	18		21	91	
Sc				1.5	2.2	1.3		1.3	1.4	
Zr				863	891	817		860	836	

Appendix A.
DHF Whole-rock data

ChemoUnit	DHF III	DHF III	DHF III	DHF III	DHF III	DHF III	DHF III	DHF III	DHF III	DHF III
Member	Abrigo	Abrigo	Abrigo	Abrigo	Abrigo	Abrigo	Abrigo	Abrigo	Abrigo	Abrigo
sample #	01TF120N	01TF131N	01TF138N	01TF143N	01TF38	01TF4	01TF5	01TF56N	01TF67N	01TF73N
XRF Major element oxides (Wt%)										
SiO2	59.84	57.78	61.10	60.18	59.41	60.47	60.34	60.28	60.48	59.04
Al2O3	19.19	18.43	18.96	19.18	18.95	18.92	18.99	19.20	18.71	18.40
TiO2	0.77	0.67	0.93	0.67	0.68	0.82	0.81	0.68	0.76	0.72
FeO*	3.23	2.95	2.98	3.02	2.88	3.02	2.98	3.01	2.75	2.78
MnO	0.23	0.22	0.16	0.24	0.23	0.19	0.19	0.24	0.20	0.20
CaO	1.28	4.57	1.43	0.91	1.14	1.83	1.43	0.73	0.95	2.60
MgO	0.42	0.34	0.83	0.29	0.28	0.53	0.46	0.24	0.51	0.77
K2O	5.62	5.47	5.02	5.98	5.57	5.29	5.55	5.69	5.80	5.64
Na2O	9.05	9.25	8.08	9.24	10.55	8.50	8.89	9.63	9.54	9.56
P2O5	0.11	0.09	0.18	0.06	0.07	0.14	0.11	0.06	0.09	0.08
total	99.74	99.77	99.66	99.75	99.76	99.70	99.76	99.75	99.79	99.79
XRF Trace elements (ppm)										
Ni	5.1	4.2	12.2	3.1	3.1	3.1	1.0	0.0	1.0	4.2
Cr	0.0	0.0	4.1	0.0	0.0	0.0	0.0	0.0	0.0	0.0
Sc	4.1	0.0	3.1	6.2	0.0	0.0	0.0	0.0	0.0	0.0
V	40	42	57	35	44	41	37	45	52	30
Ba	255	10	2121	0	19	1217	564	0	42	22
Rb	161	164	72	176	174	114	133	184	147	142
Sr	110	46	183	19	29	121	56	10	34	59
Zr	1116	1127	416	1231	1191	760	818	1253	928	952
Y	48	49	28	50	54	38	46	54	49	45
Nb	282	285	121	306	287	196	216	301	239	248
Ga	30	29	22	32	27	25	25	31	25	29
Cu	0	0	0	0	0	0	0	0	0	0
Zn	137	135	82	144	138	111	123	145	121	119
Pb	13	10	3	9	14	0	17	19	9	3
La	126	164	98	164	142	130	135	154	138	154
Ce	236	248	146	250	270	194	201	259	245	243
Th	26	26	8	27	31	7	20	33	24	20
ICP-MS traces (ppm)										
La					132		108	146	140	
Ce					215		185	237	236	
Pr					20		18	21	23	
Nd					61		59	64	74	
Sm					10.2		10.2	10.6	12.7	
Eu					1.8		2.4	1.8	2.3	
Gd					8.2		7.9	8.7	9.6	
Tb					1.4		1.3	1.4	1.6	
Dy					8.4		7.4	9.0	9.0	
Ho					1.7		1.4	1.8	1.7	
Er					4.9		3.9	5.2	4.7	
Tm					0.8		0.6	0.8	0.7	
Yb					4.7		3.5	5.2	4.2	
Lu					0.8		0.5	0.8	0.6	
Ba					33		597	15	50	
Th					28		18	31	23	
Nb					298		209	315	251	
Y					47		38	51	49	
Hf					23		16	24	19	
Ta					17		13	18	16	
U					6.2		4.1	7.4	5.4	
Pb					15		11	16	13	
Rb					166		118	177	140	
Cs					2.1		1.4	2.2	1.7	
Sr					26		66	10	29	
Sc					1.8		1.4	2.1	1.0	
Zr					1152		764	1227	915	

Appendix A.
DHF Whole-rock data

ChemoUnit	DHF III	DHF III	DHF III	DHF III	DHF III	DHF III	DHF III	DHF III	DHF III
Member	Abrigo	Abrigo	Abrigo	Abrigo	Abrigo	Abrigo	Abrigo	Abrigo	Abrigo
sample #	01TF87N	01TF89Na	TF00201	TF00202	TF00203	TF00204A	TF00205A	TF00205B	TF00208A
XRF Major element oxides (Wt%)									
SiO2	60.38	60.68	59.55	59.04	59.61	60.22	60.32	59.38	60.95
Al2O3	18.56	18.56	18.57	17.64	18.53	18.77	18.74	19.35	18.87
TiO2	0.84	0.95	0.63	0.83	0.67	0.69	0.75	0.66	0.71
FeO*	2.78	2.95	3.02	2.89	2.97	3.12	3.10	3.25	2.98
MnO	0.18	0.17	0.27	0.21	0.26	0.26	0.25	0.29	0.25
CaO	2.40	2.15	1.83	5.02	2.44	0.95	1.36	1.31	0.81
MgO	0.61	0.73	0.41	0.71	0.49	0.41	0.55	0.65	0.59
K2O	5.67	5.47	5.39	4.81	5.37	5.41	5.18	5.19	5.18
Na2O	8.27	7.98	10.00	8.46	9.35	9.85	9.42	9.59	9.36
P2O5	0.13	0.17	0.08	0.17	0.08	0.07	0.09	0.06	0.07
total	99.81	99.80	99.76	99.77	99.77	99.76	99.76	99.74	99.78
XRF Trace elements (ppm) Ni	4.1	5.1	16.5	11.4	19.5	5.2	14.4	15.6	19.4
Cr	0.0	0.0	1.0	1.0	2.1	0.0	0.0	0.0	0.0
Sc	2.0	0.0	0.0	0.0	1.0	10.3	3.1	1.0	1.0
V	41	35	24	32	41	36	36	48	30
Ba	376	781	9	832	17	154	393	18	187
Rb	104	82	148	88	145	142	125	146	126
Sr	84	94	23	51	24	9	26	30	15
Zr	619	455	1101	546	1025	1000	897	1214	912
Y	37	31	59	45	57	56	50	55	52
Nb	177	136	307	177	294	285	260	330	267
Ga	27	23	29	23	30	30	29	32	26
Cu	0	0	4	1	0	0	0	4	4
Zn	94	89	168	120	164	163	156	174	150
Pb	5	6	10	8	11	14	9	10	11
La	110	100	174	127	185	164	150	185	156
Ce	224	158	272	202	284	269	272	310	265
Th	16	12	28	13	27	23	21	31	21
ICP-MS traces (ppm) La			166	120	174	131	143	163	155
Ce			262	202	283	219	243	277	255
Pr			24	21	26	21	23	23	24
Nd			74	71	85	69	75	70	78
Sm			12.3	12.4	14.3	11.8	12.8	11.6	13.1
Eu			2.7	3.5	3.1	2.8	3.1	2.5	3.2
Gd			9.7	9.2	11.1	8.9	9.7	9.2	10.0
Tb			1.6	1.4	1.8	1.5	1.5	1.6	1.6
Dy			9.9	8.1	10.7	9.1	9.1	9.4	9.6
Ho			2.0	1.5	2.1	1.8	1.7	1.9	1.8
Er			5.5	4.0	5.7	4.9	4.6	5.3	4.9
Tm			0.8	0.5	0.8	0.7	0.7	0.8	0.7
Yb			5.0	3.2	5.0	4.4	4.1	5.1	4.3
Lu			0.8	0.5	0.7	0.7	0.6	0.8	0.7
Ba			41	824	43	152	495	43	348
Th			26	13	26	23	20	31	23
Nb			304	173	306	297	249	328	268
Y			55	43	58	47	47	53	50
Hf			22	11	21	20	17	24	18
Ta			17	11	18	17	15	18	16
U			5.9	3.0	5.9	3.7	5.1	6.4	4.7
Pb			13	8	14	14	11	15	12
Rb			140	82	141	136	112	139	122
Cs			1.7	0.8	1.7	2.3	1.3	1.7	1.4
Sr			23	49	10	7	24	25	16
Sc			1.1	1.0	1.3	1.5	1.2	1.4	1.3
Zr			1063	519	1034	987	817	1179	901

Appendix A.
DHF Whole-rock data

ChemoUnit	DHF III	DHF III	DHF III	DHF III	DHF III	DHF III	DHF III	DHF III	DHF III
Member	Abrigo	Abrigo	Abrigo	Abrigo	Abrigo	Abrigo	Abrigo	Abrigo	Abrigo
sample #	TF00209	01TF173Nb	01TF174N	01TF2	01TF64N	01TF66N	01TF78N	01TF84N	TF00150A
XRF Major element oxides (Wt%)									
SiO2	61.46	60.65	60.78	60.77	59.56	60.35	59.90	60.49	60.12
Al2O3	18.71	18.77	18.93	18.82	18.73	18.49	18.25	19.18	18.94
TiO2	0.81	0.81	0.68	0.81	0.78	0.82	0.76	0.73	0.76
FeO*	2.98	2.82	2.90	2.86	2.94	2.82	2.51	2.93	3.09
MnO	0.23	0.19	0.25	0.18	0.20	0.19	0.16	0.22	0.22
CaO	0.84	1.72	0.64	1.45	0.84	1.71	0.82	0.77	1.58
MgO	0.64	0.52	0.42	0.42	1.28	0.99	0.34	0.35	0.48
K2O	4.92	5.52	5.29	5.76	5.52	5.77	5.45	5.62	5.72
Na2O	9.05	8.67	9.82	8.66	9.86	8.58	11.54	9.43	8.75
P2O5	0.12	0.12	0.06	0.10	0.09	0.10	0.10	0.08	0.10
total	99.76	99.78	99.78	99.82	99.79	99.82	99.84	99.78	99.77
XRF Trace elements (ppm) Ni	14.3	3.0	3.0	2.0	4.1	3.1	6.2	7.0	28.9
Cr	0.0	0.0	0.0	0.0	0.0	0.0	0.0	0.0	2.1
Sc	0.0	2.0	0.0	0.0	0.0	2.0	6.2	0.0	2.1
V	37	38	35	32	42	44	36	42	44
Ba	801	534	87	152	48	39	108	50	99
Rb	101	117	129	121	148	130	102	153	161
Sr	15	75	8	30	35	35	28	22	42
Zr	669	742	961	702	971	774	605	1009	1049
Y	44	37	52	44	50	50	36	46	51
Nb	207	199	281	196	248	217	177	265	266
Ga	22	27	30	25	27	23	26	29	30
Cu	1	0	0	0	0	0	0	0	1
Zn	130	102	151	108	129	118	91	124	137
Pb	7	6	8	18	13	13	4	12	14
La	130	124	151	107	130	141	100	146	143
Ce	237	204	283	197	225	238	218	257	240
Th	17	15	22	19	26	23	11	25	27
ICP-MS traces (ppm) La	153			118	138	132			138
Ce	242			206	233	238			226
Pr	22			20	22	24			21
Nd	66			69	72	82			68
Sm	10.9			12.0	12.5	14.7			11.4
Eu	1.9			2.6	2.3	2.8			2.3
Gd	8.6			9.1	9.6	10.8			8.9
Tb	1.5			1.4	1.5	1.7			1.5
Dy	8.9			8.0	8.9	9.5			8.6
Ho	1.8			1.5	1.7	1.8			1.7
Er	5.2			4.0	4.7	4.5			4.8
Tm	0.8			0.6	0.7	0.6			0.7
Yb	5.0			3.3	4.2	3.8			4.4
Lu	0.8			0.5	0.6	0.5			0.7
Ba	25			195	89	67			163
Th	31			17	23	18			25
Nb	297			190	247	214			256
Y	52			40	47	46			48
Hf	24			14	19	15			20
Ta	17			13	16	15			15
U	7.4			3.9	5.5	4.3			6.0
Pb	15			10	13	11			13
Rb	171			112	135	117			146
Cs	2.1			1.2	1.7	1.3			1.7
Sr	25			40	41	35			42
Sc	1.6			1.3	1.3	0.8			1.7
Zr	1172			657	898	715			984

Appendix A.
DHF Whole-rock data

ChemoUnit	DHF III	DHF III	DHF III	DHF III	DHF III	DHF III	DHF III	DHF III	DHF III
Member	Abrigo	Abrigo	Abrigo	Abrigo	Abrigo	Abrigo	Abrigo	Abrigo	Abrigo
sample #	TF00151A	TF00153B	TF00165A	TF00168A	TF00174B	TF00175A	TF00190A	TF00194A	TF00195A
XRF Major element oxides (Wt%)									
SiO2	60.00	60.13	59.87	58.03	62.08	58.01	59.86	58.03	59.02
Al2O3	18.81	19.20	18.98	18.51	18.88	18.40	19.05	18.49	18.80
TiO2	0.81	0.72	0.71	0.67	0.60	0.68	0.68	0.67	0.68
FeO*	3.11	3.10	3.04	2.92	3.15	2.91	3.06	2.89	2.98
MnO	0.21	0.24	0.23	0.22	0.24	0.22	0.24	0.23	0.23
CaO	2.13	0.78	1.36	4.07	0.73	4.18	1.38	4.25	2.21
MgO	0.59	0.43	0.46	0.59	0.97	0.62	0.42	0.46	0.42
K2O	5.58	5.68	5.72	5.60	5.50	5.66	5.79	5.48	5.71
Na2O	8.40	9.41	9.27	8.98	7.53	8.98	9.20	9.17	9.60
P2O5	0.12	0.07	0.12	0.15	0.06	0.10	0.06	0.10	0.09
total	99.76	99.75	99.76	99.75	99.73	99.75	99.75	99.76	99.76
XRF Trace elements (ppm) Ni	19.6	16.4	20.6	17.6	10.6	20.9	16.9	16.5	23.7
Cr	1.0	1.0	2.1	2.1	0.0	4.2	1.1	0.0	5.2
Sc	0.0	3.1	0.0	1.0	0.0	3.1	2.1	6.2	0.0
V	31	29	37	39	27	36	39	43	36
Ba	425	4	67	20	0	3	0	0	8
Rb	136	184	172	175	190	173	185	174	177
Sr	76	18	39	67	26	64	15	36	31
Zr	897	1229	1141	1219	1351	1163	1259	1168	1194
Y	46	52	51	53	83	52	53	51	52
Nb	232	303	282	292	314	289	308	288	295
Ga	28	30	27	32	34	31	31	29	31
Cu	2	1	0	2	5	0	2	0	2
Zn	127	153	141	149	153	144	151	145	142
Pb	10	15	12	15	20	11	16	11	11
La	138	163	156	146	172	157	162	172	155
Ce	224	267	240	247	279	270	270	252	255
Th	25	31	28	29	35	28	33	30	29
ICP-MS traces (ppm) La	122	138	132	150	94	136	146	148	145
Ce	203	223	213	236	156	219	229	232	247
Pr	19	20	20	21	15	20	20	21	24
Nd	65	63	63	64	47	63	61	63	81
Sm	11.0	10.8	10.8	10.8	8.1	10.7	10.1	10.5	14.1
Eu	2.8	1.8	2.0	1.8	1.4	1.9	1.7	1.8	3.8
Gd	8.6	8.7	8.7	8.8	6.1	8.6	8.0	8.2	10.4
Tb	1.4	1.5	1.5	1.5	1.1	1.5	1.4	1.4	1.6
Dy	7.9	9.4	8.9	9.6	7.1	9.0	8.4	8.6	9.4
Ho	1.5	1.9	1.8	2.0	1.5	1.8	1.7	1.7	1.8
Er	4.2	5.5	5.1	5.7	4.2	5.1	5.0	5.0	4.6
Tm	0.6	0.8	0.8	0.9	0.7	0.8	0.8	0.8	0.6
Yb	3.8	5.1	4.7	5.5	4.2	4.8	4.8	4.9	3.8
Lu	0.6	0.8	0.7	0.9	0.7	0.7	0.7	0.8	0.6
Ba	897	18	132	12	13	43	14	27	908
Th	20	31	27	34	24	28	27	27	17
Nb	210	284	256	304	308	269	281	280	227
Y	43	49	47	52	36	49	48	50	47
Hf	16	24	22	26	24	22	23	22	15
Ta	12	17	15	17	17	15	16	16	14
U	4.7	6.9	5.9	7.6	4.0	6.2	6.5	7.2	3.7
Pb	11	16	15	17	16	15	14	14	10
Rb	115	172	157	182	169	162	158	160	104
Cs	1.3	2.2	2.0	2.3	2.7	2.0	2.0	2.0	1.1
Sr	156	10	42	8	8	37	12	40	15
Sc	1.6	1.7	1.7	1.9	1.7	1.6	1.1	1.2	1.1
Zr	771	1209	1087	1326	1184	1150	1112	1101	713

Appendix A.
DHF Whole-rock data

ChemoUnit	DHF III	DHF III	DHF III	DHF III	DHF III	DHF III	DHF III	DHF III
Member	Abrigo	Abrigo	Abrigo	Abrigo	Abrigo	Abrigo	Abrigo	Abrigo
sample #	TF00177	TF00184	TF00189	TF00191	01TF59N	01TF7	01TF8	01TF60N
XRF Major element oxides (Wt%)								
SiO2	58.82	59.66	60.68	56.91	60.42	59.47	59.42	60.90
Al2O3	18.66	19.00	18.77	18.69	18.89	18.86	18.71	18.85
TiO2	0.68	0.70	0.93	1.39	1.05	1.17	1.14	1.01
FeO*	2.98	3.08	2.90	4.35	3.23	3.42	3.32	3.05
MnO	0.22	0.24	0.16	0.18	0.16	0.16	0.16	0.17
CaO	3.18	1.70	2.40	4.49	2.34	3.09	3.42	1.84
MgO	0.43	0.46	0.82	1.38	0.78	0.93	0.96	0.65
K2O	5.59	5.76	4.89	4.11	4.41	4.45	4.54	4.86
Na2O	9.12	9.06	7.92	7.67	7.96	7.74	7.66	8.06
P2O5	0.08	0.07	0.18	0.36	0.22	0.27	0.26	0.19
total	99.76	99.74	99.65	99.53	99.47	99.57	99.59	99.59
XRF Trace elements (ppm) Ni	13.5	29.1	15.1	0.0	3.0	0.0	0.0	3.1
Cr	0.0	5.4	2.0	0.0	0.0	0.0	1.0	0.0
Sc	1.0	6.5	1.0	0.0	5.1	2.0	0.0	2.0
V	42	31	43	60	48	67	65	49
Ba	0	0	2206	2761	3836	2738	2714	2722
Rb	174	183	76	80	66	73	69	80
Sr	31	25	204	754	405	503	364	271
Zr	1157	1247	415	485	380	437	399	462
Y	51	54	30	36	30	32	33	35
Nb	286	307	119	137	110	122	113	130
Ga	29	33	20	20	18	18	16	20
Cu	6	8	5	2	0	0	0	0
Zn	144	151	86	101	91	88	89	94
Pb	11	14	7	7	9	9	9	8
La	156	164	92	90	92	75	105	88
Ce	254	270	158	172	157	168	148	171
Th	28	31	11	10	12	13	13	12
ICP-MS traces (ppm) La	130	136	79	97	88	95	86	95
Ce	211	217	139	172	152	164	148	165
Pr	19	19	14	18	16	17	15	17
Nd	59	60	51	69	57	61	56	60
Sm	10.1	10.1	9.1	12.9	10.3	10.9	10.0	10.7
Eu	1.7	1.7	3.3	4.6	4.1	3.9	3.8	3.8
Gd	8.1	7.9	6.8	9.9	7.8	8.5	7.7	8.1
Tb	1.4	1.4	1.0	1.4	1.1	1.2	1.1	1.2
Dy	8.5	8.4	5.7	7.8	6.1	6.7	6.1	6.4
Ho	1.7	1.7	1.0	1.4	1.1	1.2	1.1	1.2
Er	4.8	5.0	2.7	3.5	2.7	3.1	2.8	3.1
Tm	0.7	0.7	0.4	0.5	0.4	0.4	0.4	0.4
Yb	4.7	4.7	2.3	2.7	2.2	2.5	2.3	2.4
Lu	0.7	0.7	0.3	0.4	0.3	0.4	0.3	0.4
Ba	31	16	2342	2959	3879	2660	2832	2939
Th	28	29	10	10	8	10	9	10
Nb	260	273	115	127	111	129	114	131
Y	47	48	28	37	29	32	29	32
Hf	22	22	8	9	7	9	8	9
Ta	15	15	7	8	7	8	7	8
U	7.6	7.2	2.1	3.1	2.0	2.4	2.1	2.5
Pb	15	14	7	7	6	7	6	7
Rb	160	166	74	65	62	72	64	74
Cs	1.9	2.0	0.7	1.3	0.6	0.7	0.7	0.7
Sr	25	18	199	862	440	497	429	335
Sc	1.6	1.7	1.2	2.3	1.3	2.1	2.2	1.3
Zr	1103	1201	421	412	356	425	374	429

Appendix A.
DHF Whole-rock data

ChemoUnit	DHF I Syenite	DHF I Syenite	DHF I Syenite	DHF I Syenite	DHF I Syenite	DHF I Syenite	DHF I Syenite	DHF I Syenite	DHF I Syenite
Member									
sample #	99TF-19A	99TF-19A	99TF-19B	99TF-19B	99TF-19C	99TF-19C	99TF-19D	99TF-19D	99TF-19E
XRF Major element oxides (Wt%)									
SiO2	56.40	56.40	59.27	59.27	59.80	59.80	59.41	59.41	58.05
Al2O3	22.01	22.01	22.73	22.73	22.68	22.68	22.79	22.79	21.69
TiO2	0.45	0.45	0.34	0.34	0.35	0.35	0.36	0.36	0.52
FeO*	2.37	2.37	2.41	2.41	2.62	2.62	1.98	1.98	2.55
MnO	0.20	0.20	0.15	0.15	0.22	0.22	0.13	0.13	0.24
CaO	1.15	1.15	0.93	0.93	0.31	0.31	1.21	1.21	0.95
MgO	0.17	0.17	0.16	0.16	0.18	0.18	0.24	0.24	0.22
K2O	5.61	5.61	5.97	5.97	6.13	6.13	5.89	5.89	5.34
Na2O	11.60	11.60	8.02	8.02	7.67	7.67	7.96	7.96	10.39
P2O5	0.05	0.05	0.02	0.02	0.02	0.02	0.04	0.04	0.06
total	100.00	100.00	100.00	100.00	100.00	100.00	100.00	100.00	100.00
XRF Trace elements (ppm)									
Ni	4.0	4.0	11.0	11.0	3.0	3.0	2.0	2.0	6.0
Cr	0.0	0.0	0.0	0.0	2.0	2.0	0.0	0.0	0.0
Sc	0.0	0.0	4.0	4.0	0.0	0.0	1.0	1.0	0.0
V	11	11	16	16	35	35	19	19	17
Ba									
Rb	263	263	272	272	282	282	216	216	251
Sr	70	70	45	45	56	56	58	58	60
Zr	2208	2208	2724	2724	1690	1690	913	913	2408
Y	24	24	93	93	26	26	17	17	24
Nb	280	280	299	299	221	221	163	163	385
Ga	40	40	43	43	42	42	34	34	42
Cu	0	0	3	3	0	0	6	6	0
Zn	92	92	70	70	123	123	59	59	107
Pb									
La									
Ce									
Th									
ICP-MS traces (ppm)									
La	98		55		58		67		114
Ce	105		84		70		84		120
Pr	7		7		5		6		7
Nd	17		19		12		16		18
Sm	2.6		4.1		2.1		2.4		2.5
Eu	0.6		1.0		0.4		0.5		0.5
Gd	2.2		5.0		2.0		1.9		2.0
Tb	0.4		1.2		0.4		0.3		0.4
Dy	3.0		10.4		3.3		2.3		2.8
Ho	0.8		3.1		0.9		0.5		0.7
Er	2.9		12.7		3.3		1.8		2.8
Tm	0.6		2.6		0.7		0.3		0.6
Yb	4.9		20.3		5.1		2.4		4.6
Lu	0.9		3.5		0.9		0.4		0.9
Ba	49		27		17		15		50
Th	58		26		34		26		65
Nb	300		325		227		173		378
Y	27		108		30		18		26
Hf	40		46		31		18		41
Ta	8		12		7		7		10
U	15.1		16.6		9.1		6.4		18.1
Pb	18		14		22		13		14
Rb	260		263		276		214		256
Cs	4.5		4.6		7.2		6.6		5.0
Sr	75		50		61		60		67
Sc	0.8		1.1		0.6		0.4		0.6
Zr	2142		2599		1602		927		2162

Appendix A.
DHF Whole-rock data

ChemoUnit	DHF I	DHF I	DHF I	DHF I	DHF I	DHF I	DHF I	DHF I	DHF I
Member	Syenite	Syenite	Syenite	Syenite	Syenite	Syenite	Syenite	Syenite	Syenite
sample #	99TF-19E	99TF-19F	99TF-19G	99TF-19H	99TF-19I	99TF-22A	99TF-22B	99TF-45W1	99TF-45W2
XRF Major element oxides (Wt%)									
SiO2	58.05	58.35	57.66	59.23	60.08	58.02	57.28	57.39	57.54
Al2O3	21.69	21.93	21.36	21.99	21.80	21.41	21.82	22.19	21.79
TiO2	0.52	0.33	0.47	0.39	0.44	0.41	0.47	0.38	0.50
FeO*	2.55	2.32	2.63	2.77	2.88	2.62	2.46	2.22	2.43
MnO	0.24	0.15	0.20	0.21	0.18	0.19	0.17	0.15	0.14
CaO	0.95	0.70	0.90	1.15	0.50	0.91	1.02	0.99	1.16
MgO	0.22	0.18	0.33	0.21	0.41	0.22	0.26	0.18	0.33
K2O	5.34	5.84	5.79	5.72	5.63	5.70	5.83	5.82	5.68
Na2O	10.39	10.15	10.60	8.31	8.06	10.47	10.63	10.62	10.35
P2O5	0.06	0.03	0.07	0.03	0.03	0.05	0.06	0.05	0.07
total	100.00	100.00	100.00	100.00	100.00	100.00	100.00	100.00	100.00
XRF Trace elements (ppm) Ni	6.0	2.0	2.0	2.0	4.0	5.0	2.0	3.0	3.0
Cr	0.0	0.0	0.0	0.0	0.0	0.0	0.0	0.0	0.0
Sc	0.0	2.0	2.0	2.0	3.0	0.0	1.0	0.0	4.0
V	17	19	21	21	32	27	21	8	30
Ba									
Rb	251	220	245	261	260	260	258	260	193
Sr	60	31	45	35	34	55	45	69	121
Zr	2408	1287	1592	1811	1624	2270	1795	1653	1130
Y	24	11	29	24	25	41	24	21	17
Nb	385	208	239	253	245	288	246	266	165
Ga	42	37	36	43	38	38	39	34	32
Cu	0	0	0	0	0	2	6	0	2
Zn	107	56	48	87	55	81	104	62	76
Pb									
La									
Ce									
Th									
ICP-MS traces (ppm) La									
Ce									
Pr									
Nd									
Sm									
Eu									
Gd									
Tb									
Dy									
Ho									
Er									
Tm									
Yb									
Lu									
Ba									
Th									
Nb									
Y									
Hf									
Ta									
U									
Pb									
Rb									
Cs									
Sr									
Sc									
Zr									

Appendix A.
DHF Whole-rock data

ChemoUnit	DHF I	DHF I	DHF I	DHF I	DHF I	DHF I	DHF I	DHF I
Member	Syenite	Syenite	Syenite	Syenite	Syenite	Syenite	Syenite	Syenite
sample #	99TF-45W3	99TF-45W4	99TF-45W6	99TF-45W5	99TF-45W7	99TF-45W8	99TF-45W9	T97-6
XRF Major element oxides (Wt%)								
SiO2	57.95	58.65	60.51	58.64	59.66	58.36	59.08	60.19
Al2O3	21.32	21.64	21.84	21.90	22.19	21.72	22.99	21.28
TiO2	0.36	0.34	0.57	0.41	0.29	0.35	0.37	0.48
FeO*	2.67	2.28	2.79	3.37	2.87	2.58	2.26	2.78
MnO	0.21	0.15	0.20	0.22	0.17	0.17	0.16	0.26
CaO	0.78	0.74	0.59	0.59	0.49	0.70	0.65	0.75
MgO	0.20	0.19	0.37	0.20	0.17	0.21	0.20	0.37
K2O	5.69	6.24	5.89	5.32	5.40	5.50	5.77	4.22
Na2O	10.79	9.74	7.17	9.33	8.73	10.39	8.48	9.55
P2O5	0.03	0.03	0.07	0.02	0.01	0.02	0.03	0.12
total	100.00	100.00	100.00	100.00	100.00	100.00	100.00	100.00
XRF Trace elements (ppm) Ni	3.0	4.0	3.0	5.0	5.0	5.0	3.0	8.0
Cr	0.0	0.0	0.0	0.0	0.0	0.0	0.0	4.0
Sc	2.0	0.0	0.0	6.0	4.0	3.0	1.0	1.0
V	13	7	46	24	24	6	16	48
Ba								
Rb	281	235	222	278	263	236	242	206
Sr	22	43	90	27	23	27	60	105
Zr	2047	1185	1625	2159	1866	1453	1399	2607
Y	28	18	31	36	28	18	23	36
Nb	299	181	271	233	322	208	207	302
Ga	39	34	36	45	42	39	39	43
Cu	3	1	2	0	4	3	1	0
Zn	59	50	111	96	84	56	72	67
Pb								
La								
Ce								
Th								
ICP-MS traces (ppm) La								
Ce								
Pr								
Nd								
Sm								
Eu								
Gd								
Tb								
Dy								
Ho								
Er								
Tm								
Yb								
Lu								
Ba								
Th								
Nb								
Y								
Hf								
Ta								
U								
Pb								
Rb								3
Cs								
Sr								
Sc								
Zr								

Appendix A.
DHF Whole-rock data

ChemoUnit	DHF I Syenite	DHF I Syenite	DHF I Syenite	DHF I Syenite	DHF I Syenite	DHF I Syenite	DHF I Syenite	DHF I Syenite	DHF I Syenite
Member									
sample #	DH97-33d(i)	DH97-33d(iii)	T97-1a	T97-1b	T97-1c	T97-6	TF00148B	TF00173C	TF00182A
XRF Major element oxides (Wt%)									
SiO2	57.52	58.56	59.40	58.26	59.36	60.19	58.44	57.61	59.56
Al2O3	20.94	22.03	21.80	22.14	22.80	21.28	22.23	21.59	21.68
TiO2	0.33	0.41	0.41	0.48	0.36	0.48	0.45	0.53	0.33
FeO*	4.23	2.72	2.42	2.58	1.89	2.78	2.41	2.88	2.43
MnO	0.24	0.22	0.13	0.19	0.11	0.26	0.15	0.25	0.15
CaO	2.99	0.82	1.08	1.27	0.82	0.75	1.27	2.36	1.43
MgO	0.81	0.27	0.34	0.45	0.32	0.37	0.32	0.49	0.37
K2O	6.13	5.99	6.05	5.73	6.02	4.22	5.44	5.60	4.83
Na2O	6.73	8.94	8.30	8.85	8.27	9.55	9.00	8.22	8.88
P2O5	0.07	0.05	0.07	0.05	0.05	0.12	0.06	0.08	0.04
total	100.00	100.00	100.00	100.00	100.00	100.00	99.76	99.61	99.70
XRF Trace elements (ppm) Ni	4.0	10.0	9.0	8.0	9.0	8.0	21.4	13.1	19.4
Cr	1.0	0.0	2.0	4.0	0.0	4.0	4.1	2.0	6.1
Sc	0.0	2.0	3.0	4.0	3.0	1.0	0.0	5.1	0.0
V	19	21	25	36	17	48	26	29	57
Ba							12	0	0
Rb	317	333	247	249	214	206	239	272	214
Sr	111	58	58	75	60	105	78	79	70
Zr	3705	3269	1709	1688	1103	2607	1396	2443	1967
Y	50	38	22	40	23	36	21	30	31
Nb	589	370	241	261	159	302	242	330	233
Ga	56	47	40	42	32	43	36	45	40
Cu	25	0	0	0	0	0	0	0	5
Zn	118	164	93	83	69	67	57	181	73
Pb							7	58	19
La							72	142	96
Ce							125	199	148
Th							41	90	60
ICP-MS traces (ppm) La	181	108	84	98	46	144	61	128	79
Ce	186	114	95	121	58	147	74	139	88
Pr	11	7	6	9	4	9	5	9	6
Nd	28	18	16	23	12	23	15	23	15
Sm	4.0	2.7	2.3	3.6	1.9	3.4	2.4	3.5	2.3
Eu	0.8	0.6	0.5	0.8	0.4	0.8	0.6	0.8	0.5
Gd	3.3	2.4	1.8	3.3	1.7	3.0	2.1	3.1	2.3
Tb	0.7	0.5	0.3	0.6	0.3	0.6	0.4	0.6	0.5
Dy	5.3	3.6	2.2	4.3	2.4	4.0	2.5	3.9	3.6
Ho	1.4	0.9	0.5	1.0	0.6	1.0	0.6	0.9	0.9
Er	5.7	3.4	1.6	3.6	2.3	3.5	2.1	3.3	3.7
Tm	1.2	0.7	0.3	0.7	0.5	0.7	0.4	0.6	0.7
Yb	9.9	5.2	2.1	4.9	3.6	5.4	3.1	4.6	5.7
Lu	1.7	0.9	0.4	0.8	0.6	0.9	0.5	0.8	1.0
Ba	43	24	35	46	55	59	55	39	21
Th	118	66	46	31	25	78	42	96	59
Nb	654	376	244	285	162	327	252	335	225
Y	51	31	16	34	19	34	19	30	31
Hf	64	55	30	33	20	45	25	46	34
Ta	13	9	7	10	6	7	7	9	6
U	36.0	16.6	13.0	9.3	7.6	23.8	8.9	20.8	14.0
Pb	30	31	25	11	17	37	11	59	22
Rb	314	318	229	238	203	196	225	267	202
Cs	5.7	7.0	6.3	3.8	5.9	7.8	3.9	5.4	6.7
Sr	106	52	53	72	57	96	72	70	58
Sc	2.0	1.5	0.6	1.1	0.3	1.9	1.8	2.9	2.0
Zr							1392	2750	2034

Appendix A.
DHF Whole-rock data

ChemoUnit	DHF I	DHF I	DHF I	DHF I	DHF III	DHF III	DHF III	DHF III	DHF III
Member	Syenite	Syenite	Syenite	Syenite	Syenite	Syenite	Syenite	Syenite	Syenite
sample #	TF76-S2/2	TF9946W2	TF9946W3	TF9946W5	01TF96N	01TF97N	01TF110N	01TF162N	DH99-79b
XRF Major element oxides (Wt%)									
SiO2	58.60	60.14	59.45	59.32	60.28	60.19	60.67	61.61	61.12
Al2O3	21.44	20.44	22.15	22.15	19.61	19.49	18.77	20.10	19.41
TiO2	0.31	0.37	0.47	0.43	0.61	0.69	0.67	0.64	0.71
FeO*	2.26	2.33	2.74	2.83	2.91	2.87	3.69	2.43	2.98
MnO	0.18	0.14	0.22	0.18	0.23	0.26	0.24	0.20	0.27
CaO	0.75	0.46	0.83	0.98	0.69	0.69	0.61	0.78	0.77
MgO	0.25	0.22	0.34	0.29	0.31	0.25	0.22	0.29	0.28
K2O	5.82	5.31	6.03	5.31	5.53	5.63	5.51	5.81	5.71
Na2O	10.36	10.57	7.73	8.48	9.55	9.62	9.32	7.90	8.70
P2O5	0.03	0.02	0.04	0.02	0.04	0.08	0.02	0.05	0.06
total	100.00	100.00	100.00	100.00	99.76	99.77	99.73	99.80	100.00
XRF Trace elements (ppm)									
Ni	5.0	2.0	3.0	4.0	4.0	4.0	4.0	3.0	7.0
Cr	0.0	2.0	0.0	0.0	0.0	0.0	0.0	0.0	0.0
Sc	1.0	1.0	0.0	5.0	2.0	0.0	2.0	3.0	0.0
V	8	47	25	33	51	48	55	43	38
Ba		0	0	2	9	8	0	40	
Rb	240	173	278	252	184	181	197	169	199
Sr	48	14	63	64	16	23	12	50	41
Zr	1817	632	2641	2098	1331	1200	1591	1010	1549
Y	28	14	33	29	43	45	49	40	63
Nb	250	119	351	241	282	256	349	234	372
Ga	38	30	47	42	30	31	29	31	35
Cu	1	0	1	2	0	0	0	0	0
Zn	57	33	100	104	118	95	48	47	121
Pb		6	31	22	13	14	10	12	
La		42	111	41	100	130	100	110	
Ce		87	183	123	194	210	203	221	
Th		10	73	41	27	27	30	26	
ICP-MS traces (ppm)									
La	100				107	132	113	133	181
Ce	110				174	191	181	211	275
Pr	8				16	17	16	19	26
Nd	19				46	51	47	58	80
Sm	2.8				7.8	8.4	7.7	9.5	13.9
Eu	0.6				1.3	1.4	1.3	1.6	2.3
Gd	2.3				6.5	6.7	6.7	7.4	10.7
Tb	0.5				1.2	1.1	1.3	1.2	1.9
Dy	3.3				7.7	6.6	8.7	7.4	12.1
Ho	0.8				1.7	1.4	1.9	1.5	2.5
Er	2.9				4.9	3.8	5.9	4.1	7.0
Tm	0.5				0.8	0.6	1.0	0.7	1.1
Yb	4.0				5.2	4.0	6.5	4.2	6.8
Lu	0.7				0.8	0.7	1.0	0.7	1.0
Ba	74				33	31	31	61	56
Th	54				24	26	27	24	40
Nb	246				304	255	355	257	395
Y	28				44	43	49	42	71
Hf	32				27	22	32	21	32
Ta	7				16	12	18	15	21
U	14.0				7.9	6.9	8.8	5.7	9.3
Pb	12				14	13	12	11	20
Rb	227				181	177	190	165	200
Cs	4.1				2.0	2.2	2.7	1.8	2.4
Sr	47				14	24	13	51	44
Sc	0.9				1.5	1.4	1.6	1.4	4.5
Zr	1710				1343	1119	1572	1023	1519

Appendix A.
DHF Whole-rock data

ChemoUnit	DHF III	DHF III	DHF III	DHF III	DHF III	DHF III	DHF III	DHF III	DHF III
Member	Syenite	Syenite	Syenite	Syenite	Syenite	Syenite	Syenite	Syenite	Syenite
sample #	TF00186	DH97-38b	TF00148A	DH97-38e	TF00148C	DH97-38d	DH97-38f	DH99-79a	DH97-38c
XRF Major element oxides (Wt%)									
SiO2	60.24	60.44	59.54	61.05	61.15	60.57	60.56	60.48	60.54
Al2O3	19.05	19.47	21.19	19.35	19.45	18.85	19.34	19.78	19.59
TiO2	0.75	0.67	0.35	0.75	0.60	0.72	0.72	0.67	0.72
FeO*	3.19	3.54	2.29	3.16	2.77	3.63	2.91	2.75	3.32
MnO	0.27	0.24	0.15	0.24	0.21	0.24	0.25	0.22	0.21
CaO	0.67	0.62	0.47	0.74	0.86	0.56	0.58	0.66	0.74
MgO	0.41	0.45	0.20	0.41	0.31	0.17	0.30	0.29	0.50
K2O	5.52	5.48	5.76	5.63	5.44	5.51	5.59	5.63	5.65
Na2O	9.56	9.05	9.88	8.59	8.93	9.71	9.70	9.45	8.65
P2O5	0.04	0.03	0.03	0.08	0.06	0.03	0.04	0.07	0.07
total	99.71	100.00	99.86	100.00	99.78	100.00	100.00	100.00	100.00
XRF Trace elements (ppm) Ni	13.0	4.0	13.0	7.0	19.2	7.0	7.0	3.0	6.0
Cr	0.0	1.0	0.0	3.0	2.0	2.0	0.0	0.0	0.0
Sc	2.0	0.0	2.0	2.0	3.0	1.0	3.0	0.0	3.0
V	34	41	32	45	34	44	34	32	44
Ba	0		18		28				
Rb	198	204	183	173	156	205	193	177	174
Sr	18	50	17	34	47	26	22	40	64
Zr	1501	1542	664	1258	1063	1575	1250	1052	1123
Y	62	47	22	46	45	37	64	44	42
Nb	362	372	160	307	264	395	314	266	285
Ga	33	35	30	34	32	35	33	30	31
Cu	0	0	3	0	3	4	1	1	0
Zn	131	100	49	59	79	64	89	75	53
Pb	18		5		11				
La	183		83		140				
Ce	276		123		236				
Th	38		14		27				
ICP-MS traces (ppm) La	158	153	75	165	142	142	207	138	154
Ce	247	235	110	268	220	220	321	219	255
Pr	22	20	9	23	20	19	28	20	22
Nd	66	58	26	69	59	54	85	64	67
Sm	11.5	8.7	3.8	10.8	9.4	7.4	13.9	10.8	10.7
Eu	1.9	1.5	0.7	1.7	1.6	1.2	2.2	1.8	1.7
Gd	9.3	6.6	3.1	8.3	7.4	5.4	11.0	8.2	7.4
Tb	1.6	1.3	0.5	1.4	1.3	1.0	1.8	1.4	1.3
Dy	10.2	8.2	3.5	8.5	7.9	5.9	10.9	8.5	8.0
Ho	2.1	1.8	0.7	1.7	1.6	1.3	2.2	1.7	1.6
Er	6.0	5.3	2.3	4.9	4.7	3.8	6.1	4.7	4.5
Tm	0.9	0.9	0.4	0.8	0.7	0.6	0.9	0.7	0.7
Yb	5.9	5.9	2.6	4.9	4.6	4.5	5.8	4.6	4.6
Lu	0.9	0.9	0.4	0.8	0.7	0.7	0.9	0.7	0.7
Ba	32	64	34	71	70	29	29	41	42
Th	40	24	18	28	29	23	33	29	24
Nb	359	398	168	338	287	415	346	284	307
Y	61	48	22	48	46	35	67	48	42
Hf	29	30	14	26	23	30	26	22	23
Ta	18	20	9	19	16	22	19	16	18
U	9.8	10.0	3.8	7.5	6.7	9.1	7.6	6.6	7.0
Pb	21	15	5	13	10	17	16	14	12
Rb	200	202	181	170	152	199	192	176	173
Cs	2.6	2.0	1.5	1.1	1.8	2.1	2.4	1.9	1.4
Sr	15	50	16	35	46	25	22	44	64
Sc	1.9	1.4	1.5	1.1	2.0	1.0	0.9	0.9	0.9
Zr	1571		673		1134			1065	

Appendix A.
DHF Whole-rock data

ChemoUnit	DHF III	DHF III	DHF III	DHF III	DHF III	DHF III	DHF III	DHF III	DHF III
Member	Syenite	Syenite	Syenite	Syenite	Syenite	Syenite	Syenite	Syenite	Syenite
sample #	DH97-38a	TF00116	01TF63N	TF00173A	01TF68N	DH99-79c	TF9946W4	TF9949W5	TF9949W2
XRF Major element oxides (Wt%)									
SiO2	60.26	61.01	59.66	61.47	60.21	61.74	60.29	59.96	59.89
Al2O3	19.24	19.52	19.46	19.29	18.97	19.04	19.43	19.32	19.24
TiO2	0.67	0.69	0.71	0.71	0.68	0.83	0.66	0.65	0.74
FeO*	3.45	2.85	2.82	3.27	3.00	2.96	2.99	3.01	3.10
MnO	0.27	0.21	0.22	0.25	0.18	0.19	0.22	0.22	0.27
CaO	0.68	0.76	0.72	0.77	1.01	0.72	0.73	0.52	0.58
MgO	0.48	0.38	0.33	0.46	0.38	0.30	0.33	0.28	0.30
K2O	5.43	5.65	5.62	5.32	5.67	6.04	5.63	5.60	5.62
Na2O	9.51	8.64	10.16	8.09	9.65	8.12	9.69	10.40	10.20
P2O5	0.03	0.06	0.06	0.07	0.06	0.06	0.03	0.03	0.06
total	100.00	99.77	99.78	99.71	99.81	100.00	100.00	100.00	100.00
XRF Trace elements									
(ppm) Ni	6.0	16.1	5.1	11.1	4.1	2.0	3.0	2.0	4.0
Cr	2.0	1.0	0.0	4.0	0.0	1.0	0.0	0.0	0.0
Sc	1.0	1.0	0.0	2.0	0.0	2.0	0.0	4.0	2.0
V	49	42	49	37	45	54	46	35	41
Ba		69	24	20	36		0	0	0
Rb	203	168	170	188	190	124	191	186	191
Sr	34	57	27	42	31	43	15	17	23
Zr	1626	1063	1056	1473	842	619	1203	1294	1293
Y	58	47	48	58	35	35	27	28	74
Nb	414	272	277	388	256	190	262	300	303
Ga	38	29	28	31	27	25	30	30	32
Cu	0	2	0	3	0	2	0	0	0
Zn	156	82	70	109	56	113	55	62	79
Pb		14	5	15	8		9	6	9
La		143	154	211	123		106	129	154
Ce		259	251	319	232		207	232	268
Th		27	29	37	23		22	27	37
ICP-MS traces									
(ppm) La	199	153	134	192	139	113			
Ce	304	249	217	294	234	199			
Pr	26	23	20	25	22	20			
Nd	78	71	62	75	66	68			
Sm	12.2	11.7	10.3	12.3	10.6	11.5			
Eu	2.0	2.0	1.7	1.9	1.7	2.0			
Gd	9.0	9.3	8.2	9.9	7.6	8.2			
Tb	1.8	1.5	1.4	1.7	1.2	1.4			
Dy	11.3	9.1	8.2	10.9	7.0	7.7			
Ho	2.5	1.8	1.6	2.2	1.4	1.5			
Er	7.4	5.1	4.6	6.2	3.5	3.7			
Tm	1.2	0.8	0.7	1.0	0.5	0.5			
Yb	7.6	4.9	4.3	6.2	3.3	3.0			
Lu	1.2	0.7	0.7	1.0	0.5	0.4			
Ba	38	96	37	52	54	77			
Th	29	29	27	41	20	14			
Nb	465	299	297	389	270	203			
Y	66	51	45	58	33	39			
Hf	34	23	21	30	18	13			
Ta	24	18	18	21	19	16			
U	11.0	6.4	5.9	9.2	4.8	3.4			
Pb	21	14	5	16	9	8			
Rb	203	165	167	184	177	124			
Cs	3.4	1.8	1.0	2.1	2.4	1.0			
Sr	34	57	30	35	31	44			
Sc	1.6	1.8	1.8	1.8	1.0	0.9			
Zr		1134	1053	1588	816	605			

Appendix A.
DHF Whole-rock data

ChemoUnit	DHF III	DHF III	DHF III	DHF III	DHF III	DHF III	DHF III	DHF III	DHF III
Member	Syenite	Syenite	Syenite	Syenite	Syenite	Syenite	Syenite	Syenite	Syenite
sample #	TF9949W4	TF9949W3	TF9946W1	TF9939SY	TF9949W6	TF9965	TF9949W1	TF9940	TF9939V
XRF Major element oxides (Wt%)									
SiO2	60.28	60.03	61.87	62.79	60.34	54.22	59.89	60.69	61.33
Al2O3	19.58	18.97	19.04	16.96	19.46	20.10	19.32	16.49	17.10
TiO2	0.47	0.71	0.84	1.10	0.71	1.25	0.69	1.09	1.07
FeO*	2.77	3.01	2.94	3.79	2.92	5.43	2.92	4.61	4.21
MnO	0.15	0.24	0.21	0.32	0.20	0.29	0.21	0.37	0.28
CaO	0.61	0.67	0.83	0.64	0.71	3.13	0.67	0.73	1.05
MgO	0.27	0.36	0.37	0.63	0.31	0.81	0.32	0.56	0.79
K2O	5.74	5.60	5.95	5.26	5.63	4.86	5.62	5.02	4.67
Na2O	10.09	10.36	7.88	8.35	9.64	9.72	10.31	10.32	9.32
P2O5	0.03	0.06	0.08	0.16	0.06	0.18	0.04	0.12	0.19
total	100.00	100.00	100.00	100.00	100.00	100.00	100.00	100.00	100.00
XRF Trace elements (ppm) Ni	3.0	2.0	3.0	1.0	5.0	3.0	4.0	6.0	3.0
Cr	0.0	0.0	0.0	0.0	0.0	1.0	0.0	0.0	0.0
Sc	0.0	0.0	3.0	0.0	0.0	4.0	0.0	0.0	2.0
V	38	36	42	23	30	65	46	33	34
Ba	0	2	3	455	7	0	0	53	541
Rb	180	180	126	130	174	173	173	168	122
Sr	14	22	18	56	37	49	23	42	138
Zr	776	1173	1058	827	1078	1456	1044	1276	888
Y	24	50	52	45	41	39	47	88	65
Nb	184	279	263	207	275	372	278	350	247
Ga	30	27	29	30	31	31	29	30	28
Cu	2	1	5	2	2	5	2	2	1
Zn	61	83	104	112	117	124	74	230	170
Pb	5	9	10	10	12	14	6	13	10
La	111	162	136	97	133	144	134	192	149
Ce	200	268	285	200	223	260	245	367	265
Th	16	24	30	20	26	40	30	27	18
ICP-MS traces (ppm) La									
Ce									
Pr									
Nd									
Sm									
Eu									
Gd									
Tb									
Dy									
Ho									
Er									
Tm									
Yb									
Lu									
Ba									
Th									
Nb									
Y									
Hf									
Ta									
U									
Pb									
Rb									
Cs									
Sr									
Sc									
Zr									

Appendix B

Electron microprobe data for Fasnia Member glasses

Appendix B. Fasnia Glasses electron microprobe data

Sample ID	01TF122B_ 204	01TF122B_ 205	01TF122B_ 206	01TF122B_ 207	01TF122B_ 211	01TF122B_ 212	01TF122B_ 213	01TF122B_ 214
Na2O	7.73	8.13	7.61	7.69	9.03	7.96	8.98	9.19
MgO	0.41	0.29	0.32	0.38	0.26	0.48	0.26	0.88
Al2O3	19.53	19.99	19.97	20.00	21.33	20.19	21.39	20.80
SiO2	59.16	59.74	59.51	59.89	58.56	57.85	58.68	57.59
FeO	2.27	2.05	2.00	2.14	2.68	2.78	2.34	3.14
CaO	1.30	1.37	1.27	1.37	1.30	1.46	1.14	2.29
TiO2	0.77	0.68	0.66	0.59	0.60	0.94	0.51	0.73
K2O	6.05	6.29	6.68	6.08	5.76	5.80	5.99	5.37
MnO	0.18	0.06	0.13	0.11	0.15	0.08	0.15	0.22
Oxide total	97.39	98.61	98.16	98.25	99.66	97.55	99.44	100.21

Appendix B. Fasnia Glasses electron microprobe data

Sample ID	01TF122B_ 216	05TF82A2_ 217	05TF82A2_ 218	05TF82A2_ 219	05TF82A2_ 220	05TF82A2_ 221	05TF82A2_ 226	05TF82A2_ 227
Na2O	8.34	7.88	7.73	7.60	7.55	7.98	8.27	8.43
MgO	0.57	0.52	0.56	0.79	0.51	0.53	0.59	0.47
Al2O3	20.20	19.91	19.71	19.56	19.89	19.81	19.76	19.92
SiO2	58.00	59.70	60.15	58.52	59.50	59.37	59.68	59.58
FeO	3.08	2.66	2.60	3.04	2.47	2.46	3.01	2.51
CaO	1.76	1.68	1.67	2.32	1.41	1.78	2.16	1.33
TiO2	1.00	0.85	0.83	0.97	0.79	0.81	0.92	0.90
K2O	6.15	5.44	5.61	5.28	5.83	5.30	5.05	5.86
MnO	0.11	0.17	0.13	0.15	0.12	0.11	0.08	0.13
Oxide total	99.22	98.80	98.98	98.24	98.07	98.14	99.50	99.14

Appendix B. Fasnia Glasses electron microprobe data

Sample ID	05TF82A2_ 228	99TF8b 229	99TF8b 230	99TF8b 231	99TF8b 232	99TF8b 235	99TF8b 236	99TF8b 237	99TF8b 238	99TF8b 240	99TF8Dc_ 192
Na2O	8.07	7.69	7.54	7.61	7.72	8.35	10.08	9.85	10.05	9.88	8.17
MgO	0.48	0.36	0.36	0.35	0.33	0.39	0.15	0.13	0.20	0.12	0.53
Al2O3	19.56	19.92	20.70	20.18	20.04	20.34	22.20	22.15	22.06	21.97	19.97
SiO2	59.09	59.84	60.04	58.98	59.92	60.13	58.26	58.83	58.61	58.06	59.03
FeO	2.59	2.41	2.43	2.40	2.36	2.74	2.41	2.27	2.46	2.28	2.62
CaO	1.20	0.98	1.41	1.08	1.03	1.32	0.60	0.66	0.61	0.61	1.58
TiO2	0.83	0.66	0.66	0.67	0.65	0.66	0.32	0.28	0.29	0.27	0.82
K2O	6.25	6.08	6.09	6.56	6.31	5.85	5.51	5.54	5.55	5.69	4.88
MnO	0.17	0.17	0.09	0.13	0.05	0.12	0.19	0.27	0.19	0.17	0.14
Oxide total	98.24	98.12	99.33	97.95	98.39	99.90	99.72	99.98	100.02	99.06	97.73

Appendix B. Fasnia Glasses electron microprobe data

Sample ID	99TF8Dc_ 194	99TF8Dc_ 198	99TF8Dc_ 199	99TF8Dc_ 200	99TF8Dc_ 201	99TF8Dc_ 284	99TF8Dc_ 282	99TF8Dc_ 287	99TF8Dc_ 281
Na2O	7.80	8.13	8.22	7.99	7.94	7.47	7.16	7.57	7.41
MgO	0.60	0.51	0.54	0.45	0.49	0.47	0.52	0.48	0.53
Al2O3	19.72	19.64	19.51	19.67	19.64	19.74	19.64	19.74	19.79
SiO2	58.93	59.07	59.08	59.13	59.24	58.80	59.11	59.05	59.71
FeO	2.83	2.42	2.05	2.53	2.55	2.67	2.86	2.30	2.64
CaO	2.03	1.22	1.38	1.22	1.30	1.14	1.38	1.15	1.34
TiO2	0.86	0.83	0.84	0.85	0.86	0.76	0.92	0.84	0.90
K2O	5.24	5.86	5.53	5.97	5.98	6.36	5.91	6.41	5.89
MnO	0.15	0.14	0.60	0.15	0.12	0.15	0.13	0.14	0.16
Oxide total	98.17	97.82	97.74	97.96	98.13	97.56	97.63	97.67	98.38

Appendix B. Fasnia Glasses electron microprobe data

Sample ID	99TF8Dc_286	99TF8Dc_304	99TF8Dc_280	99TF8Dr_184	99TF8Dr_187	99TF8Dr_188	99TF8Dr_189	99TF8Dr_190	99TF8Dr_196
Na2O	7.40	7.69	7.14	9.16	10.03	10.02	9.98	10.21	9.85
MgO	0.44	0.58	0.53	0.16	0.17	0.16	0.17	0.15	0.14
Al2O3	19.97	19.73	19.82	22.29	22.06	22.09	21.91	21.84	21.80
SiO2	59.79	59.54	60.34	57.97	57.92	58.07	58.28	57.87	57.37
FeO	2.73	2.85	2.76	2.21	1.98	2.32	2.43	2.31	1.91
CaO	1.23	2.11	1.52	0.65	0.60	0.58	0.68	0.65	0.56
TiO2	0.86	0.89	0.86	0.27	0.26	0.30	0.28	0.28	0.27
K2O	6.37	5.48	5.91	5.90	5.44	5.88	5.76	5.07	5.02
MnO	0.15	0.09	0.13	0.23	0.24	0.21	0.19	0.17	0.14
Oxide total	98.95	98.96	99.01	98.84	98.69	99.64	99.69	98.56	97.06

Appendix B. Fasnia Glasses electron microprobe data

Sample ID	99TF8Dr_191	99TF8Dr_294	99TF8Dr_305	99TF8Dr_300	99TF8Dr_293	99TF8Dr_297	00TF171Wa_321	00TF171Wa_318	00TF171Wa_317
Na2O	10.12	8.82	9.03	9.80	9.29	9.50	8.21	8.12	9.02
MgO	0.16	0.16	0.17	0.15	0.15	0.15	0.24	0.21	0.21
Al2O3	22.33	21.78	22.07	22.30	22.26	22.31	21.32	22.05	21.99
SiO2	58.44	57.34	57.97	58.21	58.61	58.57	57.89	57.47	57.85
FeO	2.42	2.30	2.32	2.27	2.38	2.39	2.28	2.25	2.22
CaO	0.66	0.50	0.78	0.54	0.61	0.61	0.75	0.70	0.80
TiO2	0.26	0.25	0.32	0.31	0.30	0.27	0.34	0.36	0.40
K2O	5.29	5.33	5.82	5.31	5.57	5.84	5.47	5.68	5.49
MnO	0.19	0.23	0.21	0.22	0.20	0.22	0.20	0.21	0.23
Oxide total	99.87	96.72	98.69	99.10	99.37	99.86	96.69	97.06	98.22

Appendix B. Fasnia Glasses electron microprobe data

Sample ID	00TF171Wa_ 323	00TF171Wa_ 309	00TF171Wa_ 311	00TF171Wa_ 308	00TF171Wa_ 315	00TF171Wa_ 310	00TF171Wa_ 307
Na2O	9.48	9.45	9.20	8.71	8.49	9.15	8.97
MgO	0.22	0.17	0.21	0.20	0.18	0.20	0.20
Al2O3	21.92	21.72	22.00	22.32	21.83	21.95	22.12
SiO2	57.62	58.11	58.31	58.26	59.16	58.48	58.89
FeO	2.32	2.20	2.21	2.34	2.47	2.57	2.25
CaO	0.70	0.76	0.71	0.74	0.77	0.77	0.81
TiO2	0.37	0.37	0.31	0.29	0.40	0.40	0.35
K2O	5.52	5.63	5.58	5.91	5.59	5.73	5.68
MnO	0.18	0.19	0.20	0.17	0.20	0.20	0.28
Oxide total	98.35	98.58	98.74	98.94	99.09	99.45	99.55

Appendix B. Fasnia Glasses electron microprobe data

Sample ID	00TF171Wa_ 306	03TF16_ 333	03TF16_ 342	03TF16_ 343	03TF16_ 347	03TF16_ 344	03TF16_ 332	03TF16_ 331	03TF16_ 327	03TF16_ 326
Na2O	9.54	8.69	8.52	8.17	8.77	8.78	8.52	8.86	9.03	8.14
MgO	0.20	0.23	0.25	0.23	0.28	0.21	0.23	0.22	0.23	0.24
Al2O3	21.96	20.93	21.61	21.26	21.49	21.47	21.44	21.50	21.79	21.82
SiO2	58.89	57.51	57.58	58.54	57.76	57.97	58.67	58.76	57.89	59.28
FeO	2.40	2.11	2.18	2.15	2.49	2.53	2.04	2.07	2.45	2.27
CaO	0.72	0.80	0.75	0.90	0.98	0.81	0.80	0.93	0.81	0.78
TiO2	0.31	0.44	0.40	0.44	0.43	0.40	0.44	0.44	0.48	0.43
K2O	5.54	5.59	5.62	5.64	5.60	6.01	6.10	5.63	6.02	5.87
MnO	0.17	0.19	0.22	0.22	0.20	0.19	0.19	0.23	0.22	0.22
Oxide total	99.72	96.50	97.13	97.53	98.00	98.37	98.42	98.62	98.93	99.05

Appendix B. Fasnia Glasses electron microprobe data

Sample ID	03TF16_ 337	03TF16_ 328	03TF16_ 340	03TF16_ 350	03TF16_ 336	03TF16_ 345	03TF16_ 339	03TF16_ 324	03TF16_ 325	03TF13_ 370	03TF13_ 373
Na2O	8.67	8.65	8.63	9.22	8.97	9.56	8.78	9.40	9.04	7.12	7.41
MgO	0.24	0.25	0.27	0.22	0.25	0.20	0.22	0.26	0.24	0.42	0.44
Al2O3	21.78	21.83	21.30	21.76	21.66	21.58	21.97	21.77	21.53	19.92	20.05
SiO2	58.83	58.69	59.43	58.54	58.98	58.78	59.19	58.73	59.30	58.06	59.21
FeO	2.51	2.30	2.30	2.25	2.36	2.47	2.35	2.31	2.42	2.48	2.24
CaO	0.87	0.76	0.88	0.75	0.80	0.79	0.76	0.83	0.80	1.29	1.28
TiO2	0.44	0.43	0.52	0.30	0.43	0.40	0.41	0.41	0.46	0.71	0.71
K2O	5.71	6.23	5.85	6.29	5.91	5.56	5.88	5.77	5.94	6.11	5.66
MnO	0.14	0.18	0.18	0.15	0.18	0.22	0.07	0.20	0.16	0.13	0.04
Oxide total	99.18	99.30	99.36	99.47	99.53	99.57	99.64	99.68	99.88	96.23	97.02

Appendix B. Fasnia Glasses electron microprobe data

Sample ID	**03TF13_** 374	**03TF13_** 360	**03TF13_** 368	**03TF13_** 358	**03TF13_** 369	**03TF13_** 367	**03TF13_** 362	**03TF13_** 371	**03TF13_** 364	**03TF13_** 359	**03TF13_** 354
Na2O	7.50	7.55	7.37	6.88	7.47	7.05	7.42	7.17	7.37	6.98	7.81
MgO	0.42	0.39	0.43	0.43	0.40	0.36	0.37	0.42	0.39	0.34	0.41
Al2O3	20.10	19.95	20.04	20.09	20.13	20.44	20.27	20.25	20.28	20.11	20.31
SiO2	58.94	59.06	59.27	59.13	59.03	59.18	59.10	59.31	59.01	59.87	59.29
FeO	2.28	2.06	2.33	2.37	2.30	2.37	2.25	2.47	2.51	2.37	2.36
CaO	1.25	1.18	1.11	1.28	1.35	1.28	1.36	1.21	1.26	1.10	1.16
TiO2	0.72	0.63	0.75	0.70	0.65	0.71	0.67	0.72	0.69	0.65	0.73
K2O	6.01	6.42	5.94	6.43	6.20	6.21	6.19	6.05	6.35	6.57	6.08
MnO	0.12	0.11	0.10	0.14	0.13	0.11	0.18	0.26	0.14	0.14	0.03
Oxide total	97.33	97.33	97.34	97.45	97.65	97.71	97.80	97.87	98.00	98.14	98.17

Appendix B. Fasnia Glasses electron microprobe data

Sample ID	03TF13_ 363	03TF13_ 357	03TF13_ 355	03TF13_ 356	99TF8D_ 185	99TF8D_ 186	99TF8D_ 193	99TF8D_ 195	99TF8D_ 197	01TF122B_ 210
Na2O	7.49	7.08	7.59	7.75	11.28	9.55	7.06	2.29	6.79	7.76
MgO	0.42	0.43	0.42	0.39	0.20	0.18	0.53	1.23	1.00	0.73
Al2O3	20.32	20.46	20.53	20.34	23.05	21.01	18.37	14.21	18.91	19.63
SiO2	59.42	59.92	59.34	59.82	59.36	54.33	55.03	42.93	56.31	56.53
FeO	2.44	2.58	2.32	2.33	2.52	2.22	2.66	6.17	4.10	3.99
CaO	1.38	1.24	1.29	1.24	0.63	0.54	2.12	2.51	3.43	2.18
TiO2	0.70	0.70	0.71	0.66	0.28	0.25	0.73	3.72	1.36	1.11
K2O	5.87	5.90	6.07	6.19	5.81	5.32	4.77	3.55	3.76	5.42
MnO	0.22	0.08	0.21	0.09	0.19	0.17	0.12	5.50	0.07	0.14
Oxide total	98.25	98.39	98.48	98.81	103.34	93.57	91.39	82.10	95.73	97.49

Appendix B. Fasnia Glasses electron microprobe data

Sample ID	01TF122B_ 202	01TF122B_ 203	01TF122B_ 208	01TF122B_ 209	01TF122B_ 215	05TF82A2_ 222	05TF82A2_ 223	05TF82A2_ 224
Na2O	7.55	7.39	7.52	2.68	7.07	6.09	1.42	6.96
MgO	0.03	0.73	0.43	12.48	0.69	2.19	9.32	1.31
Al2O3	21.46	20.39	19.84	13.61	21.23	20.70	11.49	21.50
SiO2	61.81	57.98	58.82	37.22	57.64	52.65	40.73	56.09
FeO	0.31	3.50	2.29	11.23	2.87	4.16	9.13	3.36
CaO	2.48	3.84	1.25	12.42	4.52	6.55	20.09	6.44
TiO2	0.10	1.12	0.76	6.96	0.95	1.45	4.99	0.84
K2O	4.48	2.97	5.88	0.96	2.62	1.87	0.51	1.56
MnO	0.02	0.03	0.06	0.12	0.08	0.15	0.17	0.07
Oxide total	98.25	97.92	96.85	97.69	97.66	95.81	97.86	98.13

Appendix B. Fasnia Glasses electron microprobe data

Sample ID	05TF82A2_ 225	99TF8b 233	99TF8b 234	99TF8b 239	99TF8b 241	99TF8b 242	99TF8Dc_ 283	99TF8Dc_ 289	99TF8Dc_ 285	99TF8Dc_ 279
Na2O	5.81	8.43	3.64	6.96	7.08	8.31	6.49	6.84	6.98	5.69
MgO	2.18	1.34	9.11	0.21	0.16	0.15	0.51	0.48	0.47	0.54
Al2O3	17.59	19.53	13.75	18.41	21.78	21.40	19.49	19.85	19.99	19.80
SiO2	50.68	53.89	42.88	48.21	57.68	55.56	58.19	58.11	57.88	59.64
FeO	6.59	5.17	9.10	2.21	2.39	2.05	2.66	2.47	2.66	2.59
CaO	9.50	3.32	13.38	0.71	0.56	0.58	1.26	1.44	1.37	1.51
TiO2	2.43	1.41	4.60	0.28	0.28	0.29	0.79	0.91	0.83	0.85
K2O	1.28	4.79	1.59	4.71	5.56	5.62	5.80	6.12	6.03	5.74
MnO	0.15	0.19	0.15	0.17	0.22	0.18	0.14	0.05	0.17	0.17
Oxide total	96.22	98.08	98.20	81.86	95.71	94.14	95.32	96.26	96.37	96.55

Appendix B. Fasnia Glasses electron microprobe data

Sample ID	99TF8Dc_288	99TF8Dr_302	99TF8Dr_303	99TF8Dr_292	99TF8Dr_296	99TF8Dr_291	99TF8Dr_298	99TF8Dr_295	99TF8Dr_290
Na2O	6.93	6.96	0.26	7.75	7.29	7.85	8.08	8.75	8.31
MgO	0.56	0.55	0.13	0.14	0.14	0.18	0.17	0.15	0.15
Al2O3	19.86	19.48	2.08	18.98	19.25	19.58	20.17	20.94	20.83
SiO2	58.28	58.52	6.70	50.22	50.45	51.63	53.11	54.94	55.36
FeO	2.65	2.85	0.18	1.92	1.88	2.25	2.17	2.14	2.32
CaO	1.30	2.07	0.29	0.45	0.56	0.53	0.53	0.61	0.53
TiO2	0.78	0.82	0.12	0.25	0.25	0.26	0.27	0.28	0.29
K2O	6.26	5.31	0.53	4.85	5.01	5.28	5.08	5.51	5.66
MnO	0.16	0.10	0.02	0.17	0.22	0.17	0.21	0.25	0.24
Oxide total	96.80	96.66	10.32	84.73	85.05	87.74	89.78	93.57	93.69

Appendix B. Fasnia Glasses electron microprobe data

Sample ID	99TF8Dr_ 301	99TF8Dr_ 299	00TF171Wa_ 320	00TF171Wa_ 316	00TF171Wa_ 313	00TF171Wa_ 322	00TF171Wa_ 314	00TF171Wa_ 312
Na2O	10.17	10.22	3.01	4.90	4.19	7.29	7.83	7.52
MgO	0.19	0.24	0.18	0.19	0.23	0.21	0.23	0.33
Al2O3	22.58	22.30	13.07	15.80	16.41	19.70	21.29	20.84
SiO2	58.44	58.99	35.96	42.50	45.22	52.86	57.07	58.64
FeO	2.50	2.26	1.55	1.75	1.75	2.19	2.13	2.27
CaO	0.75	0.67	0.46	0.55	0.57	0.68	0.70	0.81
TiO2	0.33	0.31	0.28	0.24	0.27	0.32	0.34	0.34
K2O	5.91	6.02	4.19	4.28	4.56	5.32	5.65	5.48
MnO	0.17	0.18	0.00	0.10	0.15	0.19	0.18	0.21
Oxide total	101.03	101.19	58.70	70.32	73.34	88.77	95.42	96.43

Appendix B. Fasnia Glasses electron microprobe data

Sample ID	00TF171Wa_319	03TF16_334	03TF16_329	03TF16_330	03TF16_341	03TF16_338	03TF16_335	03TF16_346	03TF16_349	03TF16_348
Na2O	9.18	5.63	6.98	8.54	8.45	8.42	7.57	9.20	9.77	10.26
MgO	0.18	0.28	0.20	0.27	0.22	0.29	0.23	0.31	0.19	0.21
Al2O3	22.13	18.94	19.08	20.72	20.80	20.91	21.28	21.80	22.39	22.54
SiO2	58.87	50.87	51.24	56.21	56.16	56.51	58.02	59.48	58.54	59.96
FeO	2.42	2.08	2.15	2.40	2.14	2.32	2.06	2.31	2.06	2.15
CaO	0.76	0.67	0.73	0.73	0.81	0.77	0.76	0.97	0.79	0.65
TiO2	0.39	0.36	0.39	0.41	0.43	0.42	0.45	0.37	0.33	0.33
K2O	6.04	5.22	4.93	5.48	5.86	5.55	5.55	5.40	6.07	5.78
MnO	0.21	0.21	0.15	0.18	0.19	0.19	0.09	0.24	0.21	0.18
Oxide total	100.17	84.27	85.84	94.94	95.07	95.37	96.02	100.09	100.34	102.06

Appendix B. Fasnia Glasses electron microprobe data

Sample ID	03TF110_ 351	03TF110_ 352	03TF110_ 353	03TF13_ 361	03TF13_ 366	03TF13_ 365	03TF13_ 372
Na2O	6.23	5.42	1.48	7.08	7.36	5.54	6.63
MgO	0.27	0.28	0.16	0.00	0.42	0.45	0.39
Al2O3	20.76	19.97	6.21	20.67	20.21	20.34	20.13
SiO2	55.14	51.61	16.92	63.14	58.79	59.44	59.21
FeO	2.22	2.24	0.78	0.33	2.11	2.18	2.45
CaO	0.69	0.72	0.27	2.00	1.08	1.51	1.17
TiO2	0.38	0.35	0.17	0.09	0.71	0.64	0.73
K2O	6.50	5.91	2.03	5.05	5.47	6.16	6.29
MnO	0.18	0.16	0.08	0.08	0.14	0.17	0.04
Oxide total	92.36	86.68	28.09	98.45	96.28	96.43	97.04

Appendix C

LA-ICP-MS data for Fasnia Member glasses

Appendix C.
Fasnia
Glasses
LA-ICP-MS
data

Sample ID	05TF88_1	05TF88_2	05TF88_3	05TF88_4	05TF88_5	05TF88_6	05TF88_7	05TF88_8
Unit	Santo Ig.	Santo Ig.	Santo Ig.	Santo Ig.	Santo Ig.	Santo Ig.	Santo Ig.	Santo Ig.
(ppm) Ca	0.44	0.34	0.41	0.16	0.27	0.56	0.38	0.33
Sc	5.79	6.15	6.14	4.82	5.95	6.53	5.65	5.79
Ti	2,494	2,667	2,415	2,529	2,631	2,694	2,608	2,741
Rb	280	270	288	256	256	272	270	273
Sr	26.5	6.0	19.3	3.4	2.1	22.6	12.5	8.2
Y	18.3	37.9	18.8	37.7	38.8	19.2	29.2	37.4
Zr	1,337	1,311	1,394	1,275	1,341	1,346	1,354	1,370
Nb	277	437	280	425	440	280	369	437
Cs	3.78	3.33	3.72	3.08	2.91	3.66	3.62	3.42
Ba	57.9	9.2	45.8	5.0	1.8	50.0	27.1	14.2
La	86	148	87	146	150	87	128	146
Ce	126	244	124	241	246	129	200	240
Pr	8.3	16.8	7.9	17.1	17.1	8.5	13.9	16.8
Nd	21.9	45.6	21.6	46.0	46.4	22.9	39.1	46.3
Sm	2.58	5.86	2.79	6.28	6.26	3.07	5.30	6.24
Eu	0.59	1.05	0.49	1.02	1.00	0.65	0.84	0.99
Gd	2.71	6.02	2.67	5.71	6.08	2.92	4.98	6.19
Tb	0.38	0.90	0.40	0.89	0.92	0.40	0.77	0.92
Dy	2.59	5.70	2.51	5.77	5.76	2.58	4.68	5.95
Ho	0.61	1.28	0.61	1.36	1.30	0.62	1.06	1.38
Er	1.97	3.96	1.99	4.09	4.10	1.97	3.28	4.08
Tm	0.34	0.64	0.35	0.64	0.64	0.36	0.51	0.61
Yb	2.77	4.45	2.80	4.48	4.49	2.87	3.97	4.39
Lu	0.51	0.69	0.49	0.67	0.73	0.51	0.61	0.77
Hf	21.6	23.0	22.0	22.9	23.6	21.1	22.9	25.1
Ta	7.80	16.13	7.40	15.75	15.72	7.55	12.56	16.48
Pb	22.1	27.0	24.6	26.1	25.3	22.2	24.2	26.7
Th	40.5	33.6	41.2	34.4	33.1	39.4	35.5	35.2
U	14.6	11.4	14.5	10.9	11.0	14.8	12.0	11.5

Appendix C.
Fasnia
Glasses
LA-ICP-MS
data

Sample ID	05TF88_9	05TF88_10	05TF88_11	05TF88_12	05TF88_13	05TF88_14	05TF88_15	05TF88_16
Unit	Santo Ig.	Santo Ig.	Santo Ig.	Santo Ig.	Santo Ig.	Santo Ig.	Santo Ig.	Santo Ig.
(ppm) Ca	0.41	0.37	0.43	0.41	0.40	0.46	0.34	0.44
Sc	6.43	6.09	6.06	6.20	6.59	5.44	5.50	5.58
Ti	2,780	2,591	2,426	2,470	2,310	2,479	2,232	2,452
Rb	286	270	278	271	289	275	297	275
Sr	5.3	12.2	17.6	21.7	17.0	17.7	15.9	34.1
Y	41.6	27.6	18.6	18.1	18.1	20.4	18.5	18.1
Zr	1,409	1,304	1,382	1,340	1,426	1,523	1,382	1,290
Nb	460	348	284	282	290	286	279	265
Cs	3.43	3.67	3.72	3.84	4.13	3.59	4.18	3.90
Ba	4.6	28.0	43.0	55.4	40.2	40.9	38.7	64.0
La	159	117	87	85	87	97	86	80
Ce	258	187	123	122	124	130	127	119
Pr	18.3	12.7	7.8	7.5	7.5	8.5	7.7	7.5
Nd	51.3	34.7	19.9	19.4	18.4	22.1	19.4	19.5
Sm	6.23	4.46	2.57	2.64	2.35	2.97	2.71	2.57
Eu	1.07	0.86	0.56	0.57	0.43	0.58	0.52	0.67
Gd	6.46	4.25	2.22	2.59	2.64	2.77	2.45	2.80
Tb	0.98	0.65	0.36	0.38	0.38	0.42	0.36	0.39
Dy	6.03	4.25	2.45	2.51	2.42	2.78	2.56	2.57
Ho	1.44	0.98	0.54	0.60	0.58	0.67	0.65	0.56
Er	4.12	3.11	2.02	1.78	2.04	2.26	1.93	2.04
Tm	0.70	0.52	0.39	0.33	0.34	0.39	0.36	0.36
Yb	4.82	3.37	2.95	2.59	2.80	3.17	2.61	2.66
Lu	0.74	0.59	0.49	0.43	0.51	0.54	0.51	0.49
Hf	25.1	22.2	21.8	21.8	23.2	25.1	22.8	20.7
Ta	17.10	11.81	7.62	7.38	7.19	7.90	7.06	7.25
Pb	27.7	24.5	24.6	22.8	25.3	23.0	25.5	23.0
Th	35.6	35.7	42.2	39.9	43.0	45.2	43.0	38.8
U	11.3	12.0	15.2	15.4	16.6	14.3	16.1	15.7

Appendix C.
Fasnia
Glasses
LA-ICP-MS
data

Sample ID	05TF88_17	05TF88_18	05TF88_19	00TF88_20	05TF88_21	05TF88_22	05TF88_23
Unit	Santo Ig.	Santo Ig.	Santo Ig.	Santo Ig.	Santo Ig.	Santo Ig.	Santo Ig.
(ppm) Ca	0.58	0.33	0.28	0.43	0.57	0.49	0.27
Sc	5.96	4.83	4.94	6.26	6.09	5.81	5.24
Ti	2,281	3,266	3,284	2,381	2,657	2,516	3,313
Rb	289	224	198	285	272	282	232
Sr	18.1	1.2	0.7	19.1	28.6	19.3	1.5
Y	18.3	31.7	32.0	20.0	19.9	19.7	31.7
Zr	1,383	1,019	1,020	1,481	1,378	1,456	1,010
Nb	289	325	326	289	279	287	323
Cs	4.02	2.19	2.14	3.98	3.71	3.87	2.10
Ba	39.7	16.7	19.9	40.9	67.0	45.0	24.3
La	101	124	124	96	94	92	125
Ce	139	212	214	134	135	128	215
Pr	8.7	16.2	16.4	8.5	9.3	8.4	16.5
Nd	22.2	47.7	48.2	22.1	24.3	22.1	49.9
Sm	2.76	6.86	6.72	2.78	3.18	2.90	7.01
Eu	0.64	1.33	1.37	0.55	0.67	0.60	1.48
Gd	2.99	6.16	6.12	2.86	3.37	3.09	5.82
Tb	0.37	0.87	0.82	0.39	0.46	0.44	0.92
Dy	2.58	4.95	5.32	2.55	2.80	2.68	5.55
Ho	0.59	1.10	1.09	0.65	0.70	0.63	1.11
Er	2.14	3.34	3.29	2.04	2.17	2.14	3.44
Tm	0.35	0.51	0.48	0.36	0.38	0.35	0.50
Yb	2.96	3.35	3.26	2.88	3.06	2.99	3.51
Lu	0.50	0.57	0.52	0.51	0.54	0.48	0.58
Hf	22.5	17.9	17.9	23.8	22.5	23.6	18.2
Ta	7.17	12.81	13.12	7.35	7.72	7.59	13.19
Pb	25.1	17.0	17.0	25.1	20.9	23.3	16.1
Th	42.1	25.4	25.6	44.3	42.1	43.4	24.9
U	16.4	8.1	8.1	15.5	14.7	15.0	7.9

Appendix C.
Fasnia
Glasses
LA-ICP-MS
data

Sample ID	05TF88_24	05TF88_g1	05TF88_g2	05TF88_g3	05TF88_g4	05TF88_g5	05TF88_g6
Unit	Santo Ig.	Santo Ig.	Santo Ig.	Santo Ig.	Santo Ig.	Santo Ig.	Santo Ig.
(ppm) Ca	0.45	0.54	0.24	0.36	0.54	0.30	0.29
Sc	5.76	2.88	3.36	5.23	5.70	2.84	3.28
Ti	2,512	2,664	2,723	2,700	2,796	2,783	2,764
Rb	285	291	293	285	272	284	284
Sr	17.8	29.3	3.6	3.4	31.3	2.5	2.8
Y	18.8	18.2	37.5	37.1	21.6	38.2	37.5
Zr	1,353	1,320	1,308	1,307	1,230	1,306	1,289
Nb	279	279	454	443	296	449	444
Cs	3.72	3.70	3.25	3.04	3.59	3.08	3.07
Ba	41.3	59.4	3.5	2.8	77.2	2.7	2.5
La	88	90	161	158	103	163	163
Ce	125	137	287	281	169	285	283
Pr	8.1	8.1	17.8	17.1	10.6	17.8	17.5
Nd	20.6	20.5	45.9	44.2	27.1	44.9	45.2
Sm	2.71	2.86	5.96	5.78	3.70	5.97	5.76
Eu	0.51	0.53	1.01	1.03	0.73	1.03	0.94
Gd	2.55	3.35	7.07	6.77	4.29	6.81	6.71
Tb	0.41	0.40	0.87	0.85	0.46	0.87	0.86
Dy	2.52	2.34	5.70	5.52	3.14	5.42	5.47
Ho	0.55	0.56	1.18	1.32	0.68	1.17	1.21
Er	2.06	1.87	3.84	3.75	2.30	3.99	3.87
Tm	0.35	0.35	0.62	0.56	0.39	0.60	0.60
Yb	2.86	2.60	4.02	3.96	2.67	3.77	4.06
Lu	0.49	0.42	0.67	0.70	0.51	0.67	0.66
Hf	22.1	20.6	22.4	22.6	20.8	22.5	22.3
Ta	7.71	7.23	15.28	15.29	8.94	15.28	15.23
Pb	24.4	22.5	27.1	27.1	22.8	26.7	27.2
Th	40.0	41.5	33.9	34.3	39.5	35.0	34.0
U	13.8	15.7	12.2	12.1	15.3	12.4	12.4

Appendix C.
Fasnia
Glasses
LA-ICP-MS
data

Sample ID	05TF88_g7	05TF88_g8	05TF88_g9	05TF88b_g1	05TF88b_g10	05TF88b_g11	05TF88b_g12
Unit	Santo Ig.	Santo Ig.	Santo Ig.	Santo Ig.	Santo Ig.	Santo Ig.	Santo Ig.
(ppm) Ca	0.29	0.33	0.46	0.80	0.58	0.51	0.56
Sc	3.18	3.03	3.34	7.15	5.45	4.80	5.15
Ti	2,787	2,747	3,066	2,739	2,632	2,604	2,536
Rb	296	290	305	262	290	304	286
Sr	2.9	4.7	30.6	-	23.7	24.7	24.5
Y	37.8	37.7	18.5	25.2	25.8	27.1	25.6
Zr	1,287	1,277	1,340	1,748	1,874	2,023	1,888
Nb	443	433	294	288	302	318	297
Cs	3.02	3.37	4.04	3.67	3.73	4.11	3.81
Ba	2.5	5.6	66.1	-	52.8	55.0	57.4
La	160	163	100	114	120	127	119
Ce	280	281	156	142	146	154	142
Pr	17.3	17.3	9.2	10.2	10.1	10.4	9.6
Nd	44.0	44.1	22.9	27.9	27.8	27.5	25.1
Sm	5.64	6.06	2.97	3.36	3.40	3.64	3.31
Eu	0.90	0.99	0.68	0.80	0.70	0.68	0.64
Gd	4.58	4.58	2.55	6.71	5.65	5.44	4.85
Tb	0.83	0.87	0.43	0.61	0.58	0.52	0.52
Dy	5.49	5.78	2.90	3.62	3.41	3.59	3.28
Ho	1.20	1.29	0.61	0.86	0.80	0.82	0.76
Er	3.82	3.73	1.93	2.91	2.72	2.76	2.69
Tm	0.59	0.62	0.35	0.49	0.49	0.51	0.51
Yb	4.02	4.03	2.72	3.72	3.76	3.76	3.63
Lu	0.68	0.67	0.48	0.66	0.65	0.77	0.68
Hf	22.4	22.4	21.5	29.7	31.6	33.6	31.0
Ta	15.23	15.38	8.63	9.08	8.34	8.77	8.27
Pb	27.2	26.4	23.2	18.9	23.4	25.2	24.0
Th	33.6	34.5	43.6	52.6	55.4	61.1	57.4
U	12.2	12.1	16.8	13.4	14.6	15.5	14.5

Appendix C.
Fasnia
Glasses
LA-ICP-MS
data

Sample ID	05TF88b_g13	05TF88b_g14	05TF88b_g15	05TF88b_g16	05TF88b_g17	05TF88b_g18
Unit	Santo Ig.	Santo Ig.	Santo Ig.	Santo Ig.	Santo Ig.	Santo Ig.
(ppm) Ca	0.58	0.68	0.62	0.53	0.59	0.51
Sc	4.98	4.84	4.62	4.89	4.15	4.54
Ti	3,808	3,049	3,732	2,642	3,115	2,841
Rb	286	288	293	309	283	294
Sr	27.5	25.4	27.6	30.4	62.4	38.0
Y	28.9	27.3	28.2	17.4	18.6	17.5
Zr	1,474	1,784	1,524	1,216	1,157	1,214
Nb	280	300	282	275	268	269
Cs	3.30	3.63	3.50	4.02	3.51	3.81
Ba	69.8	62.8	66.3	59.8	162.9	96.1
La	126	128	124	91	93	88
Ce	172	161	169	144	150	138
Pr	13.6	11.6	13.1	8.9	10.1	8.2
Nd	41.7	32.6	39.9	22.0	25.7	21.4
Sm	6.17	4.23	5.77	3.30	3.56	2.81
Eu	1.14	0.79	1.16	0.64	0.76	0.60
Gd	7.87	6.25	7.17	3.85	4.29	3.82
Tb	0.80	0.65	0.75	0.42	0.44	0.37
Dy	4.76	3.78	4.45	2.47	2.71	2.47
Ho	0.97	0.86	0.97	0.57	0.62	0.57
Er	3.07	2.91	2.98	1.82	2.04	1.86
Tm	0.48	0.50	0.50	0.31	0.33	0.31
Yb	3.50	3.75	3.40	2.44	2.32	2.39
Lu	0.60	0.68	0.59	0.41	0.40	0.40
Hf	25.5	29.8	24.8	19.1	17.9	19.2
Ta	10.78	9.58	10.30	7.12	7.33	7.06
Pb	22.3	23.7	22.7	19.8	24.2	23.3
Th	44.3	54.0	43.6	37.8	35.7	37.8
U	10.6	13.4	10.9	15.9	14.3	15.0

Appendix C.
Fasnia
Glasses
LA-ICP-MS
data

Sample ID	05TF88b_g19	05TF88b_g2	05TF88b_g20	05TF88b_g21	05TF88b_g22	05TF88b_g23
Unit	Santo Ig.	Santo Ig.	Santo Ig.	Santo Ig.	Santo Ig.	Santo Ig.
(ppm) Ca	0.63	0.53	0.51	0.77	0.49	0.52
Sc	4.14	6.08	4.05	4.59	5.11	4.14
Ti	2,987	2,533	2,619	2,759	2,396	2,706
Rb	314	275	308	301	322	313
Sr	30.2	22.5	26.7	25.5	25.5	28.5
Y	18.1	25.5	17.2	17.1	17.0	19.0
Zr	1,209	1,874	1,242	1,272	1,328	1,351
Nb	276	292	280	290	279	289
Cs	3.91	3.60	4.13	4.18	4.38	4.00
Ba	87.0	55.5	66.0	57.7	49.0	70.0
La	89	116	92	90	89	96
Ce	146	136	145	138	138	148
Pr	8.6	9.5	8.3	7.9	7.7	8.8
Nd	22.1	25.9	21.3	20.5	18.6	22.4
Sm	2.83	3.50	2.81	2.82	2.22	2.84
Eu	0.71	0.59	0.62	0.59	0.52	0.60
Gd	3.88	6.00	3.64	3.48	2.94	3.95
Tb	0.42	0.53	0.39	0.37	0.36	0.40
Dy	2.45	3.31	2.38	2.44	2.36	2.58
Ho	0.57	0.75	0.52	0.54	0.56	0.59
Er	1.78	2.91	1.82	1.85	1.88	2.17
Tm	0.33	0.48	0.32	0.32	0.31	0.36
Yb	2.48	3.66	2.46	2.68	2.63	2.61
Lu	0.42	0.74	0.43	0.44	0.46	0.42
Hf	19.4	31.8	19.3	19.8	21.0	20.9
Ta	7.48	8.48	7.06	7.30	6.85	7.54
Pb	24.9	20.8	19.6	19.1	25.2	24.5
Th	38.0	56.5	39.1	40.2	42.3	41.5
U	15.7	14.2	16.1	16.3	17.1	15.7

Appendix C.
Fasnia
Glasses
LA-ICP-MS
data

Sample ID	05TF88b_g24	05TF88b_g25	05TF88b_g26	05TF88b_g28	05TF88b_g3	05TF88b_g31
Unit	Santo Ig.	Santo Ig.	Santo Ig.	Santo Ig.	Santo Ig.	Santo Ig.
(ppm) Ca	0.60	0.62	0.60	0.55	0.67	0.60
Sc	6.34	4.94	4.43	4.52	6.29	3.73
Ti	2,669	2,643	2,898	2,833	2,691	2,962
Rb	303	316	299	303	269	287
Sr	23.1	22.7	28.6	28.8	26.4	44.1
Y	21.8	23.4	23.2	23.2	27.2	20.4
Zr	1,557	1,734	1,629	1,596	1,927	1,413
Nb	290	309	296	295	310	282
Cs	3.84	4.17	3.83	3.76	3.47	3.84
Ba	55.5	51.1	66.5	66.5	59.1	123.8
La	108	117	113	111	121	102
Ce	147	156	153	154	146	149
Pr	9.3	9.7	9.9	9.7	10.9	9.4
Nd	24.0	24.5	26.2	26.4	29.1	24.3
Sm	2.99	2.88	3.40	3.40	3.99	3.27
Eu	0.65	0.57	0.64	0.74	0.75	0.62
Gd	4.12	4.12	4.61	4.51	6.78	4.36
Tb	0.43	0.45	0.46	0.50	0.57	0.48
Dy	2.82	2.87	3.12	3.17	3.37	2.77
Ho	0.64	0.66	0.72	0.78	0.87	0.63
Er	2.36	2.53	2.47	2.43	2.76	2.16
Tm	0.39	0.45	0.45	0.45	0.53	0.38
Yb	3.20	3.31	3.13	3.14	3.83	2.65
Lu	0.59	0.60	0.57	0.59	0.66	0.48
Hf	26.1	27.0	26.0	25.7	31.3	21.7
Ta	8.09	8.12	8.31	7.98	8.55	7.87
Pb	22.9	23.2	22.1	21.8	18.6	23.3
Th	48.9	52.7	50.0	49.4	55.8	43.6
U	15.2	16.4	15.0	15.5	13.9	15.1

Appendix C.
Fasnia
Glasses
LA-ICP-MS
data

Sample ID	05TF88b_g32	05TF88b_g5	05TF88b_g6	05TF88b_g7	05TF88b_g8	05TF88b_g9
Unit	Santo Ig.	Santo Ig.	Santo Ig.	Santo Ig.	Santo Ig.	Santo Ig.
(ppm) Ca	0.49	0.65	0.60	0.61	0.49	0.63
Sc	3.59	6.47	5.41	5.26	5.92	7.18
Ti	2,690	2,792	2,972	2,665	2,523	2,956
Rb	261	269	285	277	302	294
Sr	37.1	30.3	28.7	34.6	24.3	25.0
Y	17.7	26.6	24.7	24.4	24.9	25.3
Zr	1,183	1,892	1,701	1,720	1,969	1,778
Nb	250	297	307	295	315	297
Cs	3.30	3.62	4.08	3.72	3.78	3.93
Ba	101.9	79.4	67.7	70.5	54.4	58.7
La	88	123	117	117	114	119
Ce	131	145	151	147	141	147
Pr	8.2	10.6	10.4	9.9	9.2	10.0
Nd	21.8	29.2	28.8	26.1	24.5	27.5
Sm	2.94	4.04	4.07	3.39	2.89	3.79
Eu	0.62	0.77	0.75	0.68	0.65	0.76
Gd	3.13	6.91	6.07	5.25	5.27	5.54
Tb	0.39	0.65	0.55	0.52	0.50	0.57
Dy	2.49	3.58	3.63	3.20	3.38	3.44
Ho	0.55	0.87	0.80	0.75	0.75	0.78
Er	1.76	2.93	2.72	2.71	2.65	2.69
Tm	0.32	0.48	0.46	0.45	0.50	0.49
Yb	2.27	3.73	3.43	3.43	3.94	3.56
Lu	0.43	0.66	0.62	0.63	0.69	0.64
Hf	18.4	32.6	28.0	29.6	31.2	29.6
Ta	7.23	8.85	9.28	8.67	8.31	8.75
Pb	20.3	19.8	23.3	21.8	23.7	23.4
Th	36.4	56.7	51.9	53.7	58.7	54.3
U	12.4	14.3	14.0	14.8	16.0	14.3

Appendix D

Electron microprobe data for Fasnia Member pyroxenes

Appendix D.
Fasnia Member
Clinopyroxene
electron
microprobe
data

Sample ID	01TF51 c7	01TF51 c9	99TF10 3	99TF10 9	99TF10 10	01TF51 c5	99TF10 20	99TF10 7	99TF10 22	99TF10 18	99TF10 16	99TF10 4
Sequence	**lower**	**lower**	**lower**	**lower**	**lower**	**lower**	**lower**	**lower**	**lower**	**lower**	**lower**	**lower**
SiO_2	44.64	47.06	46.34	45.73	46.32	44.62	45.04	45.44	44.63	45.98	46.14	45.36
TiO_2	3.29	2.60	2.24	2.57	2.70	2.91	3.08	2.81	2.98	2.58	2.45	2.62
Al_2O_3	8.54	6.65	6.76	6.66	6.74	7.58	7.97	7.30	8.31	7.25	6.74	7.49
FeO*	7.59	7.15	7.09	6.77	6.26	7.04	6.92	6.66	7.11	7.17	6.53	7.31
MnO	0.09	0.13	0.10	0.05	0.08	0.05	0.09	0.08	0.08	0.09	0.10	0.09
MgO	12.33	13.35	13.48	13.43	13.25	12.97	12.80	12.99	12.63	13.14	13.66	12.99
CaO	22.50	22.83	22.98	23.42	23.89	22.60	22.17	23.21	22.71	22.87	23.30	22.89
Na_2O	0.34	0.34	0.34	0.34	0.35	0.34	0.37	0.37	0.38	0.39	0.40	0.39
K_2O	0.03	0.01	0.04	0.07	0.04	0.01	0.00	0.03	0.04	0.00	0.01	0.01
Total	99.34	100.12	99.38	99.04	99.63	98.11	98.44	98.89	98.84	99.47	99.33	99.15
Formula per 4 cations												
Si	1.672	1.743	1.725	1.708	1.721	1.685	1.697	1.702	1.675	1.713	1.715	1.695
Ti	0.093	0.073	0.063	0.072	0.075	0.083	0.087	0.079	0.084	0.072	0.069	0.074
Al	0.377	0.290	0.296	0.293	0.295	0.337	0.354	0.322	0.367	0.318	0.295	0.330
Fe^{2+}	0.119	0.118	0.067	0.037	0.055	0.071	0.114	0.065	0.078	0.084	0.038	0.068
Fe^{3+}	0.119	0.103	0.154	0.175	0.139	0.152	0.104	0.144	0.145	0.140	0.165	0.161
Mn	0.003	0.004	0.003	0.002	0.003	0.002	0.003	0.003	0.003	0.003	0.003	0.003
Mg	0.688	0.737	0.748	0.748	0.734	0.730	0.719	0.726	0.707	0.730	0.757	0.724
Ca	0.903	0.906	0.917	0.937	0.951	0.915	0.895	0.932	0.913	0.913	0.928	0.917
Na	0.025	0.025	0.025	0.025	0.025	0.025	0.027	0.027	0.027	0.028	0.029	0.029
K	0.001	0.001	0.002	0.004	0.002	0.000	0.000	0.001	0.002	0.000	0.001	0.000
Cation sum	4.000	4.000	4.000	4.000	4.000	4.000	4.000	4.000	4.000	4.000	4.000	4.000

Appendix D.
Fasnia Member Clinopyroxene electron microprobe data

Sample ID	99TF035	99TF032_2	99TF1025	99TF033	99TF108	99TF1012	99TF1017	99TF1019	99TF034	99TF101a	99TF106	01TF51c4
Sequence	**lower**	**lower**	**lower**	**lower**	**lower**	**lower**	**lower**	**lower**	**lower**	**lower**	**lower**	**lower**
SiO_2	45.35	47.34	46.29	45.18	45.58	45.75	45.78	43.98	48.54	45.56	44.87	43.42
TiO_2	2.86	2.13	2.58	3.12	2.78	2.89	2.83	3.32	1.88	2.90	3.08	3.30
Al_2O_3	7.06	5.95	6.75	7.03	7.24	7.55	6.93	8.55	5.59	7.70	7.76	9.02
FeO*	7.43	5.96	6.98	7.22	6.74	7.49	6.76	7.31	6.29	6.85	7.33	7.62
MnO	0.14	0.08	0.11	0.11	0.07	0.11	0.14	0.09	0.08	0.12	0.07	0.17
MgO	12.66	13.74	13.20	12.68	12.96	12.99	13.09	12.46	13.71	13.28	13.07	12.27
CaO	22.87	22.55	23.05	22.99	22.90	22.99	23.07	22.95	22.94	23.21	23.62	22.53
Na_2O	0.40	0.40	0.42	0.42	0.42	0.43	0.43	0.44	0.45	0.45	0.47	0.47
K_2O	0.02		0.02	0.02	0.02	0.00	0.09	0.00	0.03	0.02	0.07	0.05
Total	98.79	98.16	99.40	98.78	98.71	100.20	99.12	99.10	99.52	100.10	100.34	98.85
Formula per 4 cations												
Si	1.706	1.779	1.725	1.700	1.710	1.694	1.711	1.648	1.801	1.684	1.657	1.631
Ti	0.081	0.060	0.072	0.088	0.079	0.080	0.080	0.093	0.053	0.081	0.085	0.093
Al	0.313	0.264	0.296	0.312	0.320	0.330	0.305	0.378	0.244	0.336	0.338	0.399
Fe^{2+}	0.091	0.101	0.077	0.084	0.077	0.080	0.062	0.057	0.113	0.043	0.011	0.052
Fe^{3+}	0.143	0.087	0.140	0.143	0.134	0.152	0.149	0.172	0.083	0.168	0.215	0.188
Mn	0.004	0.003	0.004	0.004	0.002	0.003	0.004	0.003	0.003	0.004	0.002	0.005
Mg	0.710	0.770	0.733	0.711	0.725	0.717	0.729	0.696	0.759	0.732	0.720	0.687
Ca	0.922	0.908	0.920	0.927	0.921	0.912	0.924	0.921	0.912	0.919	0.934	0.907
Na	0.029	0.029	0.030	0.030	0.031	0.031	0.031	0.032	0.032	0.032	0.034	0.034
K	0.001	0.000	0.001	0.001	0.001	0.000	0.004	0.000	0.002	0.001	0.003	0.002
Cation sum	4.000	4.000	4.000	4.000	4.000	4.000	4.000	4.000	4.000	4.000	4.000	4.000

Appendix D.
Fasnia Member
Clinopyroxene
electron
microprobe
data

Sample ID	99TF1011	99TF1014	99TF032_1	99TF1013	01TF51c5	01TF116A_8e	99TF102	01TF116A_8a	99TF1015	99TF1021b	01TF116A_8c	01TF116A_8b
Sequence	**lower**	**lower**	**lower**	**lower**	**lower**	**lower**	**lower**	**lower**	**lower**	**lower**	**lower**	**lower**
SiO_2	49.00	45.56	47.58	43.56	42.50	46.67	43.95	48.52	44.77	49.65	46.06	47.96
TiO_2	1.80	2.95	2.18	3.78	3.68	2.59	3.41	2.04	3.19	1.44	3.00	2.27
Al_2O_3	3.90	7.55	6.15	9.08	9.12	5.83	8.77	4.64	8.11	3.25	6.57	5.27
FeO*	7.67	6.97	6.23	7.33	7.49	7.11	6.81	6.82	7.58	8.00	7.20	7.82
MnO	0.25	0.11	0.07	0.11	0.00	0.23	0.17	0.24	0.02	0.41	0.21	0.28
MgO	13.84	12.87	13.77	12.13	12.03	13.04	12.37	13.89	12.60	13.55	12.56	13.52
CaO	22.27	22.79	22.70	23.00	22.46	22.60	22.85	22.41	22.48	22.47	21.90	22.62
Na_2O	0.48	0.49	0.50	0.51	0.53	0.61	0.61	0.64	0.65	0.69	0.70	0.74
K_2O	0.04	0.03		0.00	0.00	0.00	0.00	0.00	0.00	0.02	0.07	0.02
Total	99.24	99.32	99.17	99.50	97.82	98.68	98.93	99.21	99.41	99.47	98.27	100.50
Formula per 4 cations												
Si	1.831	1.700	1.770	1.628	1.614	1.754	1.646	1.807	1.670	1.852	1.740	1.768
Ti	0.051	0.083	0.061	0.106	0.105	0.073	0.096	0.057	0.090	0.040	0.085	0.063
Al	0.172	0.332	0.270	0.400	0.408	0.258	0.387	0.204	0.357	0.143	0.292	0.229
Fe^{2+}	0.138	0.079	0.089	0.060	0.046	0.091	0.040	0.098	0.065	0.126	0.115	0.079
Fe^{3+}	0.102	0.138	0.105	0.170	0.192	0.132	0.173	0.114	0.172	0.123	0.113	0.163
Mn	0.008	0.004	0.002	0.003	0.000	0.007	0.005	0.008	0.001	0.013	0.007	0.009
Mg	0.771	0.716	0.764	0.676	0.681	0.731	0.691	0.771	0.701	0.754	0.707	0.743
Ca	0.892	0.911	0.904	0.921	0.914	0.910	0.917	0.894	0.898	0.898	0.886	0.894
Na	0.035	0.035	0.036	0.037	0.039	0.044	0.045	0.047	0.047	0.050	0.051	0.053
K	0.002	0.001	0.000	0.000	0.000	0.000	0.000	0.000	0.000	0.001	0.004	0.001
Cation sum	4.000	4.000	4.000	4.000	4.000	4.000	4.000	4.000	4.000	4.000	4.000	4.000

Appendix D.
Fasnia Member Clinopyroxene electron microprobe data

Sample ID	99TF06 B_6a	01TF51 B_2b	99TF10 5	01TF51 c2	01TF116 A_8d	01TF51 1g	99TF03 1	99TF10 21	99TF06 B_5a	01TF51 B_1b	99TF03 1	01TF51 B_2a
Sequence	**lower**	**lower**	**lower**	**lower**	**lower**	**lower**	**lower**	**lower**	**lower**	**lower**	**lower**	**lower**
SiO_2	50.94	49.77	45.32	49.38	48.97	51.03	51.16	51.13	50.54	50.26	50.93	49.92
TiO_2	1.01	1.40	3.30	1.25	1.86	0.99	1.04	0.77	1.46	1.40	1.31	1.56
Al_2O_3	2.37	3.36	7.28	3.09	4.11	2.29	2.34	1.98	3.26	3.16	2.77	3.49
FeO*	7.66	7.74	8.86	8.13	6.93	8.11	8.42	9.17	8.27	9.46	8.43	7.74
MnO	0.49	0.44	0.21	0.42	0.30	0.58	0.52	0.61	0.52	0.55	0.51	0.50
MgO	13.68	12.90	11.84	13.68	13.72	13.31	13.04	12.84	13.55	12.81	13.52	13.18
CaO	23.05	22.86	22.67	22.76	22.89	22.63	22.72	21.85	22.25	22.50	22.35	22.07
Na_2O	0.79	0.87	0.88	0.91	0.93	0.96	1.01	1.02	1.06	1.07	1.07	1.06
K_2O	0.04	0.02	0.00	0.04	0.02	0.03	0.02	0.02	0.00	0.00	0.02	0.04
Total	100.03	99.36	100.36	99.66	99.74	99.94	100.26	99.39	100.91	101.21	100.91	99.57
Formula per 4 cations												
Si	1.887	1.859	1.684	1.834	1.812	1.895	1.896	1.915	1.856	1.850	1.871	1.857
Ti	0.028	0.039	0.092	0.035	0.052	0.028	0.029	0.022	0.040	0.039	0.036	0.044
Al	0.104	0.148	0.319	0.135	0.179	0.100	0.102	0.087	0.141	0.137	0.120	0.153
Fe^{2+}	0.113	0.123	0.084	0.058	0.055	0.126	0.139	0.174	0.112	0.128	0.117	0.117
Fe^{3+}	0.125	0.118	0.191	0.194	0.160	0.126	0.122	0.113	0.142	0.163	0.142	0.123
Mn	0.015	0.014	0.007	0.013	0.010	0.018	0.016	0.019	0.016	0.017	0.016	0.016
Mg	0.755	0.719	0.656	0.757	0.757	0.737	0.720	0.717	0.742	0.703	0.740	0.731
Ca	0.915	0.915	0.903	0.906	0.908	0.900	0.902	0.877	0.875	0.887	0.880	0.880
Na	0.057	0.063	0.063	0.065	0.067	0.069	0.073	0.074	0.076	0.076	0.077	0.077
K	0.002	0.001	0.000	0.002	0.001	0.002	0.001	0.001	0.000	0.000	0.001	0.002
Cation sum	4.000	4.000	4.000	4.000	4.000	4.000	4.000	4.000	4.000	4.000	4.000	4.000

Appendix D.
Fasnia Member Clinopyroxene electron microprobe data

Sample ID	99TF06 B_6b	01TF51 1a	01TF51 1b	01TF51 B_1a	99TF06 PB_2	99TF06 22a	99TF06 17c	99TF06 B_4b	99TF06 25c	99TF06 B_7b	01TF51 PA_5	99TF06 B_10a
Sequence	**lower**	**lower**	**lower**	**lower**	**lower**	**lower**	**lower**	**lower**	**lower**	**lower**	**lower**	**lower**
SiO_2	49.67	50.75	50.23	49.58	50.98	51.32	51.11	51.13	51.09	51.05	51.04	50.76
TiO_2	1.57	0.87	1.19	1.40	0.59	0.49	0.46	0.47	0.50	0.48	0.45	0.48
Al_2O_3	3.41	2.13	2.70	3.32	1.82	1.42	1.51	1.59	1.58	1.32	1.41	1.52
FeO*	8.05	8.78	8.51	8.67	13.42	13.41	13.37	13.19	12.81	12.94	13.93	12.77
MnO	0.46	0.60	0.56	0.54	1.12	1.27	1.32	1.32	1.27	1.44	1.33	1.24
MgO	12.99	13.16	12.69	12.83	9.55	9.96	9.60	9.84	9.78	9.70	9.78	9.92
CaO	22.80	22.21	22.34	22.50	21.09	21.44	21.04	20.89	21.61	21.44	21.56	21.27
Na_2O	1.12	1.14	1.18	1.23	1.61	1.64	1.68	1.69	1.70	1.69	1.71	1.69
K_2O	0.02	0.06	0.03	0.04	0.01	0.01	0.01	0.02	0.07	0.00	0.03	0.00
Total	100.10	99.70	99.43	100.10	100.19	100.97	100.10	100.14	100.42	100.05	101.23	99.64
Formula per 4 cations												
Si	1.840	1.889	1.876	1.838	1.929	1.924	1.935	1.932	1.923	1.932	1.911	1.925
Ti	0.044	0.024	0.033	0.039	0.017	0.014	0.013	0.013	0.014	0.014	0.013	0.014
Al	0.149	0.094	0.119	0.145	0.081	0.063	0.067	0.071	0.070	0.059	0.062	0.068
Fe^{2+}	0.084	0.108	0.118	0.077	0.278	0.240	0.262	0.254	0.221	0.235	0.220	0.225
Fe^{3+}	0.166	0.165	0.148	0.191	0.147	0.181	0.161	0.162	0.182	0.174	0.216	0.180
Mn	0.014	0.019	0.018	0.017	0.036	0.040	0.042	0.042	0.041	0.046	0.042	0.040
Mg	0.717	0.730	0.707	0.709	0.539	0.557	0.542	0.555	0.549	0.547	0.546	0.561
Ca	0.905	0.886	0.894	0.894	0.855	0.861	0.853	0.846	0.872	0.869	0.865	0.864
Na	0.080	0.082	0.085	0.088	0.118	0.120	0.123	0.124	0.124	0.124	0.124	0.124
K	0.001	0.003	0.002	0.002	0.001	0.001	0.000	0.001	0.004	0.000	0.001	0.000
Cation sum	4.000	4.000	4.000	4.000	4.000	4.000	4.000	4.000	4.000	4.000	4.000	4.000

Appendix D.
Fasnia Member
Clinopyroxene
electron
microprobe
data

Sample ID	01TF54 px2_4	99TF06 PA_5	01TF54 px2_2	99TF06 25e	99TF10 26	99TF10 PA_1	01TF54 px1_1	01TF51 PA_5	99TF03 1_2	99TF06 PA_1	99TF10 26b	99TF06 11b
Sequence	**lower**	**lower**	**lower**	**lower**	**lower**	**lower**	**lower**	**lower**	**lower**	**lower**	**lower**	**lower**
SiO_2	50.66	51.62	50.73	51.04	50.45	50.89	49.78	50.77	51.17	51.24	50.65	51.15
TiO_2	0.46	0.51	0.45	0.45	0.50	0.50	0.46	0.48	0.68	0.44	0.45	0.58
Al_2O_3	1.52	1.63	1.42	1.42	1.58	1.64	1.44	1.40	1.90	1.33	1.47	1.77
FeO*	12.80	13.80	13.03	12.93	13.52	13.11	12.60	12.51	12.28	13.57	12.54	13.90
MnO	1.41	1.19	1.29	1.33	1.23	1.26	1.39	1.39	1.17	1.47	1.22	1.30
MgO	9.65	9.74	9.42	9.38	9.74	9.54	9.32	9.40	9.81	9.33	9.86	9.45
CaO	21.41	20.88	21.16	21.25	21.21	21.20	21.14	20.97	20.92	20.93	21.28	20.63
Na_2O	1.69	1.72	1.69	1.71	1.73	1.75	1.75	1.77	1.82	1.82	1.82	1.84
K_2O	0.00	0.04	0.00	0.04	0.02	0.02	0.00	0.00		0.02	0.02	0.00
Total	99.58	101.11	99.18	99.55	99.99	99.90	97.88	98.69	99.73	100.15	99.32	100.61
Formula per 4 cations												
Si	1.925	1.934	1.938	1.942	1.910	1.928	1.924	1.946	1.936	1.940	1.924	1.927
Ti	0.013	0.014	0.013	0.013	0.014	0.014	0.013	0.014	0.019	0.013	0.013	0.016
Al	0.068	0.072	0.064	0.064	0.070	0.073	0.066	0.063	0.085	0.059	0.066	0.079
Fe^{2+}	0.226	0.275	0.257	0.258	0.218	0.243	0.217	0.253	0.250	0.260	0.204	0.270
Fe^{3+}	0.181	0.157	0.159	0.154	0.210	0.172	0.190	0.148	0.138	0.170	0.195	0.168
Mn	0.045	0.038	0.042	0.043	0.039	0.040	0.046	0.045	0.037	0.047	0.039	0.042
Mg	0.546	0.544	0.536	0.532	0.550	0.539	0.537	0.537	0.553	0.527	0.558	0.531
Ca	0.872	0.838	0.866	0.866	0.860	0.861	0.875	0.861	0.848	0.849	0.866	0.833
Na	0.124	0.125	0.125	0.126	0.127	0.129	0.131	0.132	0.133	0.134	0.134	0.134
K	0.000	0.002	0.000	0.002	0.001	0.001	0.000	0.000	0.000	0.001	0.001	0.000
Cation sum	4.000	4.000	4.000	4.000	4.000	4.000	4.000	4.000	4.000	4.000	4.000	4.000

Appendix D.
Fasnia Member
Clinopyroxene
electron
microprobe
data

Sample ID	99TF06 22b	99TF06 B_1a	01TF51 PA_5	99TF06 B_4a	99TF06 PB_3	99TF06 PA_1	99TF06 25e	99TF06 B_7a	01TF51 PA_5	01TF54 px2_3	99TF06 PA_4	01TF54 px2_1
Sequence	**lower**	**lower**	**lower**	**lower**	**lower**	**lower**	**lower**	**lower**	**lower**	**lower**	**lower**	**lower**
SiO_2	50.92	50.74	50.95	51.05	50.47	51.58	51.10	50.96	51.39	50.15	51.32	49.99
TiO_2	0.49	0.65	0.44	0.49	0.68	0.48	0.44	0.71	0.51	0.55	0.49	0.55
Al_2O_3	1.45	1.97	1.51	1.37	2.04	1.40	1.44	2.21	1.44	1.84	1.45	1.54
FeO*	12.76	13.52	12.41	13.76	14.04	14.14	12.53	13.58	13.18	13.45	12.04	12.64
MnO	1.32	1.28	1.28	1.35	1.30	1.48	1.32	1.25	1.27	1.33	1.35	1.36
MgO	9.47	9.39	9.81	9.59	9.28	9.17	9.40	9.10	9.63	8.90	9.64	9.56
CaO	21.22	20.70	21.29	21.10	20.80	21.37	20.93	20.59	21.15	20.84	21.16	21.18
Na_2O	1.86	1.88	1.88	1.90	1.90	1.93	1.91	1.94	1.95	1.92	1.95	1.94
K_2O	0.00	0.02	0.01	0.01	0.00	0.00	0.05	0.10	0.02	0.03	0.05	0.01
Total	99.48	100.14	99.58	100.61	100.52	101.54	99.11	100.44	100.54	99.01	99.44	98.77
Formula per 4 cations												
Si	1.935	1.919	1.930	1.922	1.904	1.929	1.948	1.922	1.932	1.920	1.946	1.910
Ti	0.014	0.019	0.013	0.014	0.019	0.014	0.012	0.020	0.014	0.016	0.014	0.016
Al	0.065	0.088	0.067	0.061	0.091	0.062	0.065	0.098	0.064	0.083	0.065	0.070
Fe^{2+}	0.232	0.252	0.207	0.226	0.241	0.249	0.241	0.264	0.227	0.242	0.221	0.182
Fe^{3+}	0.173	0.176	0.186	0.207	0.202	0.193	0.158	0.164	0.187	0.189	0.161	0.222
Mn	0.042	0.041	0.041	0.043	0.042	0.047	0.043	0.040	0.040	0.043	0.043	0.044
Mg	0.537	0.529	0.554	0.538	0.522	0.511	0.534	0.512	0.540	0.508	0.545	0.545
Ca	0.864	0.839	0.864	0.851	0.841	0.856	0.855	0.832	0.852	0.855	0.860	0.867
Na	0.137	0.138	0.138	0.139	0.139	0.140	0.141	0.142	0.142	0.143	0.143	0.144
K	0.000	0.001	0.000	0.000	0.000	0.000	0.002	0.005	0.001	0.002	0.002	0.000
Cation sum	4.000	4.000	4.000	4.000	4.000	4.000	4.000	4.000	4.000	4.000	4.000	4.000

Appendix D.
Fasnia Member
Clinopyroxene
electron
microprobe
data

Sample ID	99TF06 PA_5	99TF06 16a	99TF03 1_1	99TF06 17a	99TF06 11c	99TF06 19c	99TF06 28a	99TF06 25a	99TF06 24a	99TF06 11d	01TF51 PA_5	99TF06 27a
Sequence	**lower**	**lower**	**lower**	**lower**	**lower**	**lower**	**lower**	**lower**	**lower**	**lower**	**lower**	**lower**
SiO_2	51.32	50.91	49.59	49.72	50.04	50.67	49.87	50.88	50.45	50.35	50.83	49.17
TiO_2	0.47	0.67	1.04	0.72	0.71	0.67	0.75	0.48	0.60	0.64	0.60	1.05
Al_2O_3	1.66	1.98	2.50	2.25	2.10	2.04	2.28	1.54	2.01	2.10	1.96	2.70
FeO*	12.86	14.42	13.89	14.44	13.09	14.11	14.06	13.17	12.68	12.86	12.98	13.39
MnO	1.34	1.24	1.23	1.24	1.24	1.24	1.33	1.30	1.21	1.20	1.16	1.20
MgO	9.87	9.11	8.47	8.71	9.02	9.04	8.09	9.53	9.03	9.38	9.33	8.56
CaO	21.36	19.95	20.10	20.55	20.82	20.67	20.56	20.73	20.60	20.94	20.65	20.87
Na_2O	1.99	1.98	2.00	2.04	2.06	2.09	2.06	2.09	2.10	2.15	2.16	2.16
K_2O	0.05	0.02		0.02	0.05	0.05	0.04	0.05	0.04	0.00	0.05	0.05
Total	100.93	100.30	98.81	99.69	99.12	100.57	99.05	99.80	98.71	99.62	99.71	99.15
Formula per 4 cations												
Si	1.918	1.927	1.907	1.894	1.909	1.909	1.915	1.925	1.930	1.906	1.923	1.878
Ti	0.013	0.019	0.030	0.021	0.020	0.019	0.022	0.014	0.017	0.018	0.017	0.030
Al	0.073	0.088	0.113	0.101	0.094	0.090	0.103	0.069	0.090	0.094	0.088	0.121
Fe^{2+}	0.191	0.289	0.285	0.238	0.217	0.236	0.274	0.206	0.233	0.192	0.218	0.203
Fe^{3+}	0.211	0.167	0.161	0.222	0.201	0.208	0.178	0.210	0.173	0.215	0.193	0.225
Mn	0.042	0.040	0.040	0.040	0.040	0.040	0.043	0.042	0.039	0.039	0.037	0.039
Mg	0.550	0.514	0.485	0.495	0.513	0.508	0.463	0.537	0.515	0.530	0.526	0.487
Ca	0.855	0.809	0.828	0.839	0.851	0.834	0.846	0.840	0.844	0.849	0.837	0.854
Na	0.144	0.146	0.149	0.151	0.152	0.153	0.153	0.154	0.156	0.158	0.159	0.160
K	0.002	0.001	0.000	0.001	0.002	0.002	0.002	0.003	0.002	0.000	0.002	0.002
Cation sum	4.000	4.000	4.000	4.000	4.000	4.000	4.000	4.000	4.000	4.000	4.000	4.000

Appendix D.
Fasnia Member
Clinopyroxene
electron
microprobe
data

Sample ID	99TF06 28b	99TF06 B_1b	99TF06 B_2a	99TF06 B_8a	99TF06 11a	01TF116 P_3	01TF54 px1_2	99TF06 B_2b	99TF06 19b	01TF51 PA_5	99TF06 PB_3b	01TF116 P_3
Sequence	**lower**	**lower**	**lower**	**lower**	**lower**	**lower**	**lower**	**lower**	**lower**	**lower**	**lower**	**lower**
SiO_2	50.83	49.95	50.81	49.44	50.99	49.32	48.72	49.21	49.80	50.63	49.43	48.41
TiO_2	0.65	0.89	0.68	1.14	0.60	0.73	0.69	0.87	0.80	0.68	0.65	1.10
Al_2O_3	1.93	2.42	2.03	2.73	1.93	2.13	2.11	2.49	2.15	1.95	2.00	2.44
FeO*	13.90	14.21	13.20	14.77	13.62	13.27	13.43	15.27	13.61	13.00	13.40	13.58
MnO	1.29	1.28	1.34	1.25	1.22	1.37	1.23	1.35	1.39	1.27	1.20	1.42
MgO	8.76	8.92	8.84	8.32	9.38	8.40	8.54	7.98	8.24	9.13	9.01	7.85
CaO	20.43	20.48	20.83	20.07	21.13	20.04	20.46	20.24	20.25	20.60	20.23	20.00
Na_2O	2.18	2.19	2.19	2.19	2.25	2.22	2.23	2.30	2.30	2.34	2.34	2.34
K_2O	0.07	0.01	0.02	0.01	0.02	0.01	0.01	0.05	0.02	0.03	0.09	0.02
Total	100.03	100.34	99.95	99.91	101.13	97.50	97.42	99.76	98.55	99.62	98.33	97.16
Formula per 4 cations												
Si	1.926	1.886	1.924	1.882	1.904	1.916	1.892	1.878	1.916	1.917	1.897	1.891
Ti	0.019	0.025	0.019	0.033	0.017	0.021	0.020	0.025	0.023	0.019	0.019	0.032
Al	0.086	0.107	0.091	0.122	0.085	0.098	0.097	0.112	0.098	0.087	0.090	0.112
Fe^{2+}	0.252	0.218	0.232	0.259	0.188	0.236	0.189	0.232	0.242	0.198	0.173	0.225
Fe^{3+}	0.188	0.231	0.185	0.211	0.238	0.195	0.247	0.255	0.196	0.213	0.257	0.219
Mn	0.041	0.041	0.043	0.040	0.039	0.045	0.040	0.043	0.045	0.041	0.039	0.047
Mg	0.495	0.502	0.499	0.472	0.522	0.486	0.494	0.454	0.473	0.515	0.516	0.457
Ca	0.829	0.828	0.845	0.819	0.845	0.834	0.851	0.827	0.835	0.836	0.832	0.837
Na	0.160	0.160	0.160	0.162	0.163	0.168	0.168	0.170	0.171	0.172	0.174	0.177
K	0.003	0.001	0.001	0.001	0.001	0.000	0.000	0.003	0.001	0.002	0.004	0.001
Cation sum	4.000	4.000	4.000	4.000	4.000	4.000	4.000	4.000	4.000	4.000	4.000	4.000

Appendix D.
Fasnia Member
Clinopyroxene
electron
microprobe
data

Sample ID	99TF06 PB_3b	01TF127 px1_3	01TF127 px1_4	01TF127 29a	01TF127 px1_6	01TF127 px1_5	01TF127 px1_2	01TF127 px1_1	01TF127 px3_1	01TF127 px3_2	01TF127 px3_4
Sequence	**lower**	**upper**	**upper**	**upper**	**upper**	**upper**	**upper**	**upper**	**upper**	**upper**	**upper**
SiO_2	49.67	53.04	52.57	45.56	51.65	51.54	51.60	51.64	50.50	50.46	49.67
TiO_2	0.62	0.63	0.71	2.83	0.63	0.74	0.69	0.72	1.14	1.16	1.10
Al_2O_3	2.10	3.74	3.91	7.18	3.65	3.89	3.79	3.85	4.98	5.04	4.86
FeO*	13.68	4.52	4.40	6.88	4.66	4.46	4.52	4.45	4.87	5.08	4.91
MnO	1.23	0.11	0.14	0.14	0.07	0.12	0.12	0.13	0.03	0.10	0.05
MgO	8.90	16.70	16.50	12.83	16.57	16.64	16.48	16.38	14.88	15.07	14.83
CaO	19.94	21.13	21.24	23.68	21.16	21.00	21.17	21.32	22.07	22.23	22.08
Na_2O	2.47	0.51	0.51	0.50	0.54	0.54	0.55	0.55	0.56	0.58	0.58
K_2O	0.04	0.00	0.01	0.00	0.01	0.02	0.00	0.01	0.00	0.00	0.01
Total	98.66	100.35	99.99	99.61	98.94	98.94	98.93	99.05	99.02	99.71	98.09
Formula per 4 cations											
Si	1.900	1.924	1.914	1.695	1.899	1.893	1.897	1.897	1.866	1.852	1.852
Ti	0.018	0.017	0.019	0.079	0.017	0.020	0.019	0.020	0.032	0.032	0.031
Al	0.095	0.160	0.168	0.315	0.158	0.168	0.164	0.167	0.217	0.218	0.213
Fe^{2+}	0.183	0.143	0.132	0.042	0.095	0.094	0.097	0.097	0.124	0.099	0.090
Fe^{3+}	0.255	-0.006	0.002	0.172	0.048	0.043	0.042	0.040	0.027	0.056	0.063
Mn	0.040	0.003	0.004	0.004	0.002	0.004	0.004	0.004	0.001	0.003	0.002
Mg	0.508	0.903	0.896	0.712	0.908	0.911	0.904	0.897	0.820	0.825	0.824
Ca	0.817	0.821	0.829	0.944	0.833	0.826	0.834	0.839	0.874	0.874	0.882
Na	0.183	0.036	0.036	0.036	0.038	0.039	0.039	0.039	0.040	0.041	0.042
K	0.002	0.000	0.001	0.000	0.000	0.001	0.000	0.001	0.000	0.000	0.000
Cation sum	4.000	4.000	4.000	4.000	4.000	4.000	4.000	4.000	4.000	4.000	4.000

Appendix D.
Fasnia Member
Clinopyroxene
electron
microprobe
data

Sample ID	01TF127 px3_3	01TF127 3b	01TF127 2a	01TF127 3e	01TF127 3a	01TF127 2d	01TF127 2c	00TF88 2	00TF90 px2_1	00TF90 px1_1	99TF21 px1_1
Sequence	**upper**	**upper**	**upper**	**upper**	**upper**	**upper**	**upper**	**upper**	**upper**	**upper**	**upper**
SiO_2	50.51	45.40	49.43	49.10	49.24	49.01	45.88	50.60	51.21	48.95	49.70
TiO_2	1.19	3.00	1.63	1.53	1.52	1.61	2.88	0.97	1.03	1.36	1.42
Al_2O_3	4.96	6.41	3.52	3.43	3.39	3.62	6.26	2.21	2.37	3.14	3.08
FeO*	4.73	9.67	8.66	8.05	7.64	8.06	9.66	7.43	8.04	8.14	8.44
MnO	0.10	0.37	0.44	0.40	0.44	0.43	0.37	0.53	0.60	0.52	0.55
MgO	14.97	10.80	12.59	12.43	12.89	12.68	10.97	13.28	12.92	12.77	12.85
CaO	22.22	22.31	23.11	22.90	22.81	22.81	22.63	21.90	22.50	22.31	22.37
Na_2O	0.60	0.75	0.87	0.94	0.95	0.98	0.98	1.00	1.05	1.04	1.10
K_2O	0.00	0.00	0.01	0.04	0.03	0.03	0.00	0.01	0.00	0.00	0.00
Total	99.26	98.73	100.26	98.83	98.91	99.23	99.64	97.92	99.72	98.23	99.52
Formula per 4 cations											
Si	1.861	1.728	1.837	1.847	1.846	1.834	1.726	1.913	1.907	1.849	1.855
Ti	0.033	0.086	0.046	0.043	0.043	0.045	0.081	0.028	0.029	0.039	0.040
Al	0.215	0.287	0.154	0.152	0.150	0.160	0.278	0.098	0.104	0.140	0.135
Fe^{2+}	0.106	0.168	0.125	0.116	0.097	0.099	0.125	0.141	0.151	0.097	0.108
Fe^{3+}	0.039	0.140	0.144	0.137	0.142	0.154	0.179	0.094	0.100	0.160	0.155
Mn	0.003	0.012	0.014	0.013	0.014	0.014	0.012	0.017	0.019	0.016	0.017
Mg	0.822	0.613	0.697	0.697	0.721	0.708	0.615	0.748	0.717	0.719	0.715
Ca	0.877	0.910	0.920	0.923	0.916	0.915	0.912	0.887	0.898	0.903	0.894
Na	0.043	0.056	0.063	0.069	0.069	0.071	0.072	0.073	0.076	0.076	0.080
K	0.000	0.000	0.000	0.002	0.002	0.002	0.000	0.000	0.000	0.000	0.000
Cation sum	4.000	4.000	4.000	4.000	4.000	4.000	4.000	4.000	4.000	4.000	4.000

Appendix D.
Fasnia Member Clinopyroxene electron microprobe data

Sample ID	00TF90 px1_2	01TF127 3c	00TF95 px3_1	01TF127 2b	00TF88 2b	01TF127 3d	00TF88 4	00TF88 4e	00TF91 px7_4	00TF91 px7_3	00TF91 px7_1	01TF127 27b
Sequence	**upper**	**upper**	**upper**	**upper**	**upper**	**upper**	**upper**	**upper**	**upper**	**upper**	**upper**	**upper**
SiO_2	49.99	45.64	50.31	45.57	50.09	45.41	50.83	50.93	49.63	49.55	49.56	50.85
TiO_2	1.34	2.93	0.99	2.85	1.27	2.99	0.43	0.42	0.62	0.65	0.73	0.46
Al_2O_3	3.00	6.06	2.22	6.10	2.93	6.06	1.44	1.39	2.01	2.05	2.34	1.50
FeO*	8.27	9.50	8.41	10.33	8.31	9.48	12.02	13.98	12.82	12.95	12.88	12.75
MnO	0.52	0.42	0.57	0.39	0.51	0.38	1.33	1.30	1.20	1.09	1.21	1.38
MgO	12.56	10.86	12.92	10.85	13.18	10.66	9.84	10.00	9.39	9.47	8.96	9.35
CaO	22.45	22.45	22.45	22.33	21.89	22.46	21.48	21.08	21.13	20.85	20.33	21.24
Na_2O	1.10	1.10	1.12	1.18	1.21	1.34	1.59	1.93	1.92	1.95	1.96	1.99
K_2O	0.00	0.00	0.00	0.08	0.06	0.03	0.05	0.05	0.01	0.00	0.00	0.05
Total	99.23	98.96	99.01	99.67	99.45	98.81	99.00	101.09	98.74	98.56	97.97	99.59
Formula per 4 cations												
Si	1.872	1.728	1.886	1.714	1.865	1.719	1.939	1.904	1.898	1.897	1.913	1.929
Ti	0.038	0.083	0.028	0.081	0.036	0.085	0.012	0.012	0.018	0.019	0.021	0.013
Al	0.132	0.270	0.098	0.270	0.128	0.270	0.065	0.061	0.091	0.093	0.106	0.067
Fe^{2+}	0.132	0.112	0.108	0.094	0.099	0.079	0.231	0.188	0.189	0.195	0.245	0.207
Fe^{3+}	0.127	0.188	0.155	0.231	0.160	0.221	0.153	0.249	0.221	0.220	0.171	0.198
Mn	0.016	0.013	0.018	0.012	0.016	0.012	0.043	0.041	0.039	0.035	0.039	0.044
Mg	0.701	0.613	0.722	0.608	0.732	0.602	0.559	0.557	0.535	0.541	0.516	0.529
Ca	0.901	0.911	0.902	0.900	0.873	0.911	0.878	0.845	0.866	0.856	0.841	0.863
Na	0.080	0.081	0.082	0.086	0.088	0.099	0.118	0.140	0.143	0.145	0.147	0.147
K	0.000	0.000	0.000	0.004	0.003	0.002	0.002	0.002	0.001	0.000	0.000	0.003
Cation sum	4.000	4.000	4.000	4.000	4.000	4.000	4.000	4.000	4.000	4.000	4.000	4.000

Appendix D.
Fasnia Member
Clinopyroxene
electron
microprobe
data

Sample ID	01TF12727a	00TF91px7_2	00TF884b
Sequence	upper	upper	upper
SiO_2	49.80	49.30	50.32
TiO_2	0.69	0.87	0.69
Al_2O_3	1.95	2.25	2.11
FeO*	12.60	13.12	13.53
MnO	1.31	1.22	1.27
MgO	8.76	8.93	9.30
CaO	21.15	20.70	20.08
Na_2O	1.97	2.15	2.22
K_2O	0.05	0.01	0.00
Total	98.27	98.53	99.52
Formula per 4 cations			
Si	1.918	1.891	1.910
Ti	0.020	0.025	0.020
Al	0.088	0.102	0.095
Fe^{2+}	0.221	0.195	0.219
Fe^{3+}	0.185	0.226	0.211
Mn	0.043	0.040	0.041
Mg	0.503	0.511	0.526
Ca	0.873	0.851	0.816
Na	0.147	0.160	0.164
K	0.002	0.000	0.000
Cation sum	4.000	4.000	4.000

Appendix E

LA-ICP-MS data for Fasnia Member pyroxenes

Appendix E.
Fasnia Member
Clinopyroxene
LA-ICP-MS
data

Sample ID	99TF03	99TF03	99TF03	99TF03	99TF6	01TF49	99TF6	99TF6	01TF49	01TF51	01TF49
	3_2	3_1	2_1	4_1	gmB_px5	px1	sphB_px9	gmB_px6	px3	px2	px2
Sequence	lower	lower	lower	lower	lower	lower	lower	lower	lower	lower	lower
(ppm) Sc	85.08	85.54	72.68	62.27	17.73	19.25	26.63	16.86	17.20	18.47	18.26
Sr	116.6	111.6	118.4	139.6	93.8	48.2	24.1	84.9	41.4	37.7	42.3
Y	10.03	10.58	11.62	12.76	59.32	63.52	49.66	62.37	58.49	55.78	62.74
Zr	79	97	128	159	321	349	363	363	378	385	387
Nb	0.42	0.43	0.55	0.74	3.22	1.61	2.41	3.45	1.81	1.97	1.85
Ba	0.32	0.12	0.37	0.06	0.91	0.44	0.57	0.62	0.19	0.13	0.29
La	3.93	3.69	4.09	5.38	47.69	40.62	48.92	50.02	39.45	39.99	41.65
Ce	17.61	17.87	20.51	25.69	161.59	140.68	151.67	172.30	135.59	133.38	140.35
Pr	2.28	2.29	2.80	3.20	23.36	20.58	20.94	24.92	18.55	17.38	20.21
Nd	11.58	12.20	15.22	16.97	108.70	98.95	85.43	115.25	87.83	80.82	91.98
Sm	2.94	3.31	4.03	4.49	23.83	21.86	16.96	23.81	18.78	16.91	19.55
Eu	1.05	1.13	1.28	1.62	6.78	5.27	3.69	6.52	4.24	3.80	4.59
Gd	2.56	2.64	2.88	3.65	18.43	19.40	13.36	18.10	16.97	14.58	17.71
Tb	0.38	0.40	0.44	0.52	2.71	2.78	1.99	2.79	2.38	1.95	2.47
Dy	2.06	2.37	2.39	2.85	14.64	15.51	10.97	14.34	13.11	12.25	15.26
Ho	0.34	0.41	0.41	0.43	2.54	2.74	2.01	2.52	2.27	2.14	2.47
Er	0.93	0.97	0.92	1.08	5.72	6.49	5.06	5.96	5.78	5.36	6.19
Tm	0.10	0.10	0.10	0.12	0.76	0.84	0.70	0.80	0.77	0.72	0.82
Yb	0.61	0.64	0.75	0.69	4.91	5.55	4.68	5.20	5.08	4.82	5.44
Lu	0.06	0.10	0.08	0.08	0.66	0.84	0.90	0.76	0.82	0.72	0.88
Hf	1.75	2.06	2.85	3.36	9.93	8.62	10.93	10.33	8.18	7.98	8.95
Ta	0.07	0.11	0.13	0.15	0.48	0.32	0.38	0.57	0.34	0.36	0.35
Pb	0.12	0.21	0.15	0.12	0.28	0.12	0.32	0.66	0.05	0.01	0.10
Th	0.03	0.03	0.03	0.05	0.14	0.10	0.12	0.16	0.10	0.10	0.09
U	0.00	0.01	0.01	0.00	0.02	0.01	0.01	0.02	0.00	0.01	0.01

Appendix E.
Fasnia Member
Clinopyroxene
LA-ICP-MS
data

Sample ID	01TF87 px1	99TF6 gmB_px10	99TF6 gmA_px24	99TF6 PA_22px	99TF6 PB_px2	99TF6 PB_px2_2	99TF6 gmB_px4	01TF54 px2	99TF6 PA_20px
Sequence	lower	lower	lower	lower	lower	lower	lower	lower	lower
(ppm) Sc	20.12	24.23	24.83	25.00	26.78	28.01	26.39	24.83	24.96
Sr	68.8	4.2	3.6	3.0	3.8	4.5	3.8	3.8	2.1
Y	76.25	19.63	19.73	20.65	23.78	26.55	22.63	24.63	25.45
Zr	485	889	957	992	1052	1080	1176	1338	1340
Nb	2.78	1.55	1.75	1.55	1.80	6.01	1.70	1.51	2.03
Ba	0.31	0.29	0.32	0.33	0.27	1.35	0.34	(0.06)	0.40
La	49.90	40.18	43.05	42.68	47.06	54.82	48.15	40.34	52.98
Ce	162.29	86.77	96.86	90.44	88.90	96.78	101.41	84.77	94.88
Pr	23.22	8.04	8.67	8.76	9.12	10.41	9.44	7.94	9.93
Nd	113.74	25.02	26.90	28.90	30.50	35.68	30.31	25.45	32.58
Sm	24.55	3.80	3.96	4.46	4.54	5.49	4.42	3.98	4.87
Eu	5.65	0.71	0.70	0.85	0.93	0.98	0.83	0.67	0.90
Gd	21.70	2.98	2.96	3.90	3.61	4.10	3.38	3.62	3.87
Tb	3.04	0.50	0.48	0.60	0.61	0.67	0.58	0.53	0.68
Dy	17.44	3.15	3.09	3.59	4.30	4.61	3.56	3.72	4.53
Ho	2.98	0.69	0.65	0.84	0.93	1.02	0.78	0.77	0.98
Er	7.23	2.35	2.25	3.00	3.12	3.43	2.68	2.90	3.52
Tm	0.94	0.50	0.50	0.66	0.69	0.73	0.61	0.62	0.87
Yb	5.89	6.47	6.31	7.47	8.56	9.15	7.25	7.36	10.10
Lu	0.91	1.57	1.56	2.16	2.30	2.31	1.85	1.98	2.71
Hf	11.79	20.47	22.60	29.02	29.29	29.02	30.26	24.07	40.61
Ta	0.54	0.07	0.08	0.12	0.09	0.10	0.09	0.08	0.10
Pb	0.09	0.48	0.44	0.53	0.50	2.30	0.48	0.17	0.78
Th	0.14	0.05	0.05	0.07	0.08	1.39	0.09	0.05	0.29
U	0.01	0.01	0.01	0.02	0.02	0.05	0.01	0.00	0.01

Appendix E.
Fasnia Member
Clinopyroxene
LA-ICP-MS
data

Sample ID	99TF6 gmB_px1	99TF6 gmB_px7	99TF6 gmB_px2b	99TF6 gmA_px25	99TF6 gmA_px28	99TF6 sphA_px2	99TF6 gmB_px8	99TF6 gmB_px2
Sequence	lower	lower	lower	lower	lower	lower	lower	lower
(ppm) Sc	38.15	26.67	27.44	24.16	26.25	32.67	25.85	31.63
Sr	4.3	4.1	3.8	3.7	2.9	4.8	3.3	3.1
Y	30.68	24.72	25.87	22.81	27.00	26.05	25.77	31.83
Zr	1358	1361	1363	1370	1400	1405	1460	1599
Nb	3.42	2.26	2.76	9.25	3.13	4.38	3.68	6.28
Ba	0.38	0.31	0.43	1.49	0.48	0.43	0.44	0.52
La	56.50	59.30	57.17	56.00	62.66	56.92	59.56	76.43
Ce	110.25	119.13	117.55	111.26	135.48	112.75	124.76	144.69
Pr	11.35	10.92	10.87	10.19	11.86	10.92	11.46	13.56
Nd	37.60	33.00	34.24	30.47	35.71	33.65	34.36	42.01
Sm	5.81	4.87	4.99	4.49	5.40	5.03	5.13	6.29
Eu	1.02	0.89	0.91	0.82	0.92	0.90	0.92	1.08
Gd	4.57	3.55	3.93	3.38	3.85	4.37	4.02	4.98
Tb	0.78	0.60	0.67	0.53	0.62	0.67	0.67	0.81
Dy	4.75	3.73	4.09	3.48	4.20	4.07	4.17	4.93
Ho	1.06	0.83	0.91	0.76	0.85	0.91	0.87	1.07
Er	3.45	2.86	3.02	2.62	3.01	3.15	2.97	3.52
Tm	0.71	0.63	0.66	0.55	0.65	0.69	0.65	0.78
Yb	8.76	7.91	7.99	7.03	8.07	7.34	7.60	9.09
Lu	2.09	2.00	1.93	1.70	1.96	2.12	1.87	2.23
Hf	33.29	33.09	34.28	32.01	31.74	35.44	35.98	36.79
Ta	0.26	0.13	0.19	0.37	0.19	0.41	0.28	1.30
Pb	0.55	0.44	0.54	2.36	0.50	0.51	0.52	0.47
Th	0.09	0.19	0.09	1.91	0.08	0.12	0.10	0.22
U	0.02	0.02	0.01	0.48	0.01	0.02	0.01	0.04

Appendix E.
Fasnia Member
Clinopyroxene
LA-ICP-MS
data

Sample ID	99TF6 gmA_px11	99TF6 gmA_px22	99TF6 sphA_px1b	99TF6 gmA_px27	99TF6 sphB_px3	99TF6 gmA_px19	99TF6 gmA_px16	01TF54 px1
Sequence	lower	lower	lower	lower	lower	lower	lower	lower
(ppm) Sc	28.51	27.84	32.74	33.06	34.98	27.74	29.32	30.50
Sr	4.6	4.6	2.5	2.4	3.0	2.4	2.8	3.7
Y	26.86	24.43	31.72	30.79	33.71	27.96	26.45	31.31
Zr	1617	1719	1825	1827	1866	1902	1909	2062
Nb	3.96	4.78	9.98	5.79	3.59	5.87	4.11	2.95
Ba	0.42	0.38	(0.61)	0.50	0.76	0.53	0.50	0.36
La	59.04	56.46	64.45	65.80	104.17	70.70	67.42	61.17
Ce	116.01	120.91	111.77	138.97	174.79	143.66	137.51	133.48
Pr	10.91	10.90	11.61	12.94	15.89	12.70	12.35	12.49
Nd	34.00	33.25	38.89	40.37	46.93	38.19	36.63	39.84
Sm	4.94	4.69	5.75	6.12	6.69	5.64	5.33	5.76
Eu	0.88	0.88	1.15	1.02	1.14	0.98	0.94	1.00
Gd	3.85	3.70	4.53	4.55	5.67	4.25	3.79	5.34
Tb	0.67	0.60	0.81	0.76	0.80	0.71	0.67	0.82
Dy	4.11	3.90	4.83	4.90	5.01	4.55	4.24	5.30
Ho	0.91	0.84	1.11	1.04	1.09	1.01	0.87	1.20
Er	2.99	2.90	4.22	3.43	3.90	3.43	3.14	4.23
Tm	0.63	0.63	0.96	0.71	0.84	0.76	0.69	0.95
Yb	7.99	7.85	8.40	8.62	8.54	9.23	8.34	11.03
Lu	1.92	1.84	2.58	2.02	2.32	2.20	2.04	2.82
Hf	37.95	38.68	45.93	43.59	52.51	43.41	46.98	46.52
Ta	0.31	0.36	0.83	0.44	0.32	0.43	0.33	0.34
Pb	0.46	0.49	0.53	0.49	0.54	0.47	0.48	0.41
Th	0.12	0.11	0.32	0.15	1.30	0.17	0.12	0.12
U	0.02	0.02	0.04	0.02	0.09	0.02	0.01	0.01

Appendix E.
Fasnia Member
Clinopyroxene
LA-ICP-MS
data

Sample ID	01TF54	99TF6	99TF03	01TF127	03TF172	99TF21	99TF21	03TF126	03TF126
	px1_2	sphA_px1	1_2	px3	px3	px2_2	px2	pxcor_12m	pxend_12m
Sequence	lower	lower	lower	upper	upper	upper	upper	upper	upper
(ppm) Sc	28.17	32.39	32.37	51.67	19.01	59.11	66.53	15.79	16.46
Sr	3.4	4.4	7.8	67.7	80.0	136.4	131.7	62.0	68.5
Y	31.91	33.11	29.26	6.92	13.91	21.55	21.42	42.82	47.82
Zr	2125	2141	3411	19	101	161	185	222	229
Nb	4.14	8.08	4.18	0.08	0.30	1.01	1.12	11.78	1.88
Ba	0.25	0.47	0.63	(0.02)	(0.01)	(0.08)	(0.08)	5.01	1.01
La	60.80	73.45	66.82	1.42	10.23	7.61	7.24	42.53	40.38
Ce	130.73	143.23	164.43	5.18	27.61	29.95	28.73	148.42	153.59
Pr	11.59	14.08	11.93	0.89	3.83	4.80	4.72	19.50	20.64
Nd	36.54	43.04	36.73	5.43	17.80	26.42	26.55	83.33	89.81
Sm	5.19	6.24	5.12	1.75	4.39	7.10	7.03	17.33	19.65
Eu	0.90	1.18	0.92	0.63	1.62	2.36	2.36	5.16	5.51
Gd	4.68	5.61	3.84	2.05	3.87	7.32	7.22	12.63	14.38
Tb	0.73	0.87	0.65	0.28	0.61	0.96	0.91	1.91	2.24
Dy	4.71	5.28	4.15	1.76	3.52	5.06	5.27	10.24	11.49
Ho	1.07	1.22	0.96	0.27	0.63	0.88	0.85	1.74	1.98
Er	3.82	4.03	3.32	0.72	1.52	2.08	2.06	4.10	4.66
Tm	0.82	0.86	0.70	0.09	0.20	0.26	0.23	0.51	0.56
Yb	9.29	9.18	8.14	0.53	1.33	1.41	1.39	3.64	3.96
Lu	2.33	2.57	2.14	0.08	0.20	0.17	0.18	0.54	0.57
Hf	39.85	53.38	45.12	0.71	3.04	4.93	5.90	6.27	7.06
Ta	0.33	0.74	0.40	0.02	0.09	0.25	0.31	0.57	0.28
Pb	0.47	0.50	0.42	0.01	0.94	0.05	(0.02)	1.92	1.04
Th	0.15	0.22	0.14	0.02	0.18	0.07	0.08	0.54	0.10
U	0.02	0.03	0.01	0.00	0.03	0.01	0.01	0.15	0.01

Appendix E.
Fasnia Member
Clinopyroxene
LA-ICP-MS
data

Sample ID	03TF126 pxrim2_12m	00TF91 px6	03TF126 pxrim_12m	00TF91 px5	03TF13 px2	03TF13 px1	00TF95 px3_2	00TF90 px2	00TF92 px1	00TF91 px2_2
Sequence	upper	upper	upper	upper	upper	upper	upper	upper	upper	upper
(ppm) Sc	17.07	24.04	18.62	22.76	21.14	22.89	21.66	16.92	18.76	24.42
Sr	66.1	154.9	54.4	172.6	53.7	46.0	51.0	50.6	144.4	50.4
Y	51.75	38.51	48.36	33.42	56.48	56.35	60.82	61.10	63.66	90.62
Zr	242	251	257	258	318	335	347	385	406	419
Nb	2.25	1.69	2.06	1.97	2.57	2.57	1.82	1.94	2.80	2.25
Ba	1.03	(0.04)	0.90	(0.06)	0.74	0.63	0.47	0.39	0.53	0.18
La	53.18	19.29	44.30	15.79	47.48	50.04	38.41	42.45	57.08	48.30
Ce	186.32	68.96	162.58	56.34	159.66	165.59	142.06	145.30	182.46	174.50
Pr	24.75	10.22	21.69	8.60	22.49	22.79	20.49	20.20	23.19	25.23
Nd	105.77	51.39	92.34	44.57	97.16	97.07	95.96	95.00	104.62	118.83
Sm	22.01	12.22	19.49	10.74	20.94	20.57	20.82	20.43	21.20	26.49
Eu	5.97	3.87	5.00	3.46	5.21	5.05	4.77	4.89	6.34	5.47
Gd	15.28	11.41	14.10	10.42	15.36	15.13	18.69	18.10	19.47	24.43
Tb	2.32	1.57	2.06	1.36	2.37	2.27	2.67	2.49	2.61	3.51
Dy	12.70	8.95	11.14	7.39	12.74	12.35	15.55	14.24	14.91	19.94
Ho	2.10	1.54	1.94	1.33	2.22	2.20	2.54	2.51	2.49	3.54
Er	4.97	3.46	4.70	2.95	5.21	5.28	6.14	6.36	6.22	8.89
Tm	0.66	0.44	0.59	0.37	0.72	0.68	0.84	0.85	0.79	1.17
Yb	4.02	2.83	4.26	2.07	4.52	4.99	5.40	5.53	4.52	7.03
Lu	0.59	0.39	0.59	0.29	0.69	0.75	0.79	0.87	0.61	1.04
Hf	7.34	5.84	7.34	5.93	9.20	9.77	8.34	9.25	9.39	9.26
Ta	0.40	0.37	0.29	0.42	0.41	0.42	0.35	0.34	0.56	0.43
Pb	0.43	0.01	1.93	0.03	0.28	0.27	0.22	0.09	0.09	0.09
Th	0.29	0.12	0.09	0.11	0.11	0.11	0.09	0.11	0.49	0.11
U	0.05	0.01	0.01	0.01	0.01	0.02	0.01	0.01	0.04	0.01

Appendix E.
Fasnia Member
Clinopyroxene
LA-ICP-MS
data

Sample ID	00TF91	00TF91	01TF127	00TF95	00TF95	01TF127	01TF127	00TF90	99TF21	00TF90
	px3	px4_1	GM_px2_2	px2	px4	GM_px2	GM_px3	px1	px1	px1_2
Sequence	upper	upper	upper	upper	upper	upper	upper	upper	upper	upper
(ppm) Sc	23.62	23.52	24.41	20.15	26.51	27.29	26.49	31.74	23.06	24.22
Sr	136.2	26.8	135.3	70.5	24.1	142.0	140.1	47.2	46.6	52.6
Y	57.74	56.08	48.27	69.15	51.76	47.34	50.50	68.51	72.85	77.29
Zr	444	453	462	466	471	493	503	508	540	564
Nb	2.92	1.84	5.63	3.12	2.17	5.11	4.92	2.61	3.12	2.98
Ba	0.12	0.19	2.50	0.40	0.18	0.69	0.57	0.20	0.31	2.27
La	33.73	41.57	42.93	44.59	39.63	40.72	43.14	48.36	51.86	58.76
Ce	114.67	122.62	138.27	158.77	123.12	123.58	133.24	161.31	172.46	183.82
Pr	16.12	16.59	16.95	22.53	16.38	17.82	19.22	26.87	24.01	28.00
Nd	80.04	75.53	77.82	107.96	71.32	82.74	88.51	132.48	111.07	137.40
Sm	17.72	15.81	17.44	23.46	14.79	17.60	19.32	28.26	23.70	28.25
Eu	4.97	3.16	5.07	5.78	2.95	5.45	5.84	6.48	5.34	6.07
Gd	16.23	13.90	12.70	20.12	12.59	14.29	14.88	35.37	21.02	23.94
Tb	2.27	2.02	1.97	2.88	1.74	2.07	2.24	3.90	2.89	3.47
Dy	12.97	11.77	10.38	15.92	10.52	10.98	12.00	21.11	16.57	20.19
Ho	2.27	2.14	1.87	2.79	1.90	1.98	2.05	3.67	2.88	3.60
Er	5.54	5.47	4.43	6.67	4.84	4.69	4.96	9.71	7.23	8.54
Tm	0.69	0.74	0.58	0.89	0.68	0.62	0.65	1.30	0.98	1.14
Yb	4.43	4.91	4.12	5.62	4.70	4.11	4.53	9.07	6.24	7.69
Lu	0.60	0.88	0.60	0.82	0.84	0.62	0.62	1.34	0.98	1.24
Hf	9.76	9.36	11.98	10.95	10.03	14.94	14.67	17.61	12.25	16.48
Ta	0.72	0.28	0.82	0.67	0.37	0.81	0.93	0.73	0.62	0.62
Pb	0.06	0.19	3.35	0.13	0.12	0.40	0.23	0.32	0.11	0.79
Th	0.17	0.10	5.00	0.15	0.09	0.77	0.21	0.18	0.14	0.17
U	0.01	0.01	0.09	0.01	0.01	0.03	0.02	0.01	0.01	0.08

Appendix E.
Fasnia Member
Clinopyroxene
LA-ICP-MS
data

Sample ID	00TF91 px2_cntr	03TF16 px2_1	03TF16 px2_2	01TF127 GM_px27	00TF91 px7	00TF91 px7_2
Sequence	upper	upper	upper	upper	upper	upper
(ppm) Sc	35.59	38.06	33.94	29.56	30.45	29.04
Sr	47.4	4.2	4.3	2.6	5.4	5.7
Y	83.45	30.60	29.57	26.69	32.61	31.31
Zr	663	1678	1829	1933	2107	2377
Nb	3.01	3.84	4.39	4.33	3.03	4.35
Ba	0.26	0.85	1.15	0.48	0.08	(0.02)
La	54.76	76.57	73.87	66.33	60.55	53.19
Ce	181.24	148.01	144.44	135.65	127.58	113.25
Pr	23.49	14.82	13.89	11.87	11.24	10.09
Nd	100.75	47.04	42.52	35.42	35.85	32.83
Sm	20.58	6.51	6.29	5.09	5.16	4.87
Eu	4.03	1.20	1.18	0.97	0.87	0.90
Gd	18.60	7.34	5.64	3.86	4.66	4.34
Tb	2.83	1.18	0.84	0.65	0.72	0.67
Dy	17.25	5.55	5.06	4.08	4.81	4.39
Ho	3.23	1.31	1.19	0.89	1.02	0.96
Er	8.31	4.25	3.93	2.99	3.55	3.51
Tm	1.17	0.94	0.85	0.68	0.76	0.80
Yb	7.66	11.39	10.49	8.00	8.81	8.93
Lu	1.33	2.77	2.66	1.99	2.09	2.22
Hf	13.30	48.01	50.28	48.23	39.54	39.63
Ta	0.45	0.39	0.37	0.36	0.28	0.41
Pb	0.16	0.88	0.92	0.56	0.21	0.21
Th	0.13	15.56	15.54	0.12	0.11	0.15
U	0.01	1.35	1.23	0.01	0.01	0.01

Appendix F

Electron microprobe data for Fasnia Member titanites

Appendix F. Titanite electron microprobe data

	00TF95sph3_1rT1	00TF95sph3_2cT1	00TF95sph3_3c3T1	00TF95sph3_5T1
SiO2	29.51	29.00	28.24	28.14
Al2O3	1.04	1.01	0.99	0.96
TiO2	36.28	36.31	35.41	35.20
FeO	1.32	1.30	1.36	1.28
MnO	0.12	0.09	0.13	0.12
MgO	0.03	0.05	0.03	0.03
CaO	26.91	26.61	26.53	26.52
Na2O	0.06		0.09	0.12
ZrO2	0.40	0.56	0.58	0.68
Nb2O5	0.79	0.83	0.80	0.91
F	0.35	0.24	0.72	0.12
Probe sum	96.67	95.90	94.58	94.02

Appendix F. Titanite electron microprobe data

	01TF119_2 T1	01TF119_2b T1	01TF119_2c T1	01TF127sph1_2 T1	01TF127sph3_2 T1
SiO2	30.38	29.30	29.03	29.31	29.24
Al2O3	1.06	1.06	1.01	1.09	0.96
TiO2	35.79	36.12	35.50	34.83	35.85
FeO	1.39	1.36	1.39	1.68	1.31
MnO	0.11	0.12	0.13	0.12	0.13
MgO	0.06	0.05	0.04	0.04	0.04
CaO	26.81	26.67	26.94	26.87	26.68
Na2O	0.06	0.15	0.08	0.03	0.10
ZrO2	0.46	0.76	0.57	0.89	0.61
Nb2O5	0.65	0.69	0.61	0.94	0.88
F	0.20	0.22	0.18	0.58	0.19
Probe sum	96.95	96.49	95.46	96.14	95.89

Appendix F. Titanite electron microprobe data

	99TF6_1_1 T1	99TF6_1_2 T1	99TF6_1_2b T1	99TF6_8_1 T1	99TF6_8_2 T1	99TF6_9 T1
SiO2	28.95	27.77	29.30	29.00	27.68	28.72
Al2O3	0.98	1.10	1.24	1.04	1.18	1.05
TiO2	35.87	34.86	35.05	35.66	35.80	34.85
FeO	1.49	1.71	1.79	1.37	1.49	1.74
MnO	0.16	0.16	0.11	0.11	0.09	0.10
MgO	0.04	0.06	0.03	0.03	0.01	0.05
CaO	27.12	26.83	26.74	26.63	26.57	26.46
Na2O	0.08	0.08	0.10	0.05	0.01	
ZrO2	0.65	0.84	0.74	0.48	0.46	0.81
Nb2O5	0.98	0.70	0.66	0.84	0.66	0.87
F	0.20	0.39	0.25	0.12	0.15	0.28
Probe sum	96.52	94.49	96.01	95.33	94.10	94.94

Appendix F. Titanite electron microprobe data

	00TF95sph1_1 T2	00TF95sph1_1b T2	00TF95sph1_2 T2	00TF95sph6_1 T2
SiO2	28.74	29.29	28.18	28.65
Al2O3	1.01	0.92	1.06	1.04
TiO2	36.45	36.67	35.99	35.65
FeO	1.30	1.32	1.47	1.37
MnO	0.06	0.07	0.11	0.08
MgO	0.03	0.05	0.01	0.05
CaO	26.86	27.04	26.97	27.23
Na2O				0.43
ZrO2	0.51	0.58	0.60	0.38
Nb2O5		0.84	0.74	0.69
F	0.18	0.19	0.26	0.31
Probe sum	96.88	96.90	95.29	95.75

Appendix F. Titanite electron microprobe data

	00TF95sph6_2 T2	00TF96sph4_3 T2	01TF127sph2_1 T2	01TF127sph2_2 T2
SiO2	29.06	28.79	29.09	29.15
Al2O3	1.02	1.01	1.08	1.05
TiO2	36.00	35.48	35.73	36.25
FeO	1.50	1.56	1.39	1.44
MnO	0.13	0.12	0.12	0.11
MgO	0.03	0.04	0.03	0.03
CaO	27.06	27.12	27.07	26.77
Na2O		0.08	0.04	0.05
ZrO2	0.62	0.87	0.59	0.60
Nb2O5	0.83	0.97	0.62	0.77
F	0.38	0.34	0.43	0.29
Probe sum	96.46	96.23	96.01	96.38

Appendix F. Titanite electron microprobe data

	01TF127sph2_2 T2	01TF127sph5_1c T2	01TF127sph5_2r T2	99TF6_5_1 T2
SiO2	29.69	29.13	28.94	29.85
Al2O3	1.09	0.97	1.06	1.04
TiO2	36.77	35.62	35.45	36.53
FeO	1.38	1.44	1.46	1.37
MnO	0.14	0.13	0.12	0.12
MgO	0.04	0.03	0.01	0.05
CaO	26.99	26.97	26.86	26.44
Na2O	0.04	0.08	0.11	0.04
ZrO2	0.57	0.73	0.73	0.53
Nb2O5		1.06	0.79	0.79
F	0.35	0.40	0.84	0.13
Probe sum	96.91	96.38	96.05	96.91

Appendix F. Titanite electron microprobe data

	00TF95sph2_2 T3	00TF95sph2_3 T3	00TF95sph4_1 T3	00TF95sph4_4r T3
SiO2	30	28.92	29.12	29
Al2O3	1	1.08	1.05	1
TiO2	36	35.36	36.07	36
FeO	1	1.54	1.47	1
MnO	0	0.09	0.14	0
MgO	0	0.03	0.04	0
CaO	27	27.38	26.78	27
Na2O			0.05	0
ZrO2	1	0.82	0.57	0
Nb2O5	1	0.94	0.77	1
F	0	0.48	0.16	0
Probe sum	97	96.45	96.16	96

Appendix F. Titanite electron microprobe data

	00TF95sph5_1 T3	00TF95sph5_2 T3	00TF95sph5_3 T3	00TF95sph5_4 T3	00TF95sph7_1 T3
SiO2	29.81	29.39	29.01	28.75	29.13
Al2O3	1.04	1.01	1.13	1.04	1.07
TiO2	36.58	36.22	35.62	36.20	35.87
FeO	1.33	1.34	1.57	1.47	1.45
MnO	0.12	0.08	0.12	0.14	0.10
MgO	0.05	0.04	0.03	0.05	0.06
CaO	27.17	27.11	27.01	26.60	26.91
Na2O	0.04	0.03	0.04	0.05	
ZrO2	0.53	0.56	0.82	0.64	0.51
Nb2O5	0.73	0.89	0.72	0.77	0.68
F	0.14	0.23	0.45	0.26	0.34
Probe sum	97.47	96.81	96.33	95.86	95.97

Appendix F. Titanite electron microprobe data

	00TF95sph7_2 T3	01TF127sph4_1r T3	01TF127sph6_1 T3	01TF127sph6_2r T3
SiO2	28.949	29.47	29.30	28.57
Al2O3	1.073	1.05	1.03	0.95
TiO2	36.195	36.12	34.89	35.24
FeO	1.407	1.47	1.51	1.33
MnO	0.079	0.10	0.11	0.15
MgO	0.020	0.03	0.03	0.04
CaO	27.052	26.91	27.07	26.43
Na2O		0.04	0.07	0.08
ZrO2	0.705	0.74	0.59	0.57
Nb2O5	0.608	0.85	1.02	0.76
F	0.346	0.29	0.43	0.26
Probe sum	96.288	96.95	95.87	94.27

Appendix F. Titanite electron microprobe data

	00TF95sph2_1 T4	00TF95sph3_4c3 T4	00TF95sph3_6 T4	00TF95sph4_2 T4	01TF119_1 T4
SiO2	30.08	28.48	29.86	29.23	30.34
Al2O3	1.07	1.04	1.06	1.01	1.03
TiO2	34.72	34.35	35.25	33.41	33.58
FeO	1.70	1.47	1.64	1.60	1.83
MnO	0.00	0.09	0.11	0.12	0.11
MgO	0.02	0.01	0.05	0.00	0.04
CaO	27.30	26.36	27.44	26.88	26.95
Na2O		0.10		0.13	0.14
ZrO2	1.14	1.22	1.11	1.39	1.51
Nb2O5	1.11	1.64	1.03	1.82	1.25
F	0.51	0.25	0.34	0.36	0.26
Probe sum	97.43	94.90	97.77	95.78	97.04

Appendix F. Titanite electron microprobe data

	01TF119_3 T4	01TF127sph1_1 T4	01TF127sph4_2c T4	01TF127sph4_3c T4	99TF6_10c T4
SiO2	29.51	29.60	29.42	29.37	28.42
Al2O3	1.13	1.12	1.04	1.03	1.08
TiO2	33.19	33.63	33.70	34.12	32.35
FeO	1.81	1.89	1.72	1.77	1.99
MnO	0.11	0.12	0.10	0.11	0.10
MgO	0.03	0.04	0.02	0.03	0.03
CaO	26.70	27.35	26.62	26.72	26.72
Na2O	0.17	0.11	0.18	0.17	0.02
ZrO2	2.08	1.32	1.29	1.16	2.01
Nb2O5	1.48	1.06	1.71	1.53	1.38
F	0.41	0.51	0.48	0.55	1.20
Probe sum	96.61	96.53	96.07	96.33	95.31

Appendix F. Titanite electron microprobe data

	99TF6_10c2 T4	99TF6_10c3 T4	99TF6_10r T4	99TF6_11c T4	99TF6_11r T4	99TF6_12_1 T4
SiO2	28.91	28.05	28.23	30.07	30.25	30.77
Al2O3	1.08	1.10	1.04	1.06	1.03	1.15
TiO2	33.06	33.08	33.57	34.03	33.91	34.46
FeO	1.96	1.89	1.88	1.93	1.99	2.09
MnO	0.09	0.11	0.09	0.11	0.12	0.07
MgO	0.02	0.01	0.01	0.02	0.04	0.01
CaO	26.60	26.77	26.98	27.05	27.18	27.39
Na2O	0.15	0.14	0.16	0.12	0.08	
ZrO2	2.10	2.02	1.61	1.87	1.46	1.10
Nb2O5	1.48	1.50	1.39	1.44	1.12	0.89
F	1.03	0.53	0.44	0.63	1.07	0.67
Probe sum	96.47	95.21	95.41	98.33	98.26	98.59

Appendix F. Titanite electron microprobe data

	99TF6_13_1 T4	99TF6_13_2 T4	99TF6_14_1 T4	99TF6_14_2 T4	99TF6_2_1 T4
SiO2	29.78	30.95	29.71	29.68	28.00
Al2O3	1.11	1.11	1.04	1.08	1.21
TiO2	33.17	34.36	32.30	32.95	33.98
FeO	2.02	1.94	1.91	1.98	2.32
MnO	0.09	0.10	0.08	0.14	0.13
MgO	0.00	0.03	0.00	0.01	0.03
CaO	27.19	27.30	26.72	26.96	26.56
Na2O	0.09	0.10	0.25	0.17	0.11
ZrO2	1.79	1.31	2.55	2.14	1.14
Nb2O5	1.30	1.27	1.64	1.77	0.99
F	0.68	0.71	0.49	0.46	0.67
Probe sum	97.22	99.19	96.71	97.34	95.13

Appendix F. Titanite electron microprobe data

	99TF6_3_1 T4	99TF6_3_2 T4	99TF6_6_1 T4	99TF6_6_2 T4	99TF6_7_1 T4	99TF6_7_2 T4
SiO2	29.14	29.46	29.30	29.60	28.87	29.43
Al2O3	1.04	1.09	1.07	1.07	1.12	1.15
TiO2	32.95	33.89	34.11	33.76	33.90	33.97
FeO	1.88	2.00	1.91	1.97	2.21	2.07
MnO	0.12	0.11	0.09	0.10	0.11	0.09
MgO	0.02	0.02	0.03	0.01	0.00	0.03
CaO	26.68	27.11	27.13	27.33	26.84	27.11
Na2O	0.12	0.17	0.15	0.08	0.10	0.07
ZrO2	1.81	1.43	1.51	1.70	1.25	0.99
Nb2O5	1.55	1.31	1.39	1.27	0.93	1.17
F	0.64	0.50	0.45	0.55	0.91	0.42
Probe sum	95.95	97.09	97.14	97.44	96.25	96.49

Appendix F. Titanite electron microprobe data

	99TF6_9.5 T4	99TF6_9.5b T4	99TF6A_1_1 T4	99TF6A_2_1 T4
SiO2	27.53	29.13	30.68	30.63
Al2O3	1.05	1.10	1.09	1.06
TiO2	33.74	34.23	34.25	33.48
FeO	1.91	2.00	1.95	1.85
MnO	0.18	0.10	0.15	0.13
MgO	0.02	0.07	0.02	0.01
CaO	26.15	27.10	27.26	27.26
Na2O	0.24		0.12	0.15
ZrO2	1.97	1.29	1.32	1.66
Nb2O5	1.07	1.22	1.06	1.28
F	0.35	0.52	0.73	0.53
Probe sum	94.21	96.75	98.63	98.05

Appendix G

LA-ICP-MS data for Fasnia Member titanites

Appendix G.
Titanite
LA-ICP-MS

trace element

contents

Sample ID	00TF88_gm_5sph	00TF88_gm_5sph1_2	00TF95SPH_1R	00TF95SPH_3C	00TF95SPH_3C_end
Type	T1	T1	T1	T1	T1
Lower/upper	lower	lower	upper	upper	upper
(ppm) La	3,108	2,937	3,642	3,082	3,346
Ce	8,828	8,512	8,623	8,707	8,906
Pr	1,163	1,077	1,221	1,208	1,241
Nd	4,843	4,404	5,113	5,386	5,307
Sm	876	793	939	1,043	995
Gd	603	552	670	732	683
Tb	87	81	98	105	100
Dy	450	408	506	521	500
Ho	73	68	86	85	83
Y	1,744	1,641	2,046	2,019	1,924
Er	161	154	195	184	181
Tm	19	18	23	21	21
Yb	94	95	115	101	104
Lu	10	10	13	11	11
Zr	4,310	4,111	5,154	3,887	4,276
Nb	6,246	5,777	6,693	5,477	6,014
Ta	704	606	783	710	751
Hf	121	114	146	113	127
Sr	39	37	38	76	60
Ba	31	29	29	29	29
Th	111	98	135	110	111
U	10	10	10	9	9

Appendix G.
Titanite
LA-ICP-MS

trace element

contents

Sample ID	00TF95SPH_3C3	00TF95SPH_3C4	00TF95SPH_3C6_STRT	00TF95SPH_3C7_END	01TF119_sph1
Type	T1	T1	T1	T1	T1
Lower/upper	upper	upper	upper	upper	lower
(ppm) La	3,207	3,063	3,028	2,830	2,908
Ce	8,818	8,223	8,484	7,389	8,301
Pr	1,210	1,113	1,185	1,051	1,076
Nd	5,174	4,756	4,979	4,456	4,536
Sm	979	909	964	823	825
Gd	686	635	699	593	590
Tb	100	93	102	87	86
Dy	501	463	509	435	440
Ho	83	77	87	75	75
Y	1,943	1,833	1,967	1,736	1,712
Er	183	172	188	166	166
Tm	21	20	21	19	19
Yb	102	96	106	95	95
Lu	11	10	12	10	11
Zr	4,157	4,276	4,222	3,992	4,468
Nb	5,852	5,416	5,438	5,167	5,642
Ta	735	702	643	606	599
Hf	119	126	123	117	121
Sr	54	53	55	46	40
Ba	29	28	28	26	27
Th	123	106	101	93	96
U	9	9	9	8	10

Appendix G.
Titanite
LA-ICP-MS

trace element

contents

Sample ID	01TF119_sph2	01TF119_sph3_loZr	01TF127SPH_2	01TF127SPH_3R1	99TF6sphB_sph1
Type	T1	T1	T1	T1	T1
Lower/upper	lower	lower	upper	upper	lower
(ppm) La	3,008	2,763	3,202	2,726	2,979
Ce	8,090	7,553	7,886	7,751	6,861
Pr	1,031	1,000	1,055	1,012	904
Nd	4,327	4,191	4,233	4,201	3,519
Sm	787	761	751	772	599
Gd	547	532	539	538	456
Tb	81	79	80	80	65
Dy	415	396	422	407	344
Ho	70	65	73	70	62
Y	1,593	1,607	1,708	1,625	1,557
Er	158	151	169	158	146
Tm	19	18	20	19	18
Yb	97	92	103	95	91
Lu	10	10	11	10	11
Zr	4,989	4,104	5,363	3,866	5,182
Nb	6,043	5,129	5,859	4,965	5,375
Ta	594	548	709	568	523
Hf	130	131	166	115	150
Sr	36	34	25	40	16
Ba	29	26	27	25	25
Th	98	95	111	95	93
U	10	10	10	9	8

Appendix G.
Titanite
LA-ICP-MS

trace element

contents

Sample ID	99TF6sphB_sph1b	99TF6sphB_sph8	99TF6sphB_sph9b	00TF95SPH_1C	00TF95SPH_4R
Type	T1	T1	T1	T2	T2
Lower/upper	lower	lower	lower	upper	upper
(ppm) La	3,168	3,079	2,875	3,272	2,834
Ce	7,047	8,006	7,524	7,753	7,603
Pr	893	1,077	964	1,093	1,145
Nd	3,423	4,454	3,849	4,608	5,035
Sm	569	822	703	849	985
Gd	440	608	514	615	684
Tb	63	86	74	92	101
Dy	333	438	388	476	506
Ho	60	74	69	83	83
Y	1,531	1,719	1,617	1,951	1,961
Er	143	167	152	190	182
Tm	18	20	18	22	20
Yb	89	95	88	109	97
Lu	11	10	10	13	10
Zr	6,351	4,235	4,681	5,122	3,966
Nb	6,548	5,762	5,325	5,628	4,888
Ta	645	719	566	646	605
Hf	184	123	133	152	114
Sr	12	42	23	32	65
Ba	26	28	27	27	26
Th	103	114	92	109	92
U	9	9	9	9	8

Appendix G.
Titanite
LA-ICP-MS

trace element

contents

Sample ID	00TF95SPH_5R	00TF95SPH_6C	00TF95SPH_6R	00TF95SPH_7R	01TF127SPH_2C
Type	T2	T2	T2	T2	T2
Lower/upper	upper	upper	upper	upper	upper
(ppm) La	3,245	3,402	3,321	3,568	2,852
Ce	8,205	8,197	8,227	8,696	7,412
Pr	1,134	1,104	1,137	1,235	1,023
Nd	4,769	4,555	4,779	5,407	4,371
Sm	885	822	879	1,007	821
Gd	652	602	637	721	598
Tb	96	90	96	106	86
Dy	489	476	493	535	447
Ho	84	81	84	92	77
Y	2,028	1,944	2,010	2,130	1,761
Er	188	188	191	203	179
Tm	22	22	23	23	21
Yb	109	110	112	112	100
Lu	12	12	13	13	11
Zr	5,047	5,332	5,110	4,799	4,051
Nb	5,639	5,830	5,677	6,104	5,060
Ta	664	663	683	824	603
Hf	146	155	151	146	125
Sr	40	18	40	52	40
Ba	27	28	28	29	25
Th	107	110	116	125	100
U	9	9	10	9	9

Appendix G.
Titanite
LA-ICP-MS

trace element

contents

Sample ID	01TF127SPH_2R2	01TF127sph_5R1	03TF110_SPHENE12m	99TF6sphB_sph5	99TF6sphB_sph5r
Type	T2	T2	T2	T2	T2
Lower/upper	upper	upper	upper	lower	lower
(ppm) La	3,005	3,207	3,197	2,914	2,997
Ce	7,396	7,692	8,605	7,654	7,773
Pr	956	1,040	1,045	1,081	1,082
Nd	3,671	4,233	4,050	4,725	4,655
Sm	641	756	698	894	872
Gd	441	541	550	659	644
Tb	69	81	73	93	93
Dy	368	429	382	461	467
Ho	64	75	67	79	79
Y	1,534	1,806	1,493	1,907	1,882
Er	153	175	160	173	178
Tm	19	21	20	20	20
Yb	95	106	117	98	101
Lu	10	12	11	11	11
Zr	5,076	5,455	5,058	4,202	4,197
Nb	5,469	5,876	6,005	4,933	5,771
Ta	545	681	612	581	690
Hf	143	166	158	117	121
Sr	14	25	15	52	44
Ba	24	26	27	27	26
Th	99	112	105	94	102
U	9	10	12	8	8

Appendix G.
Titanite
LA-ICP-MS

trace element

contents

Sample ID	00TF88_gm_5sph2	00TF95SPH_2C	00TF95SPH_2M	00TF95SPH_2R_END	00TF95SPH_3C_strt
Type	T3	T3	T3	T3	T3
Lower/upper	lower	upper	upper	upper	upper
(ppm) La	2,797	3,277	3,203	3,211	3,863
Ce	7,413	7,305	6,777	6,843	7,988
Pr	927	927	795	831	839
Nd	3,657	3,579	2,827	3,062	2,783
Sm	637	607	441	496	415
Gd	450	435	321	372	299
Tb	66	66	49	56	47
Dy	345	354	271	310	244
Ho	58	63	51	56	46
Y	1,449	1,501	1,273	1,384	1,167
Er	134	148	125	135	115
Tm	16	18	16	18	14
Yb	83	92	86	91	79
Lu	9	11	10	10	9
Zr	4,910	7,089	7,554	7,883	7,963
Nb	5,652	7,357	7,908	6,975	10,885
Ta	548	756	672	680	907
Hf	132	207	213	241	209
Sr	23	19	13	11	9
Ba	28	26	23	24	27
Th	87	113	110	104	141
U	10	11	12	12	16

Appendix G.
Titanite
LA-ICP-MS

trace element

contents

Sample ID	00TF95SPH_3C2	00TF95SPH_3C5	00TF95SPH_3C6_END	00TF95SPH_3C7_STRT
Type	T3	T3	T3	T3
Lower/upper	upper	upper	upper	upper
(ppm) La	3,712	3,745	3,364	3,249
Ce	7,601	7,707	6,983	6,733
Pr	810	818	769	742
Nd	2,716	2,700	2,597	2,493
Sm	394	404	393	368
Gd	289	293	282	267
Tb	44	44	43	40
Dy	244	244	243	226
Ho	45	45	45	41
Y	1,145	1,200	1,143	1,107
Er	112	117	112	104
Tm	15	15	15	13
Yb	79	82	75	73
Lu	9	9	9	9
Zr	7,671	8,142	7,925	7,316
Nb	10,584	10,837	9,337	8,914
Ta	847	879	749	680
Hf	198	205	201	183
Sr	7	7	9	7
Ba	26	27	25	24
Th	144	144	126	120
U	16	16	14	14

Appendix G.
Titanite
LA-ICP-MS

trace element

contents

Sample ID	00TF95SPH_4C	00TF95SPH_5C	00TF95SPH_7C	01TF127SPH_2R3	01TF127SPH_3C
Type	T3	T3	T3	T3	T3
Lower/upper	upper	upper	upper	upper	upper
(ppm) La	3,720	3,588	3,651	4,037	3,766
Ce	8,709	8,509	7,940	9,723	9,699
Pr	1,157	1,071	1,032	1,201	1,167
Nd	4,406	4,122	4,017	4,779	4,466
Sm	736	694	677	798	769
Gd	522	503	500	578	525
Tb	78	76	74	85	78
Dy	406	398	398	447	407
Ho	69	70	71	78	70
Y	1,702	1,725	1,736	1,825	1,672
Er	156	167	164	176	160
Tm	19	20	20	22	19
Yb	97	102	100	110	98
Lu	10	12	12	12	10
Zr	5,283	5,709	7,028	6,044	5,566
Nb	7,233	6,687	6,960	8,133	7,864
Ta	783	650	793	846	872
Hf	144	153	204	169	158
Sr	22	16	16	17	19
Ba	31	29	28	32	33
Th	133	132	117	150	137
U	10	11	9	12	12

Appendix G.
Titanite
LA-ICP-MS

trace element

contents

Sample ID	01TF127SPH_4R1	01TF127SPH_5C2	01TF127SPH_6C	01TF127SPH_6R	03TF110_1sph1
Type	T3	T3	T3	T3	T3
Lower/upper	upper	upper	upper	upper	upper
(ppm) La	3,158	3,883	3,455	3,972	3,051
Ce	7,343	8,747	7,640	8,614	7,298
Pr	825	1,054	946	1,074	773
Nd	2,871	3,946	3,507	4,118	2,658
Sm	451	647	564	711	404
Gd	330	469	417	513	286
Tb	50	70	64	77	44
Dy	266	370	350	410	239
Ho	50	66	63	73	44
Y	1,227	1,606	1,538	1,764	1,098
Er	124	158	153	170	110
Tm	16	20	19	22	14
Yb	85	101	93	110	78
Lu	9	11	11	13	8
Zr	6,664	6,139	5,547	7,996	6,588
Nb	7,058	7,803	7,609	8,811	7,200
Ta	610	729	707	957	534
Hf	194	167	156	248	185
Sr	5	14	7	18	4
Ba	25	30	26	30	25
Th	94	149	113	136	90
U	11	12	10	13	13

Appendix G.
Titanite
LA-ICP-MS

trace element

contents

Sample ID	03TF110_1sph2	03TF110_2sph2_cor	03TF110_2sph3_rim	03TF110_SPHENE212m
Type	T3	T3	T3	T3
Lower/upper	upper	upper	upper	upper
(ppm) La	3,091	2,962	2,997	3,222
Ce	7,256	7,075	7,927	8,491
Pr	778	711	893	995
Nd	2,729	2,361	3,269	3,766
Sm	426	346	520	617
Gd	307	252	375	445
Tb	45	38	56	62
Dy	247	210	300	333
Ho	44	39	52	60
Y	1,089	975	1,271	1,434
Er	107	97	125	143
Tm	14	13	15	18
Yb	75	70	83	106
Lu	8	8	9	10
Zr	7,046	8,871	6,027	5,405
Nb	7,530	8,146	6,802	6,278
Ta	566	645	603	596
Hf	192	266	176	162
Sr	11	7	11	11
Ba	27	27	29	28
Th	99	85	92	96
U	14	13	12	11

Appendix G.
Titanite
LA-ICP-MS

trace element

contents

Sample ID	**03TF110_SPHENE212m core**	**03TF126_SPHENE12m**	**03TF126_SPHENE12m2**	**00TF88_gm_4sph**
Type	**T3**	**T3**	**T3**	**T4**
Lower/upper	**upper**	**upper**	**upper**	**lower**
(ppm) La	3,026	3,247	3,038	3,073
Ce	6,427	7,783	7,665	5,745
Pr	641	876	832	537
Nd	2,191	3,288	3,005	1,712
Sm	326	529	484	234
Gd	254	400	336	177
Tb	36	58	50	28
Dy	205	309	271	161
Ho	38	55	49	30
Y	896	1,297	1,210	811
Er	97	132	116	80
Tm	13	16	15	11
Yb	81	98	87	63
Lu	8	9	8	7
Zr	7,751	6,885	6,546	12,665
Nb	8,147	6,932	6,448	9,639
Ta	531	701	626	587
Hf	207	211	189	353
Sr	11	9	9	8
Ba	21	25	24	19
Th	96	103	85	89
U	14	11	10	16

Appendix G.
Titanite
LA-ICP-MS

trace element

contents

Sample ID	00TF95SPH_2R_STRT	01TF119_sph3_hiZr	01TF119_sph5	01TF127sph_1	01TF127SPH_1C
Type	T4	T4	T4	T4	T4
Lower/upper	upper	lower	lower	upper	upper
(ppm) La	3,430	3,068	3,337	3,358	3,201
Ce	5,762	5,837	6,723	5,910	6,358
Pr	582	527	607	625	583
Nd	1,869	1,594	1,935	2,038	1,852
Sm	281	228	277	300	271
Gd	211	161	204	232	206
Tb	31	26	32	36	32
Dy	189	147	181	209	180
Ho	36	29	34	41	35
Y	967	770	865	1,037	875
Er	95	76	89	107	92
Tm	13	11	12	15	13
Yb	73	61	70	83	74
Lu	8	7	8	10	8
Zr	11,411	15,362	11,451	11,193	10,385
Nb	8,664	11,392	10,311	8,907	9,358
Ta	518	676	616	581	546
Hf	296	446	287	326	280
Sr	15	8	11	10	12
Ba	21	20	20	20	22
Th	103	92	110	112	99
U	15	18	17	15	17

Appendix G.
Titanite
LA-ICP-MS

trace element

contents

Sample ID	01TF127SPH_4C	01TF127SPH_4M	01TF51PB_7sph1	99TF6_gm_17sph2b	99TF6_gm_22Csph
Type	T4	T4	T4	T4	T4
Lower/upper	upper	upper	lower	lower	lower
(ppm) La	3,710	3,583	2,619	2,699	2,565
Ce	7,120	6,884	5,403	5,295	5,096
Pr	668	648	485	493	482
Nd	2,096	1,985	1,475	1,537	1,522
Sm	295	280	203	212	217
Gd	216	210	147	163	154
Tb	33	32	22	25	23
Dy	194	180	128	143	136
Ho	37	35	25	28	26
Y	913	888	657	706	724
Er	96	92	66	72	66
Tm	13	13	9	10	9
Yb	73	69	55	57	52
Lu	8	8	6	6	6
Zr	9,945	10,030	11,190	9,436	9,237
Nb	13,005	11,986	8,772	8,383	8,107
Ta	761	720	493	480	430
Hf	238	261	330	260	239
Sr	12	11	7	5	4
Ba	24	24	18	18	17
Th	142	130	75	77	72
U	24	20	18	14	13

Appendix G.
Titanite
LA-ICP-MS

trace element

contents

Sample ID	99TF6_gm_22Csph2	99TF6PB_3sph1	99TF6sphA_sph1c	99TF6sphA_sph1r	99TF6sphA_sph2
Type	T4	T4	T4	T4	T4
Lower/upper	lower	lower	lower	lower	lower
(ppm) La	2,819	3,151	3,268	3,157	3,180
Ce	5,462	5,507	5,433	5,370	5,523
Pr	488	514	548	547	536
Nd	1,500	1,647	1,736	1,752	1,666
Sm	209	251	251	258	239
Gd	156	177	209	209	192
Tb	24	29	30	31	27
Dy	140	160	169	170	157
Ho	26	31	33	34	31
Y	699	856	849	898	803
Er	70	82	88	89	84
Tm	9	11	12	12	11
Yb	53	63	65	65	62
Lu	6	7	8	8	7
Zr	10,387	16,189	14,643	11,058	11,314
Nb	9,453	10,553	10,020	9,231	9,678
Ta	531	640	669	551	660
Hf	275	502	440	290	322
Sr	4	7	8	9	8
Ba	19	20	21	21	20
Th	73	90	92	90	91
U	14	18	15	13	14

Appendix G.
Titanite
LA-ICP-MS

trace element

contents

Sample ID	99TF6sphB_sph10c	99TF6sphB_sph10r	99TF6sphB_sph11	99TF6sphB_sph11c	99TF6sphB_sph12
Type	T4	T4	T4	T4	T4
Lower/upper	lower	lower	lower	lower	lower
(ppm) La	3,005	2,929	2,639	2,844	3,052
Ce	5,440	5,698	5,157	5,342	5,683
Pr	501	534	494	486	546
Nd	1,514	1,600	1,488	1,522	1,637
Sm	213	226	211	214	234
Gd	170	179	169	167	187
Tb	24	25	24	24	26
Dy	136	144	136	138	150
Ho	27	28	26	27	29
Y	714	738	690	692	772
Er	70	74	68	70	77
Tm	9	10	10	10	10
Yb	56	57	55	55	57
Lu	6	6	6	6	6
Zr	14,380	9,221	10,570	11,219	8,940
Nb	10,409	8,445	8,271	9,392	8,842
Ta	680	530	505	589	515
Hf	429	255	309	341	232
Sr	11	8	5	6	6
Ba	20	21	19	20	21
Th	80	80	71	72	82
U	16	14	14	14	14

Appendix G.
Titanite
LA-ICP-MS

trace element

contents

Sample ID	99TF6sphB_sph13	99TF6sphB_sph13b	99TF6sphB_sph14	99TF6sphB_sph2	99TF6sphB_sph3
Type	T4	T4	T4	T4	T4
Lower/upper	lower	lower	lower	lower	lower
(ppm) La	3,048	2,541	2,710	3,122	3,197
Ce	5,825	4,970	4,794	5,342	5,591
Pr	526	464	465	537	564
Nd	1,618	1,421	1,425	1,694	1,802
Sm	228	204	199	243	259
Gd	177	162	159	199	211
Tb	25	23	23	29	32
Dy	144	131	135	163	178
Ho	29	26	26	33	34
Y	758	672	660	864	890
Er	73	67	68	86	90
Tm	10	9	9	12	12
Yb	55	53	51	62	67
Lu	6	6	5	7	8
Zr	9,669	10,589	14,070	12,561	12,217
Nb	9,113	8,420	8,914	9,115	8,585
Ta	549	527	553	585	500
Hf	245	311	447	356	356
Sr	7	10	4	8	6
Ba	21	18	18	20	21
Th	88	70	69	87	95
U	15	13	15	13	14

Appendix G.
Titanite
LA-ICP-MS

trace element

contents

Sample ID	99TF6sphB_sph3b	99TF6sphB_sph4	99TF6sphB_sph4b	99TF6sphB_sph6	99TF6sphB_sph6b
Type	T4	T4	T4	T4	T4
Lower/upper	lower	lower	lower	lower	lower
(ppm) La	3,299	3,073	3,220	3,378	3,296
Ce	5,572	5,264	5,428	5,831	5,891
Pr	555	530	534	556	589
Nd	1,736	1,664	1,657	1,715	1,883
Sm	250	236	233	239	277
Gd	200	197	192	194	218
Tb	28	28	27	28	31
Dy	165	159	160	162	177
Ho	32	31	30	32	35
Y	867	823	804	846	896
Er	86	81	80	81	89
Tm	11	11	11	11	12
Yb	64	61	60	62	65
Lu	7	7	7	7	7
Zr	13,632	12,141	13,515	12,227	10,987
Nb	10,362	8,914	10,038	10,304	10,242
Ta	664	554	671	659	653
Hf	394	338	397	328	301
Sr	7	6	6	8	10
Ba	21	20	20	21	22
Th	98	81	87	94	102
U	17	13	14	14	15

Appendix G.
Titanite
LA-ICP-MS

trace element

contents

Sample ID	99TF6sphB_sph7b
Type	T4
Lower/upper	lower
(ppm) La	2,887
Ce	5,191
Pr	525
Nd	1,680
Sm	245
Gd	196
Tb	29
Dy	163
Ho	32
Y	848
Er	84
Tm	11
Yb	64
Lu	7
Zr	11,364
Nb	8,525
Ta	533
Hf	326
Sr	13
Ba	20
Th	94
U	14

Appendix H

Calculated pyroxene-melt partition coefficients

Appendix H. Pyroxene-melt calculated partition coefficeients

Pyroxene	03TF126_PXCORE12m	03TF126_PXEND12m	03TF126_PXRIM212m	03TF126_PXRIM12m
	Salite	Salite	Salite	Salite
lower/upper	upper	upper	upper	upper
Glass	03TF16_10	03TF16_10	99TF8D_22SEP_8	phon_21
Glass unit	L2	L2	D	L2
E (GPa)	**278**	**309**	**259**	**315**
RSQ	**0.9857**	**0.9885**	**0.9795**	**0.9806**
La	0.48	0.46	0.59	0.53
Ce	0.87	0.90	1.11	1.09
Pr	1.37	1.44	1.64	1.75
Nd	1.76	1.90	2.06	2.46
Sm	2.43	2.76	2.72	3.38
Tb	2.36	2.77	2.79	3.46
Dy	2.39	2.68	2.62	3.25
Ho	2.12	2.42	2.44	2.77
Y	1.91	2.13	2.19	2.34
Er	1.71	1.95	2.01	2.40
Tm	1.39	1.52	1.87	2.24
Yb	1.42	1.54	1.58	1.99
Lu	1.67	1.78	1.87	1.78
Zr	0.39	0.40	0.44	0.38
Nb	0.01	0.01	0.01	0.01
Ta	0.06	0.03	0.04	0.03
Ti	1.08	1.05	1.07	1.24
Hf	0.58	0.65	0.72	0.62

Appendix H.
Pyroxene-melt calculated partition coefficeients

Pyroxene	03TF13_px2	99TF6gmB_PX5	03TF13_px1	0095px3_2	0149px1	99TF6sphB_px9
	Salite	Salite	Salite	Salite	Salite	Salite
lower/upper	upper	lower	upper	upper	lower	-
Glass	phon_21	05TF82_A2_21	phon_21	03TF16_12	03TF16_12	03TF16_12
Glass unit	L2	D	L2	L2	L2	L2
E (GPa)	**332**	**318**	**317**	**379**	**381**	**285**
RSQ	**0.9935**	**0.9967**	**0.9924**	**0.9979**	**0.9994**	**0.9944**
La	0.57	0.65	0.60	0.39	0.41	0.49
Ce	1.07	1.17	1.11	0.78	0.77	0.84
Pr	1.81	1.91	1.83	1.32	1.33	1.35
Nd	2.59	2.59	2.58	1.96	2.02	1.74
Sm	3.64	3.73	3.57	2.93	3.08	2.39
Tb	3.98	3.96	3.80	3.40	3.55	2.54
Dy	3.72	3.93	3.61	3.42	3.42	2.42
Ho	3.17	3.46	3.13	2.85	3.09	2.26
Y	2.73	3.07	2.73	2.69	2.81	2.20
Er	2.67	3.01	2.70	2.44	2.58	2.01
Tm	2.75	2.72	2.58	2.15	2.17	1.81
Yb	2.11	2.92	2.33	2.25	2.32	1.95
Lu	2.10	2.36	2.28	2.13	2.28	2.43
Zr	0.47	0.69	0.50	0.56	0.57	0.59
Nb	0.01	0.02	0.01	0.01	0.01	0.01
Ta	0.05	0.05	0.05	0.03	0.03	0.03
Ti	1.44	1.67	1.43	1.15	1.05	0.85
Hf	0.78	1.20	0.82	0.69	0.71	0.91

Appendix H. Pyroxene-melt calculated partition coefficeients

Pyroxene	99TF6gmB_PX6	0149px3	0151px2	0090px2	0149px2	0092px1	0091px2_2
	Salite	Salite	Salite	Salite	Salite	Salite	Salite
lower/upper	lower	lower	lower	upper	lower	upper	upper
Glass	05TF82_A2_21	03TF16_12	03TF56_34	03TF16_12	phon_13	03TF16_12	phon_13
Glass unit	D	L2	J3	L2	L2	L2	L2
E (GPa)	**306**	**354**	**357**	**355**	**369**	**306**	**400**
RSQ	**0.9927**	**0.9995**	**0.9965**	**0.9991**	**0.9975**	**0.9986**	**0.9992**
La	0.68	0.40	0.34	0.43	0.48	0.57	0.55
Ce	1.25	0.75	0.68	0.80	0.93	1.01	1.15
Pr	2.04	1.20	1.08	1.30	1.58	1.50	1.97
Nd	2.75	1.79	1.70	1.94	2.37	2.13	3.07
Sm	3.73	2.65	2.38	2.88	3.51	2.99	4.75
Tb	4.08	3.04	2.61	3.17	3.88	3.33	5.52
Dy	3.85	2.89	2.57	3.14	3.97	3.28	5.19
Ho	3.44	2.56	2.31	2.83	3.25	2.81	4.67
Y	3.23	2.59	2.05	2.71	2.86	2.82	4.13
Er	3.14	2.30	2.18	2.53	2.78	2.47	3.98
Tm	2.87	2.00	1.90	2.18	2.19	2.02	3.13
Yb	3.09	2.12	1.73	2.31	2.29	1.89	2.97
Lu	2.70	2.21	1.88	2.35	2.56	1.65	3.04
Zr	0.78	0.61	0.48	0.63	0.54	0.66	0.58
Nb	0.02	0.01	0.01	0.01	0.01	0.01	0.01
Ta	0.06	0.03	0.04	0.03	0.04	0.05	0.05
Ti	1.71	1.16	1.36	1.19	1.44	2.05	1.49
Hf	1.25	0.68	0.60	0.77	0.68	0.78	0.71

Appendix H. Pyroxene-melt calculated partition coefficeients

Pyroxene	0091px3	0091px4_1	0095px2	0095px4	0187px1	0090px1	9921px1
	Salite	Salite	Salite	Salite	Salite	Salite	Salite
lower/upper	upper	upper	upper	upper	lower	upper	upper
Glass	99TF8D_22SEP_1	phon_14	03TF16_12	phon_14	99TF8E_21	03TF13_G5	03TF16_12
Glass unit	D	L2	L2	L2	D	L2	L2
E (GPa)	346	330	368	312	338	432	346
RSQ	0.9993	0.9994	0.9991	0.9979	0.9997	0.9987	0.9992
La	0.39	0.47	0.45	0.44	0.56	0.64	0.52
Ce	0.70	0.80	0.87	0.80	1.02	1.32	0.95
Pr	1.11	1.25	1.46	1.24	1.58	2.55	1.55
Nd	1.63	1.85	2.20	1.75	2.26	3.95	2.26
Sm	2.39	2.65	3.31	2.47	3.44	6.26	3.34
Tb	2.78	3.06	3.68	2.63	3.91	7.85	3.68
Dy	2.67	2.90	3.51	2.59	3.67	6.91	3.65
Ho	2.40	2.62	3.14	2.32	3.25	6.05	3.24
Y	2.49	2.55	3.06	2.35	3.30	3.63	3.23
Er	2.32	2.41	2.65	2.13	2.90	5.64	2.88
Tm	2.25	2.16	2.30	1.99	2.70	4.86	2.54
Yb	1.78	1.85	2.34	1.77	2.45	4.83	2.60
Lu	1.71	2.11	2.22	2.02	2.57	5.01	2.64
Zr	0.82	0.63	0.76	0.65	0.92	0.85	0.88
Nb	0.01	0.01	0.02	0.01	0.02	0.01	0.02
Ta	0.06	0.03	0.06	0.04	0.05	0.08	0.05
Ti	2.44	1.31	1.63	1.41	1.65	1.34	1.57
Hf	0.95	0.67	0.91	0.72	1.16	1.71	1.02

Appendix H. Pyroxene-melt calculated partition coefficeients

Pyroxene	0090px1_2	0091px2_cntr	01TF127GM_PX2_2	01TF127GM_PX2	01TF127GM_PX3
	Salite	Salite	Salite	Salite	Salite
lower/upper	upper	upper	upper	upper	upper
Glass	99TF8E_21	03TF126_12	05TF82_A2_21	99TF8D_7	99TF8D_22SEP_8
Glass unit	D	H	D	D	D
E (GPa)	**337**	**438**	**279**	**295**	**300**
RSQ	**0.9993**	**0.9987**	**0.9982**	**0.9986**	**0.9984**
La	0.66	0.56	0.58	0.41	0.48
Ce	1.15	1.16	1.00	0.66	0.79
Pr	1.90	2.11	1.39	1.06	1.27
Nd	2.73	3.70	1.86	1.45	1.72
Sm	3.96	5.64	2.73	2.00	2.38
Tb	4.46	6.89	2.88	2.18	2.68
Dy	4.24	6.35	2.79	2.09	2.47
Ho	3.92	5.47	2.55	1.90	2.38
Y	3.34	4.58	2.50	1.86	2.14
Er	3.42	4.39	2.33	1.78	2.01
Tm	3.26	3.84	2.06	1.67	1.85
Yb	3.21	2.92	2.45	1.53	1.78
Lu	3.52	3.14	2.14	1.83	1.98
Zr	1.07	0.57	0.99	0.84	0.90
Nb	0.02	0.01	0.03	0.03	0.02
Ta	0.06	0.07	0.09	0.07	0.09
Ti	1.46	2.34	2.61	2.48	2.49
Hf	1.62	0.72	1.45	1.37	1.44

Appendix H.
Pyroxene-melt calculated partition coefficeients

Pyroxene	99TF6gmB_PX10	99TF6gmA_PX24	99TF6PA_22(PX)	99TF6PB_PX2	99TF6PB_PX2-2
	Na-salite	Na-salite	Na-salite	Na-salite	Na-salite
lower/upper	lower	lower	lower	lower	lower
Glass	03TF126_12	03TF126_12	01TF51pc_15	01TF51pc_6	03TF16_27
Glass unit	H	H	RAV	RAV	L2
E (GPa)	189	168	188	192	198
RSQ	0.9903	0.9886	0.9887	0.9899	0.9808
La	0.41	0.44	0.40	0.43	0.54
Ce	0.55	0.62	0.60	0.61	0.71
Pr	0.72	0.78	0.80	0.85	1.09
Nd	0.92	0.99	0.92	1.03	1.36
Sm	1.04	1.09	1.12	1.20	1.51
Tb	1.21	1.17	1.22	1.27	1.66
Dy	1.16	1.14	1.15	1.31	1.62
Ho	1.16	1.10	1.19	1.26	1.49
Y	1.08	1.08	0.92	0.97	1.25
Er	1.24	1.19	1.26	1.38	1.48
Tm	1.65	1.64	1.60	1.50	1.94
Yb	2.46	2.40	2.49	2.56	2.80
Lu	3.73	3.69	4.22	3.75	4.39
Zr	0.76	0.82	0.73	0.68	0.77
Nb	0.01	0.01	0.01	0.01	0.03
Ta	0.01	0.01	0.01	0.01	0.01
Ti	0.83	0.84	0.80	1.00	0.92
Hf	1.10	1.22	1.28	1.18	1.25

Appendix H.
Pyroxene-melt calculated partition coefficeients

Pyroxene	99TF6gmB_PX4	0154px2	99TF6PA_20(PX)	99TF6gmB_PX1	99TF6gmB_PX7
	Na-salite	Na-salite	Na-salite	Na-salite	Na-salite
lower/upper	lower	lower	lower	lower	lower
Glass	03TF126_12	03TF56_44	01TF51pc_6	01TF51pc_15	03TF126_12
Glass unit	H	J3	RAV	RAV	H
E (GPa)	182.5467	240	186	190	155
RSQ	0.9871	0.9906	0.9925	0.9941	0.9893
La	0.49	0.35	0.49	0.53	0.61
Ce	0.65	0.54	0.65	0.73	0.76
Pr	0.85	0.82	0.92	1.04	0.98
Nd	1.11	1.06	1.10	1.19	1.21
Sm	1.21	1.29	1.28	1.46	1.33
Tb	1.41	1.44	1.40	1.59	1.47
Dy	1.31	1.39	1.37	1.53	1.37
Ho	1.33	1.19	1.32	1.49	1.41
Y	1.24	1.09	1.04	1.37	1.36
Er	1.42	1.38	1.55	1.45	1.51
Tm	2.01	1.69	1.90	1.72	2.06
Yb	2.76	2.37	3.02	2.92	3.01
Lu	4.39	3.51	4.41	4.09	4.75
Zr	1.01	0.81	0.86	1.00	1.16
Nb	0.01	0.01	0.01	0.01	0.01
Ta	0.01	0.01	0.01	0.03	0.02
Ti	0.87	1.04	0.93	1.45	1.00
Hf	1.63	1.03	1.63	1.47	1.78

Appendix H.
Pyroxene-melt calculated partition coefficeients

Pyroxene	99TF6gmB_PX2B	99TF6gmA_PX25	99TF6gmA_PX28	99TF6sphA_px2	99TF6gmB_PX8
	Na-salite	Na-salite	Na-salite	Na-salite	Na-salite
lower/upper	lower	lower	lower	lower	lower
Glass	03TF126_12	03TF126_12	03TF126_12	03TF126_12	03TF126_12
Glass unit	H	H	H	H	H
E (GPa)	177	148	152	181	168
RSQ	0.9841	0.9871	0.9907	0.9831	0.9923
La	0.58	0.57	0.64	0.58	0.61
Ce	0.75	0.71	0.87	0.72	0.80
Pr	0.98	0.92	1.07	0.98	1.03
Nd	1.26	1.12	1.31	1.24	1.26
Sm	1.37	1.23	1.48	1.38	1.40
Tb	1.62	1.29	1.51	1.63	1.64
Dy	1.50	1.28	1.55	1.50	1.54
Ho	1.54	1.29	1.44	1.55	1.47
Y	1.42	1.25	1.48	1.43	1.41
Er	1.59	1.39	1.59	1.66	1.57
Tm	2.19	1.82	2.14	2.26	2.13
Yb	3.04	2.68	3.07	2.79	2.89
Lu	4.57	4.03	4.65	5.03	4.44
Zr	1.17	1.17	1.20	1.20	1.25
Nb	0.01	0.04	0.01	0.02	0.02
Ta	0.03	0.06	0.03	0.06	0.04
Ti	1.12	1.07	1.19	1.02	1.24
Hf	1.85	1.73	1.71	1.91	1.94

Appendix H.
Pyroxene-melt calculated partition coefficeients

Pyroxene	99TF6gmB_PX2	99TF6gmA_PX11	03TF16_PX2_1	99TF6gmA_PX22	99TF6sphA_px1b
	Na-salite	Na-salite	Na-salite	Na-salite	Na-salite
lower/upper	lower	lower	upper	lower	lower
Glass	01TF51pc_15	01TF51pc_15	03TF126_15	03TF126_12	00TF171W_B_14
Glass unit	RAV	RAV	H	H	N
E (GPa)	**139**	**148**	**216**	**160**	**190**
RSQ	**0.9860**	**0.9840**	**0.9581**	**0.9834**	**0.9870**
La	0.72	0.56	0.74	0.58	0.65
Ce	0.96	0.77	1.08	0.77	0.87
Pr	1.24	1.00	1.47	0.98	1.26
Nd	1.33	1.08	2.22	1.22	1.58
Sm	1.58	1.24	2.42	1.28	1.84
Tb	1.65	1.35	2.24	1.45	1.93
Dy	1.58	1.32	2.05	1.44	1.83
Ho	1.51	1.28	2.18	1.41	1.73
Y	1.42	1.20	1.52	1.34	1.48
Er	1.48	1.25	1.81	1.53	2.11
Tm	1.88	1.52	2.58	2.08	2.80
Yb	3.04	2.67	3.63	2.99	2.87
Lu	4.37	3.77	5.92	4.37	5.01
Zr	1.18	1.20	1.21	1.47	1.51
Nb	0.02	0.01	0.02	0.02	0.04
Ta	0.16	0.04	0.06	0.06	0.10
Ti	1.49	1.33	1.49	1.43	1.66
Hf	1.62	1.68	2.14	2.09	2.26

Appendix H.
Pyroxene-melt calculated partition coefficeients

Pyroxene	99TF6gmA_PX27	03TF16_PX2_2	99TF6sphB_px3	99TF6gmA_PX19	99TF6gmA_PX16
	Na-salite	Na-salite	Na-salite	Na-salite	Na-salite
lower/upper	lower	upper	lower	lower	lower
Glass	03TF126_12	01TF51pc_15	03TF126_12	03TF126_12	03TF126_12
Glass unit	H	RAV	H	H	H
E (GPa)	**178.747**	**151.076**	**113**	**154**	**146**
RSQ	**0.9938**	**0.9786**	**0.9612**	**0.9887**	**0.9914**
La	0.67	0.70	1.06	0.72	0.69
Ce	0.89	0.96	1.12	0.92	0.88
Pr	1.16	1.27	1.43	1.14	1.11
Nd	1.48	1.34	1.72	1.40	1.35
Sm	1.68	1.58	1.83	1.55	1.46
Tb	1.84	1.71	1.95	1.73	1.62
Dy	1.80	1.59	1.84	1.67	1.56
Ho	1.76	1.63	1.84	1.70	1.48
Y	1.69	1.32	1.85	1.53	1.45
Er	1.81	1.59	2.06	1.82	1.66
Tm	2.32	1.97	2.75	2.50	2.27
Yb	3.28	3.41	3.25	3.51	3.17
Lu	4.80	5.10	5.50	5.22	4.85
Zr	1.56	1.35	1.60	1.63	1.63
Nb	0.03	0.02	0.02	0.03	0.02
Ta	0.07	0.05	0.05	0.07	0.05
Ti	1.63	1.46	1.18	1.58	1.33
Hf	2.35	2.24	2.83	2.34	2.53

Appendix H.
Pyroxene-melt calculated partition coefficeients

Pyroxene	01TF127GM_PX27	0154px1	0091px7	0154px1_2	99TF6sphA_px1	0091px7_2
	Na-salite	Na-salite	Na-salite	Na-salite	Na-salite	Na-salite
lower/upper	upper	lower	upper	lower	lower	upper
Glass	03TF126_12	03TF56_44	03TF56_44	03TF56_44	01TF51pc_15	03TF56_44
Glass unit	H	J3	J3	J3	RAV	J3
E (GPa)	145	234	214	213	157	225
RSQ	0.9875	0.9806	0.9810	0.9772	0.9769	0.9856
La	0.68	0.53	0.53	0.53	0.69	0.46
Ce	0.87	0.85	0.81	0.83	0.95	0.72
Pr	1.07	1.28	1.16	1.19	1.28	1.04
Nd	1.30	1.66	1.49	1.52	1.37	1.37
Sm	1.39	1.86	1.67	1.67	1.57	1.57
Tb	1.58	2.22	1.95	1.97	1.76	1.80
Dy	1.50	1.98	1.79	1.76	1.70	1.64
Ho	1.51	1.86	1.59	1.66	1.72	1.49
Y	1.46	1.39	1.44	1.41	1.48	1.39
Er	1.58	2.01	1.69	1.82	1.69	1.67
Tm	2.25	2.61	2.07	2.23	2.08	2.17
Yb	3.05	3.55	2.84	2.99	3.06	2.87
Lu	4.72	5.00	3.72	4.13	5.03	3.94
Zr	1.65	1.25	1.28	1.29	1.58	1.45
Nb	0.02	0.01	0.01	0.02	0.03	0.02
Ta	0.06	0.05	0.04	0.05	0.09	0.06
Ti	1.35	1.42	1.63	1.67	1.71	1.85
Hf	2.60	1.99	1.69	1.71	2.36	1.70

Appendix H.

Pyroxene-melt calculated partition coefficeients

Pyroxene	**99TF03_1_2 Na-salite**
lower/upper	**lower**
Glass	**03TF126_12**
Glass unit	**H**
E (GPa)	**136**
RSQ	**0.9340**
La	0.68
Ce	1.05
Pr	1.07
Nd	1.35
Sm	1.40
Tb	1.59
Dy	1.53
Ho	1.62
Y	1.60
Er	1.76
Tm	2.30
Yb	3.10
Lu	5.08
Zr	2.92
Nb	0.02
Ta	0.06
Ti	2.21
Hf	2.43

Appendix I

Calculated titanite-melt partition coefficients

Appendix I. Titanite-melt calculated partition coefficients

Titanite	00TF88_gm_5sph	00TF88_gm_5sph1_2	00TF95SPH_1R	00TF95SPH_3C
Type	T1	T1	T1	T1
lower/upper	lower	lower	upper	upper
Glass	99TF8D_22SEP_11	99TF8D_22SEP_11	01TF122A_1	01TF122A_1
Glass unit	D	D	F6	F6
E (GPa)	373	353	415	496
RSQ	0.9913	0.9903	0.9796	0.9890
La	28	27	32	27
Ce	54	52	52	52
Pr	68	63	74	74
Nd	80	73	88	93
Sm	94	85	107	119
Tb	76	70	88	94
Dy	68	62	83	85
Ho	56	53	68	67
Y	53	49	64	64
Er	48	46	56	53
Tm	39	37	45	41
Yb	29	30	32	28
Lu	23	22	23	19
Zr	5.9	5.6	6.2	4.7
Nb	30	28	30	25
Ta	58	50	59	53
Hf	8.7	8.2	8.7	6.7
Sr	5.9	1.9	1.3	0.4
Ba	3.8	0.5	0.4	0.1
Th	2.7	2.5	3.3	2.7
U	0.7	1.0	0.7	0.7

Appendix I. Titanite-melt calculated partition coefficients

Titanite	00TF95SPH_3C_end	00TF95SPH_3C3	00TF95SPH_3C4	00TF95SPH_3C6_STRT
Type	T1	T1	T1	T1
lower/upper	upper	upper	upper	upper
Glass	01TF122A_1	01TF122A_1	01TF122A_1	01TF122A_1
Glass unit	F6	F6	F6	F6
E (GPa)	458	470	465	464
RSQ	0.9882	0.9886	0.9864	0.9880
La	29	28	27	26
Ce	53	53	49	51
Pr	76	74	68	72
Nd	91	89	82	86
Sm	114	112	104	110
Tb	89	89	83	91
Dy	82	82	76	83
Ho	65	66	61	68
Y	61	61	58	62
Er	52	53	50	54
Tm	42	42	40	43
Yb	29	28	26	29
Lu	20	19	18	21
Zr	5.2	5.0	5.2	5.1
Nb	27	26	24	24
Ta	56	55	53	48
Hf	7.6	7.1	7.5	7.4
Sr	2.0	1.3	3.8	
Ba	0.5	0.3	0.9	1.7
Th	2.8	2.8	3.0	2.4
U	0.7	0.6	0.8	0.6

Appendix I. Titanite-melt calculated partition coefficients

Titanite	00TF95SPH_3C7_END	01TF119_sph1	01TF119_sph2	01TF119_sph3_loZr
Type	T1	T1	T1	T1
lower/upper	upper	lower	lower	lower
Glass	01TF122A_1	01TF122A_1	99TF8D_22SEP_11	01TF122A_1
Glass unit	F6	F6	D	F6
E (GPa)	449	440	338	431
RSQ	0.9840	0.9930	0.9894	0.9908
La	25	25	27	24
Ce	44	50	49	45
Pr	64	66	60	61
Nd	77	78	72	72
Sm	94	95	84	87
Tb	77	77	71	70
Dy	71	72	63	65
Ho	59	59	54	52
Y	55	54	48	51
Er	48	48	47	44
Tm	38	38	38	35
Yb	26	26	30	25
Lu	18	19	24	17
Zr	4.8	5.4	6.8	5.0
Nb	23	25	30	23
Ta	45	45	49	41
Hf	7.0	7.3	9.4	7.8
Sr	1.3	1.6	0.6	0.4
Ba	0.3	0.5	0.2	0.1
Th	2.3	2.3	2.3	2.3
U	0.7	0.8	0.8	0.8

Appendix I. Titanite-melt calculated partition coefficients

Titanite	01TF127SPH_2	01TF127SPH_3R1	99TF6sphB_sph1	99TF6sphB_sph1b
Type	T1	T1	T1	T1
lower/upper	upper	upper	lower	lower
Glass	01TF122A_1	01TF122A_1	99TF8D_22SEP_11	99TF8D_22SEP_11
Glass unit	F6	F6	D	D
E (GPa)	386	427	267	250
RSQ	0.9843	0.9920	0.9855	0.9845
La	28	24	27	29
Ce	47	46	42	43
Pr	64	62	53	52
Nd	73	72	58	57
Sm	86	88	64	61
Tb	72	71	57	55
Dy	69	67	52	50
Ho	57	56	47	47
Y	54	51	47	46
Er	49	46	43	42
Tm	41	37	37	36
Yb	28	26	29	28
Lu	20	18	24	24
Zr	6.5	4.7	7.0	8.6
Nb	26	22	26	32
Ta	53	42	43	54
Hf	9.9	6.9	10.9	13.3
Sr	0.9	0.3	0.8	0.4
Ba	0.3	0.1	0.5	0.3
Th	2.6	2.2	2.3	2.6
U	0.8	0.7	0.6	0.8

Appendix I. Titanite-melt calculated partition coefficients

Titanite	99TF6sphB_sph8	99TF6sphB_sph9b	00TF95SPH_1C	00TF95SPH_4R	00TF95SPH_5R
Type	T1	T1	T2	T2	T2
lower/upper	lower	lower	upper	upper	upper
Glass	99TF8D_22SEP_11	99TF8D_22SEP_11	00TF171W_B_4	00TF171W_B_4	00TF171W_B_4
Glass unit	D	D	N	N	N
E (GPa)	**359**	**333**	**608**	**698**	**630**
RSQ	**0.9895**	**0.9887**	**0.9835**	**0.9848**	**0.9842**
La	28	26	44	38	44
Ce	49	46	106	104	112
Pr	63	56	159	166	165
Nd	74	64	223	244	231
Sm	88	75	258	299	269
Tb	75	64	218	240	229
Dy	66	58	158	167	162
Ho	57	53	109	109	111
Y	52	49	96	96	99
Er	50	45	84	80	83
Tm	40	36	59	53	58
Yb	30	27	42	37	42
Lu	24	22	25	21	25
Zr	5.8	6.4	4.2	3.3	4.1
Nb	28	26	30	26	30
Ta	60	47	117	110	121
Hf	8.9	9.6	7.4	5.6	7.1
Sr		1.8	0.9	4.1	1.1
Ba	1.4	1.4	0.3	0.6	0.3
Th	2.8	2.4	2.6	2.1	2.4
U	0.7	0.7	0.6	0.8	0.6

Appendix I. Titanite-melt calculated partition coefficients

Titanite	00TF95SPH_6C	00TF95SPH_6R	00TF95SPH_7R	01TF127SPH_2C	01TF127SPH_2R2
Type	T2	T2	T2	T2	T2
lower/upper	upper	upper	upper	upper	upper
Glass	99TF6A_5	88_g4	00TF171W_B_4	00TF171W_B_4	99TF6A_5
Glass unit	B	SAN	N	N	B
E (GPa)	**776**	**617**	**649**	**635**	**738**
RSQ	**0.9816**	**0.9833**	**0.9803**	**0.9870**	**0.9845**
La	25	32	48	38	22
Ce	61	49	119	101	55
Pr	118	107	179	148	102
Nd	175	176	262	212	141
Sm	228	237	306	250	178
Tb	163	210	252	205	125
Dy	144	157	177	148	111
Ho	91	124	121	102	72
Y	65	93	104	86	51
Er	57	83	90	79	46
Tm	40	59	61	55	33
Yb	22	42	43	38	19
Lu	14	25	25	22	12
Zr	2.1	4.2	3.9	3.3	2.0
Nb	20	19	33	27	19
Ta	100	76	149	109	83
Hf	3.9	7.3	7.1	6.1	3.6
Sr	0.6	0.9	2.1	1.6	0.1
Ba	0.3	0.2	0.4	0.4	0.1
Th	2.7	2.9	3.0	2.1	2.4
U	0.7	0.8	0.6	0.6	0.7

Appendix I.
Titanite-melt calculated partition coefficients

Titanite	01TF127sph_5R1	03TF110_SPHENE12m	99TF6sphB_sph5	99TF6sphB_sph5r
Type	T2	T2	T2	T2
lower/upper	upper	upper	lower	lower
Glass	99TF6A_5	05TF82_A2_31	00TF171W_B_4	00TF171W_B_4
Glass unit	B	D	N	N
E (GPa)	759	519	667	655
RSQ	0.9829	0.9887	0.9847	0.9839
La	24	31	39	40
Ce	58	66	105	106
Pr	111	97	157	157
Nd	162	127	229	225
Sm	210	148	272	265
Tb	147	111	221	220
Dy	130	101	153	155
Ho	84	84	105	105
Y	60	58	94	92
Er	53	58	76	78
Tm	37	43	52	53
Yb	21	34	38	39
Lu	14	20	21	22
Zr	2.2	3.9	3.5	3.4
Nb	20	27	26	31
Ta	103	75	105	125
Hf	4.1	7.3	5.7	5.9
Sr	0.7	7.2		0.3
Ba	0.3	20.2	1.1	0.1
Th	2.5	2.4	2.2	2.3
U	0.8	0.9	0.5	0.6

Appendix I. Titanite-melt calculated partition coefficients

Titanite	00TF88_gm_5sph2	00TF95SPH_2C	00TF95SPH_2M	00TF95SPH_2R_END
Type	**T3**	**T3**	**T3**	**T3**
lower/upper	**lower**	**upper**	**upper**	**upper**
Glass	**03TF110_21**	**03TF110_21**	**03TF110_21**	**03TF110_21**
Glass unit	**H**	**H**	**H**	**H**
E (GPa)	**701**	**643**	**564**	**596**
RSQ	**0.9887**	**0.9802**	**0.9857**	**0.9814**
La	19	22	21	21
Ce	50	49	46	46
Pr	74	74	64	67
Nd	112	110	87	94
Sm	165	157	114	128
Tb	125	124	94	106
Dy	99	101	78	89
Ho	74	80	65	72
Y	44	45	38	42
Er	55	60	51	55
Tm	36	40	35	39
Yb	22	25	23	24
Lu	14	16	15	16
Zr	2.6	3.8	4.0	4.2
Nb	20	26	28	24
Ta	80	111	99	100
Hf	4.6	7.1	7.3	8.3
Sr	0.2	0.6	0.4	0.4
Ba	0.1	0.3	0.3	0.4
Th	2.3	2.5	2.5	2.2
U	0.8	0.7	0.8	0.9

Appendix I. Titanite-melt calculated partition coefficients

Titanite	00TF95SPH_3C_strt	00TF95SPH_3C2	00TF95SPH_3C5	00TF95SPH_3C6_END
Type	**T3**	**T3**	**T3**	**T3**
lower/upper	**upper**	**upper**	**upper**	**upper**
Glass	**03TF110_21**	**03TF110_21**	**03TF110_21**	**03TF110_21**
Glass unit	**H**	**H**	**H**	**H**
E (GPa)	**539**	**534**	**528**	**545**
RSQ	**0.9767**	**0.9790**	**0.9804**	**0.9848**
La	26	25	25	22
Ce	54	51	52	47
Pr	67	65	66	62
Nd	85	83	83	80
Sm	107	102	105	102
Tb	88	84	84	82
Dy	70	70	70	69
Ho	59	57	58	57
Y	35	35	36	35
Er	47	46	48	46
Tm	32	32	34	32
Yb	21	21	22	20
Lu	14	14	14	14
Zr	4.2	4.1	4.3	4.2
Nb	38	37	38	33
Ta	133	124	129	110
Hf	7.2	6.8	7.0	6.9
Sr	2.5	0.5	0.5	0.2
Ba	5.4	1.1	1.1	0.2
Th	3.3	3.2	3.3	2.8
U	1.2	1.1	1.1	1.0

Appendix I. Titanite-melt calculated partition coefficients

Titanite	00TF95SPH_3C7_STRT	00TF95SPH_4C	00TF95SPH_5C	00TF95SPH_7C	01TF127SPH_2R3
Type	T3	T3	T3	T3	T3
lower/upper	upper	upper	upper	upper	upper
Glass	03TF110_21	03TF110_21	03TF110_21	03TF110_21	03TF110_21
Glass unit	H	H	H	H	H
E (GPa)	**535**	**688**	**657**	**652**	**674**
RSQ	**0.9855**	**0.9860**	**0.9835**	**0.9779**	**0.9873**
La	22	25	24	24	27
Ce	46	59	58	54	66
Pr	60	93	86	83	96
Nd	76	135	126	123	146
Sm	95	191	180	175	207
Tb	76	148	143	141	162
Dy	65	116	114	114	128
Ho	52	88	89	90	99
Y	33	51	52	53	55
Er	42	64	68	67	72
Tm	29	42	44	44	48
Yb	20	26	28	27	30
Lu	13	16	18	18	19
Zr	3.9	2.8	3.0	3.7	3.2
Nb	31	25	23	24	28
Ta	100	115	95	116	124
Hf	6.3	5.0	5.3	7.0	5.8
Sr	0.2	2.7	0.3	0.6	2.0
Ba	0.3	2.2	0.8	0.4	2.2
Th	2.8	3.1	3.2	2.6	3.4
U	0.9	0.8	0.9	0.7	0.9

Appendix I. Titanite-melt calculated partition coefficients

Titanite	01TF127SPH_3C	01TF127SPH_4R1	01TF127SPH_5C2	01TF127SPH_6C	01TF127SPH_6R
Type	**T3**	**T3**	**T3**	**T3**	**T3**
lower/upper	**upper**	**upper**	**upper**	**upper**	**upper**
Glass	**03TF110_21**	**03TF110_21**	**03TF110_21**	**03TF110_21**	**03TF110_21**
Glass unit	**H**	**H**	**H**	**H**	**H**
E (GPa)	**691**	**581**	**628**	**617**	**636**
RSQ	**0.9913**	**0.9896**	**0.9869**	**0.9811**	**0.9809**
La	25	21	26	23	26
Ce	66	50	59	52	58
Pr	94	66	85	76	86
Nd	137	88	121	107	126
Sm	199	117	168	146	184
Tb	148	94	132	122	146
Dy	116	76	106	100	117
Ho	89	64	84	80	93
Y	51	37	49	47	53
Er	65	51	64	62	69
Tm	42	34	43	43	47
Yb	26	23	27	25	30
Lu	16	14	17	17	19
Zr	3.0	3.5	3.3	2.9	4.2
Nb	27	25	27	27	31
Ta	128	89	107	104	140
Hf	5.4	6.7	5.7	5.4	8.5
Sr	0.6	0.2	0.2	0.1	3.9
Ba	0.5	0.4	0.2	0.1	5.3
Th	3.2	2.3	3.4	2.5	2.9
U	0.9	0.8	0.9	0.7	0.9

Appendix I. Titanite-melt calculated partition coefficients

Titanite	03TF110_1sph1	03TF110_1sph2	03TF110_2sph2_cor	03TF110_2sph3_rim
Type	T3	T3	T3	T3
lower/upper	upper	upper	upper	upper
Glass	03TF110_21	03TF110_21	03TF110_21	03TF110_21
Glass unit	H	H	H	H
E (GPa)	**569**	**591**	**547**	**635**
RSQ	**0.9897**	**0.9893**	**0.9852**	**0.9949**
La	20	20	20	20
Ce	49	49	48	54
Pr	62	62	57	72
Nd	81	84	72	100
Sm	105	110	90	135
Tb	83	85	73	105
Dy	68	71	60	86
Ho	56	56	50	67
Y	33	33	29	38
Er	45	44	40	51
Tm	31	30	28	34
Yb	21	20	19	22
Lu	13	12	12	14
Zr	3.5	3.7	4.7	3.2
Nb	25	26	28	24
Ta	78	83	95	89
Hf	6.4	6.6	9.1	6.0
Sr	0.1	0.3	0.2	0.5
Ba	0.4	0.3	0.5	0.6
Th	2.1	2.0	1.8	2.1
U	0.9	1.0	0.9	0.9

Appendix I. Titanite-melt calculated partition coefficients

Titanite	03TF110_SPHENE212m	03TF110_SPHENE212m core	03TF126_SPHENE12m
Type	**T3**	**T3**	**T3**
lower/upper	**upper**	**upper**	**upper**
Glass	**03TF110_21**	**03TF110_21**	**03TF110_21**
Glass unit	**H**	**H**	**H**
E (GPa)	**638**	**517**	**616**
RSQ	**0.9884**	**0.9798**	**0.9878**
La	21	20	22
Ce	58	44	53
Pr	80	51	70
Nd	115	67	101
Sm	160	84	137
Tb	117	69	109
Dy	95	59	88
Ho	76	49	70
Y	43	27	39
Er	58	39	54
Tm	39	28	36
Yb	29	22	26
Lu	15	12	14
Zr	2.9	4.1	3.7
Nb	22	28	24
Ta	87	78	103
Hf	5.6	7.1	7.3
Sr	2.4	0.3	0.4
Ba	14.7	0.2	0.5
Th	2.3	2.2	2.4
U	0.8	0.8	0.8

Appendix I. Titanite-melt calculated partition coefficients

Titanite	03TF126_SPHENE12m2	00TF88_gm_4sph	00TF95SPH_2R_STRT	01TF119_sph3_hiZr
Type	T3	T4	T4	T4
lower/upper	upper	lower	upper	lower
Glass	03TF110_21	03TF110_23	03TF110_21	03TF110_23
Glass unit	H	H	H	H
E (GPa)	607	409	420	398
RSQ	0.9914	0.9630	0.9602	0.9602
La	20	27	23	27
Ce	52	42	39	42
Pr	67	61	47	60
Nd	92	65	57	61
Sm	125	81	73	79
Tb	94	75	59	70
Dy	77	63	54	58
Ho	62	55	46	53
Y	37	36	29	34
Er	47	42	39	40
Tm	32	33	28	31
Yb	23	21	20	20
Lu	13	16	12	15
Zr	3.5	7.6	6.1	9.2
Nb	23	39	30	46
Ta	92	104	76	120
Hf	6.5	15.1	10.2	19.1
Sr	0.4	0.3	0.5	0.3
Ba	0.4	0.4	0.2	0.3
Th	1.9	2.2	2.5	2.2
U	0.6	1.2	1.3	1.4

Appendix I.
Titanite-melt calculated partition coefficients

Titanite	01TF119_sph5	01TF127sph_1	01TF127SPH_1C	01TF127SPH_4C	01TF127SPH_4M
Type	T4	T4	T4	T4	T4
lower/upper	lower	upper	upper	upper	upper
Glass	03TF110_23	03TF110_21	03TF110_23	03TF110_23	03TF110_23
Glass unit	H	H	H	H	H
E (GPa)	431	453	419	429	427
RSQ	0.9691	0.9781	0.9748	0.9591	0.9567
La	29	22	28	32	31
Ce	49	40	46	52	50
Pr	69	50	66	76	74
Nd	74	62	71	80	76
Sm	96	78	94	102	97
Tb	84	68	83	88	85
Dy	71	60	71	76	71
Ho	61	52	63	66	63
Y	38	31	39	40	39
Er	47	43	48	50	48
Tm	36	33	37	37	37
Yb	23	22	24	24	22
Lu	17	15	18	18	17
Zr	6.9	5.9	6.2	6.0	6.0
Nb	41	31	38	52	48
Ta	109	85	97	135	127
Hf	12.3	11.2	12.0	10.2	11.1
Sr	0.4	2.8	0.4	1.9	0.3
Ba	0.3	5.7	0.2	3.5	0.4
Th	2.6	2.7	2.4	3.4	3.1
U	1.0	1.3	1.3	2.0	1.5

Appendix I. Titanite-melt calculated partition coefficients

Titanite	01TF51PB_7sph1	99TF6_gm_17sph2b	99TF6_gm_22Csph	99TF6_gm_22Csph2
Type	T4	T4	T4	T4
lower/upper	lower	lower	lower	lower
Glass	03TF110_23	03TF110_23	03TF110_23	03TF110_23
Glass unit	H	H	H	H
E (GPa)	406	414	434	421
RSQ	0.9665	0.9685	0.9646	0.9513
La	23	23	22	25
Ce	39	38	37	40
Pr	55	56	55	56
Nd	56	59	58	57
Sm	70	74	75	72
Tb	58	66	61	63
Dy	51	56	54	55
Ho	44	50	47	47
Y	29	31	32	31
Er	34	38	35	37
Tm	27	29	26	26
Yb	18	19	17	17
Lu	13	14	12	13
Zr	6.7	5.7	5.6	6.2
Nb	35	34	33	38
Ta	87	85	76	94
Hf	14.1	11.1	10.2	11.8
Sr	2.2	0.4	0.1	0.3
Ba	6.6	0.7	0.3	0.8
Th	1.7	1.8	1.8	1.8
U	1.1	0.9	1.0	0.9

Appendix I. Titanite-melt calculated partition coefficients

Titanite	99TF6PB_3sph1	99TF6sphA_sph1c	99TF6sphA_sph1r	99TF6sphA_sph2
Type	**T4**	**T4**	**T4**	**T4**
lower/upper	**lower**	**lower**	**lower**	**lower**
Glass	**03TF110_21**	**03TF110_21**	**03TF110_21**	**03TF110_21**
Glass unit	**H**	**H**	**H**	**H**
E (GPa)	**417**	**421**	**426**	**411**
RSQ	**0.9553**	**0.9544**	**0.9624**	**0.9508**
La	21	22	21	21
Ce	37	37	36	37
Pr	41	44	44	43
Nd	50	53	54	51
Sm	65	65	67	62
Tb	55	57	58	52
Dy	46	48	49	45
Ho	39	42	43	39
Y	26	26	27	24
Er	33	36	36	34
Tm	24	26	27	24
Yb	17	18	18	17
Lu	11	11	12	11
Zr	8.6	7.8	5.9	6.0
Nb	37	35	32	34
Ta	94	98	81	97
Hf	17.3	15.1	10.0	11.1
Sr	3.2	0.4	3.4	1.4
Ba	11.6	0.4	7.7	2.2
Th	2.5	2.3	2.2	2.3
U	1.5	1.2	1.0	0.9

Appendix I. Titanite-melt calculated partition coefficients

Titanite	99TF6sphB_sph10c	99TF6sphB_sph10r	99TF6sphB_sph11	99TF6sphB_sph11c
Type	T4	T4	T4	T4
lower/upper	lower	lower	lower	lower
Glass	03TF110_23	03TF110_23	03TF110_23	03TF110_23
Glass unit	H	H	H	H
E (GPa)	414	421	429	418
RSQ	0.9432	0.9579	0.9632	0.9545
La	26	25	23	25
Ce	39	41	37	39
Pr	57	61	56	55
Nd	58	61	57	58
Sm	74	78	73	74
Tb	64	66	63	63
Dy	54	57	54	54
Ho	48	50	47	48
Y	31	33	30	30
Er	37	39	36	37
Tm	28	30	29	28
Yb	18	19	18	18
Lu	13	14	13	14
Zr	8.6	5.5	6.4	6.7
Nb	42	34	33	38
Ta	120	94	89	104
Hf	18.4	10.9	13.2	14.6
Sr	0.6	2.7	0.2	0.2
Ba	0.5	8.5	0.2	0.2
Th	1.8	1.9	2.0	1.8
U	1.0	1.1	1.2	1.1

Appendix I. Titanite-melt calculated partition coefficients

Titanite	99TF6sphB_sph12	99TF6sphB_sph13	99TF6sphB_sph13b	99TF6sphB_sph14
Type	T4	T4	T4	T4
lower/upper	lower	lower	lower	lower
Glass	03TF110_23	03TF110_23	03TF110_23	03TF110_23
Glass unit	H	H	H	H
E (GPa)	469	435	424	431
RSQ	0.9503	0.9422	0.9647	0.9419
La	27	27	22	24
Ce	41	42	36	35
Pr	62	60	53	53
Nd	62	62	54	54
Sm	81	79	71	69
Tb	69	66	61	61
Dy	59	57	52	53
Ho	53	52	47	47
Y	34	33	30	29
Er	40	38	35	36
Tm	31	29	27	27
Yb	19	18	17	16
Lu	14	13	13	12
Zr	5.4	5.8	6.4	8.5
Nb	36	37	34	36
Ta	91	97	93	98
Hf	9.9	10.5	13.3	19.1
Sr	0.0	2.5	0.8	0.2
Ba	0.1	8.3	0.8	0.3
Th	2.1	2.2	1.7	1.7
U	1.1	1.0	1.0	1.0

Appendix I. Titanite-melt calculated partition coefficients

Titanite	99TF6sphB_sph2	99TF6sphB_sph3	99TF6sphB_sph3b	99TF6sphB_sph4
Type	T4	T4	T4	T4
lower/upper	lower	lower	lower	lower
Glass	03TF110_21	03TF110_21	03TF110_21	03TF110_21
Glass unit	H	H	H	H
E (GPa)	419	425	417	424
RSQ	0.9578	0.9664	0.9488	0.9526
La	21	21	22	20
Ce	36	38	38	36
Pr	43	45	45	43
Nd	52	55	53	51
Sm	63	67	65	61
Tb	55	60	54	52
Dy	47	51	47	45
Ho	41	43	41	40
Y	26	27	26	25
Er	35	37	35	33
Tm	26	27	25	24
Yb	17	18	17	16
Lu	11	12	11	10
Zr	6.7	6.5	7.2	6.4
Nb	32	30	36	31
Ta	86	73	97	81
Hf	12.2	12.2	13.5	11.6
Sr	0.2	0.2	0.2	0.2
Ba	0.2	0.2	0.3	0.2
Th	2.3	2.3	2.4	2.0
U	1.1	1.0	1.4	0.9

Appendix I. Titanite-melt calculated partition coefficients

Titanite	99TF6sphB_sph4b	99TF6sphB_sph6	99TF6sphB_sph6b	99TF6sphB_sph7b
Type	T4	T4	T4	T4
lower/upper	lower	lower	lower	lower
Glass	03TF110_21	03TF110_23	03TF110_21	03TF110_21
Glass unit	H	H	H	H
E (GPa)	415	414	442	423
RSQ	0.9450	0.9420	0.9593	0.9727
La	21	29	22	19
Ce	37	42	40	35
Pr	43	63	47	42
Nd	51	65	58	51
Sm	60	83	72	64
Tb	51	74	60	55
Dy	46	64	51	47
Ho	39	57	45	40
Y	24	37	27	26
Er	33	43	36	34
Tm	24	33	27	25
Yb	16	20	18	17
Lu	11	16	11	11
Zr	7.2	7.3	5.8	6.0
Nb	35	41	36	30
Ta	99	117	96	78
Hf	13.6	14.0	10.3	11.2
Sr	0.2	0.2	0.8	0.3
Ba	0.3	0.2	0.8	0.2
Th	2.6	2.3	2.5	2.2
U	1.3	1.1	1.2	1.3